COMET Phase-I

Technical Design Report

July, 2016

The COMET Collaboration

R. Abramishvili[11], G. Adamov[11], R. Akhmetshin[6,31], V. Anishchik[4], M. Aoki[32], Y. Arimoto[18], I. Bagaturia[11], Y. Ban[3], D. Bauer[14], A. Bondar[6,31], Y. Calas[7], S. Canfer[33], Y. Cardenas[7], S. Chen[28], Y. E. Cheung[28], B. Chiladze[35], D. Clarke[33], M. Danilov[15,26], P. D. Dauncey[14], W. Da Silva[23], C. Densham[33], G. Devidze[35], P. Dornan[14], A. Drutskoy[15,26], V. Duginov[16], L. Epshteyn[6,30,31], P. Evtoukhovich[16], S. Fayer[14], G. Fedotovich[6,31], M. Finger[8], M. Finger Jr[8], Y. Fujii[18], Y. Fukao[18], E. Gillies[14], D. Grigoriev[6,30,31], K. Gritsay[16], E. Hamada[18], R. Han[1], K. Hasegawa[18], I. H. Hasim[32], O. Hayashi[32], Z. A. Ibrahim[24], Y. Igarashi[18], F. Ignatov[6,31], M. Iio[18], M. Ikeno[18], K. Ishibashi[22], S. Ishimoto[18], T. Itahashi[32], S. Ito[32], T. Iwami[32], X. S. Jiang[2], P. Jonsson[14], T. Kachelhoffer[7], V. Kalinnikov[16], F. Kapusta[23], H. Katayama[32], K. Kawagoe[22], N. Kazak[5], V. Kazanin[6,31], B. Khazin[6,31], A. Khvedelidze[16,11], T. K. Ki[18], M. Koike[39], G. A. Kozlov[16], B. Krikler[14], A. Kulikov[16], E. Kulish[16], Y. Kuno[32], Y. Kuriyama[21], Y. Kurochkin[5], A. Kurup[14], B. Lagrange[14,21], M. Lancaster[38], M. J. Lee[12], H. B. Li[2], W. G. Li[2], R. P. Litchfield[14,38], T. Loan[29], D. Lomidze[11], I. Lomidze[11], P. Loveridge[33], G. Macharashvili[35], Y. Makida[18], Y. Mao[3], O. Markin[15], Y. Matsumoto[32], A. Melnik[5], T. Mibe[18], S. Mihara[18], F. Mohamad Idris[24], K. A. Mohamed Kamal Azmi[24], A. Moiseenko[16], Y. Mori[21], M. Moritsu[32], E. Motuk[38], Y. Nakai[22], T. Nakamoto[18], Y. Nakazawa[32], J. Nash[14], J. -Y. Nief[7], M. Nioradze[35], H. Nishiguchi[18], T. Numao[36], J. O'Dell[33], T. Ogitsu[18], K. Oishi[22], K. Okamoto[32], T. Okamura[18], C. Omori[18], T. Ota[34], J. Pasternak[14], C. Plostinar[33], V. Ponariadov[45], A. Popov[6,31], V. Rusinov[15,26], B. Sabirov[16], N. Saito[18], H. Sakamoto[32], P. Sarin[13], K. Sasaki[18], A. Sato[32], J. Sato[34], Y. K. Semertzidis[12,17], N. Shigyo[22], D. Shoukavy[5], M. Slunecka[8], A. Straessner[37], D. Stöckinger[37], M. Sugano[18], Y. Takubo[18], M. Tanaka[18], S. Tanaka[22], C. V. Tao[29], E. Tarkovsky[15,26], Y. Tevzadze[35], T. Thanh[29], N. D. Thong[32], J. Tojo[22], M. Tomasek[10], M. Tomizawa[18], N. H. Tran[32], H. Trang[29], I. Trekov[35], N. M. Truong[32], Z. Tsamalaidze[16,11], N. Tsverava[16,35], T. Uchida[18], Y. Uchida[14,32], K. Ueno[18], E. Velicheva[16], A. Volkov[16], V. Vrba[10], W. A. T. Wan Abdullah[24], M. Warren[38], M. Wing[38], M. L. Wong[32], T. S. Wong[32], C. Wu[2,28], H. Yamaguchi[22], A. Yamamoto[18], T. Yamane[32], Y. Yang[22], W. Yao[2], B. K. Yeo[12], H. Yoshida[32], M. Yoshida[18], Y. Yoshii[18], T. Yoshioka[22], Y. Yuan[2], Yu. Yudin[6,31], J. Zhang[2], Y. Zhang[2], K. Zuber[37]

[1] *North China Electric Power University, Beijing, People's Republic of China*
[2] *Institute of High Energy Physics (IHEP), Beijing, People's Republic of China*
[3] *Peking University, Beijing, People's Republic of China*
[4] *Belarusian State University (BSU), Minsk, Belarus*
[5] *B.I. Stepanov Institute of Physics, National Academy of Sciences of Belarus, Minsk, Belarus*
[6] *Budker Institute of Nuclear Physics (BINP), Novosibirsk, Russia*
[7] *Computing Center of the National Institute of Nuclear Physics and Particle Physics (CC-IN2P3), Villeurbane, France*
[8] *Charles University, Prague, Czech Republic*
[9] *The Cockcroft Institute, Daresbury Laboratory, Warrington, UK*
[10] *Czech Technical University, Prague, Czech Republic*
[11] *Georgian Technical Univesity (GTU), Tbilisi, Georgia*
[12] *Insitute for Basic Science, Daejeon, Korea*
[13] *Indian Institute of Technology, Bombay, India*
[14] *Imperial College London, London, UK*
[15] *Institute for Theoretical and Experimental Physics (ITEP), Russia*

[16] *Joint Institute for Nuclear Research (JINR), Dubna, Russia*
[17] *Korea Advanced Institute of Science and Technology, Daejeon, Korea*
[18] *High Energy Accelerator Research Organization (KEK), Tsukuba, Japan*
[19] *King Abdulaziz University, Saudi Arabia*
[20] *Institute for Chemical Research, Kyoto University, Kyoto, Japan*
[21] *Research Reactor Institute, Kyoto University, Kyoto, Japan*
[22] *Kyushu University, Fukuoka, Japan*
[23] *Laboratory of Nuclear and High Energy Physics (LPNHE), CNRS-IN2P3 and University Pierre and Marie Curie (UPMC), Paris, France*
[24] *National Centre for Particle Physics, Universiti Malaya, Kuala Lumpur, Malaysia*
[25] *School of Physics and Astronomy, The University of Manchester, Manchester, UK*
[26] *Moscow Physical Engineering Institute, National University, Russia*
[27] *Nagoya University, Nagoya, Japan*
[28] *Nanjing University, Nanjing, People's Republic of China*
[29] *College of Natural Science, National Vietnam University, Ho Chi Minh City, Vietnam*
[30] *Novosibirsk State Technical University (NSTU), Novosibirsk, Russia*
[31] *Novosibirsk State University (NSU), Novosibirsk, Russia*
[32] *Osaka University, Osaka, Japan*
[33] *STFC Rutherford Appleton Laboratory (RAL), Didcot, Oxon, UK*
[34] *Saitama University, Saitama, Japan*
[35] *High Energy Physics Institute of I. Javakhishvili Tbilisi State University (HEPI-TSU), Tbilisi, Georgia*
[36] *TRIUMF, Vancouver, British Columbia, Canada*
[37] *Technical University of Dresden, Dresden, Germany*
[38] *University College London (UCL), London, UK*
[39] *Utsunomiya University, Utsunomiya, Japan*

§ deceased.

Table of Contents

Chapter 1

Executive Summary

In this document the technical design of the COMET Phase-I experiment is summarised. The COMET Phase-I experiment is seeking to measure the neutrinoless, coherent transition of a muon to an electron ($\mu-e$ conversion) in the field of an aluminium nucleus, $\mu^- N \rightarrow e^- N$, with a single event sensitivity of 3×10^{-15}. COMET stands for COherent Muon to Electron Transition. The experiment will utilize a dedicated 8 GeV, 3.2 kW proton beam extracted from the J-PARC's Main Ring via a new beamline into the J-PARC Nuclear and Particle Physics Experimental hall (NP Hall). A schematic layout of the COMET Phase-I setup is shown in Figure 1.1. Muons will be produced from the pions produced after collisions of the 8 GeV proton beam with a graphite target. The yield of low momentum muons is enhanced using a pion capture solenoid. Muons are momentum- and charge-selected using a muon transport solenoid before being stopped in an aluminium target at the centre of a cylindrical drift chamber in a 1 T magnetic field. With a total number of protons on target (POT) of 3.2×10^{19}, about 1.5×10^{16} muons in total will be stopped, which is sufficient to reach the design single event sensitivity of COMET Phase-I which, in the absence of a signal, translates to a 90% confidence level branching ratio limit of 7×10^{-15}. This is a factor of about 100 better than the current limit on gold from SINDRUM-II [1]. The primary COMET Phase-I detector for searching for the neutrinoless $\mu-e$ conversion signals is composed of a a cylindrical drift chamber and a set of trigger hodoscope counters, called the CyDet detector. The experimental setup of COMET Phase-I will be augmented with prototypes of the Phase-II straw-tube tracker and the electron calorimeter, called the StrEcal detector. As well as providing valuable experience with the detectors, the StrEcal and CyDet detectors will be used to characterize the beam and measure backgrounds to the signal of the neutrinoless $\mu-e$ conversion to ensure that the Phase-II single event sensitivity of 2.6×10^{-17} can be realised.

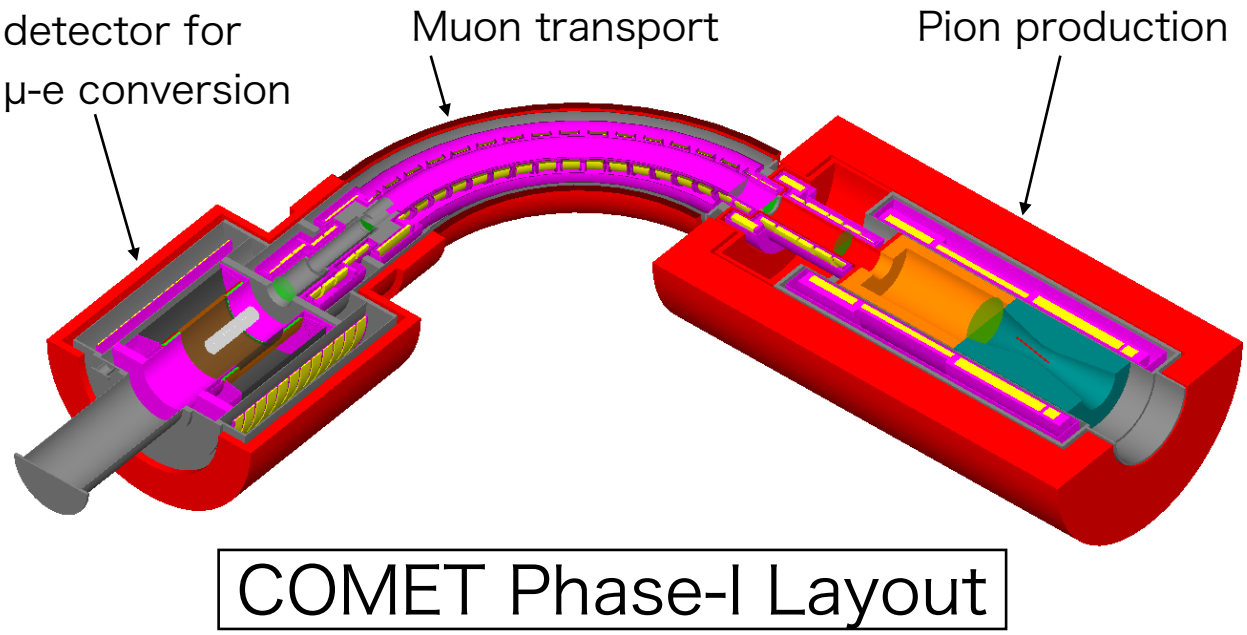

Figure 1.1: *Schematic layout of COMET Phase-I.*

Chapter 2

COMET Overview

2.1. Introduction to COMET Phase-I and Phase-II

The COMET experiment (J-PARC E21) aims to search for the coherent neutrinoless transition of a muon to an electron in a muonic atom ($\mu-e$ conversion),

$$\mu^- + N(A, Z) \rightarrow e^- + N(A, Z), \tag{2.1}$$

at the Japan Proton Accelerator Research Complex (J-PARC) in Tokai, Japan. COMET stands for COherent Muon to Electron Transition. $\mu-e$ conversion is a rare process which violates lepton flavour conservation in the charged lepton sector. Although charge lepton flavor violation is not protected by any symmetry of the Standard Model (SM), it is extremely suppressed because of the neutrino mass spectrum, and provides an excellent channel in which to search for new physics

The signal electron from $\mu-e$ conversion is mono-energetic, and its energy, $E_{\mu e}$, is given by

$$E_{\mu e} = m_\mu - B_\mu - E_{recoil}, \tag{2.2}$$

where m_μ is the muon mass, and B_μ is the binding energy of the $1s$-state muonic atom. E_{recoil} is the nuclear recoil energy. The COMET experiment will use aluminium as a muon stopping material, for which $E_{\mu e}$ is 104.97 MeV. Since the initial and final nuclei are the same, the transition to the ground state in the final nucleus is a **coherent** process, so the transition rate is enhanced, roughly scaling with the number of nucleons in the nucleus.

The COMET experiment is aiming at a single event sensitivity of 2.7×10^{-17}. This ultimate sensitivity goal is a factor of about 10,000 better than the current experimental limit of $B(\mu^- + \mathrm{Au} \rightarrow e^- + \mathrm{Au}) \leq 7 \times 10^{-13}$ from SINDRUM-II at PSI [1]. A schematic layout of the COMET experiment is shown in Figure 2.1. The experiment will be carried out in the Nuclear and Particle Physics Experimental Hall (NP Hall) of J-PARC using a bunched 8-GeV proton beam that is slow-extracted from the J-PARC main ring. Muons will be produced from the pions produced after collisions of the 8 GeV proton beam with a production target. The yield of low momentum muons transported to the experimental area is enhanced using a pion capture superconducting solenoid surrounding the proton target in the pion capture section in Figure 2.1. Muons are momentum- and charge-selected using curved superconducting solenoids in the muon transport section, before being stopped in an aluminium target. The signal electrons from the muon stopping target are detected by instrumentation in the detector section.

The COMET experiment will be carried out using a two-staged approach. Phase-I of the experiment is aiming at a signal sensitivity of 3.1×10^{-15}. This sensitivity is a factor of about

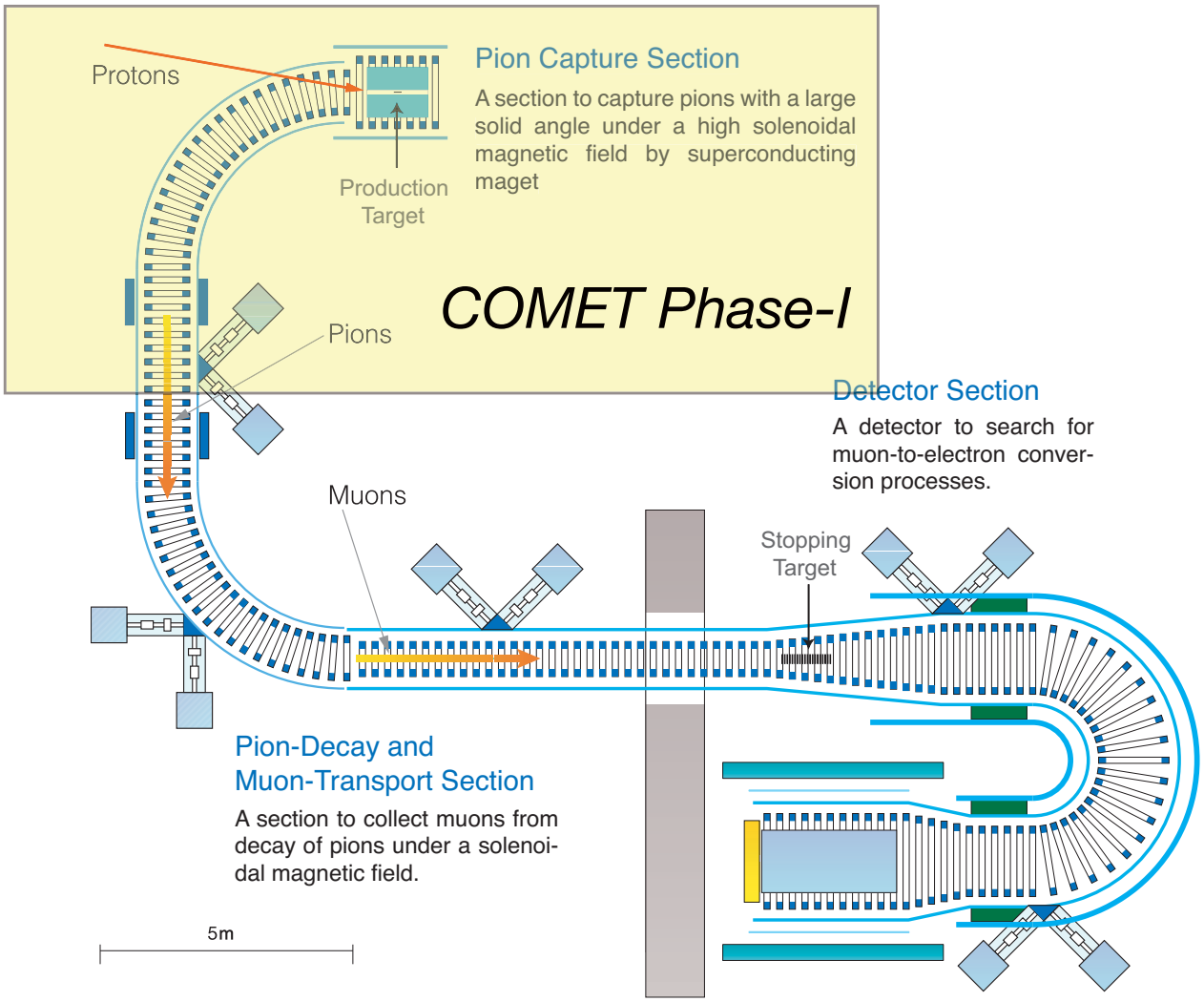

Figure 2.1: *Schematic layout of COMET (Phase-II) and COMET Phase-I (not in scale),*

100 better than the current experimental limit. COMET Phase-I will have the pion capture section, the muon transport section up to the end of the first 90° bend. The detectors will be installed after the end of this 90° bend. An illustration of how COMET Phase-I relates to Phase-II is shown in Figure 2.1. The primary COMET Phase-I detector for searching for the neutrinoless $\mu-e$ conversion signals is composed of a a cylindrical drift chamber and a set of trigger hodoscope counters, called the CyDet detector. The experimental setup of COMET Phase-I will be augmented with prototypes of the Phase-II straw-tube tracker and the electron calorimeter, called the StrEcal detector. As well as providing valuable experience with the detectors, the StrEcal and CyDet detectors will be used to characterize the beam and measure backgrounds to the signal of the neutrinoless $\mu-e$ conversion to ensure that the Phase-II single event sensitivity of 2.6×10^{-17} can be realised.

2.2. COMET Requirements

In order to obtain the desired improvement in sensitivity, the experiment requires an intense muon source, coming from a pulsed proton beam with high inter-bunch extinction factor, as highlighted below.

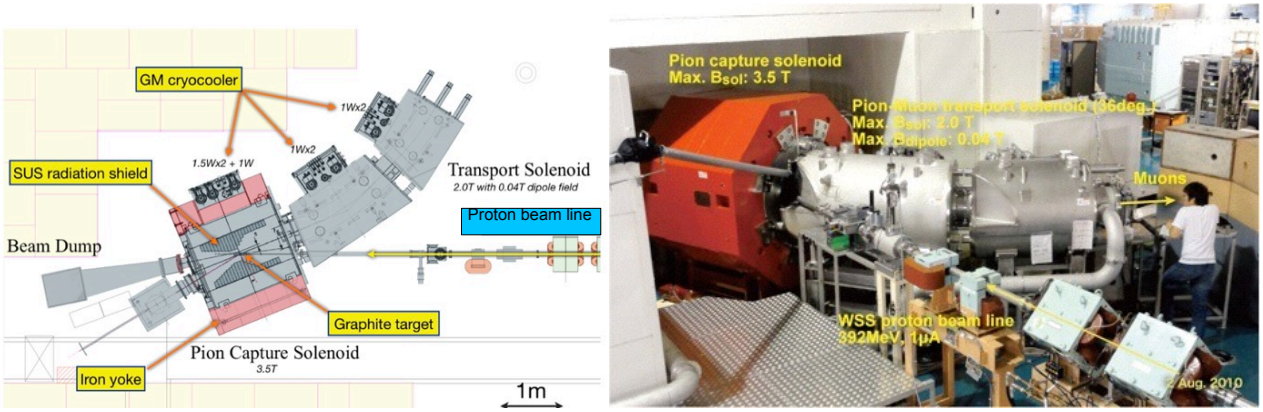

Figure 2.2: *Layout and photo of the MuSIC facility at Osaka University,*

Highly intense muon source The total number of muons needed for the COMET experiment is of the order of 10^{18} to achieve an experimental sensitivity of less than 10^{-16}. Therefore, a highly intense muon beam line has to be constructed. Two methods are adopted in this experiment to increase the muon beam intensity. One is to use a high-power proton beam from J-PARC. The other is to use a system to collect pions—which are the parents of muons—with high efficiency. In the muon collider and neutrino factory R&D, superconducting solenoid magnets, producing a high magnetic field surrounding the proton target, have been proposed and studied for pion capture over a large solid angle. With the pion capture solenoid system, about 8.5×10^{20} protons of 8 GeV will produce the number of muons of the order of 10^{18} for COMET Phase-II. The principle of the pion capture system has been experimentally demonstrated at the MuSIC (Muon Science Innovative beam Channel) facility at Research Center for Nuclear Physics (RCNP), Osaka University. By using a pion capture solenoid of 3.5 T, a factor of 1000 improvement on the muon yield per proton per proton energy has been successfully achieved. The layout and a photo of the MuSIC facility are given in Figure 2.2. The pion capture section in COMET Phase-I and Phase-II will utilise a similar pion capture system with a larger size and a higher magnetic field. Note that that the magnetic field of COMET Phase-I and Phase-II will be 5 T, instead of 3.5 T in MuSIC, because the muon beam emittance is known to be improved in proportional to the square of the magnetic field strength in the pion capture system.

Proton beam pulsing with high proton extinction There are several potential sources of electron background events in the signal energy region around 100 MeV, one of which is prompt beam-related background events. In order to suppress the occurrence of such background events, a pulsed proton beam, where proton leakage between pulses is extremely reduced, is proposed. Since a muon in a muonic atom has lifetime of the order of 1 μsec, a pulsed beam with a shorter beam width compared to this lifetime, and a beam repetition comparable to or longer than a muonic atom lifetime would allow removal of prompt beam background events by performing measurements in a delayed time window. As will be discussed below, there are stringent requirements on the beam extinction during the measurement interval. The beam extinction is defined as the number of leakage protons with respect to the number of protons in a beam pulse. Tuning of the proton beam in the accelerator ring, as well as extra extinction devices (such as kicker magnets) if necessary, need to be utilized to achieve the required level of beam extinction.

Curved solenoids for charge and momentum selection The captured pions decay to muons. The muons thus produced are then transported with high efficiency through the superconducting solenoid magnet system. Beam particles with high momenta would produce electron background events in the energy region of 100 MeV, and therefore must be eliminated with the use of curved solenoids. The curved solenoid causes the centers of the helical motion of the charged particles to drift perpendicularly to the plane in which their paths are curved, and the magnitude of the drift is proportional to their momentum.

A compensating dipole field parallel to the drift direction can be applied. For a given reference muon momentum, this will keep the centres of the helical trajectories on the bending plane. By using this effect and by placing suitable collimators at appropriate locations, beam particles of high momenta and also of positively charges can be eliminated. The combination of solenoid and dipole magnetic fields enables us to transport negatively charged muons without using an opposite-bend curved solenoid which would otherwise be needed to return the desired particles to the solenoid plane, It would make the full length of the curved solenoid useful for momentum- and charge- selections. The COMET arrangement is also unique in the choice of a 180° C-shaped muon transport. Since the muon momentum dispersion is proportional to a total bending angle, the C-shape beamline will produce a larger separation of the muon tracks as a function of momentum, resulting in improved momentum selection. Furthermore, in COMET Phase-II, curved solenoids will be used in a C-shaped electron transport system between the muon stopping target and the electron spectrometer. This allows elimination of charged particles with different momentum and charge from the 100 MeV signal electrons. It also eliminates any direct line-of-sight to the detector system from the muon stopping target, so that the detectors can be shielded from neutral particles such as neutrons and γ-rays, by adding shielding material at proper locations.

This double-C arrangement is adopted only in COMET, and not in Mu2e [2, 3, 4], which is a competing experiment in the U.S.

2.3. Outline of COMET Phase-I

The purpose of COMET Phase-I is two-fold. The first is to make background measurements for COMET Phase-II and the second is a search for $\mu-e$ conversion at an intermediate sensitivity; around a factor of 100 improvement over the current limit.

Background measurements Novel techniques are used to reduce the background events significantly to achieve the COMET Phase-II sensitivity. This necessarily implies that the background level is estimated by extrapolating the existing data over several orders of magnitude. Although there is no reason to expect gross errors in this extrapolation, the resulting uncertainties are inevitably large. To obtain data-driven estimates of backgrounds, and make the detailed design of COMET Phase-II reliable, measurements in the initial Phase-I experiment is desirable. Using a shorter 90° muon transport solenoid in Phase-I, we can investigate the secondary beam in the kinematic region that will be used in Phase-II, whose setup is highlighted in Figure 2.1. We construct a dedicated detector capable of making direct measurements of background sources, which include:

- Direct measurement of the inter-bunch extinction factor.
- Direct measurement of unwanted secondary particles in the beamline such as pions, neutrons, antiprotons, photons and electrons.

- Direct measurement of background processes that have not been measured at the required accuracy, such as muon decays in orbit and radiative muon capture.

One of the main components of this dedicated detector are a straw-tube tracker, and a segmented crystal EM calorimeter (StrEcal detector), both placed at the downstream end of the muon transport beamline. These are the candidate detectors for Phase-II physics measurement, and are described in Chapters 11 and 12. In addition, a cylindrical detector system, which is mentioned below, will be used for the background measurements, in particular backgrounds from muon decay and muon captures. The details of beam measurements and background assessments will be described in Chapters 21 and 22 respectively.

Search for $\mu-e$ conversion Even in this partial configuration, the COMET Phase-I beamline can produce a similar muon yield per 8-GeV proton to Phase-II. Therefore it is also capable to conduct a world-leading measurement of $\mu-e$ conversion and, as such, the experiment will be carried out with a dedicated detector for making these measurements. It will comprise a muon stopping target, and a Cylindrical Drift Chamber and trigger hodoscope counters (CyDet detector) located inside a 1 T solenoid magnet. This cylindrical geometry is necessary, since the curved electron transport solenoid will not be deployed in Phase-I and thus a planar type detector such as the StrEcal detector would suffer from backgrounds caused by beam related particles. The COMET Phase-I aims for an experimental sensitivity of 3×10^{-15} to the branching ratio, which is a factor of about 100 improvement over the current limit. The details of physics sensitivity and background estimations are given in Chapter 20.

Other searches In contrast to COMET Phase-II, the CyDet detector surrounds the muon stopping target directly in Phase-I, and can observe both positive and negative particles from the muon stopping target. This allows for a search for the lepton-number-violating process $\mu^- + N \to e^+ + N'$ ($\mu^- - e^+$ conversion) concurrently with the $\mu^- N \to e^- N$ search. The anticipated experimental sensitivity for $\mu^- - e^+$ conversion could be similar to $\mu^- N \to e^- N$ conversion, although a detailed estimation has not yet been performed. In addition the Cylindrical Drift Chamber will have a relatively large geometrical coverage, and thereby a coincidence measurement with a large solid angle is achievable. This allows a search for $\mu^- + e^- \to e^- + e^-$ conversion in a muonic atom, which is an as-yet unmeasured process. Using a lower intensity beam, $< 10^7$muon/s, a measurement of $\mu^- + e^- \to e^- + e^-$ can be carried out with the CyDet detector.

In summary, COMET Phase-I serves several roles that are highly complementary to the Phase-II experiment. Firstly, and most trivially, it allows for early demonstration and usage experience of many of the components to be used in Phase-II. Secondly, it enables us to directly measure background sources to conduct the optimisation of the Phase-II design, as well as reducing the ultimate systematic uncertainties. Finally it is capable of producing competitive physics results in its own right, both of the $\mu-e$ conversion process that is the primary focus of COMET Phase-II, and other processes that COMET Phase-II cannot investigate.

Chapter 3

Muon to Electron Conversion

3.1. Physics of Charged Lepton Flavour Violation

The discovery of the Higgs boson at the LHC in 2012 provided the missing piece in the Standard Model (SM) to explain electroweak symmetry breaking. However there remain many shortcomings in the SM's description of nature, notably: the lack of a dark-matter candidate; no explanation for the observed matter antimatter asymmetry in the universe; no quantum theory of gravity; and no explanation for smallness of neutrino masses. All these phenomena highlight the need for physics beyond the SM (BSM) and many of these models predict charged lepton flavour violation (CLFV) to occur at a rate that COMET can probe. The search for BSM physics through CLFV complements that being undertaken by ATLAS and CMS and potentially has sensitivity to phenomena beyond the kinematic limit of the direct searches at ATLAS/CMS and thus—like other dedicated flavour experiments—has the potential to see new physics that ATLAS/CMS cannot. In addition, the observation of new phenomena at the LHC may not be sufficient to establish the exact nature of the BSM physics and it will be necessary for other measurements to untangle models with overlapping BSM predictions and CLFV measurements have a particularly crucial role to play in this. Figure 3.1, taken from [5], compares the sensitivities of several flavour observables to a variety of BSM models. In all these models a large effect is predicted for the muon CLFV process. There are however models e.g. universal extra dimensions (UED) where no significant rate of CLFV is predicted. In the case of extra dimension models, the LHC observables are rather similar but the Randall-Sundrum (RS) and UED predictions are very different for CLFV and serve as an example of the important role that CLFV measurements will play in elucidating or constraining BSM physics in the next decade.

The neutrinoless muon to electron conversion process has a sensitivity to BSM physics from both dipole (loop) and non-dipole interactions. This is in contrast to the $\mu \to e\gamma$ process which is only sensitive to dipole interactions. A comparison between the results from MEG and COMET is therefore a powerful model discriminator. In simple BSM dipole interactions [6] the rate of the $\mu \to e\gamma$ process is 389 times that of the neutrinoless muon to conversion process (for an aluminium target). An effective Lagrangian describing both of these contributions was developed in [7] where a parameter, κ, defines the relative strength of the dipole and non-dipole interactions and Λ is the effective scale of new physics in the tree diagram. The current MEG and SINDRUM limits on κ and Λ are shown in Figure 3.2 and highlight the high effective (tree level) energy scales probed. In most BSM models the mass scales probed, *e.g.* when the tree-level BSM operators are loop-suppressed by a factor of $1/16\pi^2$, are typically in the TeV range.

	AC	RVV2	AKM	δLL	FBMSSM	LHT	RS
$D^0 - \bar{D}^0$	★★★	★	★	★	★	★★★	?
ϵ_K	★	★★★	★★★	★	★	★★	★★★
$S_{\psi\phi}$	★★★	★★★	★★★	★	★	★★★	★★★
$S_{\phi K_S}$	★★★	★★	★	★★★	★★★	★	?
$A_{CP}(B \to X_s\gamma)$	★	★	★	★★★	★★★	★	?
$A_{7,8}(B \to K^*\mu^+\mu^-)$	★	★	★	★★★	★★★	★★	?
$A_9(B \to K^*\mu^+\mu^-)$	★	★	★	★	★	★	?
$B \to K^{(*)}\nu\bar{\nu}$	★	★	★	★	★	★	★
$B_s \to \mu^+\mu^-$	★★★	★★★	★★★	★★★	★★★	★	★
$K^+ \to \pi^+\nu\bar{\nu}$	★	★	★	★	★	★★★	★★★
$K_L \to \pi^0\nu\bar{\nu}$	★	★	★	★	★	★★★	★★★
$\mu \to e\gamma$	★★★	★★★	★★★	★★★	★★★	★★★	★★★
$\tau \to \mu\gamma$	★★★	★★★	★	★★★	★★★	★★★	★★★
$\mu + N \to e + N$	★★★	★★★	★★★	★★★	★★★	★★★	★★★
d_n	★★★	★★★	★★★	★★	★★★	★	★★★
d_e	★★★	★★★	★★	★	★★★	★	★★★
$(g-2)_\mu$	★★★	★★★	★★	★★★	★★★	★	?

Figure 3.1: *The size of the observable flavour effect for a variety of BSM SUSY and non-SUSY models. Three (red)stars denote a sizeable effect, two (blue) stars a visible but smaller effect and one (black) star for no significant enhancement above the SM. Abbreviations: AC=Abelian U(1) flavour symmetry model by Agashe and Carone; RVV2= non-Abelian model by Ross, Velasco-Sevilla and Vives; AKM=Antush, King and Malinsky SU(3) flavour symmetry model; FBMSSM= Flavour-blind MSSM; LHT=Littlest Higg with T-Parity; δLL=flavour models with pure CKM-like left handed currents, RS=Randll-Sundrum model with custodial protection. Reproduced from [5].*

The lack of a direct observation of BSM physics at the LHC or a direct detection of dark matter has led to a re-evaluation of many of the BSM models proposed before LHC data taking. In particular the LHC data, should SUSY be realised, suggests high masses for the coloured SUSY particles and there is a tension with the simplest SUSY models in which the coloured and non-coloured particles are generally treated on a similar footing and the measurement of the muon $g-2$. There is no a priori reason why the two sectors should be similar and in [8] it is noted that "*Looking to (SUSY) models with a different connection between the coloured and uncoloured sector, not only seems timely now, but mandatory*". CLFV measurements will thus be vital in establishing the integrity of more nuanced models beyond the simple CMSSM type models proposed before LHC data taking. In this context it is worth noting that the LHC limits on slepton masses are rather weak ($220-290\,\text{GeV}$) in comparison to LHC squark and gluino mass limits and the LHC will not be able to probe all the slepton-neutralino phase space of interest and again CLFV experiments potentially provide the more incisive probe.

Many BSM models seek to rationalise both the fine tuning in electroweak symmetry breaking provided by a single Higgs boson (e.g. through extended Higgs models) and also provide an explanation for the significant CP violation required to explain the matter antimatter asymmetry (e.g. through the seesaw mechanism). As such there tends to be testable relationships between CLFV observables, quark-flavour observables, phenomena in the neutrino sector (e.g. neutrinoless double beta decay) and the masses of new particles in an extended electroweak sector at the LHC. There are many variants of such CLFV models and a more detailed survey

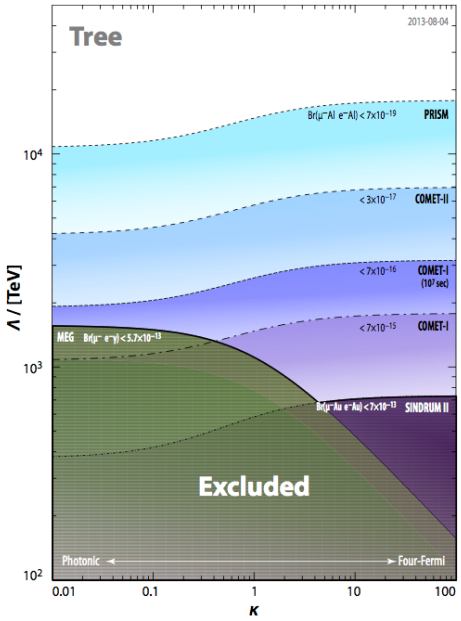

Figure 3.2: *A comparison of the parameter phase explored by COMET Phase-I and subsequent experiments in comparison to the present limits from MEG and SINDRUM. κ represents the relative contribution of dipole and non-dipole operators and Λ is an effective energy scale of the new physics (at tree-level).*

of them and their predictions are given below.

3.1.1 CLFV with Z′

Many BSM models including SUSY, extra dimensions and technicolour predict the existence of a new high mass Z boson, a Z'. The LHC experiments have searched for a Z' and have placed a lower mass limit (at 95% C.L.) of 2.9 TeV. In Figure 3.3a the rate of neutrinoless muon to electron conversion is shown as a function of the Z' mass highlighting, depending on the coupling and off-diagonal lepton mixing angles. It can be seen that the process has a sensitivity beyond that achievable at the LHC. Indeed a comparison of different muon CLFV processes, muon $g-2$ and the LHC provides a powerful constraint on the Z' model parameters.

3.1.2 CLFV with SUSY

In SUSY seesaw models [9], the neutrino mass is generated through the seesaw mechanism which introduces massive right-handed neutrinos (giving leptogenesis), and slepton mixing (giving CLFV) is induced from neutrino mixing. The magnitudes of the Yukawa couplings are model dependent and in several models e.g. SO(10) significant rates of CLFV are expected and the muon to electron conversion process can be enhanced relative to the $\mu \to e\gamma$ process. This is shown in Figure 3.3b which highlights that for large values of $\tan\beta$ and masses of the heavier (SUSY) scalar Higgs below the universal scalar and gaugino masses (at the GUT scale) that suppressions, below the canonical ratio of 389, in the range 1–100 are realised.

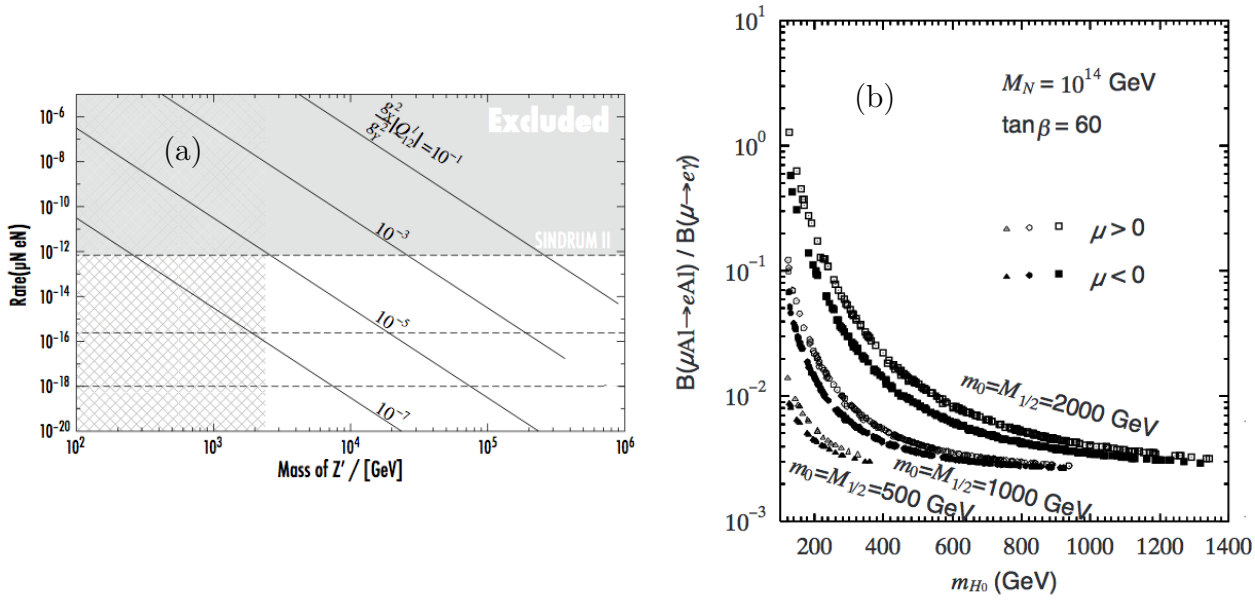

Figure 3.3: *(a): The rate of neutrinoless muon to electron conversion as a function of the Z' mass. The current region excluded by the LHC (below 2.5 TeV) is shown as is the current exclusion provided by the SINDRUM experiment for different assumptions about the Z' coupling and off-diagonal lepton mixing angles. (b): The ratio between the muon to electron conversion process (in Al) and the $\mu \to \gamma$ process in a SUSY seesaw model.*

3.1.3 CLNFV and $\mu^- N \to e^+ N$ conversion

In addition to the standard $\mu^- N \to e^- N$ conversion process, COMET Phase-I, by virtue of its lack of charge selection in the final state, can search for processes violating lepton-number and lepton-flavour (LNFV) simultaneously, *i.e.* $\mu^- + N(A, Z) \to e^+ + N'(A, Z-2)$. The rate of LNFV is typically enhanced in radiative neutrino mass models. A third conversion process that can be probed by COMET Phase-I is the $\mu^- e^- \to e^- e^-$ taking place in the orbit of a muonic atom with a sensitivity of $\mathcal{O}(10^{-15})$.

3.2. What is a $\mu^- N \to e^- N$ conversion ?

One of the most prominent muon CLFV processes is coherent neutrinoless conversion of muons to electrons (μ–e conversion). When a negative muon is stopped by some material, it is trapped by an atom, and a muonic atom is formed. After it cascades down energy levels in the muonic atom, the muon is bound in its $1s$ ground state. The fate of the muon is then to either decay in orbit ($\mu^- \to e^- \nu_\mu \overline{\nu}_e$) or be captured by a nucleus of mass number A and atomic number Z, namely, $\mu^- + N(A, Z) \to \nu_\mu + N(A, Z-1)$. However, in the context of physics beyond the Standard Model, the exotic process of neutrinoless muon capture, such as

$$\mu^- + N(A, Z) \to e^- + N(A, Z), \tag{3.1}$$

is also expected. This process is called μ–e conversion in a muonic atom. This process violates the conservation of lepton flavour numbers, L_e and L_μ, by one unit, but the total lepton number, L, is conserved.

The final state of the nucleus (A, Z) could be either the ground state or one of the excited states. In general, the transition to the ground state, which is called coherent capture, is dominant. The

rate of the coherent capture over non-coherent capture is enhanced by a factor approximately equal to the number of nucleons in the nucleus, since all of the nucleons participate in the process.

The branching ratio of $\mu-e$ conversion is defined as

$$B(\mu^- N \to e^- N) \equiv \frac{\Gamma(\mu^- N \to e^- N)}{\Gamma(\mu^- N \to \text{all})} \tag{3.2}$$

where Γ is the decay width. The time distribution of $\mu-e$ conversion follows the lifetime of a muonic atom, which depends on the type of nucleus. A list of mean lifetimes for typical muonic atoms is given in Table 3.1.

Nucleus	H	C	Al	Fe	Cu	W	Pb
Z	1	6	13	26	29	74	82
Lifetime (nsec)	2195	2027	880	200	164	78	74

Table 3.1: *Lifetimes of various muonic atoms*

Photonic and non-photonic contributions The $\mu-e$ conversion process can have two possible contributions, which are the photonic (dipole) contribution and the non-photonic contribution, which does not contribute to $\mu^+ \to e^+\gamma$ decay. For the former, the photon is internally absorbed by the capturing nucleus. For the latter, CLFV is caused by heavy virtual particles that couple to the quark system. Generically, the $\mu^- N \to e^- N$ interaction can be described by a low energy effective Lagrangian

$$\mathcal{L} = \frac{1}{1+\kappa}\frac{m_\mu}{\Lambda^2}\bar{\mu}_{\mathrm{R}}\sigma^{\mu\nu}e_{\mathrm{L}}F_{\mu\nu} + \frac{\kappa}{1+\kappa}\frac{1}{\Lambda^2}(\bar{\mu}_{\mathrm{L}}\gamma^\mu e_{\mathrm{L}})(\bar{q}_{\mathrm{L}}\gamma_\mu q_{\mathrm{L}}), \tag{3.3}$$

which has two parameters. Λ describes the energy scale of the CLFV physics and κ describes the relative strength of the two terms. The first term describes a dipole modification to the free lepton which allows it to change flavour (emitting a photon to conserve four-momentum). The second term describes a four-fermion contact interaction involving the nucleus. Only the first term contributes to $\mu^+ \to e^+\gamma$, so if κ is small there is a well-defined relationship between the rate of $\mu^+ \to e^+\gamma$ and $\mu^- N \to e^- N$. On the other hand if κ is large the $\mu^+ \to e^+\gamma$ process is suppressed to an arbitrary level below the $\mu^- N \to e^- N$ process. This complementarity between the two processes can be seen in Figure 3.2.

The long-distance photonic contribution in the $\mu-e$ conversion process has some definite relation to that in $\mu^+ \to e^+\gamma$ decay, which is a function of the mass number (A) and the atomic number (Z). It can be parametrized as

$$\frac{B(\mu^+ \to e^+\gamma)}{B(\mu^- N \to e^- N)} = \frac{96\pi^3\alpha}{G_F^2 m_\mu^4}\cdot\frac{1}{3\times 10^{12}B(A,Z)} \sim \frac{428}{B(A,Z)} \tag{3.4}$$

where $B(A,Z)$ represents the rate dependence on the mass number (A) and the atomic number (Z) of the nucleus. The values of $B(A,Z)$ are calculated based on various approximations. Some of them are tabulated in Table 3.2. For instance, by using $B_{CMK}(A,Z)$, the ratios $\mathrm{B}(\mu^+ \to e^+\gamma)/\mathrm{B}(\mu N \to eN)$ of 389 for ^{32}Al, 238 for ^{32}Ti, and 342 for ^{32}Pb are obtained.

The non-photonic CLFV interaction would provide a wide variety of possibilities of new physics models. It is known that $\mu^- N \to e^- N$ conversion is one of the best processes to study the non-photonic CLFV interaction. The short-distance non-photonic CLFV interaction could contain

Models	Al	Ti	Pb	Reference
$B_{WF}(A,Z)$	1.2	2.0	1.6	Weinberg and Feinberg (1959)[10]
$B_S(A,Z)$	1.3	2.2	2.2	Shanker (1979)[11]
$B_{CMK}(A,Z)$	1.1	1.8	1.25	Czarnecki *et al.* (1997) [12]

Table 3.2: *Z dependence of the photonic contribution in the $\mu-e$ conversion estimated by various theoretical models (after Czarnecki* et al.*, (1997)).*

heavy particles in intermediate states either at tree levels or loop levels. One of the examples of the short-distance non-photonic CLFV contribution is SUSY models with R-parity violation. They predict sizeable branching ratios of $\mu-e$ conversion [13, 14]. To calculate the rate of $\mu-e$ conversion, proper treatments from the quark level to the nucleon level, and to the nucleus level have to be made [15].The non-photonic CLFV interaction could be mediated by either (pseudo)scalar, (axial) vector, or tensor types. Another possibility that has been studied is that $\mu-e$ conversion could occur not only though the direct interaction but also through a CLFV meson exchange interaction, mediated by vector mesons or scalar mesons between leptons and nuclear currents [16, 17]. These suggest that the strange quark contribution could be large for the scalar meson exchange [18]. The CLFV neutrino-mediated interaction between leptons and nuclear system has been also discussed [19]. If the non-photonic contribution dominates, $\mu-e$ conversion could be sufficiently large to be observed, even if $\mu^+ \to e^+\gamma$ decay is small. Conversely, if a $\mu^+ \to e^+\gamma$ signal is found, $\mu-e$ conversion signal *should also* exist at an equivalent rate. The possibility of a non-photonic channel means that even if no $\mu \to e\gamma$ signal is seen, there will still be an opportunity to find $\mu-e$ conversion signals.

Rate to the ground state The $\mu-e$ conversion rates to the ground state and all excited states have been calculated by either the shell-model closure approximation [20] or the quasi-particle random-phase-approximation (QRPA) [21]. The fraction of the coherent transition to the ground state is dominant. It was calculated specifically for ^{48}Ti to be (95-99)% in the QRPA approximation, which is even larger than in the shell-model closure approximation. Also the calculation for aluminium of about 90% is available [22]. Since the transition to excited states is small, possible background associated with de-excitation from those excited states can be minimized. It was also found that among the transitions to excited states, the dipole 1^- state is large both in the photonic and non-photonic contributions [21].

Dependence on muon-stopping target material Recently, the rates of coherent $\mu-e$ conversion processes for general effective CLFV interactions (such as dipole, scalar and vector interactions) were calculated for various nuclei [23, 24]. The calculations took relativistic wave functions and the proton and neutron distributions with their ambiguities into account. Their results indicate that the branching ratios for $\mu-e$ conversion increase for light nuclei up to the atomic number of $Z \sim 30$. and high for the region of $Z = 30 - 60$, and decrease for heavy nuclei of $Z > 60$. These calculations also demonstrate that the atomic number dependence of the $\mu-e$ conversion rate would be useful to distinguish different effective CLFV interactions.

Figure 3.4 shows the dependence on muon stopping target of the physics sensitivity of muon to electron conversion in different single-operator dominance models [24]. The conversion rates normalized to the rate in aluminium ($Z = 13$) versus the atomic number Z for the four theoretical models are given : Dipole interaction (blue), Scalar interaction (red), Vector interaction with photons (magenta), Vector interaction with the Z bosons (green). The vertical lines correspond to $Z = 13$ (Al), $Z = 22$ (Ti), and $Z = 83$ (Pb)It can be seen . From Figure 3.4

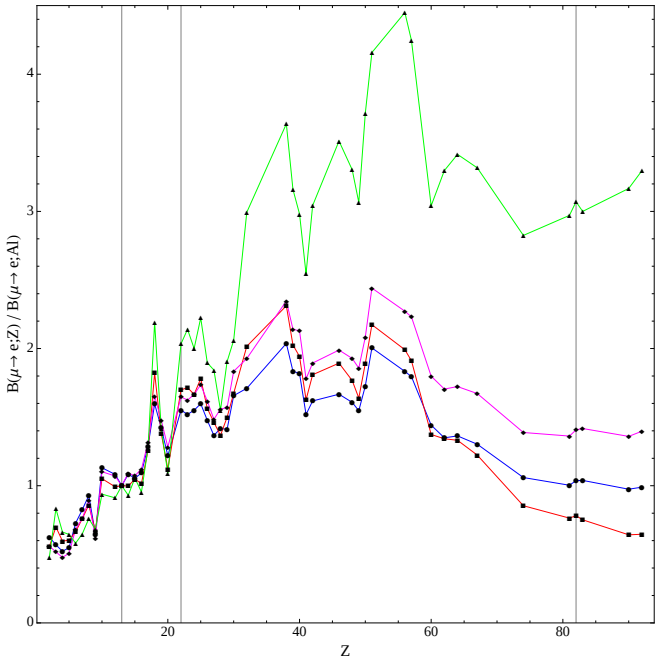

Figure 3.4: *Target dependence of the muon to electron conversion rate in different single-operator dominance models. It is given that the conversion rates normalized to the rate in aluminium ($Z = 13$) versus the atomic number Z for the four theoretical models: Dipole interaction (blue), Scalar interaction (red), Vector interaction with photons (magenta), Vector interaction with the Z bosons (green). The vertical lines correspond to $Z = 13$ (Al), $Z = 22$ (Ti), and $Z = 83$ (Pb).*

the physics sensitivity can be increased by a factor of 2∼4 by using moderately heavier nuclei than aluminium. In practice, the lifetime of the muonic atom (high-Z atoms have shorter lifetimes) should also be considered. A lifetime that is too short means that the acceptance in the COMET delayed detection time window could become smaller. Taking all these effects into account, it is found that aluminium and titanium would give similar figure of merits in sensitivity, as shown in Table 3.3. Other heavy targets are likely to be less sensitive overall, but would be interesting in the event of a discovery.

	Aluminium	Titanium
Expected branching ratio (normalized to Al)	1	1.5
Lifetime (μs)	0.864	0.330
Time acceptance (700 ns to 1170 ns)	0.3	0.2
Figure of merit	1	1

Table 3.3: *Comparison of the figure of merit for sensitivity for aluminium and titanium stopping targets. Figure of merit is scaled by a product of the expected branching ratio (normalized to the case of aluminium) and the acceptance of detection time window.*

3.2.1 Signal and background events

The event signature of coherent $\mu-e$ conversion in a muonic atom is a mono-energetic single electron emitted from the conversion with an energy ($E_{\mu e}$) of

$$E_{\mu e} = m_\mu - B_\mu - E_{recoil} \tag{3.5}$$

where m_μ is the muon mass, and B_μ is the binding energy of the $1s$-state muonic atom. E_{recoil} is the nuclear recoil energy which is small. Since B_μ varies for various nuclei, $E_{\mu e}$ will be different depending on the material in which the muon stops. The nuclear recoil energy is approximately given by $E_{\rm rec} = (m_\mu - B_\mu)^2/(2m_N)$, where m_N is the mass of the recoiling nucleus, and is small. For instance, $E_{\mu e} = 104.97\,\text{MeV}$ for aluminium (Al), $E_{\mu e} = 104.3\,\text{MeV}$ for titanium (Ti) and $E_{\mu e} = 94.9\,\text{MeV}$ for lead (Pb).

From an experimental point of view, $\mu-e$ conversion is a very attractive process. Firstly, the e^- energy of about 105 MeV is far above the end-point energy of the muon decay spectrum ($\sim 52.8\,\text{MeV}$). Secondly, since the event signature is a mono-energetic electron, no coincidence measurement is required. Thus the search for this process has the potential to improve sensitivity by using a high muon rate without suffering from accidental background events, which is a serious problem for searches using $\mu^+ \to e^+\gamma$ decay and other muon CLFV processes, such as $\mu^+ \to e^+e^+e^-$ decay.

There are several potential sources of electron background events in the energy region around 100 MeV, which can be grouped into three categories as follows: The first group is intrinsic physics backgrounds which come from muons stopped in the muon-stopping target; The second is beam-related backgrounds which are caused by beam particles of muons and other contaminated particles in a muon beam; The third includes other backgrounds such as cosmic-ray backgrounds, fake tracking events, and so on.

Intrinsic Physics Backgrounds The intrinsic physics background events are caused by muons stopped in a muon-stopping target. One of the major backgrounds in this category is muon decays in orbit (DIO) in a muonic atom, in which (unlike free muons) the e^- endpoint energy extends to the energy of the $\mu-e$ conversion signal electron, owing to a nuclear recoil effect. The endpoint energy of DIO electrons is the same as the energy of the signal electron. It is important to avoid materials whose DIO end-point energy is higher than $E_{\mu e}$. Figure 3.5 shows the DIO endpoint energy as a function of atomic number for light nuclei. From Figure 3.5, we see that if the muon stopping target is made of aluminium, materials from $Z = 5$ to $Z = 12$, such as carbon and nitrogen, should be avoided around the muon stopping target. However, helium ($Z = 2$) can be used. In fact, as seen later, COMET Phase-I uses helium gas filling the region around the muon stopping target instead of vacuum. Helium can also be used for a Ti stopping target.

Energy distributions for DIO electrons have been calculated [25, 26, 27, 28]. Since the energy distribution of DIO falls steeply as the fifth power of $(E_{\mu e} - E_e)$ toward its endpoint, where $E_{\mu e}$ and E_e are the energy of the signal electron and that of DIO electrons respectively. Experimentally, the way to eliminate such backgrounds is to improve the momentum resolution of e^- detector. For a resolution better than 0.2%, the contribution from DIO occurs at a level of below 10^{-16}.

Another prominent background process is radiative muon capture (RMC), given by

$$\mu^- + N(A, Z) \to \nu_\mu + N(A, Z-1) + \gamma, \tag{3.6}$$

followed by internal and/or external asymmetric e^+e^- conversion of the photon ($\gamma \to e^+e^-$). The kinematic end-point ($E^{end}_{\rm RMC}$) of radiative muon capture is given by

$$E^{end}_{\rm RMC} \sim m_\mu - B_\mu - \Delta_{Z-1} \tag{3.7}$$

where Δ_{Z-1} is the difference in a nuclear binding energy of the final $N(A, Z-1)$ from the initial $N(A, Z)$ nuclei in radiative muon capture. Therefore, a muon-stopping target with a

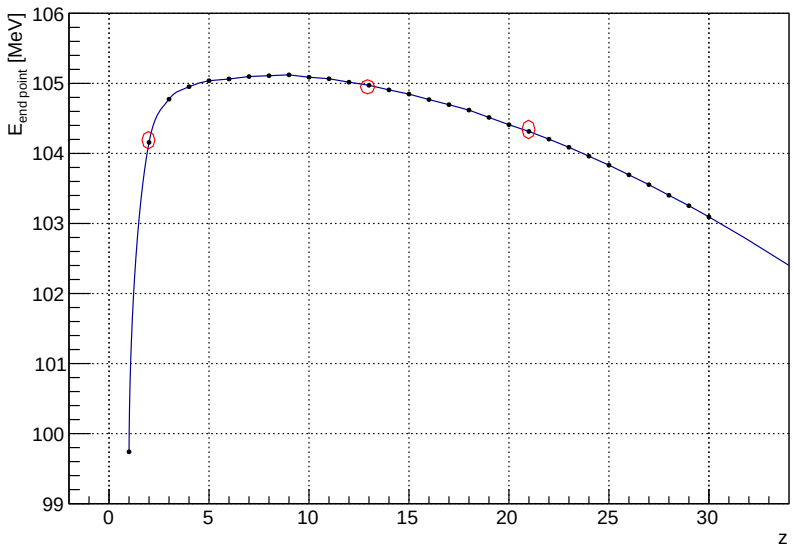

Figure 3.5: *DIO endpoint energy as a function of atomic number. Red circles represent from left to right, He, Al, and Ti as an example.*

large Δ_{Z-1} should be selected to keep a wide background-free region. The other intrinsic physics background events are particle emission (such as protons and neutrons) of after nuclear muon capture.

Beam-related Backgrounds Beam-related background events may originate from muons, pions or electrons in the beam. Muon decays in flight may create electrons in the energy range of 100 MeV if the muon momentum is greater than 75 MeV/c. Pions in the beam may also produce background events by radiative pion capture (RPC) given

$$\pi^- + N(A, Z) \to N(A, Z-1) + \gamma \tag{3.8}$$

followed by internal and external asymmetric e^+e^- conversion of the photon ($\gamma \to e^+e^-$). There are also many electrons arising directly in the secondary beam coming from the production target. To eliminate the backgrounds from pions and electrons, the purity of the beam (after transport) is highly important.

Other Backgrounds The final sources of background events are cosmic rays and tracking errors. To eliminate cosmic ray backgrounds, passive and active shielding with high efficiency is needed.

3.3. Present Experimental Status

The experimental status of searches for $\mu-e$ conversion processes is shown in Table 3.4. The latest search for $\mu-e$ conversion was performed by the SINDRUM II collaboration at PSI, which is described below, along with recent and future experiments in related channels.

Their results showed on $\mathrm{B}(\mu^- + Au \to e^- + Au) < 7 \times 10^{-13}$.

Year	Location	Process	upper limit	Reference
1972	SREL	$\mu^- + \mathrm{Cu} \to e^- + \mathrm{Cu}$	$< 1.6 \times 10^{-8}$	[29]
1982	SIN	$\mu^- + {}^{32}\mathrm{S} \to e^- + {}^{32}\mathrm{S}$	$< 7 \times 10^{-11}$	[30]
1985	TRIUMF	$\mu^- + \mathrm{Ti} \to e^- + \mathrm{Ti}$	$< 1.6 \times 10^{-11}$	[31]
1988	TRIUMF	$\mu^- + \mathrm{Ti} \to e^- + \mathrm{Ti}$	$< 4.6 \times 10^{-12}$	[32]
1988	TRIUMF	$\mu^- + \mathrm{Pb} \to e^- + \mathrm{Pb}$	$< 4.9 \times 10^{-10}$	[32]
1993	PSI	$\mu^- + \mathrm{Ti} \to e^- + \mathrm{Ti}$	$< 4.3 \times 10^{-12}$	[33]
1996	PSI	$\mu^- + \mathrm{Pb} \to e^- + \mathrm{Pb}$	$< 4.6 \times 10^{-11}$	[34]
1998*	PSI	$\mu^- + \mathrm{Ti} \to e^- + \mathrm{Ti}$	$< 6.1 \times 10^{-13}$	[35]
2006	PSI	$\mu^- + \mathrm{Au} \to e^- + \mathrm{Au}$	$< 7 \times 10^{-13}$	[1]

Table 3.4: *Past experiments on $\mu-e$ conversion. (*reported only in conference proceedings.)*

3.3.1 SINDRUM-II

The latest search for $\mu-e$ conversion was performed by the SINDRUM-II collaboration at PSI. Their experimental setup consisted of a set of concentric cylindrical drift chambers inside a superconducting solenoid magnet of 1.2 T. Negative muons were stopped in a muon-stopping target located at the center of the magnet after passing through an energy degrader. Unlike COMET, the beam at PSI provides a continuous source of muons.

Charged particles with transverse momenta above 80 MeV/c and originating from the target were detected in drift chambers. A momentum resolution of about 2.8% (FWHM) was achieved for 100 MeV/c. Figure 3.6 shows their results. The main spectrum, taken using 53 MeV/c negative muons, shows the steeply falling distribution expected from muon DIO. Two events were found at higher momenta, but just outside the region of interest. The agreement between measured and simulated positron distributions from μ^+ decay means that there can be high confidence in the accuracy of the momentum calibration. At present there are no hints concerning the nature of the two high-momentum events: they might have been induced by cosmic rays or RPC, for example. The result provides the current best limit on the conversion branching ratio of $\mathrm{B}(\mu^- + \mathrm{Au} \to e^- + \mathrm{Au}) < 7 \times 10^{-13}$ at 90% C.L. [1].

3.3.2 MECO and Mu2e

MECO was an experimental proposal at BNL [36], aiming to search for $\mu - e$ conversion with a sensitivity of 10^{-16}. The experiment was to use similar techniques for background reduction as COMET, in particular a pulsed beam and a curved transport solenoid. The MECO experiment was cancelled in 2005, due to NSF funding problems. The Mu2e experiment [2, 3, 4] is a proposal to revive MECO at FNAL, using an almost identical muon beam line and detector design to MECO. A schematic experimental layout of the Mu2e experiment is shown in Figure 3.7. The experiment received CD-1 (Approval of experimental approach and cost range) from the US DOE in 2012, CD-3a (long-lead procurement) in 2014 and CD-2/3b (phased construction) in 2015. It is waiting for the CD-3c (critical decision) in 2016. The most recent timeline given for Mu2e indicates commissioning in 2020 and physics run start in 2021. They are expecting to take 3 years of physics running.

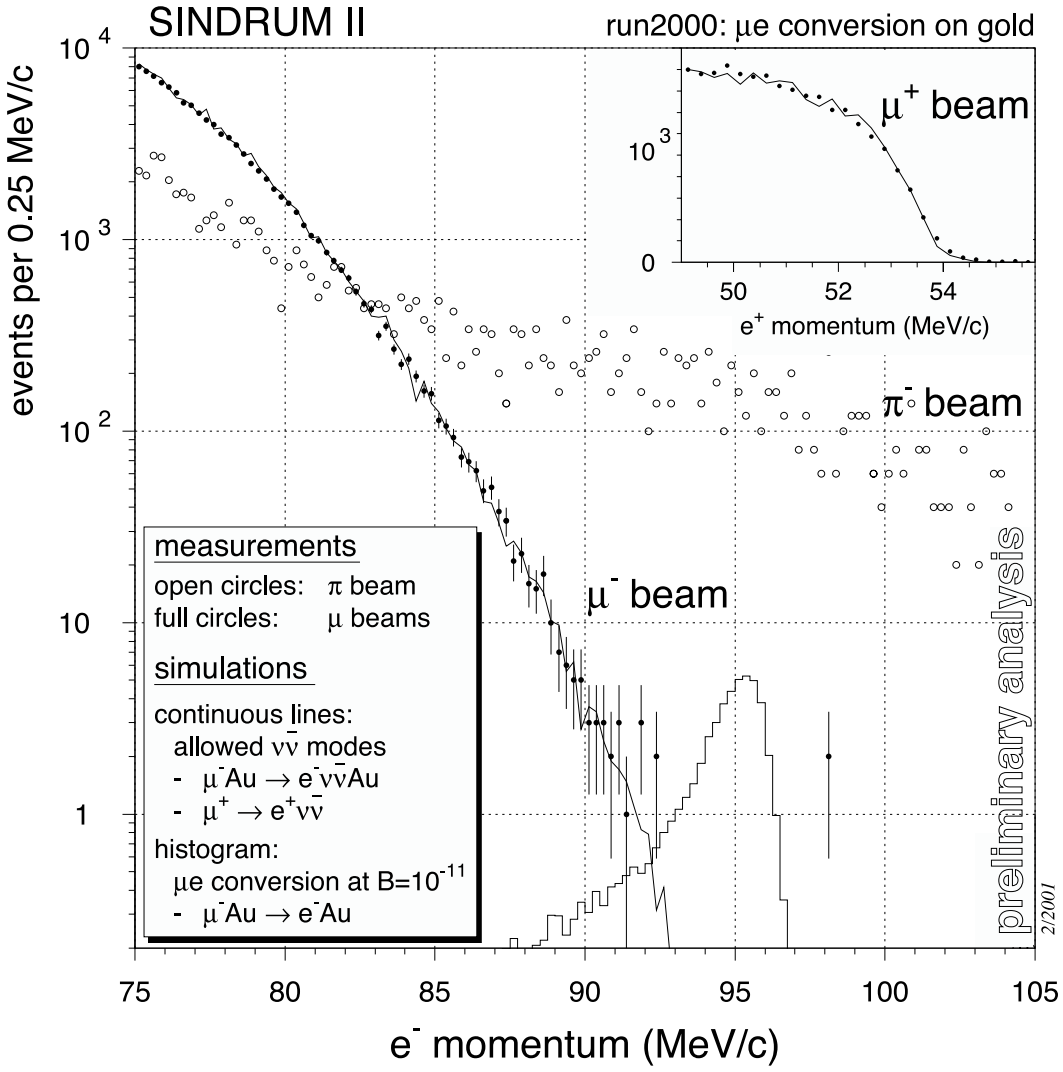

Figure 3.6: *Results from SINDRUM-II. Momentum distributions are shown for three different beam momenta and polarities: 53 MeV/c negative, optimized for μ^- stops (filled circles); 63 MeV/c negative, optimized for π^- stops (open circles); and 48 MeV/c positive, optimized for μ^+ stops (inset).*

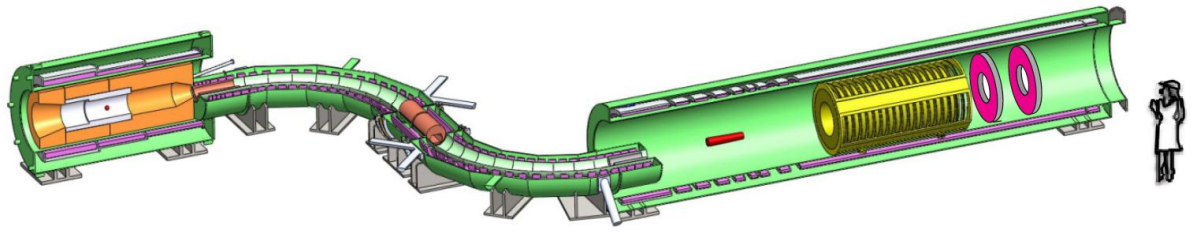

Figure 3.7: *Mu2e Experimental Layout*

3.3.3 $\mu \to e\gamma$ and the MEG experiment

A related experiment that also searches for CLFV is the MEG experiment at PSI. This uses a different final state to COMET and therefore probes CLFV in a different way:

$$\begin{aligned} \text{MEG}: &\qquad \mu^+ \to e^+ + \gamma \\ \text{COMET}: &\qquad \mu^- + N \to e^- + N \end{aligned}$$

The effective Lagrangian for $\mu - e$ conversion is given in Eq.(3.3), using the Λ, κ parametisation. As discussed earlier, while an observation of $\mu^- N \to e^- N$ would on its own demonstrate the existence of BSM physics, it can also be rapidly combined with a measurement of $\mu^+ \to e^+\gamma$ to discriminate between different new physics models. The potential benefits of this synergy are maximised if the sensitivities the two measurements are similar.

The MEG experiment [37], based at PSI, provides the current best limit [38] on $\mu^+ \to e^+\gamma$. Low-momentum muons are stopped on a thin target inside a magnetic spectrometer. The searched-for two-body decay produces one photon and one positron back-to-back, where both particles have energy $\frac{1}{2}m_\mu$. This simple topology is the basis for the detection strategy. Liquid Xenon is used as a large-volume scintillation detector for the photon, while drift chambers are used to detect positrons. The detectors are arranged so that if a signal photon is detected in the LXe detector, the recoiling positron will also be observed in the drift chambers. Backgrounds are primarily from standard model decays of the muon in accidental coincidence with a gamma ray.

The latest published result from MEG is a limit: $\text{Br}(\mu^+ \to e^+ + \gamma) < 5.7 \times 10^{-13}$ at 90% C.L.[1] As seen in Figure 3.2 this matches the sensitivity of COMET Phase-I rather well. Thus COMET Phase-I provides a comparable-sensitivity check of BSM models that have $\kappa \ll 1$, and for models where $\kappa \gtrsim 1$ it has better sensitivity. In the event that either MEG II (the upgraded version of MEG aims to achieve 10 times better sensitivity) or COMET Phase-I see a positive signal the combination of the two has a good chance to discriminate between BSM models.

[1] The final analysis of the upper limit was presented in La Thuile in March 2016, $4.2x10^{-13}$ at 90% C.L.

Chapter 4

Proton Accelerators

4.1. Requirements

The proton beam requirements for COMET Phase-I and Phase-II differ only in their power requirements. They both require a pulsed, 8 GeV proton beam, slow-extracted from the J-PARC main ring (MR) into the J-PARC Nuclear and Experimental Hall (NP-Hall). The choice of beam energy is dictated by two requirements: to minimise the production of antiprotons, the production rate of which increases rapidly for proton energies above 10 GeV; and to maximise the extinction of stray protons between proton bunches which can produce backgrounds during the live periods of the detectors. Beams of lower energies are easier to deflect and so are preferable for the extinction system, but have a higher emittance. The optimal beam energy is determined to be 8 GeV. The beam power for Phase-II is 56 kW and the beam power assumed for the Phase-I physics sensitivity estimates is 3.2 kW (i.e. 0.4 μA) running in pulsed mode with 1.17 μs between proton bunches of 100 ns duration. A beam emittance, in the RCS, of 10 π mm mrad is required and an inter-bunch proton extinction factor of at least 10^{-9}. However since the proton target and capture solenoid will be designed with the Phase-II beam power requirements in mind it would be possible, and desirable, to have beam powers in excess of 3.2 kW, e.g., by increasing the repetition cycle of the accelerator such that the detector hit rate is not affected.

A 1.17 μs pulsed beam structure is achieved by filling only four out of the nine MR buckets for MR operation at a harmonic number of nine. Also, a 1.75 μs pulsed beam structure is possible by filling only three out of the nine MR buckets. In this case the three filled buckets are distributed around the ring in such a way that two empty buckets exist between filled buckets[1]. The four filled buckets are distributed around the ring in such a way that an empty bucket exists between the filled buckets. A schematic showing the four bucket structure is presented in Figure 4.1.

4.2. LINAC and RCS operation

The LINAC requirements for COMET are almost the same as in normal operation. A chopper with a very fast rise time (10 ns) is required to ensure the RCS can be filled with high efficiency and with the appropriate gaps between bunches. Any inefficiencies in the chopper will manifest itself as stray protons between the bunches and this needs to be minimised in order not to

[1]The 1.75 μs pulsed beam structure would be better in terms of reduction of beam-related backgrounds for the COMET Phase-I cylindrical drift chamber (CDC), although the number of proton bunches is smaller.

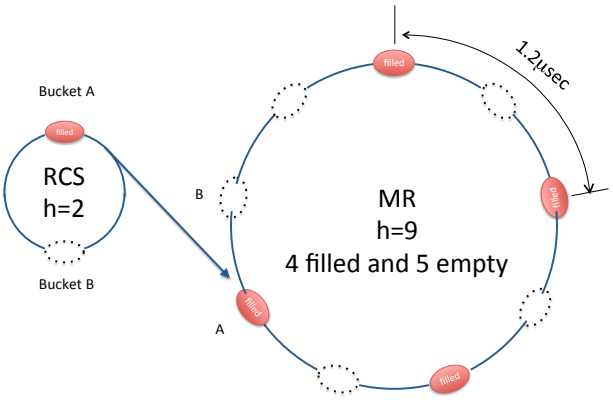

Figure 4.1: *The COMET bunch structure in the RCS and MR where four buckets are filled producing 100 ns proton bunches separated by at least 1.17 μs.*

place unachievable demands on the extinction system. Innovative methods have been proposed to remove the stray protons at the stage of injection between the RCS and MR and these will be studied extensively as part of the accelerator development programme for COMET. The RCS will accept 400 MeV protons from the LINAC and accelerate them to 3 GeV. Four sets of acceleration are performed in the RCS with two bunches (harmonic number two) for each MR acceleration cycle.

4.3. Main Ring Operation

Beam injection from the RCS into the MR using kicker magnets is a critical aspect for COMET and, due to the inter-bunch extinction requirements, will proceed differently from standard operations. Two injection methods are presently being pursued: "Double Injection Kicking" and "Single Bunch Kicking". In Double Injection Kicking, the standard kick administered when the beam reaches the end of the transfer line is augmented by a second kick (delayed by half a phase) after the two bunches have made one turn in the MR. A preliminary test of this was performed in 2010 and was found to improve the inter-bunch extinction significantly. The Single Bunch Kicking is a simpler method and is realised by shifting the injection kicker excitation timing by 600 ns such that particles remaining in empty buckets are not injected into the MR (Figure 4.2). A preliminary test in 2012 also showed this to be effective at improving the extinction significantly and the extinction level could be maintained through acceleration and extraction if the RF acceleration voltage was raised above its nominal value.

4.4. Beam emittance and collimation

In normal operation the beam emittance is limited to be less than $54\,\pi$ mm mrad in the MR by collimators in the injection line between the RCS and MR. The acceptance of the slow extraction line between the MR and NP Hall is limited to $25\,\pi$ mm mrad which can be achieved for the 30 GeV beams under normal operation. However, adiabatic damping is reduced at the lower COMET beam energy so an additional collimation system will need to be developed so that

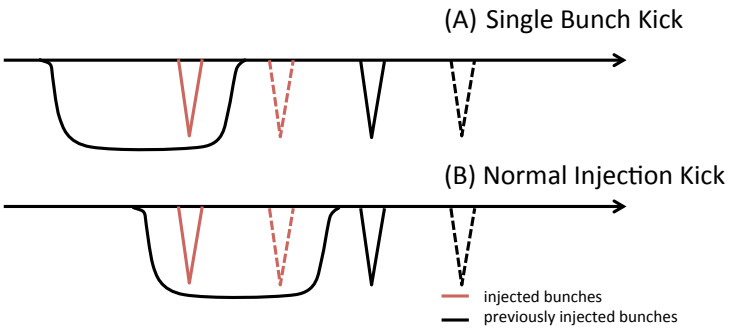

Figure 4.2: *Kicker magnets excitation timing for the single bunch kicking (A) as compared to the normal injection kicking shown in (B).*

the slow extracted 8 GeV beam can be accommodated within the $25\,\pi$ mm mrad acceptance. This system will build on work being pursued by the J-PARC MR accelerator group who are developing a"dynamic collimator" system to control emittance growth during acceleration. This system, shown in Figure 4.3, comprises: a thin target, two catcher magnets, injection bump magnets and steering magnets. Simulation studies have shown that an emittance of $20.9\,\pi$ mm mrad for 56 kW operation can be achieved at 9 GeV, increasing slightly at 8 GeV but still within the acceptance of the slow extraction line.

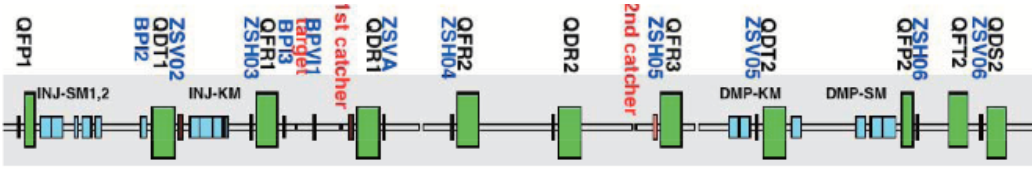

Figure 4.3: *Layout of the dynamic collimator system.*

4.5. Slow Extraction

Slow extraction for COMET will be similar to that of the 30 GeV beam into the NP Hall but needs to be modified such that the pulse structure can be maintained during extraction and for operation at the lower (8 GeV) energy. The most obvious change for this "bunched slow extraction", in contrast to the normal slow extraction, is that the RF voltages need to be maintained and not turned off during extraction. However at low RF voltages (< 100 kV) it is found that particles start to be scattered into the gaps between the bunches and the extinction is no longer below 10^{-9}. The extinction is improved by two orders of magnitude for RF voltages of 250 kV. It will be necessary to optimise the impact of the heat load (at high voltages) on the RF modules against the reduced extinction efficiency (at low voltages). Simulations have also shown that it is possible to achieve pulse widths below the required 100 ns by modifying the feedback time constant of the slow extraction (Figure 4.4).

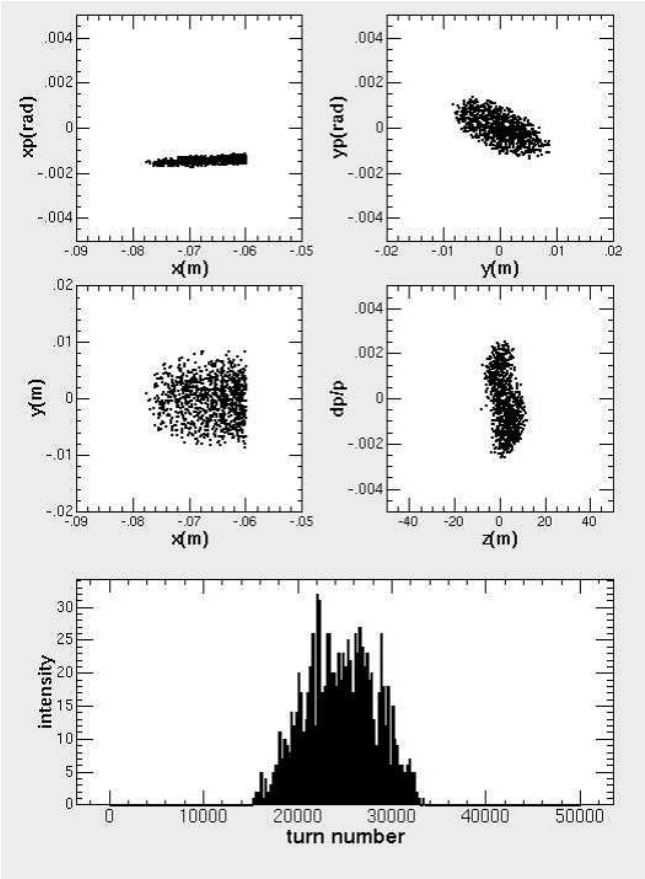

Figure 4.4: *Simulations of the phase space distributions of the beam extracted from the MR.*

4.6. Acceleration Test

A series of proton beam acceleration tests was conducted in May 2014. Every second acceleration bucket of the MR were filled with 3 GeV protons from the RCS and accelerated to 8 GeV before extraction to the abort line. Protons corresponding to 3.2 kW at 8 GeV operation were accelerated to measure various beam parameters; the accelerator configuration was then optimised for the COMET beam operation to minimise beam loss. It was also important in this test to find a possible solution to run the COMET experiment under the conditions presented by high-power operations at the MLF of above 300 kW.

Figure 4.5 shows the acceleration pattern in the MR adopted in this test. The total time necessary for one acceleration cycle was 2.48 s including injection, ramping-up, extraction and ramping-down periods.

As already described, the proton beam in COMET mode is accelerated up to only 8 GeV before extraction, which results in poorer adiabatic damping than that at 30 GeV. This would result in beam losses during the beam extraction to the NP hall, where the beam emittance aperture is limited to 25 π mm mrad, although the beam intensity is smaller in Phase-I and thus the effect will be smaller than in Phase-II. A dedicated injection method for protons to the RCS has been developed for COMET Phase-I beam operation, with beam painting during beam injection from the Linac to the RCS being optimised to minimise the beam emittance at 8 GeV. Figure 4.6 shows the horizontal and vertical beam profiles at 8 GeV, measured at 30 ms before the end of the extraction period using the flying wire method. Horizontal and vertical emittances evaluated from these data are found to be adequately small (5.6 π mm mrad

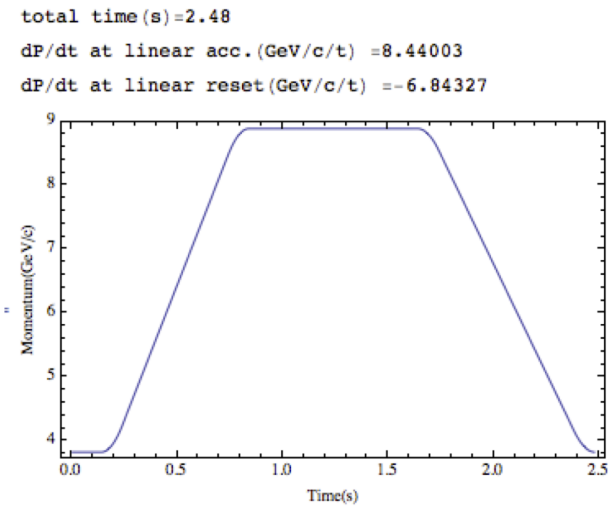

Figure 4.5: *Beam acceleration pattern for COMET 8GeV test*

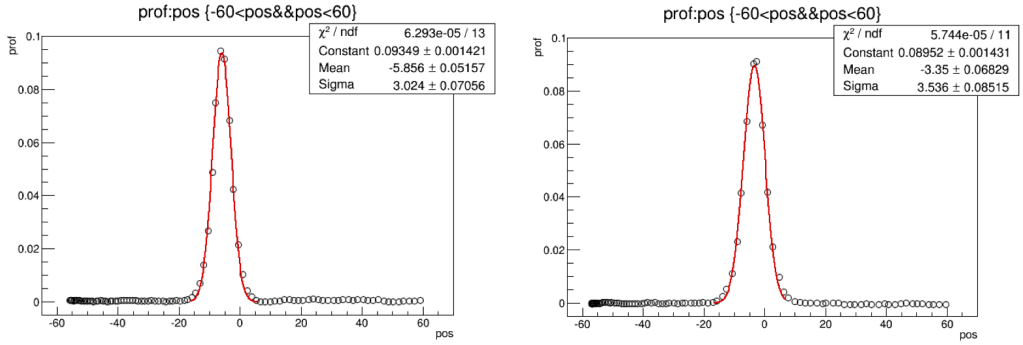

Figure 4.6: *Measured horizontal (left) and vertical (right) beam profiles for 8 GeV-3.2 kW beam at 30 ms before the end of extraction period.*

and 6.1 π mm mrad respectively) for a beam at Phase-I intensities to be extracted to the NP hall. For Phase-II beam intensities we will need to adopt an additional method, such as the dynamic collimator described above, to accommodate the emittance requirement.

Systematic studies of the proton beam extinction factor were also carried out with the extinction monitor installed in the MR abort line. The monitor is composed of a plastic scintillator viewed by four photomultipliers with different light attenuators to cover a large dynamic range of scintillation light, while remaining sensitive to single protons. The whole set-up is mounted on a movable stage which locates the monitor in the beam line when the measurement is conducted. In normal slow extraction of protons from the MR, the RF cavity voltage is usually switched off in order to give a flat time structure to the proton beam. In contrast, for the COMET beam acceleration, the RF voltage needs to be kept at a non-zero value in order to maintain the pulse structure during extraction. Figure 4.7 shows the extinction measurements at the MR abort line as a function of the voltage applied to the RF cavities before extraction. The measurement was performed by filling only one bucket with an equivalent amount of protons to that of 3.2 kW operation. The other buckets were empty and Single Injection Kicking was employed to remove any remaining particles in neighbouring buckets. We observe that accelerated particles start to be scattered along the ring when the RF voltage was reduced, and that the extinction can be reduced to as low as 10^{-12} by applying an RF voltage of 255kV, which is sufficiently small

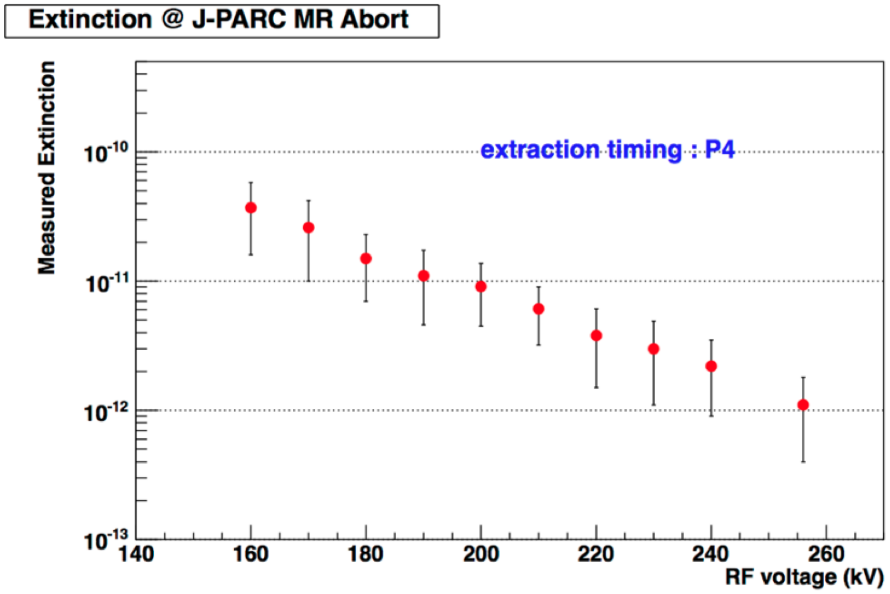

Figure 4.7: *Extinction levels measured at the MR abort line with single bucket filling with the number of protons equivalent to that of 3.2 kW operation, as a function of the applied RF voltage during beam circulation after acceleration.*

for the COMET experiment. We will optimise the voltage for long-term operations in order to keep the RF cavity temperatures stable to within the capabilities of the water cooling system.

Another study was performed to understand how protons leak from a bucket during the beam circulation (flat-top) period. The extinction was measured at the abort line at different timings by adjusting the time at which the protons are kicked out from the MR. Figure 4.8 shows the extinction measured when applying 160 kV RF voltage as a function of the time of kicking between the beginning and end of the flat-top period. A time-dependence in proton leakage can be seen. Further studies will continue in collaboration with the J-PARC accelerator group to understand the mechanism behind this effect and to ensure delivery of the beam quality necessary for the COMET experiment.

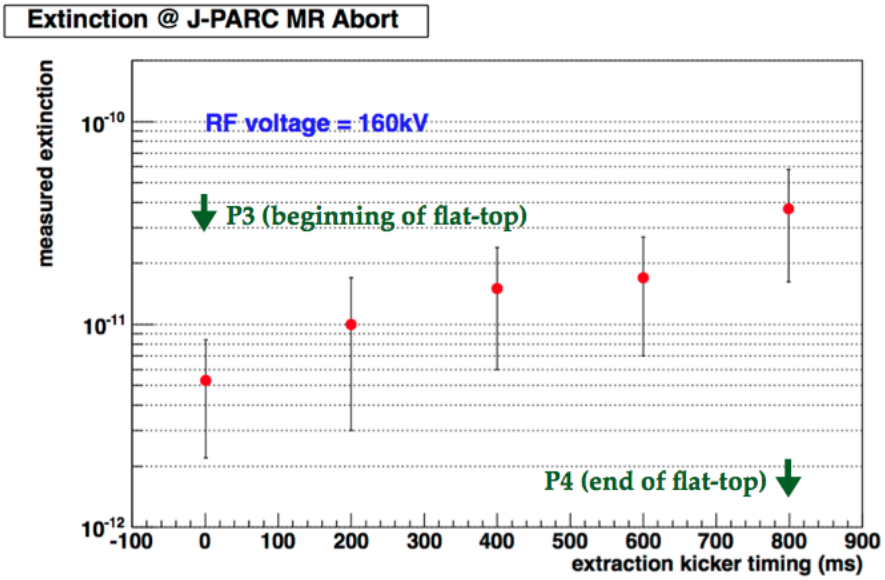

Figure 4.8: *Extinction levels measured at the MR abort line with single bucket filling with the number of protons equivalent to that of 3.2 kW operation, as a function of time between the beginning and end of the flat-top period.*

Chapter 5

Proton Beamline

The COMET experiment will be built in the NP Hall, commonly called the 'Hadron Hall'. In addition to the existing beam line (A-line) from the MR, a new beam line is being built (B-line). The B-line will serve both high-momentum (up to 30 GeV) experiments and COMET (8 GeV) and will have two branches: one from the A-line, and a second between COMET and the high-momentum experiments. During the standard high-momentum running the A-line and B-line share the beam in the ratio of 10,000:1. In the low-momentum running for COMET the entire beam is sent to the B-line. The schematic of the beam lines are shown in Figure 5.1. It is noted that the proton beamline is common for COMET Phase-I and Phase-II.

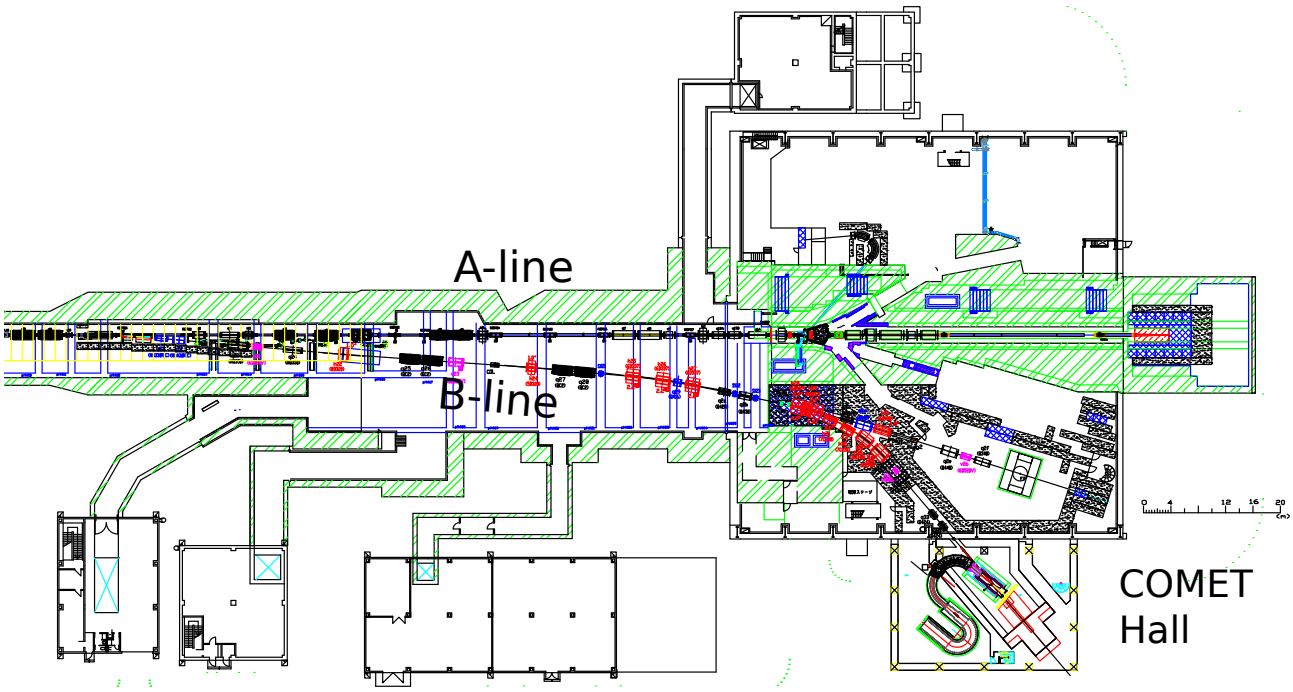

Figure 5.1: *The A and B-lines from the MR into the NP Hall. A schematic of the COMET experiment is shown in the bottom right.*

5.1. Branch between A- and B-line

To realize multiple operation modes, a Lambertson magnet followed by two septum magnets will be deployed to provide the A/B-line branches. Figure 5.2 shows the cross section of the

Lambertson magnet for the new beam line. The beam for the A-line passes through the lower hole that is free from any magnetic field. The upper hole is filled with a dipole field and is used for the new B-line. During COMET operation, the entire beam passes through the upper hole. In contrast, during the operation of the high-momentum beam experiments, only a small fraction of the beam is sent through the upper hole. A magnetic field of 0.35 T will introduce a

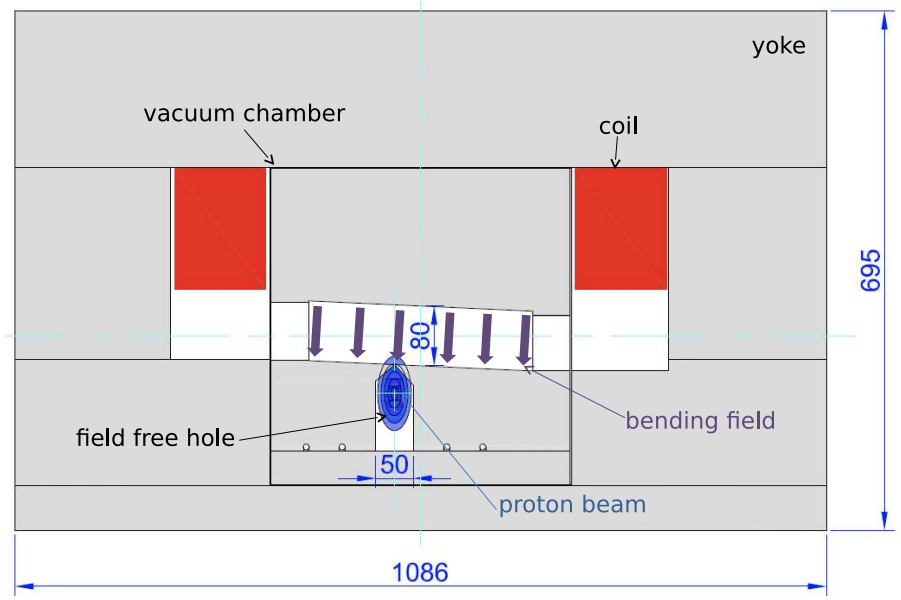

Figure 5.2: *A schematic of the new Lambertson magnet for the B-line.*

bend of 2.48° and is applied with 470 A in the coils (at 26 V) during COMET operation. The field uniformity in the dipole field region has been simulated and non-uniformities in the field are expected to be smaller than 0.1% in the region of ±36 mm from the beam axis.

Between the two different modes of operation of the Lambertson magnet (COMET and high-momentum beam experiments) the beam must shift vertically by about 76 mm. The shift is realized by two vertical bending magnets placed upstream. Figure 5.3 shows the vertical deviation of the beam centre from the nominal position obtained by a TURTLE simulation. A shift of 54 mm can be achieved at the position of the Lambertson magnet by applying a vertical kick of 5 mrad at the bending magnet located 14 m upstream of the Lambertson magnet. Meanwhile, a shift of 30 mm is possible for the 30 GeV beam operation for the existing A-line experiments. Therefore, a shift of 84 mm in total is achievable by tuning the currents of the vertical bending magnets, which is larger than the required 76-mm shift. A 3.0° tilt of the Lambertson dipole field is used to return the beam trajectory to the centre. In addition, two downstream vertical bending magnets after the septum magnets will be used for fine beam tuning.

The layout of the Lambertson and septum magnets is presented in Figure 5.4. The first septum magnet (SM1) is only excited when a 30 GeV proton beam is provided to the high-momentum beam line and so provides no bending during COMET beam operation. The second septum magnet (SM2) is used to provide 2.51° bending of the COMET beam. An important consideration in the development of the septum magnets is the clearance between the beam and beam pipe. To provide the dipole field at the septum magnets, a finite space for the magnet coil is needed between the A and B-lines. The septum magnets must be designed to make the thickness of the coil and the separation between A- and B-lines as small as possible. The coil thickness is determined to be 44.5 mm for the upstream septum magnet and 97 mm for the downstream one. This results in a minimum clearance of 36.6 mm between the beam centre

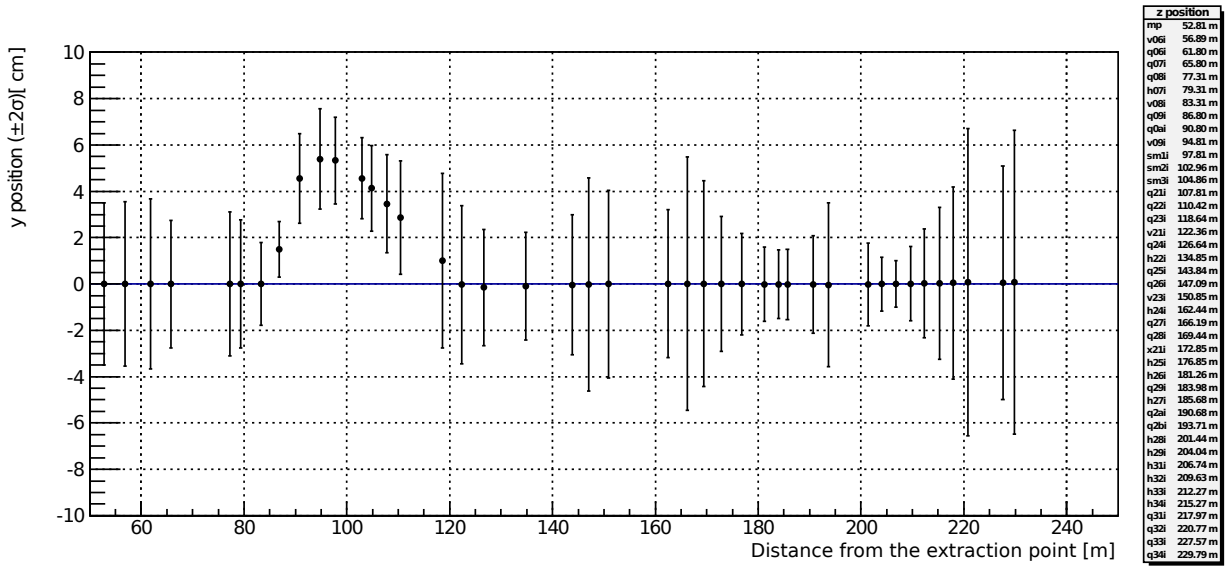

Figure 5.3: *Vertical deviation of the proton beam from the beam line centre as a function of distance from the extraction point. Bars indicate beam size in 2σ. The Lambertson magnet is 97.8 m after the extraction point.*

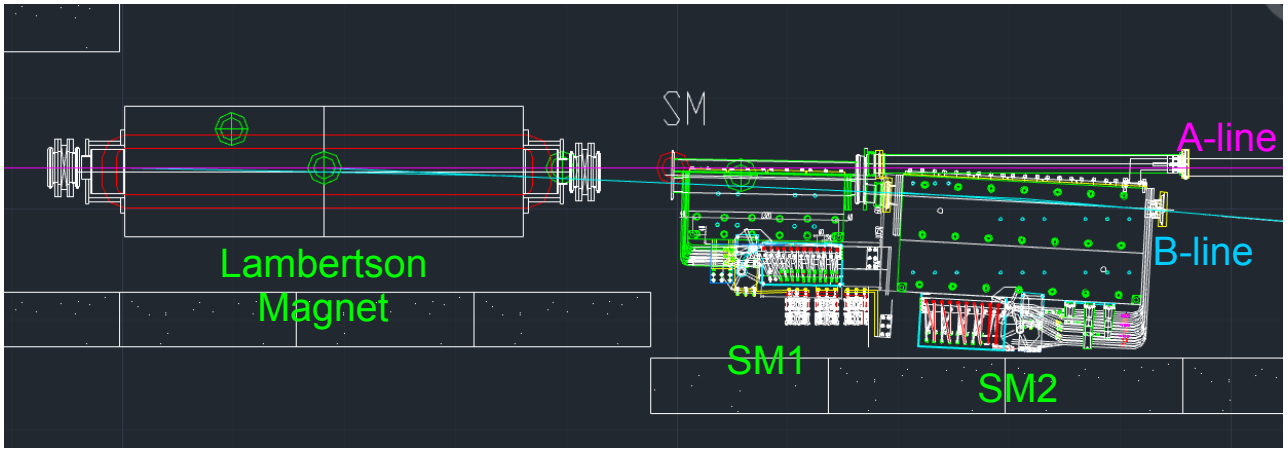

Figure 5.4: *Layout of the Lambertson and septum magnets near the branching point of the B-line from the A-line.*

and beam pipe at the exit of the upstream septum magnet, where the horizontal beam size is 7.4 mm (1σ) in the current beam optics.

5.2. Branch between COMET and High-momentum Beamline

The branch between the COMET and the high-momentum beam lines is realized by two dipole magnets. They bend the beam by 4.4° during the operation of the high-momentum beam experiments, increased to 11.6° during COMET operation. They are followed by four dipole magnets for the COMET beam line, which bend the beam by 26.4° in total. The angle between the primary proton beam line and the beam line into the COMET building is finally 49.6° . The layout of these six magnets are shown in Figure 5.1

5.3. Proton Beam Dump

The proton beam dump was designed to fulfill radiation safety requirements and this was evaluated using a PHITS[39] simulation as shown in Figure 5.5. The resulting size of the required iron dump is 4 m wide and 5 m deep as illustrated in Figure 5.6: Its height extends from 1.5 m below the beam level to 3.1 m above it. The iron dump will be surrounded by concrete shielding. A schematic view of the proton beam dump cross section for Phase-I is shown in Figure 5.6.

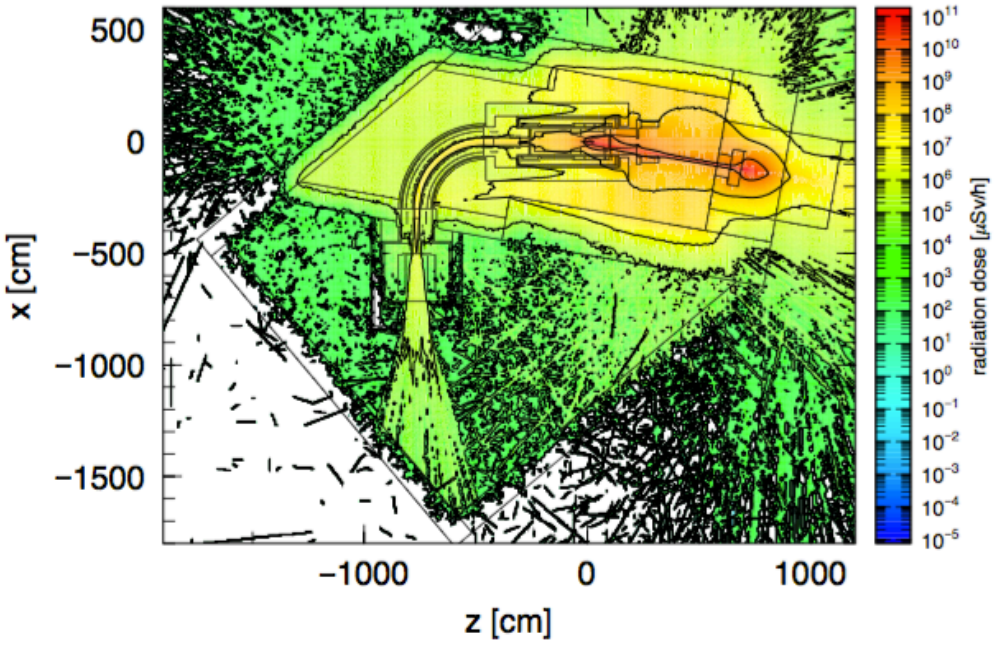

Figure 5.5: *Radiation dose around the beam dump for COMET Phase-I beam operation calculated with PHITS[39].*

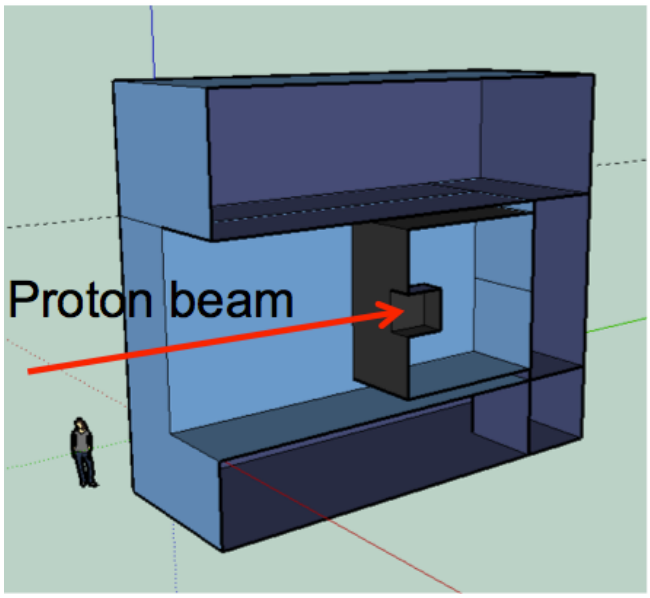

Figure 5.6: *A cross sectional view of the beam dump for the COMET Phase I.*

For safety assurance, a case study was made of the effect of full beam injection to the beam dump

due to an accelerator malfunction. If this happens in COMET Phase-I, 1.5×10^{13} protons would be injected to the dump in a short period ($\sim$5 μsec). The beam spread could be as small as 1.7 cm in horizontal and 2.6 cm in vertical directions at the surface of the dump, although these would be larger in reality owing to beam scattering at the pion production target. Figure 5.7 shows the deposited energy distribution from the beam particles. The maximum energy, J density around the center is calculated to be 10 MeV/cm^3/proton, resulting in temperature increase $\Delta T = J/C\rho < 10$K where C and ρ represent the heat capacitance (0.435 [J/gK]) and density (7.874 [g/cm^3]) of iron respectively. This is sufficiently small not to cause any unexpected problem in the facility. Note that heat generation at the dump by normal operation of the 3.2 kW beam will be dissipated by the air conditioning system in the primary beam line area, which has a cooling power more than 10 times larger than the beam power.

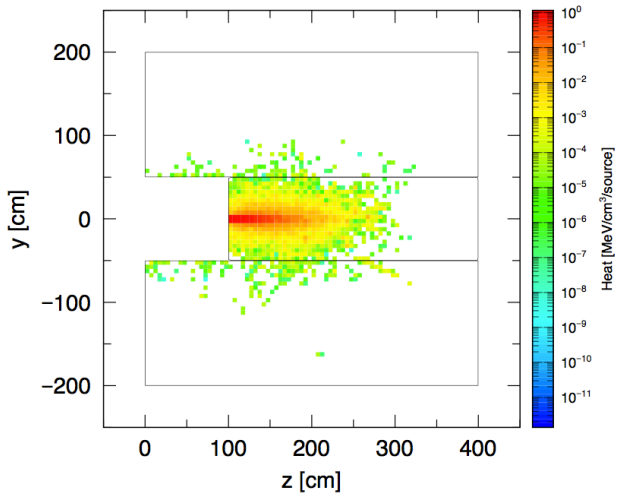

Figure 5.7: *Heat distribution for the case of full beam injection to the beam dump in COMET Phase-I calculated with PHITS. The maximum energy deposit by a proton is estimated to be 10 MeV/cm^3/proton.*

As described in later sections, the volume inside the capture solenoid will be evacuated, as is the beam duct of the primary beam line. The downstream volume between the capture solenoid exit and the beam dump will be filled with pure helium gas contained in a chamber sized to fit the downstream region. The hole in the beam dump will also be filled with pure helium gas. These are mandatory for reducing active gas production such as ozone and nitrogen oxide (NO_x) when the proton beam travels in the air. However the existence of some small air-filled gaps is unavoidable. These will be between the capture solenoid exit and the helium chamber, and between the helium chamber and the entrance of the beam dump gas volume, and their existence will simplify construction and maintenance of the beam line. We evaluated ozone and NO_x production rate using the empirical formula,

$$N = \frac{IG}{\alpha + kI} \tag{5.1}$$

where N is ozone production [g/cm^3]; I is the energy deposited [eV/cm^3/sec]; G is ozone production rate (6.4×10^{-2} [1/eV]); α is the dissociation constant (2.3×10^{-4} [1/sec]); and k is decomposition constant per radiation (1.4×10^{-16} [cm^3/eV]). Energy deposited by a proton is 1.82 MeVcm^2/g, corresponding to 5.5×10^{15} eV/cm/sec. Additional energy deposited by neutrons generated in the pion production target and beam dump is estimated to be 4.3×10^8 eV/cm^3/sec, using MARS. Supposing the total distance of air gaps along the beam line to be 50 cm, and taking the primary beam line area volume of 400 m^3, we can conclude that ozone

production in the primary beam line area will be 0.0077 ppm due to the proton beam and 0.0045 ppm from neutrons, and in total be 0.012 ppm. The NO_x production rate is known to be 0.27 times that of ozone production[40] and is evaluated to be 0.0032 ppm. Both of these values are below the environmental criteria (0.06 ppm for ozone and 0.04 ppm for NO_x in average one hour). This confirms safe beam operation of COMET with the ventilation system equipped in the facility. However, if NO_x concentrates anywhere in the primary beam line area, it would cause corrosion of metallic materials due to the formation of nitric acid. To mitigate this we will ensure forced air flow near the gaps where air concentration could potentially happen.

Upgrade of the beam dump for Phase-II operation (56 kW beam power) will be realised by replacing the central part of the Phase-I beam dump with an assembly of copper blocks in which water cooling pipes are embedded. The assembly will have a conical hole at the centre to equally distribute energy deposit by protons along the beam axis. This is a similar design to the beam dump of the hadron primary beam line, which is capable of dumping a 750 kW proton beam. Residual dose on the sliced surfaces in the beam dump after 90 days Phase-I operation and 180 days cooling time is calculated as shown in Figure 5.8. The highest dose is as high as 60 mSv/h but the average is about 1–10 mSv/h, which is manageable by remote handling with a magnetic chuck.

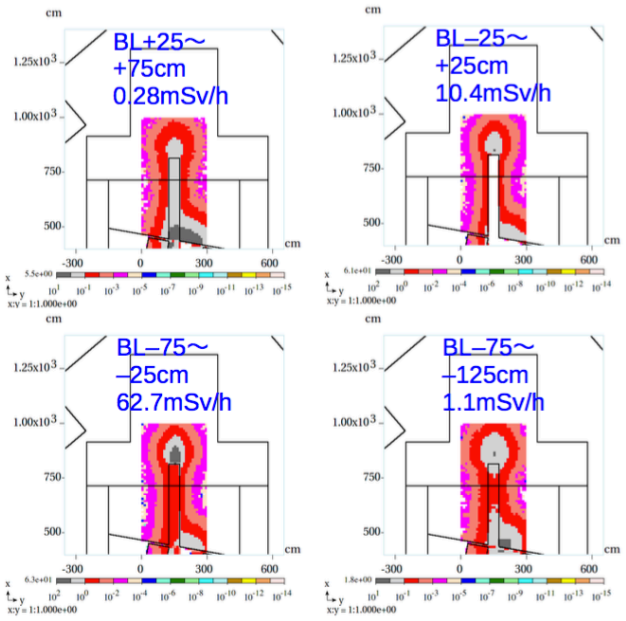

Figure 5.8: *Residual dose on the sliced surfaces in the beam dump after 90 days Phase-I operation and 180 days cooling time calculated with MARS. The beam centre is shifted 40 cm downward by the magnetic field of the capture solenoid.*

5.4. Proton Beamline Monitor

Beam profile monitors will be installed at several locations along the beam line including: downstream of the A/B-line branch; the boundary of the switch yard (the tunnel between the MR and the NP Hall); and the NP Hall, as well as upstream of the COMET building entrance. We will use the same technology, RGIPM (Residual Gas Ionization Profile Monitor) as has been used for the A-line beam monitors. For measuring the proton beam extinction factor

and beam profile for precise targeting we will employ another type of detector with a fast response and high sensitivity while operating in a high-radiation environment. Details of this detector will be described in Chapter 6. In an RGIPM the beam interacts with residual gas in the beam pipe producing ionization electrons. These are drifted by an electric field and read out by electrodes to reconstruct both the horizontal and vertical beam profile.[1] In addition to several RGIPMs, an RGICM (Residual Gas Ionization Current Monitor) will be installed near the COMET building entrance for beam intensity monitoring. The RGICM uses a similar technology to the RGIPM, but precisely measures the current of ionization electrons, which is proportional to the beam intensity. It is important to keep the vacuum pressure constant to achieve a stable monitoring system.

5.5. Power supplies and vacuum system

The power supply system for the proton beam line will be the same as is used in the A-line beam transport. It is necessary to evacuate the transport line beam pipe in order to reduce beam loss and unexpected radiation doses. The required level of 0.1 Pa can be realized without any difficulty by installing scroll vacuum pumps at about every 20 m of the beam line. Oil-free scroll pumps will be used to prevent radiation contaminated oil mist being distributed into the environment. The same type of pump that has been introduced in the A-line is available where its actual performance has already been proven.

5.6. Proton Beamline Simulation

The beam optics of the proton beam line were optimized by a TRANSPORT simulation. Figure 5.9 displays the envelope of the simulated beam optics. The 3-σ beam emittance at the extraction point used in the simulation is $42.7\,\pi$ mm mrad in horizontal direction and $81.9\,\pi$ mm mrad in vertical direction, which is based on the calculation in the MR design. These estimates are adequately safe for the beam line design because they are about 3 times larger than the extrapolation from the measurements with beam energy of 30 GeV at NP Hall ($14.8\,\pi$ mm mrad and $24.5\,\pi$ mm mrad) and are more than 7 times larger than measurements at the MR as described in the previous section. The original optics at 30 GeV operation is kept before the position labelled by MP (matching point). SM1, SM2 and SM3 in the figure indicate the Lambertson magnet and two septum magnets at the A/B-line branch. A remotely-adjustable tungsten beam collimator will be installed at the position labelled COL1.

The proton beam is eventually focused on the proton target, whose position is labelled FF (Final Focus), using the last four quadruple magnets upstream of the COMET hall. Based on the simulation, the 1σ horizontal and vertical beam sizes at the proton target are 6.0 mm and 3.3 mm, respectively.

Beam loss due to interaction of the beam halo through the proton beam line was evaluated using a TURTLE simulation. The total loss after the MP was estimated to be 0.3%.

The proton beam bends near and within the capture solenoid magnet due to its magnetic field. The trajectory of the proton beam is calculated using GEANT4 as well as TURTLE simulations as displayed in Figure 5.10. The beam position at the entrance of the capture

[1] Though signal amplifiers, such as a micro-channel plate, are often used for RGIPMs, a sufficiently large signal can be obtained with a simple electrode at the proton beam line due to the degree of vacuum in the beam pipe being relatively high compared to, for example, the J-PARC MR.

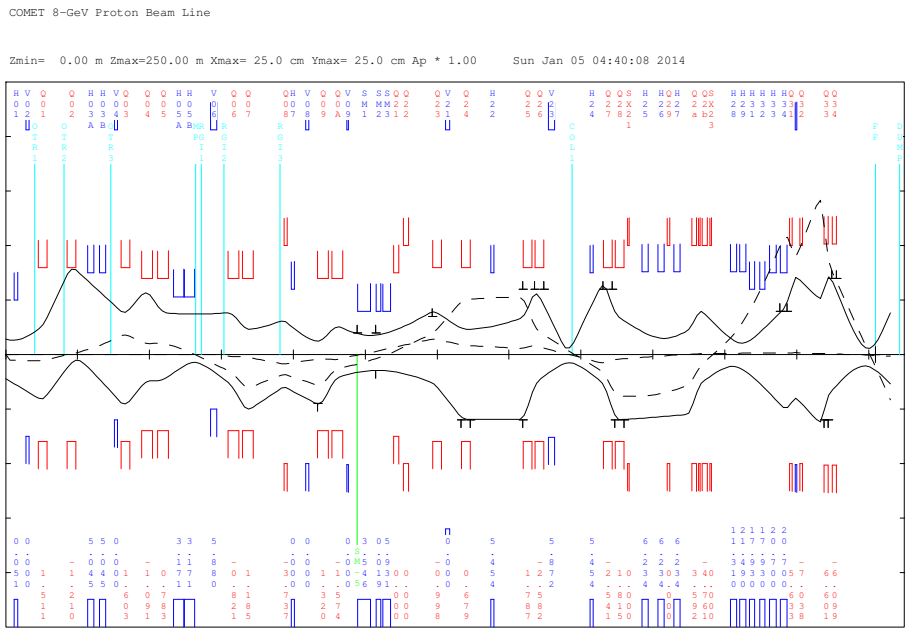

Figure 5.9: *The proton beam envelope by TRANSPORT simulation. The solid lines in the bottom and upper halves indicate horizontal and vertical beam size in 2σ, respectively. Each tick on the horizontal and vertical axes indicates 20 m and 5 cm respectivly.*

solenoid magnet is optimized so that the beam passes through the centre of the pion production target. The required beam shifts in horizontal and vertical directions are about 3 mm and -40 mm, respectively, in the GEANT4 simulation, while 4 mm and 0 mm in the TURTLE simulation. The difference between the results of GEANT4 and TURTLE comes from the fields used in each simulation. A field map obtained by an OPERA calculation with realistic magnet design is used in GEANT4, while TURTLE calculates beam trajectories based on a transfer matrix which is determined by length and radius of the magnet. The above shifts can be corrected using upstream bending magnets in the proton beam line. The horizontal and vertical beam tilts at the target centre are $dx/dz = 0.0066$ and $dy/dz = -0.047$, respectively.

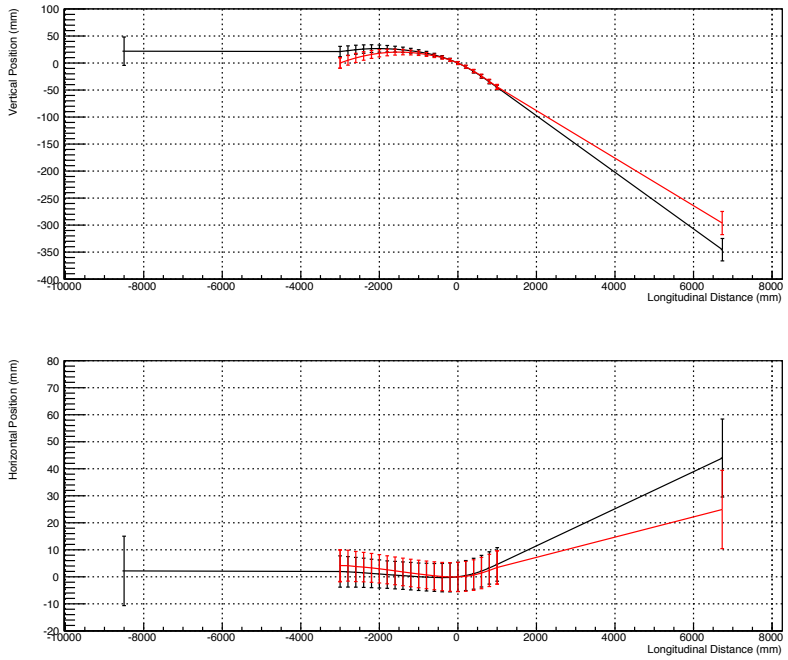

Figure 5.10: *The proton beam trajectory around the capture solenoid magnet. Black and red points are results from GEANT4 and TURTLE, respectively. The horizontal axis of the plots indicates longitudinal distance along the proton beam. Positive direction of the vertical and horizontal position in the plots corresponds to upside and left side on the beam view. The pion production target is assumed to be located at (0 mm,0 mm,0 mm) in vertical and horizontal position and longitudinal distance. The error bar of each point indicates a beam size of 1σ. The beam dump is located at 6700 mm in longitudinal distance.*

Chapter 6

Proton Beam Monitor

It is necessary to measure the bunch-by-bunch proton beam luminosity $\mathcal{L}_p$ and direction for the following reasons:

1. **Extinction monitoring:** The most important function of a bunch-by-bunch proton beam monitor is to monitor extinction of the proton bunch. An extinction factor $< 10^{-9}$ on a 10^{11} p/bunch (COMET Phase I) is specified, since stray protons can lead to secondary production in the beamline and indeterminate backgrounds in the final $\mu - e$ conversion signal. Radiation-hard semiconductor detectors are the only type capable of providing this functionality among the various beam monitor types listed in Table 6.1.

2. **Position Monitoring:** The proton beam power (3.2 kW for Phase 1, 56 kW for Phase 2)is spread over a narrow cross-section of $1\sigma = 10\,\text{mm}$ incident at a grazing angle on a cylindrical target of 20 mm diameter. A slight misalignment in the beam pointing, combined with an accidental fast extraction could trigger a worst-case scenario of the beam hitting the capture solenoid. With a fast beam profile monitor, it is possible to trip protection mechanisms when the beam centroid is measured to be well outside the nominal value. Adding multiple layers of profile monitoring detector would also give some level of redundancy in case of failure of one of the layers.

Detector type	Sampling time	Function	Readout	Beam intensity (typical)
TLD (passive)	∞	integrated dose	offline	High
Residual gas ionization current (RGICM)	$\sim$ sec	spill (beam emittance)	realtime	High
Semiconductor	$\sim$ ns	bunch-by-bunch **timing, position and extinction**	realtime	High (choice of material)

Table 6.1: *Types of detectors used for beam monitoring, with readout time scales*

6.1. Choice of semiconductor and detector materials

Solid state semiconductor detectors have emerged as the ideal choice in a high radiation environment because of their robustness: typically semiconductor detectors can tolerate high radiation

Property	Si	Diamond	Ge	GaAs
Atomic number	14	6	32	31/33
Number of atoms ($10^{22}\,\mathrm{cm}^{-3}$)	5.0	17.7	4.5	2.2
Mass density ($\mathrm{g\,cm}^{-1}$)	2.33	3.51	5.3	5.4
Radiation length (cm)	9.4	18.0	2.3	2.3
Carrier density (cm^{-3})	1.45×10^{10}	$< 10^3$	2×10^{13}	2×10^8
Resistivity ($\Omega\,\mathrm{cm}$)	2.3×10^5	$> 10^{12}$	46	3×10^8
Band Gap (eV)	1.12	5.48	0.67	1.43
Electron mobility ($\mathrm{cm}^2\,\mathrm{V}^{-1}\,\mathrm{s}^{-1}$)	1350	1800	1900	8000
Hole mobility ($\mathrm{cm}^2\,\mathrm{V}^{-1}\,\mathrm{s}^{-1}$)	480	2000	3900	400
Saturation velocity ($\mathrm{cm\,s}^{-1}$)	0.8×10^7	2×10^7		
Breakdown field ($\mathrm{V\,m}^{-1}$)	3×10^5	2.2×10^7		
Dielectric constant	11.9	5.7		
Thermal conductivity ($\mathrm{W\,cm}^{-1}\,\mathrm{K}^{-1}$)	1.48	25		
Displacement energy (eV)	13-20	43		
e-h creation energy (eV)	3.6	13	2.9	4.1
Mean MIP ionization ($e\,\mu\mathrm{m}^{-1}$)	108	36	260	173
CCD (μm)	full	$\sim$250		
Carrier lifetime (μs)	$\sim$250	250	0.001–0.01	$\sim$0.1–2

Table 6.2: *Semiconductor detector properties compared*

doses and require little servicing in hard to access areas. A bias voltage applied across the detector creates an electric field in the bulk. A charged particle passing through the biased semiconductor creates electron-hole pairs, which drift in the bias field and induce a signal in the respective electrodes. Table 6.2 lists the properties for materials typically used in solid state detectors [41, 42].

Diamond grown synthetically by microwave plasma assisted chemical vapour deposition (CVD)[43, 44] is an ideal material for beam monitoring. Polycrystalline diamond sensors up to 6 inch diameter and single crystal diamond sensors up to 10mm are available. The former have adequate response to measure beam profile, the latter have charge collection efficiency high enough to measure bunch extinction down to single proton level.

1. **Radiation hardness**: The maximum fluence including COMET Phase II is expected to be $n_{\mathrm{eq}} \sim 10^{16}/\mathrm{cm}^2$ [45]. The high proton flux necessitates a radiation-hard detector. Diamond has the highest displacement energy among the semiconductors listed in Table 6.2, making it the most radiation hard material in the list.

2. **Time response**: The beam in COMET consists of 100 ns long proton bunches separated in time by 1.17 µs. This necessitates a sensor that is capable of charge collection within a time window of a few ns to check extinction at the end of the 100ns bunch. With very high carrier mobility diamond sensors are capable of signal response at nanosecond timescale [42].

3. **Thermal and mechanical behaviour** Since the beam monitor is to be placed in the beam path, thermal effects after continuous irradiation are of concern. Diamond has high thermal conductivity, so with appropriate design of the support structure active cooling is not necessary. Charge collection in diamond has been studied up to temperature of 200 °C with no significant degradation [46].

4. **Material budget** Electrodes on the diamond sensor typically consist of a thin ($\sim 250\,\mathrm{nm}$ film of Cr+Au deposited by CVD and the diamond sensors themselves are typically $\sim$ 100–400 µm thick. Thinner diamond sensors are not mechanically stable to handle. The design envisages the beam monitor to be placed in the 1σ–2σ halo of the beam. Due to low Z of diamond and its long radiation length, the thin metallic layer would not adversely impact the beam scatter if it is placed in the beam path.

5. **Beam monitor support structure** The beam monitor scaffold does not need to bear much mechanical load. However, for an in-beam monitor, degradation of dielectric properties due to thermal heating and high fluence has to be carefully considered. Alumina ceramic substrate has been used in several high energy experiments since it is UHV compatible and can withstand integrated proton fluxes of up to $10^{20} p/\mathrm{cm}^2$[47]. Its properties are listed in Table 6.3. The beam monitor support structure will be made of Alumina, with mechanical dimensions such that it causes minimal occlusion of the beam path.

Property	Alumina	Aluminum Nitride
Bending strength (MPa) (substrate thickness $\sim$1 mm)	500	500
Specific heat (J/kg K)	800	800
Linear expansion coefficient (K^{-1})	8×10^{-6}	1×10^{-6}
Thermal conductivity ($\mathrm{W/m \cdot K}$) (up to 100°C)	24	$\geqslant 170$
Breakdown Voltage (kV/mm) (substrate thickness $\sim$1 mm)	15	15
Volume resistivity at 20° C ($\Omega \cdot \mathrm{cm}$)	$> 1 \times 10^{13}$	$> 1 \times 10^{14}$

Table 6.3: *Ceramic properties. Values of bending strength and breakdown voltage are given for a substrate thickness of* $\sim 1\,mm$

6.2. Epoxy, connectors and cables

Diamond sensors are mounted on the scaffold using a conductive epoxy that must retain its properties after high radiation and thermal stress. StayStik 571 and Epotek H31 are examples of vacuum compatible epoxies that have been widely used and tested in high radiation environments[48, 49]. These are thermoplastics filled with silver, with a very high bond strength and low resistivity. Standard radiation hard connectors and cabling (coax or ribbon) can be used to transfer the signal from the detector scaffold to the frontend electronics. The cables must be optimised for minimal RF noise pickup. Deterioration of cable insulation after prolonged irradiation has to be taken into account when selecting the cable material[50].

6.3. Location and Detector geometry

The mechanical scaffold for the detector must meet the following performance criteria:

1. Vacuum compatibility. The proton beam monitor is to be mounted in vacuum in the flange that connects the J-PARC beam tube entering the COMET experimental hall with the beam tube entering the capture solenoid as shown in Figure 6.1.

2. Minimal material placed in the beam path. Since the detector scaffold will be very close to the beam path, the quantity of material should be as small as possible to minimize beam scattering.

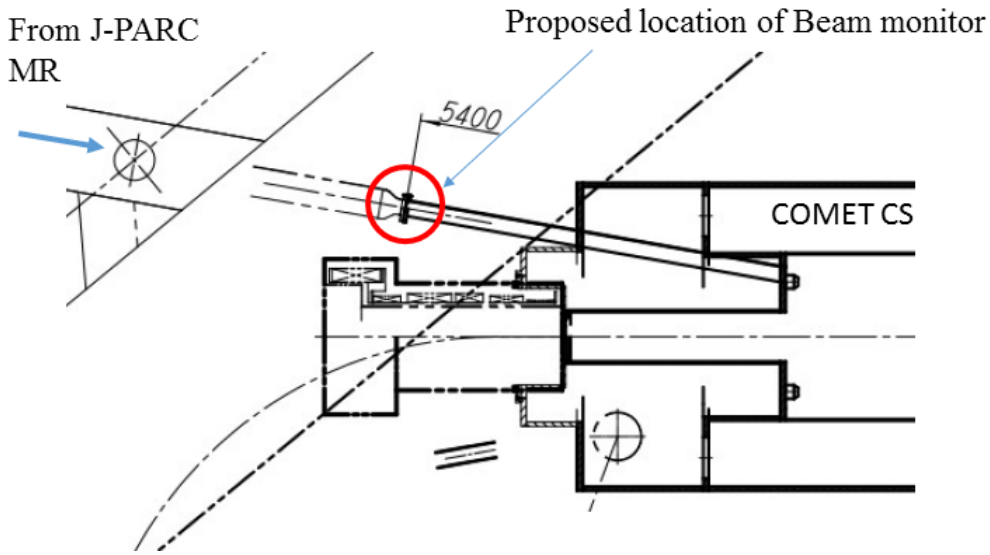

Figure 6.1: *Proposed location of beam monitor, 5. m upstream of the target. A flange connects the J-PARC beam pipe to the COMET CS beam pipe. A transition structure with multiple layers of detector can be inserted at the flange as discussed in the text*

3. Radiation hardness. the mechanical properties of the manifold must be stable after sustained irradiation.

4. Shielding from RF noise pickup. We envisage the detector manifold to contain just the active diamond sensors and the readout signal lines (which share the bias voltage). No active components are placed in the vacuum envelope. Therefore the detector manifold should have a high level of RF shielding to prevent noise pickup.

6.3.1 Geometry of sensor active area

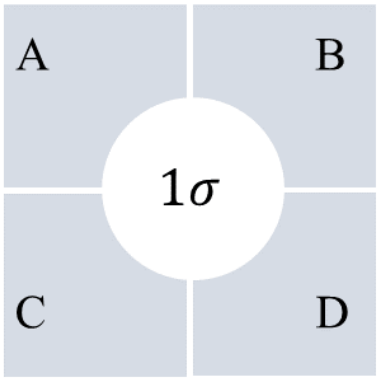

Figure 6.2: *Geometry of the four quadrant detector design. Each diamond sensor is square and arranged around the beam center. The thickness is* $d \approx 100\,\mu m$–$400\,\mu m$*, to be optimized based on material budget, mechanical rigidity and charge collection and timing response as discussed in the text.*

Since the primary function of the beam monitor in COMET is to determine the bunch-by-bunch beam position and extinction, we envisage a four quadrant detector geometry as shown in Figure 6.2. Assuming beam waist size $1\sigma \sim 10\,\text{mm}$ at the detector's location, a four quadrant

detector provides beam centroid resolution in x, y of $\sim \sigma/\sqrt{12} \sim 3\,\text{mm}$ for an intense proton beam of Gaussian transverse profile.

6.3.2 Detector support structure

It is extremely important to protect the sensor active area from RF noise pickup by enclosing it in a Faraday cage. The detector scaffold shown in Figure 6.3 indicates such a structure made on alumina ceramic substrate. A central hole of diameter $\sim 2\sigma$ of the beam waist is cutout from both the plates. Four quadrants are milled out around the central aperture to fix and align the four diamond sensors. The depth of milling in each plate is half the thickness of the sensor plus the conductive epoxy film used to affix it in place. Conductor traces extract signal from the diamond sensors—two each on either side of the scaffold. All the rest of the exposed area is at ground potential forming a Faraday cage around the active area. The width of signal traces is to be decided based on signal impedance matching considerations. The thickness and type of conductor film would be determined by the material budget of the scaffold.

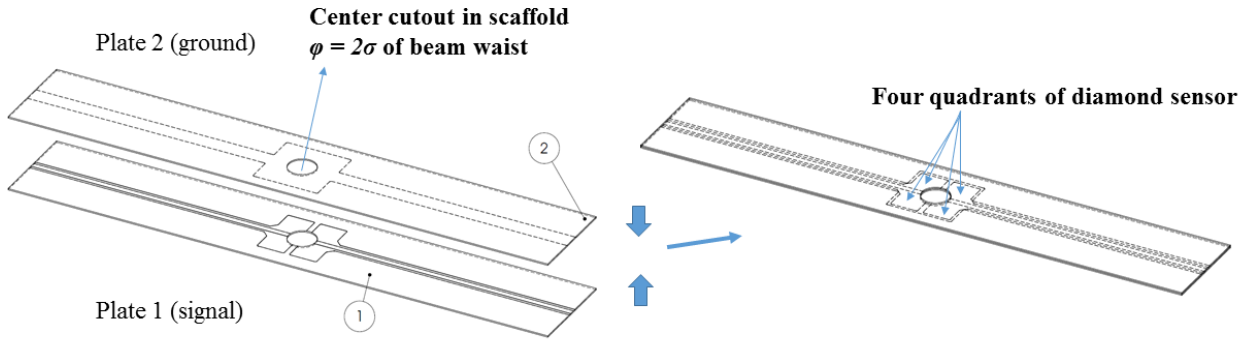

Figure 6.3: *Geometry of detector scaffold. The substrate is alumina ceramic as discussed in the text. Alignment pins and the mechanism to mount it inside the beam tube is not shown here.*

6.4. Signal extraction

The proton beam monitor has two functions:

1. During the 100 ns long bunch passage, determine the cross-sectional space profile of the beam
2. In the subsequent $\approx 1\,\mu\text{s}$ detection phase, measure the extinction of the beam at a level better than 10^{-9}

The two functions are complementary. In the beam profile phase, a flux of $10^{12}\,p/\text{cm}^2$ is expected. This will naturally lead to very large signal deposition: a detector with DC readout and fast response is required. In the extinction monitor phase, the signal goes down to the level of a few p/cm^2: a detector with linear amplification and full charge collection is required.

Two separate detectors for these two functions are used, based on the properties of polycrystalline (pCVD) and single crystal CVD (scCVD) diamond discussed in section 6.1..

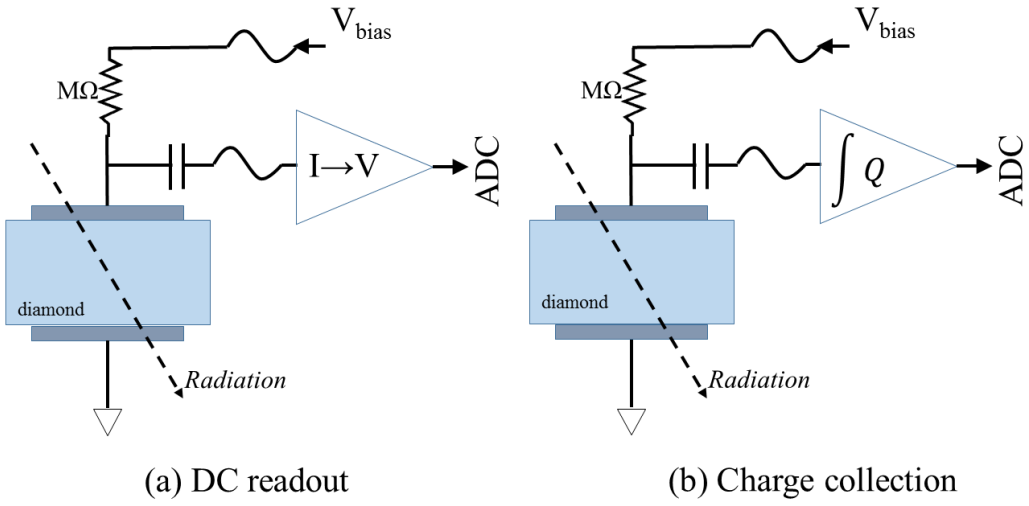

Figure 6.4: *Two readout schemes for diamond detectors. (a) is a triggerless DC readout that monitors current from the sensor. It is commonly used in setups requiring continuous beam monitoring. (b) is a triggered readout for applications where accurate charge collection measurements are required. For charge collection a charge shaping amplifier (CSA) or time-over-threshold measurement is used*

6.4.1 Beam profile monitor: pCVD

Polycrystalline diamond (pCVD) can be grown by chemical vapor deposition (CVD) [51, 52] up to large lateral dimensions (6-inch diameter wafers of up to 400 µm thickness). pCVD has shallow charge collection distance (CCD) $\approx 200\,\mu m$, but offers the advantage of extremely fast signal response at the ns level. For COMET, having a shallow CCD is not a problem, since the flux of protons per bunch is so high that the expected signal would be more than adequate. A typical number for electron-hole production by a MIP in diamond is 36 $e + h/\mu m$. With $10^{12}\,p/cm^2$ flux on a detector cross section $\approx 1\,cm^2$ with CCD $= 200\,\mu m$, the expected signal charge would be $\approx 1.15\,mC$.

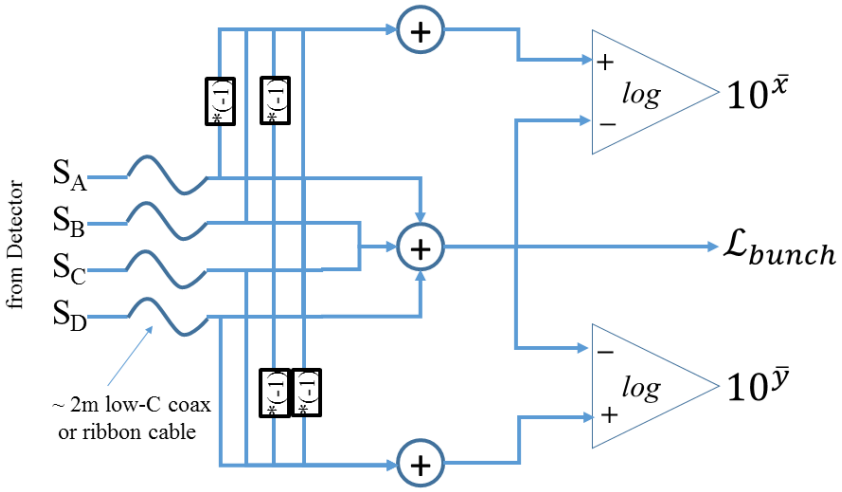

Figure 6.5: *Simple readout scheme for the four quadrant detector geometry. Signals from the four quadrants are S_A, S_B, S_C, S_D. A sequence of analog summing and logarithmic amplifiers are used to arrive at $\bar{x}, \bar{y}, \mathcal{L}_{bunch}$*

The high carrier mobility of $\approx$ 1000cm^2/Vs at a bias field of 1V/µm leads to a first order

estimation of the signal FWHM[53]:

$$t_{\mathrm{FWHM}} = \frac{\ln(2) * CCD}{v_{\mathrm{drift}}} = \frac{\ln(2) * CCD}{\mu\ E} \approx 1.4\,\mathrm{ns} \tag{6.1}$$

Bias voltage to the detector is kept on all the time at a typical value of $V_{\mathrm{bias}} = 1\,\mathrm{V}/\mu\mathrm{m}$ (i.e. 100 V for a detector thickness of 100 µm). The detector bulk is therefore active at all times. The signals S_A, S_B, S_C, S_D are read out in DC mode directly to a charge-to-voltage converting analog readout discussed below. The raw signals picked from electrical contacts to the diamond sensors can be carried up to 2 meters away from the detector location with appropriate precautions for RF noise pickup in the cabling. Due to the bunched beam structure, the signals are non-zero only during the passage of the bunch, with a decay time governed by the intrinsic detector capacitance (short) and RC delay time constant of the transmission cable. In past applications of beam monitoring at CDF, BaBar and Belle the signal has been transferred over up to 250 ft length of RG50 coax for amplification and digitization.

The centroid of the beam spot and the bunch luminosity is given by:

$$\bar{x} = \frac{(S_B + S_D) - (S_A + S_C)}{(S_A + S_B + S_C + S_D)} \qquad \bar{y} = \frac{(S_A + S_B) - (S_C + S_D)}{(S_A + S_B + S_C + S_D)} \tag{6.2}$$

$$\mathcal{L}_{\mathrm{bunch}} = \frac{(S_A + S_B + S_C + S_D)}{S_{\mathrm{cal}}} \tag{6.3}$$

where S_{cal} is a calibrated maximum value determined by measuring the total signal with a proton beam of known luminosity. The gains of signals S_A, S_B, S_C, S_D are adjusted such that the sum is always less than S_{cal} to prevent the output from saturating.

Since the beam centroid is determined from the ratios of analog signals, the calculation of Eqn 6.2 can be performed in realtime using wide-bandwidth log amplifiers. A simple readout scheme is shown in Figure 6.5. The outputs $\bar{x}, \bar{y}, \mathcal{L}_{\mathrm{bunch}}$ of the readout are digitized and fed to the upstream DAQ for recording on a bunch-by-bunch basis.

6.4.2 Extinction monitor: scCVD

Single crystal CVD diamond (scCVD) differs from pCVD in the following respects:

1. Charge collection distance is nearly equal to the thickness of the diamond sensor (we have measured up to CCD = 420 µm in sensor thickness $d = 460\,\mu\mathrm{m}$[54].
2. Signal collection down to single MIP level is possible.
3. Complete charge collection can take up to 10 ns. The convolution of the charge drift time with realistic delays of transmission cables gives the practical lower limit on the MIP charge collection time.

Hence scCVD appears to be a more suitable material for measuring the extinction phase of the beam in the 1.17 µs gap between bunches. The primary concern is that the detector bias cannot be kept on continuously. Large signal deposition during the bunch passage will cause saturation of space charge in the detector bulk and it would take significant time for the sensor to recover to the linear MIP level response regime.

The readout scheme for the extinction monitor is depicted in Fig 6.6. The detector bias voltage switches between 0 V and 100 V (1 V/µm for 100 µm thick sensor). The value of bias bypass

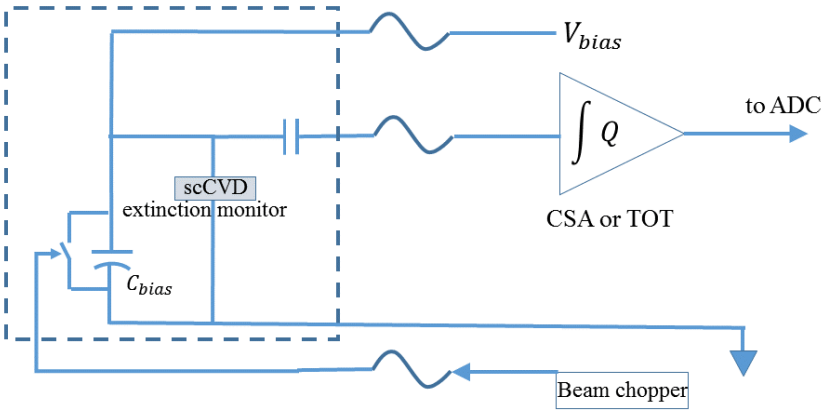

Figure 6.6: *Readout and bias control scheme for the extinction monitor made of scCVD. One quadrant of the extinction monitor is shown; others are similar. All components in the dashed box are co-located within the detector manifold*

capacitors mounted on the detector manifold close to the sensor would have to be fine-tuned to account for electronic impedances and make sure that the extinction monitor receives full bias (i.e. is active) only towards the end of the bunch passage. The bias voltage is pulled down to 0 V at the end of the extinction measurement phase by a switch triggered by the bunch synchronisation signal.

Although bias voltage to the scCVD extinction detector sensors is off during bunch passage, they will nevertheless be irradiated by the bunch. The effect of irradiation on an inactive scCVD sensor prior to application of bias is called pumping[55]. The irradiation ionizes and 'primes the detector' by pre-filling defect sites in the bandgap with charge carriers so that they are rendered inactive. When bias is applied, the signal response to further ionizing radiation is in fact slightly improved over that without pumping. This pumping effect has been studied up to fluence levels of $n_{\text{eq}} \approx 10^{10}/\text{cm}^2$ and found to be reversible. Details of the effect at levels of irradiation expected in COMET Phase-II have to be further studied in a test beam environment.

6.5. Data acquisition

The 0.4 μA proton beam is pulsed with 100 ns spill of protons separated by 1.17 μs periods of extinction to the order of 10^{-9}. As discussed in Section 6.4., we will use two set of detectors, one for beam position monitoring during the 100 ns spill and another for monitoring the beam extinction. Each detector consists of four quadrants of diamond sensors and need to be read out in the data acquisition (DAQ). Here we present a conceptual layout of the data acquisition scheme to be used for the beam profile monitoring (BPM) detector and extinction monitoring (EM) detector. The timing diagram of the proton beam monitor shown in Figure 6.7. From the BPM, the raw four quadrant signals S_A, S_B, S_C, S_D are available, along with analog signals proportional to $\bar{x}, \bar{y}, \mathcal{L}_{\text{bunch}}$ from the frontend electronics of the BPM.

The BPM runs in triggerless, deadtimeless mode. So the following options can be considered:

1. Record all the signals S_A, S_B, S_C, S_D and $\bar{x}, \bar{y}, \mathcal{L}_{\text{bunch}}$ continuously,placing markers at the bunch sync and beam spill times. These signals can also be used to compute the beam luminosity per spill for calibrations.

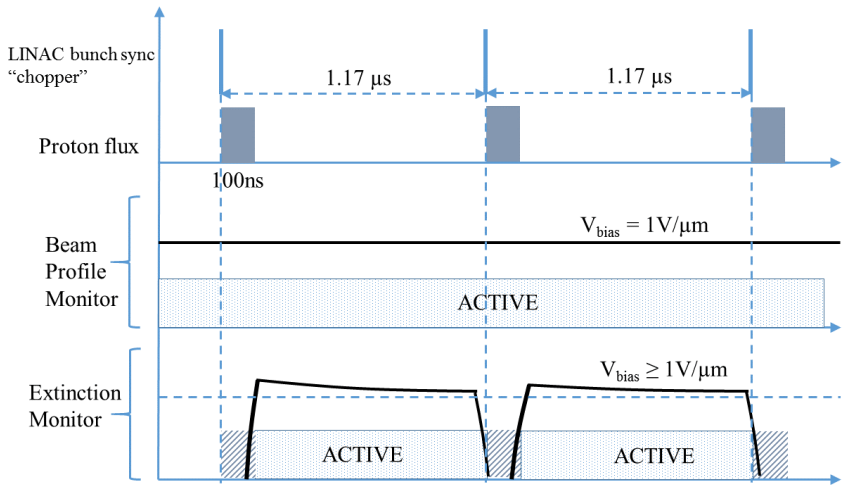

Figure 6.7: *Timing diagram for the proton beam monitors*

2. In addition, we use the signals $\bar{x}, \bar{y}, \mathcal{L}_{\text{bunch}}$ computed in realtime by the BPM frontend electronics with appropriately set threshold values to trip safety mechanisms.

The Extinction Monitor (EM) relies on a bunch sync or trigger signal to switch V_{bias} to the detector in synchronization with the required $\approx 1\,\mu\text{s}$ long extinction monitoring cycle. There are two possibilities for readout of the EM:

1. Measure and record the total integrated charge collected by the EM in the $\approx 1\,\mu\text{s}$ extinction phase. This would require a charge shaping amplifier in the front end electronics and digitization at a preset time ($1.16\,\mu\text{s}$) from the bunch sync start signal. The total charge collected during the extinction phase would be proportional to the number of particles passing through the active area of the detector. It is not possible to identify individual stray particles in this mode. However an offline can be used to veto the bunch if the collected signal in the 'quiet' phase exceeds some pre-defined threshold.

2. Perform an *event-by-event* extinction measurement. In this scenario, the EM diamond sensors are also readout in DC mode - the frontend electronics performs a charge measurement using the time over threshold technique with a very high resolution clock[56]. Thresholds can then be set to veto on the detection of single MIP level signals in the scCVD diamond of the extinction monitor.

The two options are to be evaluated in a test beam environment with consideration of the signal characteristics discussed in Section 6.4..

6.6. Radiation effects

The expected level of radiation damage to the diamond based proton beam monitor has been simulated using Fluka[57]. The beam profile and detector geometry used in the simulation are shown in Figure 6.8

We have calculated the average displacement per atom (DPA), taking into account non-ionizing energy loss (NIEL) of a high intensity beam passing through the sensor material. DPA creates lattice defects in the sensor, reducing charge collection (signal) and increasing the leakage current (noise). The expected DPA for an integrated fluence of $10^{19}p$ is shown in Figure 6.9.

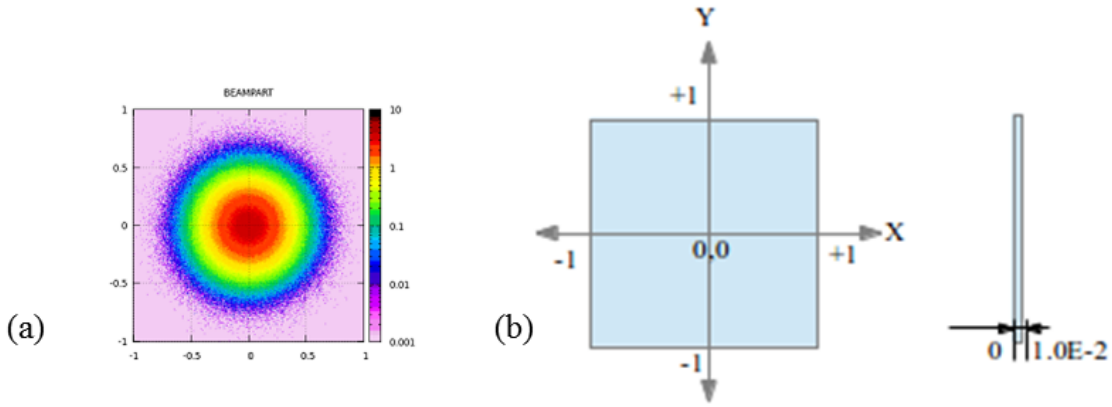

Figure 6.8: *Proton beam monitor setup for Fluka simulations: (a) Proton beam with Gaussian profile* $\sigma = 1cm$ *(b) Sensor geometry.*

The maximum DPA probability at the centre of the Gaussian beam is 1.5×10^{-21}. The COMET Phase-I beam power of 3.2 kW is equivalent to 2.5×10^{12} protons/s, which implies several hundred days of continuous operation of the diamond sensor before deep lattice defects will appear.

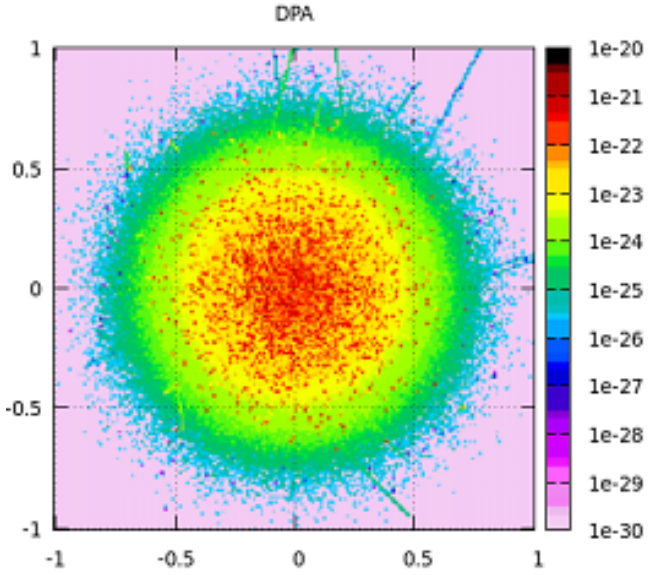

Figure 6.9: *Average Displacement Per Atom (DPA) normalized per primary particle*

To study the change in signal response as a function of fluence, we have tested a pCVD prototype module placed in the J-PARC main ring (MR) next to the beam pipe near the SX extraction point in June 2016[1]. It is not possible to insert the prototype into the main ring for operational reasons. It is positioned about 1m away from beam line, and sees some fraction of the primary proton beam bunches as well a large number secondary particles produced by the primary protons scraping along the edges of the beampipe. An OSL badge placed on the module and examined periodically measures the total dose received by the module. Figure 6.10 shows the signal distribution recorded in the prototype detector after 7 days of operation compared to that at the time of installation.

The detector has been left in place for operation during Autumn of 2016 when J-PARC MR

[1]Since the beam extraction mode at MR was SX, beam power was much lower than the power for FX, *i.e.* the beam power was 41 kW.

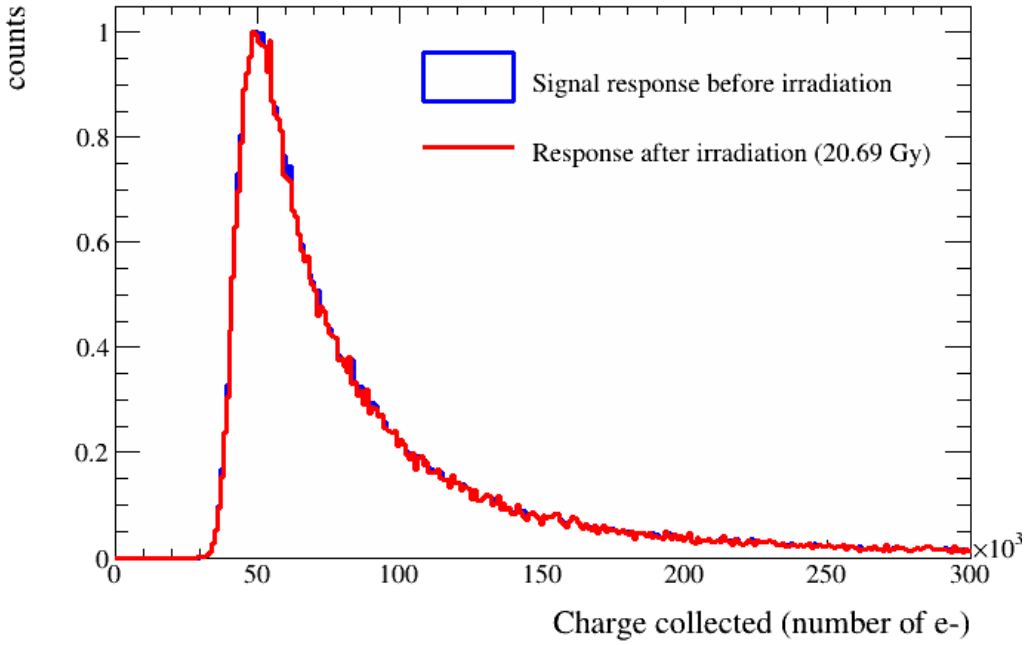

Figure 6.10: *Measured signal response of pCVD prototype placed next to JPARC Main Ring after 7 days of continuous operation. A mixture of particles is incident on the detector including secondaries generated in the beampipe.*

will operate in high power configuration which is anticipated to be 400 kW.

Chapter 7

Proton Target

The proton target is required to generate pions which will decay to muons as they are transported to the muon stopping target in the detector solenoid. The target will be installed within the bore of the capture solenoid with a configuration designed to capture low energy negative momentum pions generated by interaction with the 8 GeV proton beam from the J-PARC MR synchrotron. The designs of the target and target station will anticipate the long-term needs of the COMET Phase-II experiment while also providing hardware that is ready for Phase-I data-taking in 2018–2019. The target station and muon capture solenoid region will be designed for the Phase-II beam power of 56 kW since once constructed and activated, the target station infrastructure cannot be modified, and hence it must be able to meet the requirements of Phase-II from the start of operation. However, the target itself will be replaced between the two phases, and the target station will be designed to allow for this.

7.1. Pion Production

The COMET experiment will use negatively-charged, low-energy muons, which can be easily stopped in a thin target for the search for $\mu^- N \to e^- N$ conversion. The low-energy muons are mostly produced by the in-flight decay of low-energy pions. Therefore, the production of low-energy pions is of major interest. Conversely, we wish to eliminate high-energy pions, which could potentially cause background events.

The pion production yields from protons incident on graphite and tungsten targets in the backward and forward regions with respect to the proton beam direction are presented in Figure 7.1. It is planned to use a graphite target for COMET Phase-I, and a tungsten target in Phase-II. Generally the tungsten target produces more pions because there are more nucleons in the target to interact with incoming protons. But it would need cooling with a coolant to keep its temperature reasonable. It can be seen that the maximum total momentum for backward-scattered pions is about 150 MeV/c, whereas that for forward-scattered pions is about 200-400 MeV/c. It can also be seen that high-energy pions are suppressed in the backward direction. The yields of low energy pions are not so different, lying within a factor of two between the forward and backward directions. Thus backward pions have less high-energy pion contamination, while retaining a large low-energy pion yield. For these reasons, it has been decided to collect pions emitted in the backwards direction with respect to the proton beam direction.

Figure 7.2 shows the yields of pions and muons as a function of proton energy, calculated using Geant4. As seen in Figure 7.2, the pion yield increases almost linearly with proton

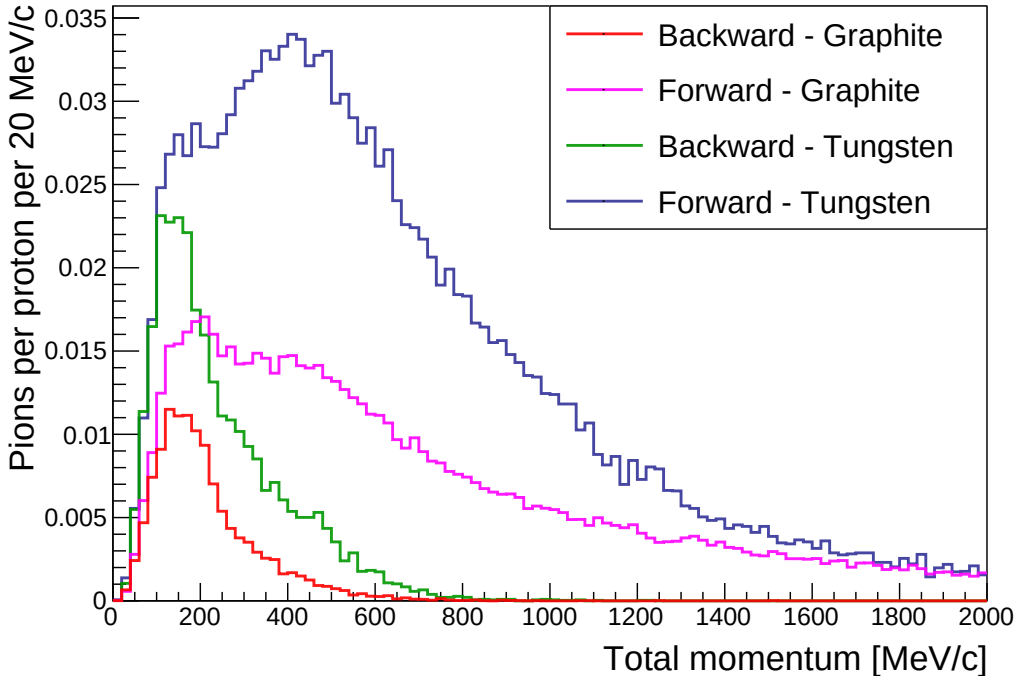

Figure 7.1: *Momentum distribution of pions exiting in the (a) forward and (b) backward regions of tungsten and graphite targets bombarded by an 8 GeV proton beam. The spectra are generated using Geant4 using the* `QGSP-BERT` *hadronisation model.*

energy, therefore with proton beam power. Also it is seen that at a very high proton energy (> 30 GeV), the pion production yield starts to become saturated.

The choice of proton energy can be determined by considering the pion production yield and backgrounds. In particular, backgrounds from antiproton production are important. The current choice of proton energy is 8 GeV, which is close to the threshold energy of antiproton production.

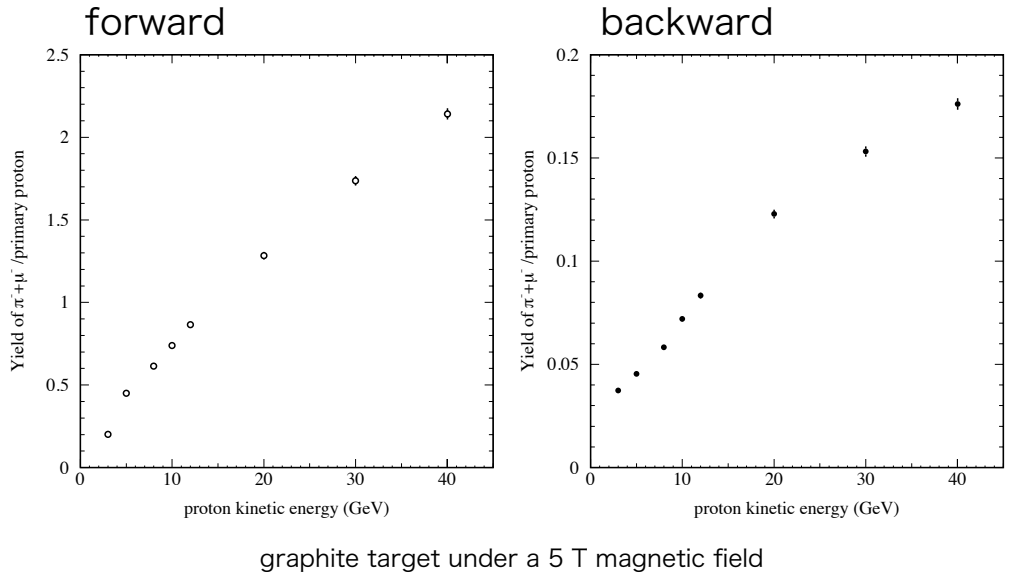

Figure 7.2: *Yields per proton of forward pions and muons, left, and backward pions and muons, right, from a graphite target in a magnetic field of 5 Tesla, as a function of proton energy.*

7.2. Material for proton target

Pion production is maximised with a high-Z material, however it is proposed to use a graphite target for Phase-I. This will minimise the activation of the target station and heat shield which will significantly ease the necessary upgrades for Phase-II operation. Also a graphite target does hold up to a few thousand degree by radiation cooling, but other high-Z material do not. It could simplify the proton target system for Phase-I.

The Phase-I beam power of 3.2 kW will deposit a heat load of approximately 100 W in the graphite target material. Figure 7.8 shows heat load and the temperature distributions for an IG-43 graphite target in COMET Phase-I. Table 7.2 summarises the properties of the IG-43 graphite. The heat load on the Phase-I graphite target can easily be radiated to the solenoid shield. A target support system will accurately position the target within the solenoid inner shield. This will be a stable and low mass structure to minimise re-absorption of the low energy pions as they follow helical trajectories within the capture solenoid.

7.3. Length and radius for proton target

The dimensions of the pion production target must be optimised. The intrinsic pion yield at low energy is almost proportional to the target length. On the other hand when the target is too long, pions produced can hit the target again and be absorbed. Also the radiation heat loads in the superconducting solenoid magnets, in which the target is embedded, should be considered; when the target is longer, it will increase the radiation heat load.

Simulations of 10^6 8 GeV protons striking graphite targets of lengths from 400 mm to 1200 mm were performed using Geant4 with the `QGSP-BERT` hadronisation model. The number of muons stopped at the muon-stopping target as a function of graphite target length is shown in Figure 7.3. The stopping yield first increases with the target length from 400 mm and be at its maximum at 700 mm. Beyond that the yield tails off. The target length of 700 mm for graphite would be the best, corresponding to about 1.5 interaction lengths. It is noted that the numbers of muons at 3 m from the proton target were used in the previous studies, but the number of muons stopped in the muon stopping target is used for the updated optimisation.

The target radius has been studied for the cases of 5 mm and 40 mm in radius, as shown in Figure 7.4. The best value is determined to be 13 mm. For cases larger than 13 mm, more pions are stopped inside the target. This could be dependent on the proton beam size. The beam spot size used in this simulation was to have two Gaussians, one of which has 5.8 mm in width and the other is 2.9 mm in σ. The proton beam has no divergence. The proton energy distribution is assumed to be Gaussian with a mean of 8.01 GeV in kinetic energy with a 0.135 MeV width. They are generated at a position 5 mm from the front face of the proton target. The dimensions of the pion production target are summarized in Table 7.1.

Target length	700 mm
Target radius	13 mm
Target material	graphite

Table 7.1: *Target dimensions and material selected for COMET Phase-I.*

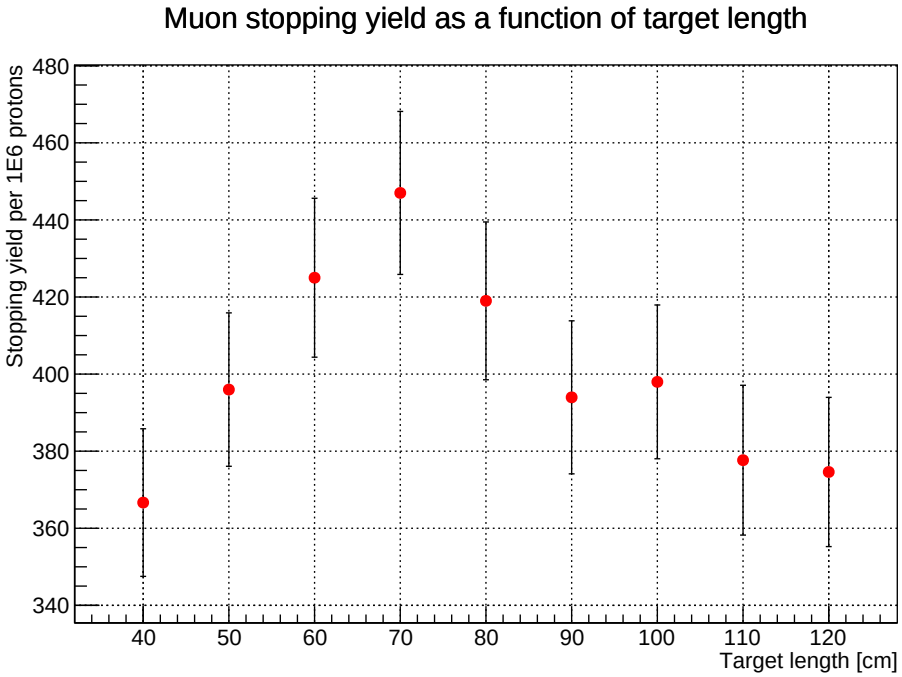

Figure 7.3: *Stopped muon yield as a function of graphite target length. The length is optimised to be 700 mm.*

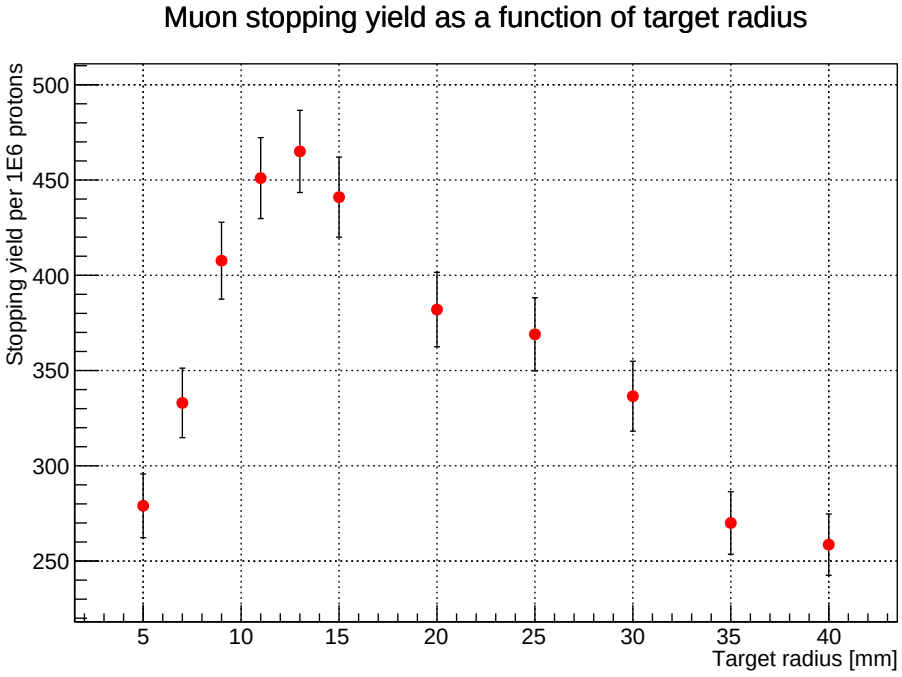

Figure 7.4: *Stopped muon yield as a function of graphite target radius. The radius is optimised to be 13 mm.*

7.4. Structure of the target holder

The target is supported by graphite spokes strung from a supporting ring made of titanium. The ring is supported by another titanium ring with a rotating shaft thus allowing the target to be tilted relative to the solenoid magnet axis. The flanges connecting the target rod and spokes are also made of graphite, to allow it to be tolerant against radiation and heat. Figure 7.5 shows a prototype of the target support inner ring for Phase-I. The supporting ring of the prototype is made of steel, and the target and flanges are made of G10, which has similar density to that of graphite. This is simply because the prototype is intended to verify design details before fabricating the real target holder. As explained in Section 5, the target has to be tilted relative

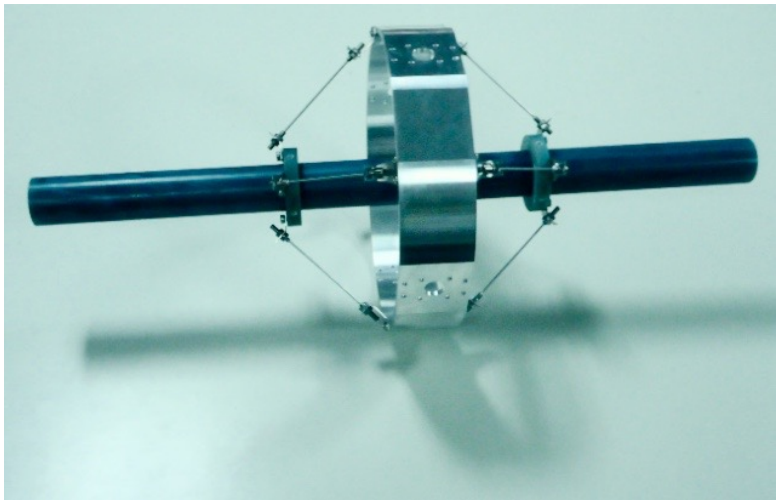

Figure 7.5: *Prototype of the target holder for Phase I with a dummy target made of G10.*

to the solenoid magnet axis to maximize the pion production yield. This is realised through the two-ring structure of the target holder. The outer ring is fixed to the magnet radiation shield with a rail system and the inner ring is tilted horizontally to align the target with the beam incident angle. Fine adjustment of the target vertical angle is realised by adjusting the lengths of the supporting spokes.

The remote handling system of the target support will be used to replace the Phase-I target with a high-Z target for Phase-II after Phase-I operation is completed. The remote handling system is also necessary in case of any unexpected failure of the target during Phase-I. The handling system is designed to be simple, to reduce any unpredictable failures caused by mechanical movement. Two rails on the inner wall of the radiation shield support the target holder from either side using metal wheels. Two additional rails with a V-shaped groove, located above and below the holder, support it and determine its position precisely both in the horizontal and vertical directions. The holder has four wheels with a rhombic cross-section on its top and bottom to fit these two rails. The groove of the V-shaped rail has larger width at the entrance and gradually narrows toward the centre of the magnet, This enables us to install the holder with sufficient position accuracy without difficulty. Two latches are prepared on each side (four latches in total) on the outer ring. These fix the target holder at the correct position. The remote handling system utilises similar latches to grasp and release the holder. When the target holder is inserted in the magnet, these latches are used by the holding arms of the remote handling system to grab the target holder. Once the holder is located at the correct position, four latches on the lateral sides fix the holder with more strength than that of the latches on the holding arms. Then, simply extracting the holding arm will release the target holder, leaving

it inside the solenoid magnet. When the target is extracted from the magnet, the holding arms are inserted and pushed further until they lock the holder at its edge for extraction. Figure 7.6 shows the prototype target holder with the holding arms. Figure 7.7 describes how the latches

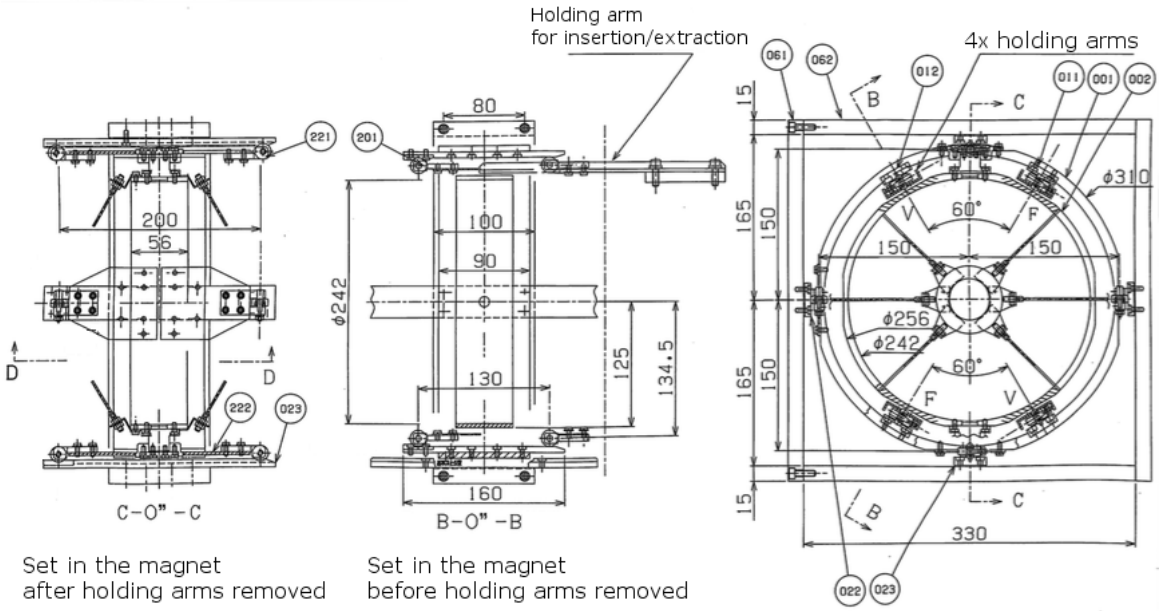

Figure 7.6: *The target holder prototype design with a holding arm insertion. 001: outer supporting ring, 002: inner supporting ring, 011&012: mating components for holding arm latches, 022: supporting rail, 023: V-shaped rail, 061&062: dummy wall of the radiation shield, 201: latch on a holding arm, 221: rhombic wheel, and 222: extension for the rhombic wheel.*

with different fixing strength work for installation and extraction of the target holder. Note that this prototype is a realistic model of the target holder for Phase-I and also for the Phase-II target with active cooling. This means that real holder construction can be carried out simply by replacing material used in the prototype with titanium and graphite once all motions and accuracies are confirmed.

The solenoid heat shield needs cooling even in Phase-I for efficient radiation cooling of the target; and the Phase-II target requires active cooling for stable operation. Therefore a cooling system using helium gas will be prepared in Phase-I. The system will be upgraded to cope with the higher beam power and larger heat deposit in the shield in Phase-II, which requires water cooling in a high radiation environment.

Property	Unit	Value
Density	(Mg/cm^3)	1.82
Hardness	(HSD)	55
Resistivity	($\mu\Omega$m)	9.2
Bending Strength	(MPa)	54
Compressive Strength	(MPa)	90
Coefficient of linear thermal expansion	$\times 10^{-6}$/K	4.8

Table 7.2: *Properties of IG-43.*

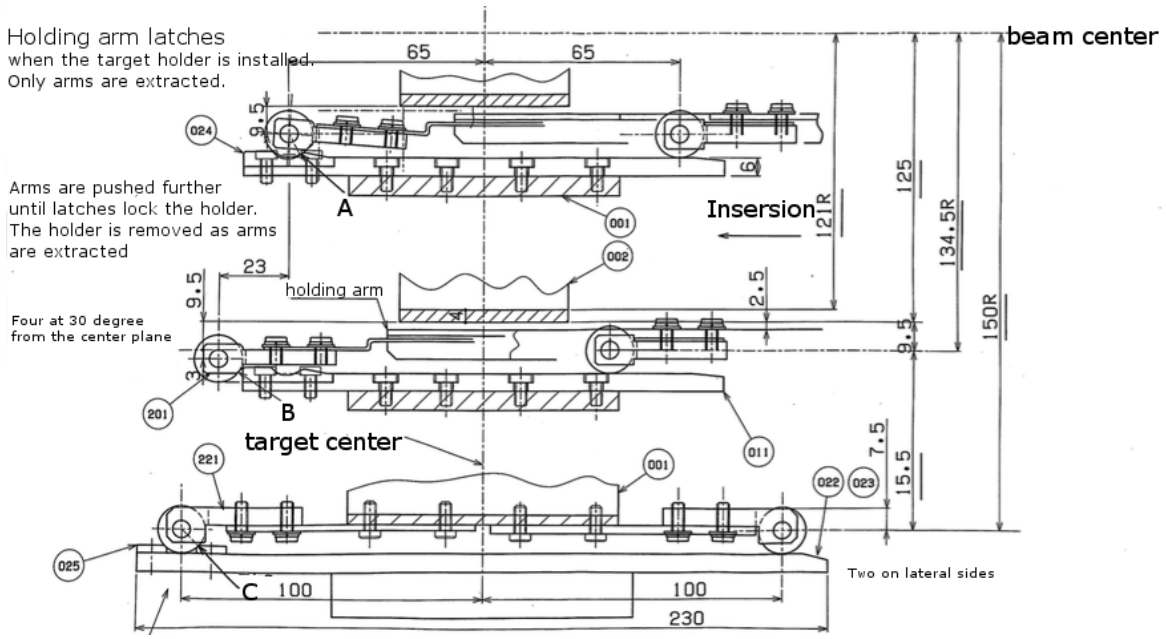

Figure 7.7: *Configuration of latches for target holder insertion and extraction. The strength of the latches are designed as A<C<B.*

Simulation Results

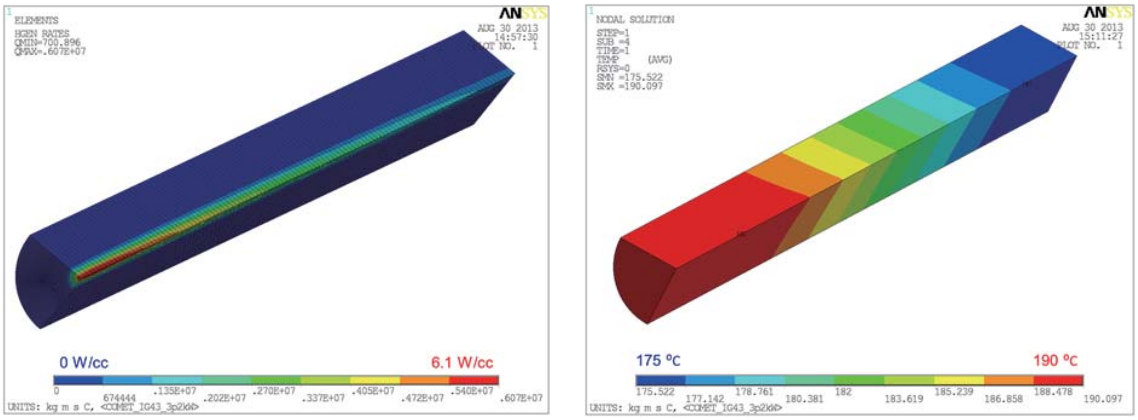

Figure 7.8: [Left] *Average heat load from an 8 GeV, 3.2 kW, proton beam with a Gaussian width of 2 mm in 4 cm diameter IG-43 graphite rod.* [Right] *Temperature distribution in IG-43 graphite rod for a material emissivity of 0.75.*

7.5. Possible degradations

The total number of protons interacting with the target for three months' operation at 3.2 kW is estimated to be 2.0×10^{19}. Possible degradation of the target material caused by the proton beam can be quantified by a factor called Displacement Per Atom (DPA). This factor expresses the number of carbon atoms displaced from their original location in the graphite molecules and is considered to be a good measure of the material degradation. For isotropic graphite such as IG-43, it is reported that the material size shrinks by 1% per DPA. Figure 7.9 shows an estimated DPA distribution in the graphite rod used in Phase-I for 8 GeV proton injection using the simulation code (PHITS [39]). The maximum DPA is located at the centre of the rod and is estimated to be 3×10^{-22} per proton on target. This corresponds to 6×10^{-3} DPA,

which is negligibly small for causing degradation of the target material property.

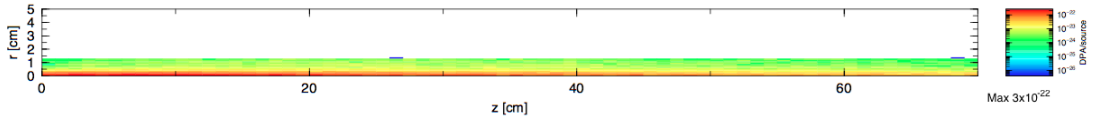

Figure 7.9: *DPA distribution in the r-z plane estimated using PHITS for 8 GeV protons injected into a graphite rod.*

Oxidization of the graphite is known to degrade the material strength. For example, the material strength is reduced by half after 4% oxidization. As described above, however, the target temperature during normal operation at Phase-I is estimated to be as low as 190 ^{o}C, which is well below the critical temperature of 400 ^{o}C where oxidization of graphite starts to become important. In addition, the COMET Phase-I target rod is located in a vacuum and thus the oxygen concentration around the target is extremely small as long as the vacuum level is maintained reasonably. Thus we can safely conclude that the COMET Phase-I target will be free from problems related to oxidization. Monitoring the temperature of the target and vacuum levels around the target will ensure that any failure of the target caused by oxidization can be avoided.

Tritium production in the graphite target is studied taking into account data for the production and release rates of tritium. According to [58] where tritium production by protons of about 12 GeV was studied, the production rate becomes independent of the incident proton energy above 2 GeV. It is also reported that the production rate has a dependence on the nuclear mass number as $\sigma(A) = 95 \times \exp(A/107)$ *mb* for heavy nuclei while a lower value of 55 *mb* is reported for aluminium (Figure 7.10). Here we take this number to make a conservative estimate for COMET Phase-I where graphite (carbon) is used as a target material. The amount of tritium produced in COMET Phase-I is estimated to be 5.9×10^{18} for a total number of protons on target of (2.0×10^{19}). This corresponds to 10.5 GBq if we ignore tritium decay during Phase-I running. It is known that release of tritium from graphite has a dependence on the graphite temperature. The maximum release rate from heated graphite is reported to be less than 5% at 870^{o}C [59] and less than 1% at 500K [60]. More precise measurements [61] indicate the diffusion coefficient of tritium in graphite is less than 10^{-12} cm$^2/s$ at 1000^{o}C. Crude estimates of the release rate indicates that 3.7×10^{14} tritium atoms will be released from the surface of the target in 10^7 seconds. In this case tritium produced in the COMET Phase-I graphite target will increase the tritium contamination level in the air of the primary beam line area by 0.0041 Bq/cc (supposing the air volume in the area of 160 m^3), which corresponds to about 1.9% of tritium directly produced in the air. Note that the temperature of the graphite target while COMET Phase-I operation is as low as 190 ^{o}C. Thus we can safely conclude that tritium produced in the graphite target by nuclear reactions will be contained in the target itself; the release of produced tritium in the target would contribute by maximum 1.9% to the air activation in the primary beam line area although this is for the unexpected case where the target temperature reaches 1000^{o}C for 10^7 seconds.

Another possible way in which the target can degrade is a decrease in its thermal conductivity, resulting in worse radiation cooling performance. A study exists on how much the thermal conductivity of the graphite decreases after proton irradiation [62]. Figure 7.12 shows changed in conductivity as a function of the radiation damage, in terms of DPA. It can be seen that the thermal conductivity reduces to below 15 % of the original after proton irradiation corresponding to 0.1 DPA. However, as already described, the damage will be as low as 6×10^{-3}DPA in COMET Phase-I, resulting in no significant decrease of the thermal conductivity.

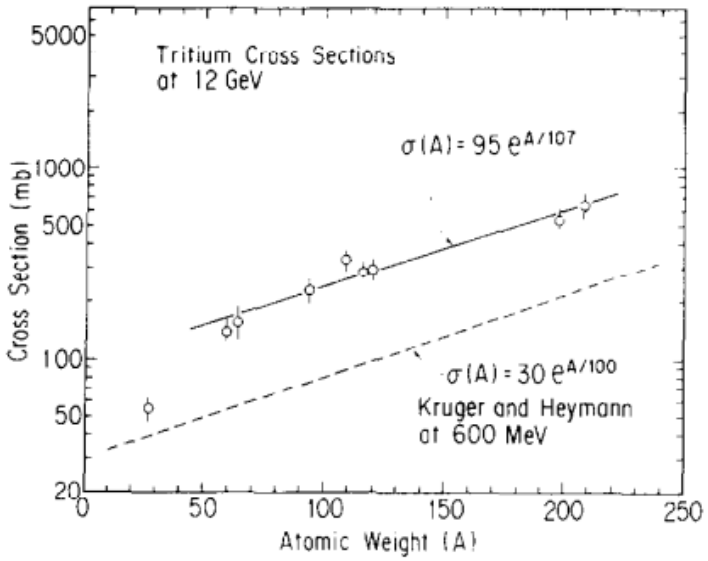

Figure 7.10: *Tritium production cross section as a function of target atomic mass number at 12 GeV. Taken from [58].*

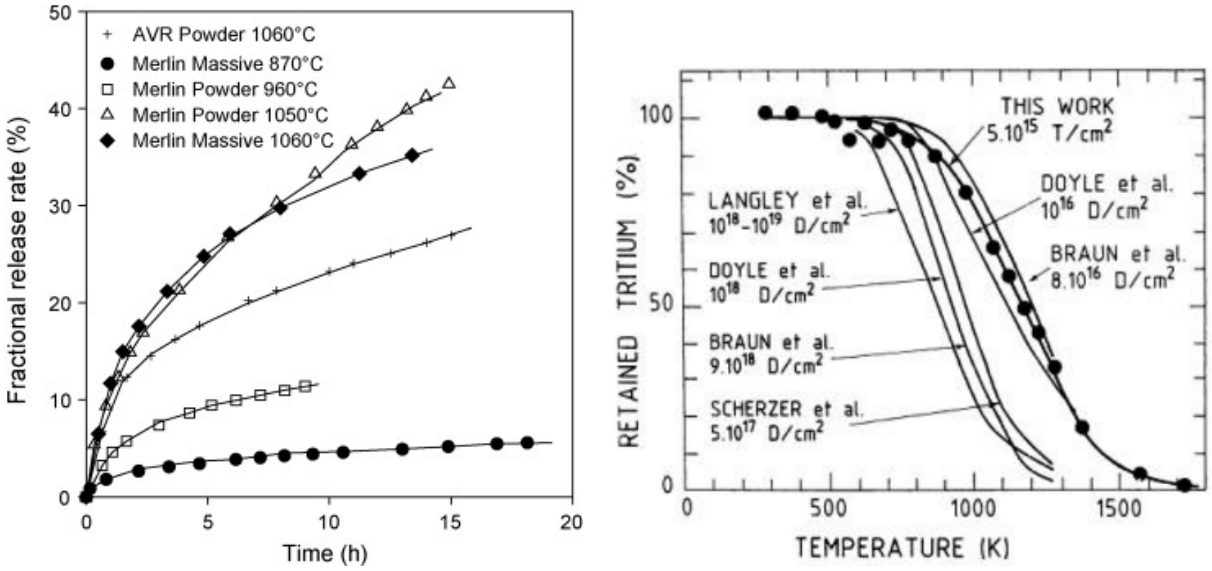

Figure 7.11: *(left) Release rate of tritium from graphite by thermal treatment. Taken from [59]. (right) Amount of implanted tritium trapped in the nuclear-surface of graphite as a function of annealing temperature. Taken from [60].*

7.6. Accident scenarios

7.6.1 Accidental fast-extracted beam pulses

One advantage of a graphite target is that it is a refractory material and so is tolerant to high temperature operation. The T2K target is helium cooled graphite with a deposited heat load of about 25 kW for the design beam power of 750 kW. The graphite experiences a temperature rise of around 100 K per fast extracted beam pulse of the 30 GeV beam during normal operation. This can be compared with an accidental fast beam extraction scenario for COMET. No adverse consequences are to be expected in this case, even for multiple pulses.

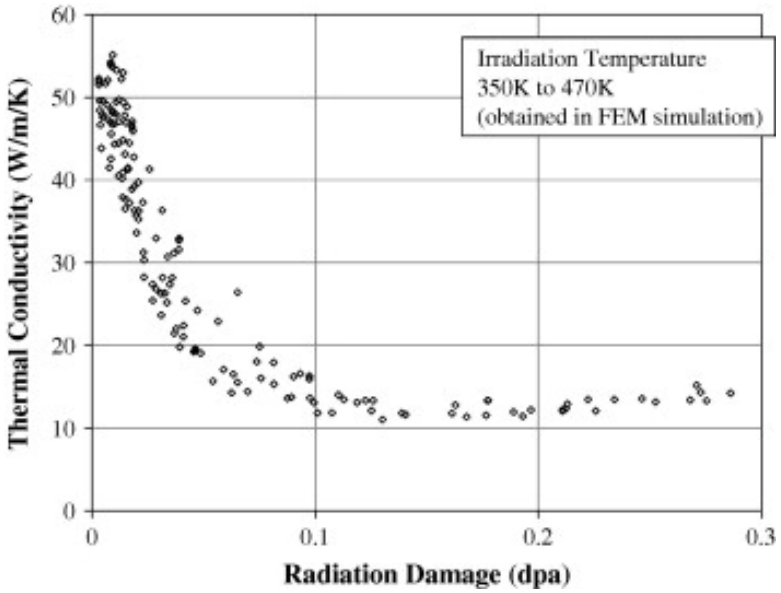

Figure 7.12: *Change of the graphite thermal conductivity as a function of radiation damage. Taken from [62].*

7.6.2 Loss of vacuum during operation

It is envisaged that the COMET target will be a bare graphite rod radiating the 100 W heat load in vacuum to the solenoid heat shield. Any sublimation or oxidation of the graphite would be extracted by vacuum pumping of the beam line. By comparison, the T2K target is housed within a metal canister which would contain any sublimation or oxidation of the material were this to occur. However, as described above, the COMET target is expected to run at a temperature well below the level where any oxidation would be a problem were the vacuum system to fail.

Risk mitigation: Due to the low heat load, it may be possible to contain the target within a thin metal capsule which would act to contain the graphite, protect it from oxidation and which would itself radiate the heat load to the solenoid radiation shield. An alternative that may be investigated is to coat the graphite with a refractory metal, e.g. tantalum or, preferably, iridium. As a further precautionary measure, the vacuum pump exhausts may be connected through a filter system to prevent the release of any material into the target station building.

Chapter 8

Muon Beam

The COMET Phase-I muon beamline consists of a section for pion production and capture (pion capture section), a section of muon transport (muon transport section) and a bridging section from the muon beamline to the detector (bridge section). These three elements are described in the following sections. At the 'downstream' end of the muon beamline is the detector solenoid. The schematic layout of the COMET Phase-I muon beam line is shown in Figure 8.1. It is noted that the muon beamline up to the end of the first 90° bend is also used for COMET Phase-II.

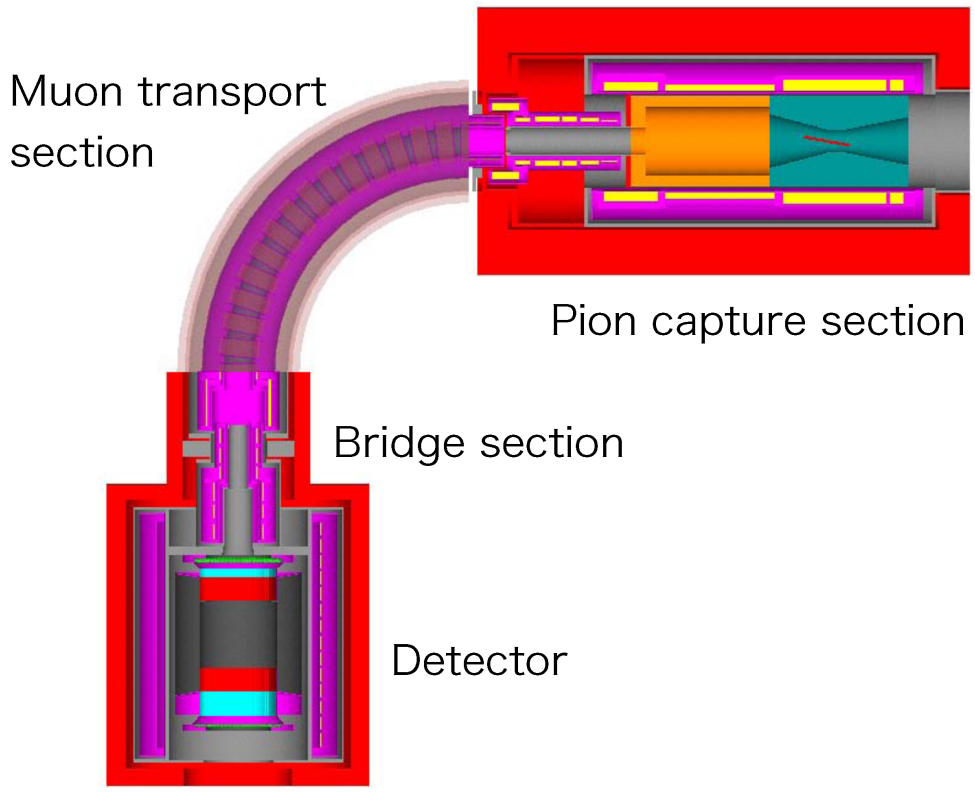

Figure 8.1: *Schematic layout of the COMET Phase-I muon beamline and detector*

8.1. Pion Collection

The COMET experiment uses negatively-charged low-energy muons, which can be easily stopped in a suitable thin target to efficiently produce muonic atoms. The low-energy muons are mostly produced by in-flight decay of low-energy pions. Therefore, the production of low energy pions is of major interest. Conversely, we wish to eliminate high-energy pions, which could potentially cause background events.

8.1.1 Pion Capture in a Solenoidal Magnetic Field

To collect as many pions (and cloud muons) of low energy as possible, the pions are captured using a high-strength solenoidal magnetic field giving a large solid angle acceptance. Figure 8.2 shows the layout of the pion capture system, which consists of the pion production target, high-field solenoid magnets for pion capture, and a radiation shield. In this case, pions emitted into the backward hemisphere can be captured within a transverse momentum threshold, $p_{\mathrm{T}}^{\mathrm{max}}$. This $p_{\mathrm{T}}^{\mathrm{max}}$ is given by the magnetic field strength, B, and the radius of the inner bore of solenoid magnet, R, as

$$p_{\mathrm{T}}^{\mathrm{max}}(\mathrm{GeV}/c) = 0.3 \times B(\mathrm{T}) \times \frac{R(\mathrm{m})}{2}. \tag{8.1}$$

A gradient magnetic field at the position of the proton target—which would cause some forward-going pions to be mirrored and captured—will not be used. Rather, the proton target is located at the position of the maximum magnetic field to maximise the solid angle for backward-going pions. The optimization of the magnetic field in the capture solenoid was performed by looking at muon yields at the exit of the transport solenoid located downstream of the capture solenoid magnet and at the muon stopping target. Note that most pions decay into muons as they pass through the transport solenoid magnet. It was found that the higher the pion capture magnetic field, the better the muon yield at the exit of the transport system. In addition, the beam emittance is better if a higher magnetic field is used for pion capture. Therefore a higher magnetic field is preferable. According to the simulation described in Section 7.1., placing $p_{\mathrm{T}}^{\mathrm{max}}$ at around $100\,\mathrm{MeV}/c$ would be sufficient. Furthermore, since we are interested in retaining muons with momentum below $75\,\mathrm{MeV}/c$, a solenoid magnet with a bore radius of 15 cm can accept most of the parent pions of these low-energy muons. Detailed optimization of the bore radius strongly depends on the available technology of the superconducting solenoid magnet. In our design, we employ conservative design values, namely of $B = 5\,\mathrm{T}$, and $R = 15\,\mathrm{cm}$.

8.1.2 Different Hadron Production Codes

In order to study the pion and muon production yields, different hadron production simulations were compared. A comparison of the predicted yields of π^- and μ^-, at three meters backwards from the proton target, using different hadron production codes is given in Table 8.1. It is found that there is a factor of 2.5 difference between different hadron production programs. Among them, the `QGSP_BERT` and `FTFP_BERT` hadron production models have the lowest yield. To make a conservative estimate, the `QGSP_BERT` hadron production model is used to estimate and optimize the muon beam.

Figure 8.3 shows the momentum distributions of various beam particles at the end of the pion capture solenoid, going towards the muon transport, produced by 8 GeV proton bombardment. This simulation used GEANT 4.9.6.p02 with `GEANT_QGSP_BERT_HP`, and the target length used is the optimised value of 70 cm.

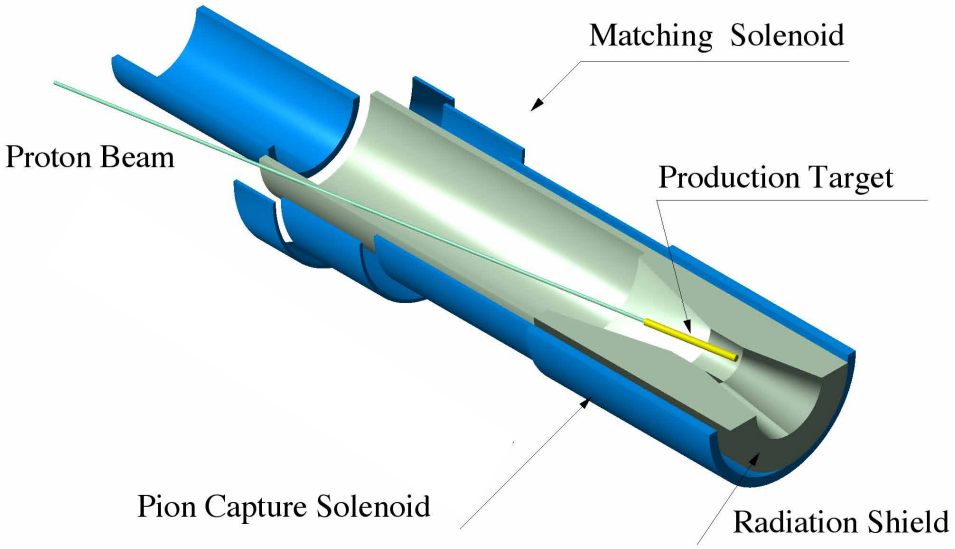

Figure 8.2: *Layout of the pion capture system, which consists of the pion production target (proton target), the pion capture solenoid magnets, and its radiation shield.*

Models	Geometry	N($\pi^- + \mu^-$)/p at 3 m
`MARS_CEM`	MARS	0.061 ± 0.001
`MARS_CEM/LAQGSM`	MARS	0.138 ± 0.001
`MARS_LAQGSM`	MARS	0.144 ± 0.001
`MARS_LAQGSM`	GEANT	0.1322 ± 0.0007
`GEANT_QGSP_BERT`	GEANT	0.0511 ± 0.0002
`GEANT_QGSP_BIC`	GEANT	0.1278 ± 0.0005
`GEANT_FTFP_BERT`	GEANT	0.0440 ± 0.0002

Table 8.1: *Comparison of the π^- and μ^- yields three meters away from the proton target for different hadron production codes. In our study of the muon yield estimation, `GEANT_QGSP_BERT` is used to ensure that estimates are conservative.*

8.2. Adiabatic Transition of Muon Beam

The pions captured at the pion capture system have a broad directional distribution. In order to increase the acceptance of the muon beamline it is desirable to make them more parallel to the beam axis by changing the magnetic field adiabatically. From the Liouville theorem, the volume in the phase space occupied by the beam particles does not change. Under a solenoidal magnetic field, the product of the radius of curvature, R, and the transverse momentum, p_T, is an invariant:

$$p_T \times R \propto \frac{p_T^2}{B} = \text{constant}, \tag{8.2}$$

where B is the magnitude of the magnetic field. Therefore, if the magnetic field decreases gradually, p_T also decreases, yielding a more parallel beam. This is the principle of the adiabatic transition. Quantitatively, when the magnetic field is reduced by a factor of two, p_T decreases by a factor of $\sqrt{2}$. On the other hand, since

$$p_T \times R \propto B \times R^2 = \text{constant}', \tag{8.3}$$

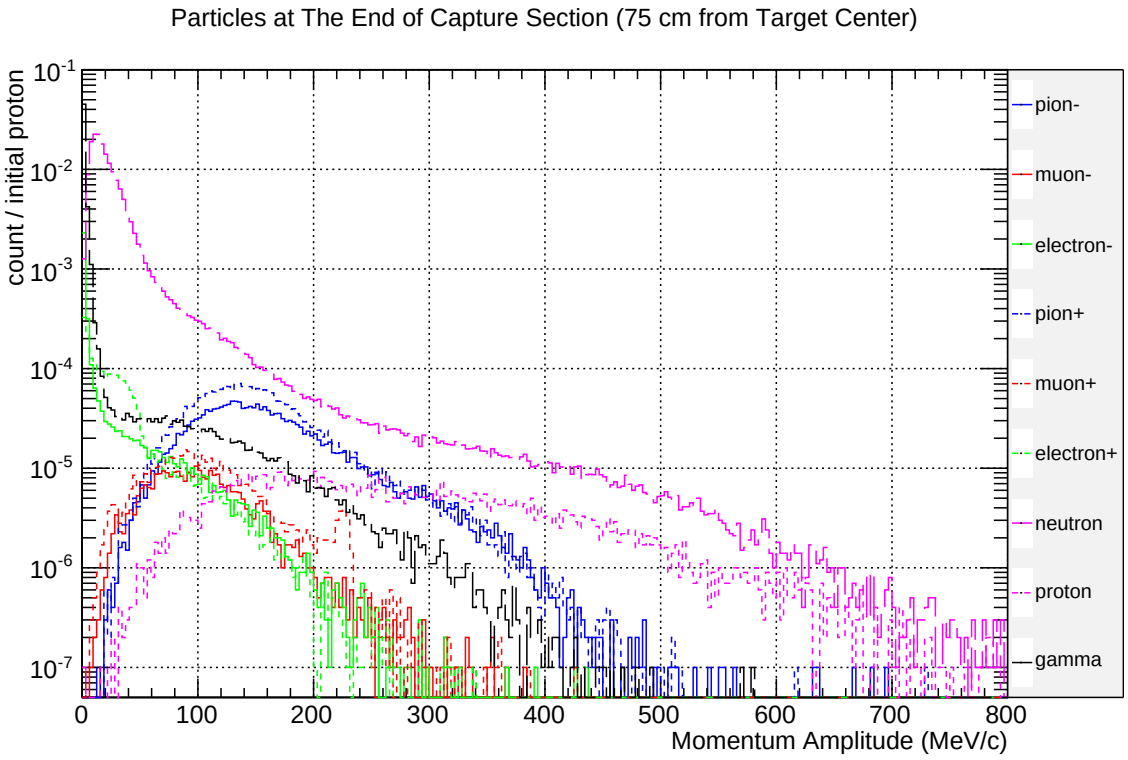

Figure 8.3: *Momentum distribution of various beam particles at the end of the pion capture solenoid section, moving to the muon transport section. For the hadron production,* `GEANT_QGSP_BERT` *was used.*

the radius of curvature increases by a factor of $\sqrt{2}$. Therefore, the inner radius of the magnet in the pion decay section has to be $\sqrt{2}$ times that of the pion capture solenoid. At the cost of an increased beam size, the pion beam can be made more parallel. Figure 8.4 illustrates the principle of adiabatic transition.

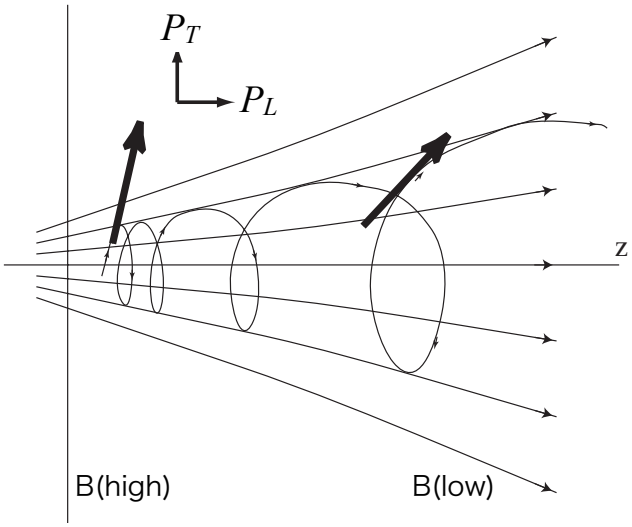

Figure 8.4: *Adiabatic transition from a high magnetic field to a low magnetic field. This adiabatic transition is executed by reducing the magnetic field. As a result, the magnitude of transverse momentum is reduced.*

8.3. Muon Beam Transport

Muons and pions are transported to the muon-stopping target through the muon beam transport, which consists of curved and straight superconducting solenoid magnets. The requirements for the muon transport section are

- the muon transport should be long enough for pions to decay to muons,
- the muon transport should have a high transport efficiency for muons with a momentum of ~ 40 MeV/c, and
- the muon transport should select muons with low momentum and eliminate muons of high momentum ($p_\mu > 75$ MeV/c) to avoid backgrounds from muon decays in flight.

The justification for the first of these criteria should be obvious. For muons to stop and be captured in the stopping target their momentum must not be too high, but it must be high enough that they make it to the target. This defines an optimal momentum to be around 40 MeV/c. Muons with higher momentum are less likely to be stopped, as well as giving rise to another background. Decays in flight of these muons produce electrons that are boosted in the lab frame, resulting in an electron background in the signal region near 105 MeV. Positive muons (which cannot be captured) are another potential source of background. In conjunction with momentum selection, a curved solenoid transport helps eliminate all these as described below.

The selection of an electric charge and momenta of beam particles can be performed by using curved (toroidal) solenoids, which makes the beam dispersive. A charged particle in a solenoidal field will follow a helical trajectory. In a curved solenoid, the central axis of this trajectory drifts in the direction perpendicular to the plane of curvature. The magnitude of this drift, D, is given by

$$D = \frac{1}{qB}\left(\frac{s}{R}\right)\frac{p_L^2 + \frac{1}{2}p_T^2}{p_L}, \tag{8.4}$$

$$= \frac{1}{qB}\left(\frac{s}{R}\right)\frac{p}{2}\left(\cos\theta + \frac{1}{\cos\theta}\right), \tag{8.5}$$

where q is the electric charge of the particle (with its sign), B is the magnetic field at the axis, and s and R are the path length and the radius of curvature of the curved solenoid, respectively. Here, s/R ($= \theta_{bend}$) is the total bending angle of the solenoid, hence D is proportional to θ_{bend}. p_L and p_T are longitudinal and transverse momenta so θ is the pitch angle of the helical trajectory. Because of the dependence on q, charged particles with opposite signs move in opposite directions. This can be used for charge and momentum selection if a suitable collimator is placed after the curved solenoid.

To keep the centre of the helical trajectories of muons with a reference momentum p_0 in the bending plane, a compensating dipole field parallel to the drift direction can be applied. If a compensating dipole field given by

$$B_{\text{comp}} = \frac{1}{qR}\frac{p_0}{2}\left(\cos\theta_0 + \frac{1}{\cos\theta_0}\right), \tag{8.6}$$

is applied, the trajectories of negatively charged particles with momentum p_0 and pitch angle θ_0 will be corrected to be on-axis.

The COMET Phase-I beamline uses one curved solenoid with a bending angle of 90°. To keep the centre of trajectory of the low energy muons, a compensating dipole field of about 0.05 T will be used.

8.4. Muon Beam Collimator System

In order to remove positive charged particles and high momentum particles that might contribute to backgrounds, particularly pions, while retaining as many muons as possible, a muon beam collimator system will be adopted. The system is required to remove particles traveling 8.5 cm above or 10 cm below the beam height. This can be realized by installing two plates made of stainless steel at the exit of the muon transport system, as displayed in Figure 8.5 (Left). [1]

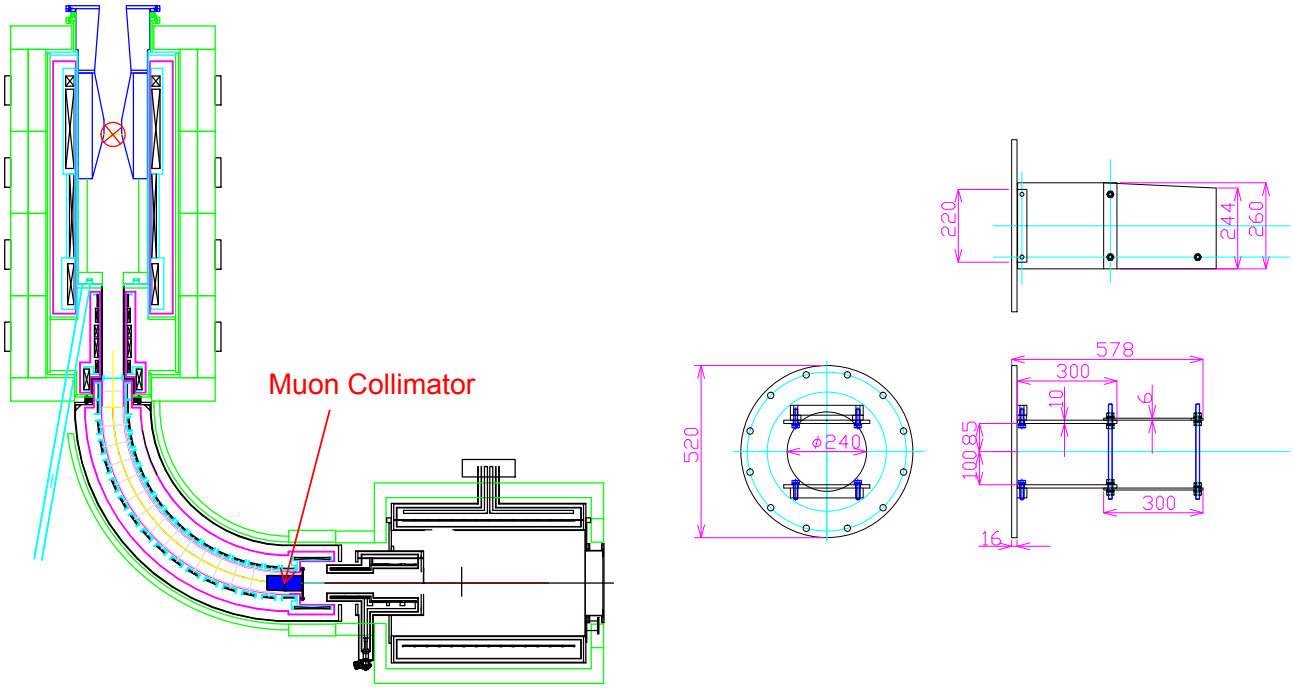

Figure 8.5: *Location (Left) and the dimension (Right) of the muon beam collimator.*

Mechanical design of muon beam collimator Two plates are placed 8.5 cm above and 10 cm below the beam height so as to form "ceiling" and "floor". The collimator has dimensions as displayed in Figure 8.5 (Right). Each plate can separate into two parts, root and head. The root part and the head part have thickness of 10 mm and 6 mm, respectively, in the current design. The total length of the collimator is 578 mm. By replacing the head part, it is possible to change the length and thickness of the collimator. The ceiling plate and floor plate are mechanically supported each other by connecting them with vertical bolts. The collimator is attached to the edge flange of the transport solenoid magnet. A total weight of about 30 kg of the collimator is acceptable for being supported by the magnet. A heat load due to interaction of beam particles with the collimator material is estimated to be much smaller than 1 W. It is small enough, in comparison to the acceptable additional heat load of 30 W of the cooling system of the magnet.

[1] It is noted that the mass production data of simulations (MC3) that were used for instance in the CyDet noise hate studies were produced based on the old design of the muon beam collimator. The old design consisted of eight vertical plates of 10 mm thick stainless steel from position of 55° from the entrance end of the muon transport to 85°, along the curved muon transport solenoids. It has been confirmed that the new and old designs have similar performance. The next mass production (MC4) will include the current collimator design described here, and when the MC4 data are available, the relevant plots will be replaced.

Momentum and arrival time distributions in the muon transport system The momentum distributions of various beam particles at the entrance and exit of the first 90° curved with the muon beam collimator are given in Figures 8.6 and 8.7 respectively. The arrival time distributions of various beam particles at the beginning and the end of the first 90° with the muon beam collimator are given in Figuress 8.8 and 8.9 respectively.

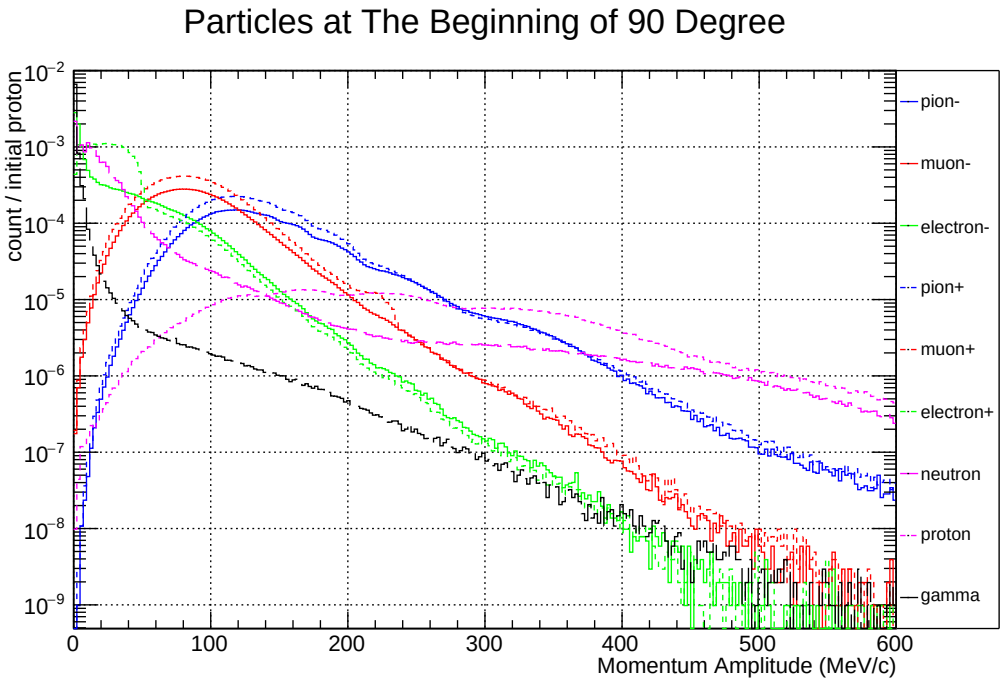

Figure 8.6: *Momentum distributions of various beam particles at the entrance of the first 90° curved solenoid, using a graphite proton target.*

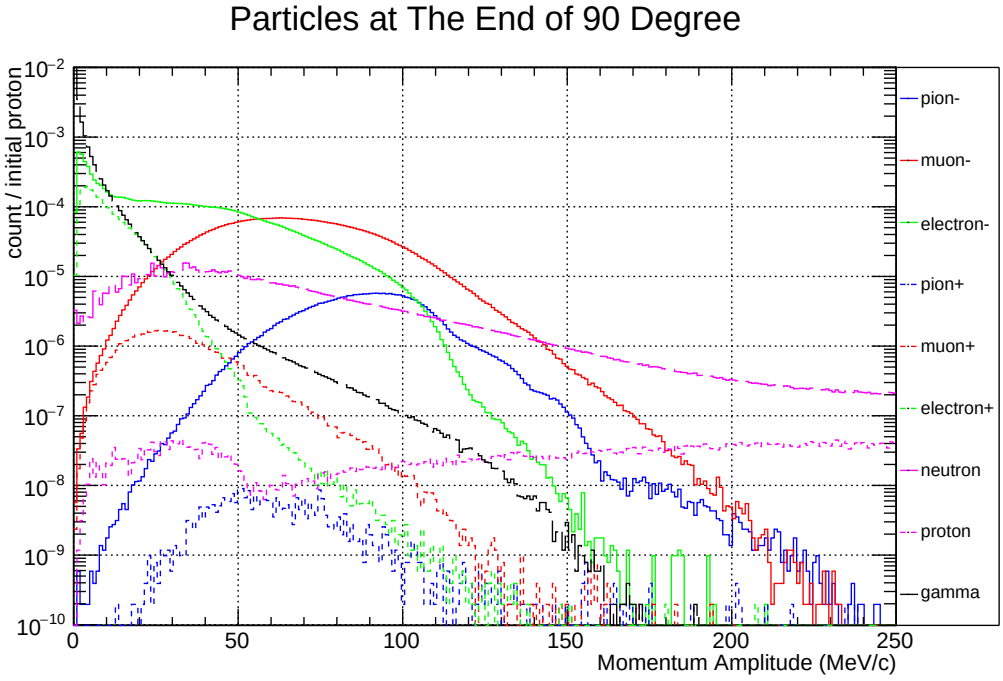

Figure 8.7: *Momentum distributions of various beam particles at the exit of the first 90° curved solenoid, using a graphite proton target.*

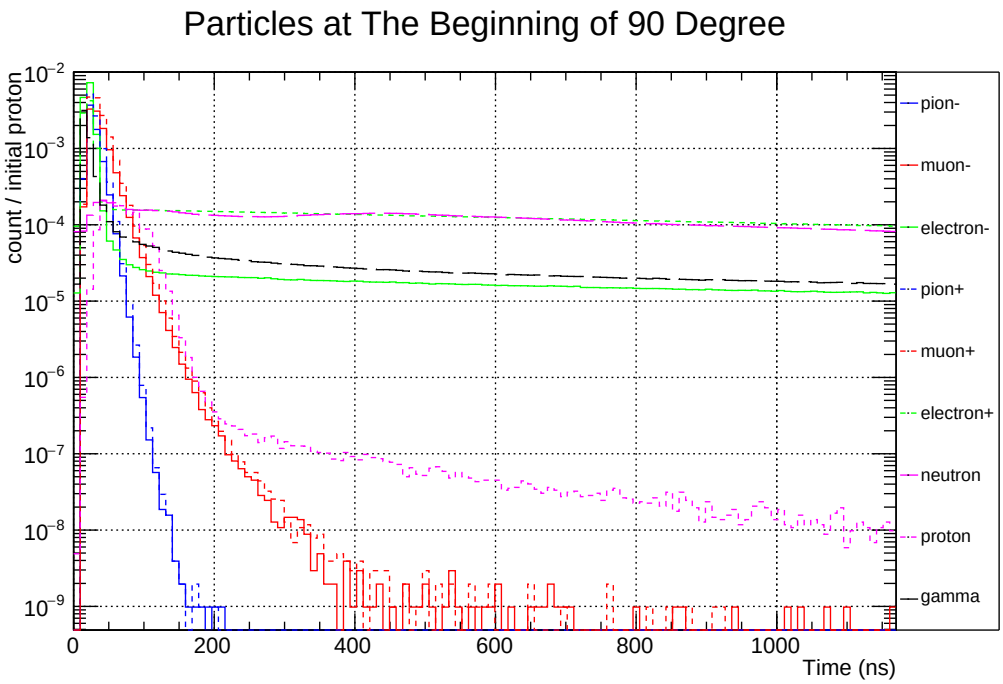

Figure 8.8: *Arrival time distributions of various beam particles at the entrance of the first 90° curved solenoid, using a graphite proton target.*

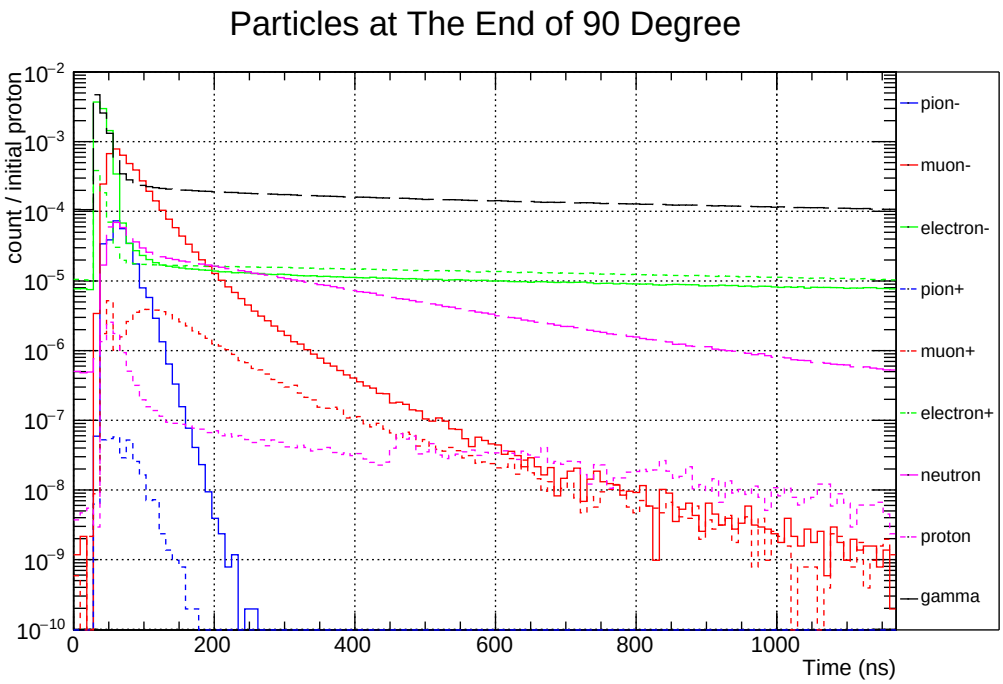

Figure 8.9: *Arrival time distributions of various beam particles at the exit of the first 90° curved solenoid, using a graphite proton target.*

The arrival time distributions of electrons and positrons have a long tail , giving almost uniformly. Figure 8.10 shows a relation between momentum and arrival time of electrons/positrons. It is found that they come from muons decay at rest in materials, as their maximum energy is 52.8 MeV. Therefore they are not harmful to cause backgrounds for the $\mu-e$ conversion search.

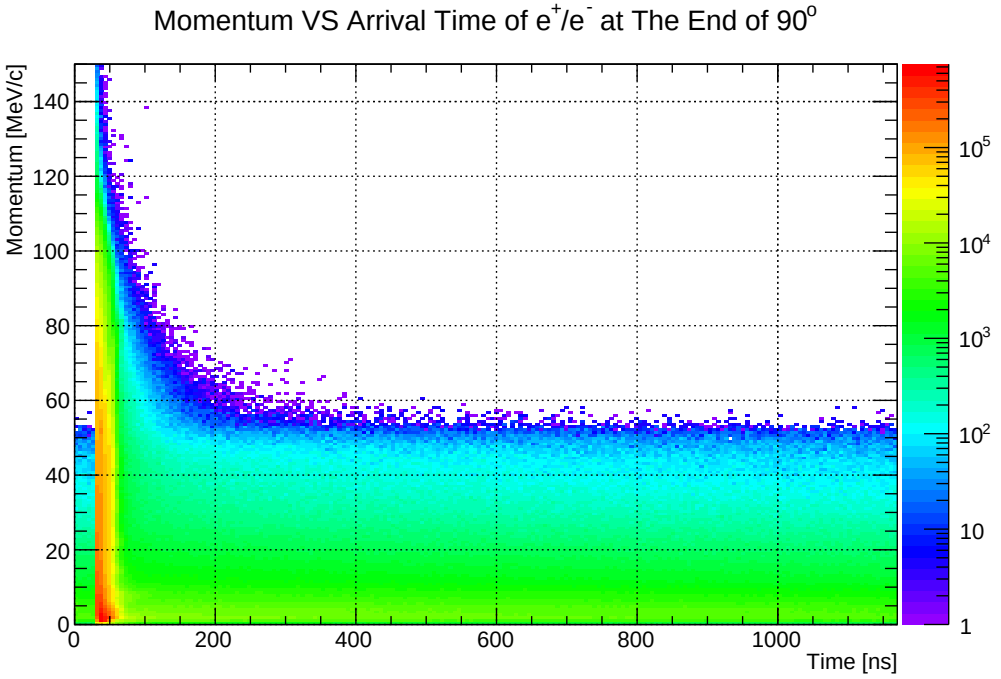

Figure 8.10: *Correlation between momentum and arrival time of electrons/positrons.*

In order to separate the muon stopping target region filled with helium gas from the muon beam line in vacuum, a vacuum window of 500 μm titanium will be installed at the exit of 90° curved solenoid. The muon transport section and the detector solenoid is connected through the beam bridge solenoid where the magnetic field is changed from 3 T to 1 T.

8.5. Muon Beam Yields

The yields of muons stopped on the muon stopping target are examined. The details of the muon stopping target is described in Chapter 10. Figure 8.11 shows the correlation between the vertical (y) positions versus momenta of the muons at locations upstream and downstream of the bridge section (BS), and at the muon stopping target. For the stopping target, the momentum distributions just before entering the target material of stopped muons are presented. Figure 8.12 shows the distributions of momentum (left), vertical (y) position (center), and arrival time (right) of the muons; where the solid black, blue and red lines are those upstream, downstream of the BS and on the muon stopping target, respectively

Figure 8.13 also shows the correlation between the vertical positions and momenta of the pions at the locations of in front of the BS, after the BS and on the muon stopping target.

Estimates using `QGSP_BERT` model of the number of muons and pions per proton with a graphite target in front of the BS, after the BS and on the muon stopping target are summarized in Table 8.2. For instance, the number of muons stopping in the muon stopping target is about 4.7×10^{-4} per proton. With a 0.4 μA proton beam, the yield of stopped muons is about 1.2×10^{9} per second. It is noted that titanium safety windows will be installed inside the muon beamline. The first window is placed in front of the muon transport section, and the second window is placed at the end of the muon transport section. Both are 500 μm thick.

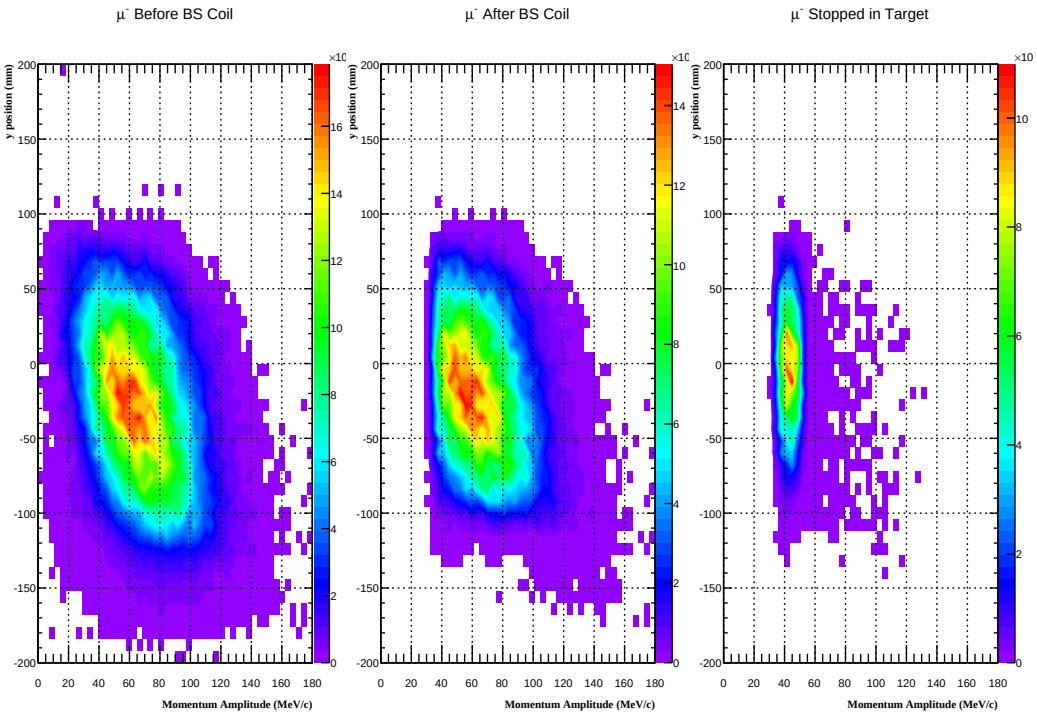

Figure 8.11: *Correlations between vertical locations and momenta of muons in front of the bridge section (BS), after the BS, and on the muon stopping target.*

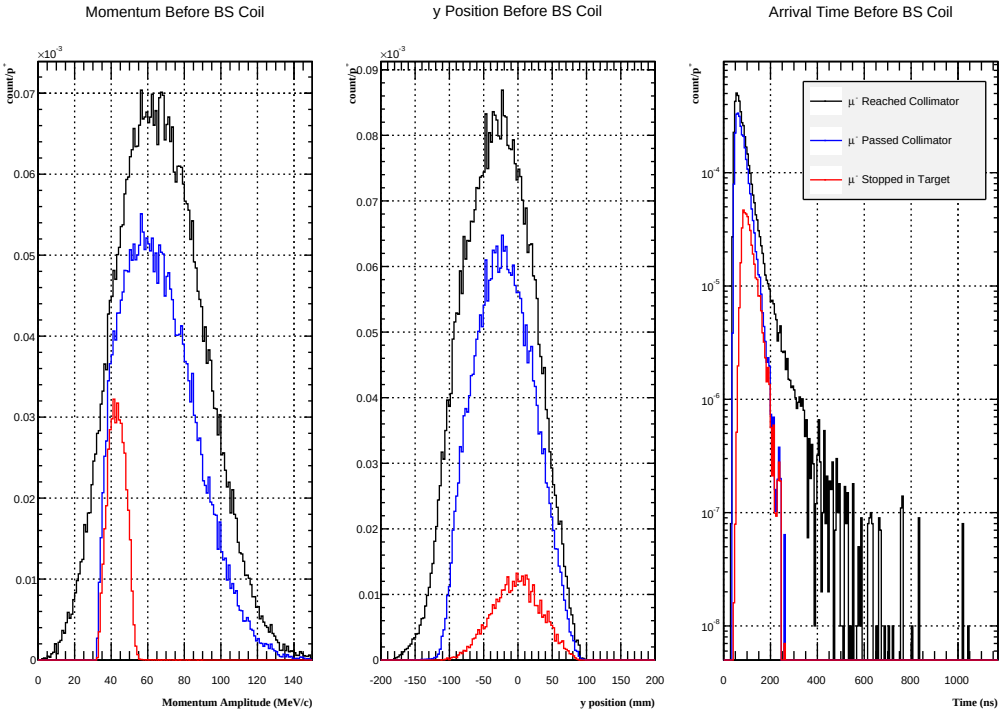

Figure 8.12: *Distributions of momentum (left), vertical (y) position (center), and arrival time (right) of muons. Black, blue and red solid lines are those in front of the BS, after the BS, and on the muon stopping target, respectively.*

Some muons are stopped and lost in these safety windows. However, given the improvement of

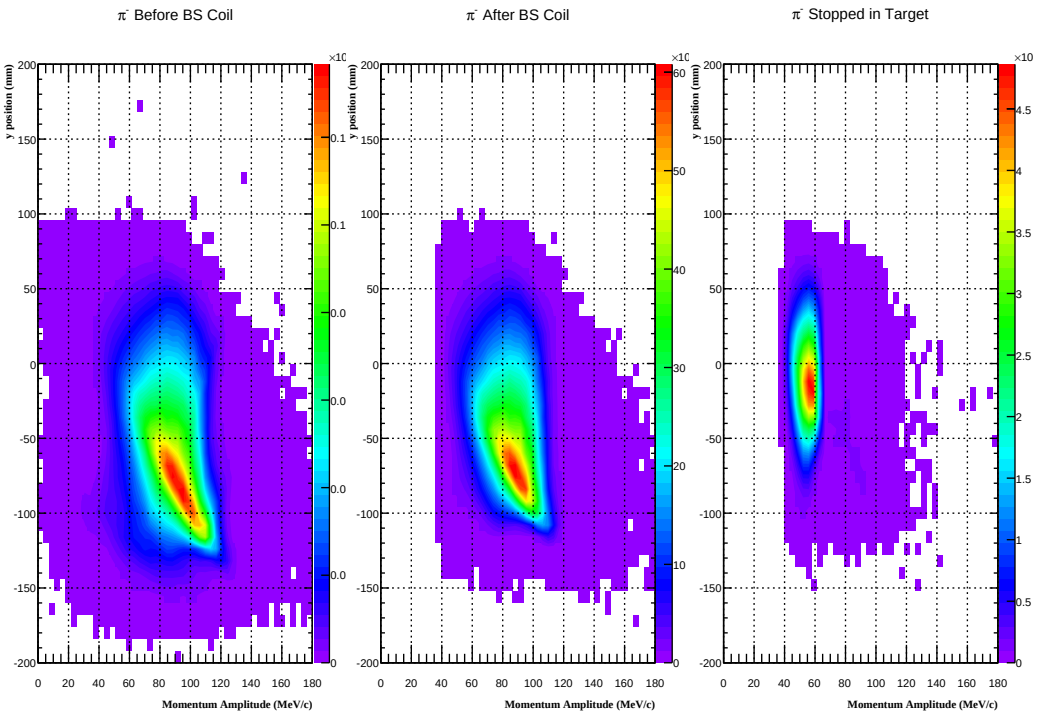

Figure 8.13: *Correlations between vertical locations and momenta of pions in front of the bridge section (BS), after the BS, and stopped in the muon stopping target.*

safety, the reduction of muon yield is acceptable.

Yield (per proton):	In front of BS	After BS	Stopped in muon target
Muons	7.4×10^{-3}	3.0×10^{-3}	4.7×10^{-4}
Pions	6.7×10^{-4}	5.5×10^{-5}	3.4×10^{-6}

Table 8.2: *Muon and pion yields per proton in front of the BS, after the BS, and stopped on the muon stopping target.*

Chapter 9

Superconducting Solenoids

The muon beam line for COMET Phase-I comprises the pion capture solenoid section (CS = capture solenoids) and the muon transport solenoid section (TS = transport solenoids), as well as a set of matching solenoids (MS = matching solenoids) between CS and TS, which are shown in Figure 9.1. Each section is composed of several separate superconducting coils, each of which is identified with an additional number e.g. CS1. In addition, the superconducting solenoid that provides a magnetic field at the detector location (DS = detector solenoid is needed. The solenoid magnets (BS = bridge solenoids) between the TS and DS solenoids is also placed to make the magnetic field smooth in field strength.

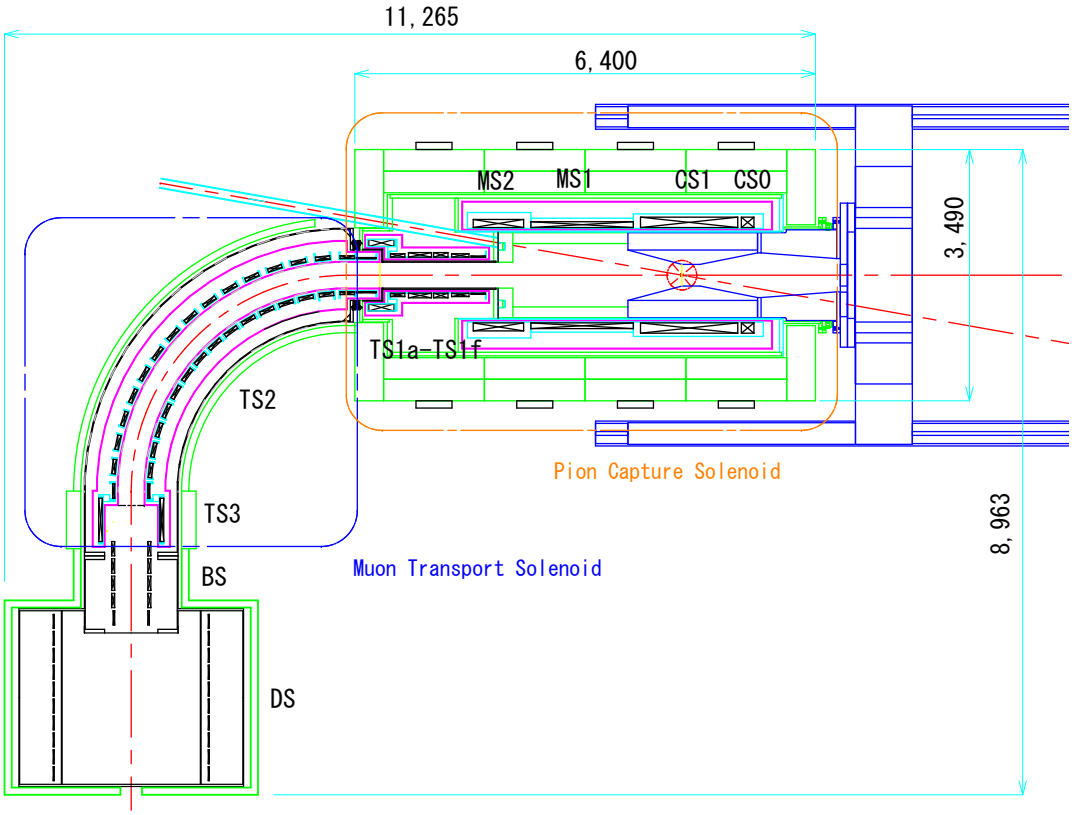

Figure 9.1: *A schematic view of the superconducting solenoid magnet system for COMET Phase-I, with coil names indicated.*

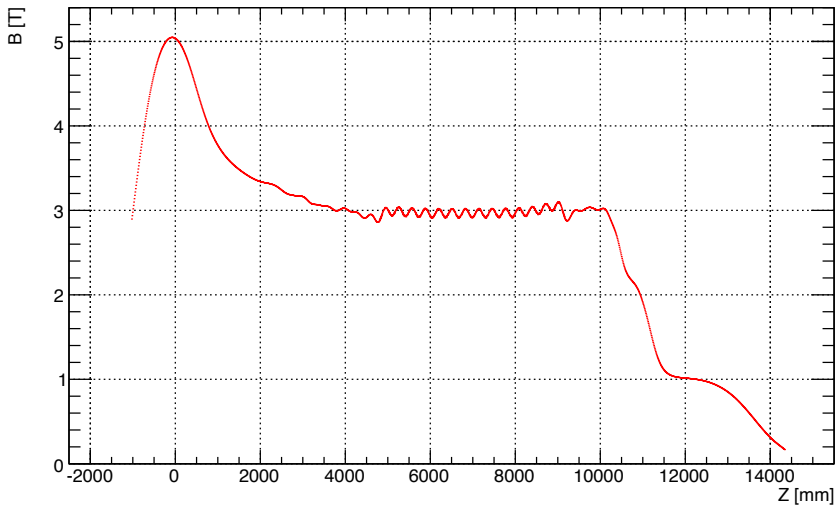

Figure 9.2: *Magnetic field strength along the beam axis for COMET.*

9.1. Pion Capture Solenoid

The pion capture solenoid is of critical importance for capturing pions from the proton beam target with a large solid angle, and transporting muons from pion decays to the muon stopping target efficiently. The muon beam line for a $\mu^- N \to e^- N$ conversion search must be long so that the number of pions in the beam, which can cause serious backgrounds for the search, is reduced through decays in flight. For COMET Phase-I, the COMET muon beamline up to the end of the first 90° bend will be constructed, as shown in Figure 9.1. The magnetic field along the beam axis is shown in Figure 9.2. The magnetic field should be smooth without any dips to prevent the trapping of, and to minimise the loss of, charged particles.

The pion capture solenoids comprise coils CS0, CS1, MS1, MS2 and TS1 and are shown in Figure 9.1. TS1 is itself composed of many coils such as TS1a, TS1b, TS1c, TS1d, TS1e, and TS1f. Strictly TS1 is part of the transport solenoid section but its coils will be situated in the same cryostat as the CS and MS and they are therefore treated as part of the pion capture solenoid system here. The strong field on the proton target is generated mainly by the CS. The coils, MS1 and MS2, function to reduce the field smoothly from the target to the muon transport solenoid section.

In the pion capture solenoid section, a magnetic field of 5 T along the direction of the solenoid axis is needed at the location of the proton target to capture the low energy pions. The magnetic field is adiabatically reduced down to 3 T in the matching solenoid section and a field of 3 T is maintained throughout the TS.

The coil layout of the pion capture solenoid system is shown in Figure 9.3. The specification of each of the coils in the system is summarized in Table 9.1. All of the superconducting coils in the pion capture solenoid are electrically connected in series with the same electric current provided by a single power supply. Aluminium-stabilised conductors will be used on all coils to reduce the heat load and radiation damage caused by secondary particles emerging from the proton target. Most coils will use the same superconductors, but the superconductors will have

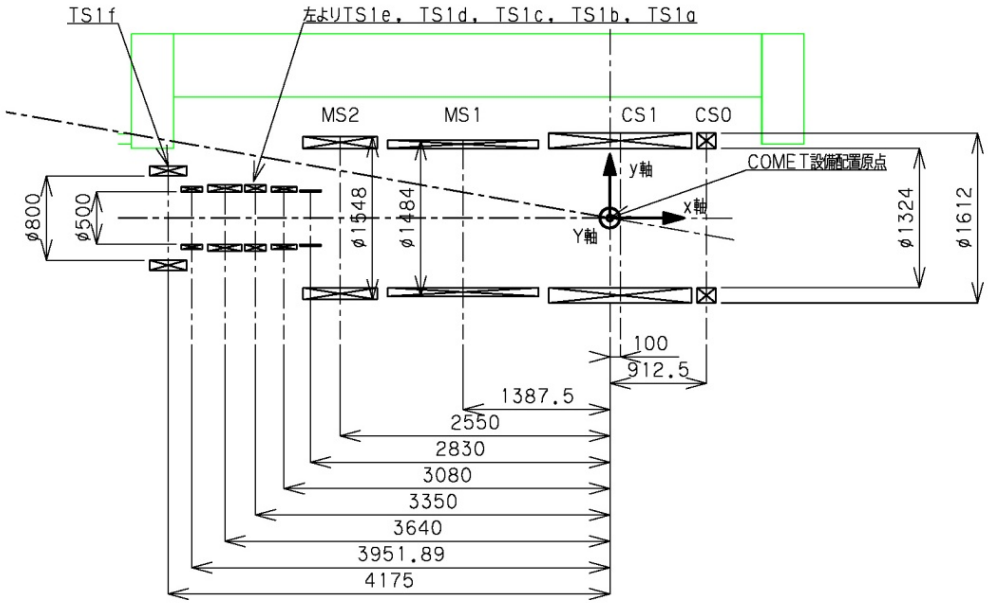

Figure 9.3: *Layout of the pion capture solenoid system.*

different keystone angles optimized for the size of coils.

Table 9.1: *Coil specifications for the pion capture solenoid system for COMET.*

Name	B_z (T)	Inner radius (mm)	Outer radius (mm)	Length (mm)	Current (A)	Current Density (A/mm^2)
CS0	4.0	662	806	175	2700	33.75
CS1	5.0	662	806	1350	2700	33.75
MS1	4.0	662	742	1425	2700	33.75
MS2	3.0	662	774	700	2700	33.75
TS1a	3.0	250	266	200	2700	33.75
TS1b	3.0	250	298	240	2581	32.26
TS1c	3.0	250	314	200	2700	33.75
TS1d	3.0	250	314	200	2619	32.74
TS1e	3.0	250	298	200	2538	31.73
TS1f	3.0	400	496	350	2916	36.45

9.1.1 Electromagnetic Forces

A simple solenoid coil is subject to hoop stress and a compressive force as it is magnetically excited and these forces are additive across all the coils. Previous studies have shown that the compressive force at the CS is 33 MPa and that at MS1 is 39 MPa. We will therefore place a flange (rib) between CS0 and CS1 so that the compressive force is reduced by the supporting shell structure which is installed at the outer edge of the CS. A flange will also be installed between CS1 and MS1. These modifications will ensure the compressive forces are reduced to less than 18 MPa. The von Mises stress in the coils has a peak of 55 MPa at CS1 as shown in Figure 9.4.

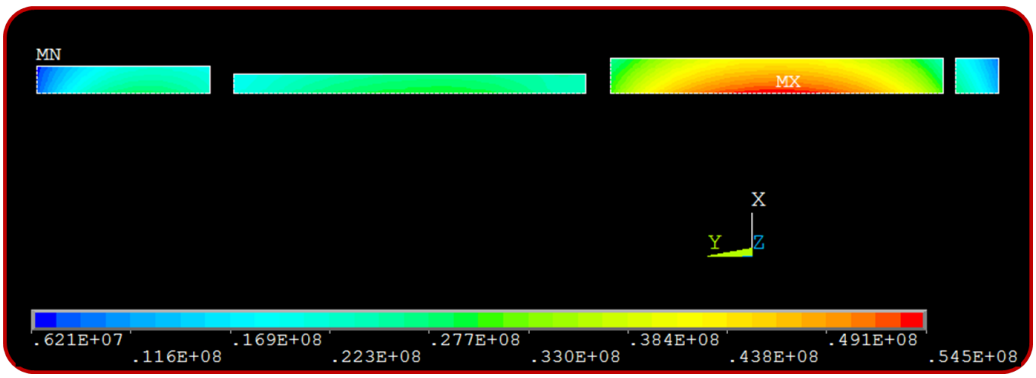

Figure 9.4: *Von Mises stress in coils of the pion capture solenoid.*

9.1.2 Radiation Heating Load

The pion capture solenoid system is subject to the radiation heat load (from both neutral and charged particles) from the proton target and the normal heat load of the cryostat and the heat load due to eddy currents when the magnet is either excited or de-excited. A radiation shield composed of copper and tungsten will be installed inside the cryostat of the pion capture solenoid system to reduce the radiation damage from the proton target. The total weight of the shield is 43 tons, and the shield is cantilevered by a supporting structure located at the end of the capture solenoid and inserted into the solenoid along rails. Deformation of the supporting structure is estimated to be less than 5 mm, from finite element analysis studies as shown in Figure 9.5. The radiation shield will be water-cooled. Figure 9.6 shows the heat loads of the pion capture solenoid system.

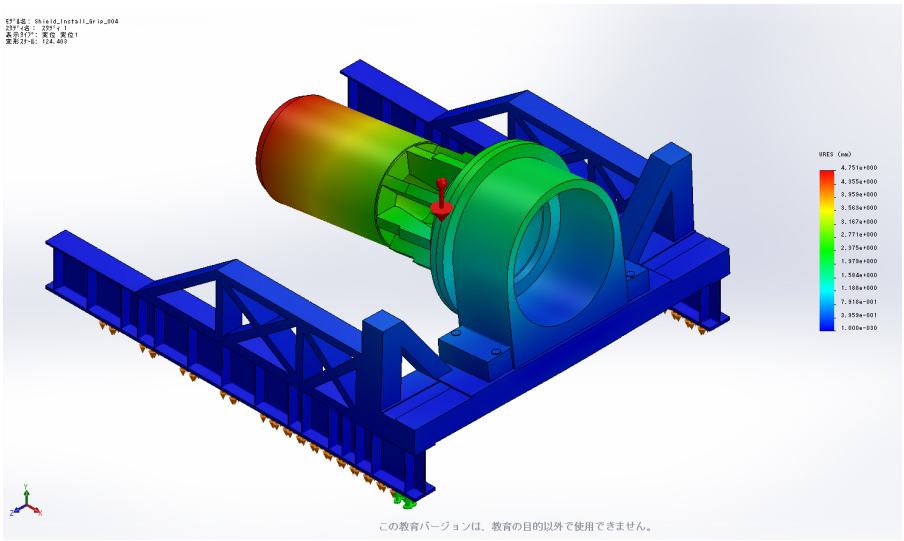

Figure 9.5: *Deformation of the radiation shield supporting structure estimated by finite element analysis.*

9.1.3 Indirect cooling of Superconducting Coils

Estimates of the heat loads for each coil in the pion capture solenoid system are shown in Table 9.2 for the cold mass. Aluminium cooling pipes are welded on to the outward surface

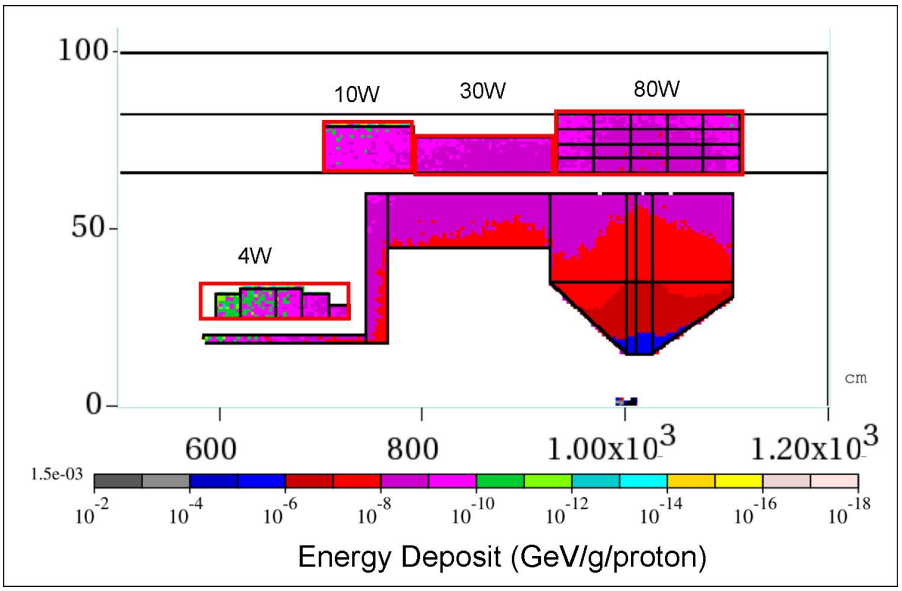

Figure 9.6: *Heat loads in the pion capture solenoid system. The plot shows a cross section in the radial plane with Z and R on the x and y axes. The colour shows the energy deposited per g per proton.*

of the supporting shell cylinder. Two-phase helium flows inside the aluminium cooling pipe. The heat load from the proton target radiation is cooled by aluminium cooling plates inserted between the coil layers.

Table 9.2: *Heat loads of the pion capture solenoid system at the cold mass (at 4 K).*

Heat load type	Heat load path	Heat load (W)	Comments
Thermal radiation	radiation	3.3	0.05 W/m^2
Supports	conduction	9.05	
Residual gas	conduction	0.16	
AC loss	eddy current	4.00	
Nuclear heating	radiation	6∼30	120 at Phase-II

An indirect cooling method is adopted as the primary method to cool the coils down to their operating temperature. This eliminates the need for a cryostat with a large liquid helium dewar, which is extremely beneficial in a high radiation environment. In normal indirect cooling, superconducting coils are cooled from the outer radial peripherals of the coils using cooling pipes with flowing coolant inside. This is not sufficient for COMET's needs particularly for the inner coil layers at small radii. Therefore additional cooling plates made of aluminium will be inserted between the coil layers. The cooling plates come out from both ends (upstream and downstream) of the coil, and connect (in a direction parallel to the ends of the coil) to the outer radii of the coil, where they are in thermal contact with the cooling pipes. Figure 9.7 shows a schematic view of the coil support shell with aluminium cooling plates at the ends.

9.1.4 Power Supply and Quench Protection

The power supply for the pion capture solenoid system consists of a main 2700 A power supply augmented with four additional power supplies of 250 A (maximum) for trim currents. When a

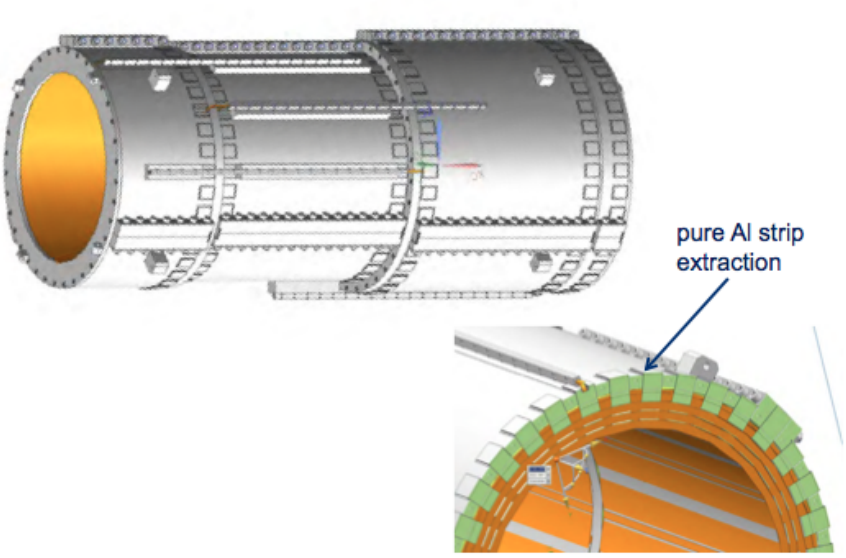

Figure 9.7: *Schematic view of the coil support shell. Aluminium cooling plates for efficient cooling will be in thermal contact with the cooling pipes.*

quench is detected, all the power supplies are shut down, and the energy stored in the magnets is dissipated in an external resistance.

9.1.5 Procurement plan

The bid for procurement of the aluminium-stabilised superconductors has already been made. The design contract of the pion capture system was accepted by Toshiba Co. in JFY 2013. Toshiba Co. has built one of the TS coils (TS1a) and a winding machine in 2014. The construction of the rest of the pion capture solenoids will be carried out at the KEK machine shop with assistance from the KEK cryogenics group using the Toshiba winding machine.

9.2. Muon Transport Solenoid

The muon transport solenoids for COMET Phase-I are those up to the end of the first 90° bend. Their layout is shown in Figure 9.8. They include the TS2 and TS3 as described in Figure 9.1[1]. TS2 and TS3 are composed of 17 superconducting coils and one coil, respectively. The first of the TS2 coils is named TS2-a, and the rest are named from TS2-1 to TS2-16. TS2 is the superconducting solenoid forming the 90° bend, which has a radius of curvature of 3 m. Each coil in TS2 spans about 6°. In TS2, a dipole coil is used to correct for the vertical beam shift owing to the curved nature of the solenoid. This vertical dipole field is parallel to the drift direction of charged tracks in curved solenoids. Table 9.3 shows the dimensions of the coils and the estimated electromagnetic forces for TS2 and TS3. The dipole field needs to be no stronger than 0.07 T. The integrated magnetic field should be 0.013 T·m over the region ±500 mm from the centre along the horizontal axis.

[1]TS1 is treated as part of the Pion Capture Solenoid

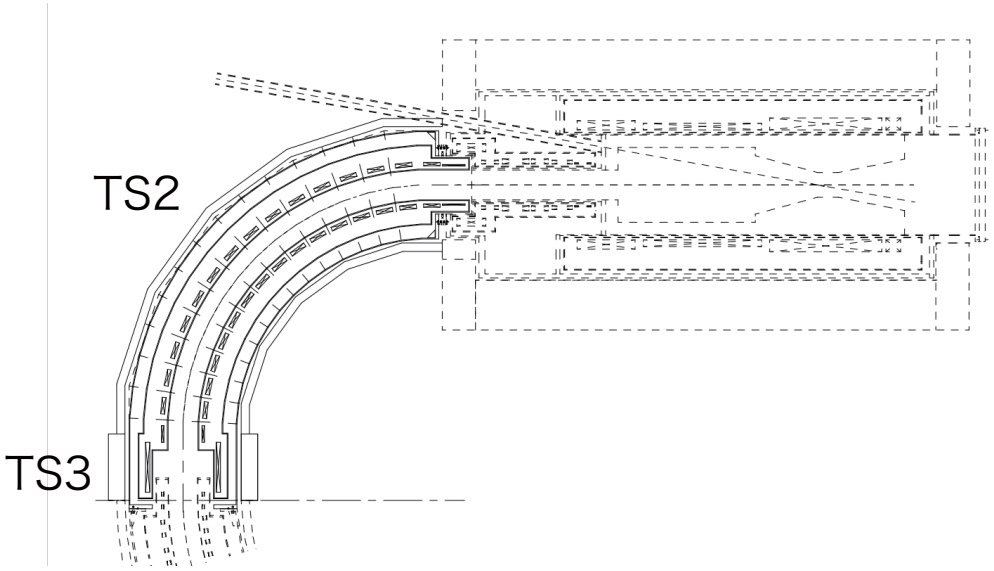

Figure 9.8: *Layout of the muon transport solenoid system (TS2 and TS3) for COMET Phase-I.*

Table 9.3: *Coil specifications for the muon transport solenoid system for COMET.*

Name	B_z (T)	B_y (T)	Length (mm)	Inner radius (mm)	Outer radius (mm)	Current (A)	Current density (A/mm^2)	Bore radius
TS2a	3	NA	255	234	249	210	72	180
TS2-1	3	0.06	205	234	264	210	95	180
TS2-2 to 15	3	0.06	205	234	272	210	95	180
TS2-16	3	0.06	205	234	254	210	94	180
TS3	3	NA	600	400	437	190 (210 in Phase-II)	85.5 (95 in Phase-II)	180

9.2.1 Radiation Resistance

The muon transport solenoid system will be exposed to a maximum radiation dose of 0.2 MGy and a neutron flux of 10^{20} $m^{-}2$ in COMET Phase-II. Both TS2 and TS3, constructed for COMET Phase-I, will be used as the first 90° of the bent solenoid in Phase-II. Polyimide, instead of polyethylene, should be used as the thermal insulator and any other organic materials deployed need to be radiation tolerant. Epoxy glues can be used with radiation levels of up to 1 MGy. The supporting structures will be made from Titanium alloy. All the lead wires such as those monitoring voltages will have polyimide jackets.

9.2.2 Cooling of Superconducting Coils

The superconducting coils in TS2 and TS3 are cooled indirectly using liquid helium. The 25 mm diameter cooling pipes are attached to the coil. Two-phase helium flows inside the cooling pipe with a flow rate of 7 g/s to 10 g/s. The cooling pipes are installed from the downstream end of TS2 through to its chimney. Radiation heating at TS2 is expected to be rather modest (0.01 W/kg at maximum); however, normal heating from the outside also has to be accommodated.

Total heat loads of 8 W at 4 K and of 120 W at 70 K are expected.

9.2.3 Power Supply and Quench Protection

A current of 210 A powers the muon transport solenoids. When a quench is detected, the power supply is shut down, and the heaters attached to each coil are used to force a quench in the non-quenched coils to prevent load heating (hot spot heating).

9.2.4 Cryostat Structure and Support for Radiation Shielding

The coils from TS2a to TS3 will be placed in a single cryostat. The cryostat will have a flange structure so that it can be connected to the cryostat of the pion capture solenoid system, as well as the downstream TS in COMET Phase-II. The cryostat of the muon transport system will have a cold bore and contain a stainless steel beam duct of 10 mm thickness for the muon beam. The heat loss from charged particles hitting the duct wall is expected to be about 0.2 W per kg. The beam duct will therefore be cooled by the flow of helium as well as being protected by thermal shields.

9.2.5 Construction

The bid for the construction of the muon transport system for COMET Phase-I was assigned to Toshiba Co., who have completed the construction of the TS. It was installed at the COMET experimental hall at J-PARC in 2015. A photograph of the installation of the TS magnet system is shown in Figure 9.9.

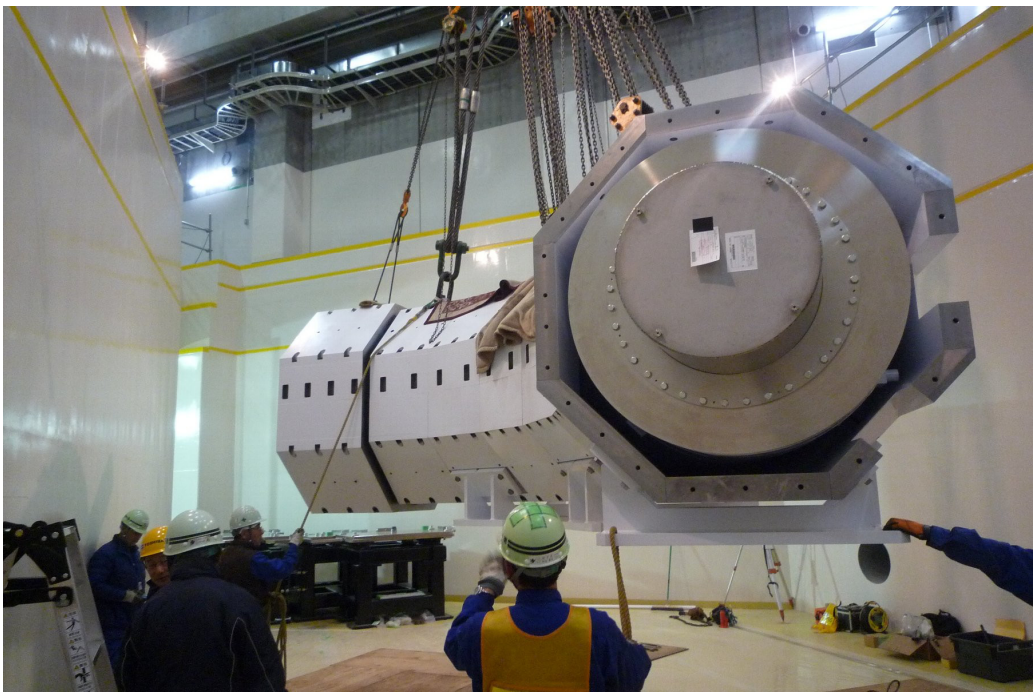

Figure 9.9: *Installation of the TS solenoid system*

9.3. Bridge solenoid

The bridge solenoid is a 1 m long superconducting magnet connecting the end of the muon beam line to the detector solenoid. It has a warm bore to allow for the gaseous helium in the CDC. It is being designed in collaboration with an external vendor. Figure 9.10 shows the magnetic field distribution calculated using the TOSCA magnetic field calculation program at the region of the bridge solenoid and the detector solenoid. The top figure in Figure 9.10 shows the schematic layout of the corresponding locations in the cross-sectional view of the bridge solenoid and detector solenoid, with muon beam trajectories in pink.

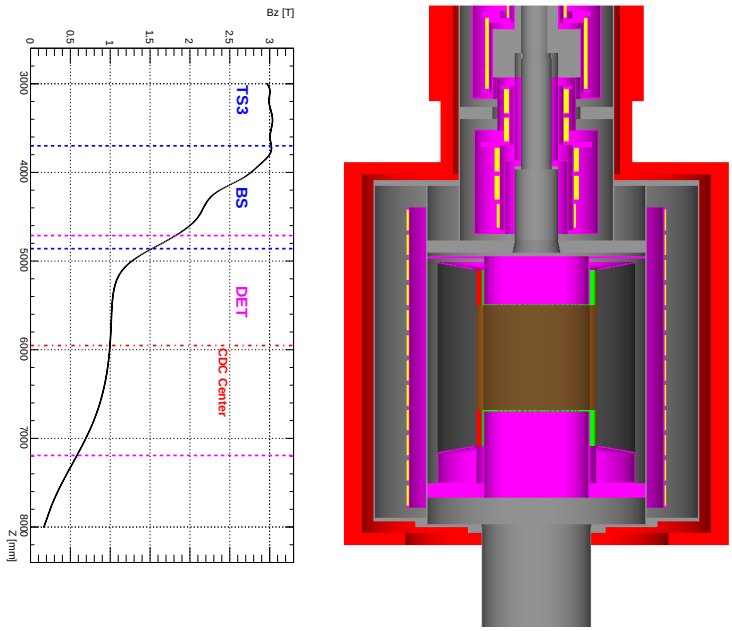

Figure 9.10: *The left figure shows a magnetic field distribution at the region of the bridge solenoid and detector solenoid. The right figure shows the corresponding locations in the cross-sectional view of the bridge solenoid and detector solenoid.*

9.4. Detector solenoid

The detector solenoid magnet produces a 1T magnetic field to allow particle charges and momenta to be measured. The CyDet and the muon stopping target are placed inside the detector solenoid. The detector solenoid has an inner bore of diameter 1800 mm and a length of 3320 mm. The inner diameter and the length of the coil itself are 2140 mm and 170 mm, respectively. The detector solenoid consists of 14 coils. Each coil is 8 mm thick, with 7 layers in the radial direction and 135 turns in total. The length of one coil is 170 mm. A current density of 131 A/m^2 is required to produce a magnetic field of 1 T. The stored energy is about 4.19 MJ. The detector solenoid has an iron yoke, with a thickness of 500 mm, which can be compared to the thickness of the iron yoke in TS3, which is 200 mm. When the CyDet is installed from the downstream side, the iron yoke at that end will be removed. The outside length of the iron yoke is about 3420 mm.

Table 9.4: *Coil specifications for the collimator and detector solenoids for COMET Phase-I.*

Name	B_z (T)	B_y (T)	Length (mm)	Inner radius (mm)	Outer radius (mm)	Location (mm)	Current (A)	Current density (A/mm^2)	Bore radius
BS1		NA	300	230	241.1	10382.39	155	111	125
BS2		NA	150	230	245.5	10657.39	155	111	125
BS3		NA	240	310	320	10902.39	155	111	180
BS4		NA	180	310	320	11162.39	155	111	180
BS5		NA	180	310	320	11422.39	155	111	180
DS1	1	NA	170	1070	1078	11397.39	191	133	910
DS2	1	NA	170	1070	1078	11607.39	191	133	910
DS3	1	NA	170	1070	1078	11817.39	191	133	910
DS4	1	NA	170	1070	1078	12027.39	191	133	910
DS5	1	NA	170	1070	1078	12237.39	191	133	910
DS6	1	NA	170	1070	1078	12447.39	191	133	910
DS7	1	NA	170	1070	1078	12657.39	191	133	910
DS8	1	NA	170	1070	1078	12867.39	191	133	910
DS9	1	NA	170	1070	1078	13077.39	191	133	910
DS10	1	NA	170	1070	1078	13287.39	191	133	910
DS11	1	NA	170	1070	1078	13497.39	191	133	910
DS12	1	NA	170	1070	1078	13707.39	191	133	910
DS13	1	NA	170	1070	1078	13917.39	191	133	910
DS14	1	NA	170	1070	1078	14127.39	191	133	910

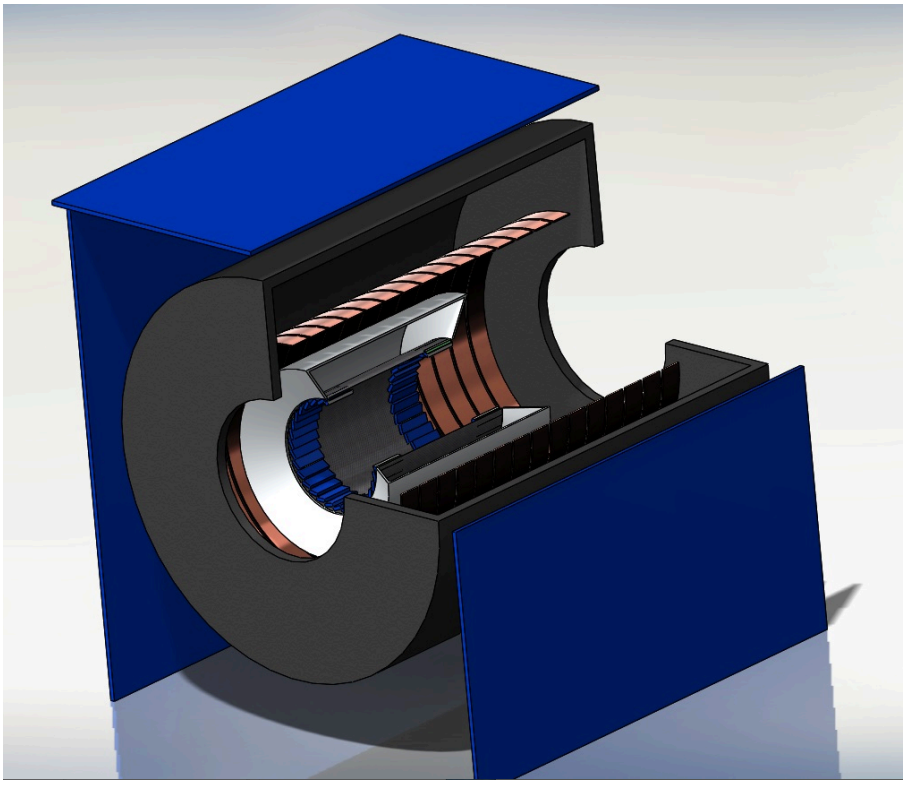

Figure 9.11: *Schematic cut view of the detector solenoid.*

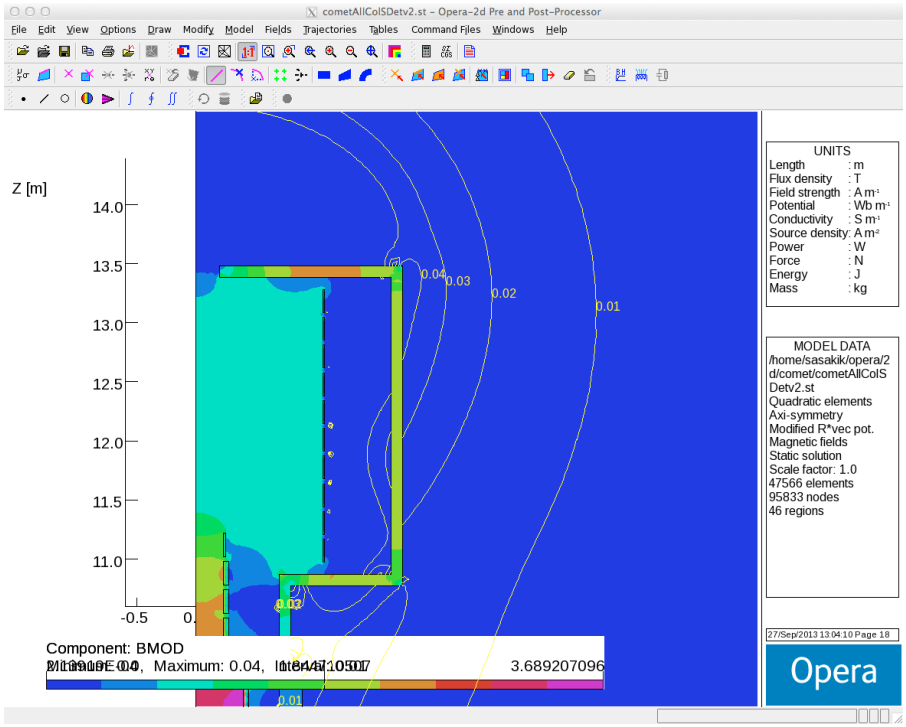

Figure 9.12: *Magnetic field of the detector solenoid.*

Chapter 10

Muon Stopping Target

The muon-stopping target is placed in the centre of the detector solenoid. The muon-stopping target is designed to: maximise the muon-stopping efficiency and the acceptance for the $\mu-e$ conversion electrons to arrive at the spectrometer and to minimize the momentum spread of electrons by reducing the energy loss as they exit the muon stopping target. The design of the muon stopping target for COMET Phase-I may not be the same as that for COMET Phase-II.

To eliminate beam-related background events arising from prompt beam particles the measurement time window will open approximately only 0.7 μs after the primary proton pulse. High-Z target materials are therefore not appropriate for the stopping target since the muonic atom lifetime decreases with increasing Z. Aluminium ($Z = 13$) with a muonic atom lifetime of 0.88 μs is preferred over titanium ($Z = 22$) and lead ($Z = 82$) which have muonic atom lifetimes of 0.33 μs and 0.08 μs respectively.

The configuration and dimensions of the muon-stopping target have been optimized using simulation to maximise the muon-stopping efficiency and minimise the backgrounds. The adopted design is composed of 17 thin circular flat disks as summarized in Table 10.1.

Item	
Material	aluminium
Shape	flat disk
Radius	100 mm disk
Thickness	200 μm
Number of disks	17
Disk spacing	50 mm

Table 10.1: *Configuration of the muon-stopping target.*

Figure 10.1 shows distributions of the number of stopped muons in 17 disks. In optimising the design, one must take into consideration that the total number of stopped muons increases with the number of target disks, but that this has a cost in the form of additional energy loss in the target. It can be seen in Figure 10.1 that the proposed target size will make a reasonable radial coverage.

A schematic layout of the muon stopping target support structure is shown in Figure 10.2. Each aluminium disk is supported by three spokes. The spokes are connected to the ring structure which is placed inside the inner wall of the cylindrical drift chamber (CyDet). The spokes are made of aluminium or a high-Z material to avoid backgrounds from muons stopped in the spokes.

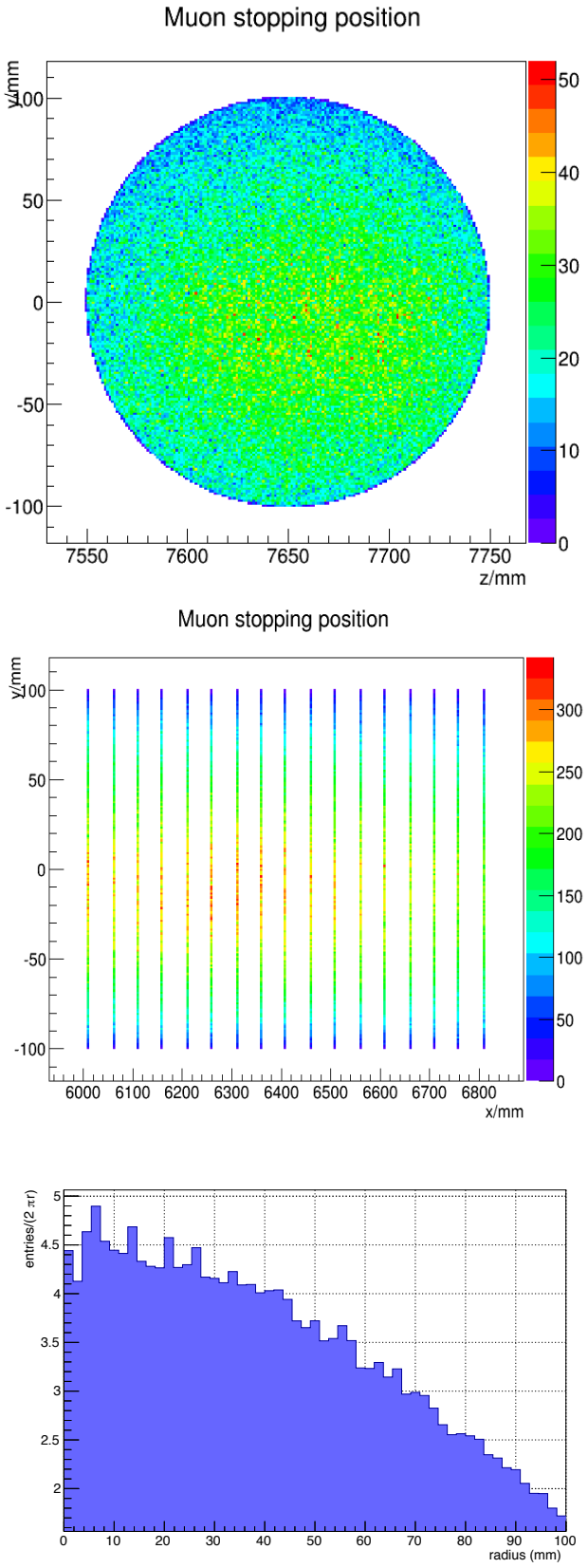

Figure 10.1: *The zy distribution of a number of stopped muon (top), distribution of the number of muons stopped projected on the x and y axis (middle) and radial distribution (bottom) are shown.*

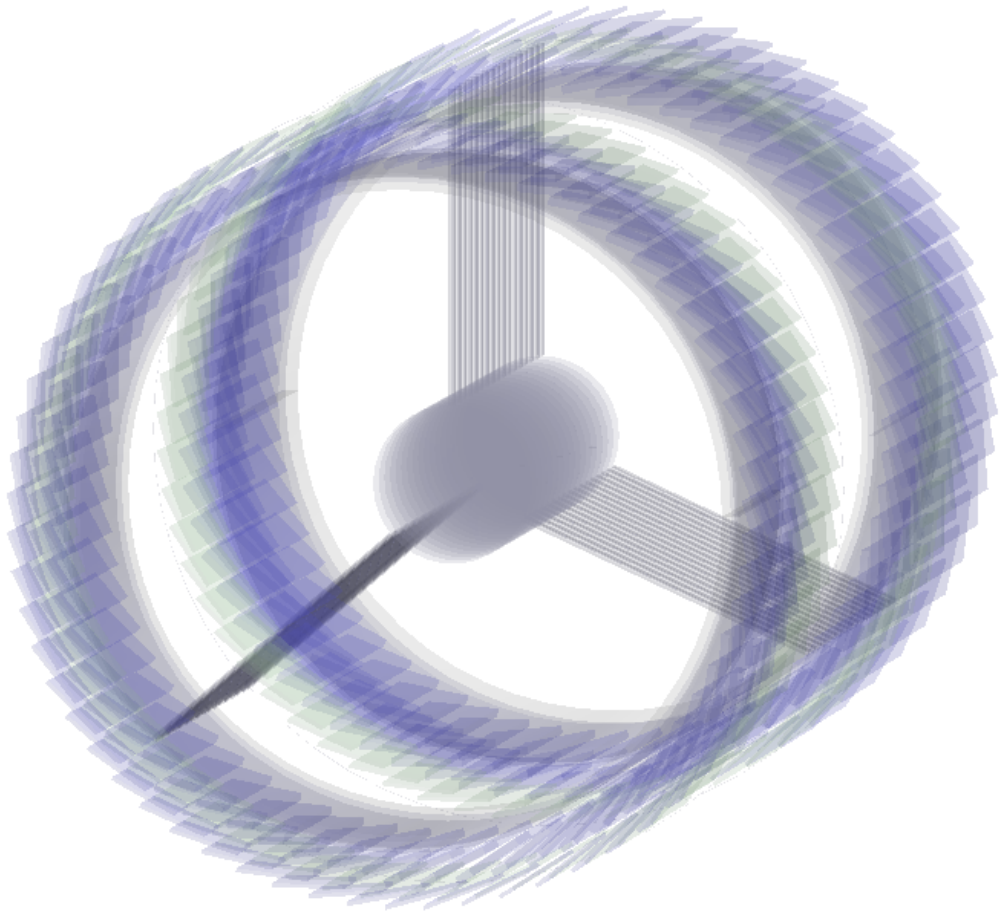

Figure 10.2: *Schematic Layout generated using the ICEDUST framework of the muon-stopping target (disk option) and its supporting system. The CyDet trigger hodoscopes are also shown as blue blocks.*

Chapter 11

Straw Tracker

The straw tracker to be developed for Phase-I is a real prototype for the Phase-II tracker and indeed could be used as is for Phase-II. During Phase-I, this detector will make direct measurements of the proton beam extinction, the rate of particle production (in particular anti-protons) as a function of beam energy and other backgrounds. The straw tracker will be inside the vacuum vessel and the solenoid magnet which has a field strength of 0.8−1.1 T. The detector needs to be able to provide a precise measurement of a particle's momentum as well as its identity, through $\mathrm{d}E/\mathrm{d}x$ information and, in combination with the calorimeter, E/p and the time of flight (TOF). For Phase-I, as shown in Figure 8.6 and Figure 8.7, many kinds of particles will reach and enter into the detector solenoid. In order to make good measurements of the many species of particle in the beam, it is essential that the volume inside the magnet is a vacuum. For Phase-II, it is not necessary to reconstruct all these particles as a beam measurement, but it is very important to measure the electron momentum very precisely, for which it is desirable to have an extremely low mass of material in the tracker components, *i.e.* the vacuum is essential not only for Phase-I but also for Phase-II. Again, the design concept of straw tracker for Phase-I is same as Phase-II in principle, thus it will be the real prototype for the Phase-II straw tracker.

11.1. Design of the straw tracker

11.1.1 Overview

The overall structure of the straw tracker is schematically shown in Fig. 11.1. Each of the five tracker super-layers, called "station" ,consists of four planes, two to measure the x coordinate and two to measure the y coordinate. Each pair of planes is staggered by half a straw diameter in order to solve left-right ambiguities. Each layer is constructed as a stand-alone unit and mounted on the detector frame which is inserted and removed from the solenoid on rails. A spare layer will also be constructed. Anode wires, made of gold coated tungsten, are extracted via a feedthrough into the gas manifold as shown in Fig. 11.1. The anode wires are held at high voltage and the straw wall is grounded as the cathode. A default gas mixture of 50%-Ar and 50%-C_2H_6 is provided from this gas manifold to the straw tube. The straws have a diameter of 9.75 mm, range in length from 692 to 1300 mm and are mounted on aluminium ring supports.

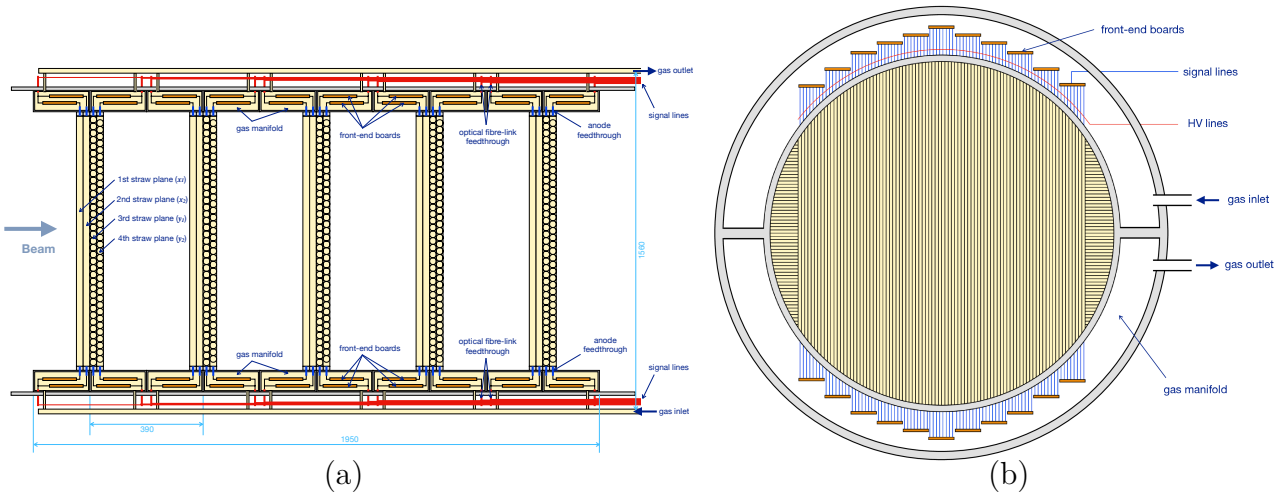

Figure 11.1: *Schematic view of the straw tracker; (a) Side view (the straw dimensions is scaled by a factor of three for clarity) and (b) cross-sectional view of a plane.*

11.1.2 Mechanical construction

The straw-tracker design assumes 9.75 mm diameter conducting straws, composed of metalised Polyethylene Terephthalate (PET) film of 20 μm thickness[1]. The straws are mounted on aluminium supports in the shape of rings, with inner and outer radii of 65 and 78 cm respectively. Gas manifolds and electrical connections are also attached to the supports. The gap between them provides a space to mount the front-end electronics, its power distributors and high voltage (HV) distributing circuit. This space should be large enough in order to contain all the front-end boards, however, the thickness should be minimised to make the fiducial tracking volume as large as possible. Thus, by putting the front-end boards along the beam direction, it is possible to reduce the space down to 15 cm. Because of this, the depth of the manifold including a clearance for cables is relatively large at 19.5 cm, which corresponds to one half of the gap between each tracker station (see Figure 11.1), and each of the five stations are properly spaced and rigidly attached to each other.

Each station, consisting of two double-arrays, is constructed as a stand-alone unit. These units are then mounted on the detector frame which positions and aligns the planes with respect to each other. The frame is inserted and removed from the detector solenoid on rails and linear bearings for access and maintenance. A spare plane will be constructed so that it can be swapped, when needed, with a malfunctioning one, reducing downtime for detector repairs. The detailed design of the support structure is shown in Figure 11.2. The left picture shows an overview of one station without straws, and also the outer rim is removed for a visualization. The right picture shows a close-up view of one station with straws. As shown in both pictures, the gas-manifold volume is separated into two volumes for each layer in order to provide gas flow by pressure gradient.

Detail of the components of the support structure is shown in Figure 11.3. The left and centre pictures show details of support-structure design as an exploded view. Almost all components are made by an aluminium since it should be non-magnetic material. The right picture shows the close-up view of the special jig which is supposed to determine the straw positioning and also provide the gas tightness. This jig determines the straw spacing which should be as

[1] There is a possibility to reduce the thickness of the straw wall, and its R&D is currently ongoing, see Section11.1.3.

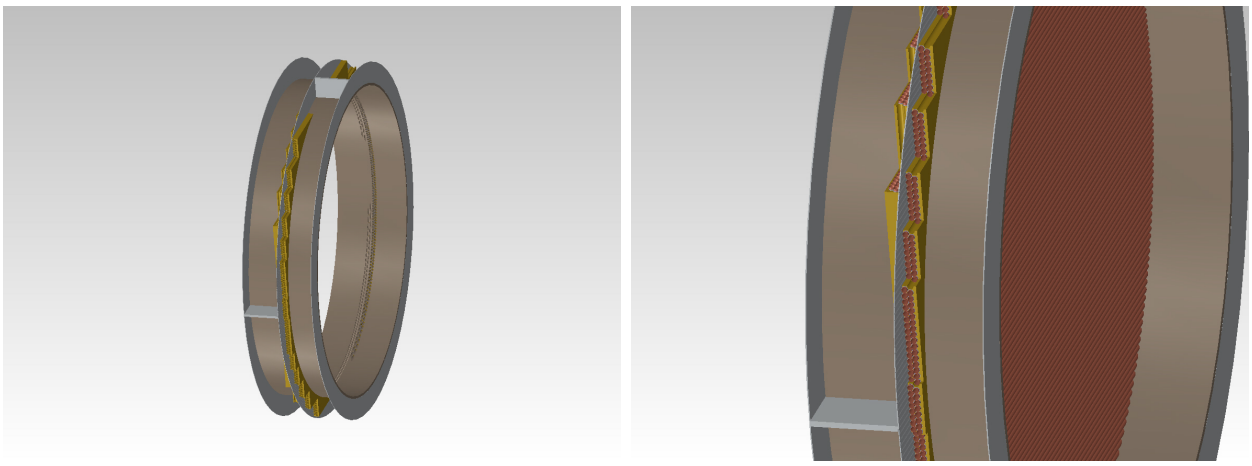

Figure 11.2: *Design of the support structure for one tracker station. (Left: Overview of one station without straws, Right: Close-up view with straws)*

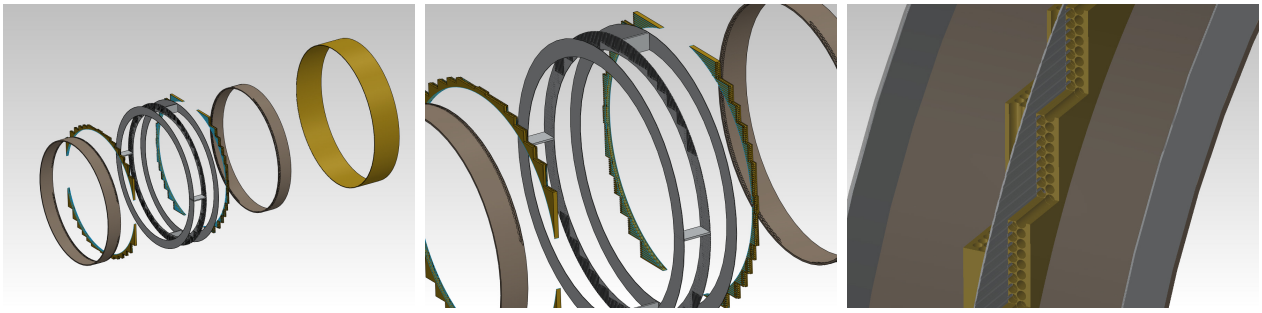

Figure 11.3: *Detail of the support-structure design. (Left: Exploded elevation view. Centre: Close-up of exploded view. Right: Straw-spacing jig)*

small as possible in order to keep the detection efficiency. Currently, by studies of the final prototype, the small spacing of 0.3 mm is enabled, as described in Section 11.5.2. By reflecting this achievement, Figure 11.3 (right) supposes to have the small gap of 0.3 mm between each straws.

During the design using CAD software, Finite Element Analysis (FEA) was performed in order to validate the robustness of this support structure against any stress, tension, and so on. In this FEA, a tension of $1.7\,\mathrm{kg}_F$ is assumed to be applied on each straws while the tension of 0.7–$1.0\,\mathrm{kg}_F$ is supposed to be applied during the detector assembly. Even if higher tension than supposed is applied, the anticipated deformation is small enough not to be concerning. As shown in Figure 11.4(Left), only $57\,\mu\mathrm{m}$ of deformation is expected at a maximum, average deformation is smaller than $10\,\mu\mathrm{m}$. As a result of straw tensions, as shown in Figure 11.4(Right), induced stress is expected to be much smaller than $1\,\mathrm{kg}_F/\mathrm{cm}^2$ for most of the volume, rising to a maximum of approximately $20\,\mathrm{kg}_F/\mathrm{cm}^2$ only for the region close to the straw roots. This maximum level is acceptably small and is consistent with the calculated deformation above.

11.1.3 Straw tube

The conceptual design for COMET straw tracker was based on earlier studies [63]. A recent design decision has been made to a new type of straw instead of the "doubly-wound" type of the original conceptual design. The doubly-wound type of straw is composed of a double layer

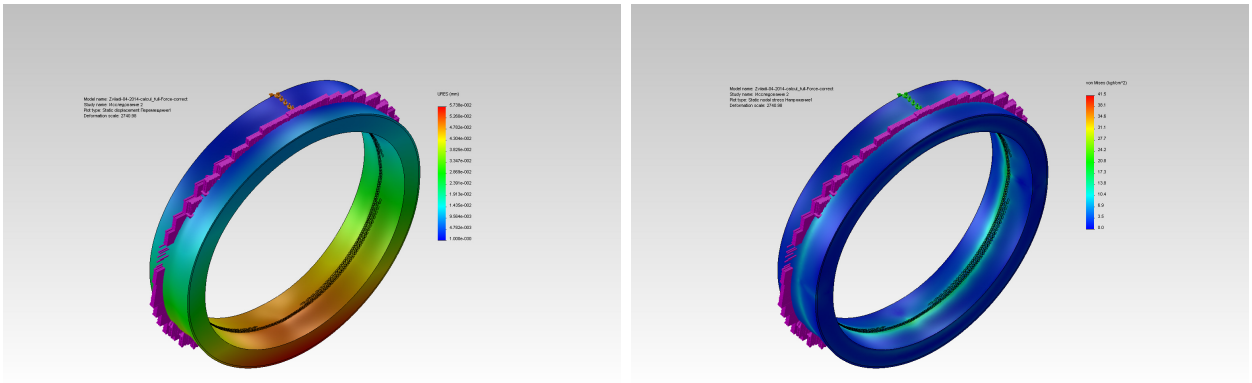

Figure 11.4: *FEA results of the support structure with the tension of 1.7*,kg_F *applying on each straws; (Left) Calculated static deformation, (Right) Calculated static stress.*

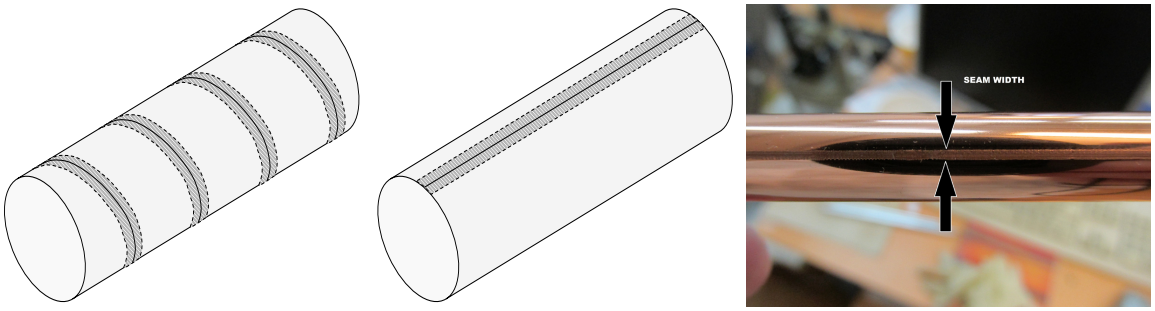

Figure 11.5: *Different adhesion styles of straw construction; (Left) the original doubly-wound style, (Centre) the new straight-adhesion style, (Right) the welding seam of a completed straw*

of spirally over-woven straws of metalised polymer film, *e.g.* Kapton, Mylar, as schematically shown in Figure 11.5(Left). The two-layer tube walls are thicker than what could be achieved with single-layer walls, but because of issues of deformation and gas leakage in vacuum, the latter option was rejected for the CDR design.

A new method of straw production, which does not require multiple over-woven layers has been developed by the JINR group for the NA62 experiment at CERN [64]. In this method, a single layer is rolled and attached to itself in a straight line using ultrasonic welding as schematically shown in Figure 11.5(Centre). This method allows the straws to be pretensioned at 1 kg_F, and guarantees constant tension of the straws over time. As shown in Figure 11.5(Right), the seam width is about 500 μm, which is small enough to maintain the circular shape of the cross-section against any pressure differences. With this new method, the amount of material used in the tracker, which is dominated by the straw wall thickness, can be reduced. The doubly-wound style requires the use of glue between the two layers, which is not needed in the new method. In addition to this, the COMET group at JINR collaborates with the NA62 group there to process the mass production of straws. Such in-house production reduces the cost for straw production dramatically.

The NA62 group in JINR provided 9.75 mm-diameter straws with 36 μm thick Mylar walls with a 50 nm deposition of copper and a 20 nm deposition of gold. Initially it was assumed that we would be able to adapt the set-up to produce 5 mm-diameter straws as with the COMET CDR design[63]. However, it emerged that the modifications and R&D that was needed to make narrower tubes were not compatible with the COMET Phase-I construction schedule, and the decision was reached to use 9.75 mm tubes as with NA62 for the COMET phase-I.

This necessitates the reduction of the straw wall thickness to compensate for the increase in material caused by the larger diameter. In principle, it is possible to reduce the thickness of PET film, and also to change the cathode metal from copper+gold to aluminium. The intensive R&D towards straws with thinner walls was made using two configurations: (A) 20 μm-thick Mylar with 70 nm aluminium deposition; and (B) 12 μm-thick Mylar with 70 nm aluminium deposition. It became apparent that the configuration (A) is reliable by the latest R&D in JINR as described below. However, the viability of configuration (B) must await the results of the additional trial.

Figure 11.6: *The latest achievement of thinner straw tube R&D; (Left) Sample tubes of 20* µm *thick wall with 70 nm aluminium deposition, (Centre) Over-pressurise test with 6 bar, (Right) Over-pressurise test with 7.5 bar*

The thinner configuration (A) straw tubes were successfully developed by our JINR colleagues with a help of NA62 group in JINR as shown in Figure 11.6(Left). Several mechanical tests were made on the new straw tubes, *e.g.* dimension measurement, over-pressure test, destruction inspection, *etc.* Deformations appeared at an over-pressure of 6 bar as shown in Figure 11.6(Centre), and the straws failed at an over pressure of 7.5 bar as shown in Figure 11.6(Right). This pressure-at-failure is sufficiently high to guarantee good mechanical stability of the new straw tubes, since the COMET experiment will use a pressure difference of only 1 bar. After these mechanical measurements in JINR, the prototype straws were shipped to KEK in order to perform further tests.

Delivered straws were carefully investigated in order to validate its reliability as a particle detector. For example, deformations of the straw and a necessary pretension on the straw were carefully investigated using the sample straws, since the pretension on the straw must be quite high to avoid deformations against the pressure difference of 1 bar when the tracker is operated in a vacuum[2]. Figure 11.7 shows the set-up of straw deformation/tension study. In this set-up, the gas supply is attached to the sample straw so that the straw inside is pressurised properly, and the one end of sample straw is fixed on the support structure, and the unfixed end is tensioned via a weight as shown in Figure 11.7 (Top). At the unfixed end of straw, capacitive sensor[3] is installed, where the change in capacitance is converted to a length, in order to measure the small displacement of straw end as shown in Figure 11.7 (Left). Here, the longitudinal deformation of straw, *ie.* elongation, is measured as a function of applied tension. On the other hand, same capacitance sensor system is also equipped at the centre of straw so that the transverse deformation of straw, which is caused by a sag by gravity and expansion due to pressure differences, is measured simultaneously as shown in Figure 11.7 (Right). The obtained sag and elongation are shown in Figure 11.8. According to the result of the sag measurement, in any pressure differences high enough tension such as higher than 1 kg_F can

[2] As a point of reference, the NA62 tracker uses a pretension of 1.5 kg_F on each straw tube.
[3] **Contrinex**; DW-AD-509-M12-390

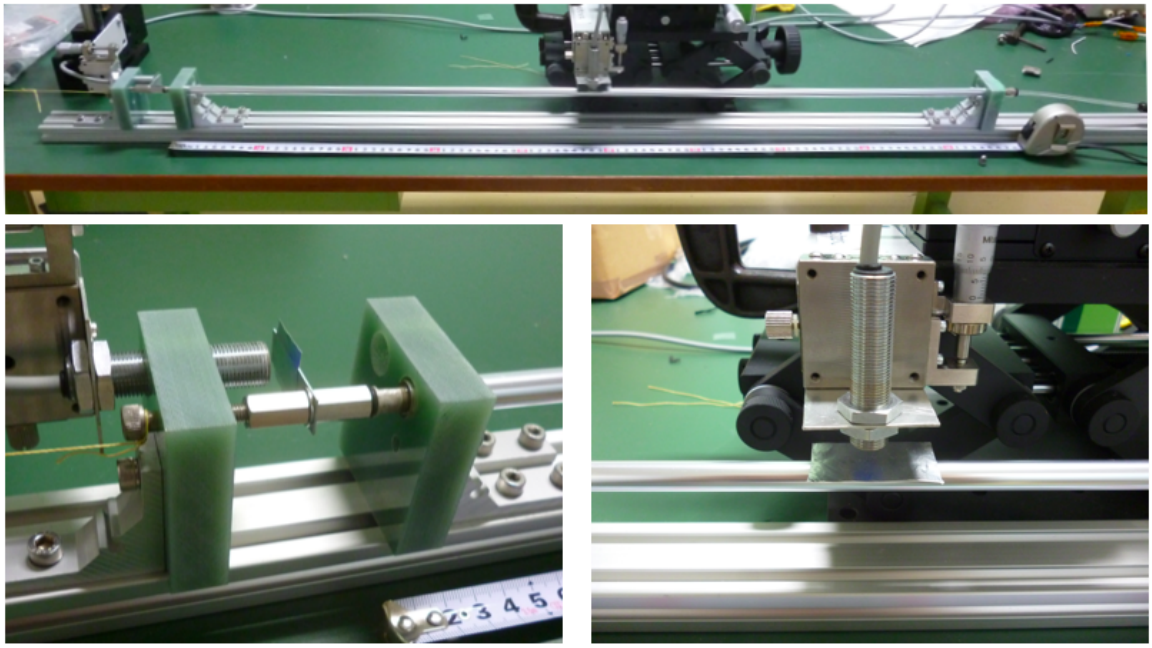

Figure 11.7: *Set-up for deformation/tension study; (Top) Whole view, (Left) Elongation measurement, and (Right) Sag/Expansion measurement*

avoid a sag. The result on the elongation measurement tells that an elongation of 1.7∼2.0 mm is corresponding to a tension of ∼1 kg_F, thus the straw deformation can be avoided by stretching the straw of 2 mm during its assembly. By this result, the new 20-μm-thick straw is acceptable for a particle detector from the point of view of mechanical strength. Further test such as a gas leak and a noise shield is performed using the small prototype detector, so-called 'One-straw Prototype', which would be discussed in Section 11.5.1.

Thus the decision reached to employ the 20-μm straw for COMET Phase-I straw tracker, and continue the R&D for 12 μm-thick straw tube toward COMET Phase-II.

11.1.4 Exterior of the straw tracker

Outside the tracking fiducial volume, the exterior section of the tracker must serve several functions including the following: electronics connections, the supplying of power and gas, and airtightness, as briefly described at the beginning of this section. The straws and wires are tensioned during their assembly and the tension is maintained by the dedicated feedthrough system[4], which also provide the gas supply.

Anode wires are extracted via the feedthrough system into the gas manifold which is attached to the ends of the straws as shown in Figure 11.1. The feedthrough system provides the gas supply from the gas manifold to the straw tubes, and the supplied gas exhaust passes through another gas manifold which is attached on the other end of straw tube. The extracted anode wires are held at HV and each conducting straw wall is grounded. The HV for each unit of 16 straws in a manifold has a filter capacitor of 8,200 pF to ground, and passes through a bias resistor of 100 kΩ to each wire. The signal is extracted through a blocking capacitor of 180 pF. Each wire is fused with a 65 mA slow-blow fuse to remove broken wires which short to ground.

[4] Straw pretensioning scheme using feedthrough has been established by the prototype study which is described in Section 11.5.1.

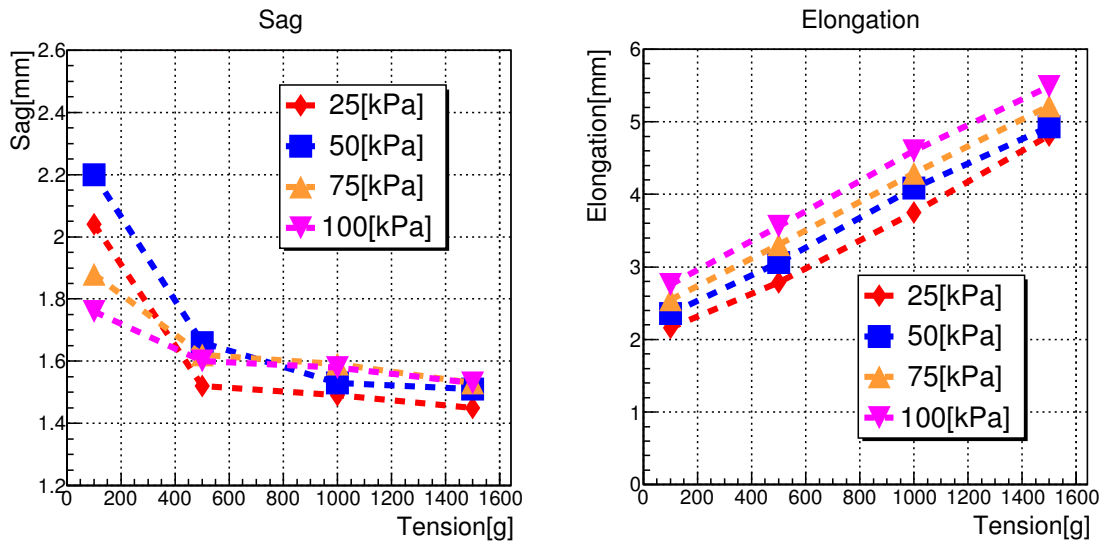

Figure 11.8: *Straw-Pretension Study; (Left) Obtained sag with various pressure differences between inside/outside straw as a function of applied tension, (Right) Obtained elongation of straw*

In the event that a short to ground occurs on a wire, the polarity of the HV is reversed and the normally back-biased diode across the bias resistor allows sufficient current to flow around the resistor and through the fuse to open the HV connection. These decoupling and HV circuits are implemented in the gas manifold so that any discharge on the HV line in a vacuum is avoided, and allows the capacitors to remain functional.

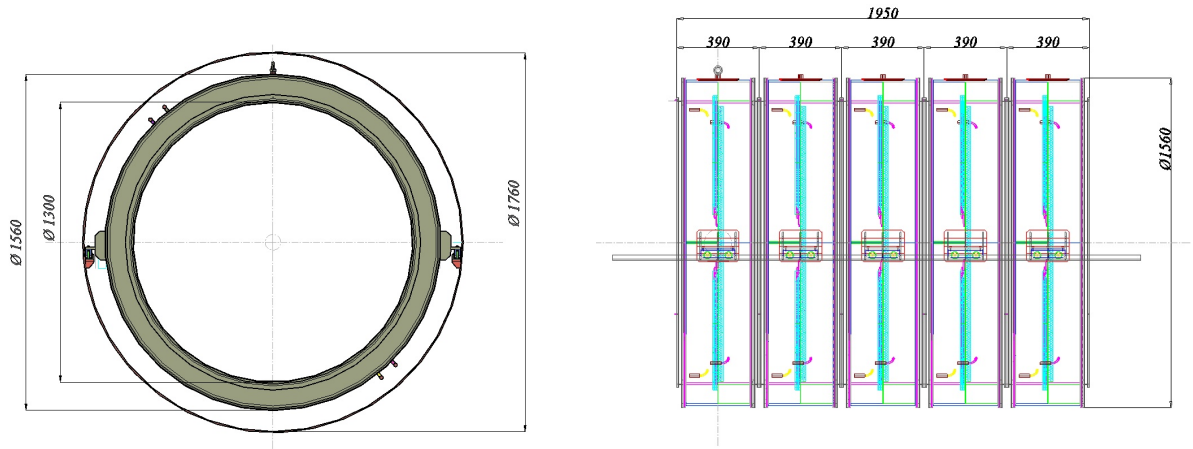

Figure 11.9: *Drawing of the tracker exterior; (Right) Front elevation of one station, (Left) Lateral view of the whole tracker (5 stations)*

The mechanical design of the tracker exterior is shown in Figure 11.9. Outside the manifold there are gas and cable service ports, which are connected to the outside of the vacuum volume through the end-cap system of the cryostat of the spectrometer magnet. Other service elements are also mounted on the exterior, such as an eyebolt on the top of the station, linear bearing system on both ends which is used for the detector installation, as shown in Figure 11.9 (Left). In the current design, as briefly described in Section 11.1.1, each all the gas manifolds are rigidly attached to each other such that each tracker station is also rigidly fixed as shown in Figure 11.9 (Right).

Figure 11.10 (Left) shows the 3-D cut-view of the one tracker station. As shown in this drawing, one station has double-sided gas manifolds on each end with different colors, and all manifold volumes are connected to the inlet/outlet gas pipes. Each gas manifold is separated into two volumes in order to provide the gas flow, so one tracker station is connected to 4 gas pipes in total and connected to the end-cap system of the solenoid. Figure 11.10 (Right) shows the

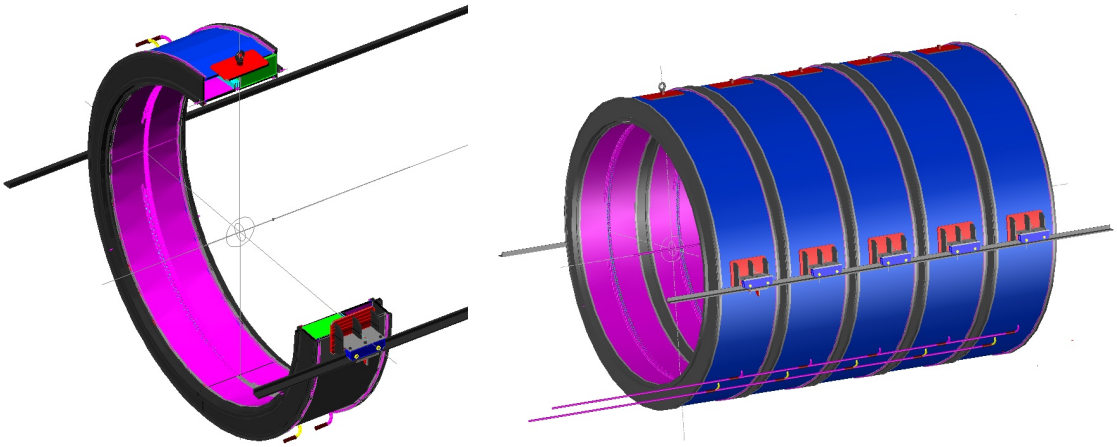

Figure 11.10: *Overview of the straw-tracker drawing; (Right) 3-D cut-view of the one tracker station, (Left) the whole tracker system*

whole tracker system.

The installation for straw tracker employs the rail system which is also intended for use by the CyDet installation described in Section 13.2.3. In order to utilize this rail system, the straw-tracker station has linear bearing system on both ends as shown in Figure 11.11 (Left) with its close-up view. As described before, each tracker stations are rigidly attached to each other so that the whole tracker system can be inserted by a combination of this linear bearing system and the rail system as shown in Figure 11.11 (Right). Development of this installation scheme is being coordinated with the CyDet group.

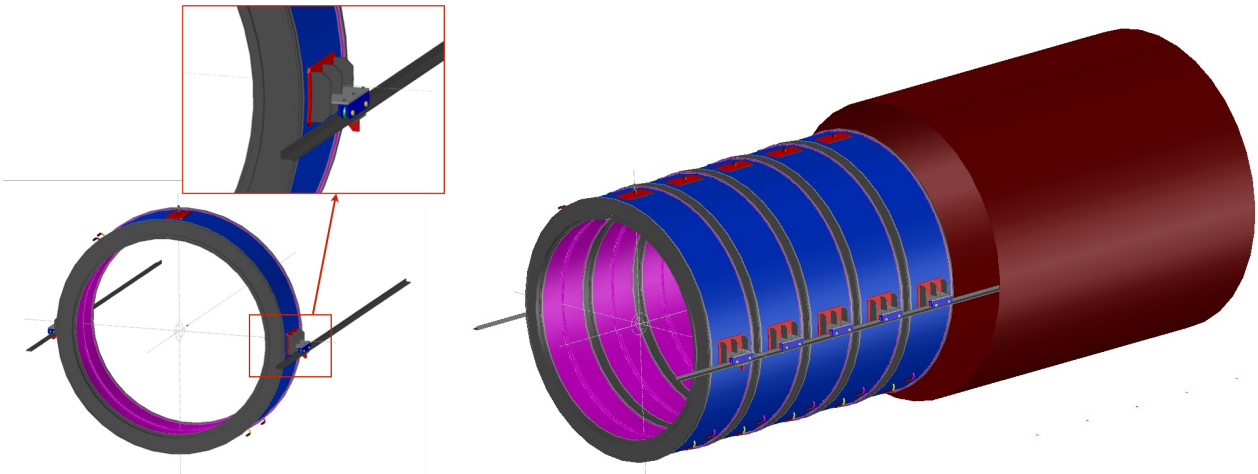

Figure 11.11: *Straw-tracker installation (Right) One station with its block system, (Left) Insertion of the whole tracker system into the solenoid*

11.1.5 Anode wire and wire supports

The sense wire is chosen to be gold plated tungsten containing 3% rhenium. This wire has excellent properties with respect to creep, which is further mitigated by using lower tensions, and pre-stressing the wires.

The sense wires are held at HV and although this requires a blocking capacitor on each read-out channel, maintaining the wires at voltage prevents a large current discharge from passing through a wire if a spark occurs, since the entire charge stored in the cathode capacitance would then flow through the spark. Note that all the straws are electrically connected to provide a common cathode ground.

As long as the straws remain stable, we do not expect to require supports for the anode wires. Wire stability can be estimated using the following equation derived from the electrostatic force on a non-central anode wire [65],

$$L_c = \pi R(CV)[2\pi\epsilon_0 T]^{1/2}, \tag{11.1}$$

where T is the tension of wire, V is the applied voltage, C is the capacitance per unit length, L_c is the critical wire length for a given tension, and R is the straw radius. Assuming a straw radius of 4.9 mm, an anode wire radius of 12.5 μm, a capacitance/length of 10.5 pF/m, a maximum voltage of 2.2 kV, and a critical length of 2 m, the required tension on the wire is approximately 70 g.

11.1.6 Chamber active gas

A gas mixture of 50%-Ar and 50%-C_2H_6 is the default choice of gas mixture. Thanks to the good drift properties of this gas mixture, such as the small Lorentz angle, small diffusion coefficient and saturated drift velocity in magnetic field, enough good spatial resolution can be achieved. At 1 T, the Lorentz angle is approximately 45° at 1 kV/cm and approximately 20° at 4 kV/cm. It is expected that the drift velocity along the radial direction will be 5 cm/μs at 1 kV/cm and 4.5 cm/μs at 4 kV/cm, which results in a resolution of 100–220 μm.[5] Detailed simulation studies to investigate these fundamental drift properties has been performed and will be discussed in Section 11.2.1.

As described in Section 11.1.3, the straw dimension was approximately doubled from 5 mm in the CDR design to the current value of 9.75 mm. In the CDR design, in order to compensate for the small number of primary ionisation in the active gas volume due to the small straw diameter, a gas mixture of 50%-Ar and 50%-C_2H_6 was specified as our default choice. However, the straw diameter is now approximately doubled so that other gas mixture is also possible. As a result, *e.g.* a gas mixture of Ar and CO_2 is also under investigation, which would be more easily handled than the default gas mixture.

- **Gas-mixture study for Phase-II**

Since we are investigating relatively low momentum particles, below the GeV/c region, using a *light* gas is more important than achieving good spatial resolution. Even if one can obtain the spatial resolution better than 100 μm, the tracking resolution cannot achieve the required

[5] Discrimination timing resolution of ≈2 ns is conservatively assumed which is easily achieved by standard readout electronics.

quality with the amount of material that is used in standard tracking detectors. That is why the inner volume of the solenoid must be evacuated and the straw chamber operated in a vacuum. Hence, it is important that we make further efforts to employ a lighter gas mixture than the default gas mixture of Ar-C_2H_6 . For example, a helium-based gas mixture such as 50%-He and 50%-C_2H_6 is also under investigation. It is well known that a helium-based gas mixture has a high ionisation potential and large fluctuations in the number of primary ionisations, which can worsen particle-identification performance [66]. However, it is not main task for the Phase-II to perform particle identification, so a helium-based gas mixture is still very attractive as it should provide excellent momentum resolution.

Such gas mixture studies are still ongoing and we will be able to make use of the Phase-I experiment to help determine, in the full beam environment, the best gas mixtures to use in the Phase-II.

11.2. Simulation study of the straw tracker

11.2.1 Fundamental process simulation

The fundamental processes in the gaseous detector: ionisations from an incident particle; the electron drift process; avalanches close to a wire; and pulse generation in the straw chamber are simulated using three simulation tools, **HEED**[67]; **MAGBOLTZ**[68]; and **GARFIELD**[69].

The **HEED** program computes in detail the energy loss of fast charged particles in gases, taking delta electrons and optionally the multiple scattering of the incoming particle into account. The program can also simulate the absorption of photons through photo-ionisation in gaseous detectors. The **MAGBOLTZ** program provides electron transport parameters for a large variety of gases and mixtures of gases. The **GARFIELD** is one of the most widely-used software packages to simulate two- and three-dimensional wire chambers and to compute the field maps, electron and ion drift lines, drift time tables and arrival time distributions, signals induced on the wires by moving ions and electrons *etc.*, and also provides an interface to **HEED** and **MAGBOLTZ**.
Figure 11.12 shows results of these simulations. Figure 11.12(a) shows the calculated drift

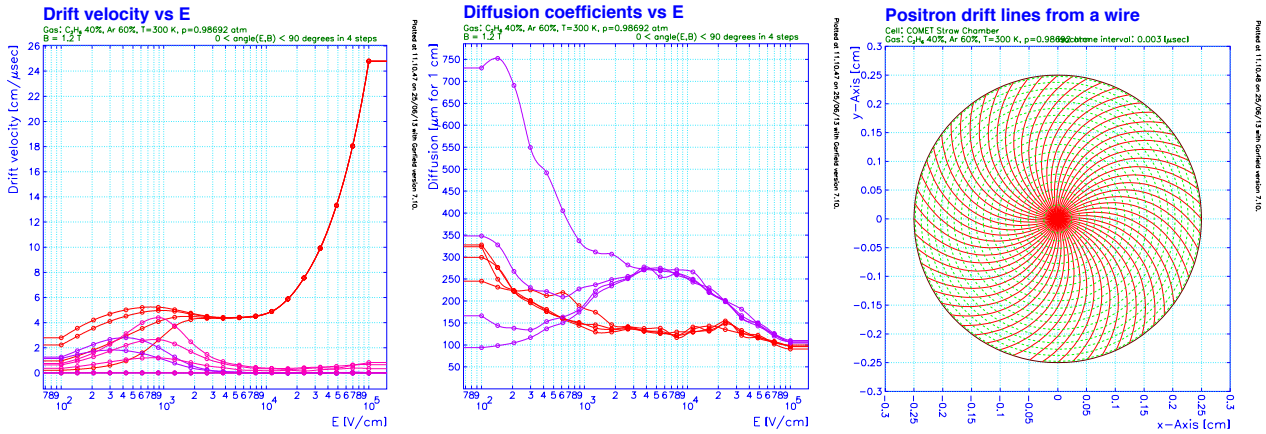

(a) (b) (c)

Figure 11.12: *Gaseous detector simulation for the COMET straw tracker by* ***GARFIELD****; (a) Drift velocity as a function of applied electric field, (b) Diffusion coefficients as a function of applied electric field, (c) Drift lines and isochrones*

velocity for Ar-C_2H_6 50:50 mixture as a function of the applied electric field, Figure 11.12(b)

shows the diffusion coefficients, and Figure 11.12(c) shows the drift lines and isochrones of drift time at 3 ns intervals, where the strength of the magnetic field is 1 T. According to this simulation study, the drift velocity is expected to be saturated at approximately 5 cm/μs for an electric field higher than 10^3 V/cm. Relatively low diffusion coefficients, roughly 100–300 μm/cm, are expected for an electric field of order of 10^3 V/cm; hence good spatial resolution can be expected.

Following these basic simulations, we have performed more detailed simulation studies, including the distance-to-time relation (the so-called "X–T function"). As shown in Figure 11.12(c), precise isochrones are obtained and the X–T relation is extracted as shown in Figure 11.13(a). Thanks to a completely axially-symmetric field, the extracted X–T relation has good linearity leading to good spatial resolution which should not be affected by a dependence on the incident angle. In order to confirm the small incident angle-dependence of the X–T relation, simulations with varying angles of incidence are shown in Figure 11.13(b), and the dependence of the X–T relation on the angle of incidence is obtained as shown in Figure 11.13(c).

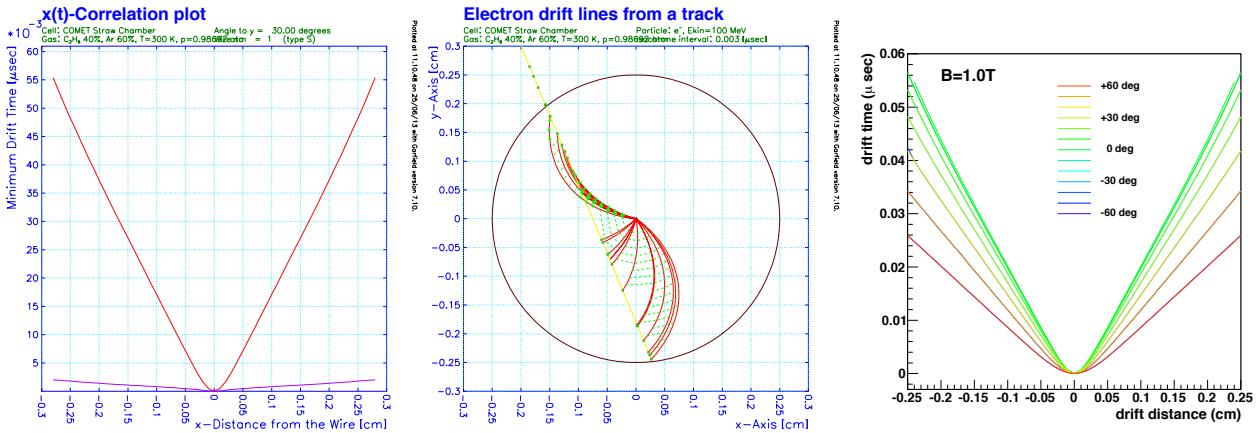

(a) (b) (c)

Figure 11.13: *XT-relation studies by* ***GARFIELD****; (a) XT-correlation plot, (b) Drift line from an electron incident, (c) XT plot with varying incident angles.*

11.2.2 Response for different types of incident particles

The basic simulations such as those shown above are important for investigating the intrinsic spatial resolution and stable operation of the straw tracker, in order to achieve a good tracking resolution. On the other hand, the straw tracker of COMET Phase-I has an another important role as a beam-background detector. Because of this, the straw tracker should be able to operate in an environment with many kind of background particles, and is required to provide sufficient information to identify particles in the beam and to measure their momenta. When charge selection is not performed in the Phase-I beam transport set-up, the following particle types will be found in the beam; p, $\overline{p}$, $e^{\pm}$, $\mu^{\pm}$, $\pi^{\pm}$ and $K^{\pm}$.

The ionisation caused by different types of incident particles is simulated and shown in Figure 11.14, in which comparison is made at an equal kinetic energy of 100 MeV for all kinds of particles. By accumulating such ionisation events, the energy-loss information is obtained for different types of particle as shown in Figure 11.15. However, as shown in Figure 11.15(comparison), it is quite difficult to identify the difference between muons and pions, and it is not possible to identify particles completely by using the straw tracker in isolation. It is essential that we combine the $\mathrm{d}E/\mathrm{d}x$ with E/p information using the energy measured in the crystal

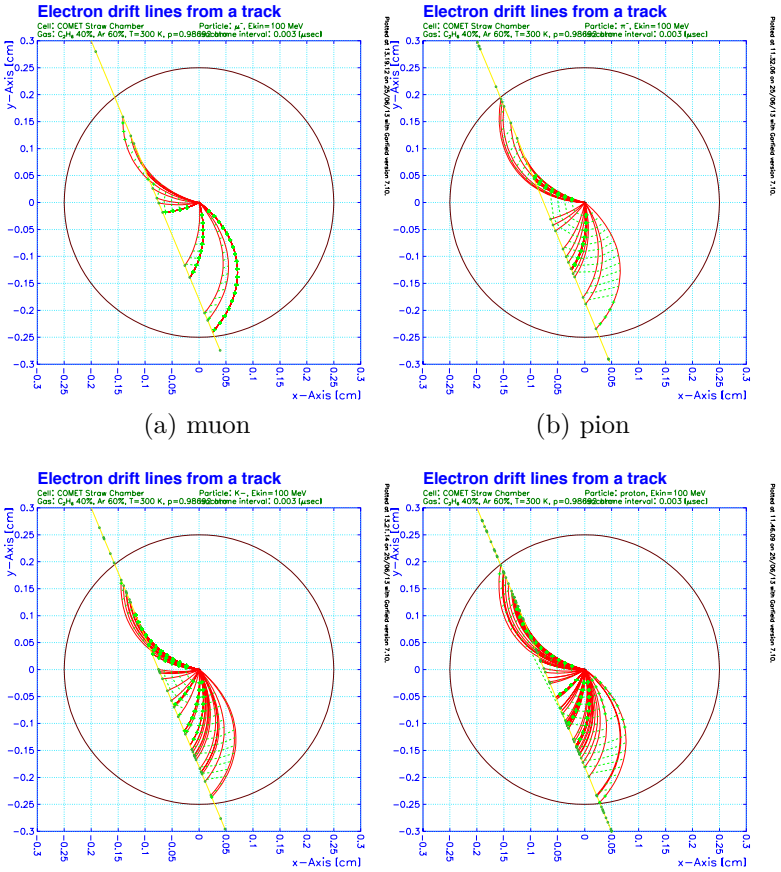

(a) muon (b) pion

(c) kaon (d) proton

Figure 11.14: *Ionisation and drift lines for different types of particles*

Table 11.1: *Characteristics of ionisation for different types of particles*

Parameter	Incident Particles (100 MeV kinetic energy)				
	e^-	μ^-	π^-	K^-	p
Number of clusters of primary ionisation	27.5	25.3	27.4	53.2	84.8
Number of electrons per cluster	1.9	2.2	2.2	2.2	2.3
Energy deposit per cluster (eV)	48	59	59	62	64
Mean $\mathrm{d}E/\mathrm{d}x$ (keV/cm)	1.38	1.53	1.67	3.37	5.56

calorimeter, to achieve more reliable identification of particles[6].

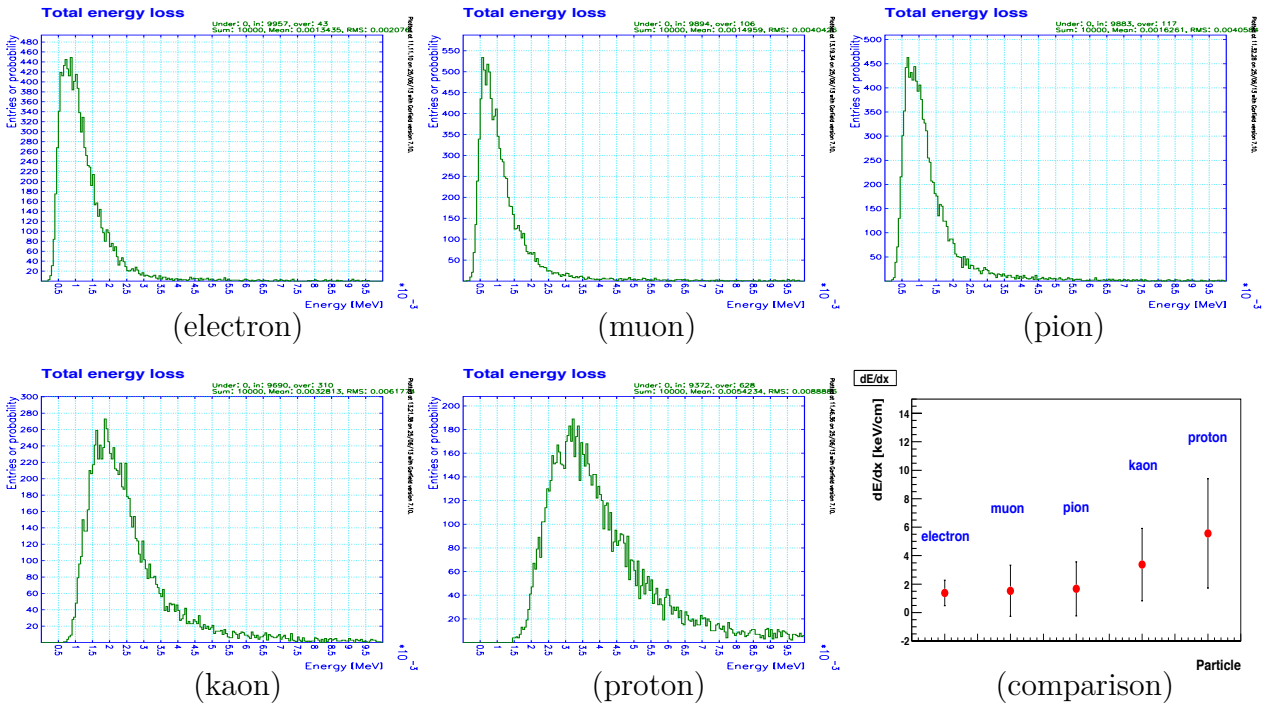

Figure 11.15: *Energy Loss for different types of particles*

Ionisation characteristics of the straw tracker, such as the number of primary ionisation clusters, the number of electrons per cluster, the energy deposited per cluster, and the energy loss per track for different types of particles are summarised in Table 11.1, where the kinetic energy for all kinds of particle are set to 100 MeV.

11.2.3 Spatial resolution estimation

In order to perform further detailed simulations such as estimation of intrinsic spatial resolution *etc.*, **GARFIELD++**[70] simulation is also processed.

At first, in order to validate the reliability of **GARFIELD++**, fundamental processes, like ionisation/drift properties, are simulated and compared with the real data and also results from old **GARFIELD** simulation[7]. For example, Figure 11.16 (Left) shows the simulated number

[6] Further studies to obtain a better particle-identification performance is ongoing, for example using TOF information by extracting from the reconstructed track length, will be discussed in Section21.

[7] Since **GARFIELD++** is developed recently and not yet well-tested, such a validation is required.

of primary electron, where the X-ray from ^{55}Fe source is irradiated, for the gas mixture of Ar/C_2H_6(50:50) and HV of 1900 V, and Figure 11.16 (Right) shows the simulated spatial distribution of the diffused drift-electron as a function of drift distance. Both results are properly

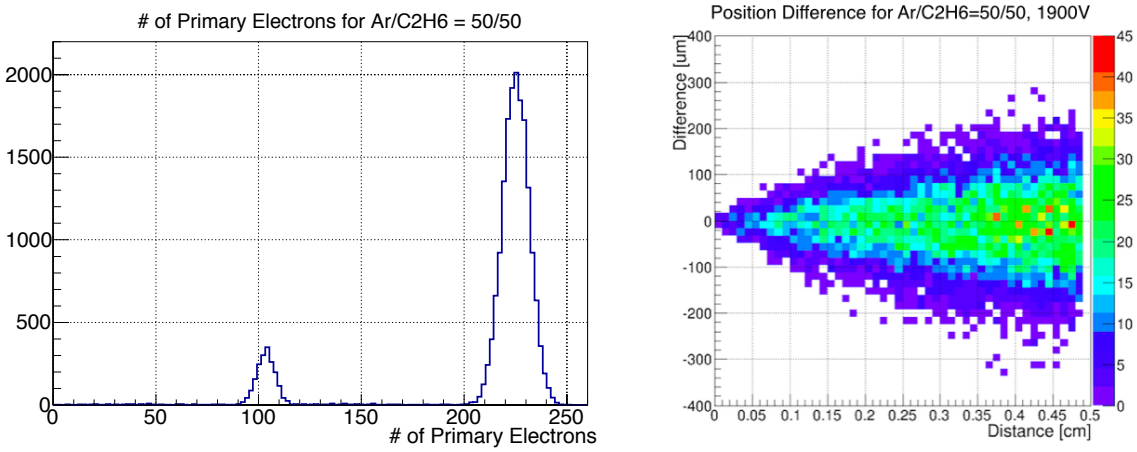

Figure 11.16: *Garfield++ simulation results 1 (Ar/C_2H_6(50:50),1900V); (Left) Number of primary electron for X-ray irradiation by ^{55}Fe, (Right) Spatial distribution of the diffused drift-electron as a function of drift distance*

validated with the real data which is obtained using the prototype detector (*cf.* Section 11.5.1), and also the old **GARFIELD** results.

Normaly, the intrinsic spatial resolution of gaseous detector is dominated by following items;

- Fluctuation of primary ionisation position along the track of incident particle,
- Diffusion of the drift electron due to the active gas,
- Electric noise.

The first contribution depends on the position of incident particle since such a fluctuation is relatively large when the particle passes near the wire while it is relatively small for the outer track. On the other hand, the second contribution also depends on the position of incident particle because the length of drift distance strongly depends on the position of particle incident. Thus the position dependence of the intrinsic spatial resolution can be precisely simulated, and it helps a lot to understand the detector responses by comparing this result with the real data. Figure 11.17 shows the first contribution, *ie.* fluctuation of the position of the closest primary ionisation, as a function of distance from the wire, and Figure 11.18 shows the second contribution, *ie.* spatial spread of the diffusion of drift electron. The first contribution does not have a normal probability distribution so that this contribution is presented as the root-mean-square (RMS), while the second contribution is normally distributed, thus it is presented as the sigma of Gaussian fitting.

By employing quadratic summation of both contributions, the intrinsic spatial resolution can be expected. as shown in Figure 11.18. Figure 11.18 (Left) shows the expected spatial resolution as a function of the distance from the wire for the gas mixture of Ar/C_2H_6 (50:50) and applied HV of 1900 V, where the incident particle is assumed to be 100 MeV/c electron. In the same way, Figure 11.18 (Right) shows the expected spatial resolution for the gas mixture of Ar/CO_2 (60:40). Here the third component, *ie.* electric noise, is not taken into account since it is not easy to expect the actual noise level precisely. In both case, the position dependence of

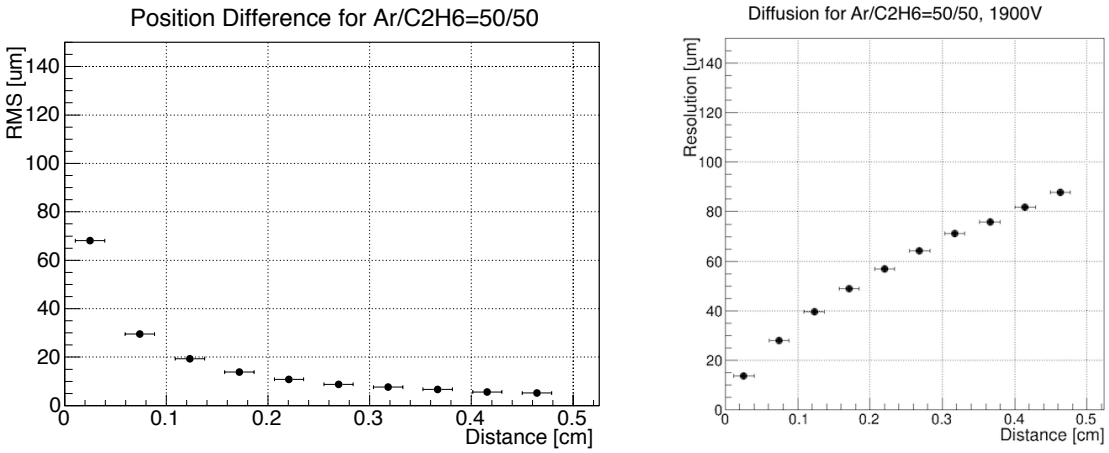

Figure 11.17: *Garfield++ simulation results 2 (Ar/C_2H_6(50:50),1900V); (Left) Fluctuation of the position of the closest primary ionisation to the wire as a function of distance from the wire, (Right) Spatial spread of the diffusion of drift electron*

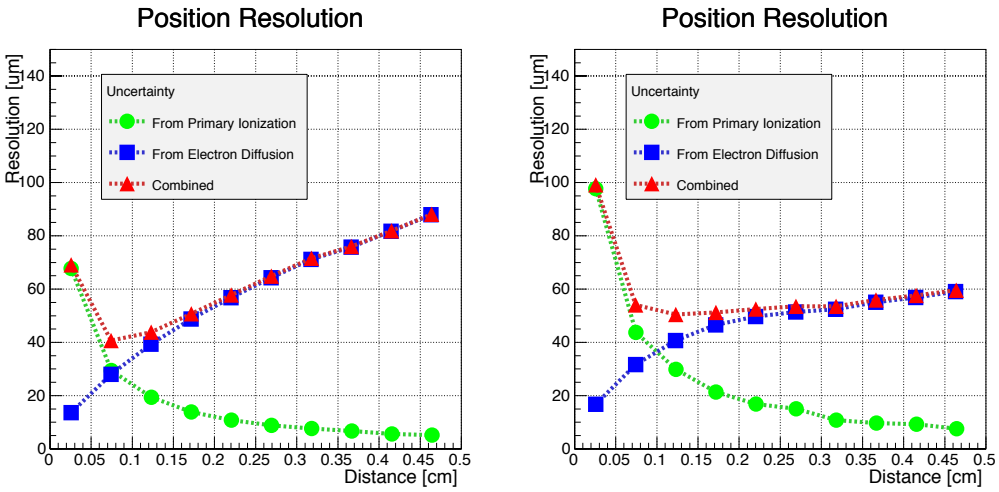

Figure 11.18: *Expected spatial resolution as a function of the distance from wire, simulated by Garfield++: (Left) Ar/C_2H_6 (50:50), 1900 V, (Right) Ar/CO_2 (60:40), 1900 V.*

the spatial resolution is clearly shown. The main difference is behaviour of each contributions. For the gas mixture of Ar/C_2H_6 (50:50), the main component is contributed by the gaseous diffusion while the main component is contributed by the fluctuation of primary ionisation for the gas mixture of Ar/CO_2 (60:40). It is difficult to conclude which gas mixture is the most suitable for COMET Phase-I straw tracker here, but it is very interesting to investigate such differences also for the real data. In Secion 11.5.1, this will be discussed again with the really obtained data by operating the prototype detector with the 100 MeV/c electron beam.

Simulation studies performed using the **GARFIELD** / **GARFIELD++** program indicate that the straw tracker will satisfy the required performance for beam background measurements using a gaseous detector, in addition to providing sufficiently good spatial resolution and stable operation, to provide tracking of charged particles.

11.3. Expected performance of the straw tracker

The performance of the straw tracker as the electron spectrometer is being investigated using MC simulation. The detailed geometry of the electron spectrometer (StrECAL), "straw tracker", "electromagneic calorimeter (ECAL)", and "solenoidal magnet", is precisely implemented in the ICEDUST framework, see Chapter 18. Figure 11.19 shows the implemented MC geometry of 5 straw-tracker stations with the reconstructed 105 MeV/c electron trajectory. All the detail of straw specification such as straw material (Mylar), straw-wall thickness (20 μm), cathode material (aluminimu), straw diameter (9.75 mm), and gas mixtures *etc.*, is precisely implemented and variable in order to perform the detailed simulation studies, *eg.* geometry optimisation. The actual magnetic field map, *cf.* Figure 9.12, is also implemented so that the charged particle trajectories are properly simulated.

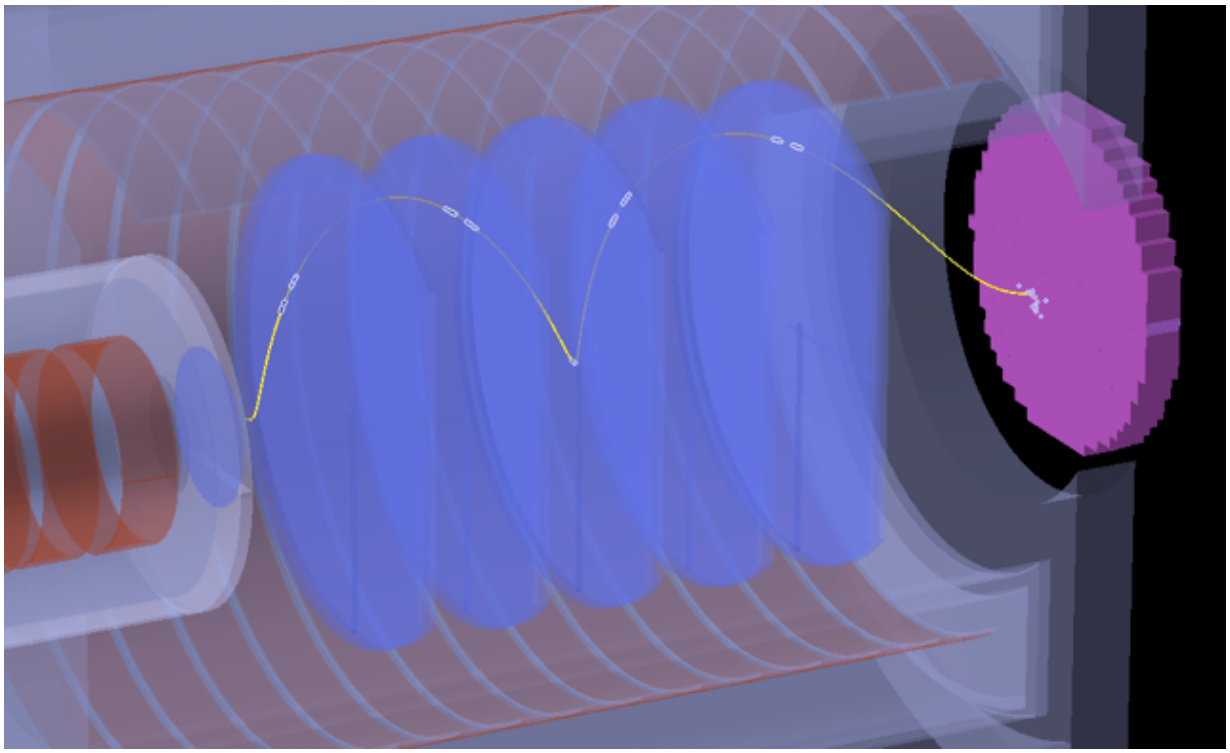

Figure 11.19: *Implemented MC geometry of the straw tracker with the reconstructed hits and electron trajectory.*

The number of hits is first studied in order to estimate the detection efficiency of the straw tracker. Here a "hit" for a station is defined by demanding that all four layers within one station record a layer hit. It is clearly shown that the number of hits strongly depends on a straw diameter and the gap between each straw. The number of hits is limited by the coverage of straw sensitive area so that larger diameters and smaller gaps improve the efficiency. The calculated efficiencies as a function of the gap between each straw are summarised in Table 11.2.

One of the most important functions of the straw tracker as a beam-background detector is the particle identification for various incoming particles. As described in Section 11.2.2, the feasibility of the straw tracker as a particle-identification detector is investigated using MC simulations with the **GARFIELD** program. According to this simulation, one can identify the difference of incident particles such as electrons, kaons and protons using charge information.

Table 11.2: *Detection efficiency as a function of the gap between each straws*

gap between each straws	0.5mm	1.0mm	1.5mm
Efficiency (N_{hit} $\geq$3)	99.1%	95.7%	87.5%
Efficiency (N_{hit} $\geq$4)	89.9%	77.1%	61.5%
Efficiency (N_{hit} $\geq$5)	56.4%	37.9%	23.1%

However, as is shown in Figure 11.15, it is quite difficult to identify the difference between muons and pions, and good particle identification is not feasible with the straw tracker alone. Using the combination of $\mathrm{d}E/\mathrm{d}x$ provided by the straw tracker and "E/p" by combining with the energy measured in the ECAL is essential to achieve more reliable identification of particles which will be discussed in Section 21

The other important performance parameters of the straw tracker is the momentum resolution. The track parameters are reconstructed by a track-reconstruction algorithm based on the Kalman-filter technique, which is known as GENFIT[71]. Momentum resolutions are extracted by fitting the residual distribution of the reconstructed momentum and the true (MC) momentum to the double Gaussians. Figure 11.20 shows the obtained momentum resolutions with various degree of vacuum. The momentum resolution is investigated with several pressures

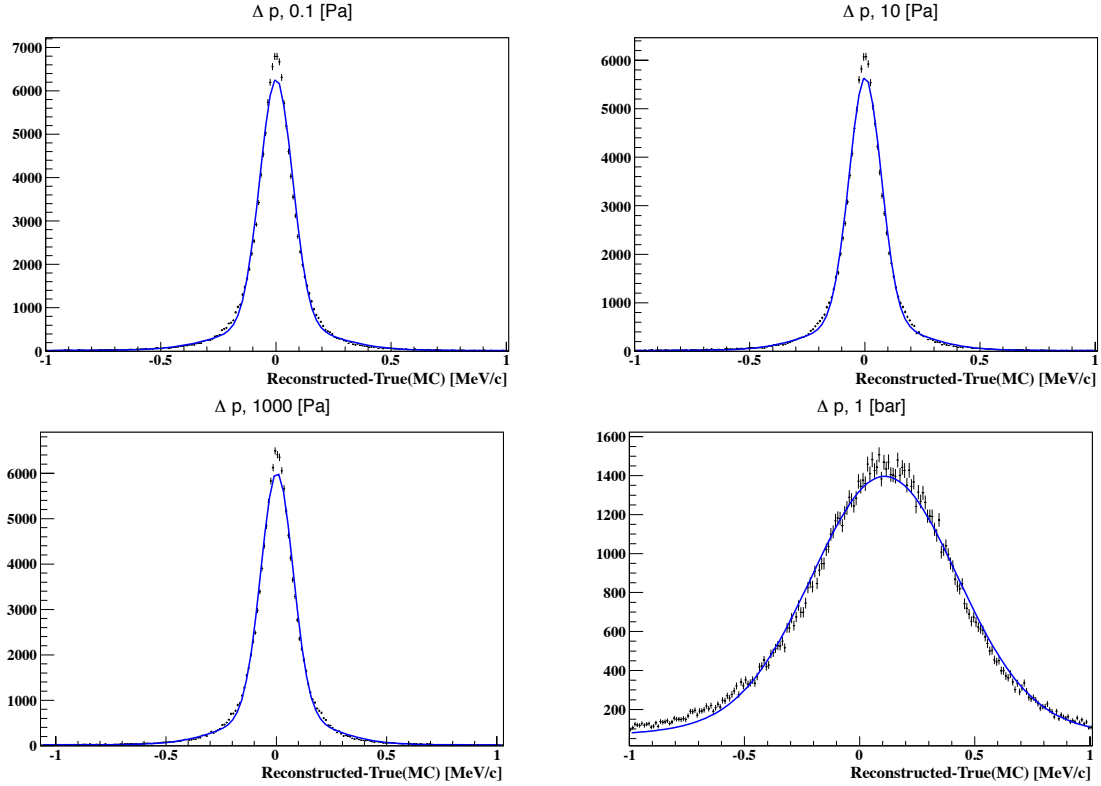

Figure 11.20: *Momentum resolution with various degree of vacuum; (Top-Left) 0.1 Pa, (Top-Right) 10 Pa, (Low-Left) 1 kPa, and (Low-Right) 1 bar*

inside the detector solenoid, *ie.* degree of vacuum. In Figure 11.20, degree of vacuum is varied to be 0.1 Pa, 10 Pa, 1 kPa, and 1 bar. The obtained core momentum resolutions found for each pressures are 72, 72, 75, and 313 keV/c, respectively. And the obtained average momentum resolutions of the double gaussian are 181, 183, 191, and 595 keV/c, respectively. The obtained momentum resolusions are good enough when the solenoid inside is pumped. However it is

noticed that they are not further improved while it is better than 100 Pa. In this study, an intrinsic spatial resolution of 200 μm is conservatively assumed, while in reality we expect it to be 100–220 μm, as detailed in Section11.1.6, which includes the alignment precision of ∼20 μm[8].

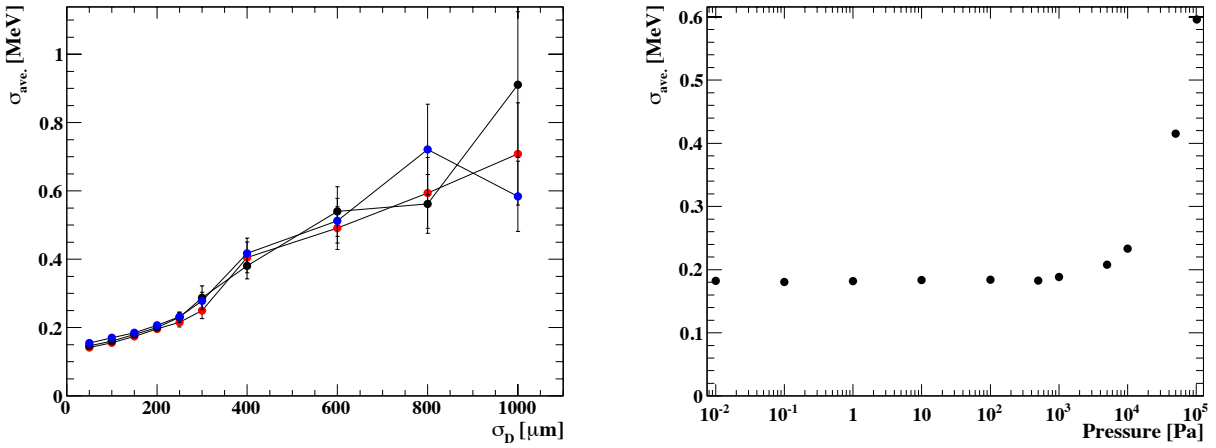

Figure 11.21: *Spatial resolution dependence and Pressure dependence of the momentum resolution. (Left) Momentum resolutions as a function of assumed spatial resolution, (Right) Momentum resolutions as a function of degree of vacuum.*

Figure 11.21 summarise the simulation studies concerning the spatial resolution and the degree of vacuum dependences of the momentum resolution. Here only the averaged momentum resolution is shown.

According to this result, the simulation studies come to the conclusion that the good enough momentum resolution can be achieved by realising the degree of vacuum better than 100 Pa and the intrinsic spatial resolution better than 200 μm.

11.4. Readout electronics

11.4.1 Tracker readout overview

As described in previous sections, the readout electronics boards will be installed in the gas manifold so that the front-end electronics operates in the vacuum inside the solenoid and can retrieve the analogue signal from anode wire directly without the use of long cables which would reduce the signal to noise ratio. All signals are digitised at the front end, and stored in digital pipelines for trigger latency. Once a trigger is presented, only those channels having signals above a set threshold are read, stored in buffers, and then serially transferred to a data acquisition system outside the vacuum wall. At this point the events are rebuilt, analysed, filtered, and finally committed to permanent storage.

[8] Currently the "off-magnet run", turning the detector-solenoid off and keeping the transport solenoid on, is planned in order to have straight charged tracks for the alignment.

11.4.2 Requirements for readout electronics

Suppose an electron track generates ∼60 electron-ion pairs in a straw tube. We propose to operate the straw tracker at a gas gain of 5×10^4 so the analogue signal presented to the front end will be 480 fC. We can assume that 10% of this charge is collected within the 6 ns which will be required for the signal to reach its peak. In order to set the discriminator threshold at approximately 16 fC or 2 primary electrons, preamplification of ∼1 V/pC of the signal is vital. To achieve the expected momentum resolution of less than 200 keV/c in straw tracker, the spatial resolution of ∼100 μm is desired as described above. Considering drift velocity in the straw as detailed in Section11.1.6, timing resolution of less than 2 ns is required in the readout board. Pileup capability is also required due to high hit rate. According to PHITS calculation with safety factor, neutron flux of $\sim 10^6$ n/cm^2/s and gamma-ray absorbed dose of ∼100 Gy are expected in Phase-I, so radiation tolerance in the readout electronics is indispensable. In general, the number of readout channels is quite large, so power consumption must be severely restricted, and cabling and the electronics footprint are constrained by space limitations.

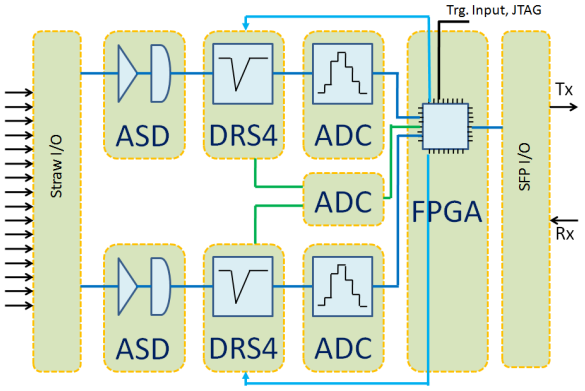

Figure 11.22: *"**ROESTI**": Front-end Board for the straw tracker.*

11.4.3 Readout electronics design

Based on these requirements, including those that are caused by the size of the gas manifold, we adopt a readout-electronics design which contains all the front-end processing; preamplification and pulse shaping, discrimination, and digitization. All this functionality is controlled by a FPGA-based readout controller, as shown in Figure 11.22. The first function, preamplification and pulse shaping, and the second function, signal discrimination, are realised by the **ASD** (Amplifier-Shaper-Discriminator) chip [9] , which has the gain of ∼1 V/pC [72]. Following this, the amplified signal is digitised by a **DRS4** chip [73] that has been developed at the Paul Scherrer Institut (PSI) for various particle-physics experiments, which has very fast sampling clock and can distinguish pileup event by offline analysis. Two blocks of input/output are implemented, corresponding to two ASD(8ch/chip) and DRS4(8ch/chip) chips. Therefore one **ROESTI** board has 16 channels of input/output. Parameters for each chip, *e.g.* signal discrimination, digitization sampling speeds etc., are controlled by the FPGA internally. For timing and jitter correction between two blocks of input/output, FPGA sends logic signal to each DRS4(1ch/chip). Finally, digitised waveform data in ADC(AD9637), correction data, and relevant metadata are sent out via an optical fibre cable through an SFP interface. FPGA has

[9] This ASD chip has been developed for ATLAS MDT/TGC front-end electronics originally, and recently modified for Belle-II CDC electronics; this version is adapted from Belle for the COMET straw front end.

some other input/output lines for trigger signal and JTAG signal. Considering neutron and gamma-ray irradiation, no flash memory is implemented on board, sp JTAG is used for FPGA firmware downloading in bit stream format.

The readout-electronics board has been developed on the basis of those described above and is called "**ROESTI**" (Read Out Electronics for Straw Tube Instrument) [10]. Development of the **ROESTI** board is supported by the KEK-Electronics group and Open Source Consortium of Instrumentation (OpenIt).

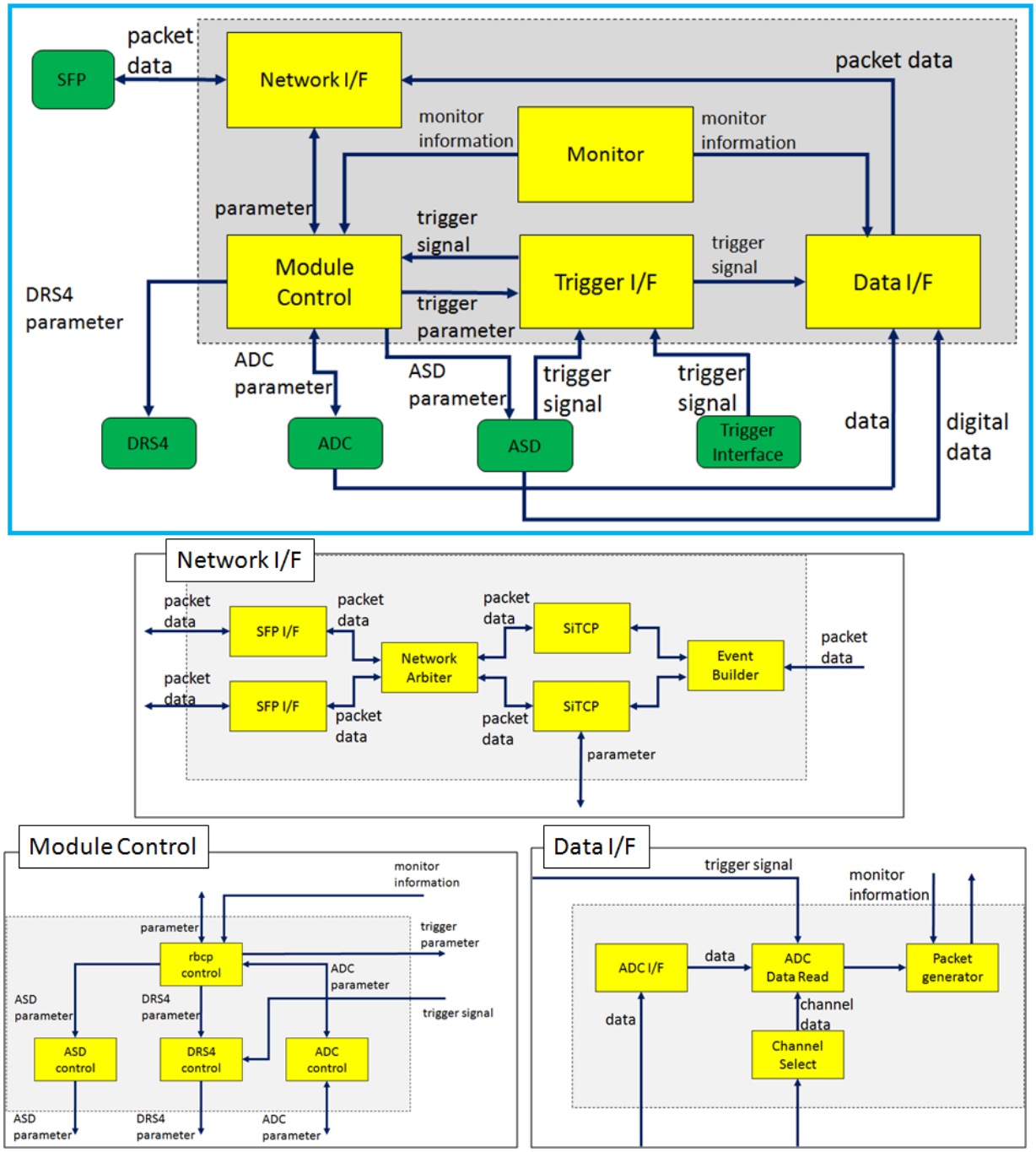

Figure 11.23: *"**ROESTI**": FPGA firmware structure*

[10] Pronunciation of **ROESTI** is ['rø:sti], same as the traditional potato dish from Switzerland, Rösti.

11.4.4 FPGA firmware design

In the **ROESTI**, one of the latest FPGAs, Artix-7 (XC7A200T-2FBG676C, Xilinx) is implemented. A block diagram of the FPGA firmware is shown in Figure 11.23. For clarity, the figure does not show the clock/reset signals and the the ADC/DRS reference clocks are likewise hidden. The firmware is composed of 5 blocks, Network I/F, Monitor, Module Control, Trigger I/F, and Data I/F. In the Network I/F block, the input/output signal can be transmitted/received between a PC and several boards via SFP I/F using TCP with SiTCP("Silicon TCP") module which provides the FPGA-Ethernet interface[74]. NetworkArbiter between SFP I/F and SiTCP determines the destination of TCP packet data and Eventbuilder controls the sequence of packet data flow, then these modules enable daisy chain connection with several boards. UDP connection for parameter control between the board and PC is also treated in this block. In the Monitor block, the temperature and voltage in the FPGA are monitored. Detection and correction of SEU(Single Event Upset) and URE(UnRecoverable Error) caused by neutron are also handled in this block. SEM(Soft Error Mitigation) module provided by Xilinx is implemented for SEU/URE in Configuration RAM. ECC(Error Correction Codes) using Hamming Codes is adopted for SEU/URE in Block RAM. Obtained monitor data is sent to Module control and Data I/F blocks. In the Module control block, RBCP(Remote Bus Control Protocol) for UDP communication is managed. Using UDP, all the chip parameters are controlled. ASD control module sets the DAC for the ASD threshold. DRS4 control module sets the offset voltage, sampling speed, and so on. When this module receives trigger signal, a start signal for sending charge information from DRS4 to ADC is issued. ADC control module sets ADC parameters. In the Trigger I/F block, trigger signal is treated and the information is sent to Module control and Data I/F blocks. In the Data I/F block, ADC output data and monitor data are received and converted to packet data, then the data is sent to Network I/F block. ADC I/F module converts the serial signal from ADC to parallel signal, and then sends the data to ADC Data Read module. In parallel, Channel Select module receives the channel information from ADC and send that to ADC Data Read module. Using the channel information, the function of zero-suppression is implemented. The parallel data is temporarily stored in the Block RAM in FPGA, and is sent to Packed generator module after receiving the trigger information. That data and the one from Monitor block are converted to packet data in a format as shown in Figure 11.24.

Header and footer are 32 bit magic words for identification of the beginning and end of the data, respectively. After the header and before the footer, some typical information data are inserted. TYPE and reserved are 16 bit data that can be set arbitrarily, which are not fixed in current version. Board number(16 bit) identifies which board sends the data as its name suggests. Length(32 bit) indicates the data packet length, which is determined by hit channels. Event number(32 bit) is also as its name suggests. SEU count(16 bit) and URE count(16 bit) show the number of counts of SEU and URE, respectively. As for the SEU, detailed information such as the memory address, error type, and so on are obtained by SEM and those are included in SEU info(32 bit) and its length is stored in SEU info size(16 bit). Pretrigger data consists of 36 bit trigger information from trigger signal and 28 bit dummy data. In the Data Packet, there are header(Data Packet Word, 16 bit), footer(Data Packet Footer, 16 word), hit channel data(ADC Data, 12 bit and 4 bit dummy), and some information data. Board number(8 bit) indicates low 8 bit of the one in Data Format, which is inserted for redundancy. Ch Number(8 bit) identifies which channel sends the data. Stop Number(16 bit) shows the number of stopped capacitor in DRS4, which is determined by trigger timing. Data length(16 bit) is as its name suggests. If no hits are detected, this is set to 0 and ADC Data region disappears. Keyword is 8 bit data that can be set arbitrarily. Check sum is set to 8 bit data for error detection.

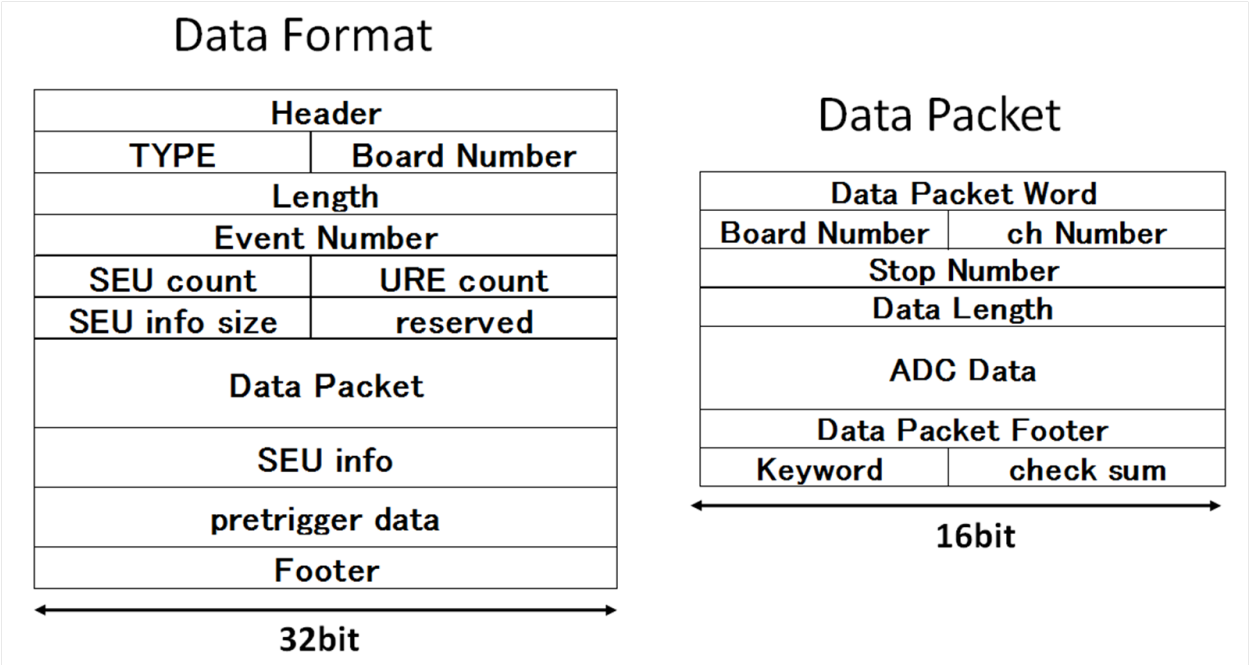

Figure 11.24: *"**ROESTI**": data format*

11.4.5 Board prototype

With support from OpenIt and KEK-Electronics group, a prototype **ROESTI** board has been developed. Currently, the prototype version 3 is under investigation and design work for final prototype is ongoing to improve the performance, correct problems discovered using prototype 3 and optimise the design. Figure 11.25(a) shows the completed prototype version 3 of **ROESTI** board. As described in the previous section, **ROESTI** can be connected with several boards via

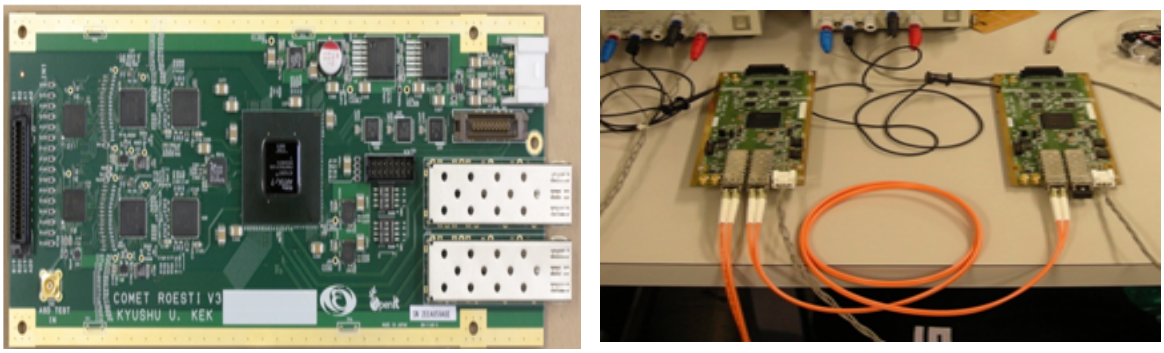

(a) (b)

Figure 11.25: *Prototype **ROESTI***
board; (a) Prototype Version 3, (b) Daisy-chained boards

SFP I/O interface as shown in Figure 11.25(b). Intensive testing and R&D work is currently ongoing. For example, Figure 11.26(a) shows the recorded waveform (red asterisks) with the test pulse input (blue line) from a function generator; gain calibration is performed using test input pulses and we have confirmed good agreement with design value as shown in Figure 11.26(b); the obtained calibration constant is 1.03 mV/fC, while 0.98 mV/fC is expected.

One of the most important performance parameters is the timing resolution of the readout. By taking two test inputs to channels 1 and 7 and reading them out at 1GSPS, the timing-

difference distribution is shown in Figure 11.26(c) that shows the timing resolution is 160 ps, which is good enough to meet the requirements for track reconstruction.

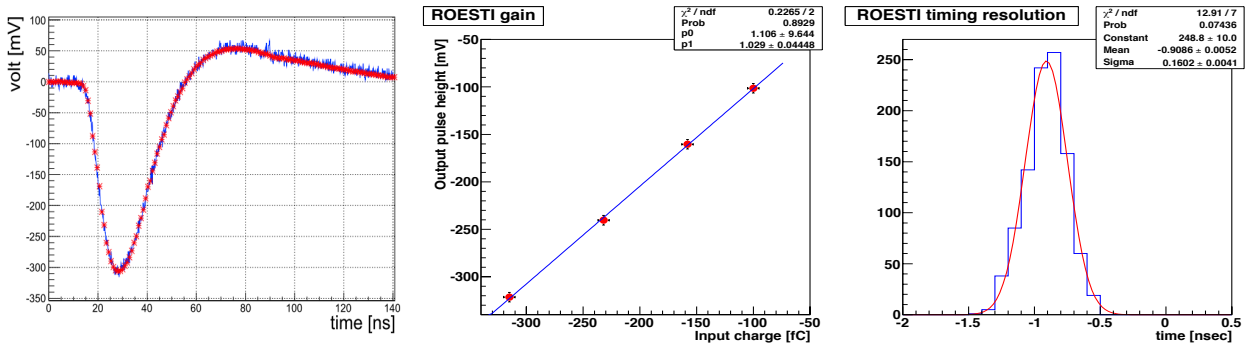

(a) (b) (c)

Figure 11.26: *Performances of* ***ROESTI*** *prototype version 2; (a) Test-pulse output, (b) Gain calibration, (c) Timing resolution*

11.4.6 Data transfer through daisy-chained boards

One of the significant feature is that a number of **ROESTI** boards can be series-connected with the daisy-chain configuration. This feature was not tested until recently, because of the difficulty of firmware implementation activating this functionality. However, this feature has been activated by implementing the dedicated firmware, and this capability was experimentally demonstrated. Figure 11.27(Left) shows the set up of daisy-chain test. In this test, three

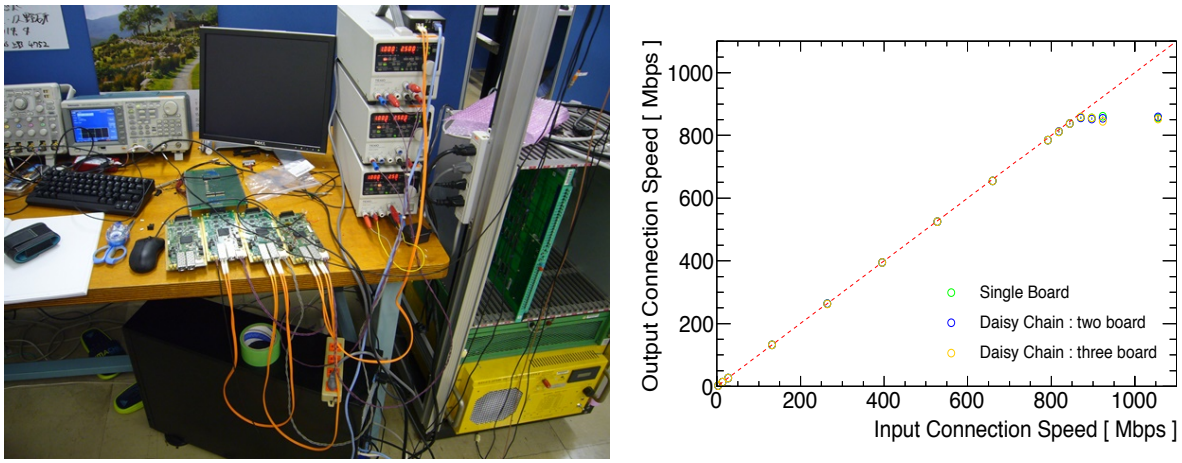

Figure 11.27: *Daisy-chain test on three* ***ROESTI*** *boards; (Left) Set up, (Right) Results*

ROESTI boards are series-connected via optical cable, and the output data packet of the second and third board is successfully recorded. Figure 11.27(Right) shows the recorded data transfer speed in the second and third board as a function of input data rates. Saturation of the data-transfer speeds all appear at same data rate, $\approx$ 830 Mbps. This demonstrates that this limitation is not caused by the daisy-chain since this saturation rate is same as stand-alone operation, indicated as "Single Board" in the plot. In addition, by using more powerful computer as a readout, it is the saturation point is improved up to 930 Mbps. Note also these ceilings are typical for Gigabit Ethernet connections.

According to this results, the daisy-chain functionality is successfully demonstrated, and it will provide a drastic reduction of connectors/channels on the patch-panel for the straw-tracker readout front-end. However, this test has just demonstrated this function, and further optimisation and improvements are planned.

11.5. Tracker prototyping and construction

11.5.1 One-straw prototype

Since the mechanical strength investigation for the COMET 20-μm straw which is described in the Section 11.1.3 was successfully performed, it was decided to build the small prototype detector, called "**One-Straw Prototype**", in order to perform the further investigation such as gas tightness, operation in vacuum, noise shielding, and so on.

Before building the one-straw prototype, one of the most important development for the straw assembly was made, *ie.* pretensioning scheme for straw stretching. As discussed in Section 11.1.3, straw stretching of 2mm is necessary which is corresponding to apply a pretension of 1 kg_F on straw tube in order to keep the circular shape of straw cross-section and avoid any deformation against the pressure difference due to a vacuum and the sag due to gravity. Then the new feedthrough system was developed by adding the specially developed 'bushing' part into the present feedthrough system. This bushing is placed between a metal sleeve that connects to the straw and gas feedthrough, and is threaded against the metal sleeve such that rotating the bushing whilst fixing the sleeve puts tension on the straw without it being twisted. This new feedthrough system provides not only the electric contact but also the straw tensioning scheme. Figure 11.28(Left) shows the pretensioning test-bench using the developed feedthrough system,

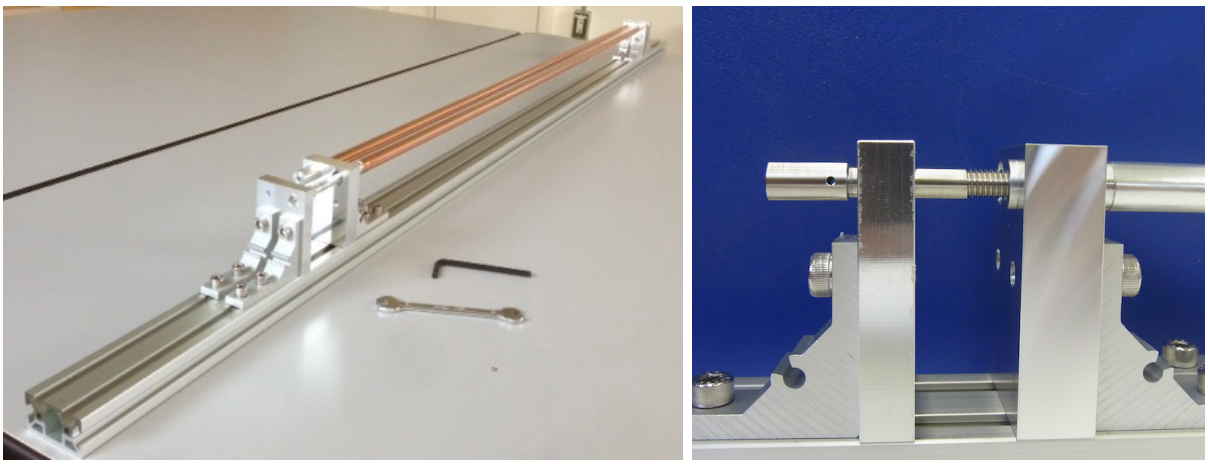

Figure 11.28: *New feedthrough development: (Left) Set up and tensioning study, (Right) Close-up of developed feedthrough*

with a close-up view on the (Right). As described above, the feedthrough system is designed to be threaded against the metal sleeve such that rotating the bushing whilst the sleeve remains fixed puts tension on the straw without it being twisted. The amount of straw stretching is measured as a function of the applied tension so that we do not have to apply pretensioning using a weight. Instead the straws are simply stretched by rotating the bushing part of the feedthrough to pull the straw tube by 2 mm, which is equivalent to a pretension of 1 kg_F.

By employing this newly developed feedthrough system, one-straw prototype was quickly built. This prototype has only one straw, however, all the accompanying items such as an anode wire, gas supply and manifolds, a HV circuit, a signal-readout circuit and so on, so that the prototype can be operated as a radiation detector like a proportional chamber as shown in Figure 11.29. Figure 11.29 (Top) shows the drawing of one-straw prototype, and Figure 11.29 (Left) shows

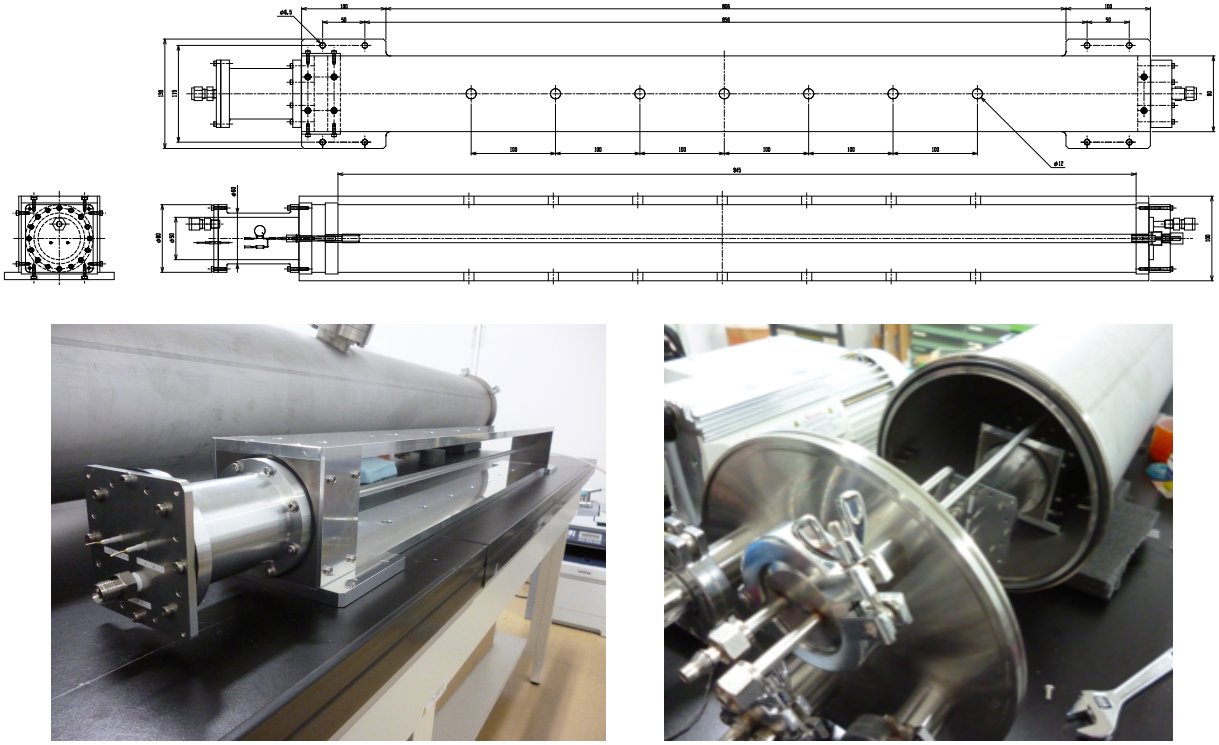

Figure 11.29: *One-Straw Prototype; (Top) Drawing, (Left) Photo of the whole view, (Right) Installation into a vacuum vessel*

the picture of whole view of the prototype. The most critical concerns for the straw chamber operating in a vacuum are (i) **gas leakage** and (ii) **deformation**, thus in order to perform the tests for this prototype in vacuum, the one-straw prototype is designed to be operational in vacuum. Figure 11.29 (Right) shows the installation of the one-straw prototype inserting into a vacuum vessel.

At first, the gas tightness was measured. The leak rate of the tubes has been measured in two different ways; (a) by measuring the pressure drop inside the tube as a function of time after it is over-pressurised to 2 bar using the Ar/C_2H_6 (50/50) default gas mixture as shown in Figure 11.30(a), and (b) by installing a straw tube in a vacuum vessel and measuring the pressure rising inside the vacuum vessel as a function of time after the tube is filled with the default gas at 1 bar as shown in Figure 11.30(b). For the measurement-(b), pressure rising was measured three times; (i) at first it was measured without anything inside the vacuum vessel to measure the out-gassing from the vessel inner wall, (ii) at second it was measured with one-straw prototype but gas flow, (iii) and at last it was measured with gas flow. Then the difference between (ii) and (iii) tells us the net leakage from the straw tube. Both tests gave consistent results. The measured pressure drop in (a) and the measured pressure rise in the vacuum vessel (b) are corresponding to a leak rate of 0.0035 cm^3/min per metre of tube. This leak rate, when scaled to the full spectrometer, is well within what is needed to keep pumping rates at modest levels.

The electrical shielding is also confirmed by operating the one-straw prototype. As described

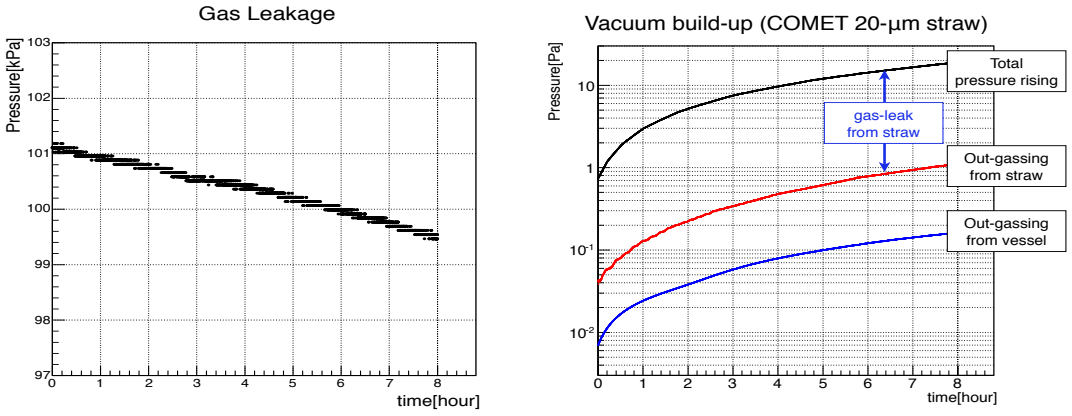

(a) (b)

Figure 11.30: *Measured gas leakage (b) Pressure drop inside the straw tube as a function of time after it is over-pressurised to 2 bar, (a) Pressure build-up as a function of the time after pump close.*

in the Section 11.1.3, the cathode material on the newly developed 20-μm straw is changed to be an only 70-nm-thick aluminium instead of Cu/Au, *ie.* there is a concern about a shielding performance since the electric conductivity can be deteriorated by the straw pretensioning described above. Figure 11.31 shows the results of signal investigation operating the one-straw prototype. In order to perform the signal investigation, the one-straw prototype is operated

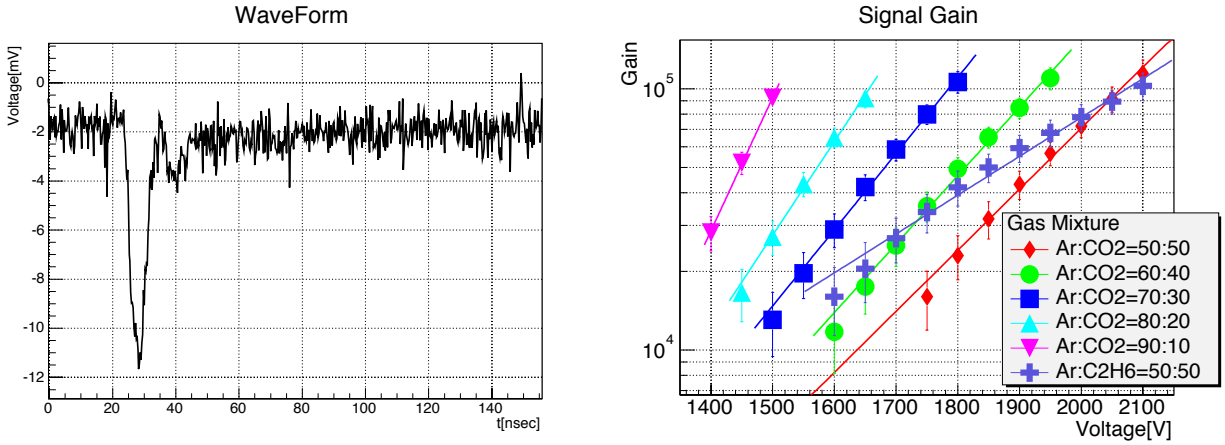

Figure 11.31: *Signal investigation of one-straw prototype; (Left) Observed signal waveform by the x-ray irradiation from ^{55}Fe source (Ar/C_2H_6(50/50), HV=2000V), (Right) Obtained gas gain with various gas mixtures as a function of applied HV.*

with several gas mixtures such as Ar/C_2H_6 and Ar/CO_2 and is irradiated by the x-ray from ^{55}Fe source. One of the observed signal waveform is shown in Figure 11.31 (Left), this waveform is extracted from the anode wire directory without any preamplification, thus a good signal shielding is confirmed. By changing the gas mixture and applied HV, gas-gain measurement is performed as shown in Figure 11.31 (Right), then the normal gas amplification is also confirmed.

According to the results of the one-straw prototyping, employment of the newly develope 20-μm straw for COMET Phase-I straw tracker is totally validated.

11.5.2 Full-scale prototype

As the last R&D before starting the final tracker assemly, it was decided to construct the large prototype, called **Full-scale prototype**. The full-scale prototype has the almost same dimension of the final tracker station, only the number of straw is small. Figure 11.32 shows

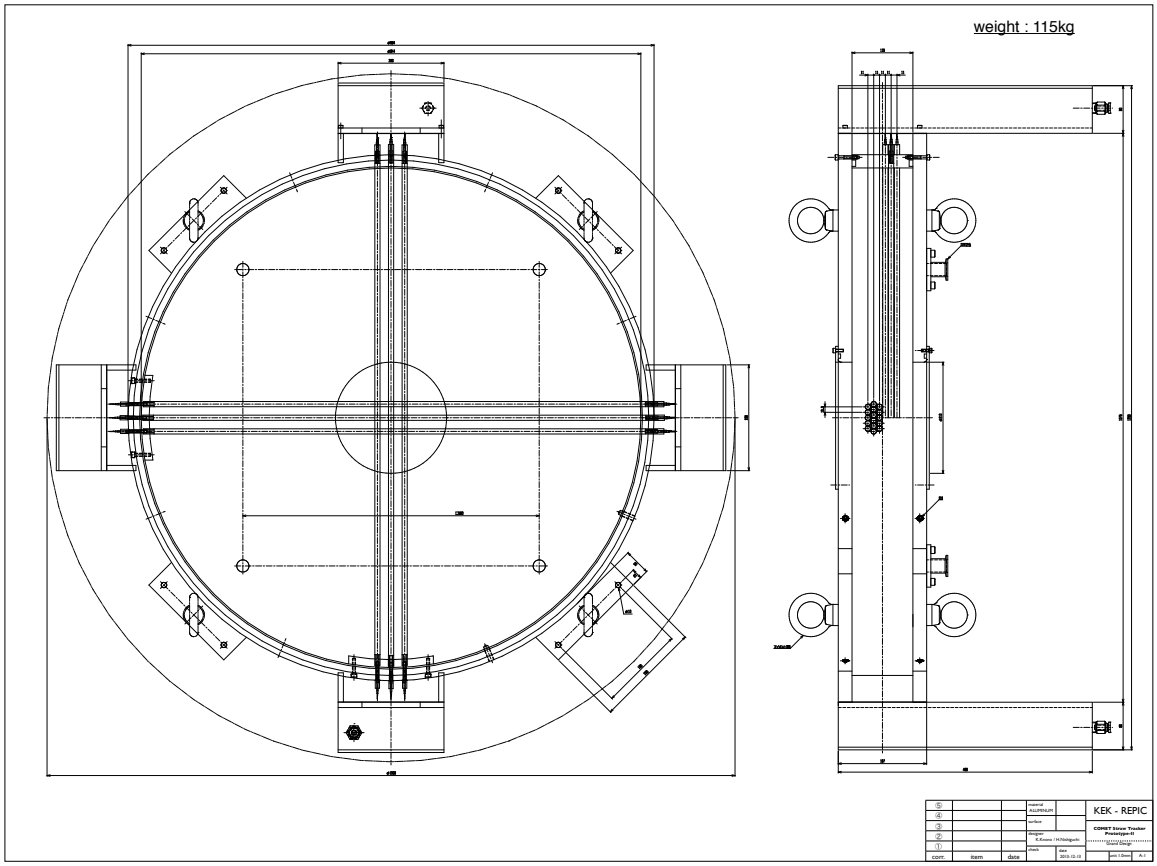

Figure 11.32: *A drawing of the assembly prototype*

the design of the full-scale prototype that consists of six straw-tube planes; x_1, x_2 and x_3 for measuring the x-coordinate and y_1, y_2 and y_3 for measuring the y-coordinate, and each coordinate is read out by 16 straw tubes. Therefore 32 straw tubes are used in total for the assembly prototype so that one coordinate (3 planes) can be covered by one **ROESTI** board which has 16 readout channels.

Newly developed 20-μm straws are mounted in the full-scale prototype using the developed feedthrough system so that no-weight is needed for the straw assembly, this feedthrough implementation is investigated precisely to provide the feedback for the final assembly. The size of gas manifold is designed to be as small as possible, while being large enough that it can hold the signal-decoupling circuits, HV-distributing line, and **ROESTI** boards. The entirety of the exterior of the full-scale prototype is covered with a vacuum wall so that the full-scale prototype can be evacuated via vacuum ports whilst operating the straws as a stand-alone detector. This allows straw behaviour studies in vacuum to be performed. Signals are transmitted through the feedthrough board which can provide the SFP I/O interface between the inside and outside of the vacuum wall. The full-scale prototype is made of aluminium so that the prototype is not affected by magnetic field.

After its operation R&D in the lab, test-beam campaign have been carried out at the Research Center for Electron Photon Science (ELPH), Tohoku University, in December 2015 and March

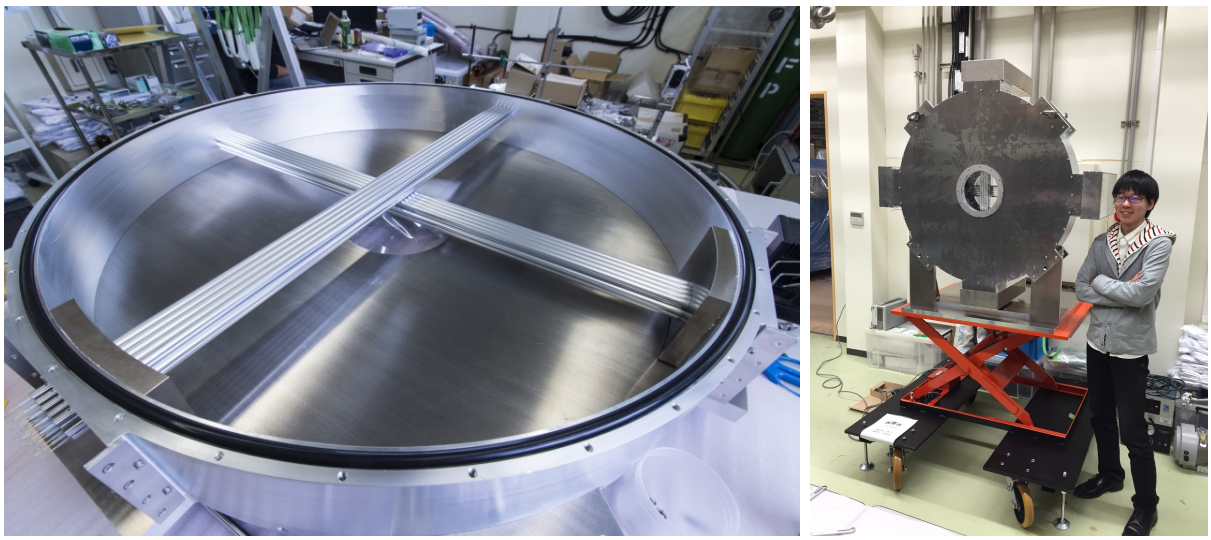

Figure 11.33: *Full-scale prototype; (Left) Partially completed without vacuum wall, (Right) Whole view of the completed full-scale prototype*

2016, with the various momentum electron beam. The setup for the beam test is schematically shown in Figure 11.34 (Left), and its photo is also shown in Figure 11.34 (Right). Here

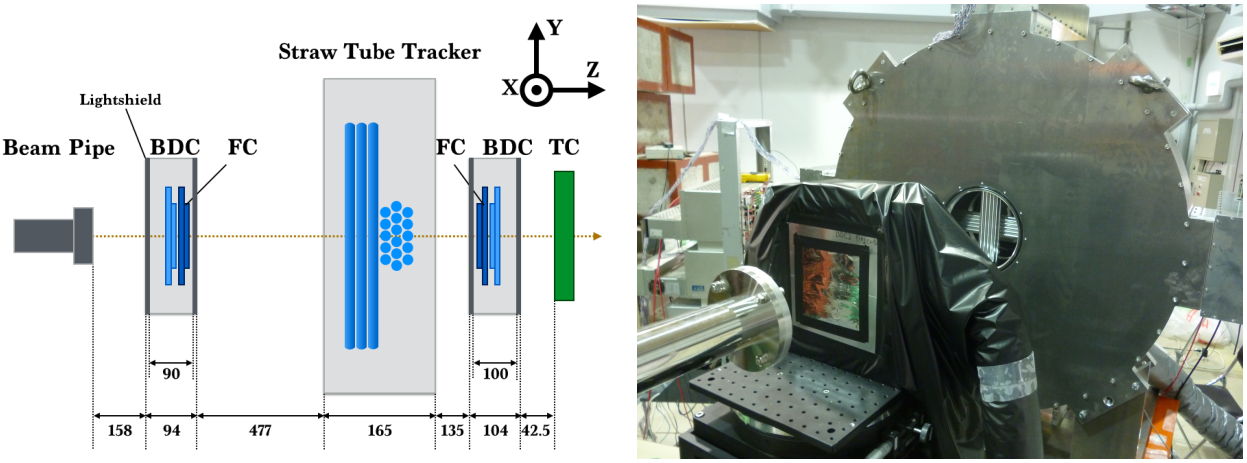

Figure 11.34: *Test-beam setup; (Left) Schematic view of the setup, (Right) Photo of set up viewing from the upstream.*

"BDC" means the "beam-difining counter" which consists of bidirectional 1-mm-thick scintifibre counters, and "FC" means the "finger counter" which consists of finger-size 1-mm-thick thin plastic schintillator counters. Trigger signal is made by the coincidence between two FCs and "TC" (Timing Counter) which consists of high light yield plastic scintillator with the fast fine-mesh PMT to provide the precise timing measurement. The electron beam momenta is varied between 50-300 MeV/c.

Figure 11.35 shows the measured detection efficiency for the gas mixture of $Ar/C_2H_6(50/50)$ as a function of applied HV. Straw single efficiency is measured by counting the number of proper hits in layer-2 and counting the number of tracks in layer-2 which is reconstructed by the hits in layer-1 and layer-3. As shown in Figure 11.35 (Left), high enough HV, higher than 1800 V, guarantees the full efficiency. However, due to the small but finite gap between each straw

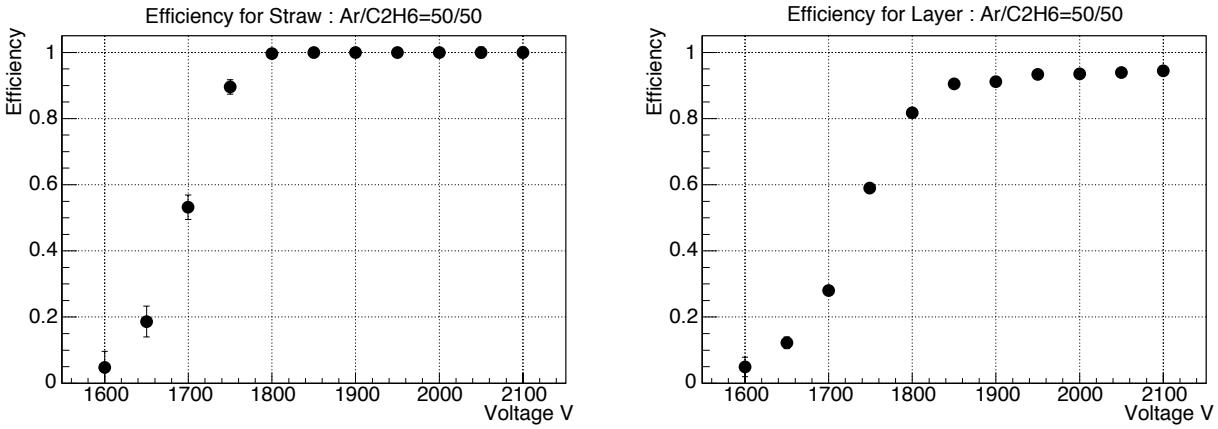

Figure 11.35: *Measured detection efficiencies; (Left) Straw single efficiency, (Right) Detection efficiency as a tracker layer*

tubes[11] a certain inefficiency should be there, thus the detection efficiency as a tracker layer is also measured as shown in Figure 11.35 (Right). Even the full-scape prototype has a certain inefficiency, high enough efficiency such as ∼95 % is obtained.

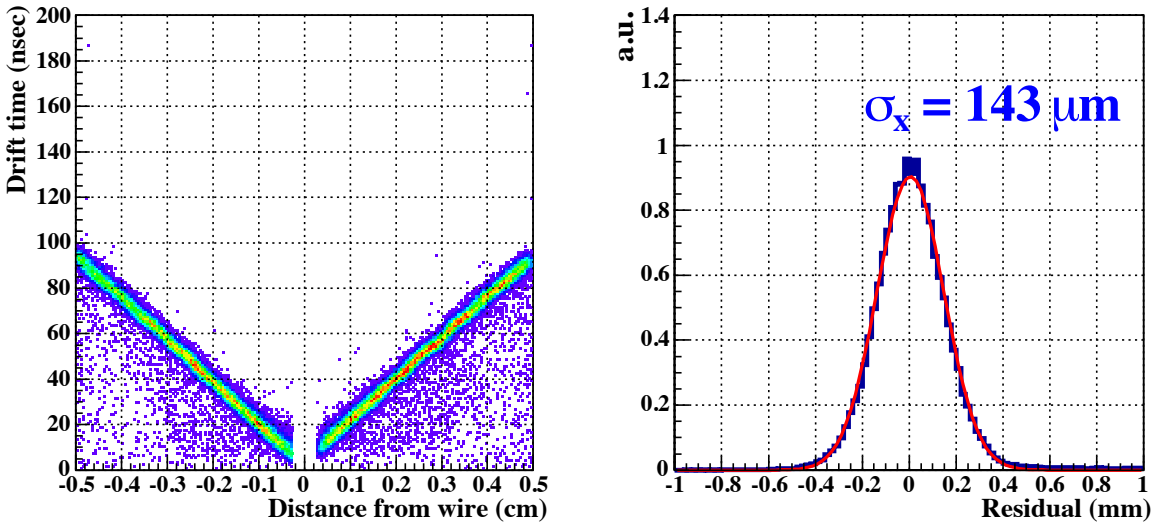

Figure 11.36: *Obtained X-T relation and its residual distribution, gas mixture = $Ar/C_2H_6(50/50)$, HV = 1900 V*

Figure 11.36 shows the obtained X-T relation (Left) and its residual distribution for tracks (Right) which is corresponding to a spatial resolution of 143.2 μm for the gas mixture of $Ar/C_2H_6(50/50)$ and HV of 1900 V. Here the obtained spatial resolution contains the uncertainties such as a precision of track reconstruction *etc.*, and the subtracted true spatial resolution could be estimated to be 119.3 μm.

Figure 11.36 (Right) is a residual distribution for whole tracks without any event selection related to the incident position. As discussed in Section 11.2.3, drift-distance dependence of the spatial resolution is interesting to have a better understanding of the tracker, and such dependences are already carefully investigated by simulation; *cf.* Figure 11.18. Figure 11.37

[11] The full-scale prototype has a small gap of 0.3 mm between each straw tubes.

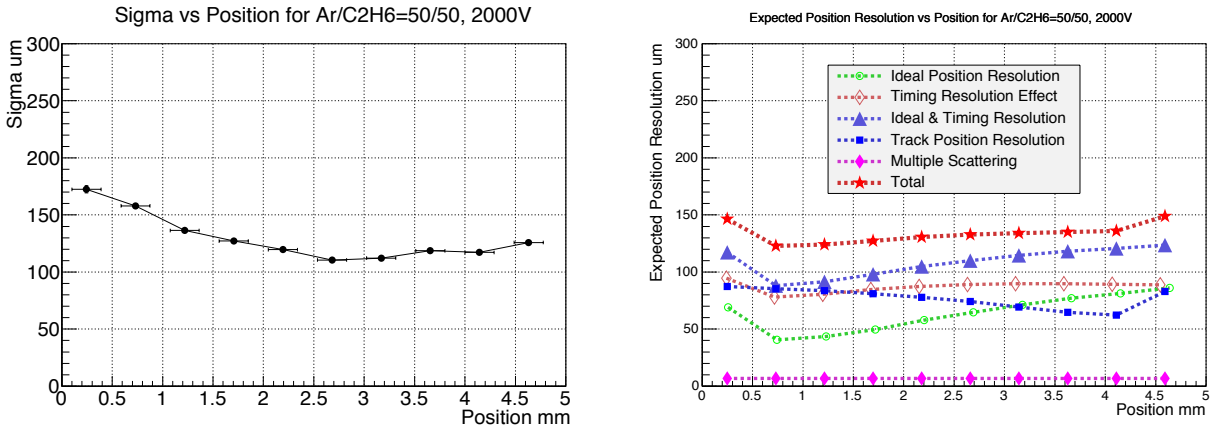

Figure 11.37: *Incident position dependence of the obtained spatial resolution, gas mixture = $Ar/C_2H_6(50/50)$, HV = 2000 V. (Left) Data, (Right) Garfield++ simulation*

(Left) shows the incident position dependence of the obtained spatial resolution for for the gas mixture of $Ar/C_2H_6(50/50)$ and HV of 2000 V. Figure 11.37 (Right) shows the result from the simulation by **GARFIELD++**. In the Section 11.2.3, two contributions are investigated, *ie.* a fluctuation of the primary ionisation position and a diffusion effect of drift electron. Now further detailed estimation is possible to take into account the other uncertainties such as timing resolution due to noise, tracking resolution, and the multipe scattering effect. Figure 11.37 (Left) shows the expected spatial resolution simulated by **GARFIELD++**, where the green (open circle) plot shows the ideal spatial resolution which is simulated in Figure 11.18. As shown in both plots of Figure 11.37, the behavior of incident-position dependence is almost reproduced in the simulation, thus the detector response is now well understood. Figure 11.38 shows the

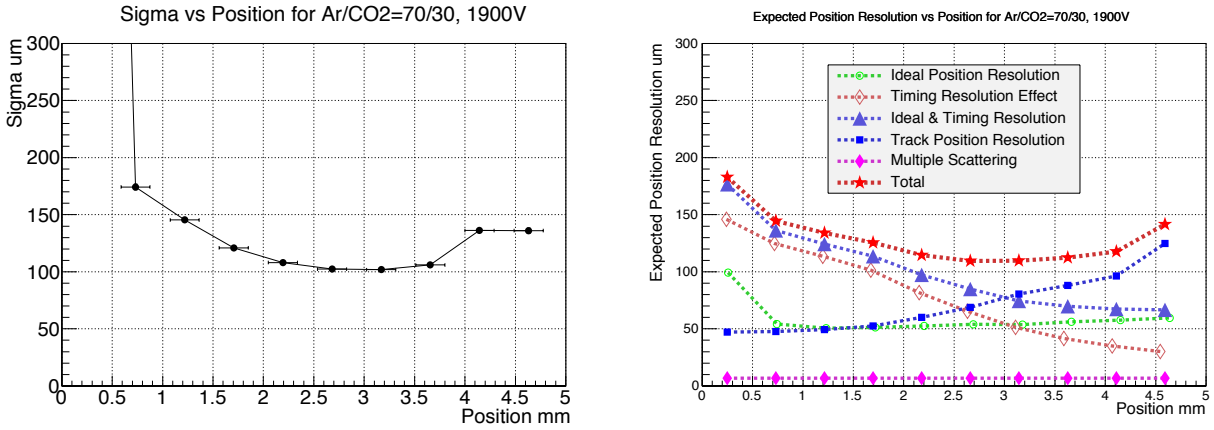

Figure 11.38: *Incident position dependence of the obtained spatial resolution, gas mixture = $Ar/CO_2(70/30)$, HV = 1900 V. (Left) Data, (Right) Garfield++ simulation*

same plots as Figure 11.37 but the tracker condition is different; gas mixture of $Ar/CO_2(70/30)$ and HV of 1900 V. In both gas mixtures, good enough spatial resolution, better than 200 μm, over all the straw region is obtained.

As described at the beginning of this section, inside the full-scale prototype can be evacuated via vacuum ports whilst operating the straws as a stand-alone detector. Figure 11.39 (Left) shows the straws viewing from outside the vacuum window. This photo was taken during

pumping the detector so the reflection in vacuum window is distorted. Figure 11.39 (Right)

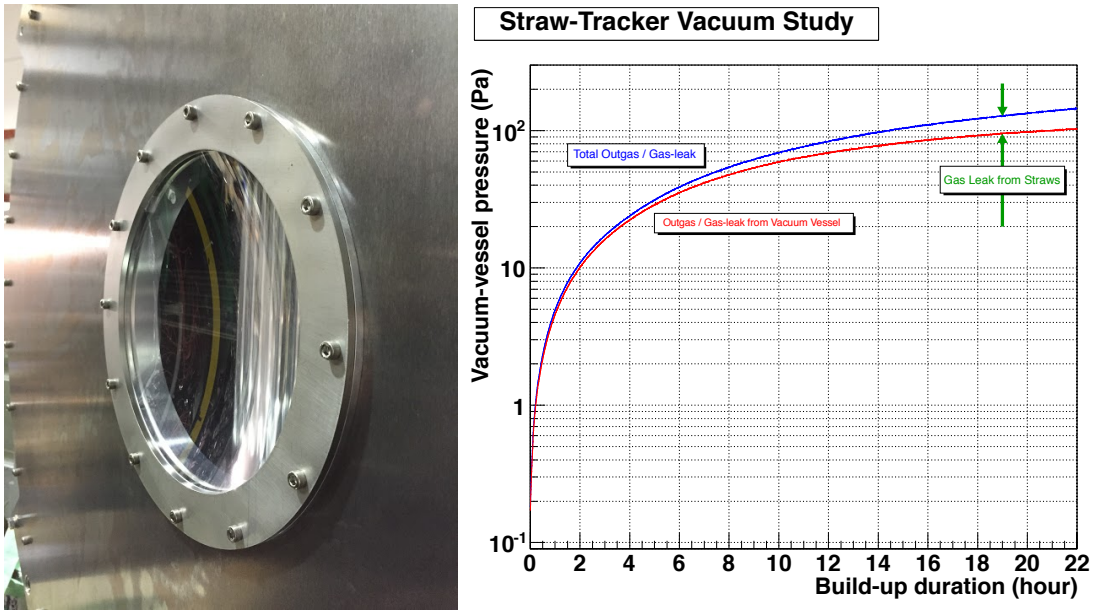

Figure 11.39: *Vacuum study for the full-scale prototype.*

shows the measured pressure rising inside the vacuum vessel as a function of the time after pump close. The total outgas/gas-leak is measured with gas flushing while the outgas/gas-leak from the inner wall of vacuum vessel and the straw tubes is measured without gas flushing. During the latter measurement, straw-tube inside is pumped, too. Then the difference between both measurements tells us the net leakage from the straw tube. The measured difference of pressure rise in the vacuum vessel is corresponding to a leak rate of 0.023 cm^3/min per 32 straw tubes, while a leak rate of 0.0035 cm^3/min per a meter of tube is obtained by the one-straw prototype as described in Section 11.5.1, Figure 11.30. The measured leak rate per one straw is 0.0007 cm^3/min which is 5 times better than the result of the one-straw prototype. The measured leak rate of the one-straw prototype contains the gas leaks at anywhere such as gas manifold, connections of piping, and so on, so that the differences can be explained. The measurement in the full-scale prototype does not contain such external gas leaks. The expected leak rate, when scaled to the full spectrometer, is 1.725 cm^3/min and well within what is needed to keep pumping rates at modest levels. The finally achieved degree of vacuum in the full-scale prototype is $\sim$0.1 Pa which is also better than the vacuum requirement of 100 Pa.

In conclusion, fundamental performances, such as a detection efficiency, an intrinsic spatial resolution, are confirmed to fulfill the requirements. And the capability to realise a vacuum inside the detector solenoid is also confirmed and expected to be better than the requirement.

11.5.3 Schedule

As described above, all the tracker R&D is just completed. Thus it is a time for final assembly.

The straw mass-production was already completed by our JINR colleagues in summer 2015, 2,900 straw tubes includeing spare of 500 tubes are already delivered to KEK, and ready for assemly.

The design of tracker body, *ie.* the support structure, is almost fixed as shown in Figure

11.2. By adding some modifications such as an attachment of the feedthrough to the front-end electronics readout, the construction will start.

The front-end electronics development is also ongoing. As described in Section 11.4.5, intensive prototyping is underway. Currently the careful investigation is ongoing for version 3. As soon as the prototype version 3 study is completed, mass production of front-end electronics will start immediately if no further development is required.

The present schedule of straw-tracker construction is presented in Figure 11.40.

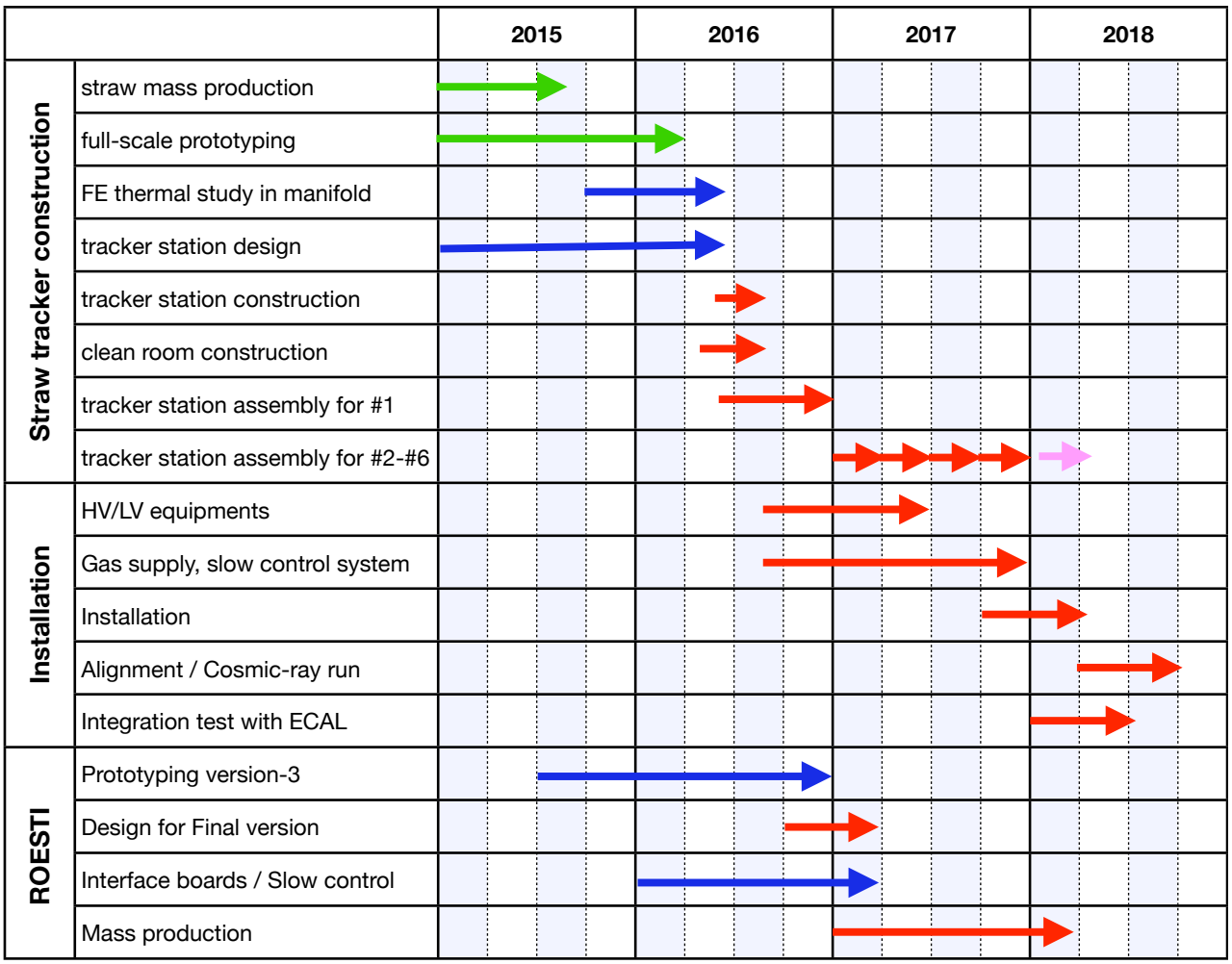

Figure 11.40: *Straw tracker construction schedule*

Chapter 12

Electron Calorimeter (ECAL)

The electron calorimeter (ECAL) system consists of segmented scintillating crystals. It is placed downstream of the straw chamber detector and serves the following three purposes : to measure the energy of electrons (E) with good resolution, to add redundancy to the electron momentum (p) measurement and to provide the ratio E/p for electron identification. The ECAL will also provide an additional hit position to the electron track trajectory at the location of the ECAL, to cross-check the tracker-based electron trajectory. The ECAL also provides the trigger signals, carrying the timing with respect to which the electron events are referenced. Independent and redundant measurements of the energy of electrons are of critical importance to separate true signals of $\mu-e$ conversion from background tracks that conspire to mimic a signal.

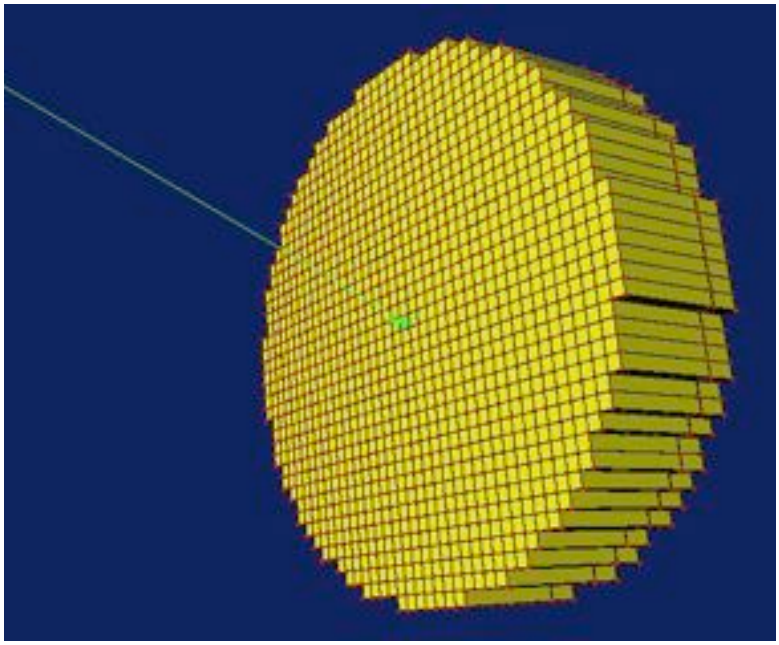

Figure 12.1: A schematic layout of the electron calorimeter system.

The ECAL is required to have an energy resolution of better than 5 % at 105 MeV and a cluster position resolution of better than 1 cm. With sufficient crystal granularity, the shower topology can also be used to discriminate electrons from neutrons and low energy photons. The crystals need to have a good light yield, and fast response and decay times to reduce pileup. A schematic layout of the ECAL system is shown in Figure 12.1. Unlike the Mu2e calorimeter, the COMET calorimeter will not require a central hole to allow the beam pass, since COMET will have a muon beam stop between the stopping target and ECAL and it has an electron transport

solenoid preventing low momentum beam particles reaching the ECAL. It is noted that the ECAL design is common for COMET Phase-I and Phase-II.

12.1. Scintillating Crystals

GSO(Ce) and LYSO are the most attractive crystals in terms of their performance. Table 12.1 summarises the characteristics of the inorganic scintillator crystals, together with PWO and CsI(pure) as a reference, which have a large light yield and a short decay constant. The choice of crystal type depends on not only its performance, but also its cost. GSO has a light yield about one third that of LYSO but the cost of LYSO is more than that of GSO. A performance-cost evaluation on GSO from Hitachi Chemical Co., Ltd. shown in Figure 12.2 and LYSO from Saint-Gobain Crystals has been undertaken. The R&D result is described in Section 12.5.. The resulting choice is to use LYSO for the ECAL.

Table 12.1: The characteristics of inorganic scintillator crystals. The superscript of f and s represent the fast component and the slow component, respectively.

	GSO(Ce)	LYSO	PWO	CsI(pure)
Density (g/cm^3)	6.71	7.40	8.3	4.51
Radiation length (cm)	1.38	1.14	0.89	1.86
Moliere radius (cm)	2.23	2.07	2.00	3.57
Decay constant (ns)	600^s, 56^f	40	30^s, 10^f	35^s,6^f
Wave length (nm)	430	420	425^s, 420^f	420^s, 310^f
Refractive index	1.85	1.82	2.20	1.95
Light yield (NaI(Tl)=100)	3^s, 30^f	83	0.083^s, 0.29^f	3.6^s,1.1^f

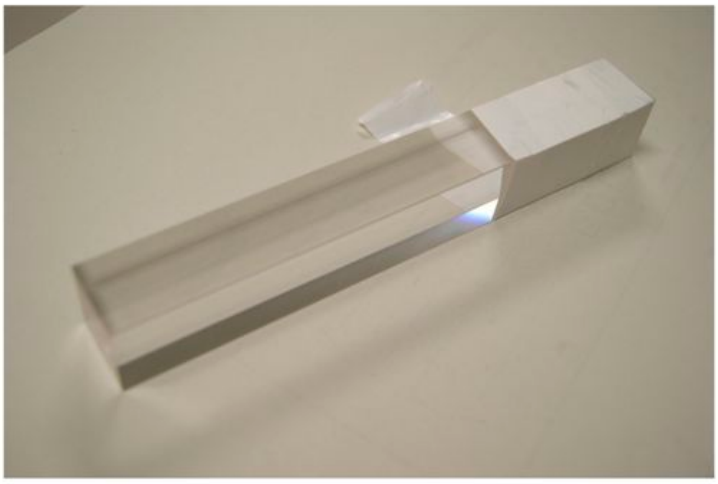

Figure 12.2: GSO crystal with a size of $2 \times 2 \times 15\,\mathrm{cm}^3$.

High segmentation is required to reduce pileup and provides good position information. The ECAL will consist of crystal modules which have a $2{\times}2\,\mathrm{cm}^2$ cross-section and whose length is 12 cm corresponding to 10.5 radiation length. The ECAL covers the cross-section of the 50-cm radius detector region and 1,920 crystals are needed which can be formed into the module and readout structure described in the following sections.

12.2. Photon Detector

Operation of the readout system of the ECAL under a 1 T solenoidal magnetic field essentially precludes the use of high-gain, low-noise photomultiplier tubes (PMTs). In order to circumvent this problem, we have two candidates for the photon readout: avalanche photodiodes (APDs) and silicon photomultipliers (SiPMs).

APDs, with typical gains of 50–100, are now generally available but require an amplifier to get a sizeable signal and their noise output depends on the APD size. They also have a high quantum efficiency of more than 70 % around the wavelength range of LYSO scintillation and have excellent linearity. SiPMs are a novel form of multi-pixel photosensor where each pixel is an APD biased to be in the Geiger mode. When all the pixels are connected together in parallel, they can provide photon-counting with gains of the order of 10^6, which is comparable to that achieved with PMTs. They also provide similar or better photo-detection efficiencies and response times. However, the excellent linearity is achieved only when the number of hit pixels is small. Typical devices have dimensions of one to a few mm squared, and pixel counts ranging from a hundred to the tens of thousands.

Because of the small dimensions of available SiPMs, and as their radiation hardness is less than that of APDs, APDs are more attractive for use in the ECAL. There is also much experience of APDs successfully utilised together with a scintillating crystal for the CMS experiment and the ALICE experiment at the CERN Large Hadron Collider. Our choice of photon detector for the ECAL is thus APDs and is specifically the HAMAMATSU S8664-55 with an active area of 5×5 mm^2. Table 12.2 summarises the characteristics of the APD. The APD has been used to develop the prototype ECAL module, where one APD was attached to one crystal, and has been beam-tested as described in Section 12.5..

Table 12.2: The characteristics of APD, HAMAMATSU S8664-55 and S8864-1010.

Type	S8664-55	S8664-1010
Active area (mm^2)	5 × 5	10 × 10
Package size (mm^2)	9.0 × 10.6	14.5 × 13.7
Spectral response range (nm)	320–1000	320–1000
Peak sensitivity wavelength (nm)	600	600
Quantum efficiency at 420 nm (%)	70	70
Breakdown voltage (V)	400	400
Nominal gain	50	50
Typical dark current (nA)	5	10
Maximum dark current (nA)	50	100
Terminal capacitance (pF)	80	270

After the successful beam-test, the APD size to be utilised for the ECAL was reconsidered. In addition to the HAMAMATSU S8664-55 with an active area of 5×5 mm^2, the S8664-1010 with an active area of 10×10 mm^2 is available as shown in Table 12.2. This larger active area APD has an advantage to collect the more scintillation photons. However, the noise output has to be carefully studied by using the next prototype preamplifier. The comparison in the noise performance of both 5×5 mm^2 and 10×10 mm^2 APDs will be carried out in a laboratory test. Based on the result from the laboratory test, the APD of 5×5 mm^2 or 10×10 mm^2 will be finally chosen and be beam-tested to confirm the expected performance.

12.3. Readout Electronics

Due to lower gain of APDs compared with that of SiPMs, fast and low noise analogue electronics is required to amplify the APD signal. We have developed a prototype preamplifier, whose circuit diagram is shown in Figure 12.3. Figure 12.4 shows the prototype preamplifier board, which reads out seven APDs.

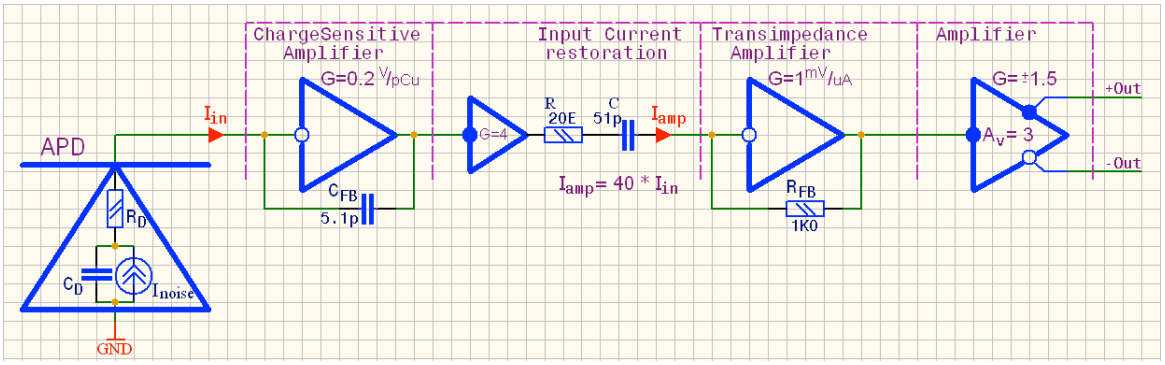

Figure 12.3: A circuit diagram of a prototype preamplifier.

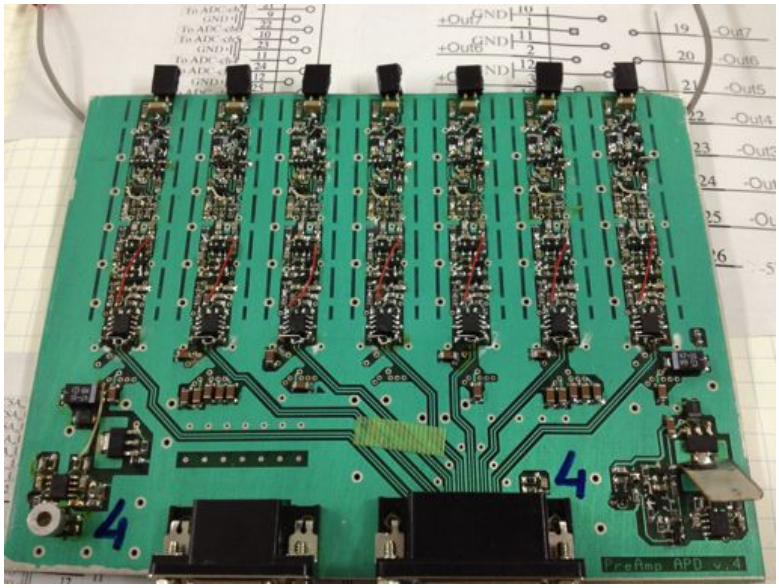

Figure 12.4: A prototype preamplifier board.

The amplifier output is designed to be differential so that the signal can be transmitted over relatively long distances without suffering from noise. The receiver circuit of the preamplifier signal is designed to convert the differential signal to the single-ended signal and to produce a trigger signal with an analogue adder. The single-ended signals are passed to a waveform digitiser. Figure 12.5 shows a schematic diagram of the whole circuit. The prototype electronics has been tested in the laboratory and also in the test experiments described in Section 12.5..

A schematic diagram of the readout electronics for the ECAL system is shown in Figure 12.6. The crystals and the APDs are located inside a vacuum vessel. The front-end preamplifier board is based on the prototype preamplifier board and has 16 channel charge sensitive preamplifiers (CSPs) for the readout and 4 channel analog adders for the trigger. The dimension of the front-end preamplifier board is 3U size and 2M width. The differential outputs of the front-end board are passed to the ROESTI board, which is developed as the readout electronics for the straw tracker. The ROESTI has wave-form digitiser chips (DRS4) [73], which is a switched capacitor

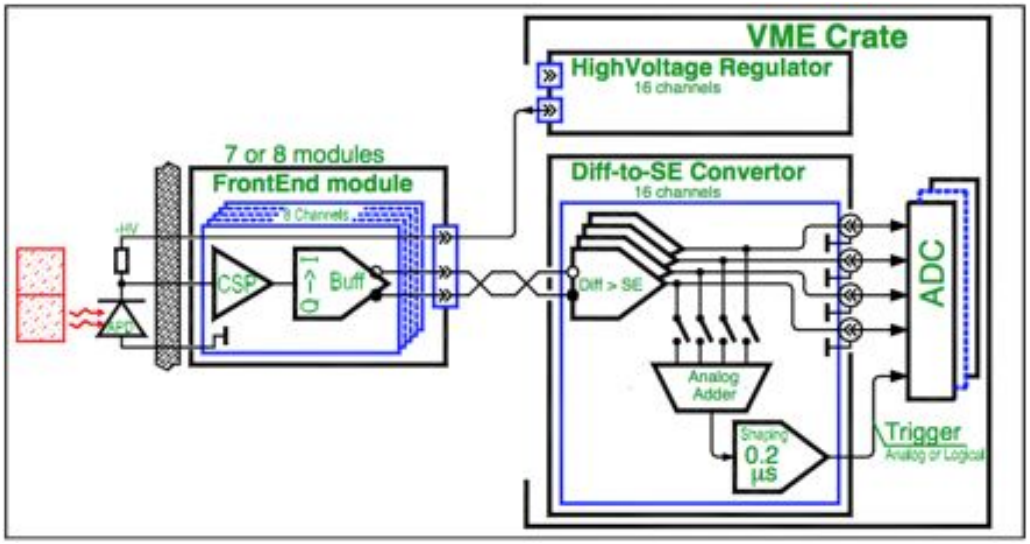

Figure 12.5: A schematic diagram of a prototype electronics.

array running with fast sampling. It has been developed at PSI for the MEG experiment. The ROESTI prototypes that were tested at KEK used an amplifier-shaper-discriminator (ASD) ASIC [72] which had been developed for a drift chamber. For the application of the ECAL readout, the ASD ASIC is not used and the converter from the differential signal to the single-ended signal is instead located on the board. The readout scheme is hence the same as that of the prototype electronics. This readout scheme was successfully tested by using the prototype preamplifier board, adding the converter from the differential signal to the single-ended signal in front of the prototype ROESTI board.

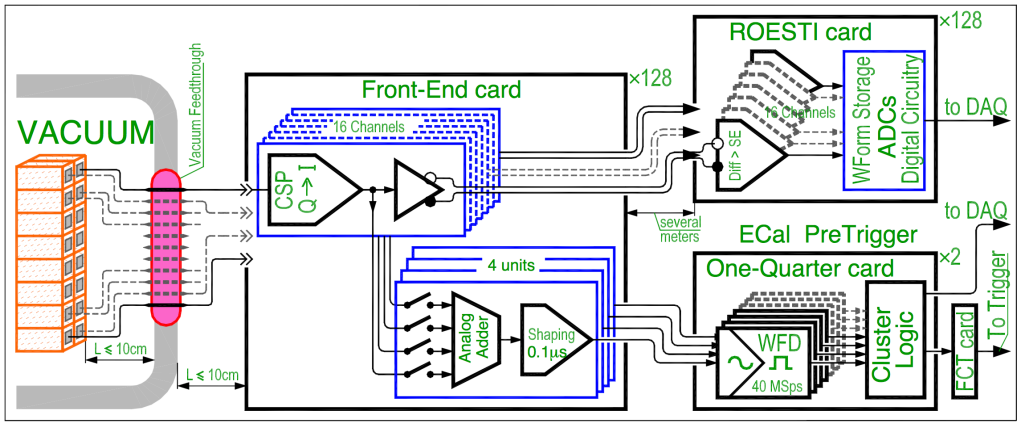

Figure 12.6: A schematic diagram of the ECAL readout electronics.

The next prototype of the readout electronics is under development. The next prototype is designed to have the same readout scheme described above and to have the form factor for the ECAL. It consists of the front-end preamplifier board, the mezzanine board of the converter from the differential signal to the single-ended signal and the wave-form digitiser board of the ROESTI. The beam test together with the close-to-final prototype detector is planned to confirm the expected performance.

12.4. Module, Readout and Mechanical Structure

The basic unit of the ECAL is a 2×2 crystal matrix module. In the ECAL system, 480 (=1920/4) modules are needed to cover the full cross-section of the detector region. Figure 12.7 shows the schematic layout of the prototype module structure together with 4 APDs, Teflon tape and a Al-Mylar case for wrapping and a preamplifier board. This module structure is designed to achieve a good light collection efficiency and its uniformity with low material budget in front of the crystals and between them. In Figure 12.7, the preamplifier board is located inside the module structure. However, in the ECAL system, the preamplifier board is separated from the module structure and is located outside the vacuum vessel as shown in Figure 12.6 for a better thermal management at an acceptable noise level.

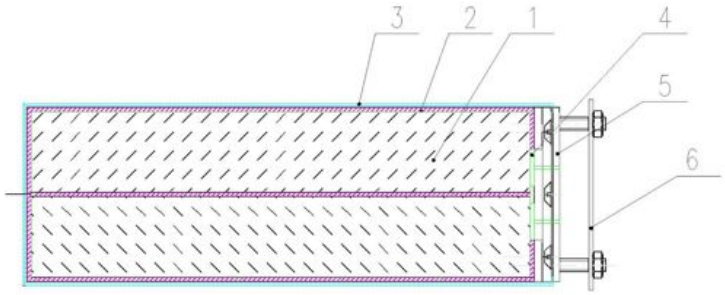

Figure 12.7: A schematic layout of the module structure. 1 : crystal, 2 : individual wrapping by Teflon tape, 3 : Al-Mylar case, 4 : APD, 5 : holder, 6 : preamplifier board.

A prototype module constructed (without the preamplifier board) is shown in Figure 12.8. The polished crystals were wrapped with two layers of 76 μm think high reflection Teflon tape from Saint-Gobain. One HAMAMATSU S8664-55 APD is attached to each crystal, using a transparent 2 mm thick silicon rubber (ELJEN Technology, EJ-560) as an optical contact between the crystal and APD. Al-Mylar sheet of 20 μm thickness was used for wrapping. This module was successfully beam-tested as described in Section 12.5..

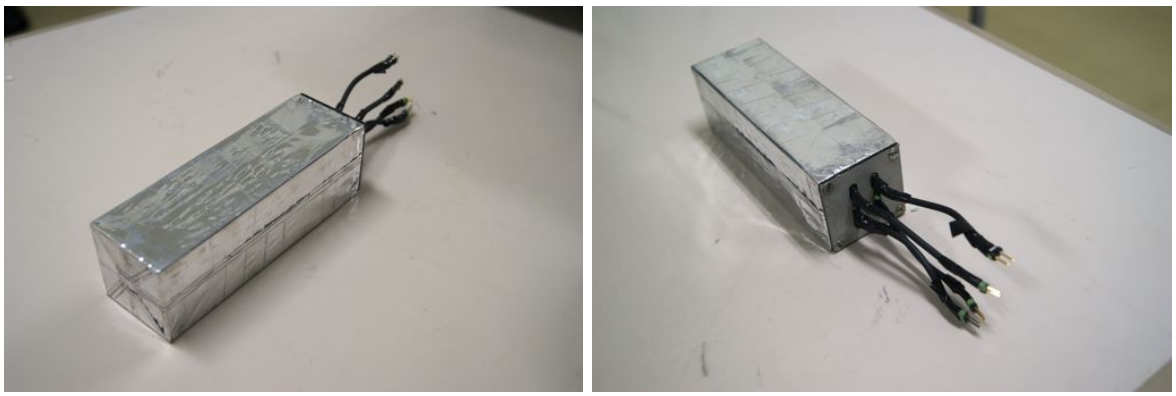

Figure 12.8: A prototype of the 2×2 crystal matrix module (without the preamplifier board).

The improved design of the module structure for the ECAL has been studied and is shown in Figure 12.9. One crystal is first wrapped by the Teflon tape together with the silicon rubber and the PCB on which the APD is attached (Figure 12.9 (a)). One LED, emitting lights with a wavelength similar to that of the LYSO scintillation photon (420 nm), is also placed on the PCB and is used to flash light for monitoring purpose. Four wrapped crystals are then used to construct the 2×2 matrix module, which is wrapped by the Al-Mylar (Figure 12.9 (b)). One resistance thermometer is implemented in one of four PCBs and is used to monitor the APDs on the module. The selection of the LED and the resistance thermometer is under way. The modules are further arranged to form a super-module (Figure 12.9 (c)). One super-module consists of 16 modules built in 4×4 matrix structure, which contains 64 (= 8×8) crystals. An intermediate board bundles all the signal and slow control lines from the super-module and is connected to the feedthrough board inside the vacuum vessel.

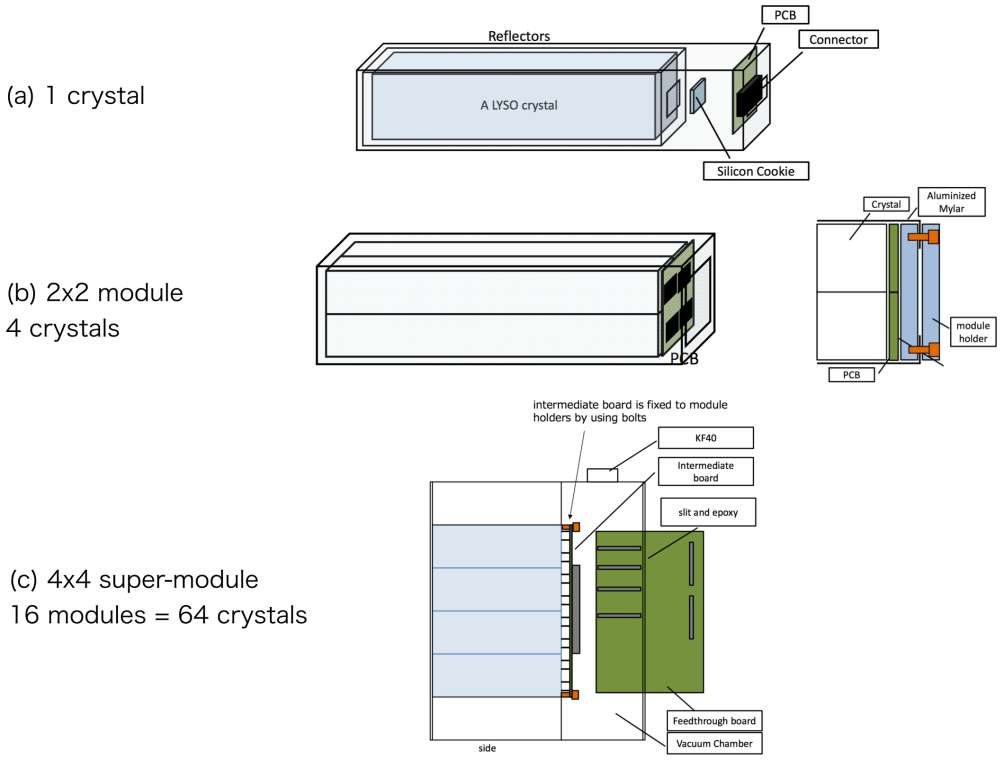

Figure 12.9: The module structure in the ECAL. (a) 1 crystal + 1 APD on PCB, (b) 2×2 crystal matrix module, (c) super-module consisting of 4×4 modules (= 64 crystals) and feedthrough

Figure 12.10 shows the feedthrough part outside the vacuum vessel, together with the arrangement of the front-end boards. The engineering design is under way. The feedthrough boards are inserted and fixed in a vacuum flange and are connected to a custom backplane. The front-end boards are connected to the feedthrough boards via the custom backplane. Each front-end board implements 16 channels for the APD readout. One high voltage filter board for the APD bias is also attached to the front-end board. In this scheme, one super-module, consisting of 64 crystals (= 4 × 4 modules, shown in Figure 12.9 (c)), is read out by using 4 front-end boards.

Outside the vacuum vessel, all the front-end boards are arranged as shown in Figure 12.11. In order to support and power all the front-end boards, a crate structure is placed downstream of the vacuum vessel. It is important to minimise the cable and connection length between the APDs and the front-end boards. Since the output of the front-end board is differential, a

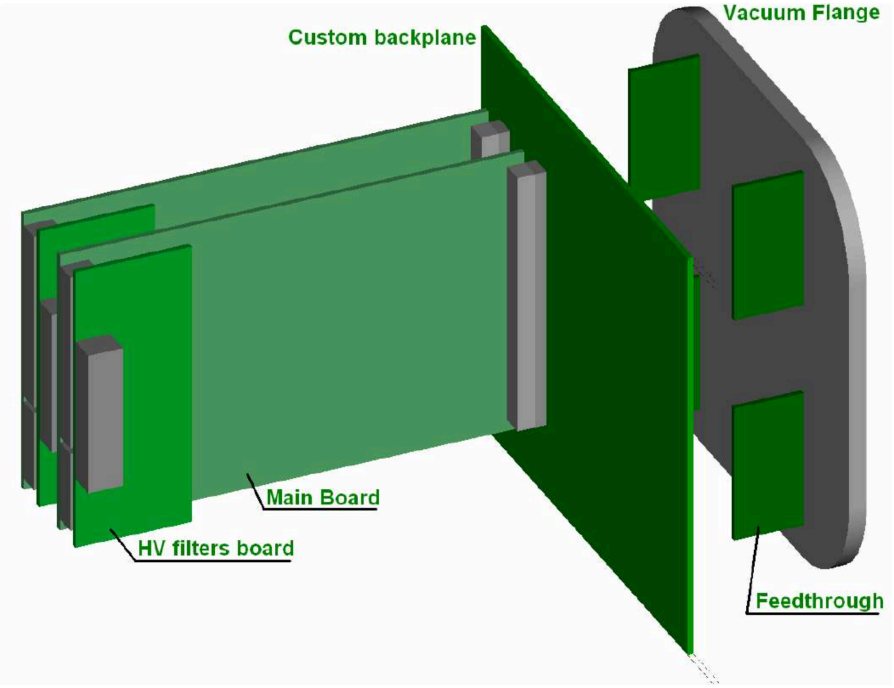

Figure 12.10: A design of the feedthrough connected to one super-module inside the vacuum vessel. Outside the vacuum vessel, the feedthrough is then connected to 4 front-end boards (shown as Main Board in this figure)via a custom backplane.

cable length from the front-end board to the ROESTI digitiser board can be a few meters. The mechanical structure of the ECAL is under design and contains all the ECAL-related devices of the super-modules, the support structure, the feedthrough and the entire electronics.

12.5. R&D Status

To evaluate the performance of GSO and LYSO, we have carried out test experiments at the J-PARC K1.1BR line and at Research Center for Electron Photon Science in Tohoku University. The J-PARC K1.1 BR beam line was capable of delivering secondary particles up to 1.1 GeV/c produced at a secondary target (T1 target) located on the primary beam line of the Hadron Hall. We used an electron beam of around 100 MeV/c for the test. The prototype electron calorimeter system consists of 7×7 crystals, 7 preamplifier boards and the prototype electronics described in Section 12.3., as shown in Figure 12.12. Figure 12.13 shows the whole set-up of the prototype electron calorimeter system located at the beam exit of the K1.1BR line. Due to limited beam time, only GSO crystals were tested. In the test experiment at Tohoku University, an electron beam at $65 - 145$ MeV/c was utilized at the GeV-γ Experimental Hall. The experimental set-up here is shown in Figure 12.14 and is essentially the same as that at the J-PARC test experiment except for the use of a scintillating fibre detector located in front of the prototype ECAL to measure the particle impact position. The results presented in this section were obtained at the test experiment at Tohoku University.

A typical waveform obtained in the beam test is shown in Figure 12.15. The waveform was fitted with a function and converted to the integrated charge. The energy calibration was carried out by taking the data with cosmic rays and using the known beam momenta. The signal from each of 49 crystals was converted to an energy deposit value and the energy deposit

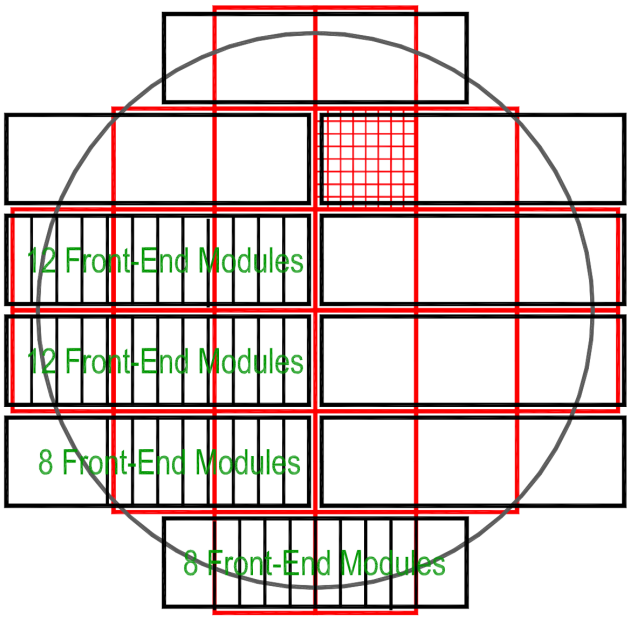

Figure 12.11: A schematic layout for the arrangement of the front-end boards downstream of the ECAL. One red box corresponds to one-super module, which is read out by using 4 front-end boards. All the front-end boards are installed in a crate structure.

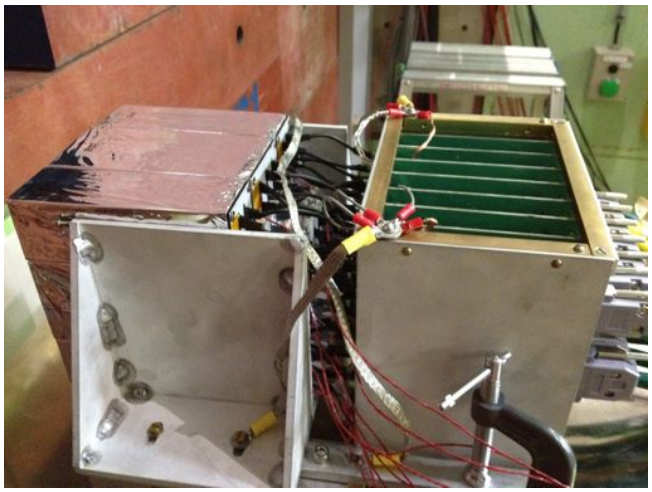

Figure 12.12: The prototype electron calorimeter system consisting of 7 × 7 GSO crystals.

in the prototype ECAL was obtained by applying a simple clustering algorithm.

Figure 12.16 shows the measured energy deposit at 105 MeV/c. A Monte-Carlo simulation was carried out to extract the energy resolution, taking into account all the material, beam size, beam momentum scale, and energy calibration using cosmic rays. The energy resolution at each momentum set-up was obtained using a width between the peak and the higher-energy tail. Figure 12.17 shows the energy resolution as a function of beam momentum. The resulting energy resolution at 105 MeV/c was 5.50 ± 0.02 (stat) ± 0.04 (syst) % for GSO and 4.91 ± 0.01 (stat) ± 0.07 (syst) % for LYSO.

Dependence of the energy resolution on the impact position was studied by using the scintillat-

Figure 12.13: The whole set-up located at the beam exit of J-PARC K1.1BR line.

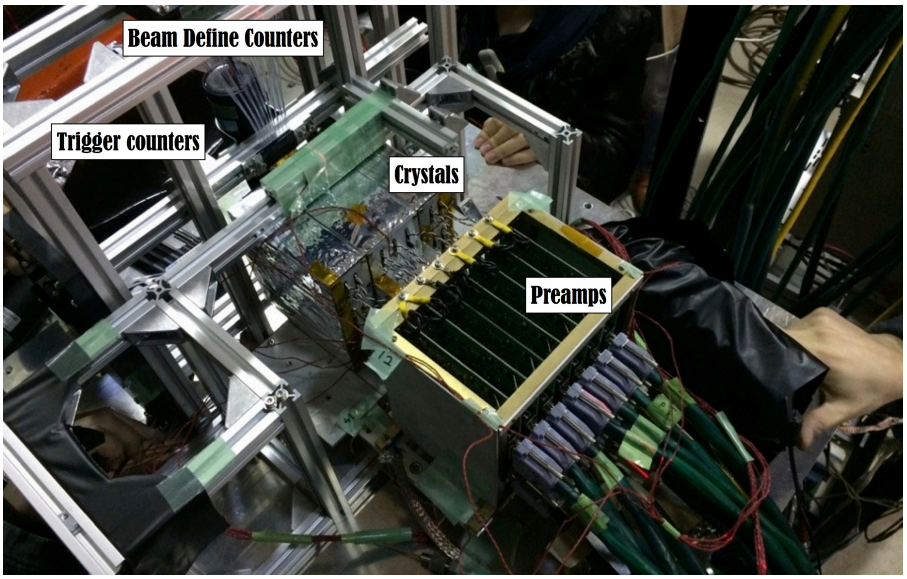

Figure 12.14: The whole set-up located at the beam exit of Tohoku University GeV-γ Experimental Hall.

ing fibre detector. The centre, border and corner area was defined by 10 mm square area with respect to the central crystal as shown in Figure 12.18. The energy resolution degraded in the border and corner area. LYSO meets the requirement of the energy resolution less than 5 % at 105 MeV/c in all the area.

The position resolution was also studied by using the impact position measured with the scintillating fibre detector and the ECAL cluster position. Figure 12.19 shows the momentum dependence of the position resolution, which decreases as the momentum increases. The impact position dependence of the position resolution is shown in Figure 12.20, where the centre, border and corner area was defined in the same way as Figure 12.18. Both GSO and LYSO meets the requirement of the position resolution less than 1 mm.

Based on the prototype ECAL results in the test experiment, the cost-performance evaluation on GSO and LYSO has been made and our decision of the crystal choice for the ECAL is LYSO.

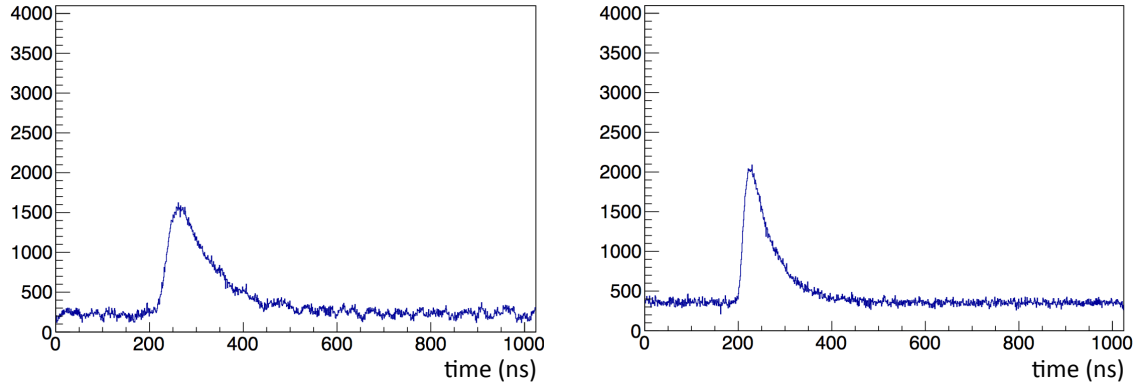

Figure 12.15: A typical waveform obtained in the beam test (Left : GSO, Right : LYSO). To adjust the dynamic range, the gain in the LYSO set-up was decreased by a factor of 4, compared with that in the GSO setup.

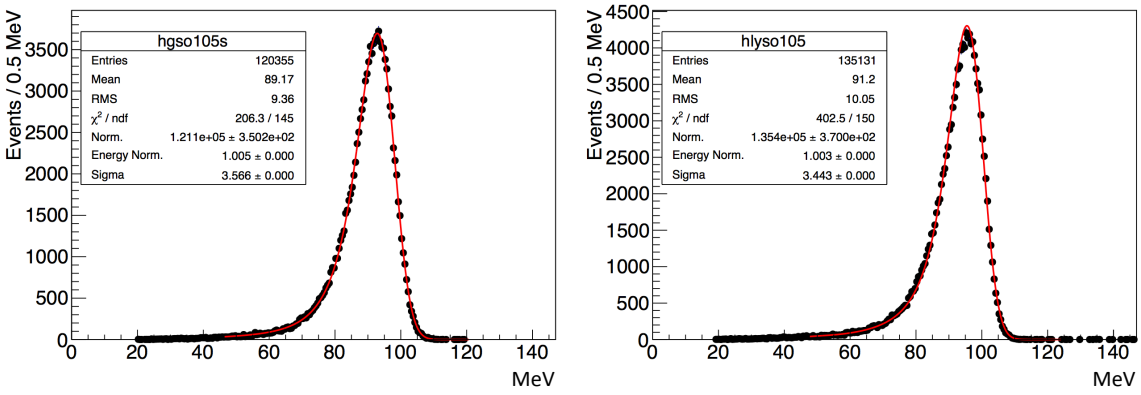

Figure 12.16: The measured energy deposit at a beam momentum of 105 MeV/c (Left : GSO, Right : LYSO). Data is shown as black points and a smeared Monte-Carlo data is shown as a solid line.

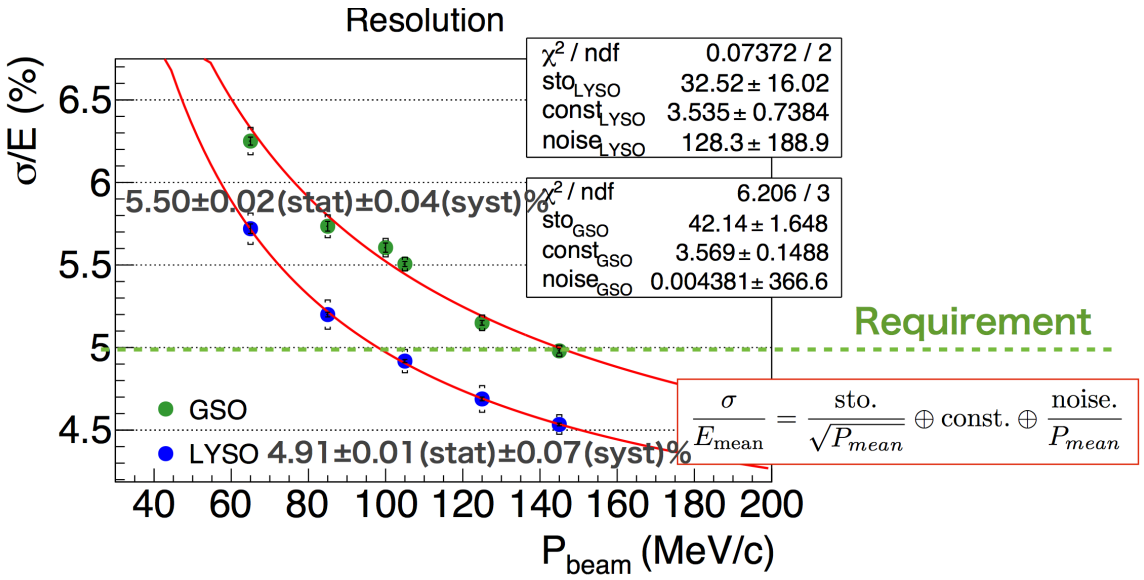

Figure 12.17: The measured energy resolution as a function of beam momentum.

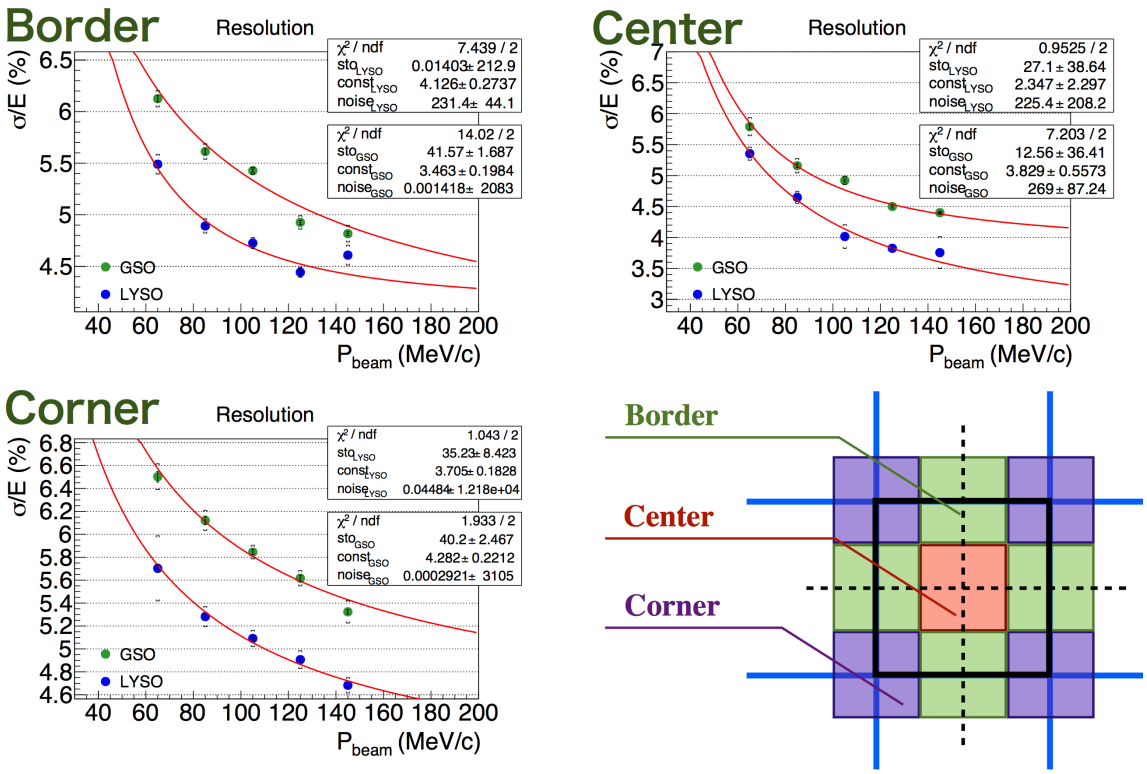

Figure 12.18: The measured energy resolution as a function of beam momentum, depending on the beam particle impact position. The definition of the centre, border and corner area is shown in the bottom-right figure, where the black solid line represents the 20 × 20 mm^2 central crystal and each area is 10 mm square.

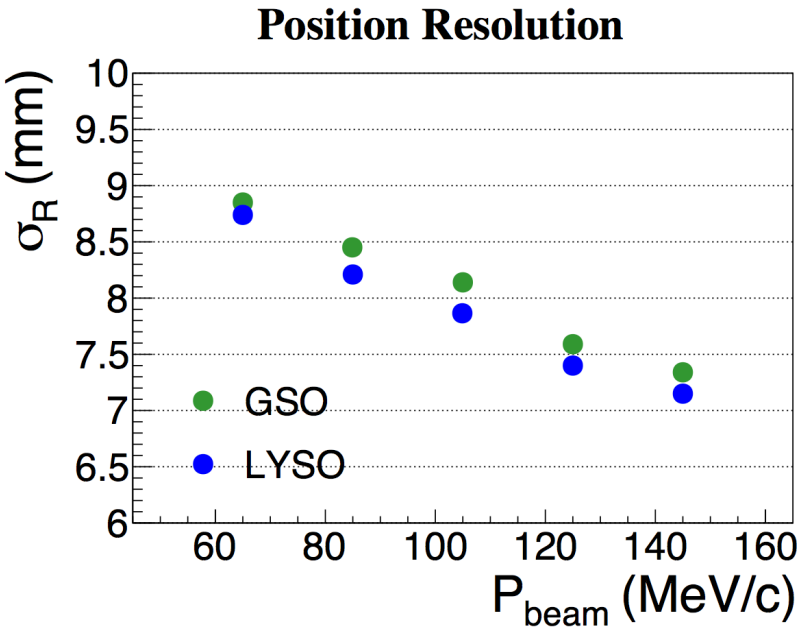

Figure 12.19: The measured position resolution as a function of beam momentum.

12.6. Future Plan of Radiation Hardness Tests of LYSO

The radiation hardness of LYSO crystals should not be a serious issue for COMET Phase-I since the exposed time to a beam is short, only during the engineering run. Nevertheless we have

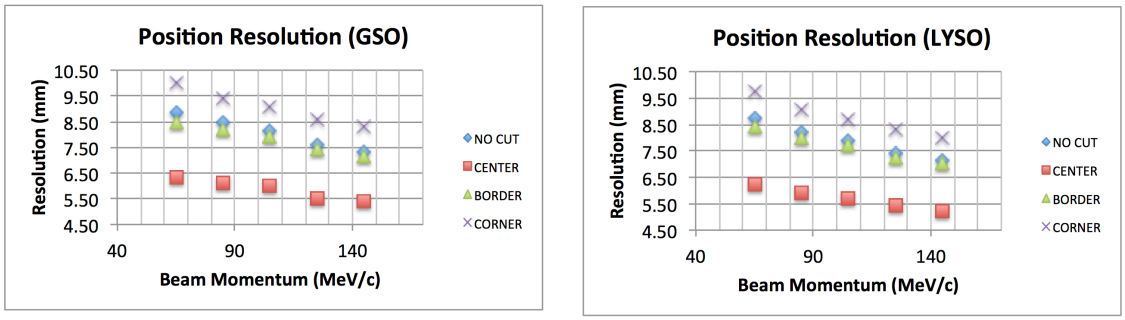

Figure 12.20: The measured position resolution as a function of beam momentum, depending on the impact position (CENTER, BORDER and CORNER defined by Figure 12.18). "NO CUT" corresponds to the resolution without using the CENTER, BORDER and CORNER separation.

to examine the radiation hardness of LYSO. The properties against radiation hardness have been studied by the CMS collaboration and also in [**?**]. We will make our radiation hardness tests. We plan to do the neutron irradiation tests at Tandem Facility at Kobe University. In addition to neutron irradiation we plan to do gamma-ray irradiation tests in Tokyo Institute of Technology, Osaka Unviersity and Kyushu University. They can be organized together with the irradiation tests described in Chapter 17.

Chapter 13

Cylindrical Detector System (CyDet)

13.1. Introduction

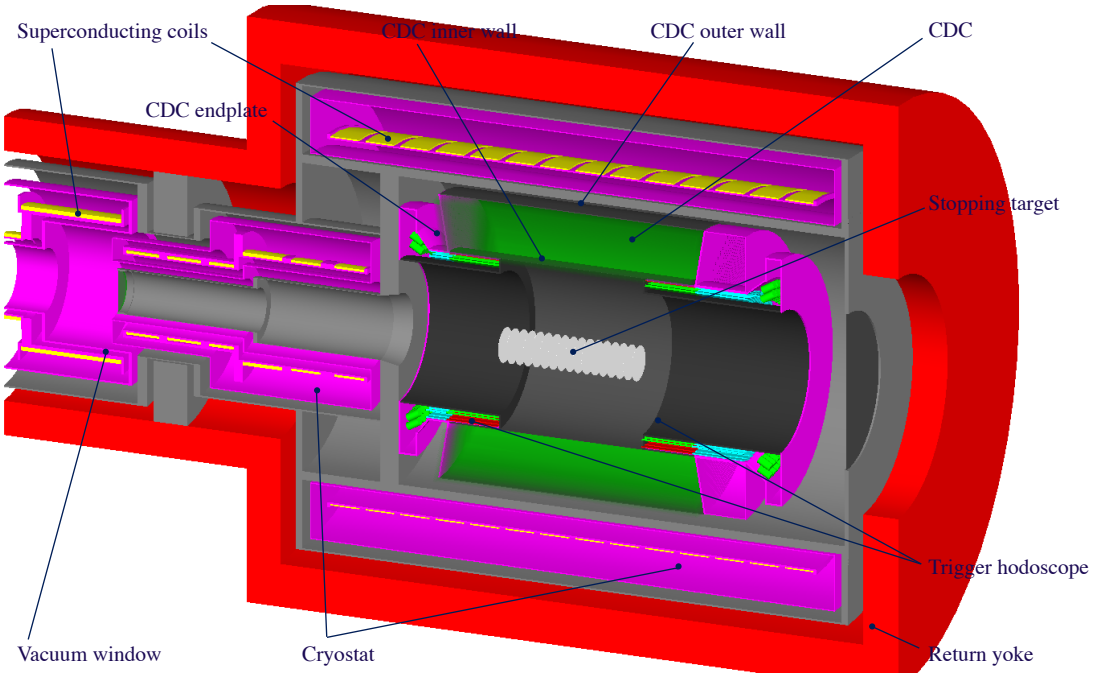

Figure 13.1: *Schematic layout of the CyDet.*

The cylindrical detector system (CyDet) is the main detector system for the $\mu-e$ conversion search in COMET Phase-I. The CyDet will not be used for COMET Phase-II. It consists of a cylindrical drift chamber (CDC) and a cylindrical trigger hodoscope (CTH). It provides the primary momentum measurement for electrons from $\mu-e$ conversion. Figure 13.1 shows a schematic layout of the CyDet. It is located after the bridge solenoid (BS) in the muon transport section, and installed inside the warm bore of a large 1 T superconducting Detector Solenoid (DS). The CyDet must accurately and efficiently identify and measure 105 MeV electrons whilst rejecting backgrounds.

There are remarkable differences in detectors and spectrometer magnets between COMET Phase-I and Phase-II. In COMET Phase-II, with a proton power of 56 kW, there will be

a curved solenoid electron transport system before the tracking detector in order to select momentum and charge of particles coming from the stopping target. On the other hand, in COMET Phase-I there will be no curved solenoid electron transport system. Although the proton beam power is reduced to 3.2 kW in Phase-I, the detectors for Phase-II may not work for the $\mu-e$ conversion search in Phase-I due to the high hit rates. This motivates the use of a cylindrical detector system that surrounds the muon stopping target in order to track charged particles. By adopting the cylindrical detector system, most beam particles that do not stop in the muon-stopping target will go downstream and escape from the detector region without leaving any hit in the detector system. The background rate is therefore reduced as well as the hit rate in the CyDet detector.

A key feature of COMET is to use a pulsed beam that allows for elimination of prompt beam backgrounds by looking only at tracks that arrive after the beam pulse. Therefore, any momentum tracking device should be able to withstand the large flux of charged particle during the burst of "beam flash" particles. The time window for the measurement of electrons from $\mu-e$ conversion in COMET will start several hundred nanoseconds after the prompt flash.

The dimensions of the CyDet are shown in Figure 13.2. The length of the CDC at the inner wall and at the outer wall are 1495.5 mm and 1577.3 mm respectively. The inner wall of the CDC is made of a 0.5 mm thick carbon fibre reinforced plastic (CFRP). The outer wall of the CDC is made of CFRP of 5 mm thickness. The inner and outer walls have thin aluminium foils glued inside to eliminate charge-up on CFRP. The endplates is conical in shape. The thickness of the endplate is about 10 mm to rigidly support the feedthroughs. Trigger hodoscopes are placed at both the upstream and downstream ends of the CDC.

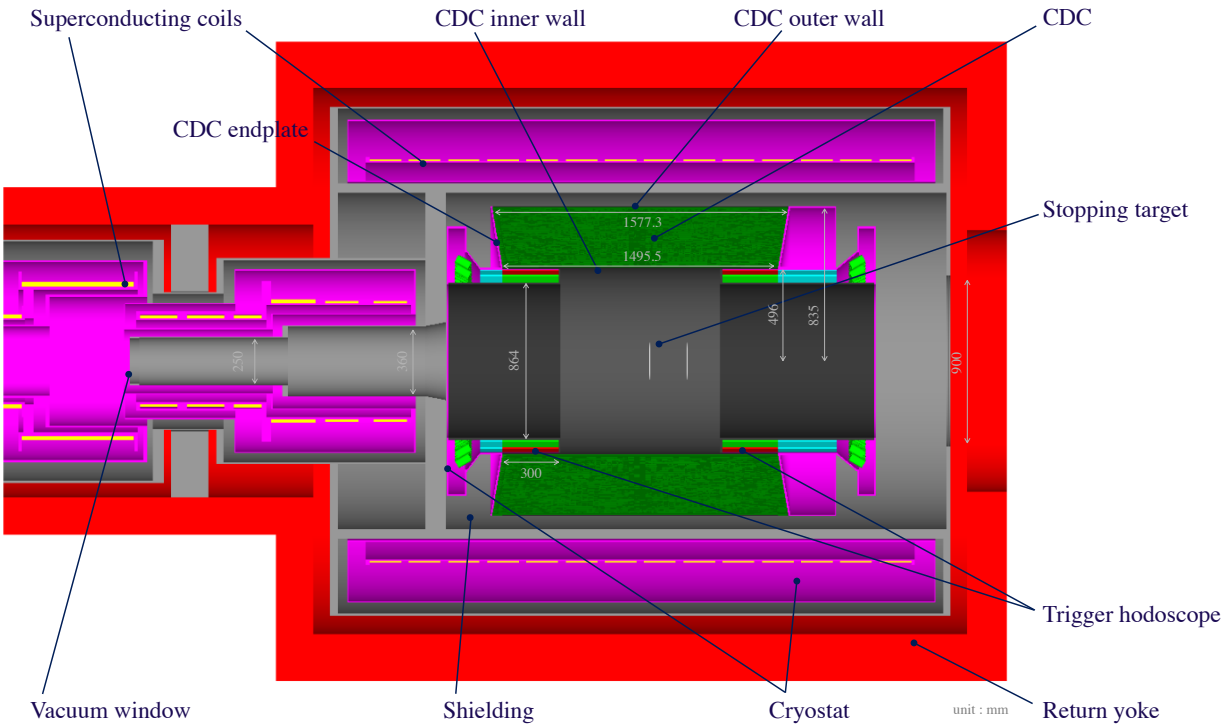

Figure 13.2: *Schematic layout of the CyDet detector*

13.2. Cylindrical Drift Chamber (CDC)

13.2.1 Overview

The cylindrical drift chamber (CDC) reconstructs tracks of charged particles in the solenoidal magnetic field and measures their momenta precisely. It is designed to avoid high hit rates due to the beam particles, muon-decay-in-orbit (DIO) electrons, and low energy protons emitted by muon nuclear capture process. Among the small fraction of particles which eventually enter CDC and leave hits, DIO electrons and low energy protons will dominate. It is noted that the hits of protons can be easily identified using energy deposit in the CDC cells, because the energy loss of a low energy proton is about 100 times larger than that of a signal electron.

The main parameters of the CDC are summarized in Table 13.1. The radii of the inner and the outer walls are determined to avoid DIO electrons with momentum less than 60 MeV from hitting the CDC and to fully cover the tracks of 105 MeV signal electrons. The momentum resolution σ_p of the CDC must be about 200 keV/c for the 105 MeV electrons to achieve the target sensitivity of COMET Phase-I. For such a low energy region the intrinsic momentum resolution is dominated by multiple scattering effects. Therefore, the CDC must be a low-mass detector. These requirements lead to the choices of the cell configuration, the wires, and the gas mixture as described below.

Table 13.1: Main parameters of the CDC.

Inner wall	Length	1495.5 mm
	Radius	496.0∼496.5 mm
	Thickness	0.5 mm
Outer wall	Length	1577.3 mm
	Radius	835.0∼840.0 mm
	Thickness	5.0 mm
Number of sense layers		20 (including 2 guard layers)
Sense wire	Material	Au plated W
	Diameter	25 μm
	Number of wires	4986
	Tension	50 g
Field wire	Material	Al
	Diameter	126 μm
	Number of wires	14562
	Tension	80 g
Gas	Mixture	He:i-C_4H_{10} (90:10)
	Volume	2084 L

13.2.2 CDC configuration

Layer configuration The CDC is arranged in 20 concentric sense layers (including 2 guard layers) with alternating positive and negative stereo angles. Cylindrical drift chambers with only stereo layers have been constructed in the past, for example, the KLOE drift chamber. The 1st and 20th sense layers have a lower HV and act as a guard layer to remove the space

charge that accumulates due to ionizations created in the regions between the inner (outer) walls and the guard layer, which would, otherwise, accumulate in the absence of an electric field. The wire configuration is summarised in Table 13.2.

Based on the wire arrangement a Monte Carlo simulation has been made. Track displays for simulated events are shown in Figure 13.3.

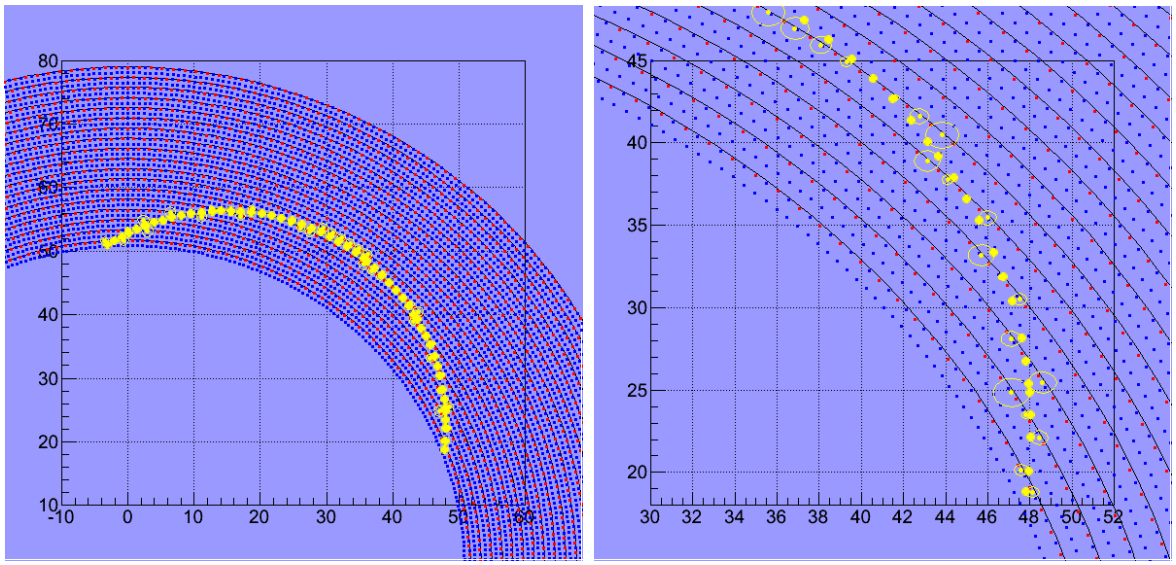

Figure 13.3: *A typical track display with a zoomed view. Closed thick dots are hit points along the track, where a hit point is defined as a point with the closest approach to a specific sense wire. Thin line circles are isochronal lines of those hit points. Blue and red thin closed dots represent field and sense wires locations projected to an endplate. Energy of the track is 105 MeV.*

Cell configuration Each cell has one sense wire surrounded by an almost-square grid of field wires. The ratio of the total numbers of field to sense wires is 3:1. The cell size is 16.8 mm wide and 16.0 mm height. It is nearly constant over the entire CDC region. Square cells are well-suited to the low momentum tracks (such as those from the $\mu-e$ conversion signal), which might enter the drift cells with a large angles with respect to the radial direction. The stereo angle ε is set to $64 \sim 75$ mrad, which is selected to achieve the longitudinal spacial resolution σ_z of about 3 mm. The CyDet will have 4,986 sense wires and 14,562 field wires.

The field wires are most massive material in the CDC tracking volume. In order to reduce multiple scattering at the field wires, aluminum is adopted as a material of the field wires because of low-Z and low density. The intrinsic momentum resolutions of the CDC were estimated for two cases of the field wire size; $\phi 80$ μm and $\phi 126$ μm as described in Section 13.5.2. The $\phi 80$ μm wire shows significantly better resolution than $\phi 126$ μm wire. If we use the $\phi 80$ μm aluminum wire as a field wire, however, the operation voltage should be below 1730 V to keep the electric field on the wire surface below 20 kV/cm, above which the wire surface starts to deteriorate. According to the past test with CDC prototype, 1730 V is not enough to get reasonable gain of the signal for any gas mixture. Also we found that the difference of the momentum resolution between $\phi 80$ μm and $\phi 126$ μm wire configurations does not change the physics sensitivity significantly. Therefore, we decided to use the $\phi 126$ μm aluminum wire as the field wire. A tension of 80 g is applied to the field wires to match the gravitational sag of the sense wires.

The sense wires are made of gold-plated tungsten, 25 μm in diameter, tensioned to 50 g. The deflection due to gravity is about 60 μm at the center of CDC. A maximum difference of the

Table 13.2: The configuration of wires in the CDC. The columns contain, respectively: wire layer ID; cell layer ID; layer type (G/F/S for Guard/Field/Sense) ; radius at the end plate; number of wires on the layer; number of holes to skip; stereo angle; angle of the first hole at the end plate.

$I_{wireLayer}$	$I_{cellLayer}$	Type	R_{EP}	N_{wire}	$\Delta N_{holeSkip}$	ε	φ_{EP}
-	-	-	[cm]	[wires]	[holes]	[mrad]	[mrad]
1	0	G	51.40	396	12	66.106	0.000
2	1	F	52.20	396	-12	-67.004	15.867
3	1	S	53.00	396	-12	-67.899	15.867
4	2	F	53.80	408	12	66.778	15.400
5	2	S	54.60	408	12	67.640	15.400
6	3	F	55.40	420	-12	-66.553	0.000
7	3	S	56.20	420	-12	-67.384	0.000
8	4	F	57.00	432	12	66.327	14.544
9	4	S	57.80	432	12	67.129	14.544
10	5	F	58.60	444	-12	-66.102	0.000
11	5	S	59.40	444	-12	-66.876	0.000
12	6	F	60.20	456	12	65.877	0.000
13	6	S	61.00	456	12	66.625	0.000
14	7	F	61.80	468	-12	-65.652	13.426
15	7	S	62.60	468	-12	-66.376	13.426
16	8	F	63.40	480	12	65.428	0.000
17	8	S	64.20	480	12	66.129	0.000
18	9	F	65.00	492	-12	-65.205	12.771
19	9	S	65.80	492	-12	-65.884	12.771
20	10	F	66.60	504	12	64.982	0.000
21	10	S	67.40	504	12	65.640	0.000
22	11	F	68.20	516	-12	-64.761	12.177
23	11	S	69.00	516	-12	-65.398	12.177
24	12	F	69.80	528	12	64.540	0.000
25	12	S	70.60	528	12	65.158	0.000
26	13	F	71.40	540	-12	-64.319	11.636
27	13	S	72.20	540	-12	-64.920	11.636
28	14	F	73.00	552	12	64.100	0.000
29	14	S	73.80	552	12	64.683	0.000
30	15	F	74.60	564	-14	-74.472	0.000
31	15	S	75.40	564	-14	-75.132	0.000
32	16	F	76.20	576	14	74.220	0.000
33	16	S	77.00	576	14	74.862	0.000
34	17	F	77.80	588	-14	-73.969	10.686
35	17	S	78.60	588	-14	-74.593	10.686
36	18	F	79.40	600	14	73.719	0.000
37	18	S	80.20	600	14	74.326	0.000
38	19	F	81.00	612	-14	-73.470	10.267
39	19	G	81.80	612	-14	-74.061	10.267

gravitational sag between the sense wires and the field wires are less than 100μm. The total tension force is 1.4 tons.

The radiation length of the proposed chamber gas, He:i-C_4H_{10} (90:10), is about 1300 m. In addition to that, the field and sense wires shorten the average value of the radiation length of the CDC tracking volume to 507 m. Another candidate of the sense wire is gold-plated tungsten with 30 μm in diameter, which changes the average value of the radiation length to 452 m.

HV of approximately +1400 $\sim$ 1900 V is applied to the sense wires with the field wires at ground potential, giving an avalanche gain of approximately 1$\sim$4 $\times 10^4$ for the gas mixture of He:i-C_4H_{10} (90:10).

Electric field at the surface of field wires should be less than 20 kV/cm to prevent corona discharge and whisker growth on the wires. The Garfield program has been used to study cell properties, including drift time isochrones, time-distance relationships, distortions and gain variations. Figure 13.4 shows the result of the Garfield calculation. For field wires of ϕ80 μm, an electric field at their surface is about 20 kV/cm with HV = 1730 V. That is the reason why we decided to use ϕ126 μm wires as field wire. We can apply +1900 V on sense wires to obtain sufficient amplification gain with a surface electric field of only 14 kV/cm. The time-distance relationship has been calculated for different gas mixtures for comparison as shown in Figure 13.5. Results of more detailed studies with different incident angles are shown in Figure 13.6 for He:i-C_4H_{10} (90:10) and He:C_2H_6 (50:50) gas mixtures.

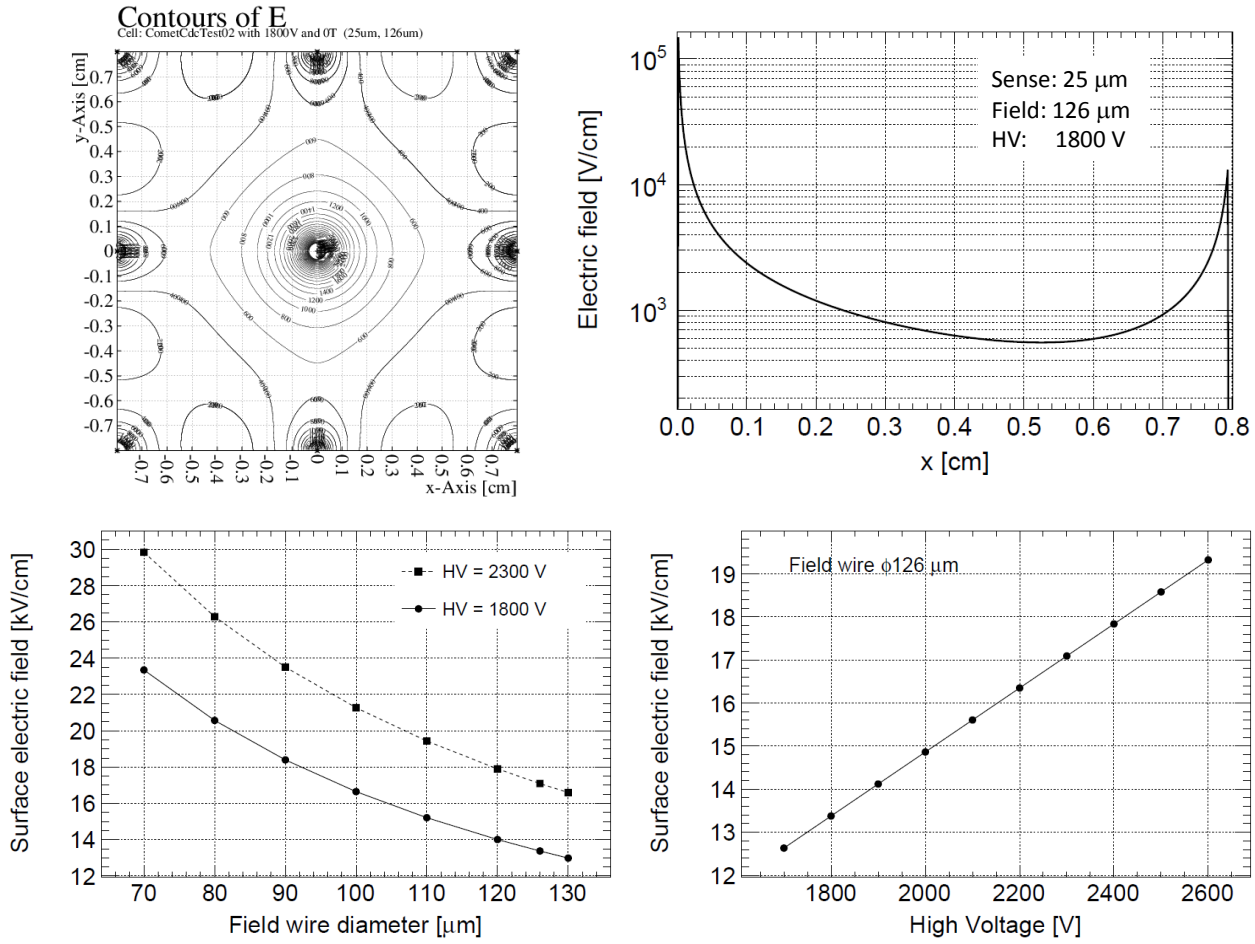

Figure 13.4: *Contours of electric field distribution calculated by* `Garfield` *for a cell of 1.6×1.6 cm*^{2}*, sense and field wires of ϕ25 and ϕ126 μm, and HV of 1800 V (top left), and the electric field distribution along the x-axis at $y = 0$ (top right). Electric field at surface of field wires as a function of the field wire diameter for HV of 1800 and 2300 V (bottom left), and that as a function of HV for the field wire diameter of 126 μm.*

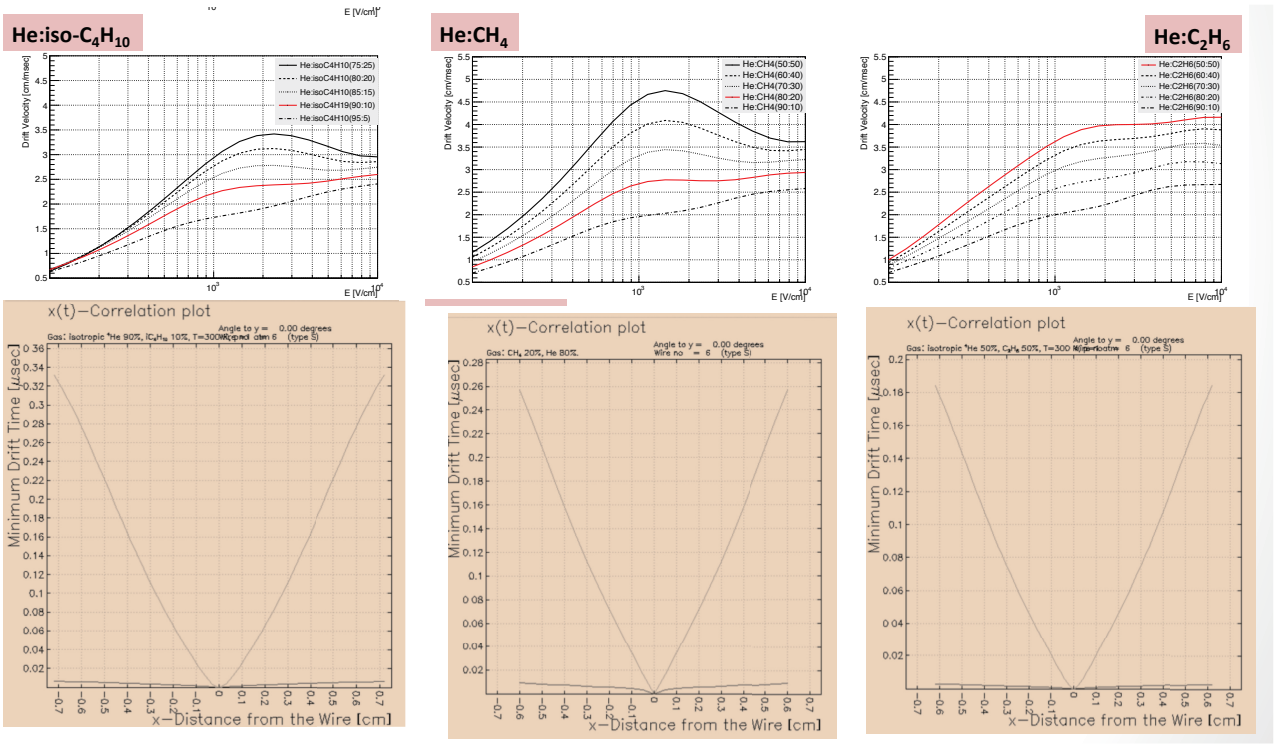

Figure 13.5: *Result of* `Garfield` *calculations with different gas mixture.*

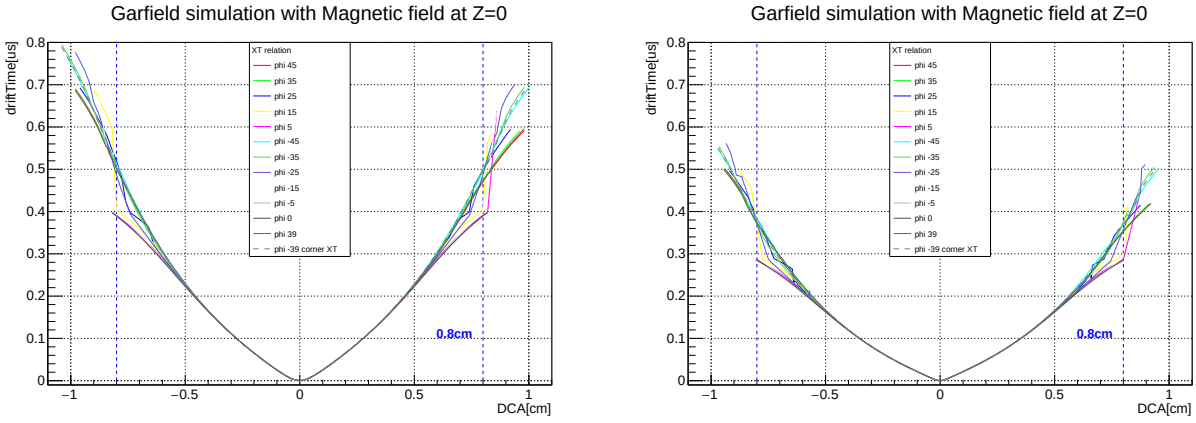

Figure 13.6: `Garfield` *studies on X-T correlation for He:i-*C_4H_{10} *(90:10)(Left) and He:*C_2H_6 *(50:50)(right) with different incident angles of electrons.*

Gas mixture A gas mixture with long radiation length and a fast drift velocity is needed in order to minimize the multiple scattering and reduce the maximum drift time respectively. Several gas mixture candidates have been studied by `Garfield` as shown in Figure 13.5. The baseline choice of the gas mixture is He:i-C_4H_{10} (90:10) and it was chosen to minimize the multiple scattering that dominates deterioration of the momentum resolution. In Table 13.3, different Helium-based low-Z gas mixtures are compared. The time-distance relationship depends on the gas mixture. Typical drift lines for a cell is shown in Figure 13.7, calculated for He:i-C_4H_{10} (90:10). Alternative gas mixture candidate is He:C_2H_6 (50:50). The performance of the baseline option has been established in KLOE. It adds little to the material budget, gives good position and energy-loss resolutions, and suppresses photon interactions owing to its small cross section to photons.

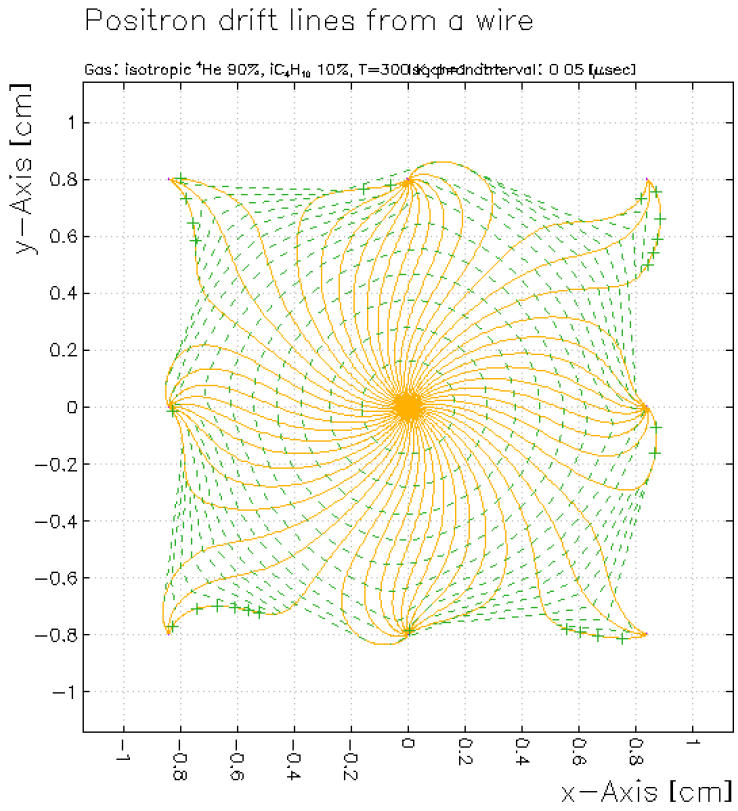

Figure 13.7: *Typical drift lines for the CDC cell under a 1 Tesla magnetic field from a Garfield simulation. The gas mixture of He:i-C_4H_{10} (90:10) is assumed.*

Gas system The present COMET gas system for CDC is designed based on that for the BELLE II CDC. Separate pure gas bottles are located in a gas stock booth outside. Gas mixing is performed using two mass flow controllers on the ground floor in the COMET building. Four gas bottles for each gas component are connected to the pressure regulators, and exhaust ports are prepared with a diaphram valves to avoid air contamination when the bottles are replaced. Only the CDC detector and a buffer tank with a pressure gauge are located in the underground experimental room. The other gas equipments and devices are on the ground floor to avoid the radiation damage on the electronics. The gas is fed into the detector though a metal gas pipe. The gas system consists of a circulation pump, flow controllers, pressure controllers, oxygen filters and monitors, a humidity monitor and three buffer tanks in the circulation line as shown in Figure 13.8. The schematic view of the COMET building can be seen in Figure 24.2. Some amout of flow rate (e.g., 2 liters/min) is required to remove oxygen efficiently from the CDC gas volume. An oil-free metal bellows pump is used to circulate the gas. A small amount of Hydrogen gas is mixed into the Oxygen filter for a Platinum catalyst. Fresh gas will be fed in at only 1/10 of the circulation flow rate to reduce gas consumption, and the exhaust flow rate is the same as feeding. The pressure in the CDC is controlled by the mass flow controller with a feedback of the pressure gauge on the buffer tank connected to the CDC output and will always be kept slightly higher than the atmospheric pressure (e.g., 1050 hPa) to obtain constant gain. The pressure of the CDC volume should be controlled within ∼1 % accuracy, to achieve the best performance although it is possible to compensate the gain fluctuation effect in offline analysis The output gas will be sent to the air exhaust port in the experimental hall. The input flow rates into the oxygen and humidity monitors are controlled with two mass-flow controllers to measure the oxygen and humidity levels correctly. The reasonable level of the oxygen concentration should be less than ∼50 ppm with the oxygen filter, and that of the water

Gas	X_0 (m)	W (eV)	$\frac{dE}{dx}^{MIP}$ (keV/cm)	n_T^{MIP} (cm^{-1})	n_p^{MIP} (cm^{-1})
He:i-C_4H_{10} (85:15)	954	38	1.14	40	18
He:i-C_4H_{10} (90:10)	1310	39	0.88	29	14
He:i-C_4H_{10} (95:5)	2102	40	0.61	19	9
He:C_2H_6 (50:50)	630	32	1.63	60	27
He:CH_4 (80:20)	2166	39	1.47	17	11
He:CH_4 (90:10)	3073	40	0.47	13	8

Table 13.3: *Comparison of different Helium-based low-Z gas mixtures, where* X_0 *is the radiation length,* W *is mean energy to generate one electron-ion pair,* dE^{MIP}/dx*,* n_T^{MIP}*, and* n_p^{MIP} *mean is energy loss per cm, the number of electron-ion pairs per cm, and the number of primary ions per cm for minimum ionizing particles, respectively.*

concentration should be ∼500 ppm, according to the study by the Belle CDC group. Three buffer tanks are installed to suppress a drastic change of the pressure. Their volumes are about 100 liters each.

Almost all the devices should be monitored and controlled remotely, to make the operation of the gas system safe and stable. The slow control system is described in Section 16.3. It is necessary to install a heating system or to locate the bottle on the ground floor (where room temperature is high enough) to avoid i-C_4H_{10} from being liquefied inside the gas transfer tubes.

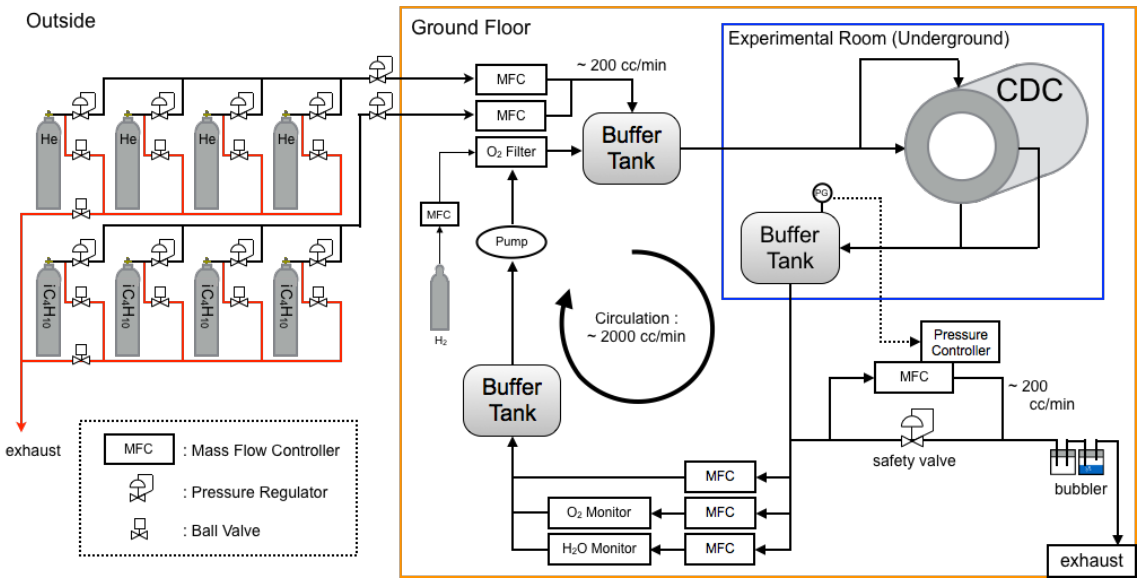

Figure 13.8: *Schematic view of the gas system for the CDC.*

13.2.3 Mechanical design

There are three main mechanical parts composing the CDC: the endplates, the inner wall and the outer wall. Two designs of the endplates had been considered in the past: a flat plate design and a cone shape plate design. In the end, a cone shape plate design is chosen to adequately support a 1.4 ton wire tension load. The outer wall of the CDC is made of CFRP with a thickness of 5 mm, and the inner wall of the CDC is made of 0.5 mm CFRP. It is noted that it

was planned originally to place a proton absorber in front of the CDC inner wall to minimizes the number of protons entering the detector from muon-capture in the stopping target. However, the latest study of the proton emission rate (discussed in Section 22.4.) indicates sufficiently low proton yield, requiring no proton absorber in front of the CDC.

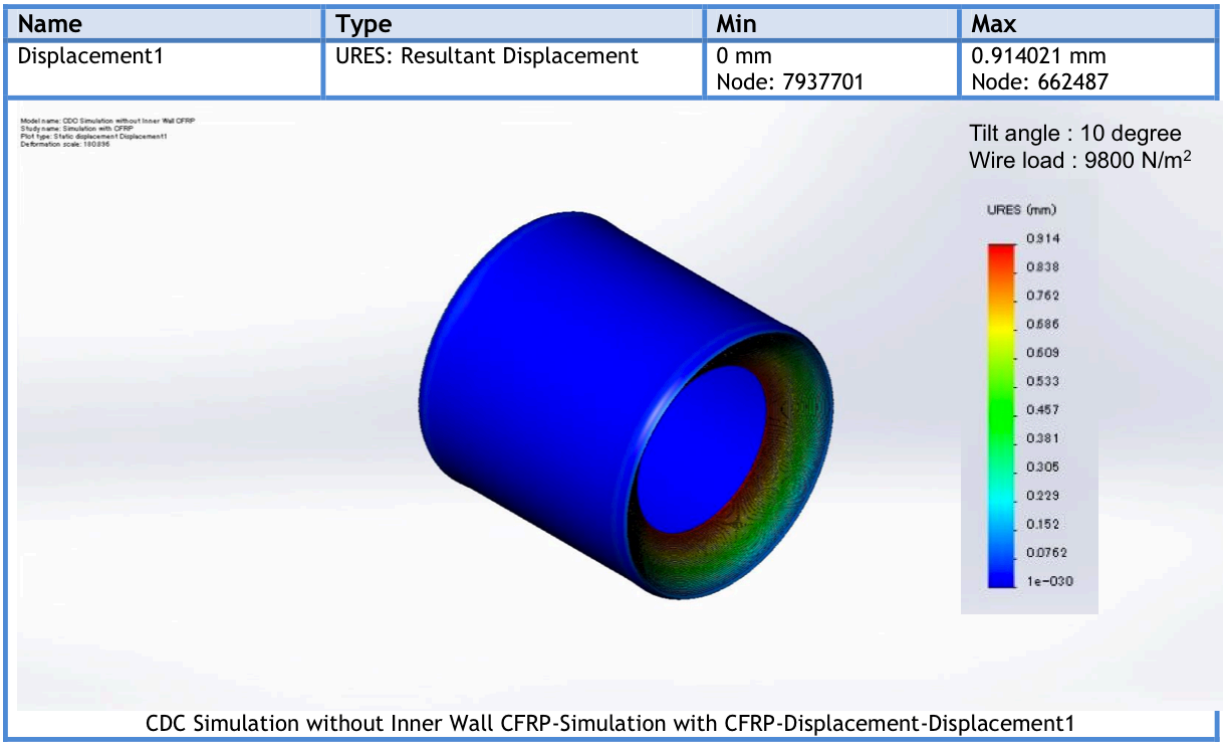

Figure 13.9: *Result of a deformation calculation of the CDC for F_{wire}=9800 N/m^2 and θ_{EP}=10 degree.*

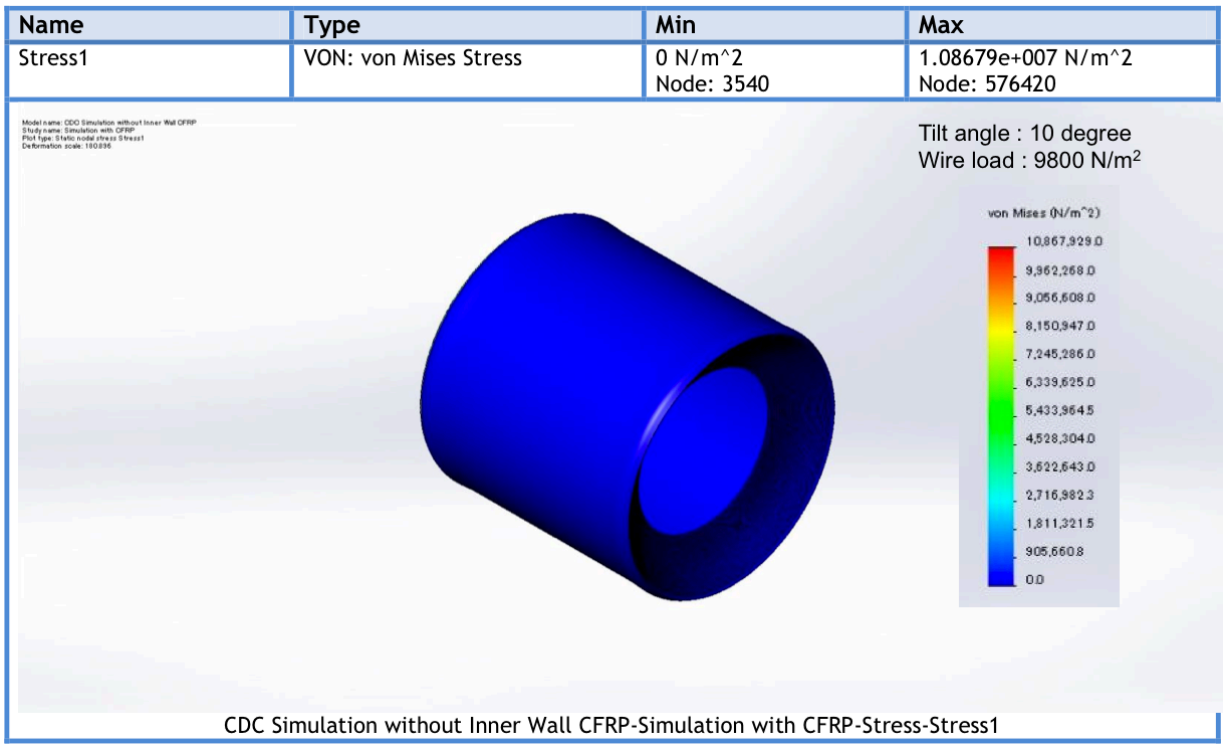

Figure 13.10: *Result of a stress calculation of the CDC for F_{wire}=9800 N/m^2 and θ_{EP}=10 degree.*

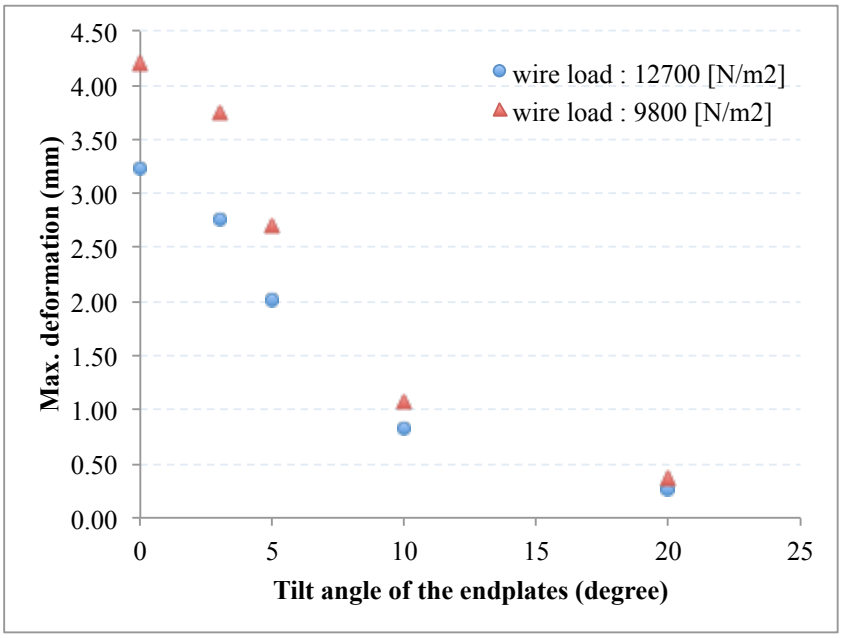

Figure 13.11: *Results of maximum deformation in the endplates and the outer wall of the CDC as a function of the endplate tilt angle for two different wire tension loads.*

The mechanical strength has been calculated using the SolidWorks (Premium 2013 x64 Edition) CAD program incorporating a Finite Element Analysis function. The wire load F_{wire} and the tilted angle of the endplate θ_{EP} were varied in the ranges of 7800∼12700 N/m^2 and 0∼20 degree to evaluate the stress and deformation of the endplates and the outer wall of the CDC. It is noted that no CDC inner wall was installed in the setup of this study strength since it is too thin to hold the wire load. Figure 13.9 and 13.10 show the results of stress and deformation calculations respectively, calculated for F_{wire}=9800 N/m^2 and θ_{EP}=10 degree. Figure 13.11 summarizes the deformation of the CDC as a function of the endplate tilt angle for two different wire tension load cases. The total wire tension load is calculated to be F_{wire}=12700 N/m^2 based on the paramters described in Table 13.1. The maximum deformation of the endplate is estimated to be 1.1 mm for F_{wire}=12700 N/m^2 and θ_{EP}=10 degree. This meets our requirements. The final tilt angle of the endplates of θ_{EP}=10 degree was determined from this calculation. Figure 13.12 shows the drawing of the whole CDC.

Prototype of the endplate The prototype of 1/12 of the endplate with feedthrough holes has been constructed to examine the accuracy of the hole positions. The total number of the holes for the prototype endplate is 1668, and the hole diameter is 3.20 mm.

The geometry of the produced test endplate was measured with 3D camera device (VMR-10080) to check the accuracy of machining. The diameter and center position of holes (x, y and θ) were calculated with automatically detected 4 points on the hole edges. The distributions of the diameter, dθ, dx and dy are shown in Figure 13.13, where dθ, dx and dy are determined as "measured value − design value". We found slightly large discrepancy and dispersion in the dx distribution (Figure 13.13(c)). This is solved by adding a proper offset in the machine coordinates, production of the real endplates started after checking the validity of the solution in another test.

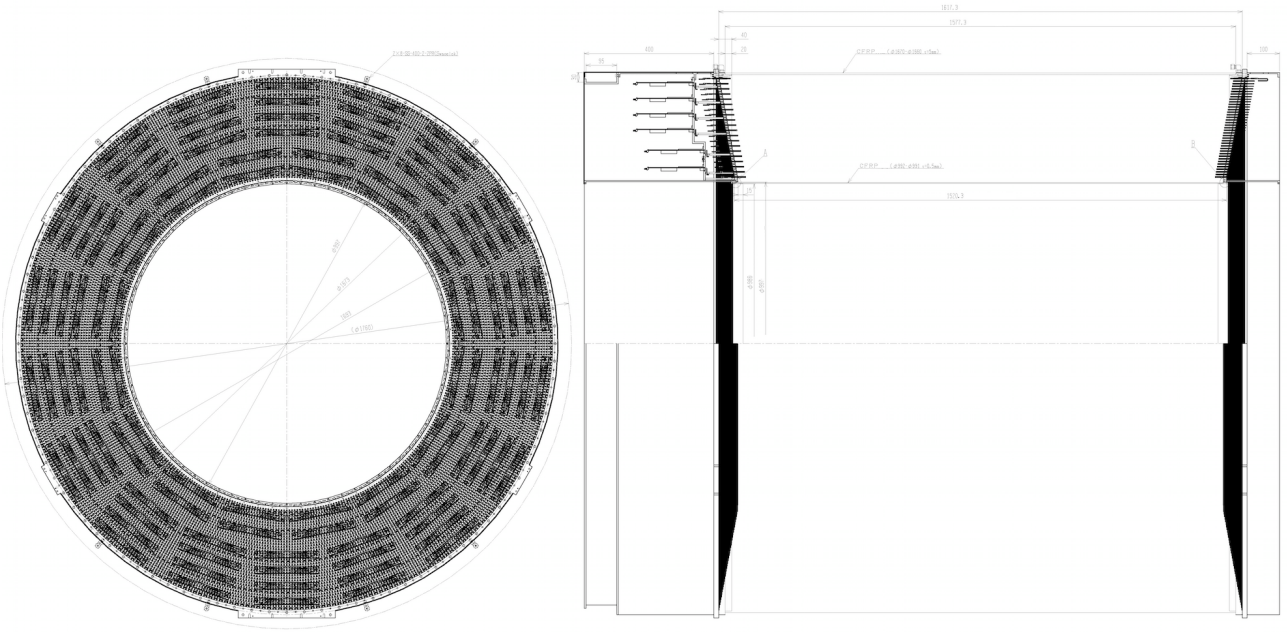

Figure 13.12: *CDC mechanical drawing. The endplates, outer wall, inner wall are shown.*

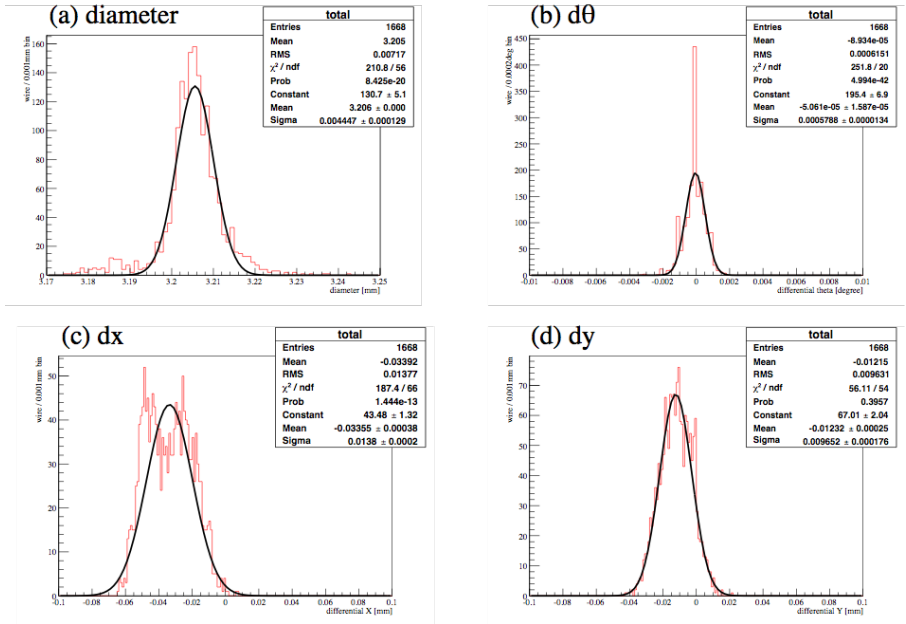

Figure 13.13: Distributions of the measured diameter and the position of all holes on the test endplate after coordinate correction.

Feedthrough The feedthrough is used to fix the wires and to ensure insulation between the high voltage and the endplate ground. We adopted the feedthrough developed for the BELLE CDC. The insulator material for the feedthrough-body is made of Noryl because of its reliable insulation performance against high voltage. The feedthrough-pin is made of aluminum. For the field wires, aluminum pins are used to hold the wire tension and are electrically connected to the aluminum endplates through additional cables. Figure 13.14 shows a photograph and dimension of the feedthrough.

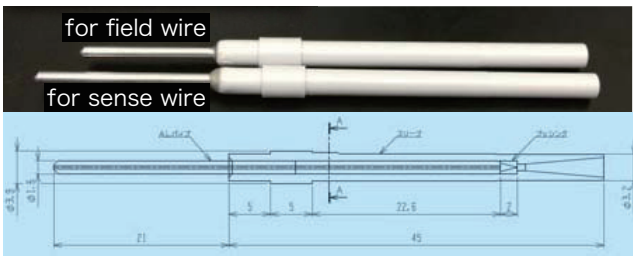

Figure 13.14: *Feedthrough for the CDC.*

13.2.4 Construction

The construction of the CDC started in summer 2014 after the design of whole CDC was fixed. In November 2014, the fabrication of the endplates completed, and then the outer CFRP pipe was fashioned in February 2015. After that, assembling of the endplates and the outer CFRP with supporting rings was operated in March. Subsequently, the assembled CDC outer structure has been shipped into the clean room at Fuji building B4 in KEK.

The prepartion work took $\sim$ 2 month for the start of wire stringing, such as cleaning, labeling the holes, installation of tension bars and set-up of the dial-gauge to measure the displacement between two endplates. Estimated sum of the tension of all wires was $\sim$ 1.4 ton, therefore, we applied 1.4 ton load burden with tension bars made of aluminum bars, spring, bolts and nuts. After burden, the distance between two endplates was found to be consistent with the calculation (0.9 mm).

In May 2015, we started to string wires. Figure 13.15 shows the number of total strung wires as function of consumed working days. There was no serious trouble, and the speed of the stringing was gradually improved. The wires were strung by traind company workers. Tension measurement of strung wires was carried out by COMET CDC crewson the same when the wires were strung. If the measured tension is 10% less or larger than the design value (50 g for sense wire, 80 g for field wire), they were re-strung. With controlled tension, the diffrence of wire sag due to the gravity is estimated to be less than 100 μm between sense and field wires.

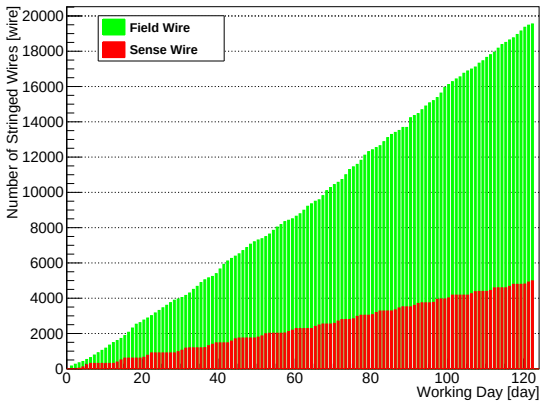

Figure 13.15: Progress plot of the wire stringing. It took 121 working days to complete all wire stringing.

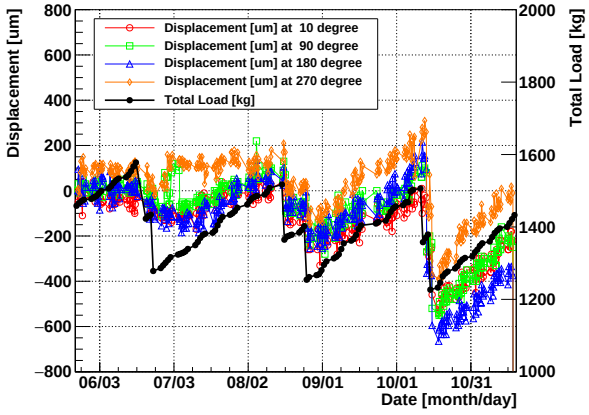

Figure 13.16: Transition of the displacement between two endlplates and total load by strung wires and tension bars.

In addition to the wire tension, displacement between upper and lower endplates was recorded with 4 dial-gauges three times per day. The transition of the displacements are in coincidence

with the total load by strung wires and tension bars as shown in Figure 13.16. The load by tension bars was alleviated by reducing spring load or removing tension bars one by one. There were 6 load alleviation, and no tension bar installed in the end. Wire stringing completed at the end of November 2015 after 121 working days. Figure 13.19 is a picture of inside CDC taken just after the completion.

After the stringing completed, the tension of all 19,548 wires was re-checked because the gap between 2 endplates was changing during the campaign. We found that aluminum wires in the inner layers have significant tension drop, $\sim$ 20 g drop compared to the 1st measurement. There is no tension bar anymore after the innermost tension bars were removed, therefore this indicates that the distance between 2 endplates became shorter by the tension burden by the inner wires. According to reduction of the distance between two endplates, reduction of the wire tension is reasonable though this is beyond our requirement. We re-defined the criteria with more practical way. Each wire sag by the gravity can be calculated with the length of wire, tension and the parameters of the material (density and diameter), and it is better to minimize the sag. In order to cope with this situation we re-examined the allowed wire sag and corresponding the wire tension; we have found that the wire sag should be less than 170 μm for the field wire and 70 μm for the sense wire. These values came from the practical calulation, and they correspond roughly to 60 g tension for the field wires, and 45 g tension for the sense wire. In addition to the wire sag itself, sag difference in a cell should be considered to avoid deformation of the cell shape. Another criterion is that the difference of the sags between a sense wire and the other field wires in the cell should be less than 100 μm. Figures 13.17 and 13.18 shows the geometry and tension of sense and field wires seen from the downstream side of the CDC. For the field wire, we can see three clear boundaries with larger tension reduction related to tension bars removal. After that, we found about 20 bad wires out of the criteria to be replaced. The tension measurement result will be incorporated in simulation, analysis and calibration of wire position.

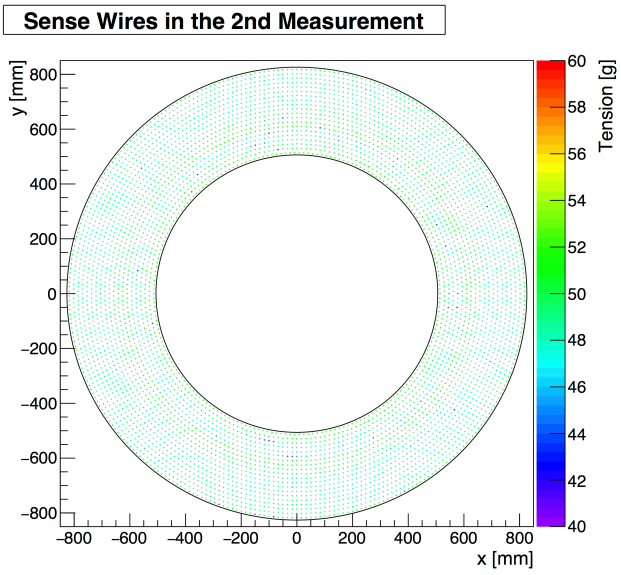

Figure 13.17: The geometry and tension of sense wires seen from the downstream side of the CDC. About 10 wires have lower tension to be replaced.

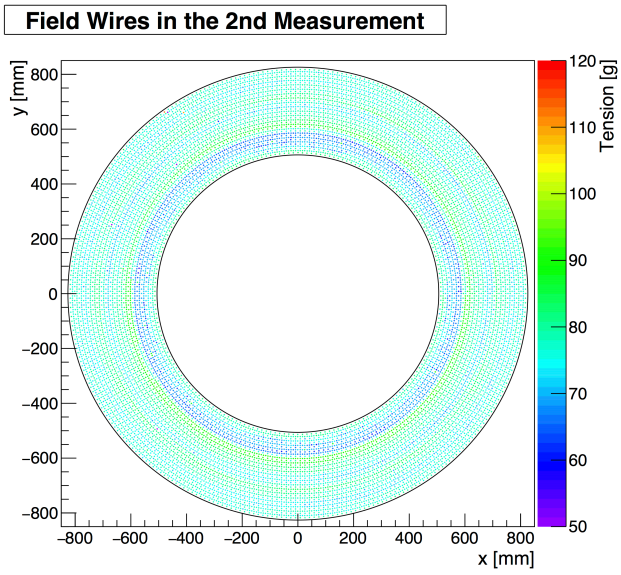

Figure 13.18: The geometry and tension of field wires seen from the downstream side of the CDC. The dependence of the tension on the wire layers and tension bar locations can be clearly seen. There are still several bad wires shown to be replaced.

The CFRP pipe for the CDC inner wall was successfully fabricated in February 2016. The

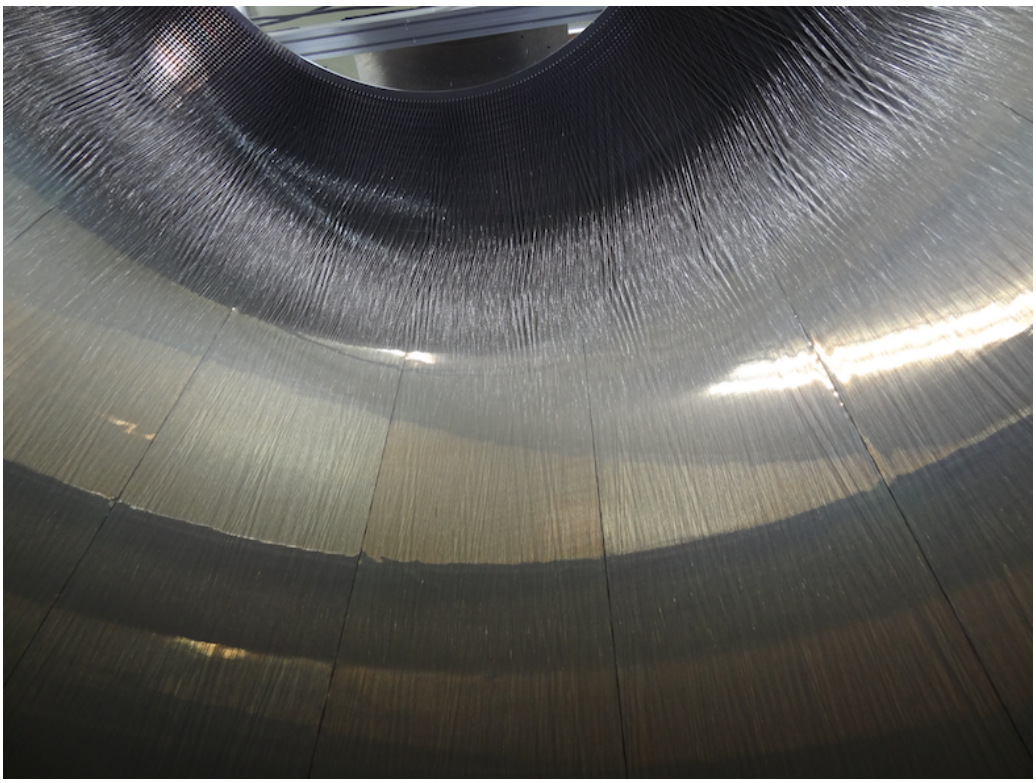

Figure 13.19: CDC wires seen from the inside of CDC.

thickness of the inner CFRP is only 0.5 mm, and the drawing as shown in Figure 13.20. There are 13 pieces of 50 μm thickness aluminum film pasted without glue on the outer side of the CFRP pipe (that is inner side of the chamber) for grounding the innermost layer. The assembled inner wall (CFRP pipe + support rings) will be shipped to KEK in April, and the wall will be installed into the CDC at the clean room in Fuji building B4. The joint parts will be sealed with silicon rubber to assure the gas tightness.

After the inner wall is installed, we check the gas tightness with herium gas in spring 2016. The Belle-II CDC group achieved $\sim$ 50 cc/min of the leak rate. Because we have less holes and joints area, we expect the leak rarte less than $\sim$ 20 cc/min, which corresponds to the 1% of the circulation flow rate in our gas system.

13.2.5 Readout Electronics

Overview The readout electronics board for Belle-II CDC (called RECBE) has been chosen as the front-end readout electronics for the COMET CDC with appropriate modifications. It has tested adequately in terms of radiation hardness at the radiation level of the Belle-II experiment. Figure 13.21 shows a photograph of the COMET CDC readout board. Each board has 48 input channels, 6 ASD (Amplifier Shaper Discriminator) ASIC chips, 6 ADCs and a FPGA of `Virtex-5` XC5VLX155T. The ASD ASIC chips made by KEK (KEK-ASD) are obsoleted, but the new ASD ASIC chip with same performance is developed by an external vender which took over the development. The acquired data is sent to DAQ PC via a SFP slot with the SiTCP technology through an optical fiber cable. The board has two RJ45 connectors, one is for JTAG line to download the firmware into the FPGA, the other is for transmitting clock, trigger and busy signals to the FCT board described in Section 16.1.. Modifications made for COMET use are,

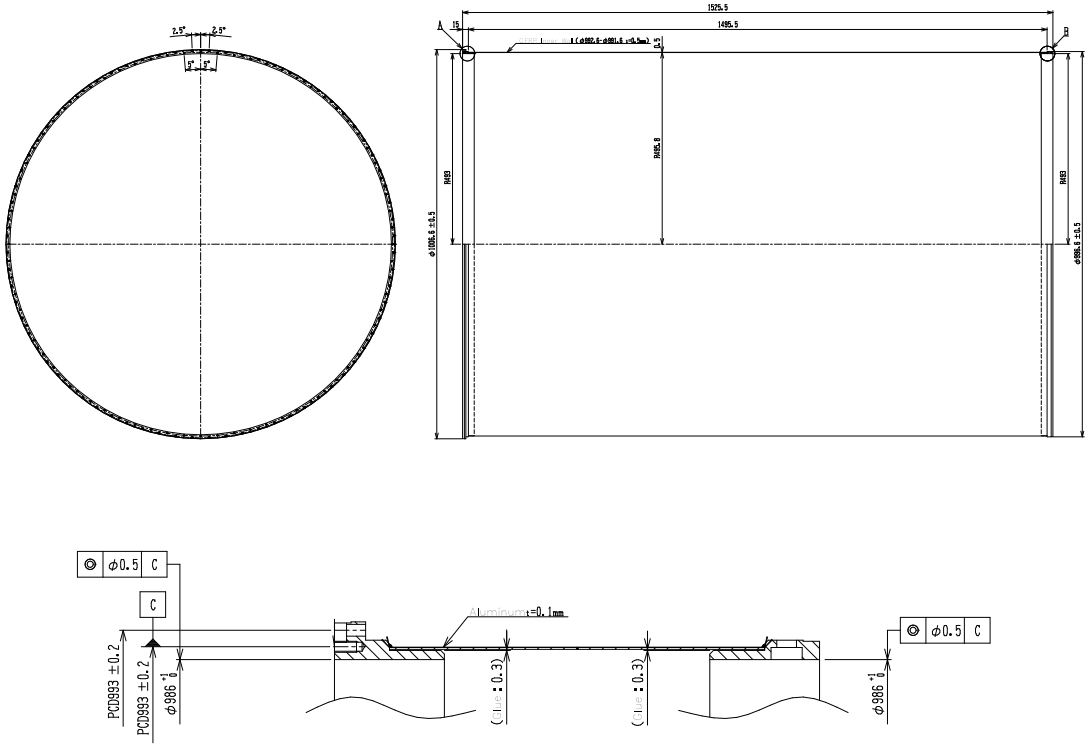

Figure 13.20: The drawing of the CDC inner wall (CFRP pipe + support ring).

- The LEMO connectors for the test are removed.
- A socket for aurora interface is removed.
- KEK-ASD ASIC chip is replaced to new one which is developed by an external vender.
- The PCB is modestly re-worked for the new ASD ASIC chips.

The readout electronic will be located on the CDC downstream endplate and the HV cables will be connected on the upstream endplate. The production of all the readout boards (128 boards with spares) has already finished by the IHEP group in China in 2015. A performance test for these new boards is ongoing. The detail is described in latter sections. Specification of the CDC readout board is summarized in Table 13.4.

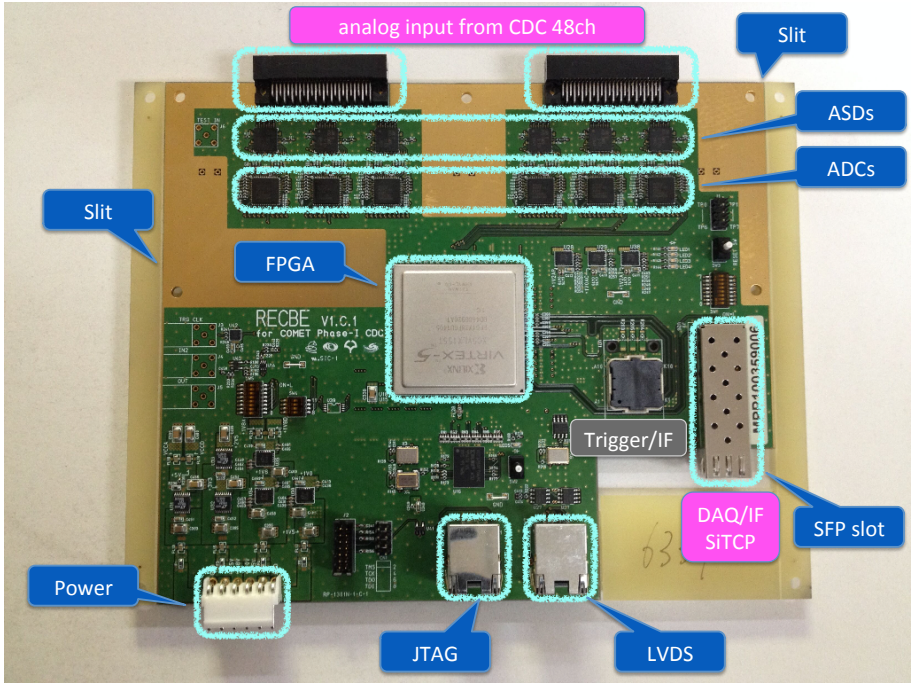

Figure 13.21: The COMET CDC front-end readout board

Size	200×170 mm^2
Thickness	1.838mm (16layers)
Power supply	+5.5V, +3.8V, +2.0V, +1.5V
Power consumption	12.5W

Table 13.4: The specification of the COMET CDC readout board.

FPGA Firmware Figure 13.22 shows a block diagram of the COMET CDC readout module implemented in the FPGA. The fast control block receives the reference clock, trigger (trigger number) from FCT board, and sends a busy signal to stop receiving triggers if the buffer is full. The CDC block arranges data of drift time and dE/dx from digitized values by the TDC and ADC. SiTCP is used to transmit the event data to the DAQ system via Gigabit Ethernet fiber link. TCP/IP provides end-to-end reliable connectivity. The Reg block, which is responsible for configuration and status, can be accessed through UDP communication. The SYS MON block is used for status monitoring of the board, such as temperature and voltage monitor.

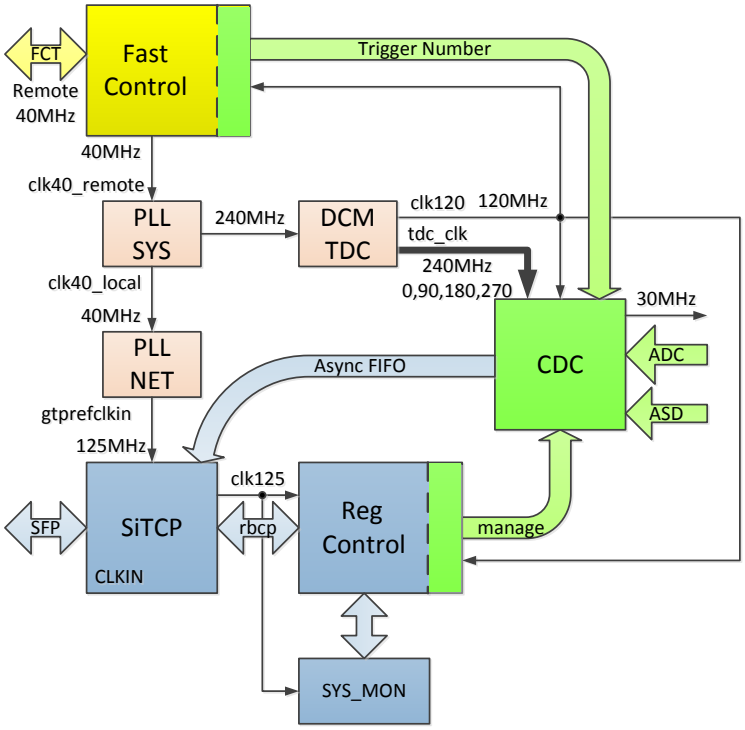

Figure 13.22: Block diagram of the RECBE firmware.

Table 13.5: Operation clocks in the FPGA firmware functions.

System Clock	120 MHz
TDC Time Resolution	1.0416 nsec (960 MHz)
ADC Sampling Rate	30 MHz

There are three clock domains in RECBE as indicated in different colors in Figure 13.22: the yellow one is is the 40 MHz domain, which comes from FCT board; the green one is 120/240 MHz domain, which manages for ADC and TDC; the blue one is 125 MHz domain, which matches the data transfer rate of the Gigabit Ethernet. The signal and data bus crossing clock domains are carefully handled to avoid metastability. No local clock or nonvolatile memory is used because of radiation issue. We need to re-configure the firmware remotely and regularly to recover from errors caused by radiation.

The size of ring buffer to store the ADC and TDC data is 256 depth, corresponding to $\sim$8.533 μsec. If a proper roll-back length is set as an offset in the ring buffer, we can acquire ADC and TDC data of $\sim$8 μsec before. Typically, the event window size for the CDC is 32 sampling, which corresponds to $\sim$1.067 μsec. Therefore, the acceptable trigger latency is $\sim$7 μsec at maximum after subtracting the typical event window size. As a downstream buffer, there are also 256 depth block RAM just before sending to the SiTCP module. Assuming the typical event window size, 8 events can be stored in the buffer.

Data Structure There are three types of data recording mode in the firmware. Figure 13.23, Figure 13.24 and Figure 13.25 show the (binary) data structure of raw mode, suppress mode and semi-suppress mode.

The common header data is inserted before the event data for each mode, to identify the packet type (mode), board ID, sent number, trigger time, data length and trigger count (number). The

packet type is an 8-bit number originated for each mode, and board ID is also an 8-bit number assigned to each readout board. The sent number is a 16-bit number to count up the number of sent data for each event. The trigger time is a 15-bit number of the timestamp synchronized with TDC clock (the highest 1-bit is un-used). The TDC time in the event data, if the trigger time is subtracted from the trigger time, is equivalent to the drift time. The data length is used to identify where the end of the data packet is, especially when the data size is reduced in suppress mode and semi-suppress mode by zero-suppression even with same event window size. The trigger count (number) is a 32-bit counter to synchronize the event with the other sub detectors and this is provided by the FC7 which is the central trigger electronics.

The three recording modes have different purposes. The raw mode provides us all information (all TDC and ADC values of all channels for each sampling clock) as described in Figure 13.23, therefore we can perform primitive analysis such as noise and baseline measurements and threshold scanning using full waveform. This raw mode will be used in the performance check with cosmic-ray and the engineering run before the physics run. The suppress mode is a main recording mode in the physics run. The information is suppressed to an ADC sum value and valid TDC value(s) only for hit detected channels. The data size of the suppress mode is much smaller than the raw mode, and the suppress mode is available in the high trigger rate (more than $\sim$ kHz) in the physics run. The third mode is an optional mode to record the waveform of the channels in which signal is detected, named semi-suppress mode. The TDC values are also suppressed by discarding invalid TDC data. The data size is in the middle of raw and suppress mode sizes. The semi-suppress mode may be used in the engineering run for waveform analysis with higher trigger rate.

The firmware has a function to select hit channels by ADC sum information. The ADC sum value of the most of hits made by signal electrons is small, whereas that from noise particles have a larger ADC sum value as described in Section 13.4.2. Only data of hit channels which have ADC sum value below a threshold level is transferred to the downstream buffer. The threshold level also can set through UDP communication. This high-charge cut function is very useful to suppress the CDC data size.

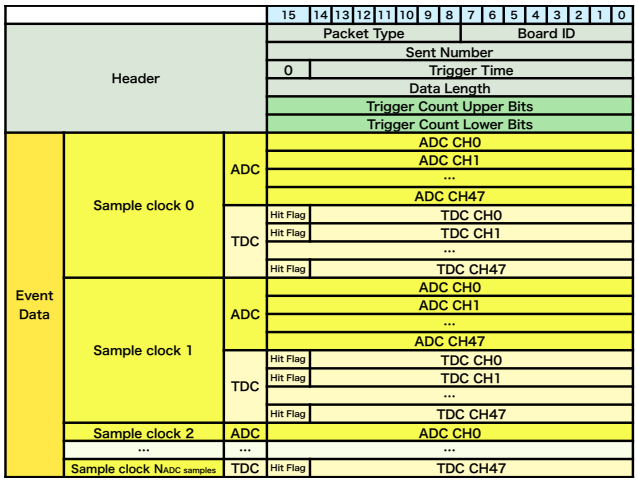

Figure 13.23: Data structure of Raw Mode.

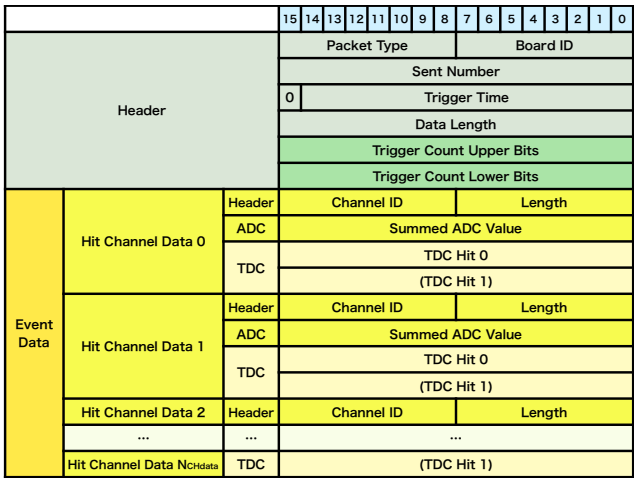

Figure 13.24: Data structure of Suppress Mode.

Mass Production The pre-production of the CDC readout electronics started in Jan. 2015. Four boards use Lead-free solder (peak temperature: 245-255 °C), and the other four boards use Tin-lead solder (peak temperature: 205-215 °C). Even with tin-lead solder, only one solder joint failure was found in pre-produced board. After completing soldering, we made a burn-in test of these boards.

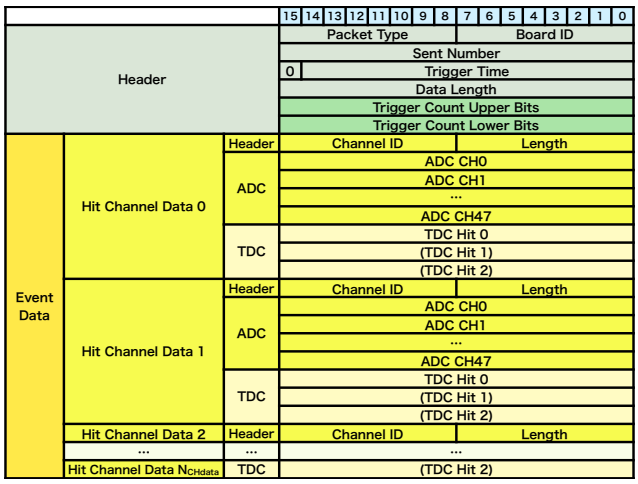

Figure 13.25: Data structure of Semi-Suppress Mode.

Table 13.6: Summary of burn-in test of pre-production boards.

No.	Category	Test item	Criteria Standard	Test Condition	Check after Test
1	environmental stress test	high temperature storage life test	GJB2423.2	85 °C, 168 hours	electrical perfomance test
2		temperature cycle test	JESD22A104-A GJB2423.2	$-40 \sim 85$ °C ramp rate: 5 °C/min hold time: 15 min	visual inspection
3		temperature and humidity bias test	GJB2423.2	85 °C, 96 hours, humidity: 85% RH	electrical perfomance test
4	life test (aging)	high temperature operationg life test	GJB2423.2	85 °C, 96 hours	

The test methods and conditions for pre-production boards are summarized in Table 13.6. If we use Arrhenius model to predict how time-to-fail varies with temperature, the acceleration factor (AF) is calculated to be 7.49 according to

$$AF = e^{\frac{\delta H}{k}(\frac{1}{T_u} - \frac{1}{T_t})}$$

where $\delta H = 0.68$, $k = 8.617385 \times 10^{-5}$, $T_u = 55 + 273.16$ K (operating temperature), $T_t = 85 + 273.16$ K (testing temperature). The burn-in tests made no significant change of the RECBE performance for both types of boards with tin-lead and lead-free soldering. Finally, we decided to use Lead-free solder, which is commonly used in the world today, for mass-production. Using the result obtained in this test, we can estimate the life time of RECBE is longer than 2.5 years ((168 + 96 + 96) hours ×8 boards ×AF).

Mass-production of 120 readout electronics boards took one and half months for soldering, assembling, function and performance testing, and aging. In the middle of August 2015, 126 products passed the aging test, to ensure the reliability. Figure 13.26 is a photograph of the 128 boards in the shelf, and the performance check is ongoing.

Figure 13.26: 128 COMET CDC readout electronics boards.

Radiation Tolerance The RECBE boards will be located at the downstream of the CDC detector, so they will be exposed to the high radiation fluence from the beam line and the target. The study of the radiation tolerance is summarized in chapter 17.

Electronics shield cover and cabling The front-end electronics of the CDC will be installed in electronics shield covers as shown in Figure 13.27. The shield covers are set on both the upstream and downstream endplates. The covers are made of mainly 3-mm thick aluminum plates and the joints are sealed with dismountable glue. Since the inside of the detector solenoid is filled with helium gas, we circulate dry air inside shield covers in order to avoid discharges in high-voltage parts.

The number of necessary cables to be connected in shield covers is summarized in Table 13.7. In addition to the 104 RECBE boards, 4 FCT and 18 COTTRI boards, described in Section 16.1., are installed in the downstream electronics shield cover. The cables are laid from each board to patch panels on the endcap of detector solenoid through connectors equipped on the shield covers. High voltage is supplied the upstream side of CDC.

Cooling System From the point of view of the detector performance, the temperature of gas detector is very important to make the gas gain stable. The electronics boards located near the downstream endplate are potential heat sources to warm up the CDC detector. Also the electronics performance is affected by the temperature, if it is too high.

The main source of the heat is read-out electronics (RECBE). There are 104 RECBE boards installed on the downstream endplate, and they are covered by the electronics cover to shield

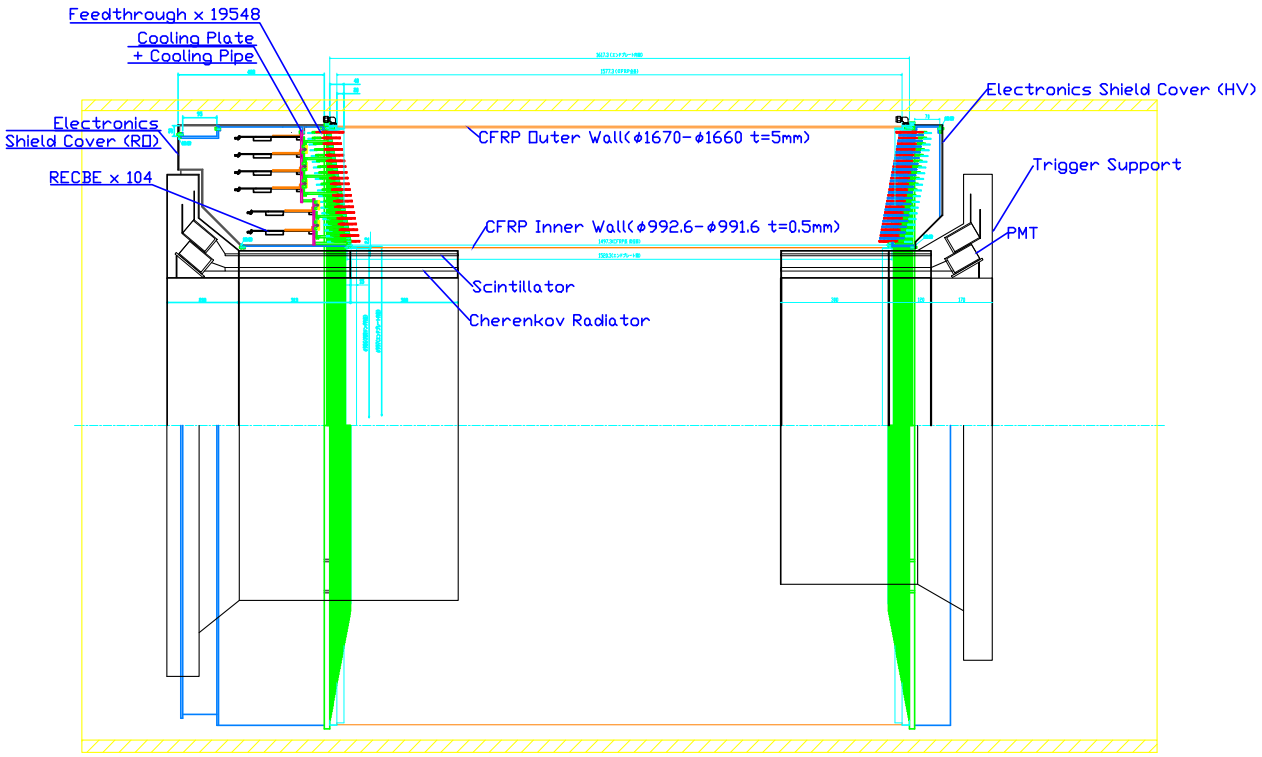

Figure 13.27: *Mechanical drawing of CDC and CTH with the surrounding structures. The right of the figure denotes the upstream of detector solenoid. Support structures of the trigger hodoscopes is shown as the black line.*

Table 13.7: *Summary of the number of cables for CDC. The forth column indicate the cable destination, i.e. upstream or downstream (U/D) shield cover.*

Description	Cable	# of cables	U/D
Data transfer from/to RECBE	Optical cable	104	D
Power supply for RECBE	Metal cable	104	D
Data transfer from/to FCT	Optical cable	4	D
Power supply for FCT	Metal cable	4	D
Data transfer from/to COTTRI-FE	Optical cable	18	D
Power supply for COTTRI-FE	Metal cable	18	D
High voltage supply for CDC	HV cable	10	U

against environmental electro-radioactive noise. The power consumption of one RECBE board is $\sim$ 15 W, therefore the total power is $\sim$ 1.6 kW as a potential heat source. In addition to RECBE, there will be 4 FCT boards and the interface boards installed inside the electronics cover. The power consumption of them is not large, and is estimated $\sim$ 5 W for each pair of FCT and interface board. As conservative estimation, we assume 2 kW as a potential heat generation inside CDC to consider the specification of the cooling system.

In a crude estimation, passive cooling power by natural air convection and heat radiation is only $\sim$ 100 W, requiring us to consider active cooling using forced air flow or liquid circulation. As for air cooling, we estimated the required air flow rate to achieve 2 kW cooling power, to be $\sim$ 6 m^3/min by assuming the difference between input and output air temperature is less than 15 °C. This flow rate is not small and we need to calculate and/or simulate the air flow path in the real condition to make the thermal gradient small. However, it is not easy to be confident with air cooling without actual measurement with the realistic configuration. Thus, we decided to adopt the water cooling system for our CDC.

Figure 13.28 shows the current design of the cooling pipe configuration on the CDC endplate. The pipes are located closer to the endplate than RECBE boards to keep the CDC temperature stable, and the pipes cool the aluminum plates where the RECBE boards are mounted. The RECBE boards can be cooled by the cooling plates and busbar connected to FPGA on RECBE. There are five circulation lines (layers) on the endplate, and the direction of water flow will be inverted layer by layer to make the thermal gradient minimum.

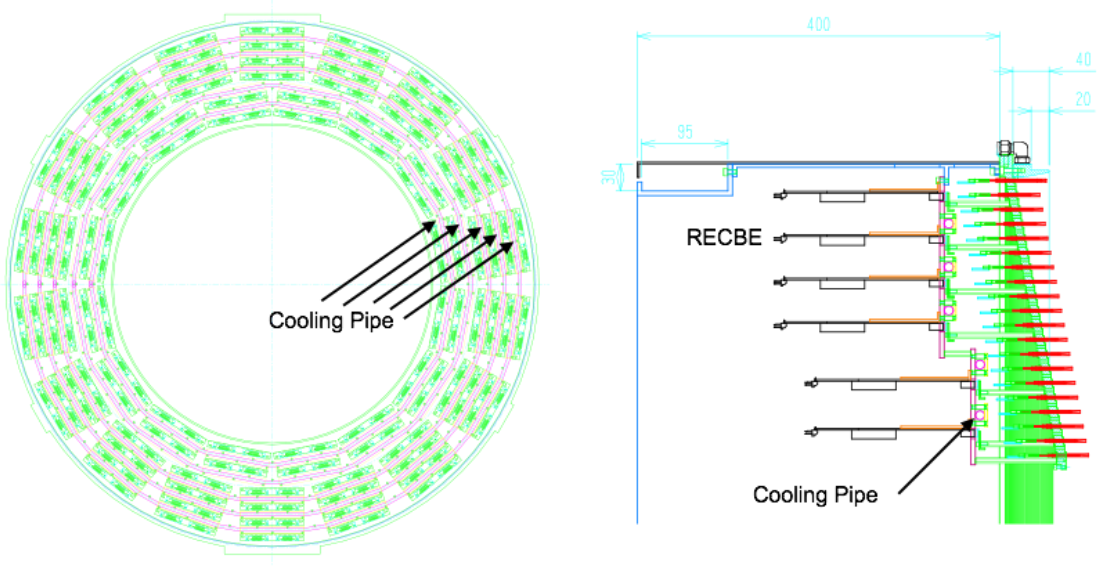

Figure 13.28: *Current design of cooling pipes on the CDC endplate.*

The required water flow rate to achieve 2 kW cooling power is $\sim$ 3 liter/min with 10 °C temperature difference between input and output. To avoid the failure of the system by water hammer phenomena, the flow speed should be kept less than 2 meter/sec, and this flow speed determines the minimum diameter of the water pipe. The size of the pipes should be larger than 1/8 inch (as nominal diameter). This is reasonable flow rate, and there are several candidates of the water-cooling apparatus (kind of thermoelectric cooling pump) to satisfy the required specification as consumer products. The current schematic view of the cooling system is described in Figure 13.29. From the point of view of the radiation safety, the whole system will be located in the experimental area (radiation controlled area) including all water pipe lines. The CDC detector is installed inside the detector solenoid. Hence it is necessary to use

feedthrough to feed/drain the cooling water into/from the detector. The output water is stored in a buffer tank of 100 liter volume. There is a sampling port at the bottom of the tank for activity measurement before discharging the water. The other line from the tank is connected to the water-cooling apparatus through a filter preventing pipe clogging. The machine should have the specification to satisfy the required cooling power ($\gg$ 2 kW) and pumping speed ($\gg$ 3 liter/min), and remotely controllable system because we can not access to the experimental area during beam time. The CDC detector is located at more than 1 meter higher than basement level to adjust the muon beam height to center of the detector. Thus the return line can harness the difference in height. The buffer tank should be located higher than the water-cooling apparatus so that water can flow to the apparatus without any pump. A corrosion prevention material will be dissolved in pure water to protect the pipes from corrosion.

Radiative products such as tritium are harmful and strictly controlled. Therefore we need to estimate the production rate in advance by neutron irradiation on the cooling water. Tritium production amount is estimated conservatively to be $\sim$ 1.8 Bq/cc after 100 days of beam time operation in COMET Phase-I with neutron radiation level; 5×10^6 neutrons/cm^2/sec in total. This amount of tritium is one order magnitude lower than that allowed to discharge by the Japanese law. We do not have to displace cooling water in the system in the whole period of the COMET Phase-I, and we can discharge it after confirming the activity level when Phase-I completed. The discharge line should be prepared to connect the buffer tank with the drain ditch in the experimental area. The discharged water will be transferred to the water disposal tank installed in the machine room in the COMET building.

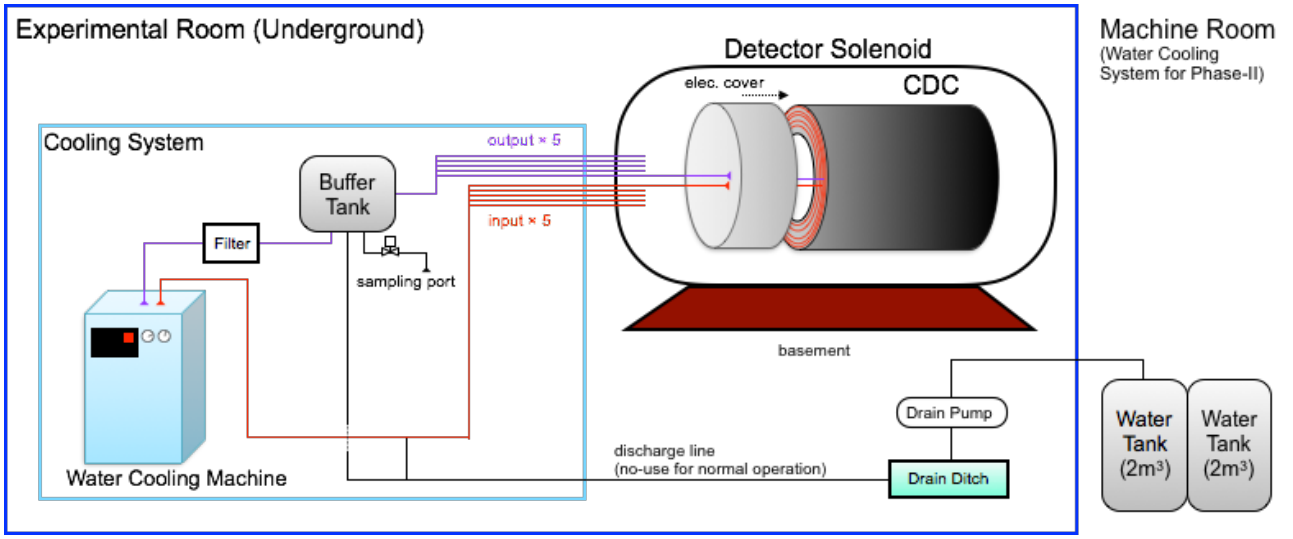

Figure 13.29: *Diagram of the water cooling system for the CDC electronics.*

As an additional concern, the cooling can lead to dew in higher humidity condition, and the dew water may damage the electronics. To keep the humidity inside the electronics cover lower, sufficient amount of dried air/nitrogen must be blown into the cover. The air/nitrogen will be fed to prevent the discharge at high voltage pins. Also, the cooling pipes in the experimental room should be covered with insulator.

13.2.6 Prototype chamber

Small-sized prototype chambers were constructed in order to examine the performance of the real CDC. Specifications of the four prototype chambers are summarized in Table 13.8.

Table 13.8: *Specifications of the prototype chambers.*

Prototype	1	2	3	4
Sense wire ϕ [μm]	30	25	30	25
Field wire ϕ [μm]	126	80	80	126
# of sense layers	11	5	5	9
# of readout channels	199	27	27	87
Stereo angle [mrad]	25	70	70	66
Wire length [mm]	600	200	200	600
Angle coverage [deg]	30	8	8	15

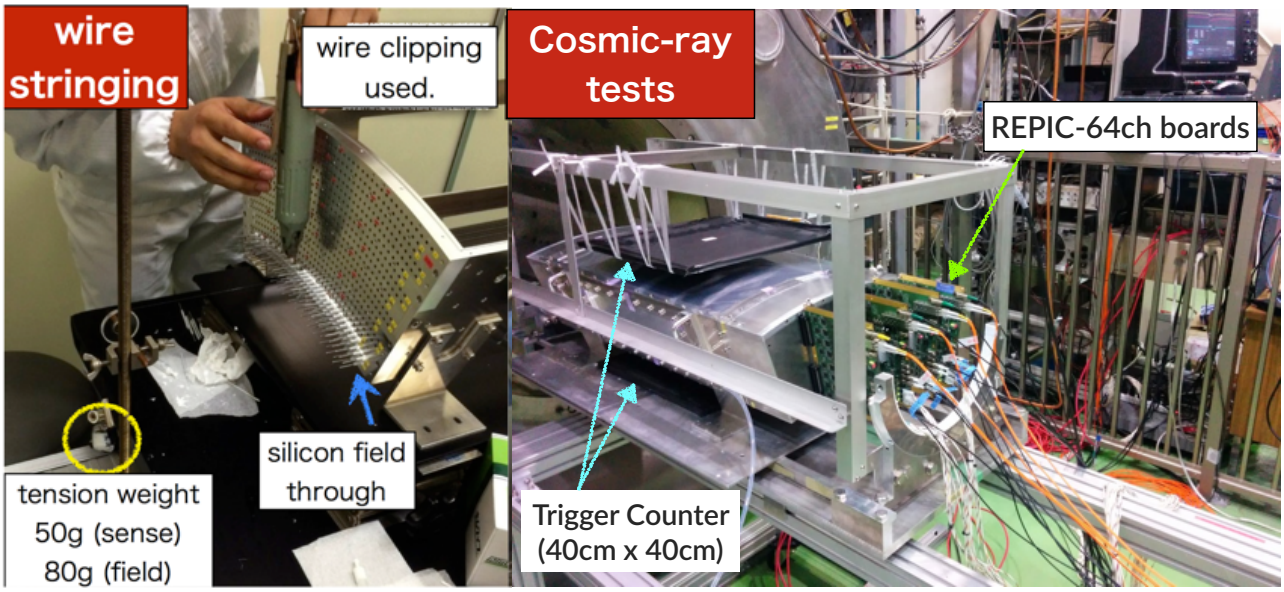

Figure 13.30: *Left: Wire stringing of the first prototype chamber. Right: Cosmic-ray test set-up of the first prototype chamber at KEK.*

Figure 13.30 shows wire stringing of the first prototype chamber (left) and the setup for a cosmic-ray test at KEK cryogenic center (right). The first prototype chamber was tested in July 2014 using cosmic rays to study spatial resolutions in the magnetic field for different gas mixtures. The data were taken for three types of gas mixtures, He:i-C_4H_{10} (90:10), He:C_2H_6 (50:50) and He:CH_4(80:20), at magnetic fields of 0.6 and 1.0 T. To estimate the spatial resolution, cosmic-ray tracks are reconstructed by using the sense layers except one used to evaluated resolution. Figure 13.31 shows the residual distributions for each gas mixture and magnetic field. Assuming the track interpolation uncertainty of 200 μm, the spatial resolutions were found to be less than 200 μm for the three gas mixtures at 1 T magnetic field.

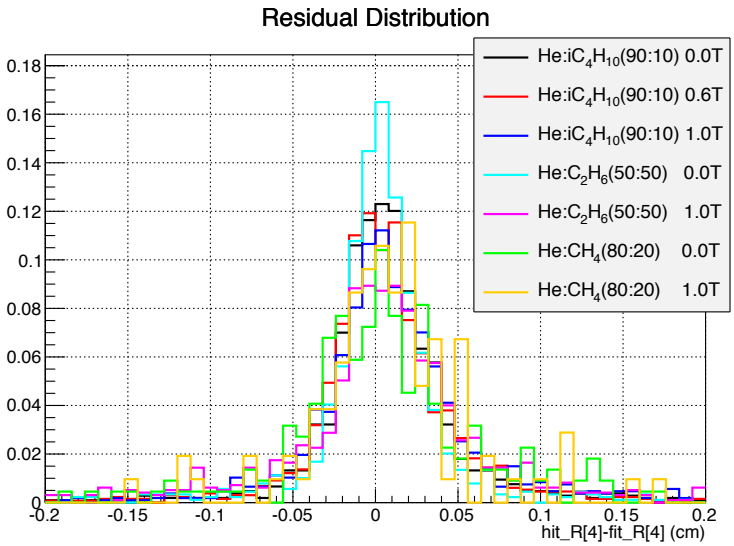

Figure 13.31: *Residual distributions measured with the first prototype chamber using cosmic-rays.*

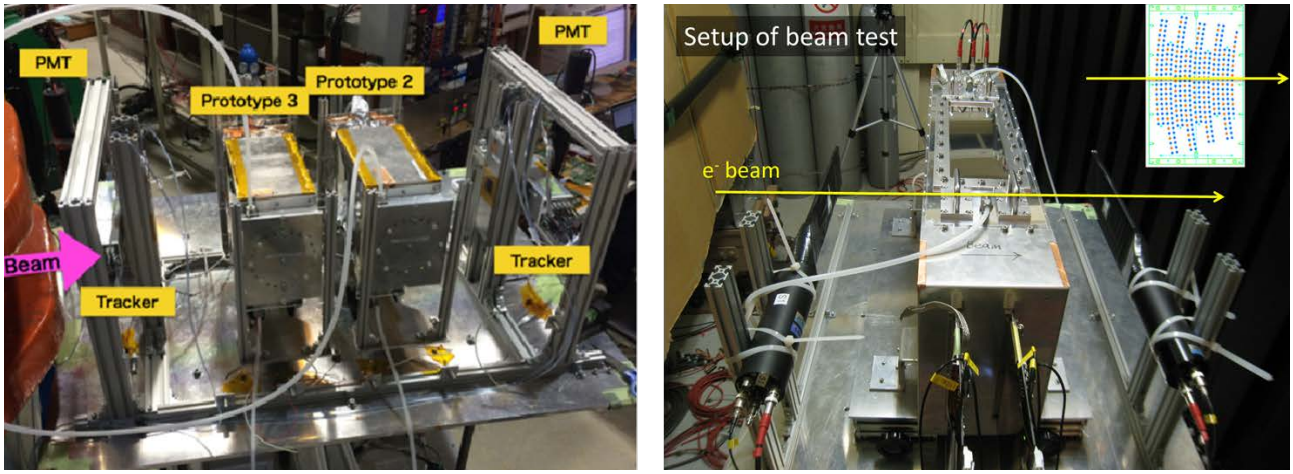

Figure 13.32: *Setups of the beam test of the second and third prototypes at ELPH/Tohoku Univ. (left), and the beam test of the forth prototype at LEPS/SPring-8 (right).*

The second and third prototypes are simple box-type chambers with their sense wire diameters of 25 and 30 μm, respectively. They were constructed for the beam test at ELPH, Tohoku University in December 2014. Electron beams were irradiated to two chambers for three gas mixtures as shown in Figure 13.32 (left). Electron tracks were reconstructed by using reference trackers installed in front and rear of prototype chambers. A hit efficiency is defined as the ratio of the number of events with the residual within 600 μm to the number of reconstructed

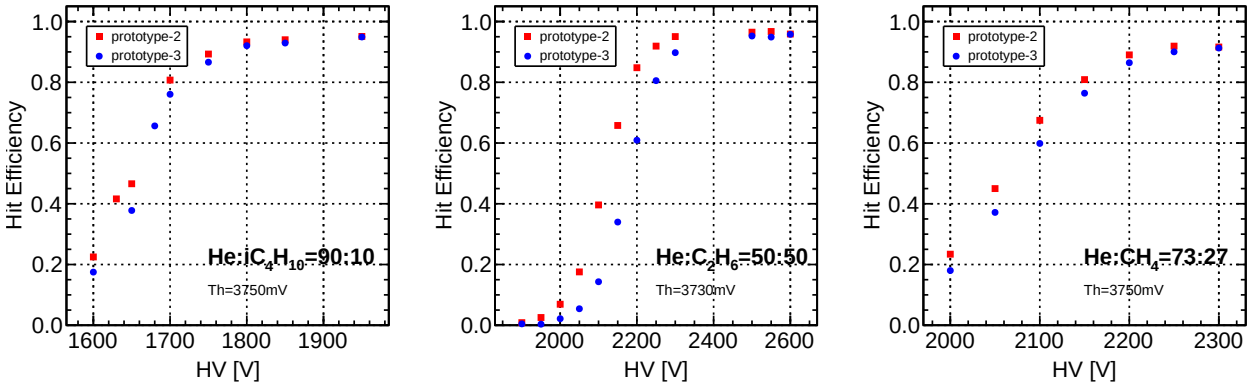

Figure 13.33: *Hit efficiency of the second and third prototypes for gas mixtures of He:i-C_4H_{10} (90:10) (left), He:C_2H_6 (50:50) (middle), and He:CH_4(73:27) (right). The second and third prototypes have sense wire diameters of 25 and 30 μm, respectively.*

tracks. Figure 13.33 shows the hit efficiency as a function of the applied high voltage for each gas mixture. We confirmed that the operation voltage should be higher than 1800 and 2300 V for He:i-C_4H_{10} (90:10) and He:C_2H_6 (50:50), respectively, to achieve sufficient efficiency. The result led to the decision of the field wire diameter of 126 μm as described in Section 13.2.2.

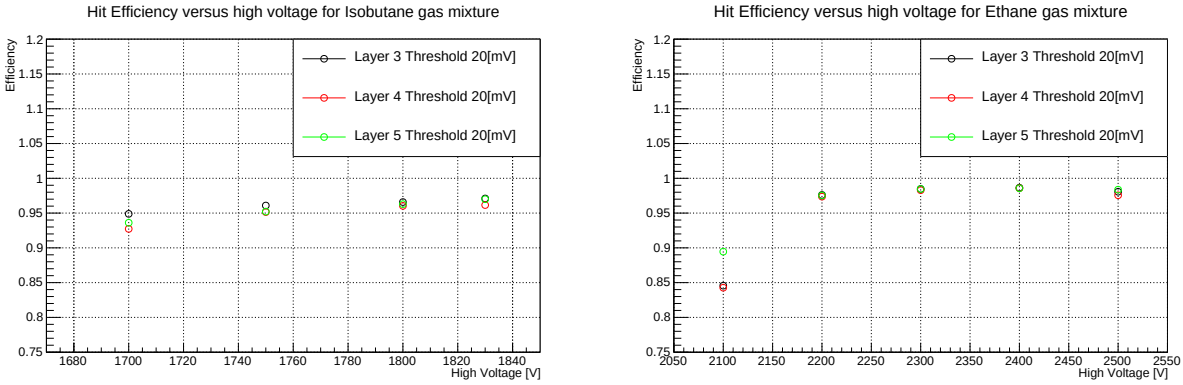

Figure 13.34: *Efficiency for central three layers of the forth prototype as a function of high voltage for gas mixtures of He:i-C_4H_{10} (90:10) (left), and He:C_2H_6 (50:50) (right).*

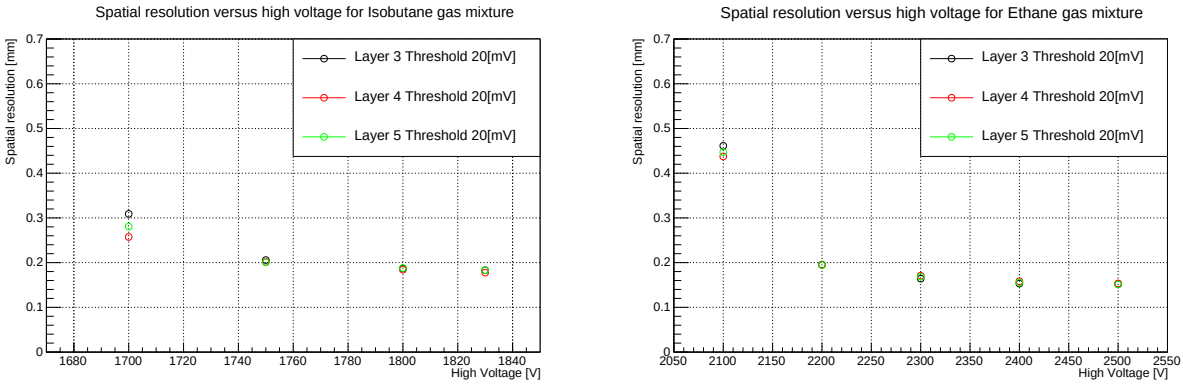

Figure 13.35: *Spatial resolution for central three layers of the forth prototype as a function of high voltage for gas mixtures of He:i-C_4H_{10} (90:10) (left), and He:C_2H_6 (50:50) (right).*

After determining all the mechanical specification of the CDC, we constructed the fourth (final) prototype chamber as a partial copy of the real CDC design. It can be used to study the

performance of the CDC under more realistic conditions. A beam test was conducted at LEPS/SPring-8 in July 2015 to examine the performance for three different gas mixtures in a systematic manner. Electrons converted from photon beams were irradiated to the chamber as shown in Figure 13.32 (right). The hit efficiency, spatial resolution, and drift velocity for different applied high voltage and different threshold values were studied. Electron tracks are reconstructed by using hit information of the other layers except for the layer of interest. The hit efficiency is defined as a ratio of the number of events within 3σ of the residues to the number of reconstructed tracks. Figure 13.34 shows a hit efficiency as a function of applied high voltage. The spatial resolution are shown as a function of applied high voltage in Figure 13.35.

These prototype studies concludes that both He:i-C_4H_{10} (90:10) and He:C_2H_6 (50:50) gas mixtures satisfy our requirements on efficiency and spatial resolution. Detector responses of the CDC such as the X-T relation based on results from the beam tests and `Garfield` were modeled in our `Geant 4` simulations to study effects on the DAQ system and physics sensitivity.

Plan for future studies

We plan to carry out the following tests with the fourth (final) prototype chamber to study more detailed detector responses of the CDC.

1. Cosmic-ray tests in a magnetic field: In order to study effects of the electric field deformation in the cells from a magnetic field, the final prototype chamber will be located in a 1 T solenoid magnet at the KEK cryogenic center. The X-T relations for various z positions in the chamber are compared with the `Garfield` predictions, and tracking codes will be developed with the data.

2. Low energy proton tests: Low energy protons emitted from muon and pion capture processes enter the CDC and make a large energy deposit in the CDC cells. This might cause a cross talk among neighboring cells. This effect will be studied using a DC proton beam provided by the AVF cyclotron of RCNP, Osaka University, hopefully in this year.

3. Beam flush tests: The CDC needs to receive a high hit rate at beam prompt timing for about 200 ns. We plan to inject muon beams at the D2 beam line of the J-PARC MLF Muon facility. A 25 Hz pulsed muon beam with a 100 ns wide and intensity of about 10^6 muons/sec is available there. The CDC responses will be studied changing the intensity and momentum of the beam. Furthermore, we will try to measure the secondary particles emitted after negative muons stopped at an Aluminium target. Low energy negative pulsed muons from the D2 beam line are stopped in a Al target. The final prototype chamber will be located near the target. By adjusting a distance between the target and the prototype chamber, we will take data of different rates and reconstruct tracks of the secondary particles.

13.3. CyDet Trigger Hodoscopes (CTH)

13.3.1 Overview

The CyDet trigger hodoscopes (CTH) are placed at the upstream and downstream ends of the CDC to make the first level trigger. Figure 13.36 shows a schematic layout of the CTH in the CyDet detector. Each hodoscope consists of 64 trigger hodoscope modules. One module is made up a pair of a plastic scintillator and a Lucite Cherenkov counter, as shown in Figure 13.37.

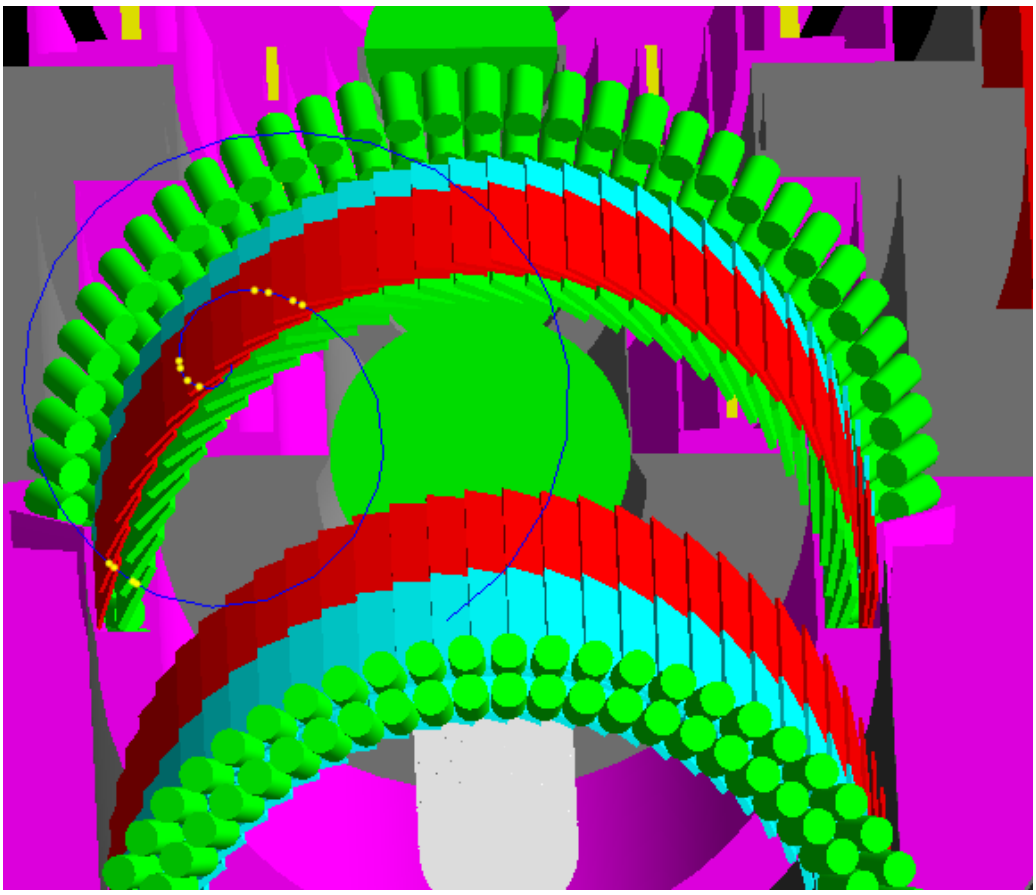

Figure 13.36: *Cutaway showing layout of the CTH in the CyDet detector. The red pannels are plastic scintillators, and the green pannels beneath the scintillators are Cherenkov counters made of lucite. An example track is also shown.*

The Cherenkov counters, together with scintillation counters, are chosen so as to identify electrons against other particles such as protons from nuclear muon capture and cosmic-ray muons. Each of the Cherenkov and scintillation counters are tilted by specific angles to the tangent of the concentric circles so that four-fold coincidence (two-fold in both Cherenkov and scintillator rings) can be made with a high acceptance for the signal electron tracks. The four-fold coincidence allows further reduction of fake triggers caused by γ-rays as shown in the right handed side in the 'pull out' cartoon in Figure 13.38, whereas a simple two-fold coincidence may not be sufficient to reduce fake trigger rates caused by energetic γ-ray conversions.

Optimization of length The length of the CTH counter has been optimized to maximize the geometrical acceptance. With the total length of the CDC fixed, a longer CTH results in the fiducial region (the central region where tracks enter the CDC) being shorter. Therefore, the CTH length has to be optimized taking this acceptance of the fiducial region into account. Figure 13.39 shows geometrical acceptances for $\mu-e$ conversion signal events, which were generated according to the simulated muon stopping distribution with electrons emitted isotropically. The blue and red points show single-turn tracks and multiple-turn tracks respectively. The sum of single- and multi-turn acceptance is shown with black points. The geometrical acceptance was evaluated by the numbers of triggered events, which are also described in Section 13.3.6. The requirements for geometrical acceptance are given in Section 20.1.1. It is concluded from Figure 13.39 that the optimal length for the CTH is 30 cm.

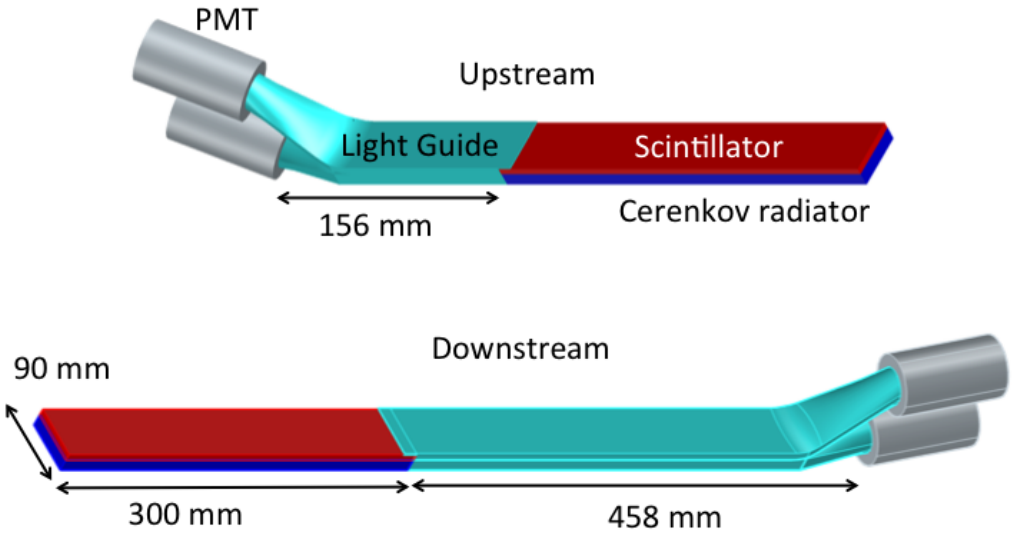

Figure 13.37: *Schematic layout of the trigger hodoscope modules for both upstream and downstream, showing one segment each of scintillator and Cherenkov radiator.*

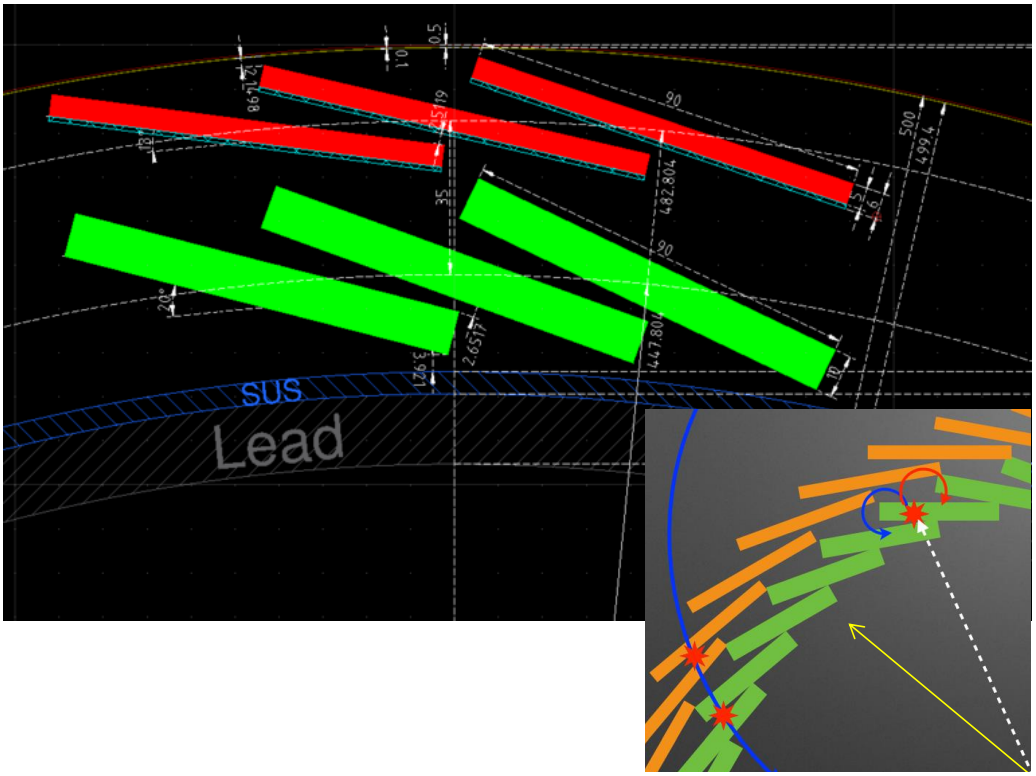

Figure 13.38: *Detailed layout of the hodoscope rings. Counters are tilted and located shifting half width so that four-fold coincidence with the neighboring counters can be required, in order to reduce accidental coincidence.*

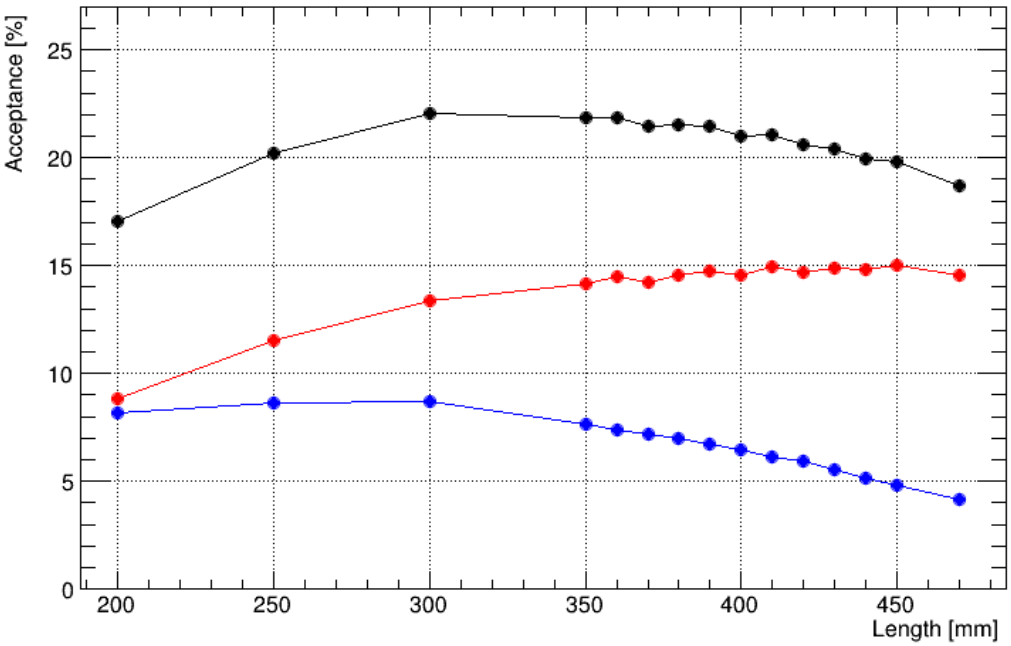

Figure 13.39: *Optimization of the CTH length. Blue, red, and black lines are for single turn tracks, multiple turn tracks, and the sum of the two, respectively.*

13.3.2 Requirements for the CTH

The requirements for the trigger hodoscopes are listed in Table 13.9. The trigger hodoscopes must be operated in a 1 T solenoidal magnetic field and in a high neutron-fluence of about 10^{11} (1 MeV-equivalent) neutrons per cm^2. To provide triggers and timing information for the track reconstruction, the signal-noise ratio S/N needs to be larger than 20, and the time resolution is required to be less than 1 ns. Despite the high magnetic field, the photosensor that best meets these requirements is a fine-mesh PMT. MPPCs and APDs were also considered. However, MPPCs would not survive the neutron irradiation and APDs would not provide a sufficiently good S/N.

Magnetic field tolerance	> 1 T
Neutron radiation tolerance	$> 10^{12}$ neutrons/cm^2
Signal-to-noise ratio	> 20
Time resolution	< 1 ns

Table 13.9: *Requirements for the trigger hodoscopes.*

13.3.3 Module design of the trigger hodoscopes

Each module has two layers: $300 \times 90 \times 5\,mm^3$ ultra-fast PVT-based scintillator (ELJEN EJ-230) [75] and $300 \times 90 \times 10\,mm^3$ UV-transparent acrylic plastic as a Cherenkov radiator to identify the electrons. The acrylic plastic and the plastic scintillator are separately wrapped with a radiant mirror film (3M Vikuiti ESR). They are also attached to light guides at the ends. A fine-mesh type photo multiplier tube (PMT), Hamamatsu H8409-70 [76], is attached to the light guide. The PMT has a small transit time spread of 0.35 ns and a high gain of $\sim 10^7$. It

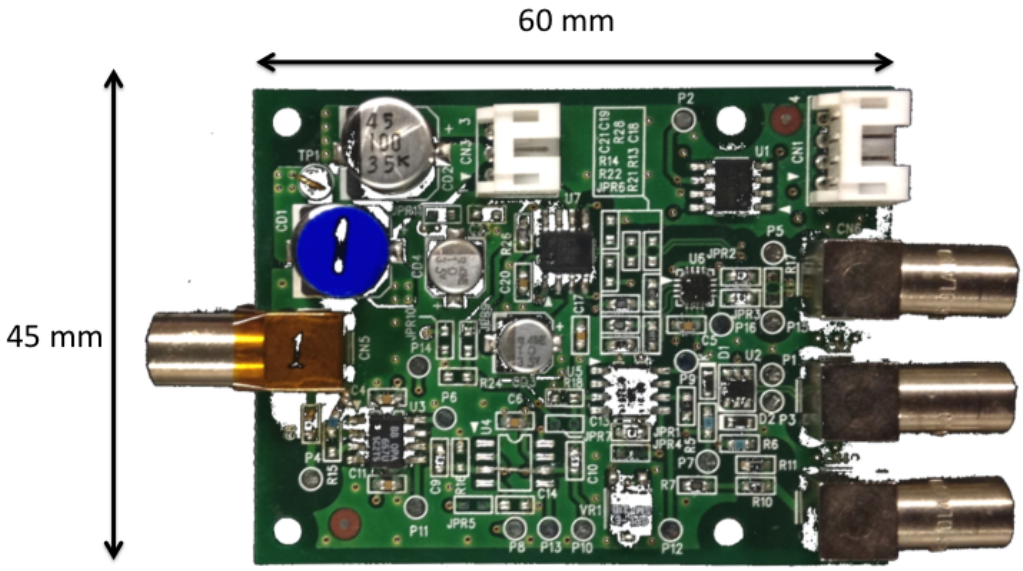

Figure 13.40: Prototype for the front-end board.

is possible to operate them in 1 T magnetic field, although their gain is somewhat reduced. To compensate for the drop in gain, signals from the PMT are amplified by a front-end board. A picture of a prototype of the front-end board is shown in Figure 13.40.

13.3.4 Support structure

A drawing of the CyDet and a schematics of the support structure of the trigger hodoscope are shown in Figs. 13.27 and 13.41. This support structure not only supports the modules but also isolates them from the helium gas that surrounds the muon stopping target. Helium gas causes degradation of PMTs due to increased after-pulsing. For this reason, the support structure is designed to be helium-tight. EVOH (ethylene vinyl alcohol) film and aluminized mylar are candidate materials for the helium barrier. In addition to the barrier, dry air will be pumped around the PMTs to flush out any helium gas. We plan to test the quality of the helium shield and the PMT degradation using a prototype of the support structure.

13.3.5 R&D Status

A beam test using 155 MeV/c electrons was carried out to evaluate detector performance without a magnetic field. The front-end boards were not yet available, therefore the signals were processed with a stand-alone waveform digitizer. Figure 13.42 shows typical waveforms measured in the beam test. The corresponding pulse height distributions are shown in Figure 13.43. As expected, the scintillator modules produce more light than the Cherenkov modules. Higher light yields are also recorded for the upstream modules, which have shorter light guides. For all four modules types, the readout met the required S/N ratio.

Figure 13.44 shows the distribution of the difference in detection time between the Cherenkov

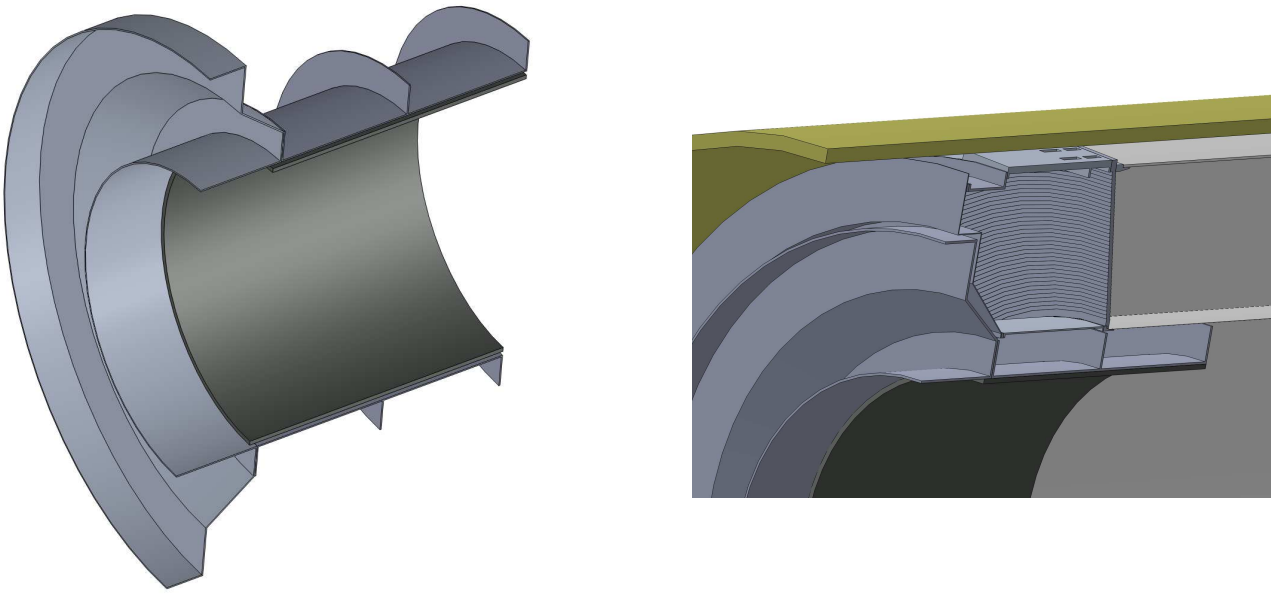

Figure 13.41: CAD image of the support structure.

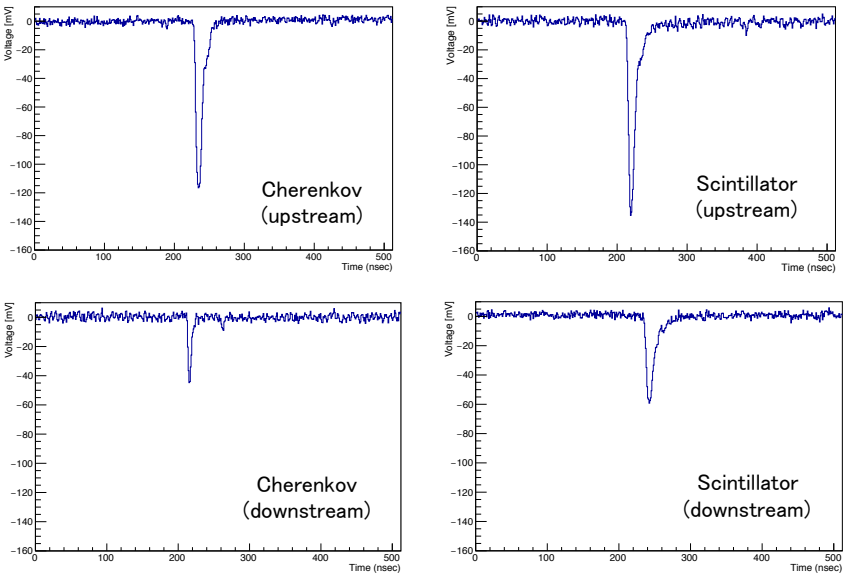

Figure 13.42: *Waveforms from the Cherenkov detector (left) and the scintillator (right).*

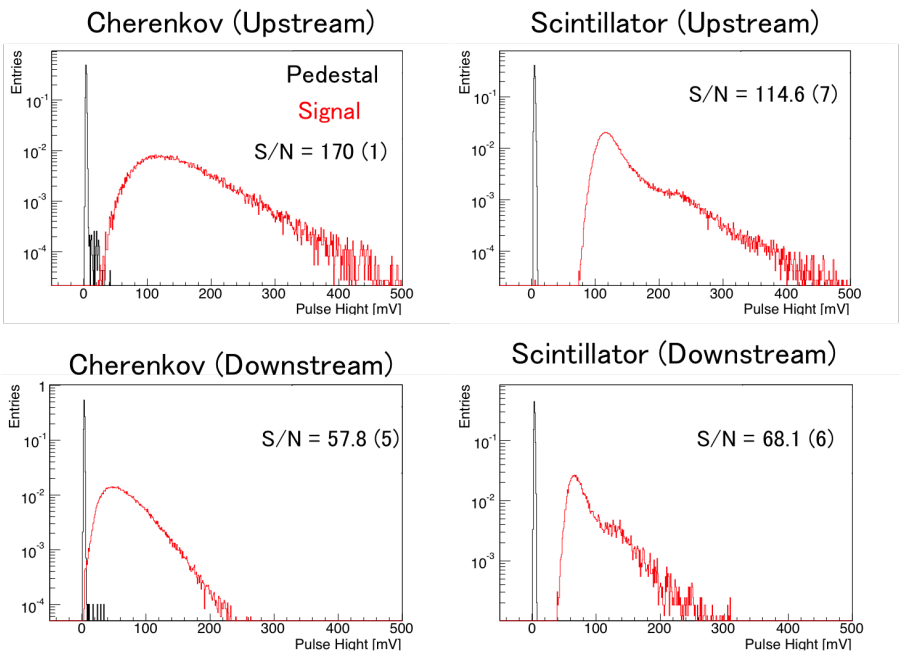

Figure 13.43: *Pulse height distributions of the Cherenkov detector, left, and the scintillator, right. Black histograms show the pedestal distribution, whilst the red histograms show the signal response. All areas are normalized to unity.*

detector and the scintillator (Both were arranged closely so that the electron beam hit both counters). From fitting the distribution, the combined ΔT resolution is measured to be 0.8 ns. The individual time resolutions, which must both be lower, therefore meet the requirement of resolution better than 1 ns.

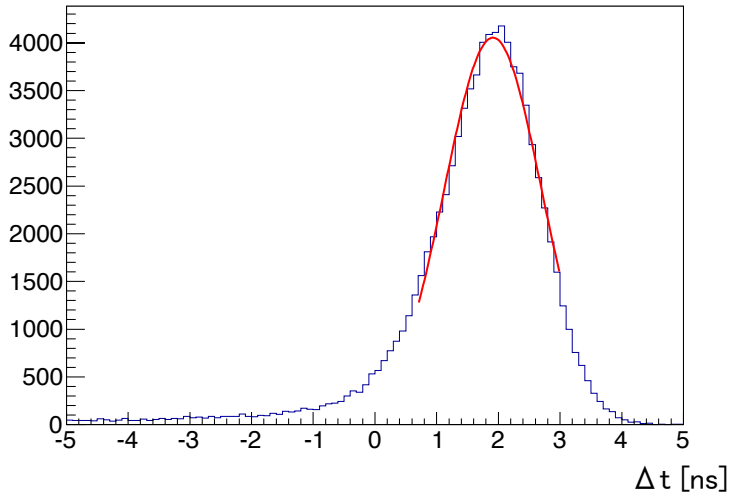

Figure 13.44: *Detection time difference between the Cherenkov detector and the scintillator.*

13.3.6 CTH trigger rates

A CyDet trigger is made by a four-fold coincidence of two adjacent CTH pairs of a scintillation counter and a Cherenkov counter. An example event is shown in Figure 13.38. The trigger rate was estimated by simulations with all possible accidental hits taken into account. The trigger coincidence window was set at 10 ns. The time window of measurement is either from 500 ns to

1170 ns or 700 ns to 1170 ns, as described in Section 20.1.4. Major background sources for fake trigger signals in the time window of measurement come from photon conversion in or near the CTH. Most photons are Bremsstrahlung from Michel electrons produced in muon decay at rest in the muon stopping target. In order to reduce fake trigger signals, it is found that additional lead (Pb) shielding of about 16 mm thick is required beneath the CTH, facing to the muon stopping target. With this lead shielding, the trigger rates of 26 kHz and 19 kHz are estimated for the time window of measurement from 500 ns and 700 ns respectively. These rates are the sum of the seperate upstream and downstream CTH rates. These trigger rates still result in a rather high data rate, dominated by backgrounds. Therefore an online trigger selection using the CDC hit information will be implemented; this is discussed further in Section 16.1.

Time window	500 – 1170 ns	700 – 1170 nsec
Trigger rate	26 kHz	19 kHz

Table 13.10: *Estimated CTH trigger rates for different time windows of measurement. These are the sum of the trigger rates from the upstream and downstream CTH.*

Table 13.11 shows different trigger configuration to compare trigger rates and acceptances. Here, the three-fold coincidences require a two-fold coincidence plus one more hit on either neighboring scintillator or Cherenkov counter. The two and three-fold coincidences produce still very high trigger rates although the later can reduce it down to 100 kHz. On the other hand, the four-fold coincidence achieves a further trigger rate reduction of $\sim 1/20$ and preserves about 71% signal electrons, compared with the two-fold coincidence. Therefore, it is concluded that the four-fold coincidence is definitely required.

trigger configuration	trigger rate [kHz]	relative acceptance
two-fold	497 ± 13	1
three-fold + scintillator	132 ± 7	0.94
three-fold + Cherenkov	97 ± 6	0.96
four-fold coincidence	19 ± 3	0.71

Table 13.11: *Comparison of the trigger rate and acceptance between four trigger configurations.*

13.3.7 CTH hit rates

The single hit rates of the CTH have been evaluated with the lead shielding of 16 mm in thickness, mentioned in the above. They are useful in order to estimate a rate capability and data rates to be transferred to DAQ. The estimation was made using a full simulation data set. During the beam prompt of about 200 nsec duration, the CTH hit rates are expected to be very high. After the beam prompt, the CTH hit rates are dominated by background products from muon decays.

Prompt hit rates Table 13.12 shows average charges deposited in each of the CTH counters, integrated during the beam prompt period of 0 to 200 nsec. The charges are normalized to the charge deposit by a minimum ionizing particle (MIP).

The effects of this beam flash in the CTH, in particular to photomultipliers, have been examined experimentally. We used an experiment setup of the CTH counter, which consists of a plastic

	upstream scintillator	upstream Cherenkov	downstream scintillator	downstream Cherenkov
Deposit charge (/MIP)	0.6	0.8	1.2	4−5

Table 13.12: *Estimated integrated charge deposit during the beam prompt (0−200 nsec).*

scintillator and a Cherenkov counter, with two LED's. One of the LEDs was used to make a beam flash pulse, and the second one was used to make signal events in a delayed time window of measurement. In this test, we prepared three signal pulses from the second LED so as to simulate a realistic situation (given in the next paragraph). The light yield of the second LED was adjusted so that it corresponds to the light yield of one MIP. By changing the light amplitude of the first LED, the gain drop of the following pulses from PMTs was measured. From the test, it has been found that the degradation of gains of the CTH scintillator counter and of the CTH Cherenkov counter start for the amount of beam flash of more than 25 MIPs and 120 MIPs respectively. The test results are summarized in Figure 13.45. From the simulations, the average beam flashes for the CTH scintillator counter and of the CTH Cherenkov counter are less than these limits of gain degradation, and it is concluded that the effect of beam flash will not cause any loss of the measurement of signal electrons.

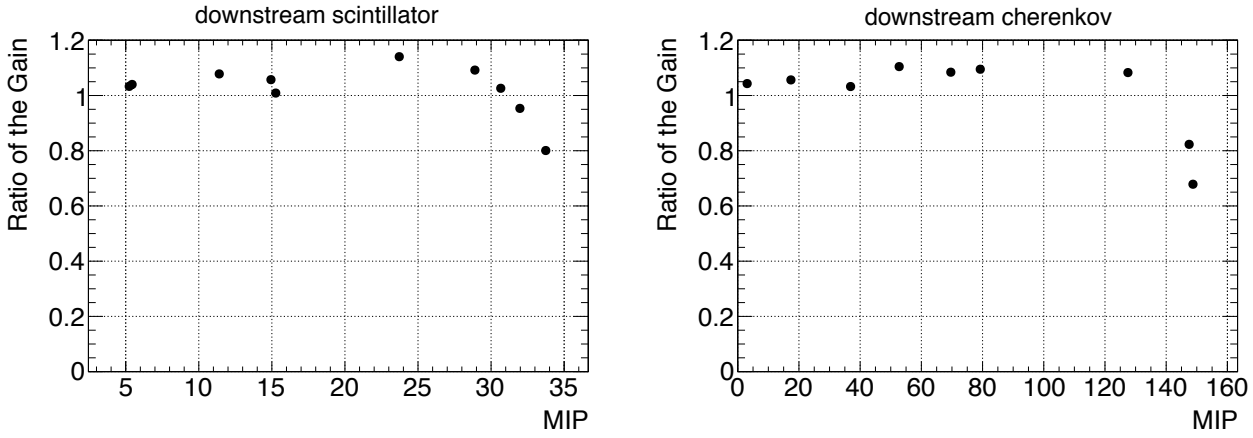

Figure 13.45: *Gain drop of the CTH scintillator counter (left) and CTH Cherenkov counter (right), measured by the second LED pulses, as a function of the pulse height of the first LED to simulate different amplitude of a beam flash. The gain drops of the CTH plastic scintillator and CTH Cherenkov counter start from 25 MIPs and 120 MIPs equivalent respectively.*

Hit rates after beam prompt The instantaneous rates after the beam prompt are estimated for each counter of the upstream CTH and downstream CTH separately as shown in Table 13.13. It is noted that they are average instantaneous rates during the time period.

	upstream scintillator	upstream Cherenkov	downstream scintillator	downstream Cherenkov
Average rate (MHz)	3.5	$1.5 - 2$	4	3

Table 13.13: *Average instantaneous hit rates during the time period after the beam prompt of 200 nsec to 1170 nsec.*

13.4. CyDet Performance

13.4.1 CDC Hit Rates

The CDC hit rates have been studied with `GEANT 4` simulations. Potential sources causing noise hits are grouped into three categories:

- muons and pions at the muon stopping target and its vicinity, which create secondary (or tertiary) particles coming to the CDC,
- a prompt beam flash, and
- neutrons which are either in a beam or from the proton target or a proton dump.

The first group includes electrons from muon decays in orbit (DIO), and protons, deuterons and other light nuclei emitted from nuclear muon and pion capture, and Bremsstrahlung photons from DIO electrons and others. Bremsstrahlung photons generate electrons (and positrons) by Compton scattering or photon conversion at the CDC inner wall, endplates, field and sense wires, and gas. The particles from a stopped muon have a time distribution following a lifetime of a muonic atom. The second group includes all charged particles (muons, pions, electrons) and γ rays associated with a beam flash. These contributions occur at a beam prompt timing. The third includes secondary and tertiary particles from neutron interaction. In the following, each of the contributions is described in details.

Hit rate contribution from stopped muons and pions The contribution of DIO electrons from stopped muons are estimated. The hit rates of each CDC cell at different layers are shown in Figure 13.46. The contribution to the rate decreases quickly at deeper CDC layers, since the DIO momentum spectrum drops as a function of an electron momentum, as shown in Figure 13.46. From Figure 13.46, the time-averaged rate for the innermost sense wire (layer ID=2) of at most 4 kHz/cell is obtained, yielding the instantaneous rate of about 12.5 kHz /cell by taking care of a duty factor of the J-PARC MR proton beam cycle. It implies the hit occupancy for one bunch cycle of 1.17 μsec is about about 1.5 %.

The contributions of proton emission from muon capture is studied. The emission rate of protons from nuclear muon capture on aluminium, which was measured by the AlCap experiment at PSI, was used. As described in Section 22.4., the time-averaged hit rate on a single cell is estimated to be 1.4 kHz. The detailed description should be referred to Section 22.4.

Other than the DIO electrons and protons from nuclear muon capture, several other sources such as Bremsstrahlung photons, muonic X-rays, neutrons from nuclear muon capture, γ-rays from the final state nucleus after nuclear muon capture and so on, were considered. The energies of muonic x-rays are several hundred keV, and Compton scattering produces low-energy electrons in the CDC. Neutrons are also emitted from nuclear muon capture. For the case of aluminum, an average rate of about 1.26 neutrons per muon capture is expected. The

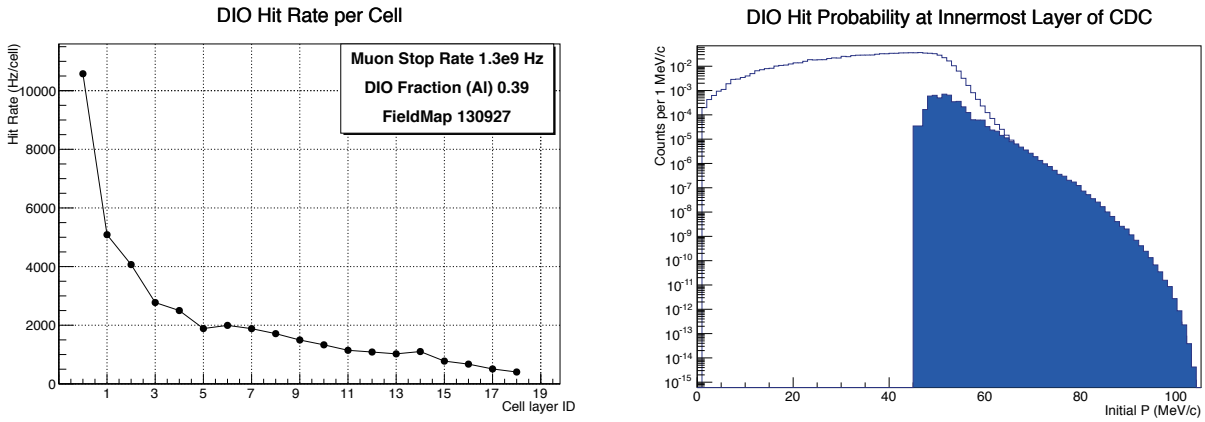

Figure 13.46: *(Left) DIO electron hit rate for each CDC cell layer, and (Right) Momentum distribution of the DIO electrons. The blue histogram shows those of electron hits the CDC.*

neutron energy spectrum was measured but the interpretation is very difficult. In this study we use the `QGSP_BERT_HP` physics model in `Geant4` to generate neutrons after muon capture.

The magenta points and lines in Figure 13.50 summarize the CDC occupancy caused by stopped muons. All the processes mentioned above have been considered. As a result, the total occupancy is about 7% to 10%, depending on different layers.

Hit rate contribution from stopped pions also has been studied, and the occupancy caused by stopped pions is summarized with the cyan points and lines in Figure 13.50. Their contribution is vary small compared to the other categories.

Hit rate contribution from beam flash The contributions to hit rates from beam flash, such as pions, muons, electrons, neutrons and photons in a beam are studied. beam flash occur at a prompt timing of the beam. However, the CDC hits associated with a beam flash come with an additional drift time after the prompt. The distribution of drift times could be different for different gas mixtures, as described in Section 13.2.2. In fact, the drift time distributions were measured by using the prototype IV at SPring-8 for different gas mixtures of He:i-C_4H_{10}

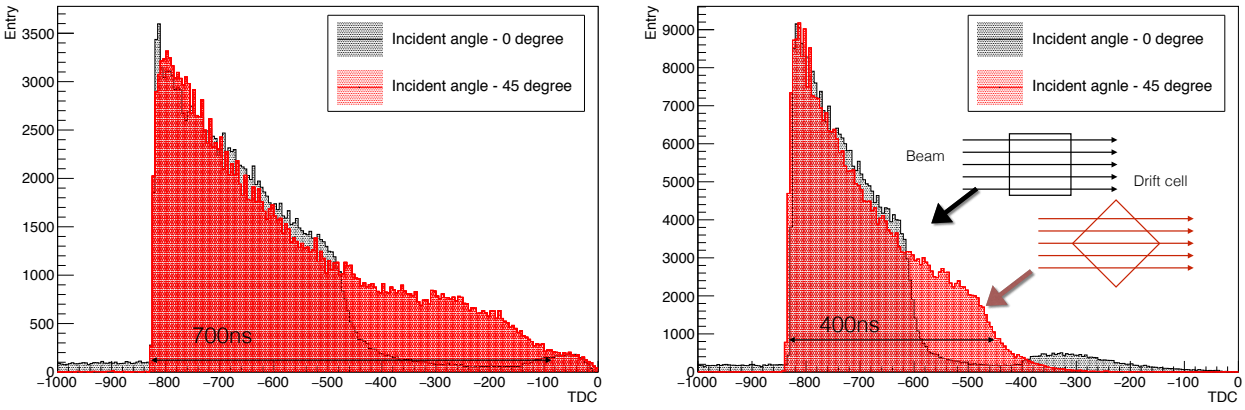

Figure 13.47: *Distributions of a drift time for gas mixtures of He:i-C_4H_{10} (90:10) and He:C_2H_6 (50:50). The former has a maximum drift time of about 700 nsec and the latter has that of about 400 nsec.*

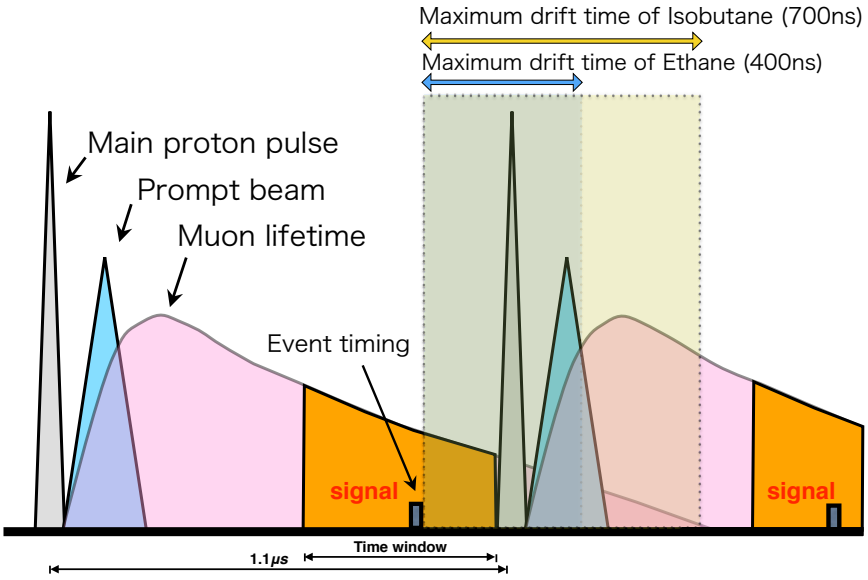

Figure 13.48: *Relation between beam prompt, event timing in the time window of measurement, drift time of hits in a time period of two beam cycles.*

(90:10) and He:C_2H_6 (50:50) and they are shown in Figure 13.47. From this, it is known that the maximum drift time comes from hits in the corner of the cell. The maximum drift times, which is contributed from the hits in the cell corners, are 700 nsec and 400 nsec for He:i-C_4H_{10} (90:10) and He:C_2H_6 (50:50) respectively. Figure 13.48 shows the relation between beam prompts, event timing in the time window of measurement, and drift time of hits. For the case of He:i-C_4H_{10} (90:10) where the maximum drift time is 700 nsec, the following beam prompt might come within the drift time of 700 nsec. Therefore beam flash cannot be avoidable in the drift time window. The CyDet detector should be tolerable to beam flash. Major sources in beam flash to create noise hits in the CDC are photon and neutron interaction. They strongly depends on the muon beam design, in particular the muon beam collimation. Furthermore, radiation shielding to prevent photons hitting the CDC (in particular the endplates) would be effective. The total contribution from beam flash will lead to around 4% occupancy as shown in Figure 13.50. It turns out the current design of the beam line and shielding would be sufficient to reduce the effect of beam flash to the CyDet. In Figs. 13.51 and 13.52, sample event displays with beam flash are shown. The events in Figs. 13.51 and 13.52 occur at 1090 nsec and 784 nsec after the beam prompt, and therefore their time periods to open hits cover the following beam prompt. As can be seen in Figure 13.51 and 13.52, it can be seen that noise hit rates are not too large.

Hit rate contribution from room and beam Neutrons Room neutrons are thermal in energy, and beam neutrons are fast in energy. Capturing thermal neutrons produces low energy photons, which pair-produce an electron and a positron. This capture happens at the endplates, the inner wall, and the outer wall. They are simulated with both `PHITS` and `GEANT`. According to the design with Paraffin shields installed along beam line, hit rate induced by room and beam neutrons can be very small.

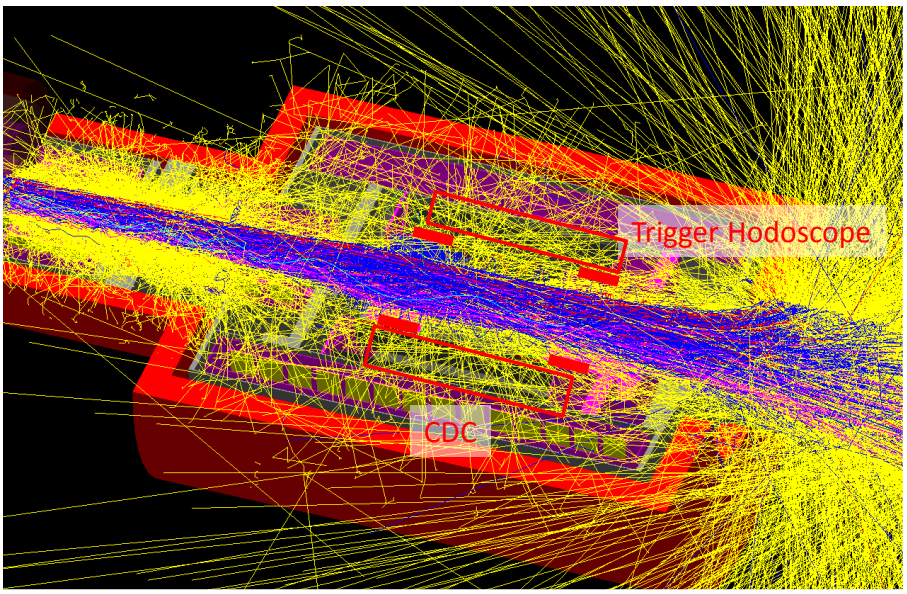

Figure 13.49: *Simulated event displays for beam flash, where yellow lines are photons which might create pairs of electrons and positrons.*

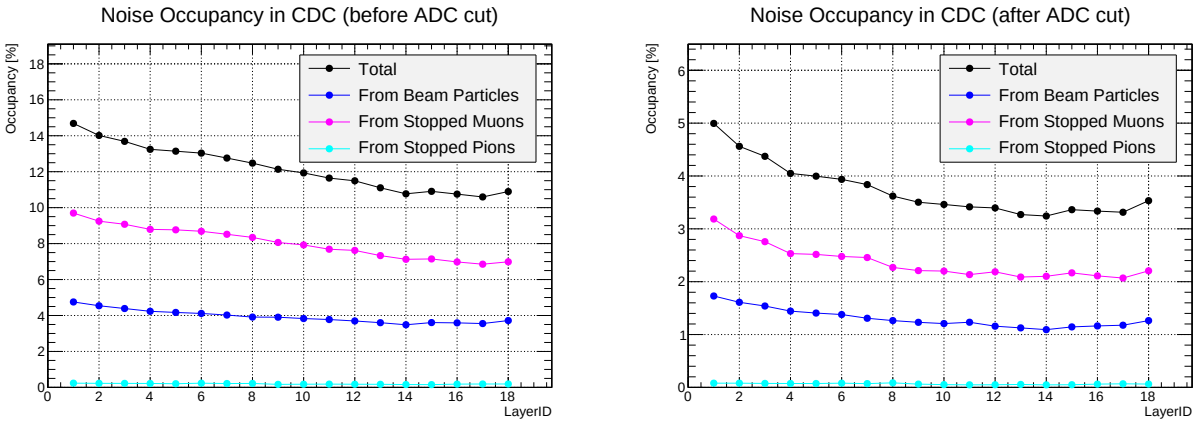

Figure 13.50: *CDC single hit occupancy as a function of the CDC layers for a gas mixture of He:i-C_4H_{10} (90:10). The left and right figures are respectively those before the energy deposit cut and after the cut, which selects hits with energy deposit smaller than 5 keV. The closed circles filled with blue, magenta, cyan, and black are respectively from beam particles, stopped muons, stopped pions, and total occupancy.*

Net Single Hit Rates Figure 13.50(Left) shows the net single hit occupancy before the energy deposit cut for a gas mixture of He:i-C_4H_{10} (90:10). It includes hits from beam flash (blue closed circles), stopped muons (magenta closed circles), and stopped pions (cyan closed circles). The sum is shown using the black closed circles. An average rate of about 12% occupancy for a gas mixture of He:i-C_4H_{10} (90:10) is obtained with a duty factor of the accelerator cycle included. There is no significant layer dependency.

Some examples of event display in the CDC are simulated. Different gas mixtures with different radiation lengths are checked since noise hits caused by γ-rays. Simulated event displays for different gas mixtures of He:i-C_4H_{10} (90:10) and He:C_2H_6 (50:50) in Figs. 13.51 and 13.52, respectively. In Figs. 13.51 and 13.52, hits in red, green, cyan, magenta and blue are respectively from signal tracks, DIO tracks, proton/ion tracks from pion capture, proton/ion tracks from

muon capture, and other noise hits. The hits in open circles and closed circles are respectively those with energy greater and smaller than 5 keV. It is noted that the former has a radiation length of 1310 m, while the latter has a shorter radiation length of 630 m. From this point of view, the gas mixture of He:i-C_4H_{10} (90:10) could be better.

13.4.2 Charge Measurement

Most noise hits are either associated with low energy electrons or positrons created by photon conversion, electrons from DIO decays of muons, and protons created from nuclear muon capture. For the low energy electrons or positrons, their typical energies are a few MeV and their helical trajectories have a very small radius. As a result, they are likely to stay in the same CDC cell for a long time. In some cases, they are created at one of the endplates, travel along the CDC, and reach the other endplate. Therefore it is expected that many of these noise hits will have a *large* charge in the hit cell. Protons, by virtue of being heavily ionizing, also tend to deposit a lot of energy in a CDC cell.

The CDC readout system is capable of measuring total charges with 33 MHz sampling. Figure. 13.53 shows the total energy deposit for electron signals of $\mu-e$ conversion and noise hits. From that plot we can see that about 68% of the noise hits can be identified and removed by only retaining hits with an energy deposit smaller than 5 keV, while 99% of the signal hits can pass this selection. Figure 13.50(Right) shows the hit occupancy after this selection. The original hit occupancy of 12% would be reduced to about 3.5% by the selection. This high-charge cut is carried out in the RECBE firmware as described in Section 13.2.5. Because of its simplicity a cut of this kind could be useful to the online system, both for deciding what to readout and as input to a trigger system. This is discussed further in Chapter 16. The event display in Figure 13.54 shows the benefit even more clearly.

13.4.3 Ageing Effects

The deterioration by ageing is a function of lifetime-integrated charges on the sense and field wires. One of the potential issues regarding the CDC is that the CDC hit rate is quite high and the these hits are expected to include many protons from nuclear muon capture. These protons leave a localised energy deposit about 100 times larger than minimum ionization particles.

Figure 13.55 shows results of a test of gain degradation due to ageing effects performed by the KEK-Belle group. They used a gas mixture of He:C_2H_6 (50:50) and X-rays to irradiate the chamber. The test indicates material selection for the gas system is important to reduce the ageing effect. Using stainless steel (SUS) pipes and an O_2 filter, the gain reduction could be kept below 1% even at a total accumulated charge on the sense wire of 153 mC/cm.

Detailed simulations have been made to estimate the integrated charges on the CDC. To do this, the rate and spectrum of proton emission after muon nuclear capture was added to the `Geant4` physics lists, based on the measurements discussed in Section 22.4.. Contributions to the total charge from noise hits, which are discussed in Section 22.4., are also taken into account. Figure 13.56 shows the estimated integrated charge (mC/cm/day) for each CDC layer.

It is found that a CDC inner wall of 0.5 mm thickness is sufficient to reduce the number of charged particles (in particular, protons) entering the CDC to tolerable levels. With a running period of O(100) days, the expected total integrated charges is much less than 200 mC/cm, which is the maximum acceptable value according to the Belle group's studies of ageing effects.

It is noted that the proton emission rate after nuclear muon capture was originally expected

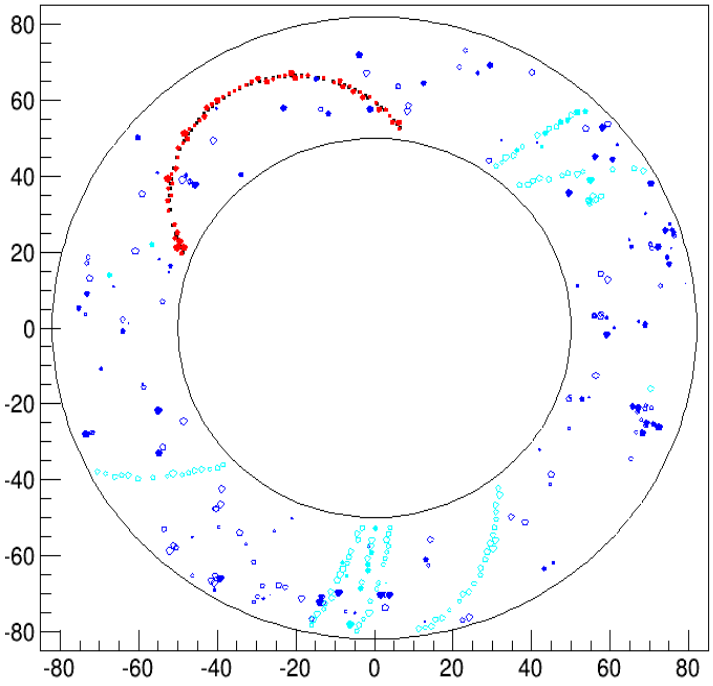

Figure 13.51: *Simulated CDC event display for a gas mixture of He:i-C_4H_{10} (90:10). This event occurs 1090 nsec after the beam prompt. Hits in red, green, cyan, magenta and blue are respectively from signal tracks, DIO tracks, proton/ion tracks from pion capture, proton/ion tracks from muon capture, and other noise hits. The hits in open circles and closed circles are respectively those with energy greater and smaller than 5 keV.*

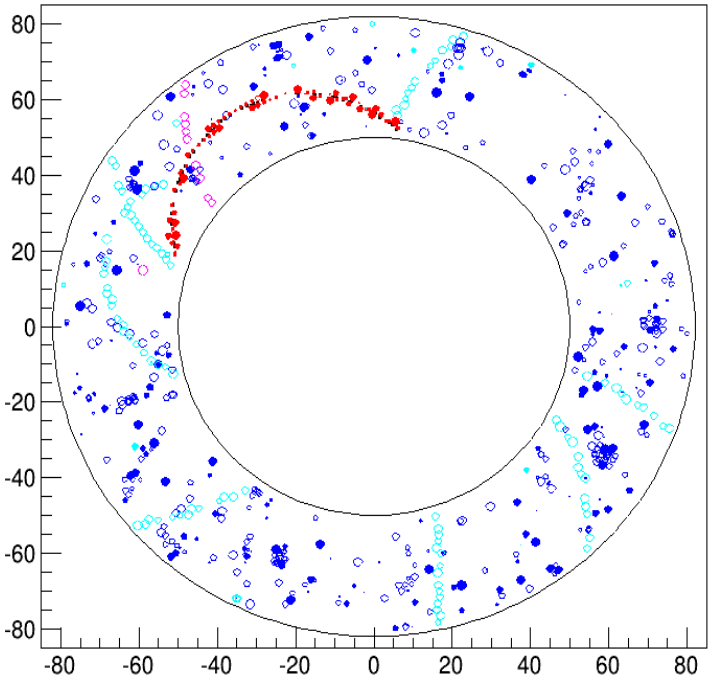

Figure 13.52: *Simulated CDC event display for a gas mixture of He:C_2H_6 (50:50). This event occurs 784 nsec after the beam prompt. Hits in red, green, cyan, magenta and blue are respectively from signal tracks, DIO tracks, proton/ion tracks from pion capture, proton/ion tracks from muon capture, and other noise hits. The hits in open circles and closed circles are respectively those with energy greater and smaller than 5 keV.*

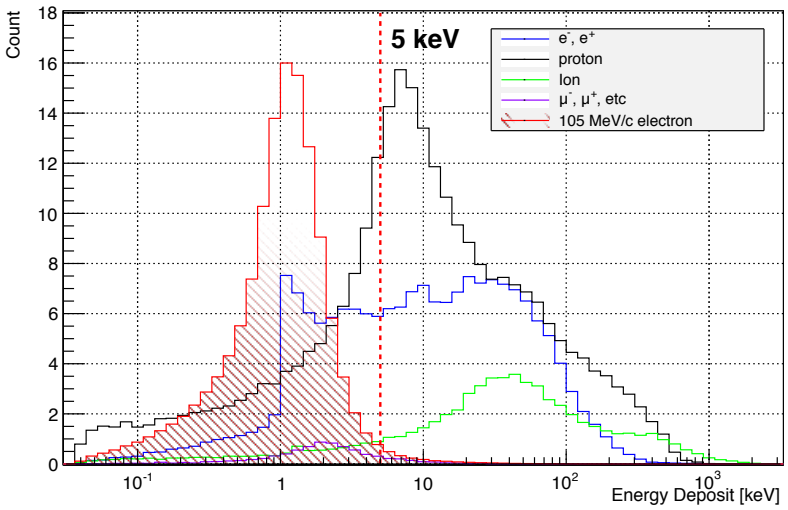

Figure 13.53: *Total energy deposits per cell for signal electrons and noise hits. The signal electrons are shown in the red shaded histogram; noise hits from various sources are shown in other histograms. A 5 keV threshold line (as used in the event displays) is also shown.*

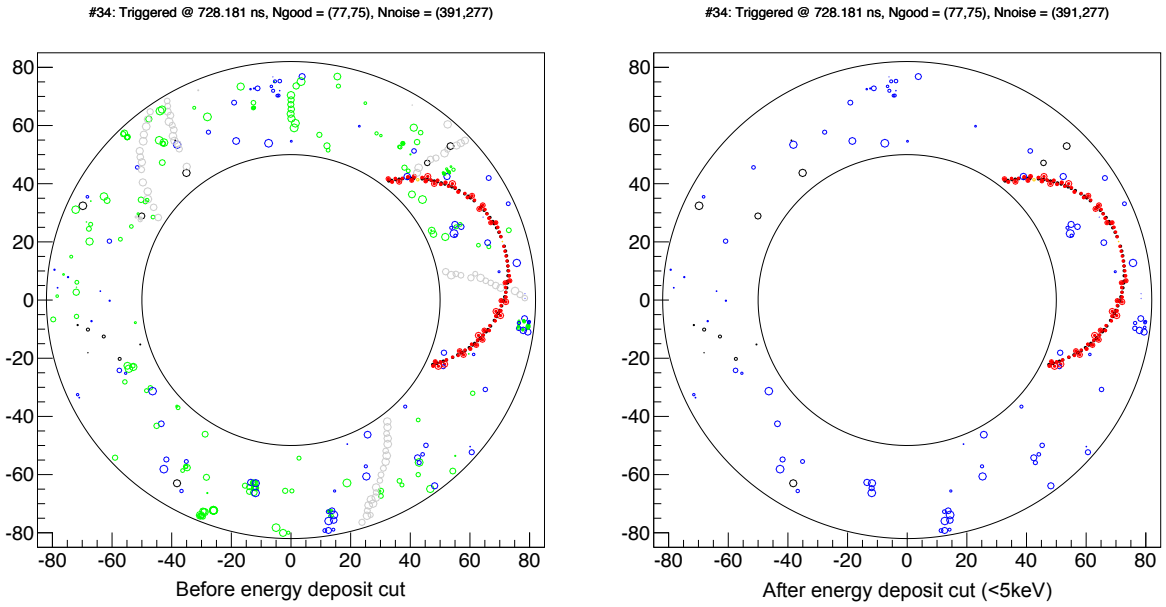

Figure 13.54: *Typical event displays (from simulation) for He:i-C_4H_{10} (90:10). The left figure is an original event display before the energy deposit cut, while right figure just shows hits that passed the energy deposit cut (i.e. cells which have an energy deposit smaller than 5keV). Here circles with different colors represent different types of hits: red for signal hits, blue for noise hits that passed the energy deposit cut, green for noise hits that didn't pass the energy deposit cut, black for proton hits that passed the energy deposit cut and gray for proton hits that did not pass the energy deposit cut.*

to be substantially higher and therefore a thicker CDC inner wall (or placing an additional proton absorber) was seriously considered. However the AlCap measurements, described in Section 22.4., show that the proton emission rate is rather lower than assumed. Because of the smaller proton emission rate, a CDC inner wall of 0.5 mm thickness turns out to be sufficient to

keep the ageing effect low. A thinner wall is desirable as energy loss in the wall would degrade the momentum resolution.

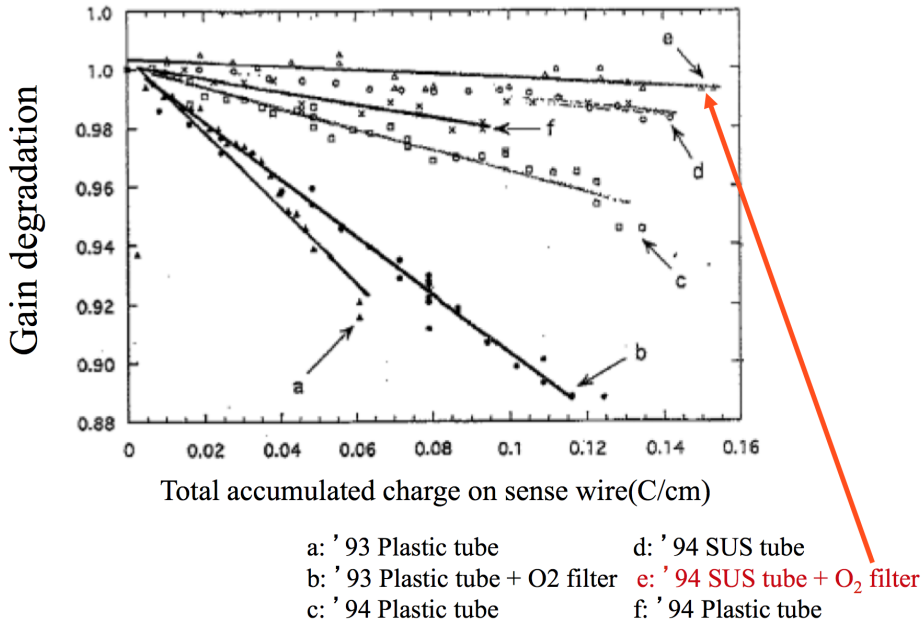

Figure 13.55: *Results of ageing tests performed by the KEK-Belle group [77]. A gas mixture of He:C_2H_6(50:50) was used in these tests. The chamber was irradiated using X-rays. The condition "e", which use a gas system with stainless steel (SUS) pipes and O_2 filter, resulted in a gain degradation of about 0.993 at a total accumulated charge on the sense wire of 153 mC/cm.*

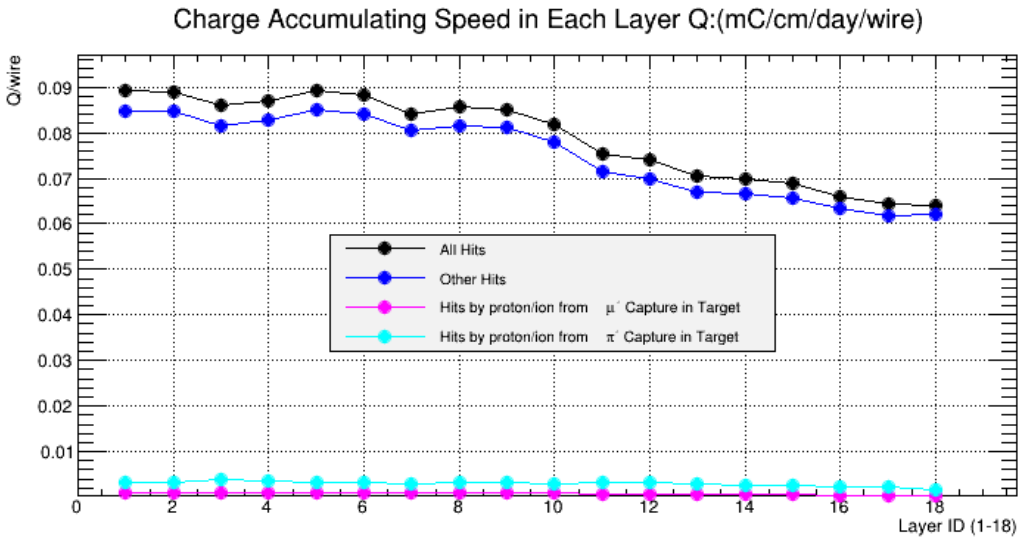

Figure 13.56: *Estimated integrated charge (mC/cm/day) for each CDC layer. The contributions of protons and other particles from muon capture (magenta), those from pion capture (cyan), others (blue) and the total (black) are given.*

Ageing Test

A preliminary ageing test was performed in July 2014 at Osaka University. A test chamber for testing the ageing effect was produced with Au-W sense wires of $\phi 25$ μm and Al field wires of $\phi 80$ μm. The drawing of the test chamber is shown in Figure 13.57. The central sense wire is a

wire to be tested for the ageing effect. There are two holes on each of the sides, the front back sides, to irradiate X-rays with a ^{55}Fe source. The hole named "Side A" is used to give charges with two ^{90}Sr sources, and "Side B" is used for reference as a not-aged sample wire.

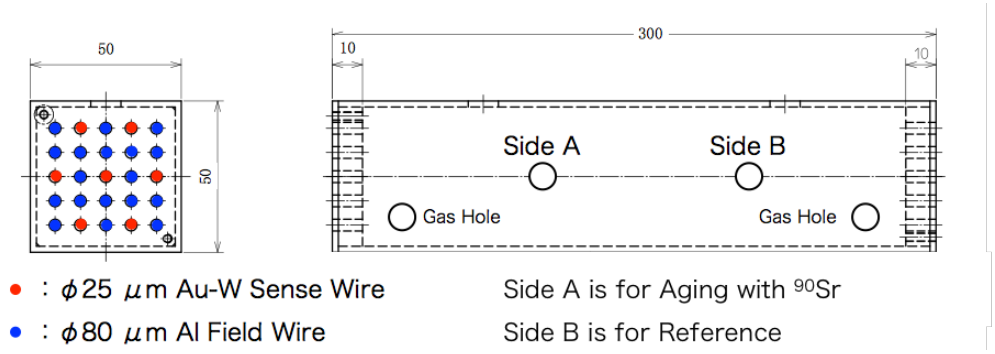

Figure 13.57: *Drawing of the test chamber for the ageing test. There are 25 wires including 7 sense wires. The central wire is used for a wire to be tested and evaluated for the ageing effect. There are 3 × 2 holes to expose the wires by radiation sources, and 2 gas ports to flush the mixed gas.*

Figure 13.58 shows the experimental set-up. The gas mixture was He:i-C_4H_{10} (90:10) controlled with two area flow meters, and the flow rate was set to 20 cc/min in total: 18 cc/min and 2 cc/min for He and i-C_4H_{10} respectively. All gas pipe lines consist of metal(SUS) tubes, and there is no filter. Before filling the mixed gas, the gas pipe lines and chamber were flushed with a large amount of nitrogen gas to suppress the effect of outgassing from the system. The central sense wire (test wire) and surrounding 6 sense wires were connected to different channels of the HV module to monitor the current of the test wire. The HV was supplied by a CAEN N1471ET module, which can be remotely controlled and monitored via an Ethernet port. To accelerate the ageing (charge accumulation), the applied HV value of the test wire was set to 2600 V when the wire is exposed to ^{90}Sr sources, and a HV of 1500 V was applied to the other 6 wires. In this condition, we obtained an electric current of $\sim 6.5\ \mu A$ on the test wire. On every 30 minutes of exposing to two ^{90}Sr sources, the ^{90}Sr sources were replaced by a ^{55}Fe source for the gain measurement with 5.9 keV X-rays. The gain was measured with an ADC module of LeCroy 2249W by subtracting the pedestal value taken for each measurement. During the gain measurement, the HV value was set down to 1800 V.

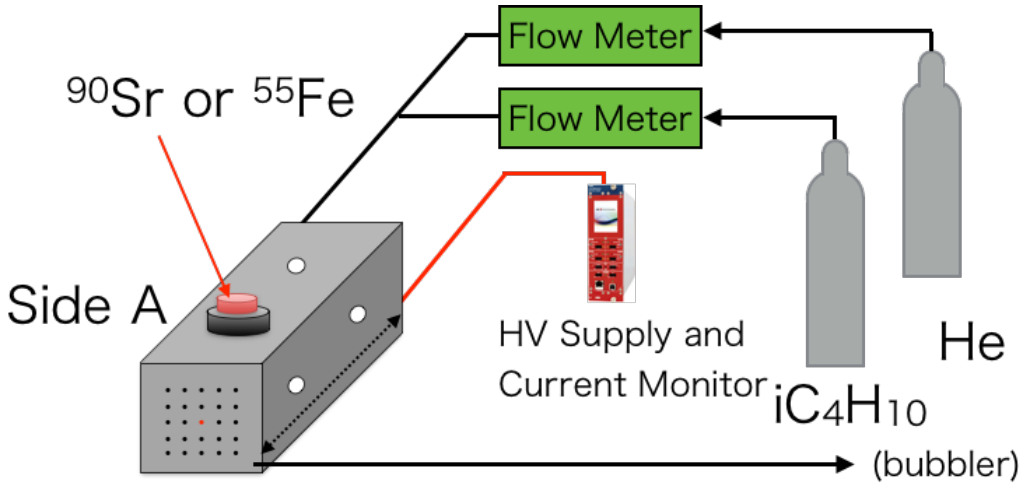

Figure 13.58: *The set-up of the ageing test in Osaka University. All gas pipe lines are made of metal tubes, and gas flow rates are controlled with area flow meters. The HV module is CAEN N1471ET to apply HV and monitor the electric current on the wires.*

After the measumrent of $\sim$ 21 hours, an accumulated charge reached about 47 mC/cm. A ratio of the ADC values of "Side A" against "Side B" is shown in Figure 13.59. The black points indicate the results of the gain measurement with only statistics uncertainties, and the red line is a fitted function with the points and fixed offset (= 1.0). The systematic uncertainty is not considered here. The best fit value of the gradient is -0.0013, corresponding to the gain drop of 0.13 %/mC/cm. The temperature, humidity and atmospheric pressure were recorded in the experimental room during the measurement, and there was no significant changes observed.

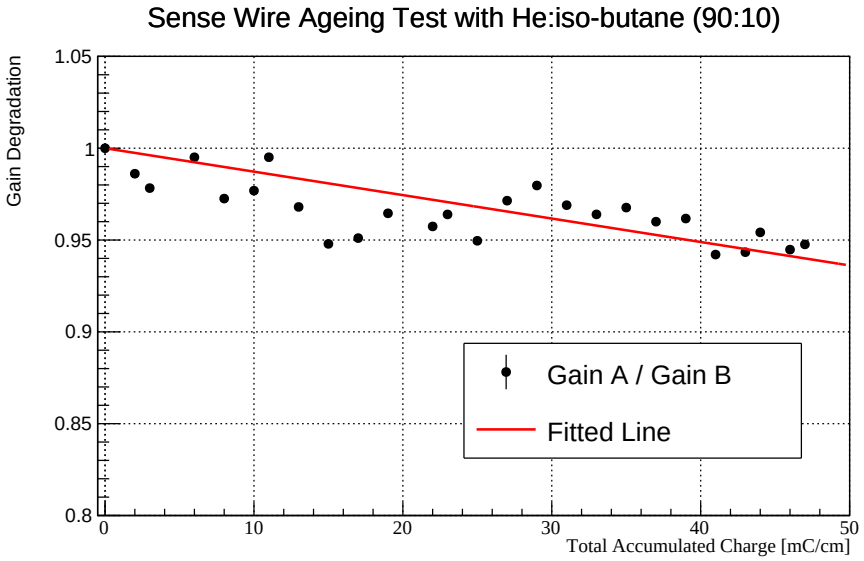

Figure 13.59: *The first result of ageing test with He:i-C_4H_{10} (90:10). The black points indicate the gain drop as ratio of the measured gain against the gain not-aged area (Side B). The red line shows the fitted result with the data. The best fit value of the gradient is* -0.00132*, corresponding to the gain drop of 0.13%/mC/cm.*

According to the study of accumulated charges on the wires (Figure 13.56), it should be 0.09 mC/cm/day/wire at most (in the inner-most layer). By considering our running period in Phase-I (O(100) days), the accumulated charge should be less than 2 mC/cm/wire. The estimated gain drop at the end of COMET Phase-I is only 0.3%. It is sufficiently small. Even if the gain drop is 10 times worse, it can be recovered and corrected offline. The measurement was, however, performed only at a specific condition. Therefore, we plan to perform further ageing tests with different conditions.

Prospects for further ageing tests

The preliminary ageing test was made, but we might continue further studies, since it was made with one cell prototype chamber, being different from the real situation. For example, the test chamber has only one cell. Therefore, the surrounding wires were used as guard wires with a lower HV, and the electric field is slightly different from the real CDC. Also, the diameter of Al field wire ($\phi 80\ \mu m$) is different from that of the real CDC ($\phi 126\ \mu m$). The preliminary test was performed with a short time. Also the HV value was higher than the usual operation value to accelerate the ageing. In addition, there was no oxygen filter and monitor for the water concentration level in the chamber gas. The ratio of the flow rate and the chamber volume was much different from the real condition.

We plan to perform further ageing tests with the following conditions to confirm the aging effect in more realistic conditions;

- by using the 9-cell chamber with same wires as those in the real CDC,
- by changing various HV values,
- by changing various gas flow rates, and
- with an oxygne filter and/or a water level monitor.

13.5. CyDet Track Reconstruction

The CDC track reconstruction consists of track finding process followed by track fitting process. The former does selection of good hits in order to identify track-like structures and eliminate background noise, whereas the latter does track fitting with Kalman filtering to determine which hits are most probably part of the track, whether a single continuous track is a good interpretation of the hit pattern, and (assuming it is) thereby find the best estimate of the momentum of the charged particle that made the track. In the fitting process it will be necessary to consider both single-turn and multiple-turn tracks.

13.5.1 Track Finding

The CyDet offline track finding algorithm outlined in this section filters out background hits using three main stages. First, it uses a Gradient Boosted Decision Tree (GBDT) to classify the hit as signal or background based on the properties of the hit itself, i.e. "local features", and the properties of neighbouring hits, i.e. "neighbour features". It then performs a circular Hough transform on the output of this GBDT, reweights the result, and inverts the transform to recover information about which hits form a circular path with signal-like hits. Next, a new GBDT uses this information, the local features, and the neighbour features to classify hits as signal or background. The output at this hit-filtering level suppresses nearly 98% of background hits while keeping 99% of signal hits.

This work has been completed in collaboration with the Yandex School of Data Analysis[1], namely with Alex Rogozhnikov. The analyses uses the `scikit-learn` [78] package in Python 2.7.

Machine Learning in CyDet Tracking

The CyDet is designed to operate in a high intensity environment. By design, the CDC is able to reduce the amount of noise hits using a cut on the energy deposited in each hit, as discussed in Section 13.4.2. This reduction can be greatly improved by using other features of the hit, such as timing of the hit and the radial distance of the hit from the target, in a machine learning algorithm.

Boosted Decision Trees Boosted Decision Tree (BDT) methods utilise a binary tree structure, as shown in Figure 13.60. The classifier starts with all hits in one sample or "root" node. It determines which feature will provide the best separation between background and signal, and scans this feature for the optimal cut value. The sample is then split on the basis of

[1]Yandex is the leading search engine in Russia, and have lent their expertise in machine learning to this study.

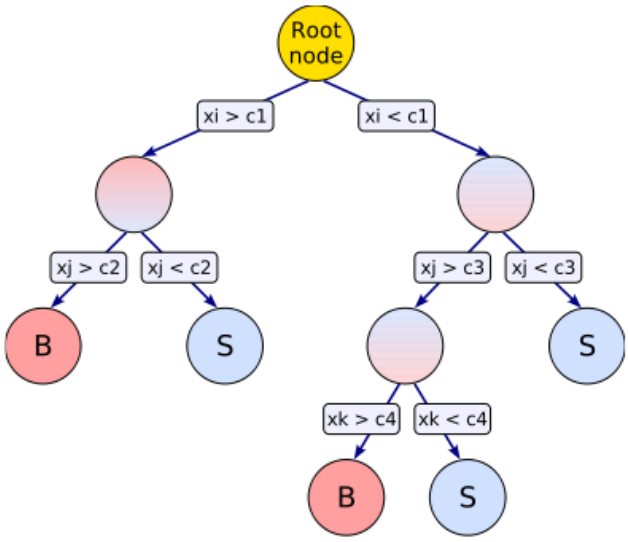

Figure 13.60: A decision tree, where the features are labelled as $\{x_i, x_j, x_k\}$. The first cut is on x_i at value $x_i = c_1$. This cut creates two daughter nodes, the first of which is cut at $x_j = c_2$, while the second is cut on $x_j = c_3$. This process is continued until some stopping criteria is reached. The leaf nodes are labelled as background, B, or signal, S.

this cut, after which the process of selecting the optimal feature and value is repeated on the resulting "daughter" nodes. The process is iterated until some stopping criteria is satisfied. The stopping criteria used in the tracking algorithm is that a decision tree can only be three nodes deep. The final nodes are referred to as the leaf nodes. During training, each leaf node is classified as background or signal depending whether it contains more background or signal hits. The testing sample is then run through the same decision tree, where each hit is classified as signal or background by which leaf node it ends up in. This process defines a single decision tree, which are not nearly as powerful as ensembles of decision trees.

Gradient Boosting is a technique that combines the result of an ensemble of weak decision-tree classifiers into one far stronger classifier. Each individual tree will assign each event as signal or background, hence for a hit with a vector of features $\mathbf{f}$, we define the result of a classifier as $h_i(\mathbf{f}, a_i) = +1$ or -1, respectively[2]. The output of the each classifier h_i is then individually reweighted by parameter b_i. Their outputs are then summed, yielding the combined classification result, $y_{\text{Grad.}}$:

$$y_{\text{Grad}}(\mathbf{f}, \mathbf{a}, \mathbf{b}) = \sum_{i=0}^{N_{\text{trees}}} b_i h_i(\mathbf{f}, a_i). \tag{13.1}$$

From here, the loss-function is defined, which is built to quantify the inaccuracy of the classifier on the training sample. The one used currently in this study is the deviance of the classification, $F(y_{\text{Grad}}, y)$:

$$F(y_{\text{Grad}}, y) = -2\left[y \cdot y_{\text{Grad}} - \ln\left(1 + e^{y_{\text{Grad}}}\right)\right] \tag{13.2}$$

Minimising this function with respect to the parameters $(\mathbf{a}, \mathbf{b})$ fully determines the GBDT. This is achieved using a steepest-descent approach. The current gradient of the loss function with respect to the full set of parameters is calculated and used to determine the direction

[2]Note that each decision tree has been allowed to be be independently parameterised by a_i. This is an extra degree of freedom not utilised in this study, but available to gradient boosted techniques in general.

in parameter space that minimises the loss. The parameters are updated in this direction. This is repeated until a minimum is reached. For more details on the GBDT in used from `scikit-learn`, see Section 4.5 in [79], which details the relevant L_k_TreeBoost algorithm.

The CyDet Tracking Finding Algorithm

The primary functionality of track finding is to remove the noise hits, and pass the results to the track fitting algorithm. The algorithm described uses simulation data generated using GEANT4 and ICEDUST, which are discussed in Section 18.1.. This algorithm relies on using local and neighbouring features to recover a strong separation between background and signal hits. This separation is improved using shape based information via a reweighted inverse hough transform method.

Data Sample The data sample used in this study was generated using the ICEDUST framework. The total sample size is background-only 10,500 bunch-events. Each bunch-event is constructed from 8×10^6 proton-on-target events, which are simulated from the pion-production target level. To ensure the validity of this result, no events were resampled, meaning that every hit analysed is unique.These proton-on-target events are spread out in time by 100 ns to form a bunch. The spacing between bunches of 1170 ns is used. The detector response is applied, and only hits within the $700 < t_{\text{hit}} < 1620$ are considered, where t_{hit} is the time the hit is detected in the CDC, i.e. including drift time and detector response time.

The default sample discussed in this analysis uses 8×10^6 proton-on-target events per bunch, which is the expected yield. This uses 5,000 bunch-events. This is further divided into 2,500 events for the training sample, and 2,500 events for the testing sample. Signal tracks can be generated as needed, and superimposed on the background event to form a signal event. The signal tracks have 74.0 signal hits on average, while the background events have 493 background hits on average. This totals to an average occupancy of 567 hits, or 12.7% occupancy. The results from this sample are used to judge the performance of the algorithm in general.

To test the algorithm's robustness to larger occupancy rates, the algorithm was tested against a background-rich sample, where the number of proton-on-target events per bunch-event was doubled from 8×10^6 to 1.6×10^7. This sample used a total of 5,250 bunch-events, which was divided evenly into training and testing sample with 2,625 events each. The average number of background hits in these bunch-events nearly doubles to 921, while the average number of signal hits remains at a similar level at 73.1 per event. The total occupancy of this sample is 994 wires, or 22.2%, filled on average. The results of this sample are used to demonstrate the algorithm's robustness to high occupancy, which is discussed in detail in Section 13.5.1.

Data Sample and Event Structure Figure 13.61 gives an example of a truth-labelled input event. The blue points are the signal hits, while the red points are the background hits. The event shown has an uncommonly high occupancy of 728 wires for the default sample, or 16.3%, to show illustrate the performance of the algorithm.

Neighbour-Level GBDT The algorithm begins by considering three "local-level" classification features of each hit wire. The first of these is the energy deposition of the hit. Background protons deposit far more energy than signal electrons as they pass a wire, causing the energy deposition in the hit to be the most powerful feature. A cut on this feature alone can reduce the background hits by 68% while retaining around 99% of signal hits. These values are taken

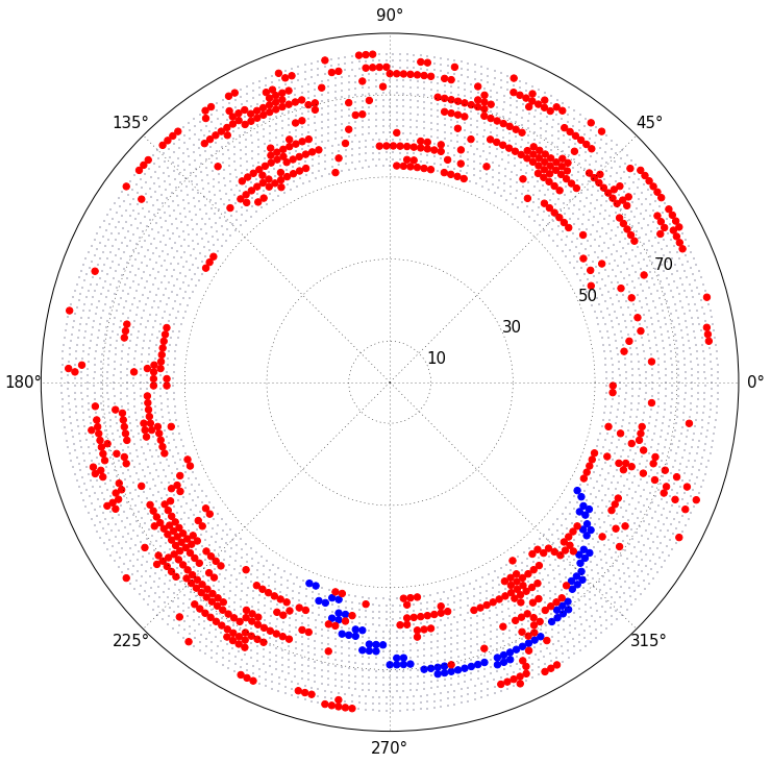

Figure 13.61: A 16.3% occupancy event in the CyDet. This is a projected view from the central plane of the detector, looking in the direction of the beamline. The red points are hits caused from background processes, while the blue hits correspond to the signal electron. The remaining points are the inactivate wires.

as a baseline for judging the performance of the algorithm. The second feature is the timing of the wire hit relative to the timing of the hit in the CTH trigger system. Signal hits tend to occur soon after these trigger hits, while background hits occur randomly with respect to the trigger timing. The third feature is the hits radial distance from the centre. The magnetic field and geometry is tuned so that signal tracks curve through the fiducial volume, rarely reaching the outer layers, yet always passing through the inner ones. The background hits in used data distribute more evenly throughout the layers, peaking slightly at the inner and outer CDC layers. A GBDT trained only on these features is discussed in the performance section for reference, but not implemented in the algorithm itself.

The separation power of these features are further exploited by defining features that describe the neighbouring wires of a hit, i.e. the "neighbour-level" features. Due to the alternating stereo angles, the features on the neighbouring wires in the same layer are more powerful than adjacent layers. These are referred to as the left and right neighbours of a hit. Along with the local features, the left-right timing and energy deposit features are used. This defines seven input features for the GBDT, referred to as the neighbour-level GBDT. Its output is visualised in Figure 13.62.

Circular Hough Transform A crucial part of correctly identifying signal-like hit lies in the ability to check that the hit forms a track shape with other signal-like hits. To recover information about this shape, a circular Hough transform is used. This is best illustrated with the aide of Figure 13.63. In Figure 13.63a, the collection of blue points will be tested to see if they are all on the red circle of radius, R, whose centre lies at the origin. To do so, the green circles of the same radius R are drawn around each blue point, as shown in Figure 13.63b. Each green circle represents all the possible centres for circles of radius R that contain the respective blue

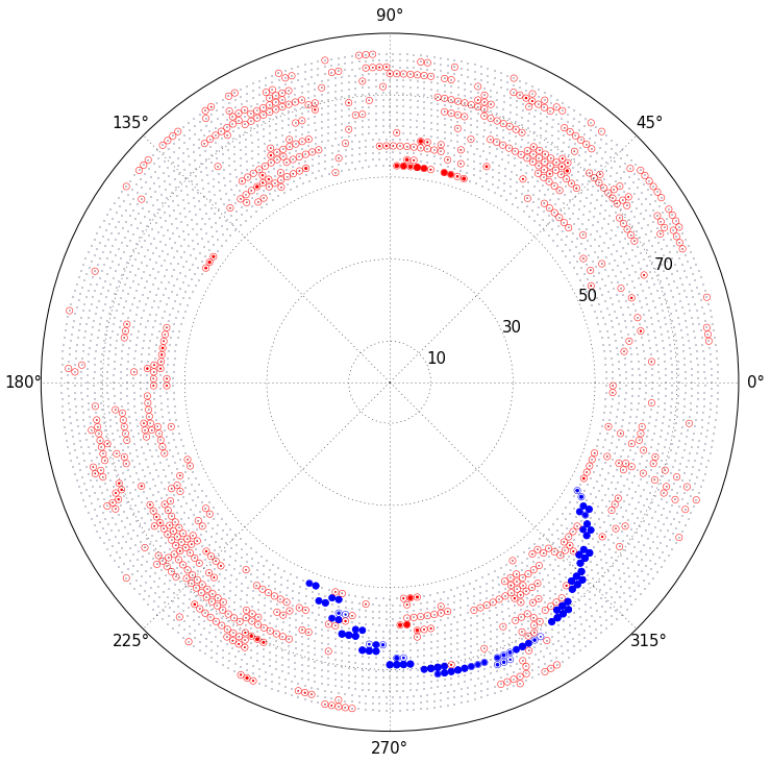

Figure 13.62: A visual representation of the neighbour-level GBDT applied to the event shown in Figure 13.61. The locations of the hits are shown by the outlines of the hits. The fill is scaled with the output of the GBDT, where a full circle corresponds to a signal-like response.

point. Since all the green circles intersect at the origin, all of the blue points must lie on the same circle, i.e. the red circle whose centre is at the origin.

While this method assumes the radius is known beforehand, it is possible to allow for some level of uncertainty in this parameter. This is highlighted using the lighter green bands around the green circles. These green bands represent a probability spread that the blue point belongs to a circle centred somewhere near the green circle. This probability peaks for circle centres at a distance R from the blue point and decays as the circle centre deviates from this target radius. Reshaping the probability spread gives the algorithm more flexibility to accommodate a range of shapes that are close to circular, which is important in signal detection in the CyDet wire array.

Reweighted Forward Hough Transform While local and neighbour features alone yield promising results, there are still some isolated clusters of misclassified background hits, as well as a diminished response for isolated signal hits. To correct this, a circular Hough transform is used on the output of the GBDT to determine which hits lie in a circular pattern with other signal-like hits. This is done by defining a transformation to map from a collection of points in (x, y) space to tracks-centres that lie in (a, b) space. As shown in Figure 13.63b, this means considering the contribution from all points in (x, y) space to a given track centre in (a, b) space.

This contribution as a function of distance has been tuned to the distribution of signal hits around the target radius. To do so, the transverse momentum of the signal electron at each of the hits in an event were averaged. This momentum was converted to the corresponding radius of curvature for an electron in a 1 Tesla solenoidal field. The distribution across all events is shown in Figure 13.64.

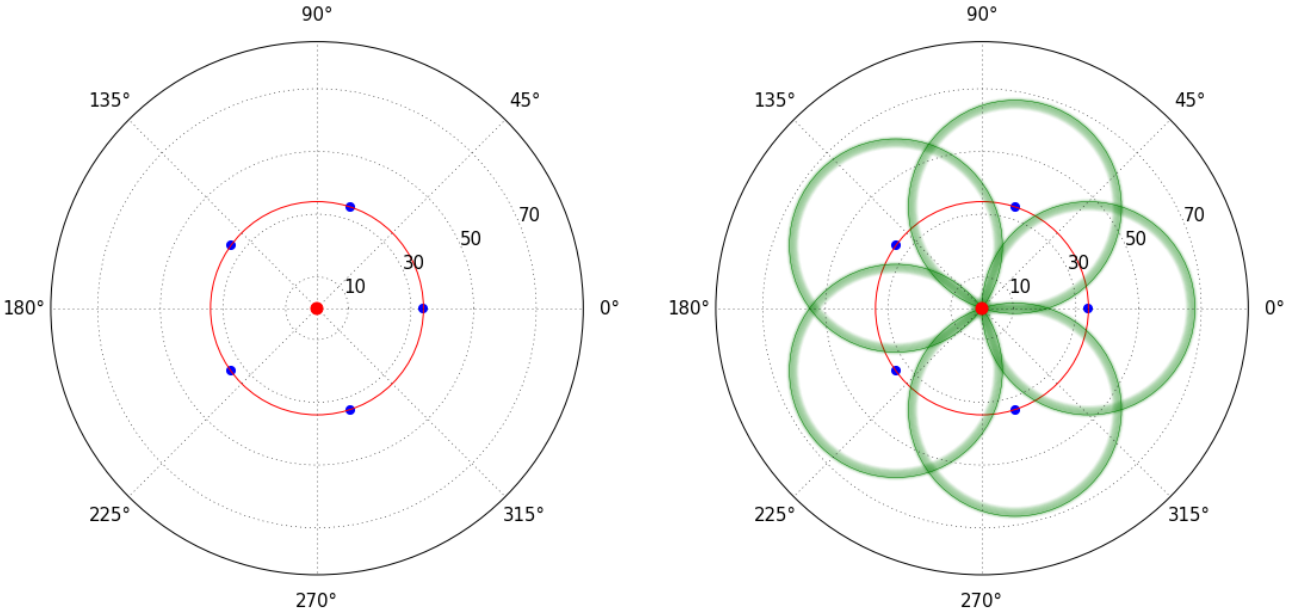

(a) Points in (x, y) space, blue, thought to be on a circle, red, whose centre lies at the origin, orange.

(b) A mapping from the points in (x, y) space, blue, to possible circle centres in (a, b) space, green.

Figure 13.63: Demonstration of a circular Hough transform.

The distribution was fit with a half-Gaussian for radii smaller than the peak, and a linear drop off for radii larger than the peak. This fit was used to define the contribution to a track centre at $\mathbf{r}_i$ from a wire at $\mathbf{r}_j$ as:

$$T(\mathbf{r}_i - \mathbf{r}_j) = T_{ij} \propto \begin{cases} \exp\left(\frac{[|\mathbf{r}_i - \mathbf{r}_j| - r_{\text{sig}}]^2}{2\sigma_{\text{sig}}^2}\right) & : \; r_{\text{min}} < |\mathbf{r}_i - \mathbf{r}_j| < r_{\text{sig}} \\ 1 - \frac{|\mathbf{r}_i - \mathbf{r}_j| - r_{\text{sig}}}{r_{\text{max}} - r_{\text{sig}} + 0.1} & : \; r_{\text{sig}} < |\mathbf{r}_i - \mathbf{r}_j| < r_{\text{max}} \\ 0 & : \; \text{else} \end{cases} \tag{13.3}$$

The four parameters of this fit at the target signal radius, r_{sig}, the minimum signal radius, r_{min}, the maximum signal radius, r_{max}, and the width of the half-Gaussian, σ_{sig}. The red curve in Figure 13.64 defines the contribution function as a close fit to the distribution of signal radii across all events. While this works well as a first guess, the contribution function used is the green curve, which is far more narrow, has a slightly larger target radius, and a tighter width on the Gaussian. This is the same contribution function can be seen in 2D in Figure 13.63b, where it is used to draw the green circles and their spread around the blue points. The exact values used are $(r_{\text{min}},\ r_{\text{sig}},\ r_{\text{max}},\ \sigma_{\text{sig}}) = (31.5\text{cm},\ 34.0\text{ cm},\ 34.5\text{ cm},\ 2.0\text{ cm})$.

Now that the contribution to a track centre at $\mathbf{r}_i$ from a hit wire at $\mathbf{r}_j$ as a function of $|\mathbf{r}_i - \mathbf{r}_j|$ is defined, it is calculated for all wire and track centre pairs, i.e. ij pairs, and saved as a matrix, T_{ij}. Once the track-centre space in (a, b) is discretised, the Hough transform is fully defined. To help illustrate this, consider the vector of all wires, $\mathbf{W}$, and the vector of track-centres, $\mathbf{C}$. Given a hit at wire j, we can assign $W_j = 1$. The contributions from all hits to track-centre i is given by the forward Hough transform in equation (13.4). This transform is inverted by taking the inverse of the matrix T_{ij}[3].

[3]Note the following equations are implicitly summed on repeated indices.

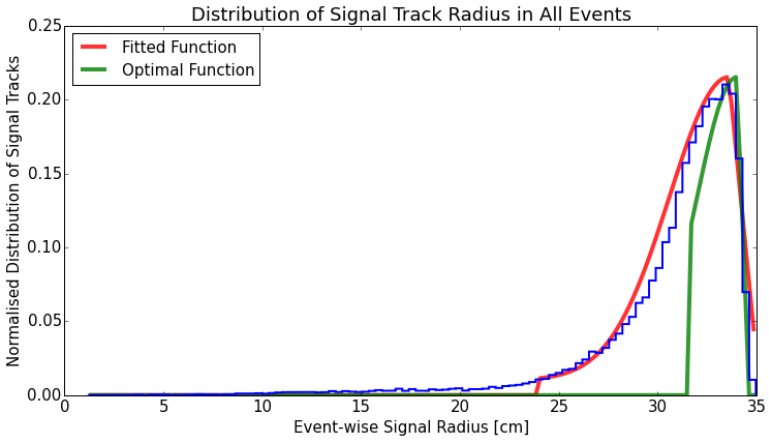

Figure 13.64: Distribution of signal track radius in the data sample. The red curve is the fitted function that closely follows the distribution. The green curve is distribution used to define the Hough transform used. Both curves are described by equation (13.3).

$$\begin{array}{ll} \text{Forward Transform} & \text{Inverse Transform} \\ \text{Hit property} & \text{Track property} \\ \underbrace{T_{ij}}_{\text{Hough}} \overbrace{W_j} = \underbrace{C_i}_{\text{Track centres}} & \underbrace{(T_{ij})^{-1}}_{\text{Inv. Hough}} \overbrace{C_i} = \underbrace{W_j}_{\text{Wire Hits}} \end{array} \tag{13.4}$$

To limit the search for tracks to signal-like tracks, the contributions from each hit are weighted by their output from the GBDT. For wire j with the set of features $\mathbf{f}_j$ and GBDT classifier output $y_{\text{Grad.}}$, this reweighting implies:

$$W_j \to W'_j = y_{\text{Grad.}}\left(f_{1j}, \cdots, f_{Nj}\right). \tag{13.5}$$

This function returns one for a signal-like feature set, and zero for a background-like feature set, which naturally suppresses contributions from background hits in the Hough transform. The application of this weighted transform is visualised in Figure 13.65. Note that due to the width in the Hough transform contribution function, the stereo angles of the wire array, and the imperfections in the track, the signal track peak is spread over two main centres.

Reweighted Inverse Hough Transform The information in track-centre space is now inverted to recover information about long-range structure in the hits. To achieve this, the set of outputs in track-centre space C_i can be reweighted to cut out noise and isolated background, while reinforcing the strong, signal-like structures. To remain sensitive to complex, multipeaked structures in Hough space, all track-centres are reweighted exponentially:

$$C_i \to C'_i\left(\alpha\right) = \exp\left(\alpha C_i\right). \tag{13.6}$$

This reweighting process can be thought of as looking as using an "inverse-logarithmic" scale. The larger the difference between two track centres in C_i, the more orders of magnitude difference they will have in $C'_i\left(\alpha\right)$. It introduces a new parameter α, which controls the scale of the reweight. Once this reweighting in complete, the result is mapped back to the wires to give $W''_j\left(\alpha\right)$, which is the likelihood that the j-th wire lies on a circular track of target radius with signal-like hits. The result can be seen in Figure 13.66.

At this stage, α is tuned to yield an inverse Hough transform output, $W''_j\left(\alpha\right)$, that compensates for the error in the GBDT classifications, W'_j. It does this by determining the value for α that

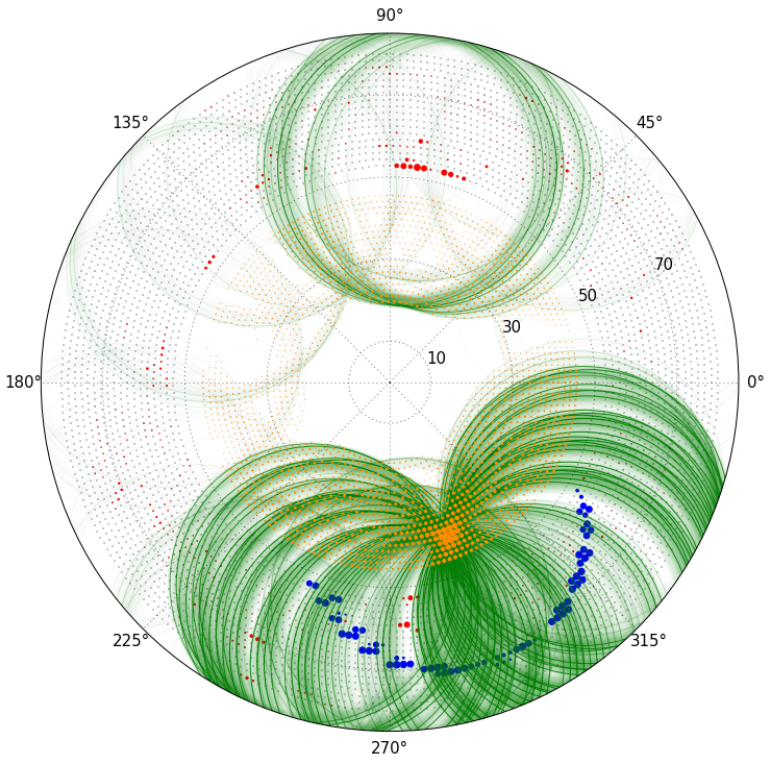

Figure 13.65: A visual representation of the Hough transform applied to the GBDT output shown in Figure 13.62. Each point in the wire array has a green circle to represent its contribution to the orange track-centre points, which is defined by equation (13.3). The weight of the green circle matches the size of the corresponding hit, which in turn corresponds to the wires GBDT output, as defined in equation (13.5). The orange track-centres are scaled with respect to the Hough transform output C_i, as defined in equation (13.4).

best relabels the hits that were mislabelled by the GBDT. To achieve this, a mislabel weight, γ_j, is defined for each hit as:

$$\gamma_j = \left(W'_j - L_j\right)^2, \tag{13.7}$$

where L_j is the truth label as to whether the hit is signal or background. From here, the following metric is calculated for each value of α:

$$H\left(\alpha_k\right) = \sum_{j}^{N_{\text{wires}}} \gamma_j \left[W''_j\left(\alpha_k\right) - L_j\right]^2, \tag{13.8}$$

Track-Level GBDT Even without accounting for the stereo angles, the Hough transform does improve the classification of signal-hits. The W''_j values are defined a new feature of the hits. They are used alongside the previously defined local and neighbour features in a new GBDT, referred to as the track-level GBDT. Its output is visualised in Figure 13.67. Note that there is no overall cut placed on this output. The isolated background hits have been suppressed, while some of the signal hits on the inner layers have been restored. A few background hits close to signal track remain, but these points will always be difficult to classify correctly. Should their overall impact on track fitting be substantial, further efforts will be taken to correctly classify them.

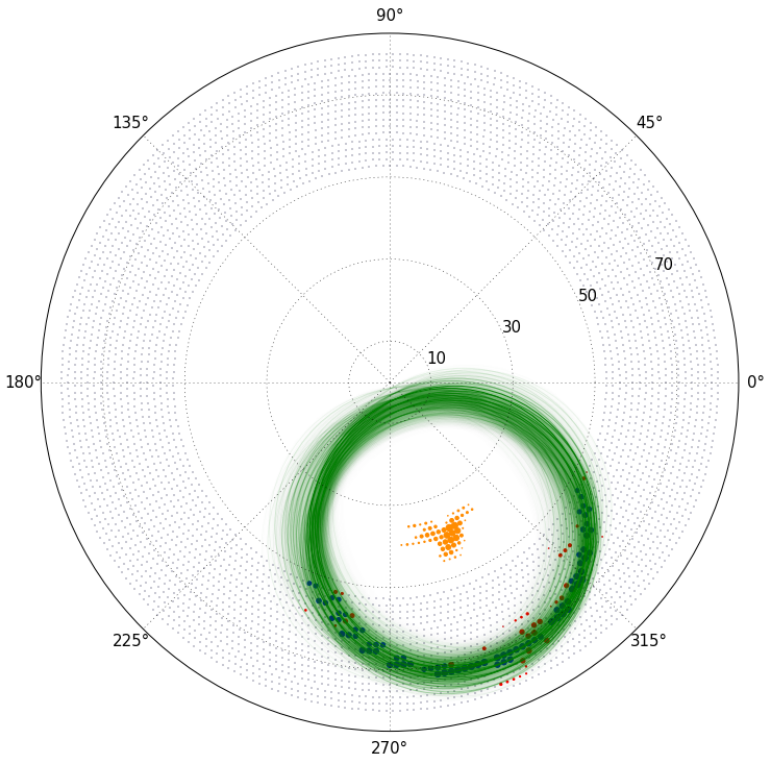

Figure 13.66: This shows the effects on reweighting the track centre values exponentially, as given in equation (13.6), and inverting the transform, as given in equation (13.4). The value used here for α here is 2, which yields a suppression to all centres except those directly neighbouring the maxima.

Performance

The following performance metrics measure the performance of the algorithm on the default sample with 8×10^6 proton-on-target events per bunch, as discussed in Section 13.5.1. To measure this algorithm's classification abilities, the distribution of the track-level GBDT is shown in Figure 13.68. This distribution shows a strong improvement over the baseline result of cutting on the energy deposition alone.

Classification Results To better compare these results, ROC curves are used to plot the algorithms' ability to reject background as a function of its ability to retain signal. Each point along the ROC curve corresponds to a cut value of the GBDT output that would yield the corresponding classification efficiencies. The ROC curves for this algorithm are plotted in Figure 13.69. These plots compare the performance of the neighbour-level GBDT and the track-level GBDT to the baseline separation power of the energy deposition of a hit. As a benchmark, consider the background rejection rates at a signal efficiency of 99%. A cut retaining this signal efficiency would remove 68% of background using the energy deposition alone, 82% using the local-level GBDT, 92% using the neighbour-level GBDT, and nearly using the 98% track-level GBDT. The track-level GBDT consistently outperforms the neighbour-level GBDT, as intended. This performance increase becomes more dramatic as the signal efficiency increases.

Feature Performance The performance of each feature can be measured by both its "feature importance" and by its correlation with other features, as shown in Figure 13.70. The feature importance measures the frequency that the feature is used when training the GBDT. It is clear from Figure 13.70a that the reweighted inverse Hough output is the most used feature. This

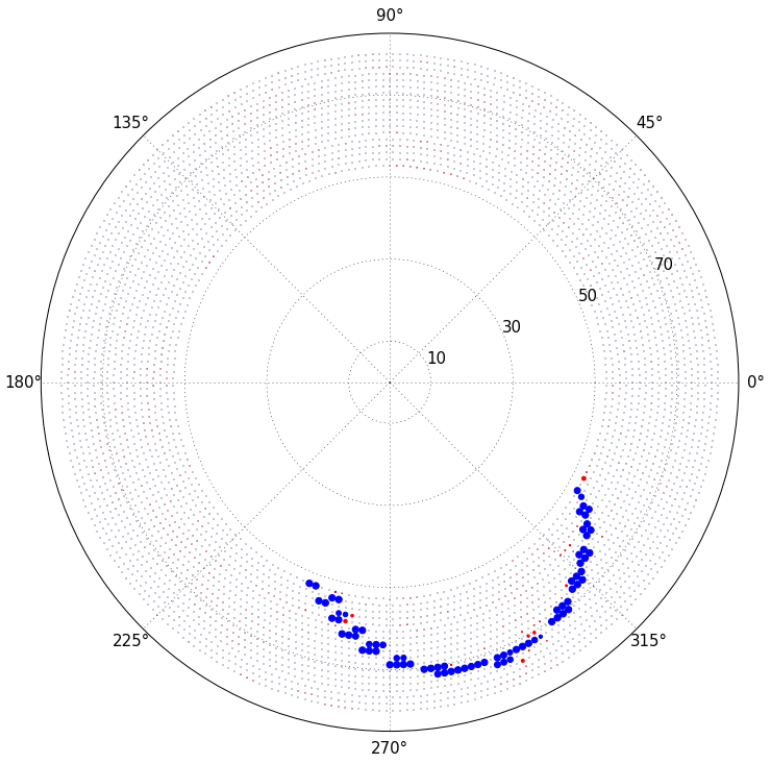

Figure 13.67: This is the final output of the algorithm. Note that the local clusters of background that were mislabelled in the neighbour-level GBDT output in Figure 13.62 have been removed.

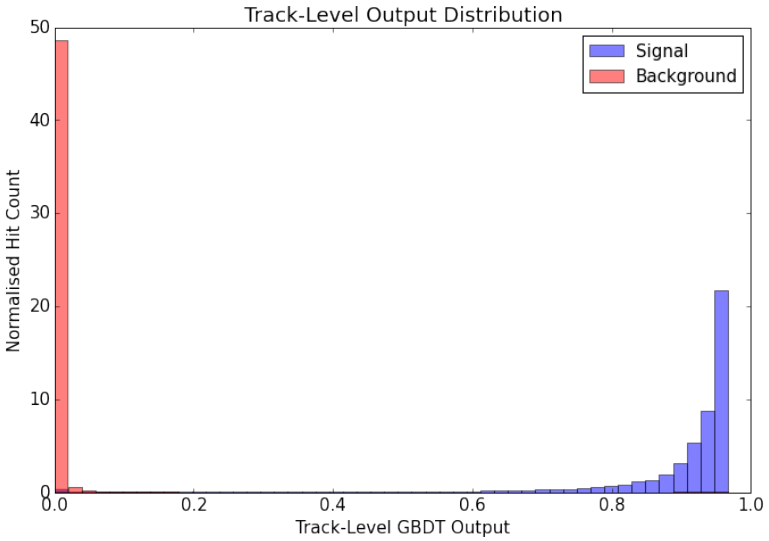

Figure 13.68: Distribution of the output of the track level GBDT, comparing response from signal hits to the response from background hits.

is to be expected given that it was constructed using Hough transforms over the output of the neighbour-level GBDT. The second performance measure is the correlation matrix, which helps describe the relationships between features. Figure 13.70b shows no strong correlations between any of the seven neighbour-level feature and features the Inverse Hough Transform feature. This suggests that the shape-based feature does bring new information to the classification process.

Occupancy Rates Descriptions of the occupancy rates before and after classification are provide a useful metric for evaluating the hit filtering abilities of the algorithm. The occupancy

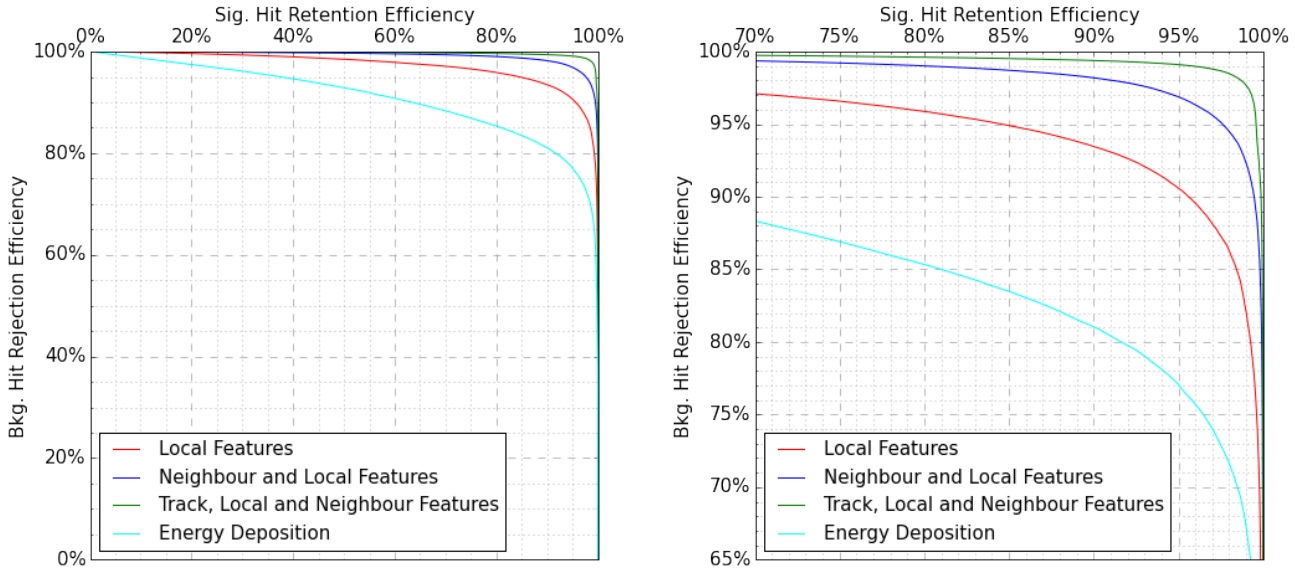

(a) ROC curves at full scale.

(b) ROC curves with zoomed scale.

Figure 13.69: ROC curves for three independent classifiers. The red curve is from a GBDT trained on energy deposition alone, the blue curve is from the neighbour-level GBDT, and the green curve is from the track-level GBDT.

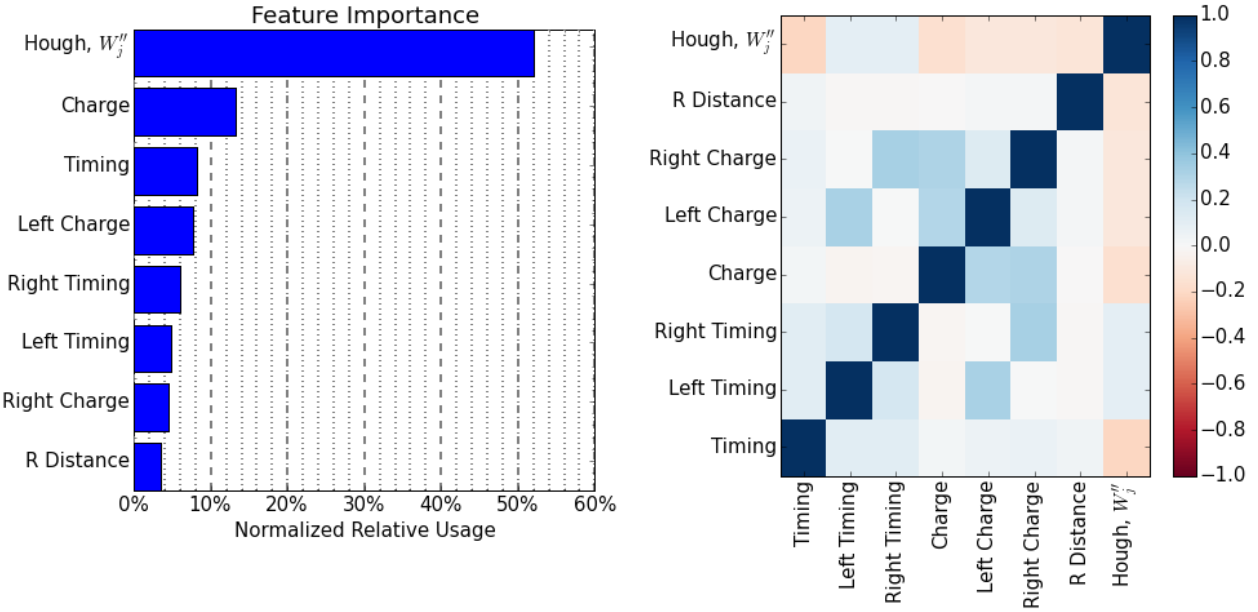

(a) The importance of each feature. This is determined by the frequency this feature is used to split a node when training the GBDT.

(b) The correlation matrix between each feature. This is determined by the linear correlation constant between the two features

Figure 13.70: Metrics to assess the performance of each feature.

distributions of all events in the default sample and background-rich sample, described in Section 13.5.1, are shown in Figure 13.71.

Hits are classified using the distribution in Figure 13.68. Using the benchmark previously discussed, the cut that ensured 99% of signal hits survived was used. The results of this cut for both the default and background-rich sample are shown in Figure 13.72. These show that the signal occupancy is not greatly effected, while the background reduction is significant. The default sample demonstrates a background hit rate of tolerable levels, although not ideal.

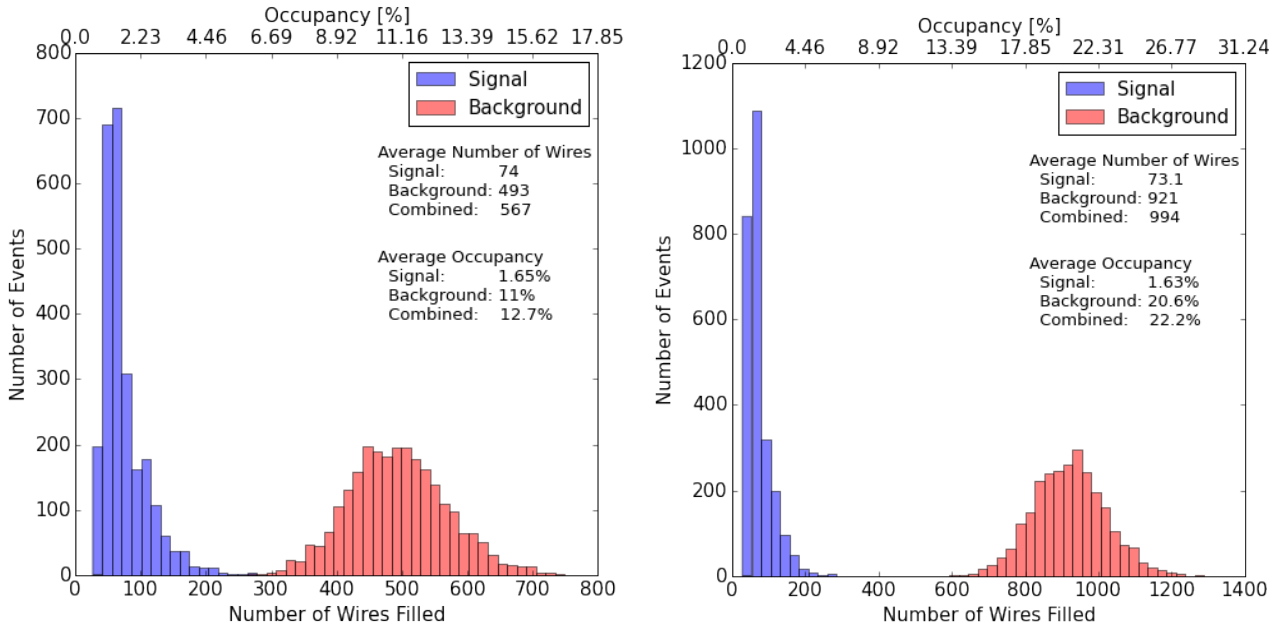

(a) Default Sample

(b) Background-Rich Sample

Figure 13.71: Occupancy rates and total number of wires filled for the default sample and the background-rich sample, before classification.

The background-rich sample shows that the performance of the algorithm suffers in a higher occupancy setting, and is not usable at this benchmark in its current version. With this said, the parameters of the algorithm have been developed and optimised using the default sample. Performance in the high occupancy case may be improved with a different parameter set, namely for the reweighted inverse hough transform.

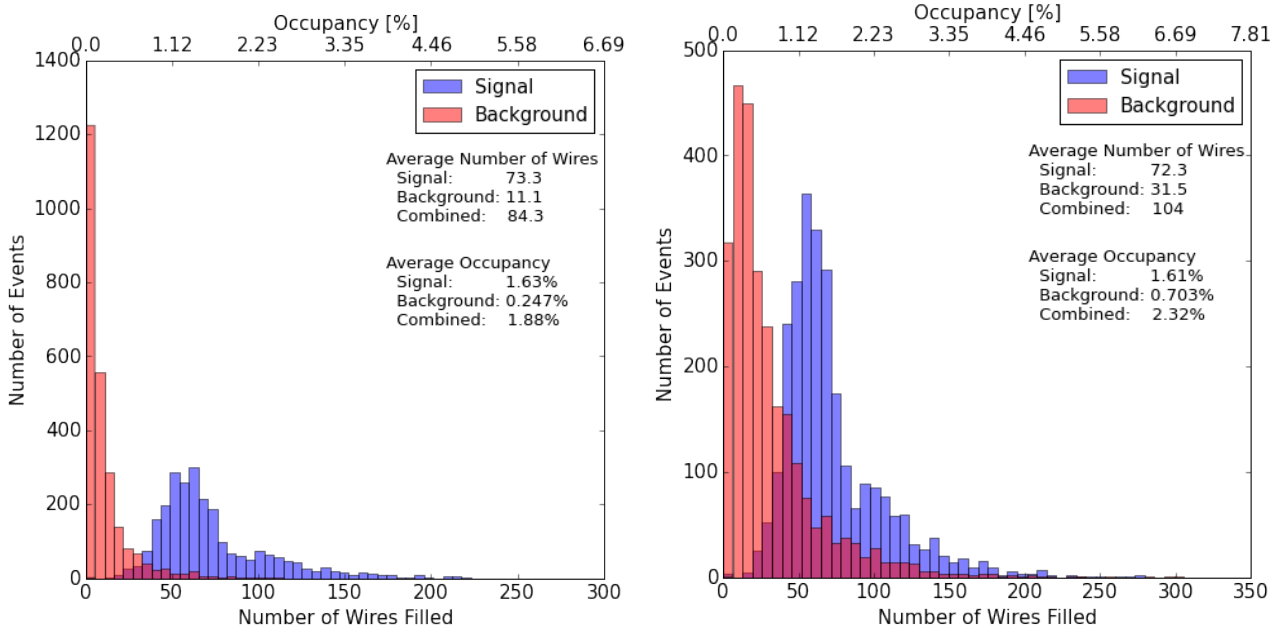

(a) Default Sample

(b) Background-Rich Sample

Figure 13.72: Occupancy rates and total number of wires filled for the default sample and the background-rich sample, after classification that retains 99% of signal hits.

While 99% signal hit retention rate does not yield usable background hit rates in the high

occupancy sample, a looser requirement can be used to improve the situation. To compare, a cut that still retains 95% of signal hits was used. The results are shown in Figure 13.73. The background-rich sample after this cut has a similar background level to the default sample after the previous cut. This shows that even in its current version, the algorithm can recover the needed background suppression should the occupancy be much higher than expected. While we have lost 4% more signal hit points using this cut, this does not mean the overall signal efficiency suffers by 4% as well. Further study will inform which is the optimal cut to take in terms of overall signal efficiency and momentum resolution. The default sample response to this loose cut shows the best background suppression of the four plots after classification.

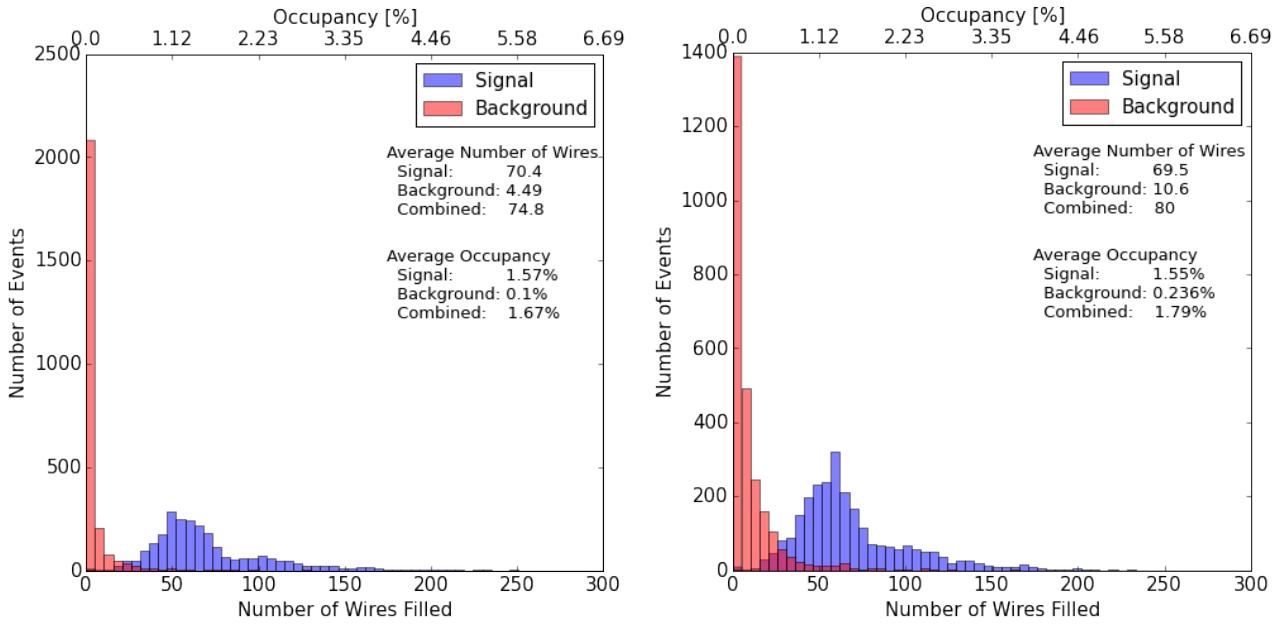

(a) Default Sample

(b) Background-Rich Sample

Figure 13.73: Occupancy rates and total number of wires filled for the default sample and the background-rich sample, after classification that retains 95% of signal hits.

Further Study The current version of the CDC track finding demonstrates an ability to filter out a large majority of background hits while retaining signal hits. This ability suffers somewhat in the face of higher occupancy samples. Even so, it can be tuned to achieve increasingly higher levels of background suppression at larger costs to signal hits.

The optimal balance between signal hit retention and background hit rejection relies heavily on the steps taken in track fitting. A full optimization of the algorithm will done against the track fitting stages of the algorithm. Additionally, an intermediate "pre-fitting" technique may be introduced. The aim of this step would be to remove isolated islands of background hits that survive the hit filter by fitting a model to the track-level GBDT output. Even without a full optimization, this algorithm performs well as a hit filtering technique that is flexible and robust in the face of high occupancy events.

13.5.2 Track fitting

A tracking program using `GENFIT` with a Kalman filter has been developed. In the `GENFIT` program, `GeaneTrackRep2` was originally used as a Kalman filter, but we decided to use another code `RKTrackRep` instead. This allows for tracking in a large angle arc, and is needed to perform

multiple turn track fitting. An alternative tracking program based on the tracking code for the BES-III experiment at IHEP, China has also been developed and is used to cross-check the fitting. Here we describe the performance of the `GENFIT`-based algorithm.

Signal tracks which hit the CTH are selected and split into two groups: single turn tracks and multiple turn tracks. The ratio between single turn and multiple turn tracks is roughly 8:5. It is noted that in the current track fitting, multiple turn tracks are treated initially as a set of a few single turn tracks, and then they are combined to form one multiple turn track.

Tracking and track quality cuts

In order to select good curving tracks and eliminate bad tracks with poor momentum resolution, the following good-track selection criteria are required. They are:

NL5 : Tracks must reach the 5th sense layer. This requirement ensures that tracks record a sufficient number of hits in the CDC that the reconstruction will be reliable. It also ensures that selected tracks have a large transverse momentum component (p_{T}). Figure 13.74 (top-left) and Figure 13.75 (left) give the distributions of the deepest layer number that signal tracks can reach for the two groups of single turn and multiple turn tracks respectively.

NFIT : To ensure a decent resolution we also require that the signal tracks provide at least one whole turn in the CDC to be fitted. The number of the successfully fitted tracks is defined as `NHIT`, and the requirement is `NHIT`=1. It should be noticed that the maximum number of turns used in the current fitting scheme is temporally two. Figure 13.74 (top-middle) and Figure 13.75 (right) give the distributions of `NFIT` for the two groups of single turn and multiple turn tracks respectively. Given this number in Figure 13.75 (right), multiple turn tracks are further split into the single turn and multiple turn tracks respectively : multiple turn tracks with only one turn successfully fitted (*1-turn-fit tracks*), and multiple turn tracks with more than one turns successfully fitted (*2-turn-fit tracks*).

NDF30 : The number of degree of freedom should be greater than 30. The distributions of the number of degree of freedom in the CDC for single turn tracks, *1-turn-fit tracks*, and *2-turn-fit tracks* are shown respectively in Figure 13.74 (top-right), Figure 13.76 (top-left) and Figure 13.76 (bottom-left). This also helps to ensure the reliability of the fitted track.

χ^2 : The normalised χ^2 ($=\chi^2/N_{\mathrm{DOF}}$) should be less than two. The distributions of the normalised χ^2 for single turn tracks, *1-turn-fit tracks*, and *2-turn-fit tracks* in the multiple turn tracks are shown respectively in Figure 13.74 (bottom-left), Figure 13.76 (top-middle-left), and Figure 13.76 (bottom-middle). This χ^2 is required to be less than two. Since signal tracks are rarely scattered from a helical trajectory they rarely fail this cut, but those that do will generally have poor momentum reconstruction.

CL3 : It is required to have at least 3 consecutive hit layers at both the entrance and exit of the CDC (`CL3Enter` and `CL3Exit`) for single turn tracks and *1-turn-fit tracks*. For *2-turn-fit tracks*, a difference between the two fitted p_{L} in each of the two turns ($\Delta_{p_{\mathrm{L}}}$) must be smaller than 20 MeV/c. Here, in general, the resolution of the longitudinal momentum (p_{L}) is not as good as that of the transverse momentum (p_{T}). The determination of p_{L} is based on reconstructing the pitch ($\sim p_L/p_T$) of the particle. This can be deduced from how far the particle travels longitudinally while it make an arc in the CDC. For single turn tracks and *1-turn-fit tracks*, it is required that the track should have hits in the 3 innermost sense layers at both the entrance and exit of the CDC, in order that the z

positions can be well-determined. Figure 13.74 (bottom-middle and bottom-right) and Figure 13.76 (top-middle-right and top-right) show the distributions of `CL3Enter` and `CL3Exit` for single turn tracks, *1-turn-fit tracks* correspondingly. For *2-turn-fit tracks* the reconstruction of p_{L} can be easily controlled by requiring $\Delta_{p_{\mathrm{L}}}$ smaller than $20 MeV/c$. Figure 13.76 (bottom-right) shows a typical distribution of p_{L} of *2-turn-fit tracks*. These two criteria give us the longest possible lever arm to determine p_{L}.

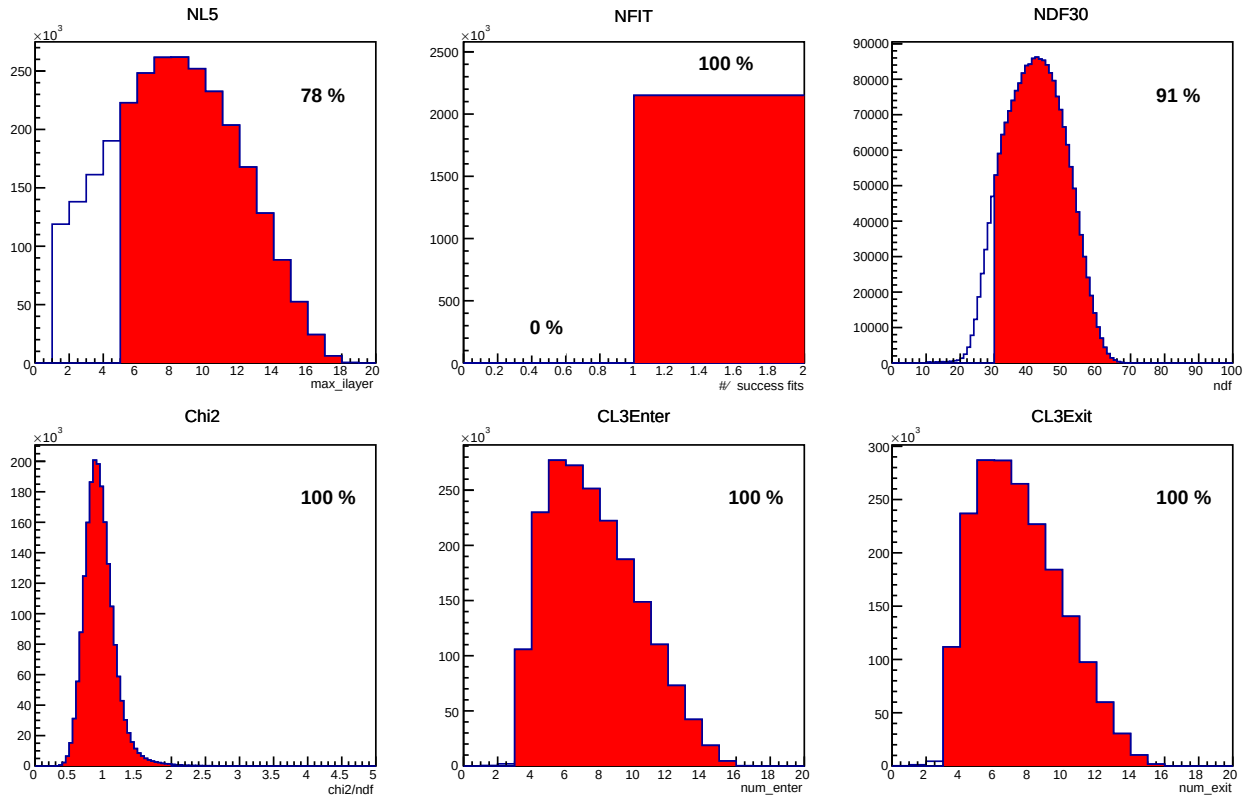

Figure 13.74: *Distributions of track quality cut parameters for single turn tracks of signal events. The regions highlighted in red are accepted in the track quality cuts. Each of the cuts is applied in the order of* `NL5`, `NFIT`, `NDF30`, χ^2, `CL3Enter` *and* `CL3Exit`, *and the distributions show only events that pass the requirements of the preceding cuts*

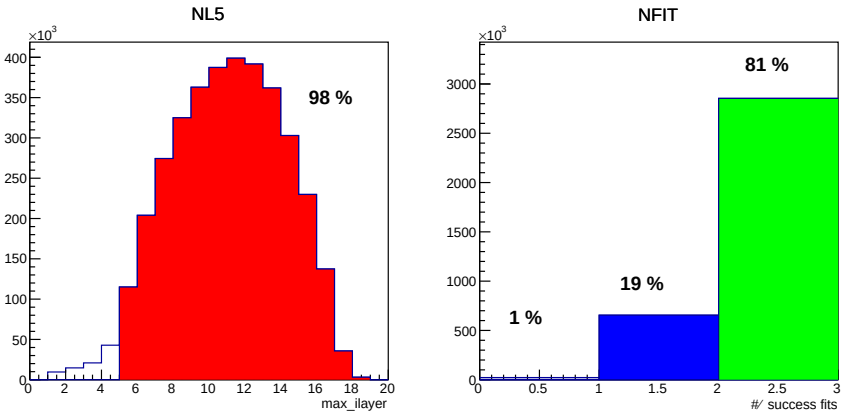

Figure 13.75: *Distributions of track quality cut parameters for multiple turn tracks of signal events. The regions highlighted in red are accepted in the track quality cuts. Each of the cuts is applied in the order of* `NL5` *and* `NFIT` *and the distributions show only events that pass the requirements of the preceding cuts*

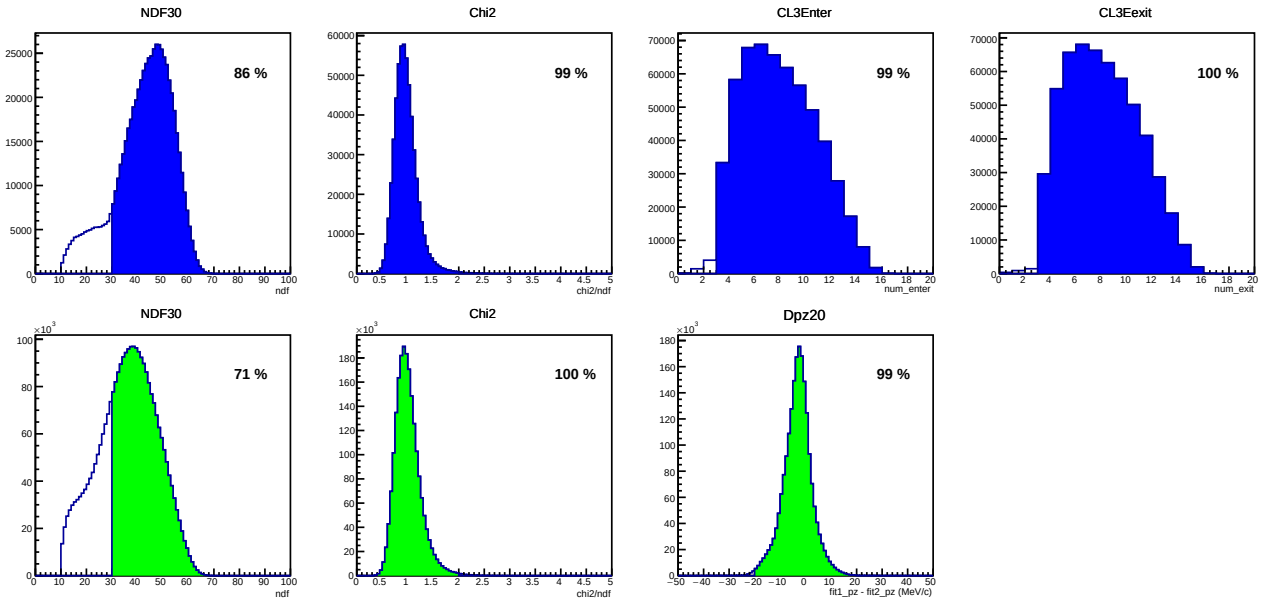

Figure 13.76: *Distributions of track quality cut parameters for multiple turn tracks of signal events. The upper row shows the distributions for 1-turn-fit tracks, while the lower row shows the distributions for 2-turn-fit tracks. In each row, the regions highlighted in red are accepted in the track quality cuts. Each of the cuts is applied in the order of* `NDF30`*,* χ^2*,* `CL3Enter` *and* `CL3Exit` *(for 1-turn-fit tracks),* Δ_{p_L} *(for 2-turn-fit tracks), and the distributions show only events that pass the requirements of the preceding cuts*

For single turn tracks all the hits after track finding will be used for fitting. For multiple turn tracks, among the hits selected by track finding, a candidate set of hits for the first turn is selected. A `GENFIT` tracking is tried using the selected set of hits, if remaining hits are less than 30. This is the case when the second turn track goes away CDC without leaving enough hits. It is referred to as a *1-turn-fit track* in the above. If more than 30 hits remain, then another set of hits for the second turn is selected. `GENFIT` trackings are tried for these two sets of hits to determine the first and second turn. Since the charged particle will lose some momentum as it travels, a track with higher p_L is determined to be a first turn track. Until above track quality cuts are met the trackings continue using different sets of hits. This is referred to as a *2-turn-fit track* in the above.

Intrinsic momentum resolution

The intrinsic momentum resolution is defined as the difference between the reconstructed and true momenta *at the first sense wire layer*. For simulation, a gas mixture of He:i-C_4H_{10} (90:10) is assumed, and a position resolution of 200 μm is used. The quoted momentum resolutions for single and multiple turn tracks are obtained by fitting single or double Gaussian functions to the momentum resolution distribution, and are summarised in Table 13.14. Multiple turn tracks generally have a better *total* momentum resolution since the contribution of p_L in multiple turn tracks is smaller than that in single turn tracks. However the tracking efficiency for multiple turn tracks is lower than that for single turn tracks. More detailed discussions on the efficiency and geometrical acceptance are given in Section 20.1.1. It should be noted here that the effect of multiple scattering at field wires is significant.

Type	Single Gaussian (core)	Double Gaussian (core)
Single turn	236 keV/c	174 keV/c
Multiple turn	197 keV/c	115 keV/c

Table 13.14: *Intrinsic momentum resolution of the CyDet for single turn and multiple turn tracks.*

Effect of flight time to the trigger hodoscope

The reference time of the CyDet comes from the timing of electron tracks hitting the CTH. Since most of electron tracks curl through the CDC at least once before reaching the trigger hodoscopes, the time of flight (TOF) of the tracks to the CyDet trigger hodoscopes should be corrected to obtain the proper drift time of hits in each cell. Because of the detector geometry, the TOF has a bunched distribution, which depends on a number of turns the tracks makes before reaching the CTH. Figure 13.77 shows the TOF distribution between the first hit cell and the trigger hodoscopes for the electron tracks of different numbers of turns and different momenta. Reading from this Figure, for a single turn track of 100 MeV/c (in green), the TOF can ranges from 2 ns to 4 ns and the RMS of the distribution is less than 1 ns. Since an RMS distribution of 1 ns introduces only a 50 µm position uncertainty (drift velocity $v \sim 2.5$ cm/µs) which is smaller the intrinsic positron resolution of 150–200 µm, the effect of TOF can be ignored in the initial track fitting, and then be corrected in subsequent iterations.

To study how we can correct for the TOF effects, a simulation was made where TOFs are added to the true drift times for all the hit cells. Then TOF corrections, based on track fitting, was made. The intrinsic momentum resolution with TOF correction for single turn tracks was found to be about 200 keV/c, which is about the same as for the ideal case without TOF effects.

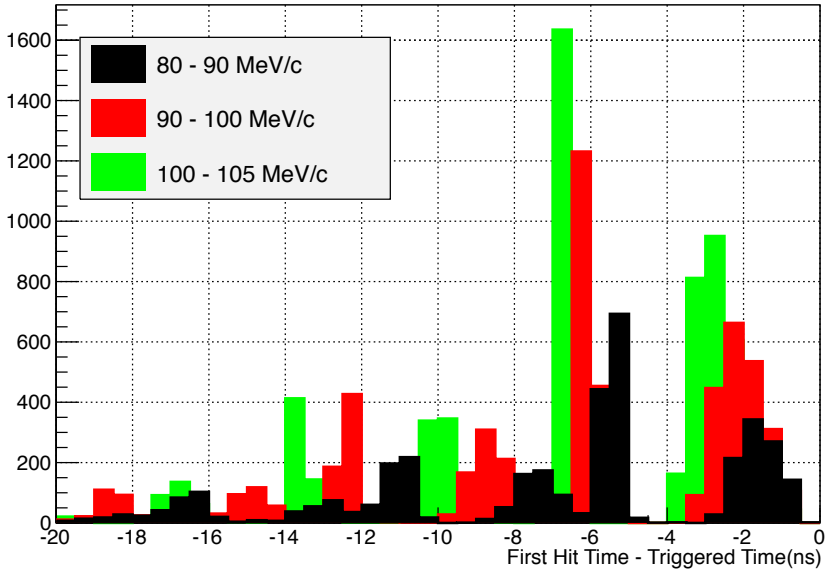

Figure 13.77: *Time of flight distribution for electron tracks with different momentum and different numbers of turns. It shows bunched structures for given momentum. Each bunch corresponds to different numbers of track turns, with the rightmost bunch corresponding to single turn tracks*

13.5.3 Momentum resolution at birth

The momentum resolution for the $\mu-e$ conversion signal will be affected by the energy loss and energy straggling in both the muon stopping target and the CDC inner wall. The tail at the lower momentum side is caused mostly by energy loss in the muon stopping target. The tail at the higher momentum side, which becomes more important for background suppression, is caused by energy straggling in the muon stopping target and the CDC inner wall. The momentum distribution of the $\mu-e$ conversion signal is given in Figure 13.78. To eliminate intrinsic backgrounds from regular muon decays, the momentum resolution (in particular on the higher momentum side) is extremely important. As shown in Fig 13.78, the sigma of the core Gaussian, and that of the tail Gaussian at the high momentum side are 195 keV/c and 226 keV/c, respectively.

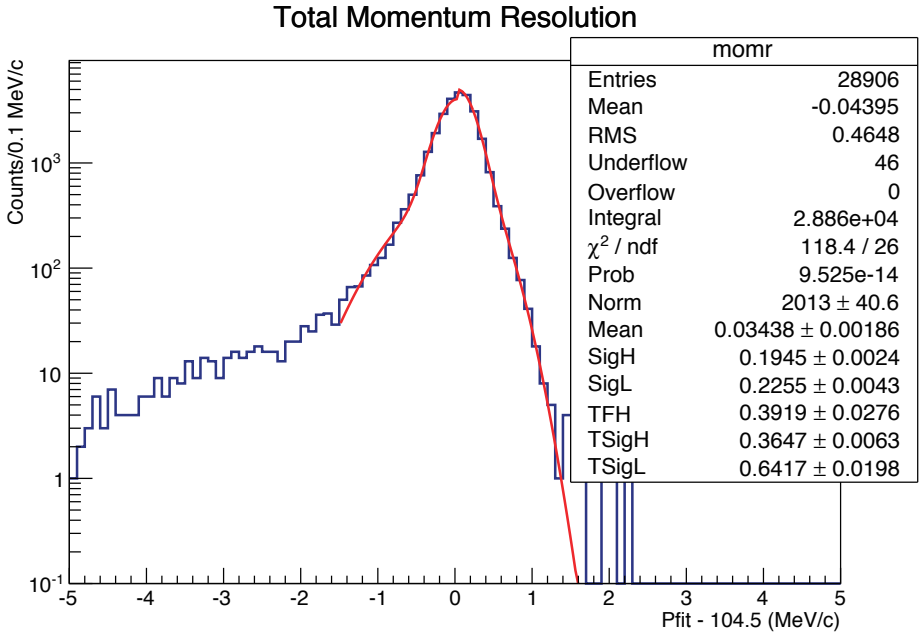

Core	σ of high-momentum half-Gaussian (`SigH`)	195 keV/c
	σ of low-momentum half-Gaussian (`SigL`)	226 keV/c
Fraction in tail distribution (`TFH`)		39%
Tail	σ of high-momentum half-Gaussian (`TSigH`)	365 keV/c
	σ of low-momentum half-Gaussian (`TSigL`)	642 keV/c

Figure 13.78: *The distribution of the fitted momentum minus 105.0 MeV (for the $\mu-e$ conversion signal) for a 0.5 mm thick CFRP inner wall.*

13.6. CyDet Momentum Calibration

The CDC momentum calibration procedure is under consideration. There are several options to make this calibration. One of them is to use the $\pi^- + p \rightarrow n + \gamma$ reaction, followed by $\gamma \rightarrow e^+ + e^-$. The maximum energy of photon is 129 MeV. Another possible process is the $\pi^- + p \rightarrow n + \pi^0$ reaction, followed by $\pi^0 \rightarrow \gamma + \gamma$ with photon conversion. The maximum energy of these photons is 83 MeV. For both these processes, a photon converter may be necessary. It is noted that a photon converter placed in front of the CDC is also being considered for a measurement of the photon rate arising from radiative muon nuclear capture (RMC) in aluminium (see Section 22.3.).

A third reaction that can be used for the CDC calibration is the $\pi^+ \to e^+ + \nu$ decay, where the e^+ is monochromatic, at 70 MeV/c. The diameter of curvature of 70 MeV/c tracks is about 46 cm, and they cannot normally reach the CDC, as its inner radius is 50 cm. However, if a special muon stopping target with a larger radius (such as 20 cm instead of the nominal 10 cm) some π^+s can stop in the outer region of the target, and e^+s from $\pi^+ \to e^+ + \nu$ can reach the CDC. Such electrons are mono-energetic and are very useful for the CDC calibration. Another option is to use the electrons from muon decay in orbit (DIO). In this case, the spectrum above 80 MeV/c has not been measured, so it would have to be compared to the theoretical calculation, which is available. Once this spectrum is measured in COMET Phase-I, it can be used for the calibration. A dedicated set of simulation runs to study the CDC calibration is in progress.

Chapter 14

Normalization of Muons Stopped

The number of muons stopped in the muon-stopping target is needed to know in order to determine the branching ratios. It can be measured in several different ways. The baseline solution is observing the characteristic X-rays from muonic atoms using a germanium detector. The detector and its electronics are designed to handle high count rates which is expected in the COMET Phase I environment. We also consider alternatives in case the hit rate on the germanium detector is prohibitively high for its normal operation.

14.1. Muonic X-rays measurement

The number of muons stopped in the muon-stopping target (N_μ) can be estimated by:

$$N_\mu = \frac{F_{i\to j}}{A_{i\to j} \times \Omega \times \varepsilon} \tag{14.1}$$

where $F_{i\to j}$ and $A_{i\to j}$ are, respectively, the number of counts in the muonic X-ray peak and the transition probability from the muonic atomic states of i to j per negative muon captured. The latter is given in the literature [80]. Ω is the solid angle covered by the X-ray detector and ε is the efficiency of detection of the $i \to j$ transition X-ray.

The major X-ray transition that we will use for monitoring the number of muons stopped is the 2p $\to$ 1s X-rays for aluminium since it has the highest yield with a relatively low background. The second candidate is the 3d $\to$ 2p transition for which a semiconductor detector has a better detection efficiency. The drawback of this X-ray is a potentially very high background of characteristic X-rays from other materials. Other transitions with sizeable intensities, such as 3p $\to$ 1s or 4p $\to$ 1s, might also be observable. Cross checks using various X-ray lines can be used to reduce the systematic uncertainties. Table 14.1 summarises the energies of the most intense muonic X-rays for aluminium.

We plan to use an n-type, coaxial germanium detector (Figure 14.1) to measure the X-rays. The detector is of GMX type manufactured by ORTEC, optimized for low energy gamma and X-ray measurements with an ultra-thin entrance window of 0.5-mm-thick beryllium, and a 0.3-μm-thick ion implanted contact. This detector is equipped with a transistor reset preamplifier which enables it to work in an ultra-high rate environment up to 10^6 counts/s at 1 MeV. The crystal is 52.5 mm in diameter and 55.3 mm long with a hole of 9.9 mm in diameter and 47.8 mm deep.

The germanium detector was already tested in the AlCap experiment at PSI. The AlCap experiment is designed to measure the rate of proton emission after muon nuclear capture on

Table 14.1: *Energies and relative intensities of muonic X-rays from aluminium.*

Transition	Energy (keV)	Relative Intensity (%)
2p → 1s	346.828 ± 0.002	79.8 ± 08
3d → 2p	66.11 ± 0.02	67.6 ± 1.7
3p → 1s	412.87 ± 0.05	7.62 ± 0.15
4p → 1s	435.96 ± 0.10	4.87 ± 0.10

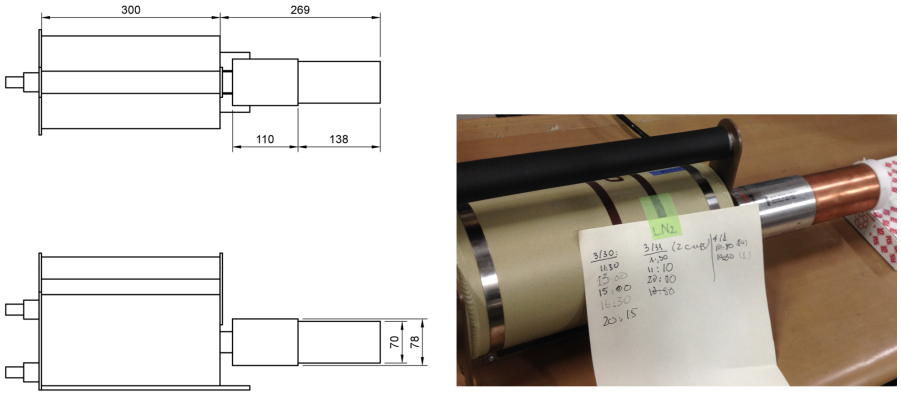

Figure 14.1: *Germanium detector and its dimensions.*

aluminium for COMET. We took data with 100-μm-thick and 50-μm-thick aluminium targets. The detector was placed about 30 cm far from the target position. The absolute detection efficiency ($\Omega \times \varepsilon$) of the 2p → 1s line was determined to be 3.56×10^{-4}. One measured spectrum is shown in the Fig. 14.2 where the 346.8 keV line is clearly visible. The 3p → 1s line is also recognisable around 410 keV region. The 4p → 1s line is however dominated by double peaks, 431 and 438 keV, from the lead shielding.

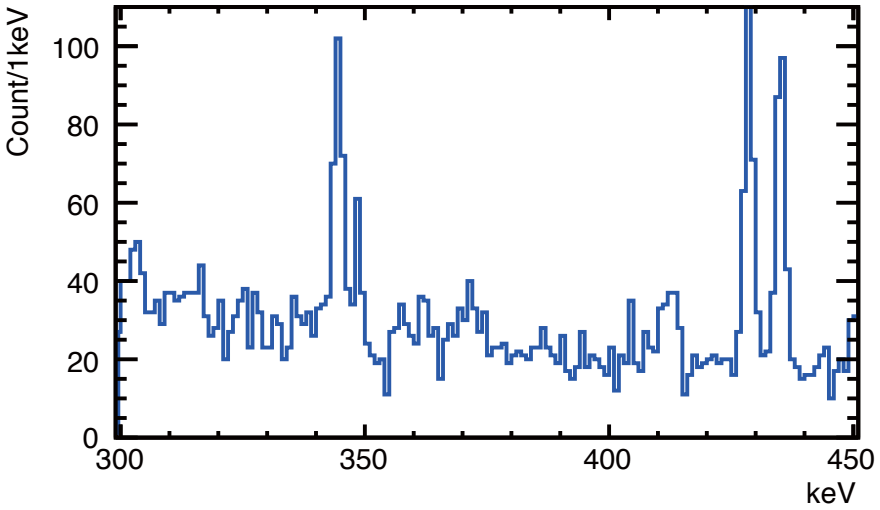

Figure 14.2: *Muonic X-ray spectra taken at PSI. The 2p → 1s muonic X-ray of 346.8 keV is clearly seen.*

In the COMET Phase-I, the germanium detector will be placed about 3.5 metre downstream of the centre of the detector solenoid, as shown in Fig. 14.3, since there will be no open space

for it at the upstream side. The detector will view the stopping target at an angle of 12 degrees to avoid attenuation of X-rays in the iron yoke of the solenoid. The magnetic field strength at this position is about 10^{-2}T, low enough for the normal operation of the detector. For the sake of long term operation, the portable dewar will be detached and the detector will be cooled by a cooler.

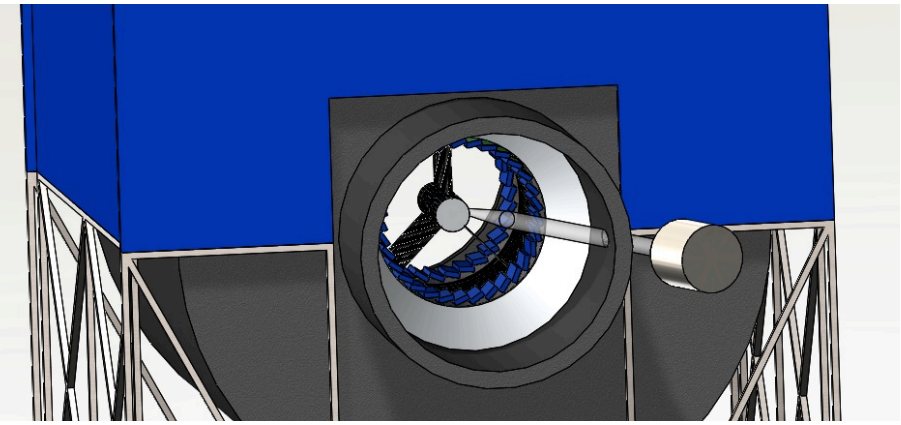

Figure 14.3: *Schematic layout of location of the X-ray detector. A cylinder from the X-ray detector to the target region is drawn to guide the eye, and it is not physical. The hole in the cryostat vessel will have a window for X-rays.*

Calibration of detector acceptance in the proposal above is not trivial because of the long distance from the muon stopping target to the detector, and the target consists of 17 aluminium discs. We plan to build a set up at Technical University of Dresden for this calibration where highly radioactive sources, and a well-shielded irradiation laboratory are available. A mock-up version of the target will be made, the acceptance of the detector with respect to each target disc will be measured by substituing that disc by the radioactive source.

Germanium detectors are known to be vulnerable to fast neutron radiation, and the manufacturer quotes that our detector will show significant deterioration in energy resolution after being exposed to a fluence of 10^{10} cm^{-2}. The neutron fluence at the detector location during the COMET Phase I is expected to be about 10^{12} cm^{-2} - 100 time higher than the tolerance level of the detector. It is clear that a scheme of neutron shielding is necessary. A preliminary design of the radiation shield has been made based on a Geant4 simulation study (Figure 14.4). The shield consist of an thick outer lead layer, a neutron moderation and capture layer and several graded layers to absorb gammas and X-rays (see Table 14.2). The simulation study shows that a 10-cm-thick borated polyethylene is sufficient to reduce the fast neutron fluence by 100 times. The inner graded shield is necessary to absorb 478-keV gammas from the capture of thermal neutrons on ^{10}B.

Possible background contributions to the muonic X-ray measurement with the pulsed muon beam during the $\mu-e$ conversion search are still under investigation, and shielding design in Figure 14.4 are provisional.

14.2. Alternatives

As mentioned above, one of the main concerns is bremsstrahlung generated when electrons in the beam hit the stopping target, as well as other materials. The electrons arrive just before the muons, and produce bremsstrahlung promptly. If the hit rate caused by bremsstrahlungs

Table 14.2: *Compositions of the radiation shield for the germanium detector*

Layer	Material	Thickness (mm)	Weight (kg)
1	Lead	50	320
2	Borated polyethylene	100	37
3	Lead	10	23
4	Copper	10	15
5	Plastic	5	<1
	Total weight		416

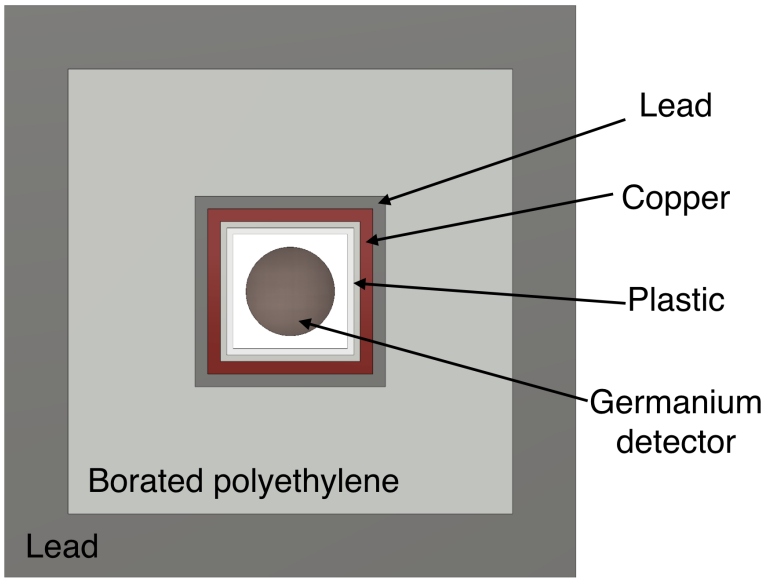

Figure 14.4: *Conceptual design of a shielding system for the germanium detector.*

is higher than 1 MHz, the germanium detector will not be able to work normally. Several other solutions are being considered in preparation for this scenario. These methods will be calibrated against the muonic X-rays method in a dedicated beam time where a reduced beam power will be used.

Cadmium-zinc-telluride (CdZnTe) detector

One way to deal with the high counting rate is using a detector suitable for the environment, namely a pixelated cadmium zinc telluride (CdZnTe) detector. Cadmium zinc telluride is a promising material for room-temperature X-ray detectors with good energy resolution and high detection efficiency. Pixelation will help with high rate tolerance during the beam flash.

Decay-in-orbit (DIO) electrons spectrum

If the background contributions, in particular from photons and neutrons, are serious, an alternative is to use the partial rate and energy spectrum of the DIO electrons. Although the DIO electron spectrum are theoretically estimated [25], it should be measured experimentally to confirm its absolute partial rate at the high energy region.

It is estimated that about 1.3×10^{12} stopped muons are needed in order to measure the DIO spectrum in the range from 80 to 90 MeV/c at 10% uncertainty. That is equivalent to about 4 hours of beam time at 1/10 designed beam power. The germanium detector should be able to function in this environment and will be used to calibrate the DIO rate.

It should be noted that the DIO spectrum will be used for the normalization of the number of stopped muons for the COMET Phase-II, since there will be no place to locate the germanium detector there.

Protons from nuclear muon capture

Also the measurement of protons emitted from nuclear muon capture in aluminum can be used, since the partial branching ratio and the spectrum of the proton emission are being measured precisely by the AlCap experiment at PSI. This can be made as a redundant consistency check on the determination of the muon normalization.

Activation measurement

Another way to count the number of stopped muons is measuring the activities of residual activated isotopes created during the beam time. One candidate is the ^{24}Na ($T_{1/2} = 14.96$ hours), which can be produced via the $^{27}\mathrm{Al}(\mu^-, \nu\mathrm{p2n})^{24}\mathrm{Na}$ reaction. The production crosssection is unknown, but can be estimated from other channels to be about 13×10^{-3} per muon capture. It should be noted that the ^{24}Na can also be induced by other particles such as pions, and neutrons. These contributions should be estimated in order to have an accurate number of stopped muons. The activation measurement would be taken every two days of irradiation.

Chapter 15

Cosmic Ray Veto

Cosmic rays (CR) will be a background source to the $\mu-e$ conversion signal (Section 20.2.5). CR muons can decay in flight or interact with the materials around the area of the muon-stopping target producing signal-like electrons in the detector region. Basic background estimates for the COMET experiment show that the veto system must provide a rejection power of about 10^4 for CR muons. For COMET Phase-I, the area of the cylindrical drift chamber (CyDet) has to be protected against CR to prevent cosmic ray induced backgrounds. The first prototype measurements and dedicated MC simulations indicate that the proposed design is expected to satisfy this requirement.

Both passive and active shielding will be used to protect the region around the detector. The passive shielding consists of concrete—the experiment uses a high intensity beam and must in any case be shielded for this reason—and the iron yoke of the detector solenoid. Low-angle cosmics are also shielded by the surrounding earth as the detector is located underground. This shielding will reduce the flux of cosmic rays significantly.

Active shielding is provided by a scintillator-based veto system, covering the CyDet area. Figure 15.1 shows a cross-section view of the CyDet including the active veto system surrounding the detector area for COMET Phase-I. The length along the solenoid axis is 4500 mm, the width is 4400 mm and the height is 4000 mm from the floor.

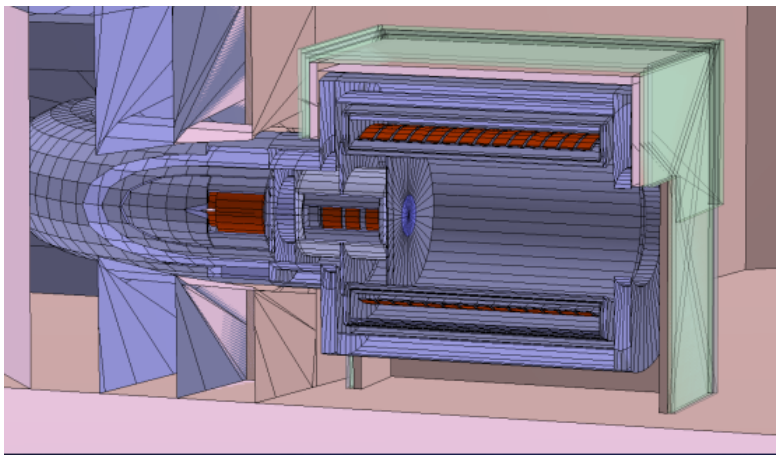

Figure 15.1: *Cross section view of the Cydet including cosmic ray active veto system for COMET Phase-I. The green plates represent the cosmic ray active veto system.*

The veto system consists of 8 supermodules, 2 above the CyDet, 2 on either side and 1 each

for the front and rear ends. The supermodules will be assembled from modules, which will be produced, restrained and transported as a single unit. The modules are formed from 15 scintillator strips placed in parallel. The weight of a module is about 10 kg or less. To provide a high detection efficiency four modules will be installed in each supermodule.

Each strip will have the same profile with a total cross-sectional area of $0.7 \times 4\,\mathrm{cm}^2$ and a length of about 220 cm or 110 cm. They will be made of a polystyrene-based scintillator, produced by Uniplast (Russia), and finished with a matte surface to provide diffuse reflection of light. Each strip is equipped with a 1.2 mm diameter wavelength-shifting (WLS) fibre in a central groove. The fibre is glued into the groove with a special gel, which assures good optical contact between the scintillator and the fibre and hence increases the light collection efficiency.

The fibres are mirrored at the one end and read out at the other by $1.3 \times 1.3\,\mathrm{mm}^2$ active area silicon photomultipliers (SiPMs). We consider two possible types of SiPM: MPPCs from Hamamatsu Photonics and Russian-made MRS APDs. A SiPM is mounted on the strip with a special plastic connector to fix its position and guarantees a small air gap to the fibre.

The proposed strip design has the following advantages over a wider strip with several WLS fibres:

- Light from a MIP is not shared between different SiPMs. This allows for very high efficiency even with a high signal threshold. Our measurements demonstrate the efficiency for a MIP in the worst case of it crossing the far end of the strip to be larger than 99 % for a 7-pixel threshold. As will be shown below, at such a threshold the MPPC noise rate is less than 10 Hz, i.e. below the CR rate.
- It is easier to estimate the efficiency of each strip with cosmic muons using coincidences with other strip signals.
- In case of problems with one channel only a small part of the detector is affected.
- A time resolution of about 1 ns can be achieved.

For each module, the SiPMs are read out with 15 differential preamplifier channels, which allow the signals to be transferred over greater distances. This preamplifier has been tested and a compact 15 channel layout will be developed shortly.

To form each module, both sides of a set of 15 strips are glued to a 1.5 mm-thick plastic support. The insensitive area between strips is about 300 μm for tracks with normal incidence. This corresponds to less than 1% of the total area. Four layers of scintillator strips should provide a perfect geometrical efficiency, requiring signals coinciding in time in at least two layers, due to the single-layer efficiency being greater than 99%. A second layer is then fixed to the first with no additional support. As described above, the layers are shifted by 2 mm in x in order to avoid alignment of gap positions (see Figure 15.2). This installation procedure is repeated for the next two layers, which are shifted by about 3 cm in z to avoid dead zones between super-modules. All four layers will be covered by black plastic to protect strips from external light sources.

Modules are fixed inside the super-modules with u-beam channel bars. Supporting plates are used to align the modules inside a super-module. A shift of about 2 mm between neighbour layers allows us to avoid efficiency losses near the edges of modules. To avoid dead zones, the super-modules will be connected with shifts of layer positions between super-modules and at their ends. A space of 1 cm has to be allocated for SiPMs on one side of each super-module to readout signals.

There are three types of inactive zones in the veto counter: inter-strip gaps, inter-module gaps, and gaps between layers, as shown in Figure 15.2. In the area within a gap the muon signal

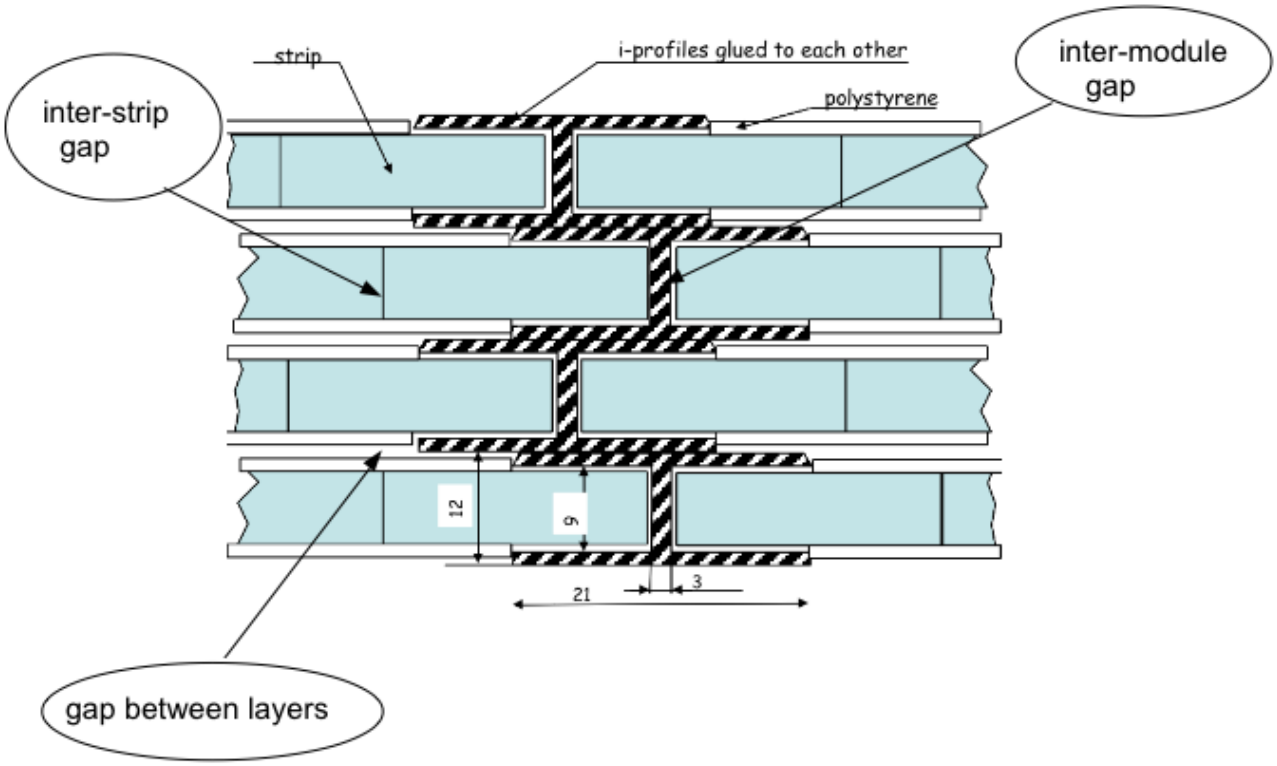

Figure 15.2: *One of the possible strip layouts.*

efficiency falls sharply. The gaps were included in simulation, which demonstrated that despite the inactive zones, muon detection efficiency meets the integrated value of 99.99%, assuming moderate gap sizes.

SiPM noise signals above threshold can cause a fake muon passing signal, resulting in dead time. This is caused by the random coincidence of SiPM noise signals occurring for two layers and within the spatial and time resolution range which would not be distinguishable from the signal of a real muon in these layers. Data from the vetoed windows would be excluded from the physics analysis, while in fact there was no cosmic muon.

Potential problems for the cosmic veto system appear due to a large neutron flux in the experimental hall. The main sources of neutrons are interactions of protons with the pion production target (above 1 MeV) and the beam dump (below 1 MeV). Neutrons cause two problematic effects, which must be taken into account: firstly they can interact with material of strips resulting in a high level of noise signals, and secondly they cause long-term neutron irradiation which can damage SiPMs.

During data taking the noise frequency of SiPMs grows with irradiation by neutrons which damage the p-n conjunction of the SiPMs. It is known that the dark current of the SiPM incrases after significant irradiation above 10^8 neutrons/cm^2 [81], causing noisy response of a detector. However the decrease in SiPM gain is about 50% even after 7×10^{11} neutrons/cm^2 irradiation [81], which allows us to keep the detector efficiency by adjusting the threshold properly.

The evaluation of the time loss caused by SiPM noise has been done for different irradiation doses received by the SiPM. It has been shown, that operating with a threshold level above 7 pixels can keep the fraction of dead time at a level of a few percent. The disadvantage of working at high thresholds is a reduced muon detection efficiency. However, MC simulations of the muon detection efficiency demonstrated that it would still meet the COMET requirements

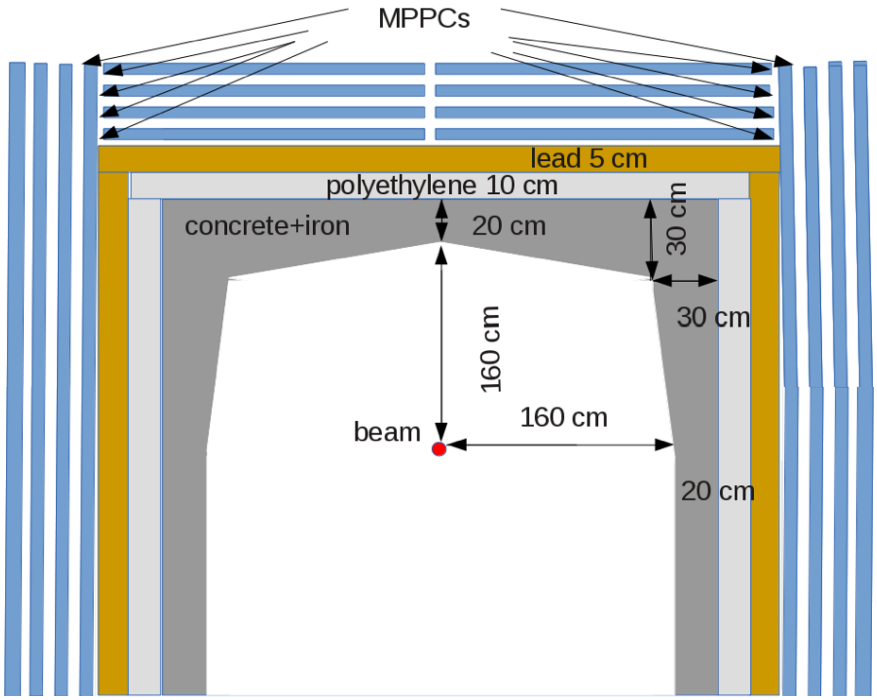

Figure 15.3: *CR veto inner shield with an arched shape (not to scale) showing the read out (in this case SiPMs) locations.*

of 99.99% even at an 11-pixel threshold. On the other hand, both the noise frequency and the neutron detection efficiency are lower when operating at high thresholds, which results in a smaller dead time.

Neutrons are abundantly emitted by nuclei of aluminium of the muon stopping target after muon capture at a rate of $\sim 10^9$ Hz. Signals from background neutrons in the veto counter result in the effective loss of data taking time. The fraction of lost time is determined by the neutron detection efficiency and the neutron fluence at the veto counter. In order to minimize the frequency of neutron signals, scintillator strips as well as SiPMs must be protected against the large neutron flow by an inner shield. Since the spectrum of neutrons from muon captures stretches up to tens of MeV, the shield should comprise layers of different materials: iron, polyethylene and lead that protect against medium-energy neutrons, fast neutrons and hard photons respectively. The optimal configuration of the shield is an arched shape. Such a shape accounts for the signal attenuation along strips and additionally protects SiPMs, which are located at the outer ends of the strips, Figure. 15.3.

In order to develop the design of the inner shield, `Geant4` simulations were performed, which includes details of signal coincidence between scintillator strips, and the time and transverse spatial information from strips were studied. The presence of a 10 cm thick return yoke as well as reinforced concrete as the material of the inner shield were implemented in the simulation. The results show that a mixture of iron and concrete, volume fractions being 0.33 and 0.66, performs quite well. In conjunction with the iron yoke, a shield composed of this mixture, plus polyethylene and lead, drastically reduces the neutron flux at the counter strips. With such a shield, the time loss due to fake veto signals from neutrons in strips can be reduced to a tolerable value of 1% of data-taking using a 40–50 cm thick shield, depending on specific details of composition. The current design is composed of 20 to 30 cm of the iron-concrete mix, 10 cm of polyethylene and 5 cm of lead. Such a shield reduces the flux of fast and more energetic neutrons at photo-detectors by 2 orders of magnitude. Therefore, no substantial decrease in

the photo-detector efficiency is expected throughout the full period of data taking.

Cosmic ray veto system at the Bridge Solenoid area

As discussed in Section 20.2.5, the area of the CyDet has been protected very well by the current design of the CR veto mentioned in the above. However, from further studies it is found that the area of the Bridge Solenoid (BS) is needed to be covered by a veto system (BS-CRV). The area is not large, about 1 meter, and a similar veto system to that covering the CyDet will be deployed. A design study is ongoing.

Chapter 16

Trigger and Data Acquisition Systems

The COMET Phase-I experiment consists of two sets of detectors, the combined Straw Tracker and Ecal (hereafter referred to as the StrEcal) and CyDet, and these are effectively operated and read out independently. They will have two separate data acquisition (DAQ) systems and slow control and monitoring system, although these will have a similar structure and components to keep as much commonality as possible. In addition, there are a few common detector components, such as a beam monitor and an X-ray monitor (to determine the muon beam profile and number of muons captured in the target, respectively) that are needed for both systems. These will be common detectors which have readouts for each DAQ system. If these detectors are operated in parallel the readout needs to be parallelised so that information is duplicated in both streams, and this needs to be taken into account.

The trigger and DAQ system for Phase-I has been designed to be conservative, meaning the hardware is generally not at the cutting edge of available technology and most of it is commercially available, with only a few of the custom components having any significant complexity. It is also designed to be scalable, such that the same concept (and ideally most of the same hardware) can be reused for Phase-II.

Each system consists of six main parts:

The fast control system, which distributes a common clock and all time-critical signals, such as triggers, to all detectors in each system.

The trigger system, which determines when to read out the detectors. This is distributed with a fixed latency.

The readout system, which transfers the event data from the detectors to disk when a trigger occurs.

The configuration system, which transfers data to the detectors to set parameters to control their performance.

The online software to operate the system.

The slow control and monitor system.

Those six systems are related such that the trigger system generates most of fast control system; the fast control system invokes readout system for selected events; the configuration system uses the fast control system hardware; and the online software works all behind of these systems. The fast control and trigger systems are run on common hardware, mainly custom electronics,

using the GBT protocol; the two systems send data in opposite directions. The configuration and readout systems also run on common hardware—in this case based on commercial network components—using ethernet; again, the two systems send data in opposite directions. The slow control and monitor systems are largely independent of these other systems, the main connection required is at the software level. However, the slow control will need to monitor both the custom boards of the readout system, and standard off-the-shelf sensors, and thus needs to be fairly flexible.

16.1. Trigger System

The triggers for the two separate systems are quite different, although in both cases the information is transmitted and processed over the gigabit optical links. The trigger decision along with fast control and timing signals are sent back to readout system through the same links. In the StrEcal (Figure 16.1), the ECAL provides the event trigger. In the CyDet (Figure 16.2), the baseline plan is that Cherenkov trigger hodoscope (CTH) provides the beam trigger, however, considering the high hit rate in CTH, a trigger using CDC hit information is being developed. The cosmic ray detector can provide veto or calibration trigger, as well as be used for debugging of both detectors. In all cases, the trigger is handled by a central trigger processor implemented in the FPGA of an off-the-shelf board.

The trigger system, which is composed of a number of subdetector trigger systems, should be located near the subdetector frontend electronics, or at least near the detector solenoid, to reduce the trigger latency. However, those areas are typically high radiation areas, meaning that the subdetector trigger systems are supposed to be radiation-hard. Conversely, the fast control system is composed of off-the-shelf FPGA board mounted in a commercial crate, of which the radiation-hard design techniques are not applied in most cases. This requires to locate the fast control system at non-radiation area, while at the same time, the distance to the subdetector trigger system should be minimized for smaller latency.

16.1.1 Fast Control and Timing

The fast control and timing systems need to distribute a common clock to all detectors to ensure the data can be correctly aligned offline, and distribute all time-critical signals needed by detectors, such as the trigger, accelerator beam timing, calibration pulses, etc.

Figure 16.1 shows an overview of the implementation of the fast control and trigger components for the StrEcal detector, while Figure 16.2 shows the same for the CyDet. The systems consist of a central trigger processor, currently implemented by a FC7 board [82], which distributes the fast control signals and a 40 MHz clock using the GBT (GigaBit Transceiver)) protocol [83] over fibre. These signals and clock are received by custom fast control and timing (FCT) boards which either pass the signals on to the detector front-end electronics, or interface to trigger boards which in turn connect to the detector electronics. In the latter case, trigger information is passed back to the FC7 using the same GBT protocol. The FC7 then makes trigger decisions based on these data.

FC7 board The FC7 board is a general-use FPGA board supporting multi-gigabit data transfer, designed for use at CMS by CERN (See Figure 16.3). The pre-production version had been available since 2015, and the official production have started in February, 2016. The FC7 supersedes the previous GLIB board [84] which was used for trigger and fast control purpose in CMS

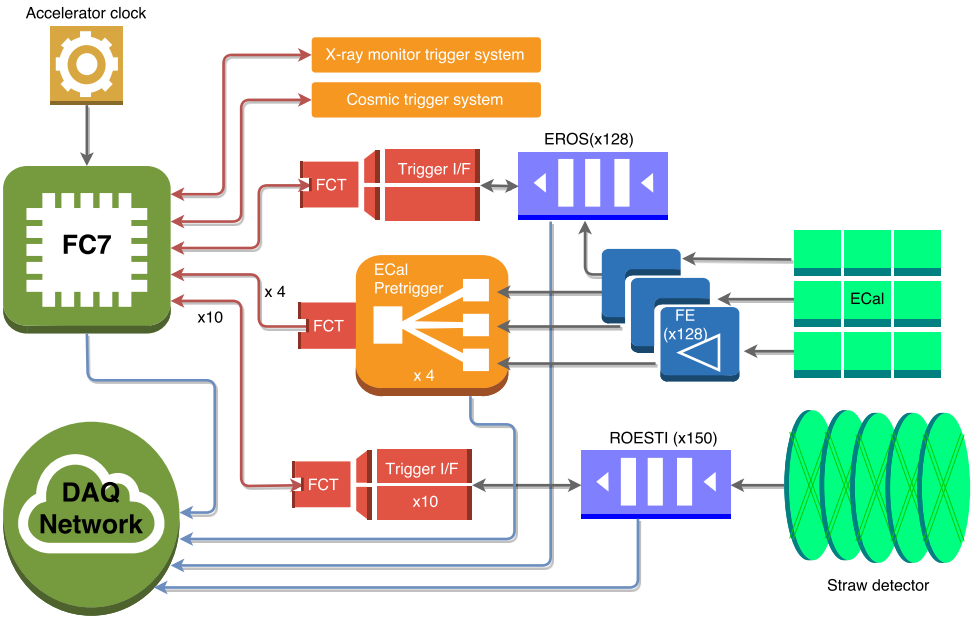

Figure 16.1: *Block diagram of the StrEcal fast control and trigger systems.*

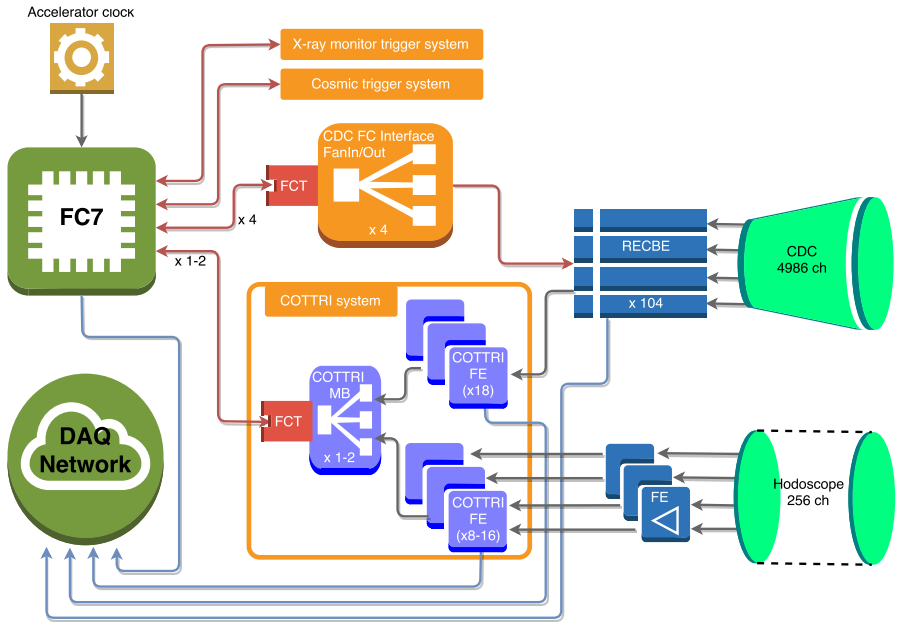

Figure 16.2: *Block diagram of the CyDet fast control and trigger systems.*

experiment. In COMET, it will be used as the source of fast control signal distribution, as well as the central trigger processor. Both GLIB and FC7 boards will be housed in a μTCA [85] shelf and controlled over Ethernet connection. Comparing FC7 and GLIB boards, the FC7 can drive up to 16 GBT links, rather than 8 for GLIB, and has a more powerful Xilinx 7-series FPGA. Consequently, while the previous design of fast control system used two GLIB the new design uses only one FC7 board. This enabled the handling of more complex trigger algorithms and makes implementing the fast control systems significantly easier. Currently, the test setup for fast control and trigger system and performance evaluation uses one GLIB board, which will be replaced to the FC7 board within the year 2016.

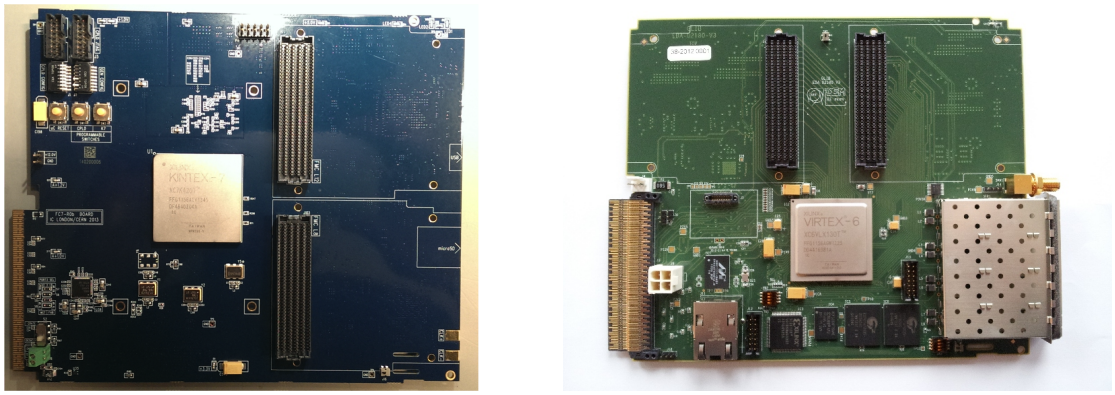

Figure 16.3: *Left: The FC7 board. Each of the large connectors to the right of center takes a mezzanine card with eight SFP connectors, and so eight GBT fibres per connector. Right: The GLIB board. The cage at the lower right houses four SFP connectors for four GBT fibres. The connector at the upper right can take a mezzanine card to allow another four SFP connectors to be used, giving four more GBT links. The connector on the upper left will be used to input the accelerator signals.*

GBT protocol and Fast control signals The GBT (a.k.a. GigaBit Transceiver) protocol is an implementation of radiation-hard data transmission to ASIC chipset and HDL code, used between detector and outside electronics system through optical link and developed by CERN. The GBT protocol provides a fixed-latency, two-way data link, allowing timing signals and data to be transferred with predictable delays. One GBT link sends 120-bit serial data at 4.8 GHz speed, so effectively 40 MHz data frame rate, which enables the 40 MHz clock recovery from the link. Out of 120 bit serial data lines, 84 bits are usable for custom data, and remaining 36 bits are reserved for the packet header and error correction information of GBT protocol. For the outbound link from the FC7, the fast control system will use 14 of the 84 bits, with the remainder allocated for trigger data, firmware loading, and other control or monitors. For inbound link to FC7, 64 bits are allocated for trigger data transfer. The Table 16.1 shows detailed GBT link implementation.

The set of fast control commands which will be sent on the GBT links in COMET are summarized below. Not all signals are required in the consummer board of fast control signals, however, the clock, busy and trigger decision signal are the most important in the readout board.

- The “Trigger” signal is the actual trigger for the experiment. Rather than one single bit signal, the readout system requires trigger number data to distinguish the triggered event. The trigger number will be sent through dedicated 32 bit lines, of which the leading two bits are set to one (to identify the trigger itself) and the remaining 30 bits give the unsigned trigger number within the run, sent LSB first. This number therefore has a range up to around 10^9, which at a 30 kHz sustained average trigger rate would allow runs of up to 10 hours.

- “BeamTime” gives a pulse in time with the nominal beam arrival at the detector; this requires input to the FC7 from the accelerator timing system.

- The “SignalWindow” is generated internally in the FC7. It is high for the duration of the period between beam pulses when signal event triggers will be taken. This will be around 800 ns after the BeamTime and will last for around 800 ns; both the start and end will be configurable.

- The "PreBeamTime" signal is also generated internally in the FC7. It is issued a configurable delay after "BeamTime", intended to be after the signal window but before the next beam pulse. It can be used as a clear signal for any detector which needs to be reset before each beam pulse.

- "SpillWindow" is a line which is high during the beam spill period of around 0.7 s. This again requires accelerator timing information to be input to the FC7.

- "Busy" is a global indicator that no further triggers can be taken. It is an OR of all possible sources of full buffers, etc, throughout the hardware. It is raised by the FC7 for the duration of the transmission of the trigger number (800 ns) after which time other systems should have raised their Busy levels if necessary.

- "HardReset" is intended to generate a complete reset, including reloading FPGAs. This would require the whole DAQ system to be restarted and so would only be used rarely. It is initiated by a software command.

- The two "TimingPulse" signals are generic timing signals under three different frequency domain, 40 MHz, 80 MHz, and 160 MHz This is to allow more precise relative timing of these signals, namely to 6.25 ns, than would be possible on the 40 MHz clock. Their use would be for generating calibration signals to test front-end electronics, etc. The two signals have identical functionality and both are provided for cases where two precise timing signals are required. They are generated by the FC7 and their times and lengths are configurable.

FCT board The FC7 GBT links are each received by the FCT board, which is a FPGA board with GBT implementation on it, intended to be located inside the high-radiation area and connecting to FC7 via GBT link. The FCT board provides a standardized interface and serializing/deserializing, between the GBT timing and data protocol provided by the FC7, and the specific needs of each detector. It also provides an interface to the readout system for all the trigger electronics. One FCT board handles one GBT link, meaning 10 FCT boards are needed for the StrEcal and 14 are needed for the CyDet. The FCT FPGA firmware will be able to be reprogrammed in situ using the GBT link from the FC7. The FCT board is common to both the StrEcal and CyDet DAQ and trigger systems and will be used by all subdetectors in each system. A prototype of the FCT board is shown in Figure 16.4.

Each FCT board is connected via the FMC connector to a detector-specific board. These provide the interface for the required signals for each particular detector, fanning out clock and control to all the readout electronics of each detector and gathering any BUSY signals when necessary to prevent further triggers. Some interface boards also gather the trigger information for transmission to the FC7 (see below). In most cases, these boards are reasonably straightforward and do not require FPGAs. These boards will have an identifying number hardwired into their connectors, allowing the FCT board to know which detector it is handling. The FCT and detector board will have one pair of Multi-Gigabit Transceiver (MGT) link and its clock connection, as a high bandwidth backup. For example, the trigger number from FC7 handed downto FCT can be transmitted to ROESTI board through MGT link. The signal definition of FMC connector are summarized in Table 16.2.

Table 16.1: *List of GBT links for FC7 and FCT.*

Direction	Name	Number of GBT lines
Outbound	Fast control: Trigger	1
	Fast control: BeamTime	1
	Fast control: SignalWindow	1
	Fast control: PreBeamTime	1
	Fast control: SpillWindow	1
	Fast control: Busy	1
	Fast control: HardReset	1
	Fast control: (Spare)	1
	Fast control: TimingPulse0	3
	Fast control: TimingPulse1	3
	(Spare)	2
	Trigger event number	32
	Generic write interface	16
	FCT control command and data	20
	Total Outbound	84
Inbound	Status flag: FPGA fault	1
	Status flag: Wrong board ID	1
	Status flag: Busy	1
	Status flag: Data line active	1
	FCT control and status data	16
	Trigger data	64
	Total Inbound	84

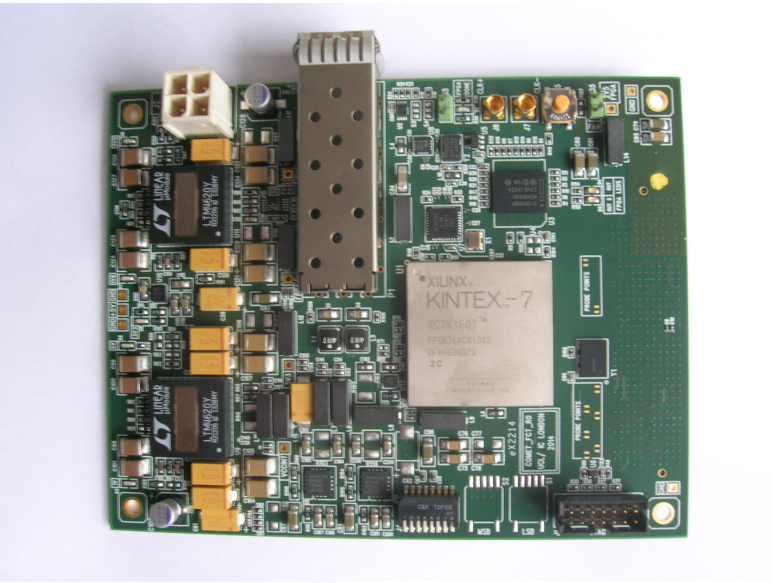

Figure 16.4: *Photograph of the prototype FCT board. The SFP+ housing for the GBT fibre is at the upper left and FPGA is to the right of this. The empty space along the right edge is for the 400-pin FMC connector, which is mounted on the opposite side of the board.*

Table 16.2: *The signal definition of FMC connector at FCT, which corresponds the data between fast control / trigger system and the readout or subdetector trigger system. FCT is assumed starting point of signal, therefore, the direction "Out" or "In" means the signal from FCT to detector board, or from detector board to FCT, respectively.*

Use	Name	No. of bits	Direction	Format	No. of pins
Fast control	40MHZ clock	1	Out	LVDS	2
	80MHZ clock	1	Out	LVDS	2
	160MHZ clock	1	Out	LVDS	2
	Trigger	1	Out	LVDS	2
	Beamtime	1	Out	LVDS	2
	Signal window	1	Out	LVDS	2
	Pre-beamtime	1	Out	LVDS	2
	Spill window	1	Out	LVDS	2
	Busy	1	Out	LVDS	2
	Hard reset	1	Out	LVDS	2
	Timing pulse	6	Out	LVDS	12
Configuration / generic interface	Generic read	8	In	LVDS	16
	Generic write	8	Out	LVDS	16
	FMC JTAG	4	In/Out	Single-end	4
	FMC MGT	3	In/Out	LVDS	6
Status	Detector board ID	8	In	Single-end	8
	Status	4	In	LVDS	8
	Trigger data	64	In	LVDS	128
	FMC presence	1	In	Single-end	1
Others	Power				11
	GND				159
	Not connected				11
Total					400

16.1.2 StrEcal trigger

The ECAL consists of up to ∼2000 crystals in an approximately circular array. The trigger is required to give a good time resolution (to keep the readout windows around the trigger time as narrow as possible) and good energy resolution (so as to select energy clusters in the signal region rather than background). Since the energy deposition will be divided among several crystals, it is necessary to do a summation over crystals to reconstruct the full energy. The necessary size of the summation area depends on the radius of the showers to be triggered on (i.e. the planar distance around the entry point where most of the energy is reliably contained). At energies of $\sim 100\,\text{MeV}$, the necessary radius is somewhat smaller that the lateral size of the ECAL crystals. Thus, if we take the sum of 4×4 crystals, when the particle enters in the middle 2×2 crystals, effectively all the energy will be included. It is therefore proposed to select the basic trigger unit (cell) as a group of 2×2 crystals (corresponding to one crystal module of the ECAL), and to determine the total energy by using the sum of an array of 2×2 trigger cells (i.e. 4×4 crystals). All possible combinations of the sums of 2×2 trigger cells will calculated and the maximum energy found in one of these combinations will be used. This is illustrated in Figure 16.5.

A trigger condition would correspond to an energy deposition in the signal window E_{min} (for

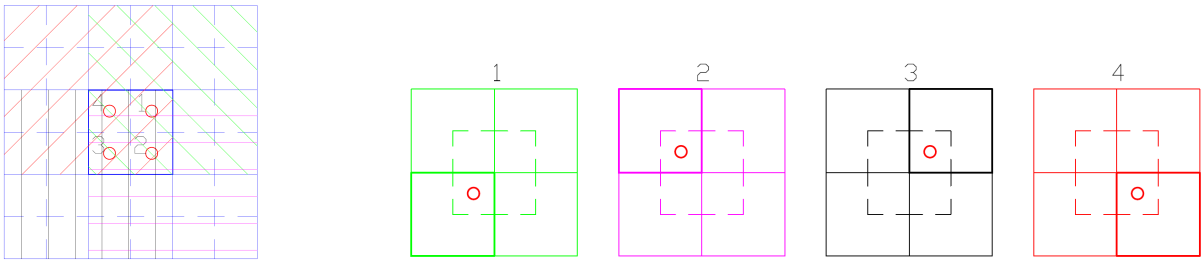

Figure 16.5: *Crystal regions which are summed within the ECAL trigger. Left: Illustration the entry point of particle (red dot) in the trigger cell (2 × 2 crystals) and the summation areas (4 × 4 crystals). Right: Illustration of the calculation of all possible combinations of the trigger cell (2 × 2 crystals) and their summation areas.*

example, 95 MeV) $<$ E (around 105 MeV) $<$ E_{max} (for example, 115 MeV). However, energy deposits outside this window, such as between 85 and 95 MeV, would also be used for triggering, with a prescale factor so as to only trigger after a fixed number of such trigger conditions. Hence, sufficient information to allow the FC7 trigger processor to make such triggers must be provided. Since 64 bits are assigned for trigger data between FCT and detector electronics system, the trigger data sent from ECAL to central trigger system can be composed of a energy histogram, trigger cell information with the highest energy deposition, and other diagnostic information, as defined in Table 16.3.

Table 16.3: *The trigger data from ECAL to central trigger system.*

Definition	Bits	Note
E(highest energy trigger cell)	8	
ID of the highest energy trigger cell	4	
N(trigger cell; $E > (10 - 20)$ MeV)	4	All trigger cell with hit
N(trigger cell; $E > (30 - 40)$ MeV)	4	Median threshold
N(trigger cell; $E > (70 - 80)$ MeV)	4	DIO core and CE
N(trigger cell; $E < 90$ MeV)	4	DIO core and background hits
N(trigger cell; $90 < E < 95$ MeV)	4	DIO tail
N(trigger cell; $95 < E < 100$ MeV)	4	DIO tail
N(trigger cell; $100 < E < 104$ MeV)	4	DIO tail and CE tail
N(trigger cell; $104 < E < 106$ MeV)	4	CE core
N(trigger cell; $106 < E < 110$ MeV)	4	CE tail
N(trigger cell; $110 < E < 200$ MeV)	4	Sideband for continuum background
N(trigger cell; $E > 200$ MeV)	4	High energy background particle
Diagnostic information	8	
Total	64	

Detailed structure of ECAL electronics system is shown in Figure 16.6. The trigger electronics will be implemented using custom PCBs. The analog adder for energy summation of trigger cell will be located on the frontend card. The signal of the trigger cell is formed in the preamplifier by analogue summing. Therefore, as outputs from each preamplifier, there are 16 signals (one per crystal) going to the digitizing readout board and 4 signals (one per trigger cell) going to a dedicated pretrigger board, where they are also digitized. The pretrigger board will be located several meters away from the frontend card, outside of the detector solenoid. The total diameter of the ECAL for Phase-I is not yet known, but it will be too large for a single PCB

to cover its back surface, so four trigger board PCBs will be used, each covering one quarter, as shown in Figure 16.7. To avoid any inefficiency at the edges of these quadrant PCBs, it is necessary to transmit around 15 analogue trigger cell signals from one board to the next. In this baseline ECAL design, a quarter of ECAL is occupied by 6 of 4×4 trigger cell modules, plus 6 of 2×2 trigger cell modules, so in total, 120 trigger cells. Therefore, total number of ECAL trigger cells is $120 \times 4 = 480$, which corresponds to 1920 crystals of ECAL baseline design. The detailed map of the transmitted signals will be determined later considering above trigger cell allocation map.

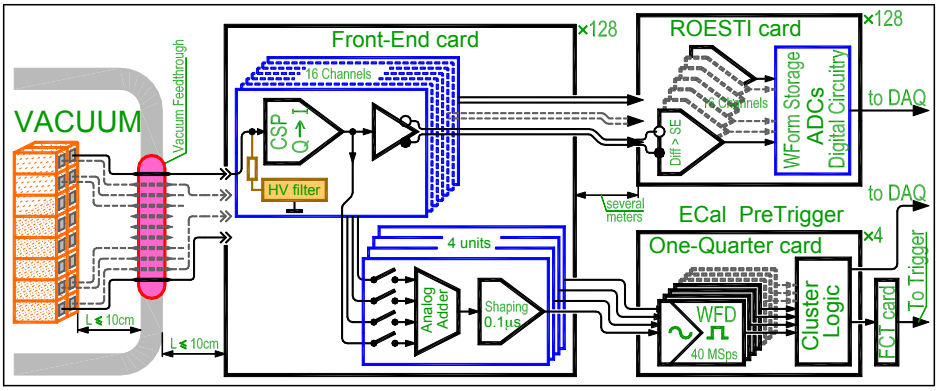

Figure 16.6: *The electronics system for ECAL.*

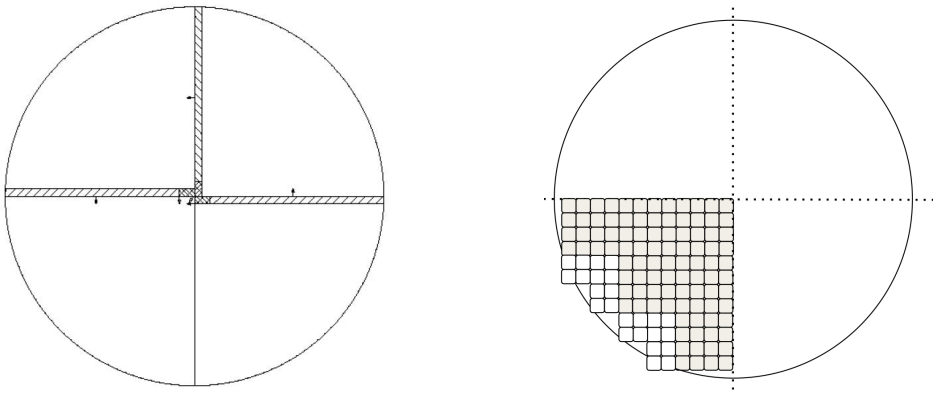

Figure 16.7: *Left: Conceptual diagram of the four quadrant ECAL trigger PCBs mounted on the rear of the ECAL. Right: Conceptual trigger cell allocation for a quadrant of ECAL.*

ECAL Pretrigger board The ECAL pretrigger boards will digitize analogue signals from the trigger cells and pass the resulting waveforms through some filters, implemented in an FPGA. Following the filtering, the digitized waveforms passed are then summed into four groups (i.e. each containing 16 crystals) in the FPGA. From these, estimates of the energy and time of the clusters in the ECAL will be calculated. These act as the trigger primitives.

Each pretrigger board for a quarter of ECAL will have an FMC connector to interface to an FCT board. The FCT board will supply the 40 MHz detector clock to the trigger board to enable the ADC digitizations to be synchronized. It also collects the trigger primitives and transmits them to the FC7. Hence, the energy and numbers of the activated trigger cells consistent with

each 40 MHz clock period will be sent to the FC7, which will then impose a trigger condition on them for each clock period. The whole trigger must work with fixed latency and fit within the required latency budget.

Large PCBs can have problems with component reliability and clearly make spares expensive. Hence, almost all analogue components and the ADCs will be implemented on small daughter boards, with the large PCB being mainly passive, although it will hold the signal processor FPGA. The prototype pretrigger board is equipped with 20 mezzanine digitizer cards, with 8 channel, 10-bit, 40 MSPS ADC, which receive analog energy sum signals of 8 trigger cells (i.e. 32 crystals) and digitize them. Therefore, each pretrigger board can handle $20 \times 8 = 160$ trigger cells, which is sufficient for a quarter of ECAL (120 trigger cells). A conceptual design of the final mezzanine PCBs is shown in Figure 16.8, where the prototype pretrigger board is shown in Figure 16.9.

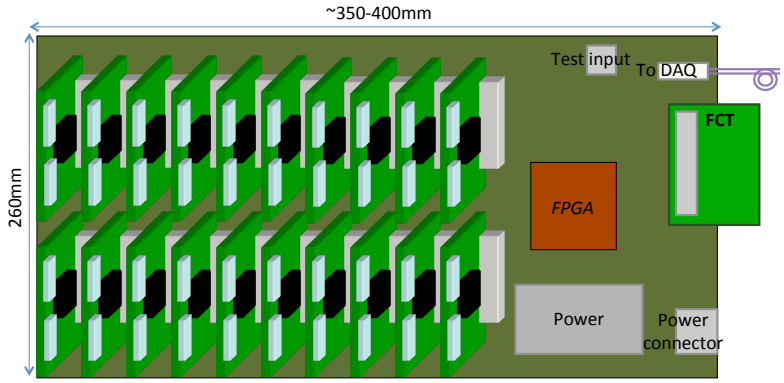

Figure 16.8: *The conceptual design of ECAL pretrigger board. One pretrigger board contains 20 digitizer mezzanine modules, each of which digitizes 8 channels.*

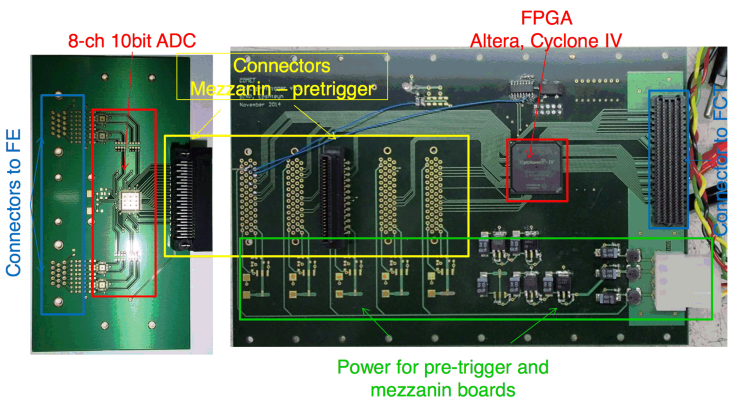

Figure 16.9: *The prototype version of ECAL pretrigger board.*

Other trigger system in StrEcal The StrEcal cosmic trigger is needed for tests and calibrations when not running with beam. This will be based on the cosmic veto system and simple coincidences of hits in different layers of bars close to each other should be sufficient. It will be necessary to implement discriminators and some OR logic on the detector before sending the resulting logic levels to the trigger. The cosmic veto trigger should be very fast as there is little logic and the scintillator signals are fast. Hence, the trigger latency will be larger for the ECAL trigger. Because the cosmic veto trigger and the ECAL trigger will have different latencies, the GLIB will have a configurable delay on these triggers so that they are aligned to a fixed latency, independent of the trigger type.

The straw detector system does not provide any trigger primitive in the current baseline design. It is linked to FC7 system to receive fast control and central trigger decision so that the readout board (ROESTI) can issue selected data transfer to DAQ system.

Latency estimation For the StrEcal detector, the upper limit on the latency requirement is assumed to be set by the ROESTIs. They contain a 1k deep analogue buffer which is filled at 1 GHz and so fills in 1 μs. For a particle passing close to a sense wire, there is effectively no drift time and hence relevant data will be lost if the trigger does not arrive before these data reach the end of the buffer. There must also be allowance for the signal spread and trigger jitter, as well as ensuring that a background hit just before the event is seen, so a sensible latency maximum is 800 ns, while the aim will be to achieve a conservative target of 700 ns. A preliminary estimate of this for the ECAL trigger indicates that 700 ns should be feasible, as shown in Table 16.4.

Table 16.4: *Estimate of latency of StrEcal detector ECAL trigger.*

	Source	Time (40 MHz clock periods)	Time (ns)	Total time (ns)
ECAL specific	ADC latency	8	200	200
	Transfer from ADC to FE FPGA	1	25	225
	Peaking time	4	100	325
	FIR calculation	1	25	350
	Clustering	2	50	400
	Histogramming	1	25	425
Common	Interface to GBT	1	25	450
	Transfer on FO to GLIB	2	50	500
	Interface from GBT	1	25	525
	Trigger decision in GLIB	1	25	550
	Interface to GBT	1	25	575
	Transfer on FO to detectors	2	50	625
	Interface from GBT	1	25	650
	Internal processing on detectors	1	25	675
Total		27	675	

16.1.3 CyDet trigger

Baseline plan with CTH In the baseline plan for the CyDet trigger, the Cherenkov Trigger Hodoscope system (CTH) provides the trigger primitive. The CTH consists of double planes,

each containing a Cherenkov radiation counter and a scintillator counter, both read out with fine-mesh PMTs. There are two rings of double planes, one at each end of the CDC, and there are 64 planes in each ring, giving a total of 128 channels per ring and so 256 channels in total. The trigger condition for the hodoscope is generally a coincidence of two hits in the counters. For triggers during beam running, these would normally be from the two counters in the same double plane. However, the trigger should also allow for a coincidence in the counters of neighboring planes to catch particles which scatter or bend in the magnetic field, and so hit one layer in each of two planes. Examples of these triggers are shown in Figure 16.10. In all cases, both for beam and cosmic triggers, the times of the hits may vary between counters due to differences in cable lengths, threshold slew, etc. Hence, there must be some allowance for time-offsets in forming coincidences.

The signals from fine-mesh PMT need to be amplified and discriminated. One frontend amplifier board (Figure 16.11) will be attached to each fine-mesh PMT, and the amplified signal will be digitized and discriminated using a COTTRI board. The COTTRI board is described in detail below. The jitter-adjusted digital signal for CTH trigger will be sent from COTTRI to the FC7 board, the central trigger system.

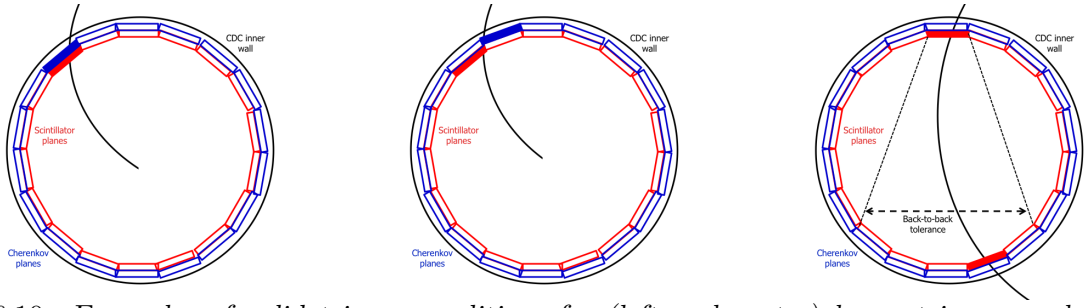

Figure 16.10: *Examples of valid trigger conditions for (left and center) beam triggers and (right) cosmic triggers. The last of these indicates an example of the range of back-to-back matching which might be required by the trigger. These diagrams have only 18 hodoscope planes for clarity (compared with 64 in the actual detector), with the inner scintillator layer in red and the outer Cherenkov layer in blue.*

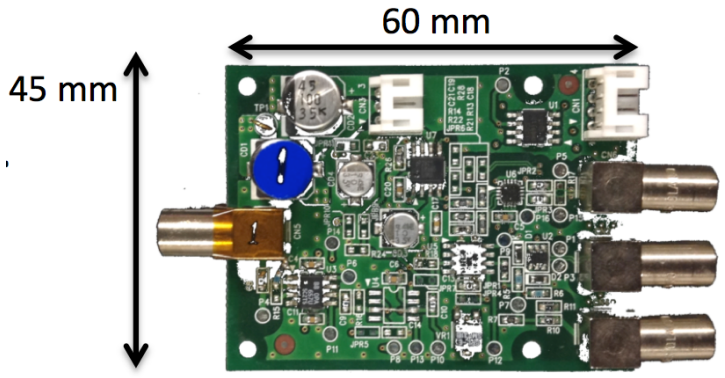

Figure 16.11: *The prototype CTH frontend amplifier board.*

When the CTH generates a trigger pattern, the signal goes to FC7 and (assuming the system is not in a Busy state, and taking into account any prescales) it issues a trigger that is distributed to CDC through fast control system to process readout. The CDC readout is performed using 104 RECBE boards (see Sec. 13.2.5 and Ref. [86]), Each RECBE board has an RJ45 "Belle2Link" connector which must receive the 40 MHz system clock and trigger to

allow the board to operate. It is assumed that it can also receive a TimingPulse to operate an on-board electronics calibration pulse. The RECBE board has no deadtime following each trigger. However, the data are stored in a finite number of event data buffers before being read out. When all buffers are in use, there must be no further triggers and it is assumed that the RECBE board raises a Busy signal during these periods; this must be returned to the fast control within less than 800 ns after the trigger (the FC7 trigger deadtime) to ensure there is no possibility of another trigger. It is assumed that this Busy signal is available externally in LVDS format on the same connector.

The interface between the fast control system and the RECBE boards will consist of four of the CDC interface boards. A conceptual layout of the interface board is shown in Figure 16.12. It is assumed that each interface board will handle up to 32 Belle-II boards and so the four interface boards can handle up to 128 Belle-II boards (compared with the expected 104 boards), allowing for spare channels in case of faults. The interface boards will have an FCT board as a daughter board to deliver the clock, trigger and time pulse and to collect the Busy signals. It will also have 32 RJ45 connectors to take short cables from the board, with each cable going to one Belle-II board. Only 27 out of the 32 connectors will be needed per interface board. The interface board will fan-out the 40 MHz clock, trigger and time pulse signals to each connector and gather the returned Busy signals into the FCT board, therefore, this consists 4 links between FCT and each RECBE. This allows the OR of all the Busy signals to be implemented in the FCT board FPGA and then returned to the FC7. There will also be a 32-bit mask register in the FPGA to allow the Busy signal of any faulty or unconnected channels to be disabled. This mask will be programmed through the FCT board.

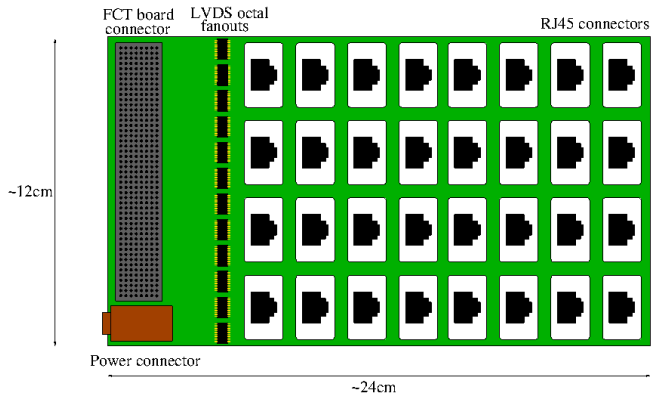

Figure 16.12: *Conceptual layout of the central drift chamber fast control interface board.*

Conceptual trigger design using CDC hit information From studies of COMET simulations, the trigger rate from CTH was found to be very high, around 500 kHz, mostly due to the background hits from beam. Because the CTH does not provide information to discriminate between CE or DIO electrons and background particles, it is necessary to use CDC hit information to reduce the trigger rate to a manageable level by avoiding triggering from background particles. The track patterns for CEs or high momentum DIO electrons are quite different from low momentum particles, which are distinguishable by the radius of helical trajectories in CDC. A full hardware level reconstruction of these helical trajectories is time-consuming and cannot supply fast trigger signals. However, a simple combination of hit pattern and energy deposition can yield sufficiently fast trigger with high efficiency and background rejection power, resulting in a manageable trigger rate of a few kHz.

To use CDC hit information in trigger, it is necessary that the CDC frontend electronics provide fast hit information. The precursor Belle-II CDC board design was capable of providing discriminated hit information through an optical link. The optical transceiver was removed in the later RECBE board due to the production cost, however it is still possible to provide such fast hit information for further trigger processors by applying the relevant firmware functions in the FPGA, and attaching an appropriate connector. The current RECBE firmware is designed to be capable of applying selection on the charge of CDC wire hit, to reject hits from low energy background electron as well as highly ionizing heavy particle such as proton. The 'hit' wire information from this selection will be sent from RECBE to the next level of trigger processing.

In order to reject CTH triggers from background particles, the discriminated CDC hit information requires further processing to find patterns corresponding to high momentum tracks, or to combine with CTH hit information. This requires another detector-level trigger processor board which is capable of receiving hit information from a large number of CDC channels, making a detector-level trigger decision, and communicating with the central trigger system of the FC7 through the GBT link. The COTTRI (COmeT TRIgger) board is designed for this purpose.

The proposed trigger algorithm using COTTRI is visualized in Figure 16.13. Once the CTH provides trigger, the COTTRI system searches the CDC wire hits near the CTH hit and count the number of the CDC hit region. If required, a simple track reconstruction can be performed using those CDC hits. Based on these features, the COTTRI system makes a trigger decision and sends it to the central trigger system as well as relevant CTH and CDC hit information. The final trigger word communicated to the FC7 consists of 64 bits which should be more than enough to encode the information required to make a trigger decision, as shown in Table 16.5.

Table 16.5: *An example of COTTRI trigger output.*

Definition	Bits
Number of CTH hits	8
Number of CDC hits	13
Number of CTH hits with CDC coincidence	4
Number of CDC hits with CTH coincidence	10
Diagnostic information	29
Total	64

A more sophisticated algorithm is also being pursued and is described in Sec. 16.1.3. This makes greater use of the energy depositions in the CDC and is expected to be more selective. Such an algorithm would likely require more detailed state information from the RECBEs, so the granularity and complexity that can be achieved will depend on the bandwidth available across the trigger system. Further study of this approach will need to be done once development of the COTTRI and RECBE firmware is more advanced.

The COTTRI board The COTTRI system is divided into the frontend boards (COTTRI FE) and a mother board (COTTRI MB), which is shown in Figure 16.14. The FE for CTH and CDC application can be different boards sharing the same FPGA architecture and communication protocol to the MB, however, different processing algorithm of incoming data and the its connection protocol. The COTTRI FE performs the initial processing of analog or digital trigger signal, when the COTTRI MB combines all detector trigger signals to generate higher level trigger signal which will be sent to the central trigger system and distributed to

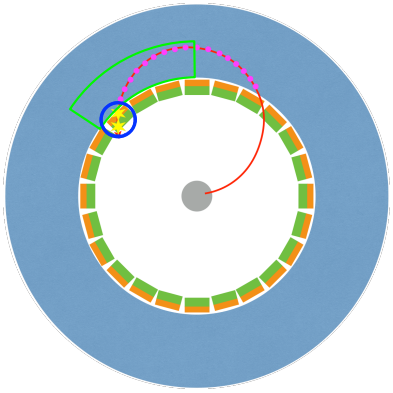

Figure 16.13: *Trigger concept using COTTRI system. The CTH hit (shown in blue circle) information is sent to COTTRI system. Next, the CDC region (green arc box) near the CTH hit is defined, and the CDC wire hits (magenta circle) inside this region are counted. The track (red line) is reconstructed if necessary. The COTTRI system decides on a trigger request using these information.*

the detector readout system. The conceptual design of COTTRI FE and MB are shown in Figure 16.15.

For use with the CTH, the FE board digitizes the amplified analog signals from CTH, applies discrimination, and sends the digitized trigger inputs to the MB. The 100 MSPS 8-bit, 16 or 32 channel ADCs are equipped for analog signal digitization. The FPGA will perform digital discrimination and generates digital trigger signal. Assuming 16 channels can be processed by a single FE, 16 COTTRI FE boards will be required to process CTH signals. Those will be located inside CTH support structure, therefore, a radiation hard design is necessary.

For CDC application, the digitized hit information is multiplexed and sent to the MB. The FPGA will be capable of handling 16 multi-gigabit transceivers, and one is reserved for SFP connector to communicate with a readout system. Two multi-gigabit transceivers will be assigned for each of 6 RECBE connections, which means 18 FE will be required to process 104 RECBE board trigger signals. Those boards will locate inside the CDC readout box.

The number of COTTRI MB will be one or two depending on the number of FE boards. It will have three slave FPGAs, each of which will have connection with 6 FEs. The slave FPGA multiplexes the incoming trigger signal and the master FPGA will have an implementation for trigger processing, trigger decision and the control of slave FPGAs. The connection protocol between FE and MB is under study with a few options such as DisplayPort [87], Ethernet, or InfiniBand [88]. All of these protocols are capable of multi-gigabit serial data transfer. Another option under investigation on COTTRI MB functionality is to use multiple "slave" FC7 boards which collects CDC trigger information from COTTRI FB, and communicates with "master" FC7 board of central trigger processor.

Performance estimation For the baseline CyDet trigger system, the trigger latency mostly comes from the signal transmission between FC7 and COTTRI (for CTH signal digitization) and the digitization time in COTTRI. The latency from transmission is estimated to be around 300 ns, but the COTTRI digitization time is not estimated yet. For the CyDet, the required trigger latency is around 5 μs, due to the buffer size of RECBE (8 μs). Table 16.6 summarizes current estimation on the latency of CyDet system.

Because of the buffering of data in the RECBE system, there is no significant jitter requirement on the trigger to retain data. The buffers are long enough that data will not be lost within any

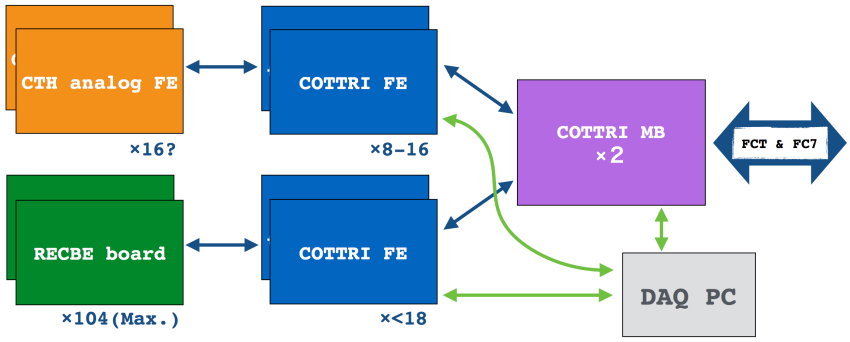

Figure 16.14: *Conceptual design of COTTRI system.*

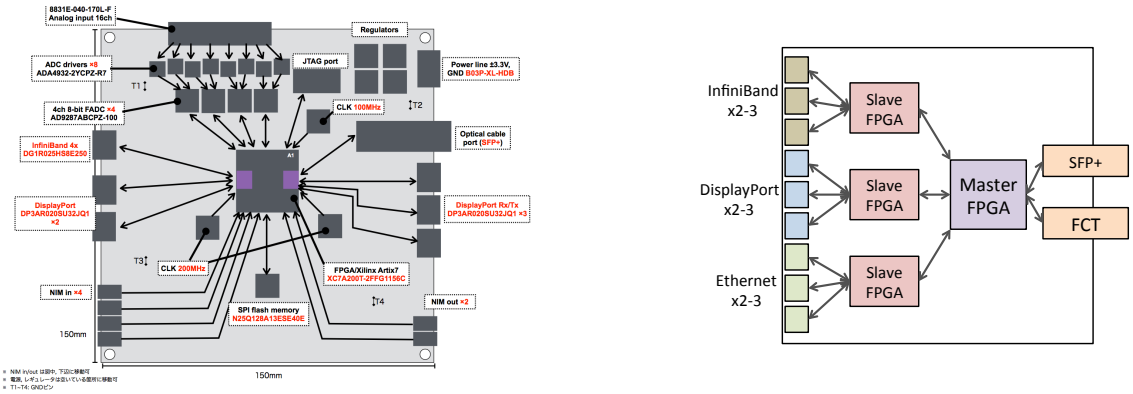

Figure 16.15: *Left: Conceptual design of COTTRI frontend board (FE). Right: Conceptual design of COTTRI mother board (MB).*

reasonable jitter, such as ±1 clock period. However, the result of such jitter will increase the required width of the event data window retained for readout. This then contributes directly to the data volume read out and hence can impact the event data rate of the system.

Table 16.6: *Estimate of latency of CyDet detector trigger with COTTRI system.*

Source	Time (ns)	Comment
CTH to COTTRI FB	< 25	
ADC processing in COTTRI FE	80	8 clocks at 100 MHz
Processing in COTTRI FE	20	4 clocks at 200 MHz
COTTRI FE to MB	< 200	Depending on protocol
Processing in COTTRI MB	$25 - 250$	Depending on algorithm
FCT – FC7 – FCT	250	StrEcal estimation
FCT to RECBE	10	
Total	$385 - 835$	

CyDet Track Trigger

Current estimates show that the data rates for the CyDet are higher then the hardware can handle. A further 10–100 times suppression is needed. Due to this time constraint, a Bonsai

Boosted Decision Tree (BBDT) [89] is being used, which is a Boosted Decision Tree (BDT) [90] classifier optimised for quick classification. The algorithm begins by classifying each wire as signal or background. It then analyses these results on the layer level and passes one to two features per layer that describe their signal hit content. The final decision is made using these values. While the current algorithm shows promising results, further development and optimisation is still needed. For a more in depth introduction to machine learning in the CyDet detector, including a description of the events used here, see Section 13.5.1

Bonsai Boosted Decision Tree While gradient boosted decision trees are powerful classifiers, a highly efficient algorithm is needed to perform well in an online environment. A Bonsai Boosted Decision Tree aims to speed up classification by reducing the complexity of the possible set of features. This is done by rebinning features on each hit wire into much coarser values. To demonstrate this technique, consider binning a continuous feature such that all possible values falls into one of ten bins. Doing the same for two other features would yield 1,000 possible unique sets of feature values, i.e. a factor ten for each rebinned feature. Each hit wire must be described by one of these feature sets.

A boosted decision tree is then trained over these rebinned features and its response to each possible combination is stored in a lookup table. Classification then becomes a matter of determining the rebinned feature set of a given wire and finding the corresponding BBDT response in the lookup table. Rebinning the feature space comes at a price, as the distinction between background and signal is harder to determine in a coarse feature space. With that said, the number bins and the location of their edges offer a great deal of control over this information loss, as well as the corresponding speed up of the classifier.

Wire-Level BBDT The online trigger BBDT starts at the wire level by defining four local features for classification. These features are the energy deposition on the wire, the energy deposition on either of the neighbouring wires that are in the same layer and the radial distance of the layer from the beamline. Noting there are 18 layers, the radial distance is already "binned," although further rebinning is possible. Denoting the energy deposition on wire j as e_j, the energy features are rebinned to define binned energy b_j as follows:

$$b_j = \begin{cases} 1 & : \ 0 < e_j \leq 5 \text{ keV} \\ 0 & : \ e_j = 0 \ \text{ or } \ e_j > 5 \text{ keV} \end{cases} \tag{16.1}$$

This binary binning scheme results in the smallest number of possible energy-feature combinations. The size of the resulting lookup table is $2 \times 2 \times 2 \times 18 = 144$ entries, where each energy feature contributes a factor of 2, and the radial distance contributes a factor of 18. This performance increase is further enhanced by the ability to analyse each layer in parallel on different processing units in the online environment. In this instance, 18 different lookup tables can be defined, each with 8 entries. The features themselves could be defined using only 3 bits, which minimises the overhead of passing energy information to the relevant processing centres. This also minimises the information that would need to processed, as all three energy features are pooled from the same set of energy deposition data.

This rebinning scheme shows a substantial performance improvement over using only the energy deposition on the wire. A simple cut defining hits with $b_j = 1$ as signal removes 83% of background while retaining 99% of signal. Once the neighbouring bins and radial distance are considered, this performance improve to 93% background suppression at 99% signal retention. The ROC curves in Figure 16.16 give a more detailed breakdown of performance in terms of achievable background rejection rates and the corresponding signal retention rates. From

these curves, it seems the rebinning procedure has little effect on the high signal retention region, while incurring a small penalty for signal efficiencies less that 95%. Overall, the wire classification performs well enough to continue to the layer level.

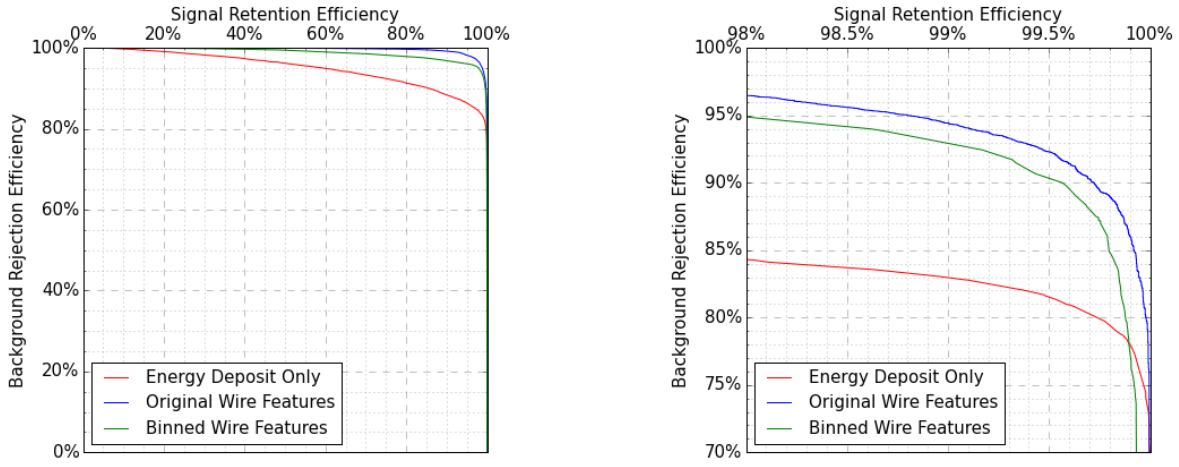

Figure 16.16: ROC curves for three independent classifiers of wire-level BBDT, in full scale (left) and zoomed scale (right). The red curve is from a BBDT trained on energy deposition alone, the blue curve is from the unbinned wire-level features, and the green curve is from the rebinned wire-level features.

Layer-Level GBDT In an online environment, long-range hit structure can be quickly recovered by analysing the varying distributions of signal-like hits across groups of wires. This can be tuned to match the architecture of the readout hardware, such that each group is analysed in parallel. Currently, the algorithm groups the wires by layer, although this will be updated to match the wiring and structure of the readout hardware. Each layer is able to classify all the hits it contains as signal or background using the wire-level BBDT, and return a smaller set of features describing the layer. The current algorithm returns the sum of the BBDT output across all wires in the layer. This feature space has not been explored fully, but ideas for future development include returning the longest chain of hits, the sum of the BBDT output on the longest chain of hits, and other similar features.

Performance A GBDT is trained on the sums returned from each layer, with each sum defining a feature. While a GBDT will not be possible in a live environment, it serves as a good performance benchmark for this early stage of development. Figure 16.17 shows ROC curves from GBDTs trained on the sums from all of the layers and sums from only the nine inner most layers. While statistics are low, it is clear that there is little to no performance hit from only considering the values returned by the inner most layers. With that said, this may bias the signal acceptance towards tracks that only enter the inner layers. Careful considerations must be taken in future studies to ensure these biases are avoided. As of now, this algorithm can produce a factor 20 background suppression at only a 10% signal loss. In order to further optimise, a larger simulated data sample is needed. Additionally, this algorithm must be integrated into the readout hardware system, which will require some restructuring of how the algorithm groups the wires at the higher, layer-level GBDT.

Conclusion Even in its relatively early stage presented here, a BBDT-based track-level trigger shows promise as a flexible discriminator that would be robust against the high occupancy

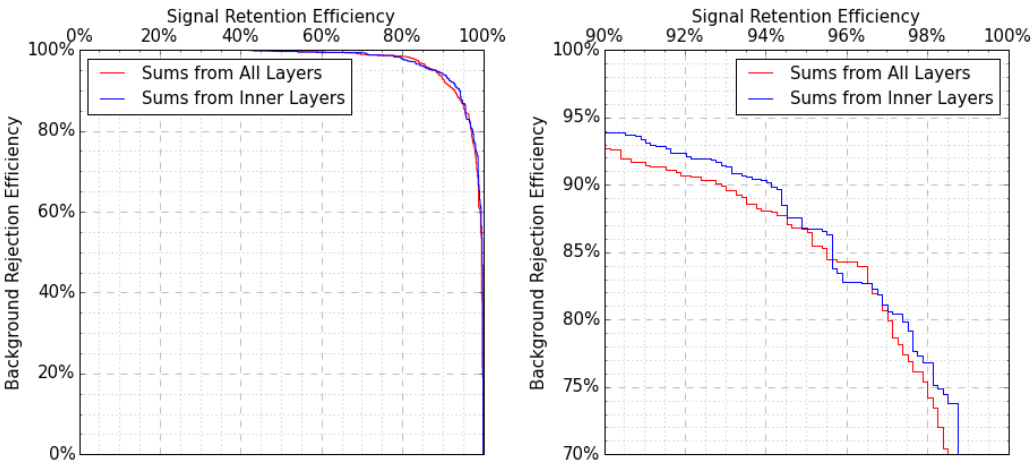

Figure 16.17: ROC curves for two independent classifiers of layer-level GBDT, in full scale (left) and zoomed scale (right). The red curve is from a GBDT trained on the layer-wise sum of the wire-level BBDT output for all layers. The blue curve only considers these sums from the inner most layers.

predicted in the CyDet. Further work includes refining the input features and flow of the algorithm, grouping the hit wires by readout board to match the intended hardware structure, and writing the firmware implementation of the algorithm. A larger simulation sample is needed to move forward with this study. This simulation sample is currently being produced using the ICEDUST framework.

16.1.4 Trigger performance evaluation plan

For successful operation of trigger system on Phase-I experiment, the trigger latency, efficiency, and rate should be evaluated before beam data taking. The topography of event for cosmic muon events are quite different with the case of beam data, that it is not helical shape and there is generally no coincidence with CTH hits with CDC hits of CyDet. Therefore, the proposed CyDet trigger algorithm using CDC can not be applied to cosmic event trigger, and a dedicated trigger algorithm should be developed for cosmic data taking of CyDet. This new trigger logic, which can be implemented in COTTRI system will make different processing delay with beam event trigger logic utilizing BDT, resulting different trigger latency. This means, to evaluate trigger performance for CyDet, the engineering run with lower beam power will be necessary rather than cosmic data taking.

In the CyDet engineering run, the trigger rate should be low due to lower beam power. In this case, the CTH can be used as the only trigger source. By reconstructing trigger events in offline, and comparing with COTTRI trigger result, the trigger efficiency and trigger latency of COTTRI trigger system utilizing BDT algorithm can be obtained. The CTH trigger rate can be also compared with simulation results, even though it will not increase linearly on beam power increase. The trigger efficiency of CTH can be obtained in cosmic data run, by using CRV as the primary trigger source.

The ECAL pretrigger system is the only trigger source of StrEcal detector. The ECAL pretrigger generates cluster information and energy sum by using rather simpler algorithm than COTTRI system. The central trigger system makes trigger decision by using those information. This trigger decision logic will be different but similar with that of beam data case, therefore not much difference is foreseen in trigger latency of ECAL pretrigger system. Trigger efficiency of ECAL pretrigger can be obtained by using CRV as primary trigger source, as in the case of

CTH of CyDet. Therefore, StrEcal trigger system test under cosmic data run will be possible. The trigger rate test of StrEcal is not important in Phase-I because the beam power will be low.

The FC7 board can be fully controlled and monitored through UDP network in real time, and this functionality can be utilized to generate arbitrary random trigger. A test run with this random triggers can be used to test the noise performance of detector and readout system.

16.2. Data Acquisition System

16.2.1 Overview

For both the StrEcal and CyDet, the readout system is based on standard Ethernet networking, and implemented using commercially available off-the-shelf networking components. The readout and control networks for the StrEcal detector are shown in Figure 16.18, and for the CyDet in Figure 16.19. The factors influencing these designs are discussed in the following sections.

The underground area where the detector sits is a comparatively high radiation environment, and is assumed to be unsuitable for off-the-shelf computing equipment. Therefore all switches and PCs will be housed outside of the underground area, on the control room floor of the building. Since transmission in the readout network is essentially one way, and the control network is "slow", this should not present any latency issues, provided all the long cable runs take similar routes. In practice there are only a few $\mathcal{O}(10)$ cm diameter service pipes out of the underground area. Using standard optical cables for Gigabit Ethernet, each DAQ would require about 1 service pipe dedicated to the transmission of (digitised) data. Optical cables are preferable as they have smaller cross section, eliminate the possibility of cross-talk within the bundle and simplify grounding considerations, however it should also be possible to use cat 6/7 twisted-pair. To reduce the possibility of damage to the cables a trunk line, including several spares, can be installed through the shielding, with passive patch panels at each end to which the readout cards and PCs are connected. If the StrEcal and CyDet are only to be used sequentially and not in parallel this also allows the same trunking to be used for both DAQs.

Most of the custom elements will be in the underground area, as control and triggering impose latency requirements. In the case of read-out electronics it is also necessary to house these in (or very close to) the detector so that signals can be amplified and digitised without degradation. However, a few elements (most notably the FC7) are fully digital, and their location is primarily constrained by the (less strict) requirements of latency. It may be possible to situate these on the ground floor, as shown in the figures. Alternatively they could be located in an enclosure in the underground area. The enclosure would have additional shielding to reduce the neutron flux for these elements.

A run control PC sends commands to start and stop runs, configure hardware, etc, (using the MIDAS [91] DAQ software) over a "slow" 1 Gbit/s control network. These commands are distributed via network switches to a set of PCs which are dedicated to the readout of particular parts of the detectors and they react as appropriate. All data are transferred on the network using standard protocols (Ethernet, UDP, TCP/IP). Most readout cards will use TCP to communicate with the controlling PC, but may use different protocols to communicate between themselves.

When a trigger occurs, the event data are stored in buffers in the front-end electronics of each system. When the buffer has a whole event it will be sent as a packet (or packets)

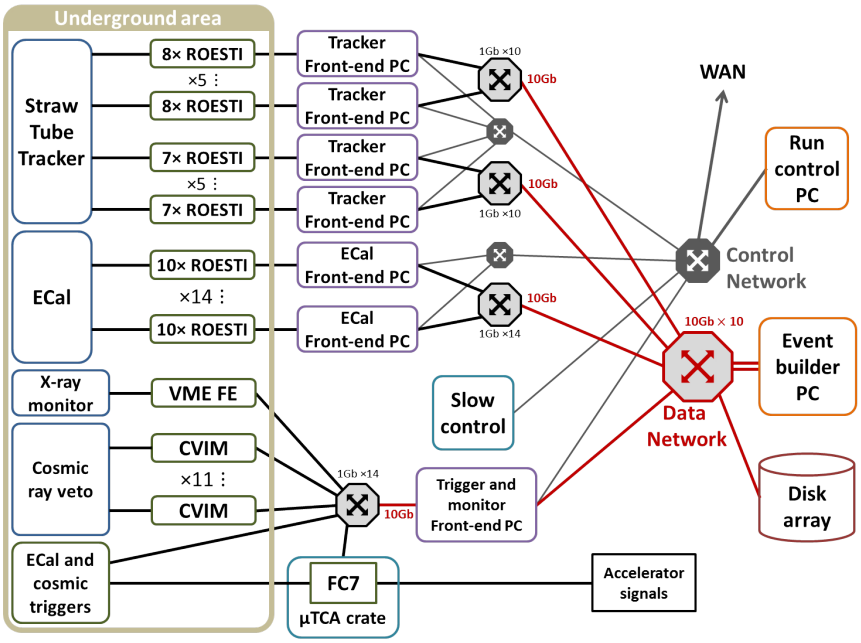

Figure 16.18: *Block diagram of the StrEcal readout and configuration system.*

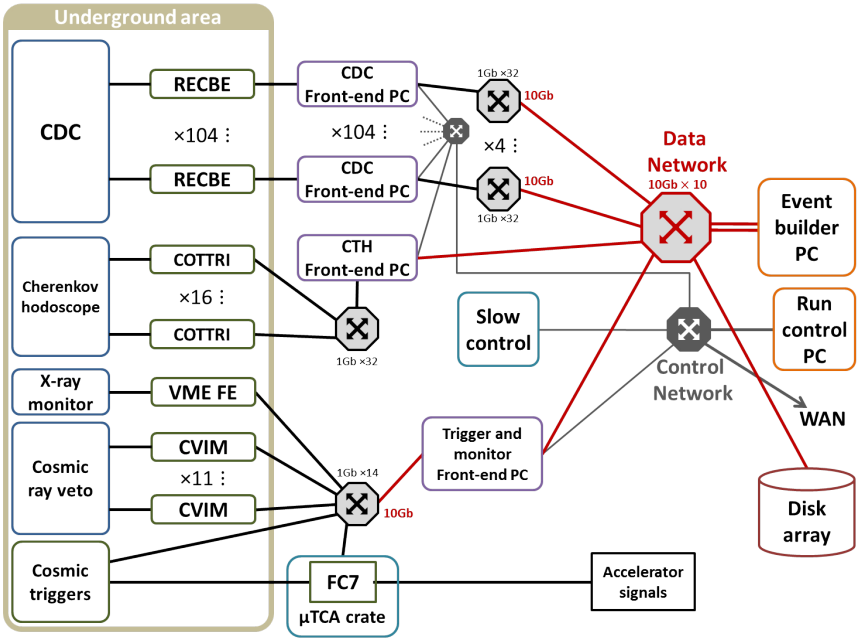

Figure 16.19: *Block diagram of the CyDet readout and configuration system.*

of data to a PC. In some cases the data will travel initially on custom data links (within the front-end hardware), but these will be translated to standard network links as soon as convenient. Packetising will be conducted such that minimal translation is required; the data volume will fit within standard network packet size and headers will be placed to ease the load on hardware. To avoid the PCs polling and then requesting data under software control, ideally data destinations will use flow control to prevent packets being sent when they are busy. This will be at the packet level, so there will be no need for a low latency signal here. For example, a PC will assert (i.e. send a message to the front-end electronics) saying "ready for a packet", meaning it has enough resources available to receive the largest possible packet (and one more). While receiving the packet it can assert/send a "not ready for packet" signal/message and the front-end will continue and finish the current packet, but then wait for an update for the PC.

Ethernet pause frames can also be accommodated. Once the data is collected on a PC all further transmissions are over standard computer networking.

16.2.2 MIDAS Front-ends and back-end

As far as the high-level MIDAS DAQ is concerned the basic unit of readout is a single 'equipment'. This equipment wraps all the activity of a subset of the readout electronics and communicates it back to MIDAS in the standard MIDAS format. It also acts as the receiver for MIDAS commands. Standard protocols such as VME can also be used and are understood by MIDAS, but with a custom-designed board it is simpler to interface with MIDAS directly. This can be done at hardware/firmware level (for example, on an on-board FPGA) or in software running on an intermediate PC. The model chosen for the main detectors (CDC, ECAL and Straw tube tracker) is to use intermediate PCs (designated *front-end PCs* and is inspired by experience with T2K's ND280 which used both firmware and software implementations. For some of the smaller detector systems with low bandwidth requirements a similar approach could be used, or one of the standard protocols understood by MIDAS. This decision should be guided by development of the readout for these systems. The remainder of the chapter concentrates on the larger subsystems, and assumes the smaller detectors can use a similar model.

Both ROESTI and RECBE will communicate using SiTCP, which is an FPGA-based implementation of TCP[1]. The data content of the TCP packets has no special restrictions, and is assembled into an appropriate format by the SiTCP firmware. The front-end PCs will receive data packets from the electronics and decode them according to shared knowledge of the format used. A dedicated Rx/Tx (Receive/Transmit) process is used for this and will naturally include TCP drivers for network communication. It is possible for one PC to handle multiple boards; in the case of the ROESTI this is natural as they are daisy-chained together. Communication from the MIDAS DAQ (e.g. configuration data) can also be encoded and transmitted to the electronics by this process.

The other part of communication by the front-end PCs is with MIDAS. The process communicating with MIDAS responds to commands sent by the DAQ, but most communication (at least by byte count) is the transmission of readout data to the central Event Builder PC. The process fulfils the MIDAS role of 'frontend'[2] and needs to wrap the data coming from the readout in a MIDAS recognised data format, which is essentially a short MIDAS header followed by user-defined data block.

These two processes running on the same PC need to transmit data between themselves, and this will be achieved by using shared memory segments. Between the two will sit a third process: a data processor. This communicates over shared memory with both the Rx/Tx and the MIDAS Frontend Process (MFP). The strength of this model is that the data processor can perform some additional work on the data as it passes through the front-end. This could include data compression such as zero suppression; noise detection and removal; or the processing of summary data for monitoring purposes. It also allows for the aggregation of data from non-synchronous devices, such as the X-ray monitor, that may be used to monitor the experiment even outside of the trigger periods. A schematic of the triplet of processes running on a front-end PC is shown in Fig. 16.20

Provided sufficient shared memory, the front-end PCs also naturally act as buffer between the electronics and the MIDAS DAQ and disk. This is potentially a very useful feature as it allows smoothing of the data rates to disk, which is expected to be the most important bottleneck

[1] In addition the COTTRI boards will also use a firmware-based TCP implementation

[2] This has a specific meaning within MIDAS, see [91]

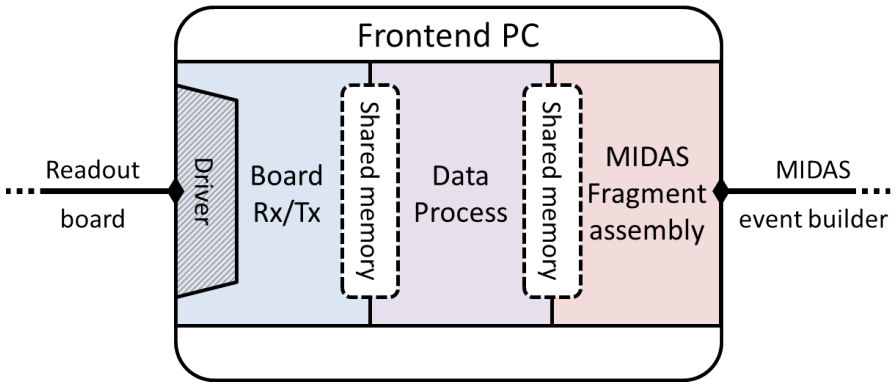

Figure 16.20: Schematic of the processes running on a front-end PC

in the system. The design shown in Figures 16.18 and 16.19 is the most conservative, using the maximum number of front-end PCs, to allow for greater buffering in parallel and more complex operations by the intermediate data processor. This is not an intrinsic requirement however, with better understanding from testing of prototypes, and more tightly specified running conditions, it may possible to use a lower number of frontends, with each PC handling multiple electronics cards (or chains in the case of the ROESTI).

The front-end PCs will be housed in an server room near the control room. The 100+ PCs could fit easily into a single full-height server rack, although it would be preferable to spread them out to simplify access, cooling and the provision of UPS power. All PC racks should be supplied with UPS systems to smooth the power supply, and allow for an orderly shut down in case of loss of power to the server area. In such cases the system should stay up for at minimum of 30 minutes on battery power, and preferably longer.

The front-end PCs will typically have two (optical) Gigabit Ethernet ports on a dedicated network interface card.[3] The first of these connections for direct communication with the electronics, as already described. The second port (which may instead be 10GbE for some PCs, if they are aggregating several inputs) communicates with the DAQ back-end over the data network.

The backbone of the data network will be 10 Gigabit Ethernet, as it needs to channel data from all of the front-end PCs. Where 1 Gbit links are used from the front-ends these will fan-in to the 10 Gbit network via suitable switches. Because the front-end PCs are not located inside the underground area they can be housed in racks adjacent to the back-end, therefore the entire data network is physically compact and located in the server room. The equipment used therefore does not require any unusual standard of radiation-tolerance.

The back-end of the DAQ is based on more standard MIDAS components. The central element of the MIDAS back-end is the PC that runs the event builder process. This requests and collects 'fragments' directly from all the front-end systems to a memory buffer, and when every expected fragment is received, it sends the completed event (which consists of a few headers plus the aggregated fragments) to a logger that is responsible for writing the event to disk.

The logging functions can be run as a process on the same PC as the event builder, but it is more likely to be set up on a separate PC that is set up as a disk server. In either case the data disk(s) must be attached on a high-bandwidth bus (e.g. PCIe to SAS2). Assuming a separate disk server PC, all data must at some point be pass from event builder to the logger, so the link between the two must also be high-speed. The baseline design has the logger communicating

[3]There should also be an standard Fast Ethernet (or better) port for the control network. Almost all PC motherboards have one such port.

with the event builder PC over the central data network, but it could alternatively be via a direct link between the two.

16.2.3 Readout elements

The number of readout channels is an important consideration for the hardware topology and eventual data rates. Here we summarise the channel counts for the three high-multiplicity detectors: the CDC, Straw Tracker and ECAL. Although the Cosmic Ray Veto and hodoscope also have multiple readout channels, the number is significantly smaller and will not dominate the overall system.

For the Straw Tracker, the current design uses 150 ROESTI boards, across five tracking stations with two projections at each station, corresponding to 15 boards in each manifold. The ROESTI is designed to be daisy-chained, but the length of the chain is limited by the bandwidth of the top link. It may be possible to have all 15 boards from a manifold in a single chain, here we conservatively assume that two chains are needed. Each ROESTI can digitise 16 channels, corresponding to 2400 channels overall.

For the ECAL the channel data is also read out via a (variant) of the ROESTI card, again digitising 16 channels per card. The number of active channels in the Phase-I ECAL is constrained by the cost and lead-time to grow scintillator crystals, so is not known, however the completed design envisages full coverage of the ECAL face would require around 2000 crystals, so this can be taken as an upper limit. We assume 128 ROESTIs divided up among 14 chains of up to 10 boards, but the exact topology is somewhat flexible as the ECAL ROESTIs are mounted together.

The CDC design has a little under 5000 sense wires. Each RECBE card can read-out up to 48 channels, so the cabling scheme requires 104 RECBE cards.

16.2.4 Aggregation of data

The front-end PCs communicate with their associated readout boards over 1 Gbit/s links. These data will be stored in the front-end PC memory until the associated MIDAS event readout command is sent, at which point the data are copied to the MIDAS event buffer and transferred out of the front-end PC. Initially this is over a 1 Gbit/s link but after passing through aggregating switches it will traverse a 10 Gbit/s network, using a fast switch. The event data from all the front-end PCs are merged in a global event builder PC and written to disk. Hence, the run control path and event data path are kept separate, with the latter running on a fast dedicated network to ensure a high rate and few bottlenecks.

The parallelisation of readout between the electronics and associated front-end PCs means that the effective bandwidth at the front-end is equivalent to a few times 10 Gbit/s. There are likewise multiple 10 Gbit/s links connecting these front-ends to the main network switch. The main bottlenecks come from the connection to the MIDAS Event Builder PC which is at best 10 Gbit/s, and the connection between this PC and the disk. Of these, the most critical bottleneck is likely to be the disk. A fast mechanical hard disk is limited to about 80 MByte/s. It is possible to get improvements over this number (e.g. a RAID0 arrays of solid-state drives are able to reach a few hundred MByte/s), but practically it is desirable to keep the average data rate to disk well below 1 Gbit/s, not least because this drastically reduces the need for cutting-edge hardware (which typically has higher rates of failure). Note that peak theoretical rate to the disk controller is substantially higher than this 'limit' (e.g. 4 Gbit/s, with SAS2 /

Table 16.7: Experiment operating parameters assumed in this section. In most cases these are not fixed and will be optimised.

Accelerator cycle time[a]	$\mathcal{O}(1)$ s	
Slow extraction duty factor	0.5	
	4 bunch	3 bunch
During slow extraction:		
Normal bunch spacing	1170 ns	1755 ns
Signal window	800 ns	1300 ns
Signal window active fraction	0.68	0.74
Number of bunches extracted	$\mathcal{O}(10^6)$	

[a] 30 GeV SX currently operates with a cycle time of 6 s during which a spill will last around 2 s.

SATA-III) but these rates cannot be maintained by standard hardware for long periods.

If a rate of 80 MiB/s is sustained, a 10 TB data storage disk will be filled in around 35 hours. Hence, there will be several such disks which can be swapped over as they get filled. The primary data archive is likely to be provided by KEK computing at Tsukuba. To ensure this archival process does not disturb data taking, the conservative assumption is that full disks will be disconnected from the experiment and then connected to a high-bandwidth WAN in order for the data to be copied to permanent storage. Transferring from the DAQ disks is unlikely to be substantially faster than the data is produced by the experiment, so several disks will be used on rotation.

16.2.5 Data rates

Both detector systems need to operate assuming the accelerator is operating continuously for an indefinite period of time. However the beam is not continuous so peak rates are higher than time averaged rates. While the electronics (and maybe associated front-end PCs) need to operate at the peak rate, higher levels of the DAQ can be 'protected' by buffering data, allowing them to operate at the lower average rate. The operating parameters assumed in the following section are shown in Table 16.7. The baseline operating mode is to fill four of the nine RF buckets in the MR, giving a minimum spacing between successive proton bunches of twice the standard MR bucket spacing. An alternative mode of operation is under consideration where every third bucket is filled, giving a 50% longer window between proton bunches. To maintain the event rate the three-bunch mode would have correspondingly more protons in each bunch, however this has secondary effects on the data rates since the detector would only be read out during the Signal window. Unless noted, the 4-bucket mode is used for data rate estimates as that is expected to result in higher rates overall.

For the StrEcal The trigger rate can be tuned by adjusting the parameters of the trigger algorithm, and the nominal target is to obtain a rate secondary beam particles (mainly pions) of 1 kHz during the spill period. The gap between spills leads to a duty factor of 0.5, so the average trigger rate over a full accelerator cycle will be correspondingly reduced. This benefits the high-level DAQ, provided there is enough buffering to smooth the rates over the accelerator cycle time.

If the rate of beam particles reaching the ECAL is 1 kHz, and $\mathcal{O}(10^6)$ bunches are extracted in a $\mathcal{O}(1)s$ spill, we expect a such secondary beam particles to arrive roughly once in 1000

bunches. The actual rate at which moderately energetic particles hit the detector is somewhat higher than this since they can also be produced due to interactions in the beam channel. In addition there is a large number of electrons and positrons produced both in the target and other locations, although these are mostly at low momentum. As a result the actual trigger rate would be somewhat higher than the 1 kHz of hadronic secondaries and their daughters. A pion must have momentum $\gtrsim 40\,\mathrm{MeV}/c$ to reach the ECAL, which sets the minimum energy for a pion trigger to be about the pion mass. The total number of charged particles reaching the ECAL will be higher than this and mostly made up of muons and high energy electrons. The trigger rate would therefore need to be somewhat higher than 1 kHz in order to retain 1 kHz of (benchmark) pion events, however MC indicates this factor is not much larger than unity. We assume a trigger rate of 1 kHz, since the rate can be controlled by adjusting thresholds in the trigger algorithm, however it may be desirable to tune this slightly higher, depending on what the data actually looks like.

The event sizes for the StrEcal detector are calculated using some reasonable assumptions about the level of detail required in waveform digitisation and the channel occupancy. The ROESTI card used by the Straw Tracker and ECAL will have two DRS4 chips (total 16 channels) which store the analogue waveforms. The DRS4 will be operated at 1 GSPS for both systems[4] and has a waveform buffer of 1024 samples, thus a full DRS4 waveform has a duration of around $1\,\mu s$. The ADC used by the ROESTI has a bit depth of 12, requiring a two-byte integer to store a single digitisation or, more aggressively, packing two samples into three bytes.

The data rate calculations start from an estimate of the number of particles traversing the StrEcal. This is rather higher than the trigger rate and is dominated by low energy electrons and positrons, as shown in Figure 16.21. This Monte Carlo suggests there could be several hundred of these for each triggering particle. The exact ratio may vary by a small numerical factor because of the uncertainties relating to secondary production, so we conservatively assume this ratio could be as high as a few thousand. The corresponding particle rate could therefore be as high as ~ 10 per bunch within the 800 ns signal window. The Straw Tracker has 20 active planes arranged so that each particle intersects once with each plane, therefore 10 particles would result in ~ 200 hit straws. Because of drift time in the straws and trigger jitter, waveforms will be kept if they begin within 200 ns of a trigger, so we estimate 50 (rounded up to 100) hits to be recorded in each trigger, i.e. about five particle tracks in the trigger window.

It is assumed that it is sufficient to record zero-suppressed data, using approximately 16 samples for each waveform. Properly packed, this corresponds to 24 bytes ($= 16 \times 12$ bits). An additional three bytes are needed to pack a timestamp, number of samples, and channel identifier, resulting in 27 bytes per hit. In addition it is necessary to take some complete waveforms for monitoring and calibration. A full waveform for one channel is 1.5 kiB ($= 1024 \times 12$ bits). For calculational convenience this is treated as if we do a full readout of a small number of channels (on the order of 3 per trigger, so that each channel is sampled unsparsified at ~ 1 Hz) and include it in the regular data stream, which adds about 5 kiB per trigger. Overall this results in a data size from the Straw tracker of around 8 kiB per trigger.

Complete ECAL coverage uses around 2000 crystals, and we consider that case here. If fewer crystals are available during Phase-I, the data rates will be correspondingly lower[5]. The ~ 10 charged particles in each signal window are assumed to leave a deposit in four ECAL crystals on average. This is probably an over-estimate as many of these particles will not be very energetic.

[4]It is expected that the ECAL could tolerate a slower sampling frequency, but most DRS4 chips do not function properly below 700 MSPS. Therefore we assume the raw readout will be at the same 1 GSPS as the Straw Tracker.

[5]This can be assumed to scale linearly with the number of crystals on the basis that the covered region will be picked to minimise biases.

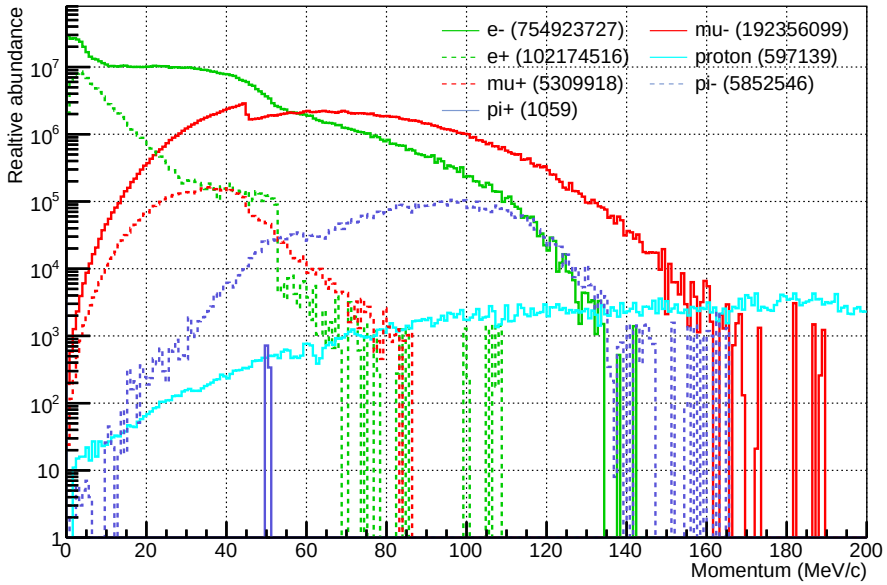

Figure 16.21: Relative frequencies of hits in sensitive volumes for the most common particle types entering the StrECal, as a function of momentum.

Conversely there will also be some crystals hit by photons radiated upstream of the ECAL, but this number is expected to be quite small. Because there is no drift time, the trigger coincidence window can be shorter than for the straw tracker, 80 ns is assumed, thus we estimate fewer than 40 hit crystals per trigger.

For the ECAL, a shaper amplifier with characteristic time of $\sim$ 200 ns will be used, and full waveforms should be retained, although it should be acceptable to resample them at a lower sampling rate. We assume that 200 (re-)samples is sufficient, requiring about 300 bytes per hit. This results in a total readout of 12 kiB per trigger. As with the Straw Tracker, it is desirable to take regular unsparsified data for calibration, and we assume here that this adds another 10 kiB to each trigger for a total of 22 kiB

For the smaller sub-systems the data rates should be much lower. The sub-system with the largest channel count after the main detectors is the CRV. This consists of six or ten super-modules of scintillator strips. One super-module will be slightly larger than 2 m $\times$ 4 m and has 4 layers of 4 cm-wide scintillator strips, thus there are approximately 500 strips per super-module. If all channels are read out independently, this is in the region of 5000 channels. Since each trigger window will be $\sim$ μs long the average number of cosmic rays in each trigger will be small, so we assume that the hit rate in the CRV is dominated by noise and take a conservative 10% occupancy. The CRV readout uses a tuned threshold discriminator to produce a binary output once per GBT cycle, thus each channel requires just an ID and a timestamp, expressed in GBT frames. This requires 3 bytes per hit, and therefore about 1.5 kiB per trigger. If a coarse charge readout were recorded this would require an additional 0.5 kiB per trigger.

We assume that the X-ray monitor will operate by building up a spectrum of the X-rays observed between triggers. Depending on the lines monitored this might require multiple histograms in different regions of interest, or in different gated time periods. The data could be summarised in a few histograms, and would be a fixed data volume per event. Assuming two bytes per bin of the spectrum, 250 bins per histogram, and four histograms recorded in parallel, then this would be 2 kiB per trigger.

There are two trigger systems for the StrEcal, which will also write out diagnostic information. The primary trigger comes from the ECAL and uses cells of 2 $\times$ 2 crystals as the base unit, so

there are ~ 500 cells total. Assuming four bytes per cell that gives a total of 2 kiB. The other possible trigger comes from the CRV. It is assumed that a CRV trigger would use a coarser granularity than the readout, such as a single bit for each 15 bar module. This would result in a trigger-word of a few hundred bits, well below 1 kiB.

The FC7s will capture the full fast control bit transfer for a period of around 1 µs around the trigger, corresponding to 40 GBT clock cycles. This is the fast control data from the FC7 and from the FCT boards connected to the FC7. Most of the data returned by the FCTs is the history of the trigger state, so detectors that are not integrated into the trigger system will produce much less data. Fast Control and Busy lines for an FCT on a non-triggering system correspond to 3 bytes per cycle, giving a data volume of 0.12 kiB. For an FCT involved in the trigger system, up to eight additional bytes (64 bits) of trigger primitives may be written, totalling 0.44 kiB. There will additionally be a few bytes for the FC7 state itself.

In the StrEcal, there will be 5 triggering FCTs (ECAL and CRV) and up to 11 non-triggering FCTs. Allowing for headers and information about the FC7 state this totals at most 5 kiB, and is a fixed volume per event.

Table 16.8 shows the summed contributions to the data rate and gives a total of around 42 kiB/trigger, corresponding to an average of around 22 MiB/s at the nominal 1 kHz trigger rate and 50% duty factor in slow extraction. This is comfortably below the rate estimated for the maximum the DAQ is capable of sustaining (due to the disk bottle-neck). With operating experience the data rate could be increased, either by loosening the trigger condition or by increasing the proton beam current. Note that increasing the beam current increase both the trigger rates and the amount of overlay, so the data rate increases roughly as the square of the beam current.

The yield of backward-going pions is somewhat poorly known however, so we should also consider what happens if the real data rate is too high. In this case additional throttling measures may be necessary. It should be possible to tune the trigger to a lower rate, as well applying more compression (e.g. by recording waveforms with some form of delta encoding). As a final protection, the DAQ will be able to self-throttle by the sending of busy signals, but it would be sensible to supplement this with a 1-in-N prescaler to ensure that the accumulation of busy signals does not bias the data recorded, or result in instabilities. A prescaler would be particularly useful in the case that special runs are taken with naturally higher rates, for example runs with a looser trigger condition.

Table 16.8: *Estimated event (i.e. single trigger) sizes for StrEcal detector DAQ system. The nominal trigger rate is 1 kHz and a 50% beam duty factor is assumed.*

Detector	Event data size /kiB	Average data rate /MiB s^{-1}
Straw tube tracker	8	4
Electromagnetic calorimeter	22	11
X-ray monitor	2	1
Cosmic veto	2	1
Fast Control	5	3
ECAL trigger	2	1
Cosmic veto trigger	1	1
Total	42	22

For the CyDet The basic trigger rate is not easily to tune, as it derives directly from the hodoscope trigger counters. Without shielding, the hodoscope would trigger at a rate of a few hundred kilohertz, which results in a very high data rate. However this is mostly due to low-energy scattered particles, so some lead shielding is enough to reduce the frequency of triggers substantially. The resulting trigger rate is estimated from Monte Carlo simulations (see 13.3.6) to be around 26 kHz, and is still dominated by low-energy particles (i.e. not high-energy electrons). The estimate is derived from the planned beam current, in effect it is averaged over the accelerator cycle, so the instantaneous rate during the spill would be somewhat higher. This rate could still saturate the high-level DAQ, therefore a higher-level trigger using the CDC hit information is being developed to reduce the a data rates to manageable levels. Initial estimates based on Monte Carlo 'truth' quantities (See Section 16.1.3) suggest this higher-level CDC trigger can reduce background trigger rates by a factor of 20, to a more manageable 1.3 kHz.

Signal-like triggers (from the high energy tail of DIO) should pass the high level trigger with probability close to 1, and as such represent a minimum floor for the online readout rate. Because such events are rare compared to the overall number of muon stops it requires a large sample of Monte Carlo events to estimate the rate in detail. In older simulations that don't incorporate the latest software developments we find a rate of a few hundred per second. This can be confirmed by a back of the envelope calculation: The CDC by design imposes a minimum threshold momentum for electron tracks to be observed of at least 70 MeV/c, and the rate of DIO electrons above 70 MeV/c is around 600 Hz. Summing both triggers from background and signal-like electrons we estimate an overall trigger rate of around 2 kHz.

It may be useful, especially in the early stages, to relax the trigger conditions and take minimum bias data at higher rates. In this mode the number of triggers taken during a single spill could be (assuming around 26 kHz) of order 10^4 or higher. To ensure the highest possible capacity in the DAQ we will make use of the gaps between spills for load averaging. This will require significant buffering in the readout chain. The PCs used will need to have plenty of memory, in excess of 4 GiB.

The event sizes for the CyDet are calculated assuming the existing *Suppress*[ed] readout of the RECBE boards is used. This is based on a Belle-II mode which essentially corresponds to reading out an integrated ADC value and timestamp for channels above some zero-suppression threshold. The RECBE has a 10-bit ADC, so an integrated wave form should fit into 2 bytes.

The RECBE firmware also provides a *Raw* readout mode where all digitised waveforms are recorded, however this amount of information is too much to even send off-board at high trigger rates. An alternative readout mode (*Semi-supress*) for COMET is under study that would preserve full waveforms over 1 µs (32 samples) only for channels that pass above threshold. Another addition to the firmware for COMET is an *upper* threshold, above which readout is suppressed. This is because of the unusual nature of COMET Phase-I beamline, which results in a significant instrumental background of low energy electrons at high radii. Although they are low energy, these electrons leave large charge depositions on individual wires, or small clusters of wires.

Here we assume the suppress mode (including a high-charge cut-off) will be used for standard data-taking, but that the COMET raw and semi-supress modes will be available and used for calibration and check-out runs operating at a lower trigger rate. It should be noted that actual operation could be a hybrid mode, where the RECBEs read out using the COMET semi-supress mode, and the front-end PCs reduce this to something resembling the suppressed mode format in the DAQ output stream. But in parallel with the DAQ output, the front-end PCs could then use the waveform data for online monitoring tasks.

The data volume per trigger is calculated starting with a projected occupancy of 20% out of around 5000 sense wires, corresponding to ~ 1000 hits in a signal window. However the majority of these hits would be eliminated by the high-charge cut. Simulations suggest the fraction of channels that would be read out after such a cut is lower, around 3.5%, so we assume 200 hits in the signal window. Because the drift time in the CDC is projected to be around 0.4 µs, it will be necessary to consider a coincidence timing about as large as the signal window itself, so there will be no significant reduction from applying a trigger window. The Suppressed mode requires two bytes each for a channel ID, integrated ADC, and TDC values for the integration start and stop. This totals 8 bytes per hit channel, or an average of 16 bytes per board. The boards add a header of 12 bytes, but we assume this can be checked and then suppressed by the front-end PCs. Scaling up to 104 boards across the CDC gives 1.7 kiB per trigger.

Using the raw mode and retaining the high charge hits it is projected that hit channels would require 52 bytes (allowing 12 bits per sample plus a TDC and channel ID), or an average of 500 bytes per board and around 52 kiB per trigger. This would not be possible in normal running, but should be available for special low-intensity (or pre-scaled) runs.

The only other CyDet subsystem that needs to be evaluated is the trigger hodoscope. The baseline design uses 64 two-layer segments at each end, totalling 256 channels. The expected rates in each hodoscope element depend on the element's location, but the rates can range as high as a few megaHertz in the most frequently hit counters. (The fact the trigger rate is 'only' 26 kHz is by achieved by requiring a 4-way timing coincidence between adjacent elements.) The readout window for the CTH counters should not need to be as wide as for the CDC, as there is no drift delay. However in initial running it will be useful to retain the CTH information from the entire readout period, which is aproximately 1 µs. In such a broad window, most counters will recieve at least one hit. In this case the an efficient readout format is a fixed-ordering. The data for each counter would consist of a one byte 'header' indicating how many hits were recorded followed by the same number of TDC-ADC pairs. These are assumed to need two bytes for an accurate timestamp, plus one byte for a coarse ADC value. A few bits of the header can be used as a simple checksum to confirm the readout ordering. In this scheme, the total data read out would be aproximately 2.5 kiB ($= 256 \times 1$ header bytes $+ 800 \times 3$ TDC-ADC bytes), which is not problematic but is a large contribution to the overall event size.

Once experience is gained (e.g. to demonstrate stable latency, and rejection of background tracks) the CTH readout window could probably be reduced to a few tens of nanoseconds around the trigger time, which would reduce its contribution below 1 kiB. For the purposes of the overall data rate estimate, we conservatively assume the long trigger window, and correspondingly large contribution.

The remaining subsystems are common to both the CyDet and the StrEcal, and we reuse the numbers from there. The estimates from the X-ray Monitor and the Cosmic Ray Veto detector are the same, although the CRV *trigger* would almost certainly not be used during beam running because of the high rate and long readout window. The Fast Control data is estimated the same way as for the StrEcal. In the CyDet case the design calls for two triggering FCTs and (assuming an FCT each for the X-ray monitor and CRV) six non-triggering FCTs. This totals 1.6 kiB. In this case we expect that the CRV FCT will not be enabled for triggers during beam time.

The overall data per trigger and rates are shown in Table 16.9. It is notable that the small sub-systems contribute somewhat more overall than for the StrEcal because the average trigger rate is higher. In particular a large fraction comes from the hodoscope counters which (as discussed above) will almost certainly run with a smaller readout window after inital check-out runs.

Table 16.9: *Estimated event sizes for CyDet DAQ system, using the Suppressed mode, and considering two possible average trigger rate (2 kHz as estimated above, and 8 kHz, assumed to be representative of a low-bias mode).*

Detector	Event data size /kiB	Data rate at 2 kHz /MiB s^{-1}	Data rate at 8 kHz /MiB s^{-1}
Central drift chamber	2.0	4	16
Trigger hodoscope	2.5	1	20
Cosmic veto	1.5	3	12
X-ray monitor	2.0	4	16
Fast Control	1.6	4	13
High-level trigger	0.5	1	4
Total	10.1	20	81

Intermediate designs for the CyDet had unexpectedly high projections for the data rates to disk. These are now controlled by improvements on two fronts:

1. Event size per trigger is significantly reduced by suppressing high charge CDC hits caused by low-energy electrons. A more detailed estimate of Fast Control monitoring data also allows a confident estimate of lower rate form this subsystem.

2. The addition of thin lead shields around the hodoscope counters drastically reduces the low-level trigger rate from backgrounds. After further suppression by the high-level trigger, the background trigger rate is comparable to the rate of 'signal-like' high-momentum DIO electrons.

The baseline rate is now comfortably below the 80 MiB/s target level. It will be possible to 'ease off' some of the trigger and readout thresholds, recording additional data for some events according to a tuneable prescale factor set as part of run configuration, and even switch to full Waveform mode for limited calibration and diagnostic runs. It is expected that further gains will be possible, particularly for the Fast Control monitoring data which should be fairly predictable, and thus easily compressed. However such estimates can only be reliably made after experience with full-scale test systems and during commissioning, so the current estimate remains conservative in this regard. The rate in a low-bias mode is noticably higher, but is likewise beleived that this estimate is slightly pessimestic.

As with the StrEcal, a variable trigger prescale will be implemented, allowing some fine tuning of rates. Finally, the busy mechanism will provide the ultimate guarantee of a maximum data rate even in the case where the average rate is higher than estimated here, be that due to instrumental effects, higher muon yields or some combination of the two.

16.2.6 Online Software

MIDAS will be used for the DAQ software and it must support selective writing to disk, conversion from a MIDAS data file to a ROOT data file that is compatible with the offline software, and live monitoring of the experiment to quickly identify problems should they arise. The online software system will be split into several parts. As already discussed, there will be several front-end PCs, each running: detector-specific Rx/Tx programs that will read directly from the hardware; a MIDAS frontend process to store these data into MIDAS banks; and an intermediate processing step. The back-end PCs runs an event builder program that will

combine the MIDAS banks from several front-ends into a single MIDAS file; an "online converter and monitor" program that will produce histograms for live monitoring of the experiment and also to convert the data into ROOT format for offline analysis; a "logger" to write the MIDAS data to disk; and a "run control" program to start, stop and monitor runs.

MIDAS provides a logging program, an event builder and run control web page ("mlogger", "mevb" and "mhttpd" respectively) that can be used with no or minimal modification. The online converter and monitor program will need to use the MIDAS to ROOT interface libraries supplied by ROOTANA for the conversion process and will probably be based on the ROOTANA example analyser. Most, if not all, of these programs would need to be implemented within COMET's ICEDUST software framework. MIDAS is also sufficiently modular that it is possible to replace these elements with other programs that fulfil the same roles. As a baseline we assume the MIDAS tools are used, but replacement with more modern or more user-friendly programs is worth considering, assuming they also provide equivalent or better performance. A possible exception to this policy of minimal modification is the event builder process, for which a modification is already under consideration, as detailed in the Section 16.2.7.

The front-end programs need to implement the specific readout of the actual hardware used and also to define the MIDAS bank format that they will use. The hardware access itself can be completely specific and will require dedicated software.

MIDAS has the concept of "equipment", which it regards as the basic readout unit. The hardware itself will not be defined as "equipment" in this sense; shared memory in the dedicated detector PCs will form this level. Hence, MIDAS will not interact directly with the actual hardware. The programs doing the hardware access will run independently of MIDAS. These programs can receive data from the front-end electronics whenever it is available, asynchronously with any run. The data packets will be buffered in a shared memory in the detector-specific PC. MIDAS will communicate with the PC and request data for an event. The MIDAS process on the PC will then extract the relevant data to fill the MIDAS event banks. Once copied, the shared memory associated with that event will be flagged as free. (As discussed before, these programs actually communicate through an intermediate process, but the basic concept is unchanged.) This structure means the detector-specific readout code which interacts with the hardware can be optimised independently of MIDAS and also allows a dedicated process to be running which should maximise the data rate from the detector.

In addition, the MIDAS bank formats from the various detectors are also likely to be very specific. For each, an access class in the online converter and monitor program will be used to directly map the memory buffer containing the data to be written. Using these, the data can be unpacked into a standard, easily-utilised format. This means that access to the data is controlled through a single software implementation and it also makes the data more easily interpreted since any evolution of the data format can be mapped through a well-defined interface.

At some level the offline data format used in the reconstruction and downstream software must be common to both data and simulation. The simulation will not write out MIDAS-format (".mid" file) data, so the actual raw data written from the DAQ system must be converted to a data format containing the same information which is common to both data and simulation. This offline raw data format can then also be used for simulation output to ensure equivalent treatment of both.

The conversion will use the data-specific mapping class mentioned above to give a well-defined interface to the online raw data format. Wherever possible, the offline (common) raw data format should remain the same even if changes are made to the online (MIDAS) version, with any changes to the latter being converted or substituted during the online-to-offline conversion.

One major benefit of the ICEDUST software framework is it is based on the T2K-ND280 framework, which also uses MIDAS, and as such already has libraries to do exactly these transformations. By recognising the MIDAS bank name as it is read and behind the scenes instantiating a suitable data parser, the software is able to present all MIDAS data blocks in a user-defined structure, using the Python-inspired pattern of a forward-iterable generator. Thus, the data is available in a logically-structured way regardless of any optimisations made for online storage. The model even allows the online system to decide on an encoding 'on the-fly' (for example using different formats depending on the channel occupancy) and will present the data to the user in the same logical format.

Data monitoring will be done on a separate PC to the actual DAQ data flow path. A dedicated PC will run the online conversion and monitor program to read the data on disk (in MIDAS format) and produce standard plots of detector responses which can be checked by the shift crew. The first step of this program will be to do the online-to-offline raw data conversion into a compatible ROOT format. This means all data monitoring code will work with the offline data format and so can be developed using the offline files.

Another important element of data monitoring is an event display. This is a very useful tool to check for problems which can be identified by a human but not easily by software. Again, the first step will be to run the conversion of the raw data to the offline format, after which the offline event display (albeit with preliminary alignment and calibration constants) can be used.

16.2.7 Adaptions for high radiation environment

Initial studies suggest that the firmware in development for the RECBE FPGA may suffer upsets due to high neutron flux inside the detector solenoid. Other readout cards, such as the ROESTI, may also be affected, however the rate is expected to be lower as these cards are situated further from the beam axis. Additionally, the StrECal readout will normally be run with a less intense proton beam. The higher-level electronics (primarily the μTCA crate housing the FC7) can be situated further from the production target, either in a shielded enclosure underground, or on the ground floor. Thus the question of radiation induced upsets is most important for the CDC frontends, but the DAQ should be able to apply similar considerations to other subsystems.

Many upsets only affect transient data and can be isolated offline, however a small fraction of upsets will lead to firmware malfunction. The exact rate of such occurrences is difficult to estimate at present, as the prototype firmware does not yet incorporate the usual techniques (e.g triplicated logic) for high-radiation environments, and irradiation tests using the COMET RECBE have yet to be made. However it is important to consider the implications for the DAQ system. The easiest approach is simply to invoke a full run restart when board needs to be reset, but this could result in a lot of deadtime if the failure rate was high. We consider here some contingency techniques to enable a run to survive a firmware reset.

Dealing with gaps in the data stream

In these cases where the FPGA does not automatically recover from the radiation event, it must be reloaded which can take several seconds. This reload should be triggered automatically by logic local to the board so the main DAQ should not be involved, but an upset necessarily results in a gap in the data record from the affected board. The default MIDAS event builder does not provide any sophisticated alignment of data fragments, instead assuming that fragments from each frontend arrive sequentially without gaps. In order to present a continuous stream to the event builder the frontend PC would need to provide dummy fragments in the case the

RECBE is unresponsive, but this is somewhat tricky because the frontends do not receive a direct trigger signal, so have no idea how many dummy fragments to provide, at least until the RECBE recovers and starts sending fragments (which will record the central trigger number).

A much better alternative is to modify the central event builder process so that if a fragment buffer remains empty for a specified timeout period (which will need to be tuned based on a semi-complete systems but is probably several milliseconds) it continues to complete the events without the missing fragment stream. When the rebooted RECBE resumes sending of event data the event builder also needs to realign this buffer with the remainder of the detector, which requires that it inspect the fragment to determine the trigger number at which the data stream restarted. To do this efficiently also places constraints on the fragment format: the trigger number should be near the start of each fragment and ideally at a fixed offset. This would almost certainly be true in any case, so is not a taxing requirement.

Loading of runtime parameters

It is likely that the RECBE will need to reload various configurable parameters after a new firmware is flashed. In a normal run start sequence these are communicated from the run control (MIDAS "Online DataBase") to the RECBEs via the front-end PCs. In order that at RECBE can reinitialise mid-run, the relevant parameters will need to be cached by the front-end PC and provided when requested by the RECBE (i.e. they should be *pull*ed by the RECBE rather than *push*ed by the Rx/Tx process). This parameter pulling should also occur as part of the normal run start, in this case the pull may be prompted by the Rx/Tx process. By caching the parameters at the front-end for the duration of the run, we ensure that the configuration remains stable throughout the run. There is no difficulty foreseen in implementing the configuration this way, but it requires slightly more co-operation between the RECBE firmware and the processes on the front-end PC.

Raising of busy

Another question that should be addressed is whether the FC7 should continue allowing triggers to be issued while a RECBE is resetting. The initial failure that results in malfunctioning firmware is inherently somewhat unpredictable, so it is likely that the initial upset could result in both in the board reporting 'busy-high' and 'busy-low' states. Because of this it is desirable that the DAQ can continue functioning for a time, but once the firmware reset is initiated it would be preferable to lock the behaviour to one mode or another. Which mode is chosen depends on whether such data would be considered acceptable for offline analysis, and on the frequency of upsets requiring a reset.

It is difficult to dynamically mask out the busy signal from the RECBE, so to guarantee a particular behaviour may require logic at the level of the electronics (which may or may not be configurable). However, this is not an important decision for the wider DAQ, as in order to coping gracefully with the initial failure it must be be able to keep working in either condition.

16.3. Slow Control and Monitor System

In order to adequately operate an experiment in safety, the slow control system must be implemented in the experiment. We need to prepare the system for each sub-detector, sub-system and equipment for the integrated operation of COMET Phase-I.

The main purposes of slow monitor system are

- Controlling the start and stop of experiment sequence
- Checking the current status of each detector, system, and equipments,
- Logging the environment and control data for all operation period, and
- Controlling the parameters for the experiment operation, such as high/low voltage supply values.

The slow monitoring data will be stored in a dedicated database server, which is independent to the experimental data storage. These data and information will be useful for both the offline analysis and detector performance evaluation. The slow control system must be able to maintain or change the setting and parameter of each (sub-)detector/system for the desirable operation.

In principle, the monitor and control should be performed via network as long as possible, sharing the DAQ network, that is to say remote monitor and control. This is because the experimental area may not be accessed immediately during running period due to the high radiation level.

16.3.1 Software and User Interface

The baseline plan of the software package of the slow control and monitor system is MIDAS [91], which is developed at PSI and TRIUMF for data taking and experiment control purpose. As described in the previous section, the MIDAS will be employed as DAQ software, therefore the development take advantages of computing and human resource sharing, resulting easier implementation and concurrent operation.

The EPICS [92] is another candidate system which is widely used in the accelerator system control and monitor. The accelerator group at J-PARC also uses the EPICS, which enables easier implementation and coherent operation with accelerator.

Considering the benefits of these two system, we decided to use EPICS for the communication interface with the J-PARC accelerator system, and to use MIDAS for the (graphical) user interface for experiment control. A local resources, DAQ and control softwares and communication tools for sub-detector are already available, and they will be integrated into the MIDAS for the user interface.

Figure16.22 is a conceptual diagram of the slow control system with MIDAS (DAQ), suggested by BINP/NSU group, from their experience on CMD-3 experiment. By using the similar system and implementing to COMET under the help of CMD-3 experience, no significant difficulties are expected in constructing COMET slow control system. The CMD-3 control system is a variant of the original MIDAS, that the control software is written in Python language, however still providing capability of communication with MIDAS DAQ and database by using MIDAS library. The interface plug-ins which allow to communicate with sensors of the particular type are also prepared.

16.3.2 Slow Control System for CyDet

CyDet consists of several sub-detectors systems and equipments described in the Section 13. Table 16.10 shows the items for slow control system of CyDet, categorized by each detector/sys-

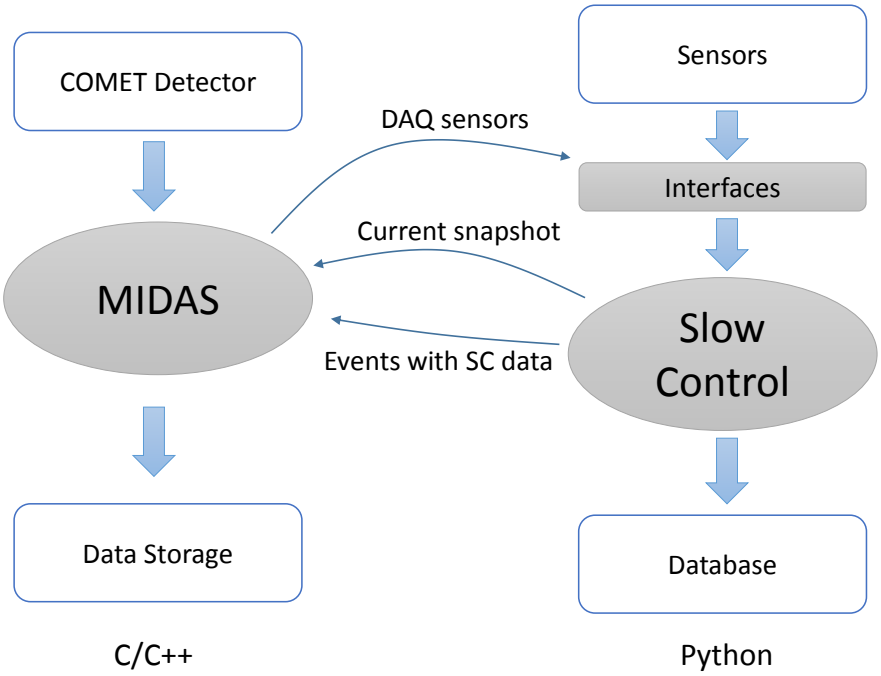

Figure 16.22: The conceptual diagram of slow control and monitor system with MIDAS of COMET experiment.

tem. Some items will be not only monitored but controlled remotely.

In case of High voltage and low voltage monitor and control, the WIENER MPOD High Voltage (ISEG) and Low Voltage (WIENER) supply modules will be employed. For each mainframe, 48 high voltage channels can be individually controlled, or configured as low- or high-voltage only operation. The high voltage operating range is from 500V to 10kV, and low voltage operation range is between 0 to 8V or 0 to 120V. As well as the manual control using LCD monitor of the mainframe, the MPOD controller will be connected to the MIDAS DAQ system through Ethernet, to utilize the MIDAS libraries for HV/LV module control and monitoring. The software development for these slow control and monitor system is foreseen to be very straightforward.

The gas flow rate into the CDC can be controlled by a system of mass flow controllers. The baseline plan is to adopt the HORIBA PE-D20 controllers which offer manual and remote operation. For remote operation, the Serial Peripheral Interface (SPI) can be used as a communication interface between a master (usually a CPU) and multiple slave devices. A schematic is shown in Figure 16.23. Here, the slave devices are the digital potentiometers AD5206. This chip provides 6 channels with 256-position digitally controlled variable resistors. Each channel can be connected to a remote-controllable equipment, like the PE-D20 and by modifying the value of resistance, we are able to control the gas flow rate into the CDC. The SPI protocol can also be used to monitor the gas flow rate using the Master Input Slave Output (MISO) logic signal which is in reverse to the earlier discussed Master Output Slave Input (MOSI) logic signal. This protocol can be extended for use with other environmental monitors.

Other monitoring items and time interval of monitor are not decided yet, because most of these hardwares still under development. However, there is very few difficulty to construct the system once they have been determined because the slow control system is not brand-new, and well established in the other experiments.

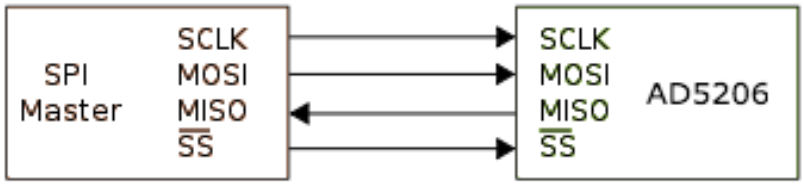

Figure 16.23: A typical SPI bus. The SPI master here is connected to a CPU, usually via USB port. The slave is the digital potentiometers AD5206 connected to the mass flow controllers.

Table 16.10: *The slow control and monitor items of CyDet.*

Definition	# channel	Interval
Electronics of CDC		
High Voltage Module (Voltage/Current/Status)	10	1 sec
Low Voltage Module (Voltage/Current/Status)	4×104	1 sec
Temperature on FPGA	104	1 min
Temperature of Sensors (3-5 sensors will be installed near electronics)	~ 5	1 min
Flow rate into Electronics Region	1	1 sec
Cooling System of CDC		
System Status (ON/OFF, alert)	1	1 sec
Temperature at input/output of cooling water	2	1 min
Flow rate	2	1 sec
Gas System of CDC		
Pressures of CDC	3	1 sec
Temperature at several points	~ 5	1 min
Input/Output Flow Rate (Mass Flow Controller)	7	1 sec
Oxygen Level Monitor	1	1 sec
Water Level Monitor	1	1 sec
Circulation Pump (ON/OFF/Status)	1	1 sec
Pressures of Target Region (He)	1	1 sec
Cherenkov Trigger Hodoscope		
High Voltage Module for PMT	256	1 sec
Low Voltage Module for Amplifier	256	1 sec
Detector Solenoid		
Status	1	1 sec
Magnet field (reference probe)	2	1 sec
Temperature	2	1 min
Environment Monitor		
Atmospheric Pressure	1	1 min
Temperature (experimental room)	1	1 min
Temperature (outside)	1	1 min
Humidity (experimental room)	1	1 min
Humidity (outside)	1	1 min
Total	~ 1069	-

16.3.3 Slow Control System for StrawEcal

StrawEcal is consists of two detectors, Straw Tracker (in the section 11) and Electron calorimeter (in the section 12), and the integrated slow control system must be prepared for each same as CyDet.

16.4. Schedule

The schedule for the DAQ components and trigger electronics is dependent on the available resources.

For the fast control and timing, then the central custom component is the FCT board and this has been given highest priority. Several prototype FCT boards were produced in summer 2014 and have been used in integration tests with CyDet and Ecal prototypes. A few FCT boards have been used for irradiation tests, which are currently ongoing, and some will be used for beam tests for CyDet and StrECal.

The FC7 boards for central trigger system are also important, because the FC7 design itself is under test before production. A nearly-final prototype FC7 was produced in the middle of 2015 with a few errors that required *ad-hoc* fixes. We have two of these board for firmware development and to be used for beam tests. More FC7's will be ordered and delivered in 2016.

As the COTTRI will play the central role in CyDet trigger system, its development is very important. The design of production version will be prepared at the end of 2015, and it will be produced in 2016. The final full chain test with COTTRI will be the middle of 2016, however, one year contingency is prepared considering the COMET Phase-I schedule.

The other components are much simpler and can only be defined when the detector-specific front-end electronics are fully specified. For the CDC, this is already the case, as it will use RECBE readout boards, which have a well-defined interface to the fast control system. Hence, the next custom board to be designed will be the CDC interface board, with a target of the first board being available early in 2015.

For other trigger electronics, the most complex part is the ECAL trigger, which needs two significant boards to be designed and firmware to be written. At the time of this writing, all prototype boards are being tested successfully, and the final version will be produced in 2016.

Most of the readout hardware is commercially available networking, PCs and disk. Hence, this can be purchased whenever required as long as the funding is available, which will benefit to the lower cost and higher performance. The custom components are the readout boards, specifically the RECBE and ROESTI boards. A few RECBE boards have already been produced in 2015, and the version 3 prototype ROESTI board is currently being evaluated.

Chapter 17

Radiation Hardness

17.1. Radiation Environment Study

17.1.1 Overview

Some electronics for each sub-detector and trigger system are located near the detector systems as described in previous chapters. High radiation environment is expected near the detector region due to very high intensity beam. Then, the radiation hardness of those electronics should be considered carefully. It is well known that especially neutron and gamma-ray affect some electronics and cause unexpected performance and deterioration in those electronics parts. Neutrons infrequently collide with silicon atom's nucleus in electronics parts which have transistors, for example FPGA, flash memory, and so on. This produces a burst of electric charge which can cause a single transistor to flip its state. This phenomenon is called Single-Event-Upset (SEU). SEU is not permanent damage for the parts which can reboot or in which the logic circuit can be rewritten, but changes digital information in memory or induces errors in logic circuit. Gamma-rays secondary effect induces ionization in the electronics parts and its charge forms fixed charge, interface state in the parts by cumulative long-term exposure of gamma-rays. Those cause deterioration of the parts. This phenomenon is called Total-Ionizing-Dose-effect (TID). TID is mostly permanent damage, so the careful selection of the parts which has few TID is indispensable.

In the COMET experiment radiation environment, a large number of neutrons and gamma-rays will be generated. For stable data taking, we need to cope with the SEU on the electronics boards. To avoid the TID, we need to select the parts for electronics development. In order to satisfy those requirements, we have performed radiation environment study with simulation for the estimation of radiation level, and several irradiation test of electronics parts.

The results of simulation studies on radiation environments are described in Section 17.1.2. The statuses of irradiation studies with neutrons and gamma-rays are described in Section 17.2. and Section 17.3., respectively. Finally, the future plan for these studies is described in Section 17.4..

17.1.2 Simulation Study with PHITS

A simulation study was done for estimation of the radiation on detector region by by using the PHITS code [39]. The investigation of the benchmark of spallation models by D. Jean-Christophe et al. showed that the intra-nuclear cascade + de-excitation models gave acceptable results [93], therefore, the INCL4.6 with GEM (from the range of 20 MeV to 3 GeV) is employed

in this simulation. The nuclear data library, JENDL is also used below 20 MeV. Figure 17.1 shows the geometry for the radiation study. A lot of detail parts, such as the CDC, the CRV detector, liquid helium transfer tube which contains the thermal shield and pipe, are included into this geometry.

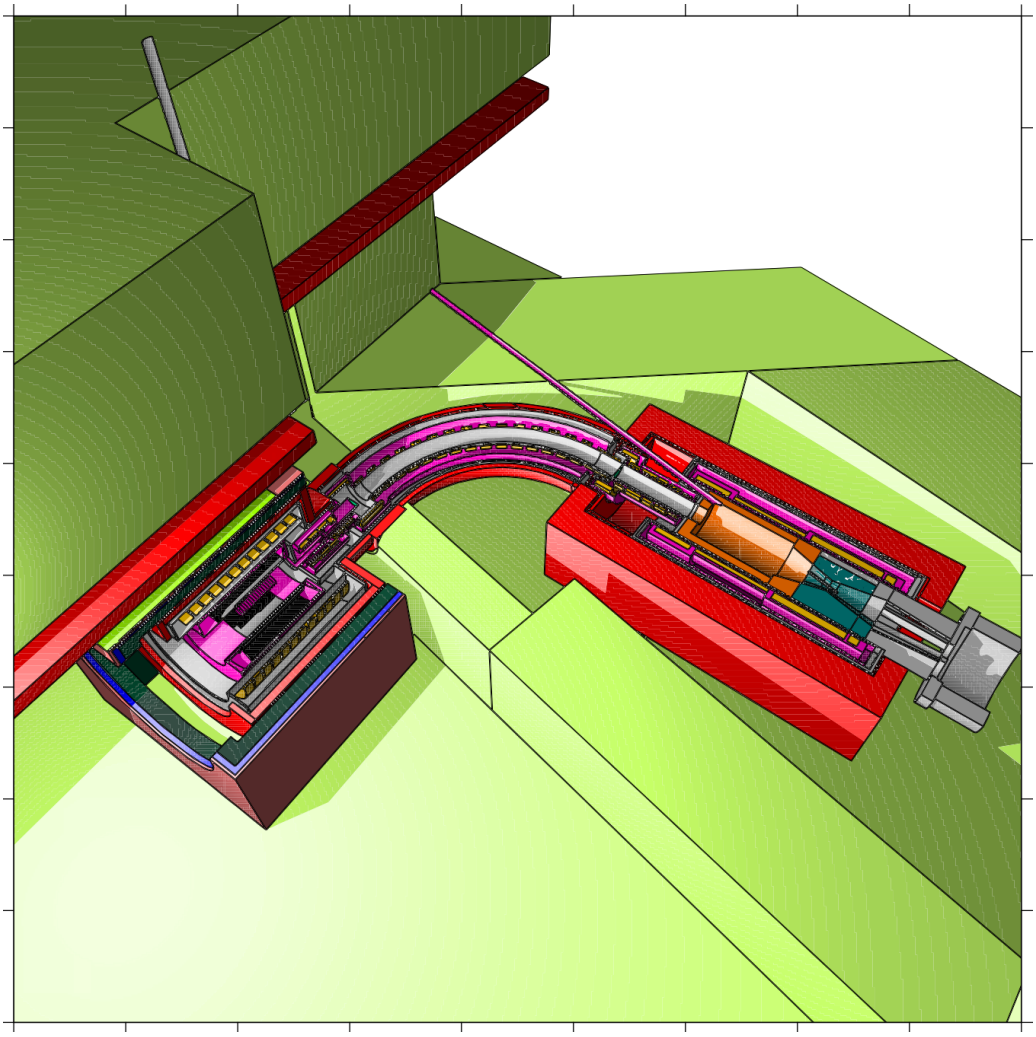

Figure 17.1: *PHITS geometry of COMET Phase-I for the radiation study.*

for CyDet

The CyDet is located at just after 90 degree bending of the muon beamline. As shown in Figure 17.2, the CDC detector is inside the Al support structure, and 104 readout electronics boards (RECBE) are located with 6-layers-structure at the downstream of the CDC detector.

Table 17.1 summarizes the result of this simulation for each readout board. 1 MeV equivalent neutron flux is converted from radiation damage factor for silicon which is shown in Figure 17.3.

The cherenkov trigger hodoscope detectors are located downstream and upstream of CDC, respectively. A proton absorber is employed in front of trigger. As the result, the estimated neutron flux is 4.0×10^5 n/cm^2/sec at maximum, which corresponds to 9.1×10^4 n/cm^2/sec as average. The dose rate is estimated about 12 μGy/sec.

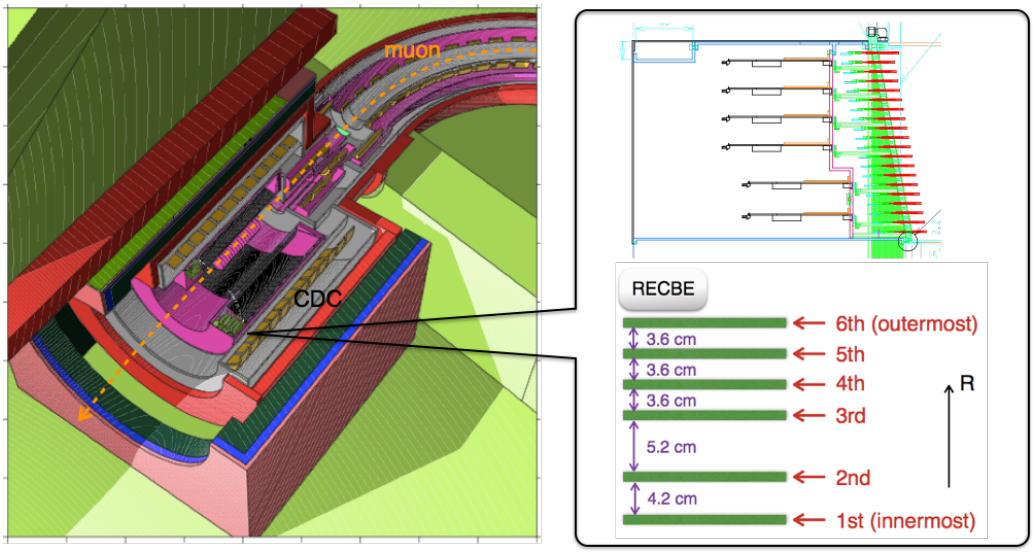

Figure 17.2: *CyDet geometry for PHITS simulation.*

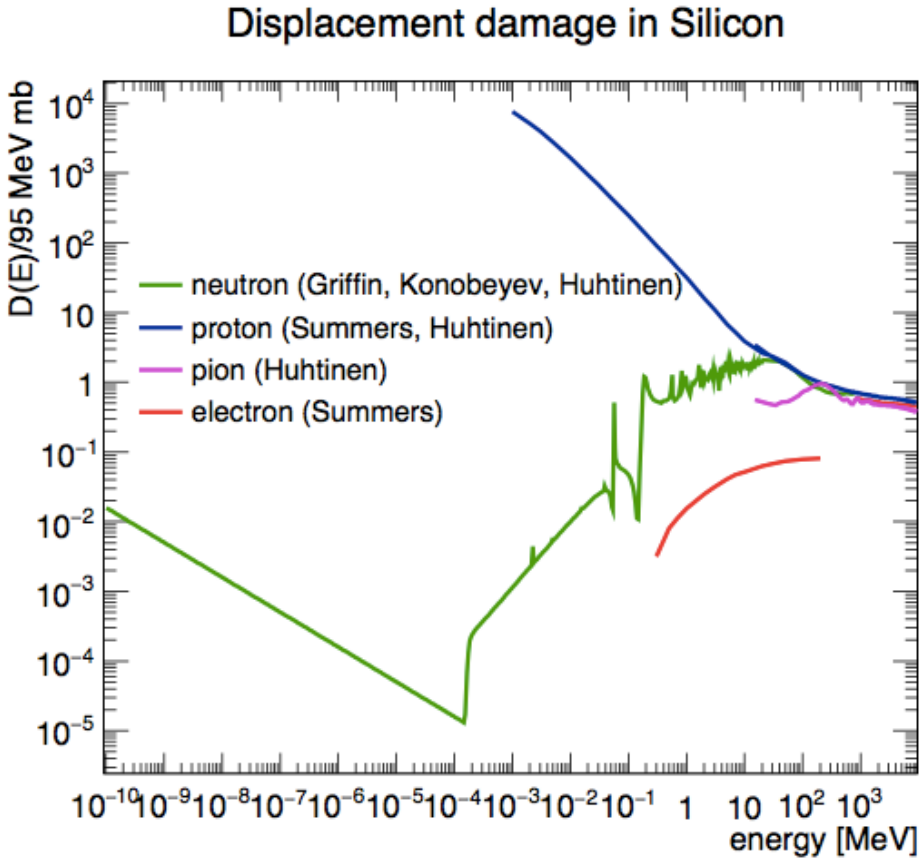

Figure 17.3: *Radiation damage factor for silicon.*

Layer	Neutron flux [n/cm^2/sec]	1 MeV eq. neutron flux [n/cm^2/sec]	Dose rate [μGy/sec]
1^{st}	4.65×10^4	2.46×10^2	8.35
2^{nd}	1.02×10^5	2.76×10^2	6.99
3^{rd}	1.05×10^5	2.89×10^2	
4^{th}	9.28×10^4	3.45×10^2	4.65
5^{th}	9.53×10^4	3.31×10^2	
6^{th}	1.01×10^5	6.40×10^1	4.19

Table 17.1: *Summary of neutron flux and dose rate at each position of RECBE boards. The 1st is the position at the first innermost layer, and the 6th is the positon at the outermost layer.*

for StrECAL

As shown in Figure 17.4, the geometry for the StrECAL in this simulation is implemented and switched from the CDC. It consists of one cylindrical simple straw tube station with ROESTI board and ECAL with APD. ECAL has 52 LYSO crystals with dimension of 2 cm $\times$ 2 cm $\times$ 10 cm, and APD is behind the ECAL with the thickness of 1.76 mm.

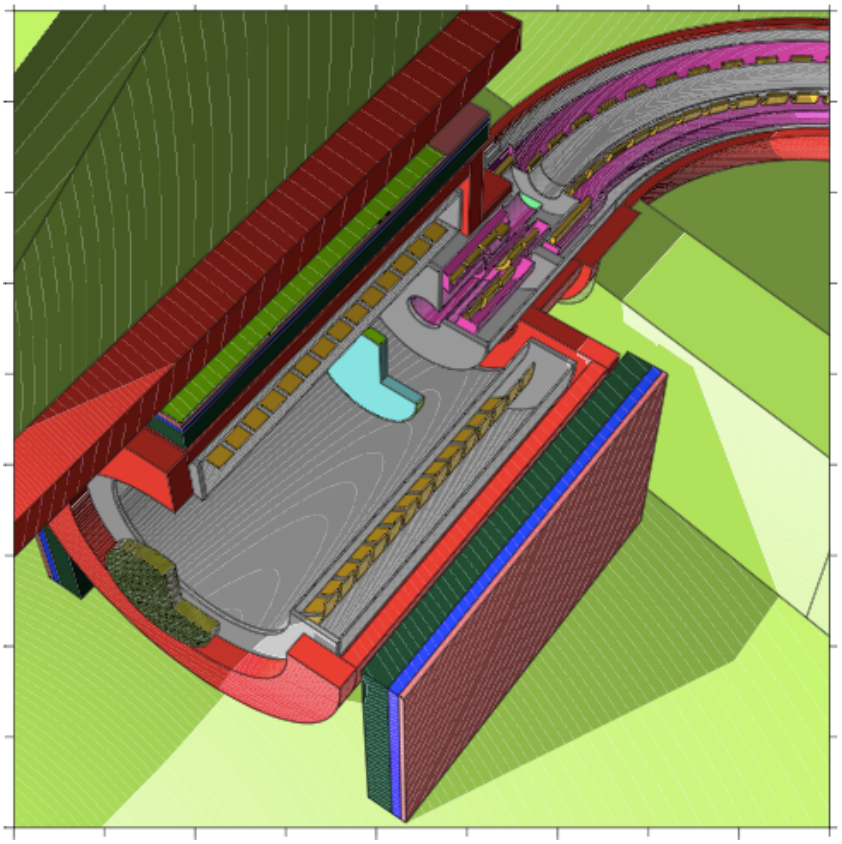

Figure 17.4: *Geometry for estimating the radiation for StrECAL.*

Figure 17.5 plots the distribution of the 1 MeV equivalent neutron flux (a) and neutron fluence for 200 day operation (b) for APD, respectively. Because the ECAL is on the beam axis and most of energy is stopped in LYSO crystal, the maximum dose rate and 1 MeV equivalent neutron flux for APD become 2.3 mGy/sec and 5.8×10^4 n/cm^2/sec. Apparently, the dose rate is three orders higher than the case of CDC and Trigger, therefore the beam intensity must be reduced for the background measurement. As for the ROESTI, the estimated 1 MeV equivalent neutron flux is 1.7×10^2 n/cm^2/sec.

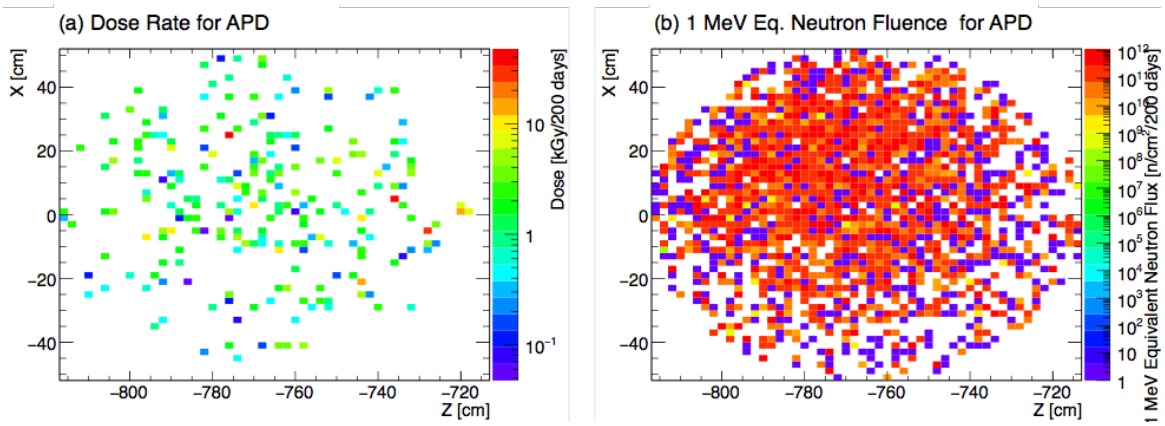

Figure 17.5: *Dose rate and 1 MeV equivalent neutron fluence for APDs (200 days).*

17.2. Neutron Tolerance

17.2.1 Neutron Irradiation Test in Kobe University

We have used the Tandem electrostatic accelerator at Kobe University[94] for our neutron irradiation tests. The tests have been performed several times in the past, and are planned for further studies. The accelerator has five beamlines of which we have used one for ion beam irradiation.

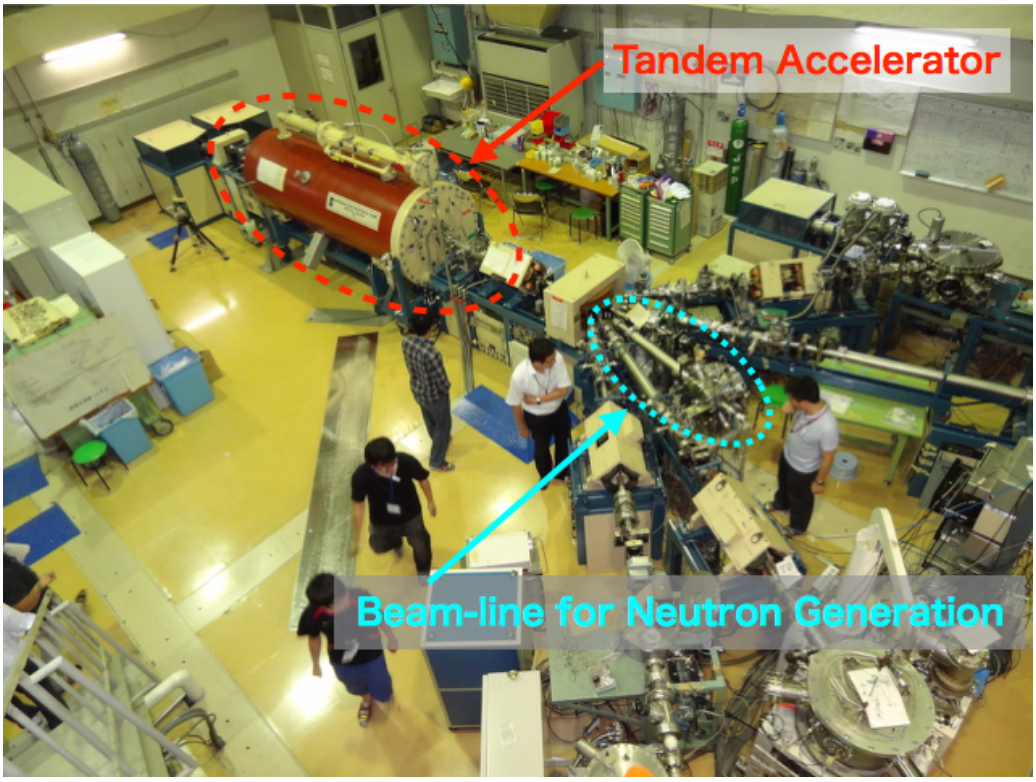

Figure 17.6: *Photograph of Tandem electrostatic accelerator in Kobe University. The accelerator has five beam lines, and we used one of them for the generation of neutrons.*

Figure 17.6 is a photograph of experimental area for the Tandem accelerator at the facility, and the accelerator and the beam line we used for the generation of neutrons are indicated.

The neutron is generated by ^{9}Be(d, n) reaction, and the energy of the deuterons is 3 MeV. The electric current of the deuteron beam is measured with a probe connected to the ^{9}Be target and the values are recorded with the logger during the beam time to evaluate the neutron flux.

The neutron flux was measured using CR-39 (BARYOTRACK-P made by Nagase Landuer Co., Ltd) with a group in Tokyo University. The size of a CR-39 is $10 \times 16 \times 0.9$ mm^3. Many CR-39s were exposed to the neutron flux at several distances and several angles from the ^{9}Be target and with some different beam conditions in July 2015. They gave us the result, and the neutron flux of the accelerator we obtained was 1.9×10^6 neutrons/cm^2/μA at 10 cm distance from the ^{9}Be target. The flucence, however, is only a half of the past study by the group in PKU. According to their study [95], they gave 3.8×10^6 neutrons/cm^2/μA at the same distance with a similar Tandem accelerator in China, therefore, we adopt larger uncertainty for the neutron flux in the accelerator, corresponding to $(1.9 - 3.8) \times 10^6$ neutrons/cm^2/μA at 10 cm distance from the ^{9}Be target. Further study of the neutron yield measurement is ongoing and planed, and these efforts are described in Section 17.4..

The test materials were located at various distances from the target, therefore the neutron fluence and flux are estimated with a simple assumption that it decreases as the inverse square of the distance.

17.2.2 Neutron Toreleance Study for CyDet

CDC readout electronics (RECBE)

The readout electronics for the CDC named RECBE which is described in Section 13.2.5 is located at the downstream of the CDC. As described in Section 17.1.2, the neutron flux was studied at the position of RECBEs. The FPGA on RECBE is `Virtex-5` XC5VLX155T, and the SEU/MBU effect must be studied in such a high neutron flux described inSection 17.1..

The self-repairing module (SEU controller) is implemented on the FPGA to repair SEU's caused by neutrons. The SEU controller can detect SEU and repair the flipped bit by using general ECC (Error Correction Code) method with 60 MHz clock timing. Also it can detect MBE ("Multiple Bit Errors", multiple SEUs occurred at the same time), but sometimes it fails to repair due to the principle of the ECC method. The numbers of SEU and MBE are counted and could be read-out via UDP communication, therefore we can monitor the status of the SEU/MBE in an almost real-time way depending on the frequency of the read-out. As of March 2016, we have confirmed the functionality of the SEU controller in the CRAM (Configuration Random Access Memory) region. Further development is necessary to implement the function for the other memory regions.

The functionality of SEU controller was confirmed in the beam test performed with TANDEM accelerator at Kobe University, with neutron flux of $\sim 10^6$ neutron/cm^2/sec at several centimeter distance from the neutron target. The SEU controller worked out well, and we were able to measure the SEU rate against neutron flux. In addition to SEU, we observed URE (UnRecoverable Error) caused by MBE, unrecoverable SEU, communication lost, accidental change to detection mode from recovery mode or other known/unknown reasons. Once URE happened, RECBE was able to be recovered by downloading the firmware or power-cycling. The latest result of SEU rate^{-1} is $(2.12 - 4.25) \times 10^8$ neutron/SEU/Virtex-5 with neutron incident from the back side. The URE rate is roughly proportional to the SEU rate, and the ratio of SEU and URE was measured to be 283 ± 19(stat.) SEU/URE with neutron incident from the back side. Figure 17.7(a) shows the relationship between the number of SEU and integrated neutron flux, and the ratio of SEU and URE is shown in Figure 17.7(b), both with

neutron incident from the back side. With neutron incident from front side, the SEU rate^{-1} is relatively larger (it means higher tolerance), so we employ the worse rate (from back side) for conservative estimation.

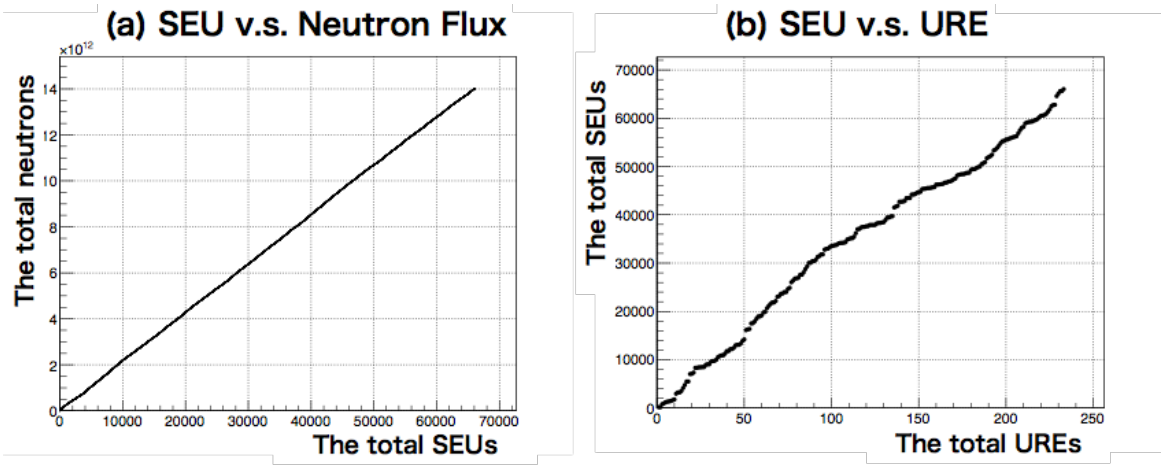

Figure 17.7: *The measurement result with neutron incident from back side. (a) shows the SEU rate against integrated neutron flux, and (b) shows the URE frequency against number of SEU.*

The URE rate in COMET Phase-I is estimated with the measurement result and the simulation result. In practice, the effective neutron flux is estimated with the PHITS simulation for each energy region summarized in Table table:cdcreadoutneutronflux and the calculation of the cross sections for each neurton energy with PHITS studied in [96]. The URE rate corresponds to $(5 - 10)$ min./URE/104 RECBEs. We need to re-download the firmware into one of 104 RECBEs every 5 or 10 minutes. It takes about 15 seconds at most to re-download the firmware during which the data cannot be acquired from the corresponding RECBE. Further efforts will be made to speed up re-download using more suitable device or method.

Table 17.2: *Summary of neutron flux and fluence in each energy region estimated with PHITS for the Phase-I (200 days). The values are averaged of every positions of RECBEs*

Neutron Energy (E_n) [MeV]	$E_n < 0.1$	$0.1 < E_n < 5.0$	$5.0 < E_n < 10$	$E_n > 10$
Neutron Flux [n/cm^2/sec]	5.89×10^4	2.95×10^4	8.03×10^2	1.36×10^3
Neutron Fluence [n/cm^2]	1.02×10^{12}	5.10×10^{11}	1.39×10^{10}	2.35×10^{10}

The implementation of TMR (Triple Modular Redundancy) may help to make the SEU and URE rate smaller. We started to implement the TMR function into the firmware and have a plan to test its effectiveness. In addition, we should care not only CRAM but also BRAM (Block Random Access Memory) to provide assurance of data quality. From a view of data taking, we might continue data taking even during re-downloading period. It is also alternative to reduce the SEU/URE rate by locating local shields around RECBE boards to reduce the neutron flux physically. We need to consider the shield seriously if the URE rate with the TMR is too high to accept. We will continue the study to cope with the neutron radiation effect for more stable and efficient operation.

CTH readout

Neutrons affect the fine-mesh PMT and semiconductor devices of the CTH front-end (FE) board. It is known that neutrons degrade the permeability of the window glass on PMTs and semiconductors.

We carried out neutron tolerance test of the fine-mesh PMT, Hamamatsu H8409-70, at the tandem accelerator facility in Kobe University. Neutrons up to the fluence of 10^{11} neutrons/cm^2 were irradiated and no significant difference was seen. A CTH FE prototype board was irradiated with 10^{12} neutrons/cm^2 at the facility. DAC, Microchip MCP41050, on the board had no problem. The uncertainty of the measurement setup was too large to evaluate degradation of the CTH FE precisely although the board continued amplifying signals during the test.

A neutron tolerance test at the facility is planned in 2016. A fine-mesh PMT and a CTH FE prototype board will be irradiated with 10^{12} neutrons/cm^2. Some candidates of regulator, which is not mounted on the current CTH FE prototype, will be also irradiated in the test. If we found problems with them, they will be altered into suitable parts confirmed enough radiation tolerance.

17.2.3 Neutron tolerance study for StrECAL

Readout electronics for Straw Tracker and ECAL (ROESTI and EROS)

The readout electronics for the Straw Tracker named ROESTI is located near the tracker as described in Section 11.4., and the one for the ECAL named EROS is located downstream of the detector solenoid, which is described in Section 12.3.. As well as the RECBE, the neutron fluence was studied with PHITS simulation in Section 17.1.2 and the SEU/MBU studies in the FPGA on ROESTI/EROS (Artix-7, XC7A200T-2FBG676C) were performed.

In both firmwares for ROESTI and EROS, SEM (Soft Error Mitigation) module provided by Xilinx is implemented for SEU/MBE in CRAM region, which can detect SEU and repair the flipped bit with general ECC and can detect the MBE in real time. The numbers of SEU and MBE are counted and could be monitored by UDP and JTAG communication, then the status of CRAM can be monitored in almost real time. When the URE including MBE is observed, DAQ is stopped and the firmware is downloaded via JTAG cable immediately. On the other hand, ECC using Hamming Codes is implemented for SEU/MBE in BRAM (Block RAM) region, which can also detect SEU and repair the flipped bit and can detect MBE. As well as the CRAM, those can be counted and monitored. Those information are also added in the readout data and then we can cope with the data with MBE in offline.

The functionality of both SEM for CRAM and ECC for BRAM were confirmed in the beam test performed with TANDEM accelerator at Kobe University as well as the RECBE. Both SEM and ECC worked well, and we measured the SEU rate against neutron flux. Figure 17.8 shows the numbers of SEU/URE in CRAM and SEU/MBE in BRAM as a function of the elapsed time corresponding to the neutron flux of $\sim 3 \times 10^6$ neutron/cm^2/sec with neutron incident from the front side. The latest results of SEU and URE rates^{-1} in CRAM are $\sim 3 \times 10^7$ neutron/SEU and $\sim 8 \times 10^9$ neutron/URE, respectively. The SEU and MBE rates^{-1} in BRAM are $\sim 1 \times 10^8$ neutron/SEU and $\sim 9 \times 10^{10}$ neutron/MBE, respectively.

The URE rate in CRAM at the environment of COMET Phase-I was also estimated with the measurement and the simulation results. Utilizing the same way to the RECBE and considering the safety factor to the simulation result, the URE rate corresponded to a few hours/URE/125 ROESTIs. It is expected to be reasonable, but more detailed simulation studies, for example

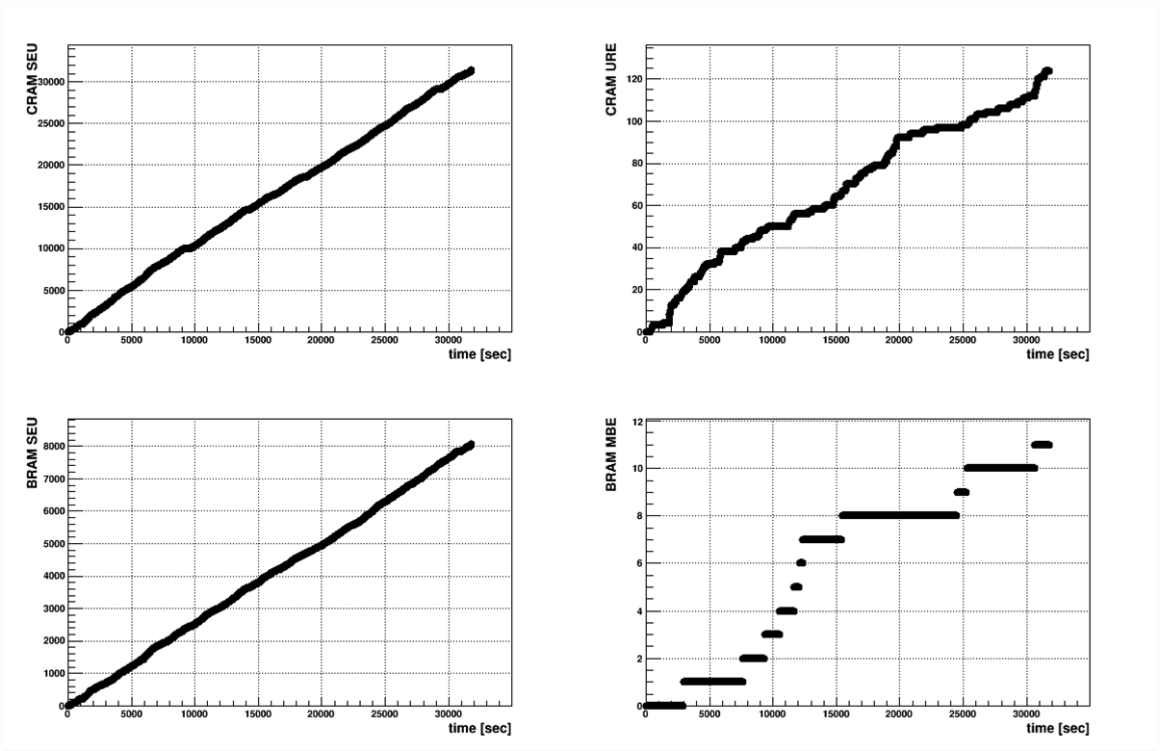

Figure 17.8: *The numbers of SEU, URE, and MBE as a function of the elapsed time corresponding to the neutron flux of* $\sim 3 \times 10^6$ *neutron/cm*^{2}*/sec in ROESTI. Top left and top right show the numbers of SEU and URE in CRAM, respectively. Bottom left and bottom right show the numbers of SEU and MBE in BRAM, respectively.*

comparison with other simulation tool, detailed validation test of the simulation model, and so on, are needed and we will continue to study the radiation tolerance.

17.2.4 Neutron tolerance study for trigger board

FCT and FCT interface board

The neutron radiation tolerance of the FCT board was tested by irradiating two of them with 10^{12} neutrons/cm^2, whose energy spectrum is similar with COMET simulation. We did not find any problem in FPGA firmware status and its reloading. The bias voltage was stable, which means power regulators were stable after neutron irradiation. For optical link, although the optical link failure was observed during and after neutron irradiation, it was not possible to isolate the reason of failure to any of optical link related parts. For example, SFP is the important part of optical link, however, in general, it is known that SFP is weak to gamma radiation but strong against neutron radiation. In our study, the SFP on FCT was found enough hard against gamma radiation (Section 17.3.). Therefore, the neutron radiation hardness of FCT should be carefully re-examined, specially neutron radiation hardness of optical link related parts will be tested carefully.

Trigger board (COTTRI)

Although the neutron radiation tolerance of COTTRI has not been done yet, almost all parts can be commonly used in COTTRI final version and other electronics boards, such as RECBE

for which neutron radiation tolerance has been well verified since the design of the COTTRI final version is still in preparation. We will have a neutron irradiation test for COTTRI prototype in 2016 to confirm the radiation tolerance of each chip used in the COTTRI prototype.

ECal pretrigger board

Neutron Irradiation tests with pre-trigger board v.2 will be in July in Kobe University, Japan. The plan of the test is next:

1. Testing of flash memory (EPCS16, EPCS64) on the board, which is used to configure the FPGA. The firmware will be remotely checked by read of the check-sum.
2. Testing the ADC (AD9212) radiation resistance. To download to ADC strictly defined sequence of data, and use two identical memories in the FPGA for readout. For these tests will used FCT (v.1) and GLIB.
3. Testing the data inside the pre-trigger FPGA (Cyclone IV), using an internal simulation memory. The data from pre-trigger board will be read by FCT and GLIB.
4. Testing all voltage regulators (NCP1117, LM1117) on the boards from the nominal values under exposure to radiation.

17.3. Gamma-ray Tolerance

CyDet According to the Belle-II group study, their RECBE board has tolerance against ∼8.8 kGy of the gamma-ray irradiation at least. In principle, the RECBE board for the COMET has same tolerance because the parts, chips and PCB are almost the same as those of Belle-II RECBE. However, we plan to confirm the tolerance with irradiation test in 2016. The estimated gamma-ray level by the simulation study gives roughly ∼0.2 kGy around the CDC detector.

For CTH, a fine-mesh PMT and a CTH FE prototype board are required to be tolerant to 2 kGy corresponding to 200 days operation with safety factor. A gamma ray tolerance test in Kyushu University is planned in 2016.

StrECAL ROESTI and EROS are expected to be exposed to gamma radiation. Based on the simulation results and safety factor, 1 kGy was estimated to be irradiated to the boards in the worst case. Using the prototype of ROESTI, the irradiation test with gamma-ray from ^{60}Co gamma radiation source was performed at National Institutes for Quantum and Radiological Science and Technology (QST), Takasaki. It was observed that some parts had problems. One power regulator had changed the output voltage during irradiation and stopped the output after 400 Gy irradiation. One DAC stopped the output voltage after 200 Gy irradiation. And one SFP link failed after irradiation. As for the SFP, we investigated and it was found that the optical converter chip was dead after irradiation. On the basis of those results, we have searched other regulators, DACs, and SFPs for parts selection. More irradiation test for those and new parts on the boards should be continued. In June 2016, we had the gamma-ray irradiation test with 1 kGy gamma from ^{60}Co for the new candidates of regulators and DACs and new parts at Tokyo Institute of Technology. We found that some regulators and DACs worked after 1 kGy irradiation, but slightly change in the DAC was observed. We will continue to search the

candidates of the parts on boards and to have more detailed irradiation tests for final design of the ROESTI and EROS.

Trigger system The only trigger component exposed to hard gamma radiation are FCT board and COTTRI front-end board. The radiation tolerance of FCT was tested by irradiating two FCT with 1 kGy gamma from ^{60}Co radiation source, which corresponds the worst gamma radiation level of Phase-I. It was found the FPGA was not affected by this irradiation, however, the bias voltage changed by up to 15% after irradiation, which means unreliable operation of power regulators, even though the FCT operation was possible. The some problems of optical link were observed, such as RX loss or link lock failure.It is expected that the problem might not be the effect of irradiation and the SFP failure due to irradiation, but might be caused by the other parts like clock and jitter cleaner chip. Detailed investigation is ongoing. More irradiation test will be performed with radiation harder design and power regulator chip selection.

For the COTTRI front-end, we will choose regulators that are found to be gamma-ray radiation tolerant in several irradiation tests performed by ourselves or well confirmed by other experiments such as regulators on RECBE board. Therefore, the only remaining gamma-radiation-tolerant parts we have to test are ADC and SFP+ that will be used in the final version of COTTRI. In June 2016, we had the first gamma-ray irradiation test with 1 kGy gamma from ^{60}Co for ADC chip on COTTRI (AD9287) and we confirmed that a chip works fine after the irradiation without problems. We will have more detailed test for more ADC chips together with several SFP+ candidates in order to confirm the final design of COTTRI in 2016.

17.4. Future Plan

The next neutron irradiation test is planed in the end of July 2016 at Tandem Facility in Kobe University, and many materials will be tested together among COMET group. There are two main motivations, one is to test the SEU/URE issues on each FPGA, and the other one is to investigate the deterioration for various devices and materials. Everything which will be located in the high neutron environment in COMET Phase-I has to be tested with enough safety factor before the start of the installation.

In addition to the neutron irradiation test, there are some plans for gamma-ray irradiation test in Tokyo Instutute of Technology, Osaka University, and Kyushu University. We will individually test, or work together for common electronics parts like SFP+ modules.

In the following sections, we describe future plans for some important items.

17.4.1 Neutron Yield Measurement

In addition to the past measurement with the group in Tokyo University, we also performed the measurement with CR-39 in January and March 2016. To reduce the uncertainty of the imagery analysis for CR-39, we are trying to improve the analysis method.

Another effort is planed to measure the neutron flux with silicon photo diode. The silicon photo diode has a behavior of the linear response for the leakage current to the neutron fluence, and it is widely, deeply and well studied in the field of high energy physics. We will try the measurement in July 2016 for the Tandem accelerator in Kobe University.

17.4.2 Regulators for Low Voltage Distribution

A part of regulators for low voltage distribution to the electronics are located near the detector system. It is well known that some regulators cannot be used in high gamma-ray environment, but it is not well investigated which one can be used. As described in section17.3., it is experimentally found that some regulators are not available in high gamma-ray environment. Thus, we need to search the candidates used in final version of the electronics and they should be tested. We have already found that one candidate may be available but careful investigation should be done, so more gamma-ray irradiation tests will be performed in 2016. In parallel, we continue to search other candidates for safety and those test will also be done. After the tests, we will determine the suitable regulators for the final version of the electronics.

17.4.3 Optical Tranceiver (SFP+)

It is known that an optical transceiver can be broken by high gamma-ray dose, and there are many optical transceivers commonly used for the electronics located at the experimental area in the COMET experiment. We need to carefully choose the transceivers to avoid the communication failure due to the gamma-ray dose. Although it depends on the location and dose rate there, we need to test the tolerance of the optical transceivers for all electronics against the gamma-ray.

We plan to have some gamma-ray tests in 2016. Some kind of optical transceivers will be tested with various electronics board to communicate during gamma-ray dose.After the tests, we can choose the suitable transceiver for our usage.

Chapter 18

Offline Software

Until March 2013 simulations of COMET had been done on an ad-hoc basis with little collaboration-wide integration. The majority of simulation used MARS [97] to cover the proton interactions in the pion production target and then a GEANT4-based [98] simulation (called comet_g4) to track the products through the whole experiment.

A new offline software framework has since been set up that facilitates the processing of both simulated and real experimental data through the full calibration-reconstruction-analysis chain. This section summarises the offline software and simulation plans for Phase-I.

18.1. ICEDUST Framework

For the calibration, reconstruction and analysis of data from COMET Phase-I, it is essential to have an offline software framework that treats this data in the same way as for simulated data. Since the development and testing of a new framework is a significant undertaking, it was decided that the COMET framework be based upon an existing framework that has been well tested in a real data-taking scenario.

To determine the framework that best fits the needs of COMET, a requirements document was written to define the key features needed of the offline framework. A number of existing frameworks were compared against the specified requirements and it was decided that the framework used for the near detector for the T2K experiment [99] at J-PARC, known as ND280, would be the best choice. This framework has the advantage of being tested at J-PARC and therefore much of the data model (including the calibration loop) can be re-used.

The ICEDUST (Integrated Comet Experimental Data User Software Toolkit) framework was then developed based upon the framework used for the ND280 experiment and the simulation features provided by comet_g4 have been incorporated. The major components of ICEDUST and the data flow between them are illustrated in Figure 18.1.

Since so much of the ND280 framework has been re-used, we only summarize here the key parts of the framework and consider in more detail only major changes or additions that have been made. For more depth on the unchanged aspects of the framework, primarily the low-level parts of the framework, please see sections 4.5 and 4.6 of [99]. Nonetheless, it is important to stress that the physics contents of the software is being significantly changed given the differences between the experiments.

To ensure that software developed for ICEDUST is done in a consistent way across the collaboration, a number of naming and coding conventions have been defined (see Appendix A for

details).

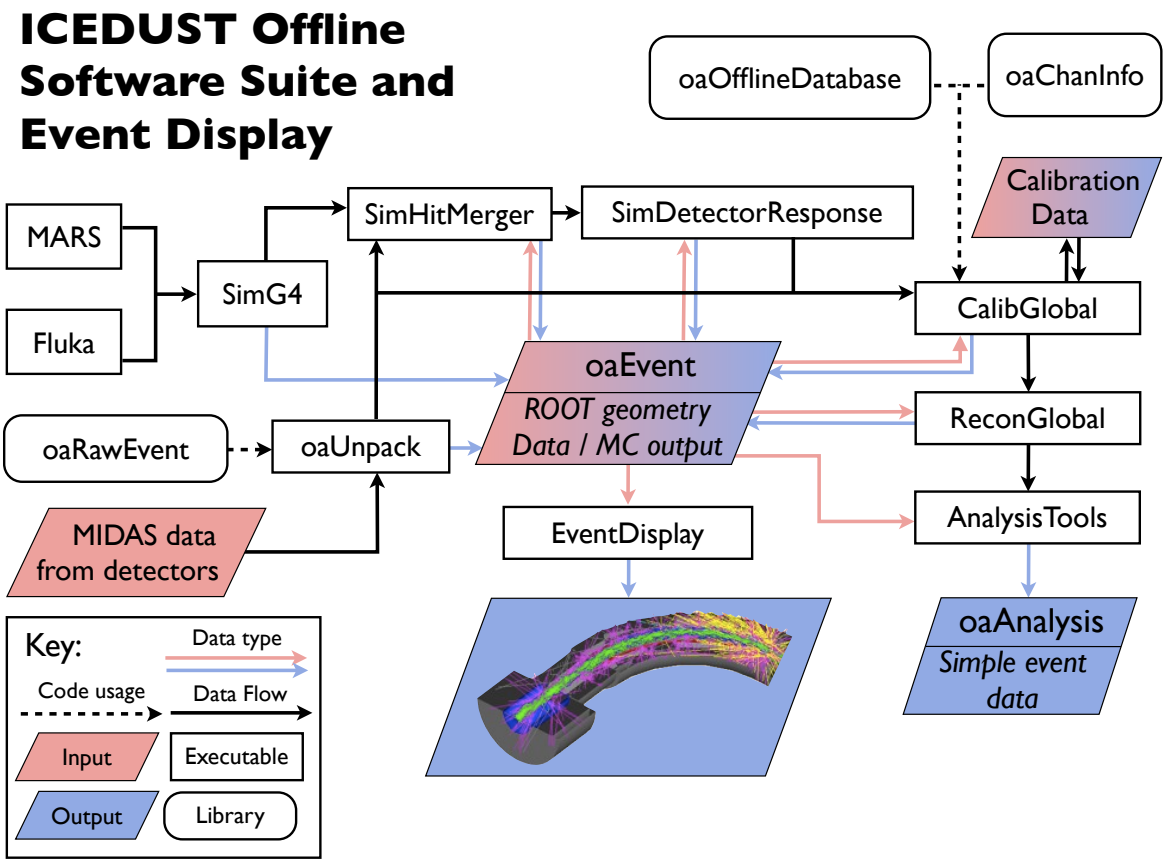

Figure 18.1: *An outline of the ICEDUST framework. The structure is largely based on the ND280 framework.*

18.2. Data Formats

The ICEDUST framework has inherited the offline and online data formats from the ND280 framework. The key strength of the approach used is the ability to treat experimental data on such an equal footing as the simulated data. This is achieved in two ways:

- An unpacking mechanism which converts the raw MIDAS data into offline root files.
- A wrapping package which can provide a semi-transparent method to process raw data.

The offline format consists of a structured ROOT file, known as the "oaEvent" format. This format provides room for header information such as a description of the geometry in the experiment, experimental conditions such as temperatures and times, and magnetic field information. Alongside this the actual event data is stored in a container specific to the current stage of data processing (calibration, reconstruction or simulation).

The description of the geometry is stored alongside the data, either in the form of a hash tag pointing of a particular archived geometry which is automatically retrieved as needed, or else as a persisted ROOT format. The ROOT format uses the various TGeo classes which

implement all geometry needs such as navigation, mass calculations, material descriptions and visualisation. This means that all packages throughout the framework use a common geometry description as well as providing an easy book-keeping mechanism.

For more information on the file formats, see the oaEvent manual from ND280 [100] and [99].

18.3. Simulation

The simulation of COMET has been sub-divided into smaller tasks. The standard simulation chain for production Monte-Carlo data is:

1. **Simulate production target** This is done separately so we can use packages that include different hadron production models.
2. **Particle tracking in GEANT4 (SimG4)** GEANT4 has a highly optimised tracking algorithm as well as many well tested experiment-based physics models. This package tracks particles from the production target to the various detectors and produces the simulated energy deposits.
3. **Detector Response Simulation** Energy deposits produced by SimG4 are converted into realistic detector outputs such as ECAL crystal waveforms or CyDet wire hits. Various detector effects such as finite resolution, cross-talk and random noise can be added here.
4. **Rare-process selection** Occasionally we may wish to focus a study on one of the rarer signal or background processes. Since this would normally require the simulation of a lot of unimportant processes, a package is being developed to merge hits from rarer processes together to artificially increase their statistics.

Up to truth information, steps 1 and 2 can be done by any of the various external Monte Carlo packages that have been incorporated into ICEDUST. These are GEANT4 [98], MARS15 [97], PHITS [101] and FLUKA [102, 103]. We describe the use of GEANT4, MARS and FLUKA within ICEDUST below.

18.3.1 Geometry Definition

SimG4 is the package tasked with running GEANT4 tracking and producing geometry files that all other packages use through the ROOT format described above. This task is made non-trivial by the necessity for a highly detailed description of the geometry in order to check all possible sources of backgrounds combined with COMET's staged approach meaning the experiment is likely to change quite drastically throughout its lifetime.

To meet these requirements despite the challenges, a modular design has been implemented whereby the entire experiment is divided into *components*. Each component is defined by a *geometry*, which gives the various volumes to use and how to nest them, and a *controller*, which provides the various parameters needed to define the size and position of each volume. A controller uses a GEANT4 *messenger* to provide a user with run-time control of the parameters. This division of labour is illustrated in Figure 18.2. For each Component, we define 3 classes:

- Geometry - Defines the various solids and shapes that need to be assembled to produce the Component. The Geometry is essentially "dumb" in that it does none of the calculations

necessary to define and place each solid. A Geometry is aware of the Geometries of any Sub-Components and of its own Controller.

- Controller - The brains of the Component. Responsible for providing the Geometry with the parameters it needs, but can do this however it needs. Information can be passed between Controllers (see below) or obtained from a user via a Messenger. If needed, it can translate a more natural parameterisation of the Component, from the users perspective, into the raw parameters needed by the Geometry.

- Messenger - The entry point for a user. Values to certain parameters are fed into this using standard GEANT4 style commands. The Messenger is at the very end of the information chain, and has no knowledge of anything, but itself.

In practice, a user writes the geometry in C++ code, then defines all the parameters in a GEANT4 macro which is processed by the messenger and controller. These parameters can be defined using complex expressions involving other parameters, which provides a flexible way for building the geometry.

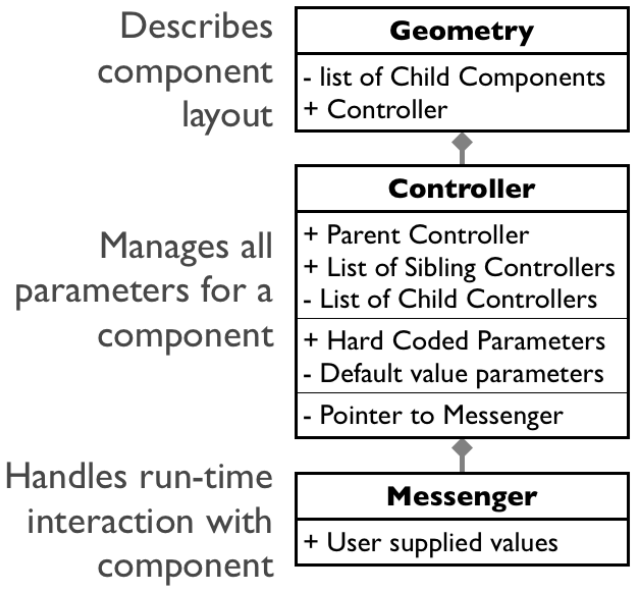

Figure 18.2: *Class structure of the Geometry-Controller-Messenger model.*

Access to parameters between components is provided, but in a restricted manner so that dependencies between logically isolated components are kept to a minimum. This is achieved by only allowing a given component direct access to parameters of components that are either immediate daughters, siblings or predecessors. This is illustrated in Figure 18.3 where Component 1.a has access to parameters of any component within the larger red blob.

The World Component is the top-most component in the component hierarchy and which World to build is specified at runtime. This allows people to simultaneously develop simulations for both Phase I and II but also provides the ability to specify single Components to be used just for testing. Different World implementations are expected to re-use Components as much as possible and Components have been implemented with this aspect in mind.

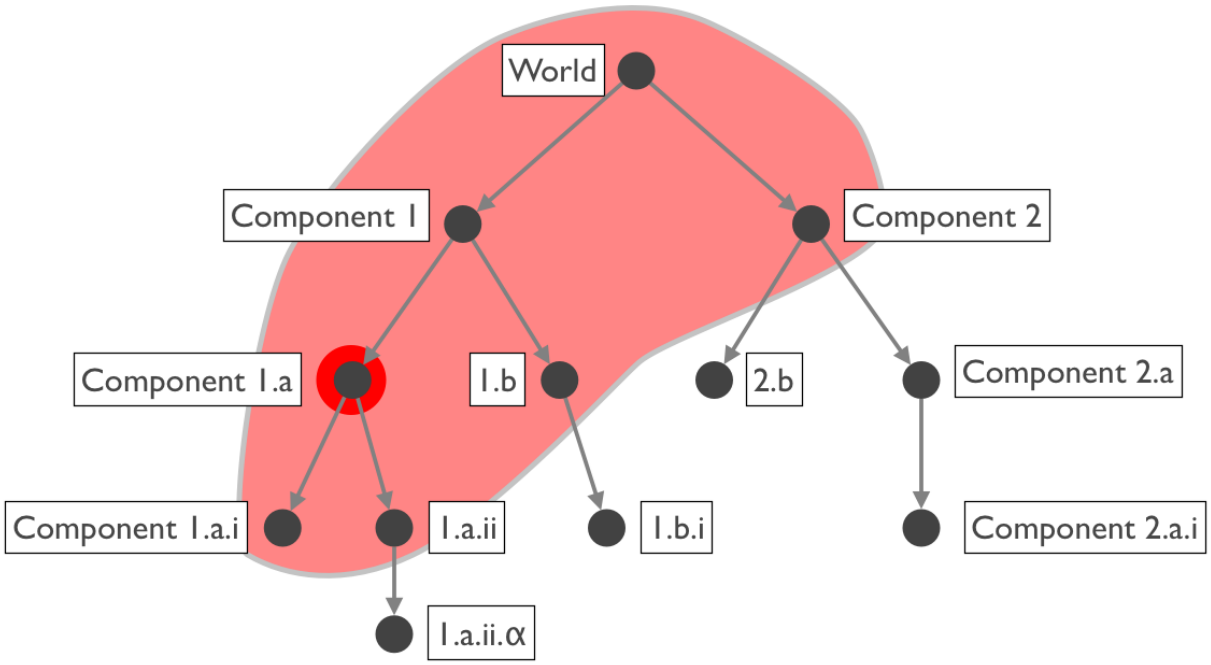

Figure 18.3: *How parameters are shared amongst different components. The Controller of the component circled in red has access to the parameters managed by Controllers of components contained in the larger red region.*

18.3.2 Custom GEANT4 Processes

Custom modelling of physics processes has been developed within the GEANT4-based simulation to provide models that match experimental data and models that include the latest theoretical updates. In particular, modelling for negative muons stopping in Aluminum has been implemented into ICEDUST, and the class diagram can be seen in Figure 18.4. The implementation of the modelling should be robust to future GEANT4 updates, but also allows new spectra to be included easily as they become available.

18.3.3 Hadron Production Models

There is a large variation in the pion and muon yield predicted by different hadron production codes. It is therefore essential that the simulation has the ability to use different hadron production codes. Currently, simulations have been done using FLUKA [102], GEANT4, MARS and PHITS and these codes have all been integrated into the ICEDUST framework. Ensuring the consistency of the geometry requires careful consideration when using FLUKA and PHITS as they do not have native support for the ROOT geometry.

Since these packages contain very accurate, experimentally supported hadron interaction models, they are particularly useful for studying and simulating the pion production target and running shielding calculations.

When simulating the interaction of the proton beam with the production target particles that pass through a cylindrical surface just outside the production target are stored to a ROOT file. All packages can read back in these files to start a subsequent run. Careful consideration must be given to mirrored or high helical-pitch-angle particles since they will cross the read-out surface multiple times resulting in the over-counting of such particles.

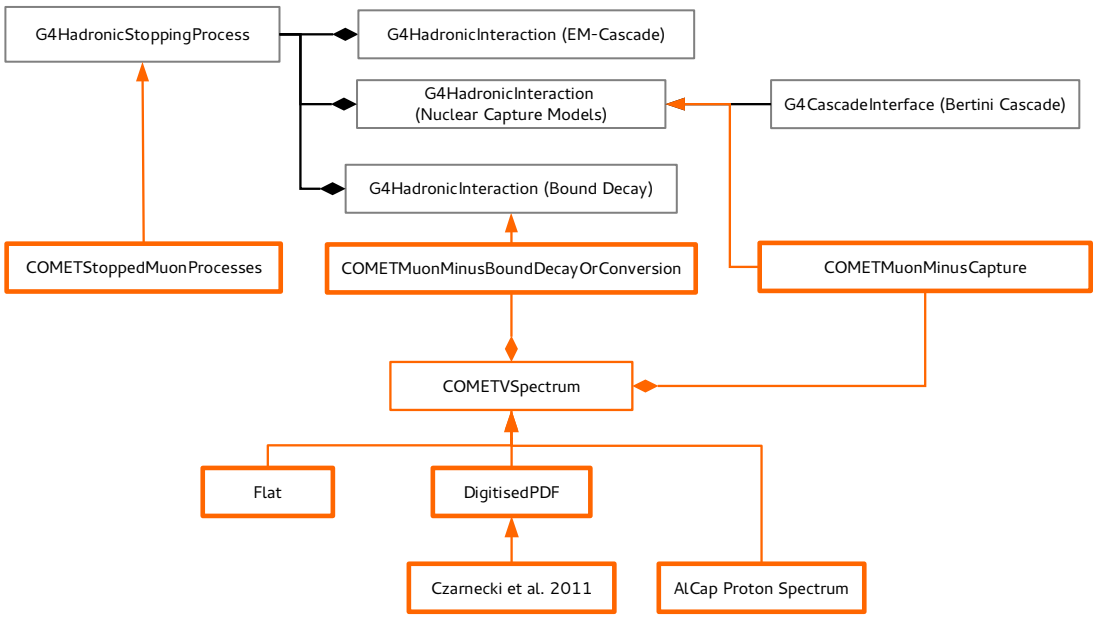

Figure 18.4: *Class diagram showing how custom muon physics models are included in SimG4.*

FLUKA

FLUKA [102, 103] is a Monte Carlo code produced by CERN and INFN for simulation of the interactions and propagation of particles through matter. It can model a wide range of particles and their interactions from keV to TeV scales.

For COMET, FLUKA can be used to model the production target and surrounding region and output particles either on the surface of the target or at the entrance to the first transport torus. This is necessary to find the absolute and relative fluxes of particle species entering the transport line, their spatial and momentum distributions and for optimising the target design.

FLUKA is written in Fortran. It consists of a core binary, user routines that can be compiled and linked into the binary and a set of utility scripts. The user routines can be used to customise input and output and to hook in to physics models and tracking. The GFortran compiler is required for creating these routines. A FLUKA run is controlled by an ASCII input file, composed of "cards" that describe the geometry, materials, source simulation settings and scoring (output).

Unlike codes such as GEANT4, the user has limited options to adjust the physics models used by FLUKA. The user can adjust cuts for production and transport, and disable some processes such as photo-nuclear interactions. Simulations were performed with both the default (NEW-DEFA) and precision (PRECISIO) settings. The precision settings have lower cuts, for example down to thermal neutrons, and use about 10 times as much CPU time. The physics models are described in detail in section 1.2.1 and the user settings in section 7.12, of the FLUKA

manual [103]. A 1 ms simulation time cut was found to be necessary to prevent rare instances of low energy electrons travelling in small loops in vacuum, using many hours of CPU time.

In FLUKA, geometry is described by regions composed of bodies. Bodies represent fundamental shapes, such as cubes, spheres, infinite planes and cylinders, placed in physical space. Regions are formed by Boolean operations on those bodies. Regions are assigned a material and optionally a magnetic field. Regions must not overlap, so space for internal regions must be explicitly subtracted from surrounding regions. It is encouraged that the same bodies are used as the boundaries of neighbouring regions.

FLUKA reads its geometry from a simply formatted ASCII file. For ICEDUST this geometry is generated by a Python script. This allows geometry parameters to be read from an external source and to calculate the locations of objects.

The geometry includes the target, surrounding shielding and the magnet coils, as shown in Figure 18.5.

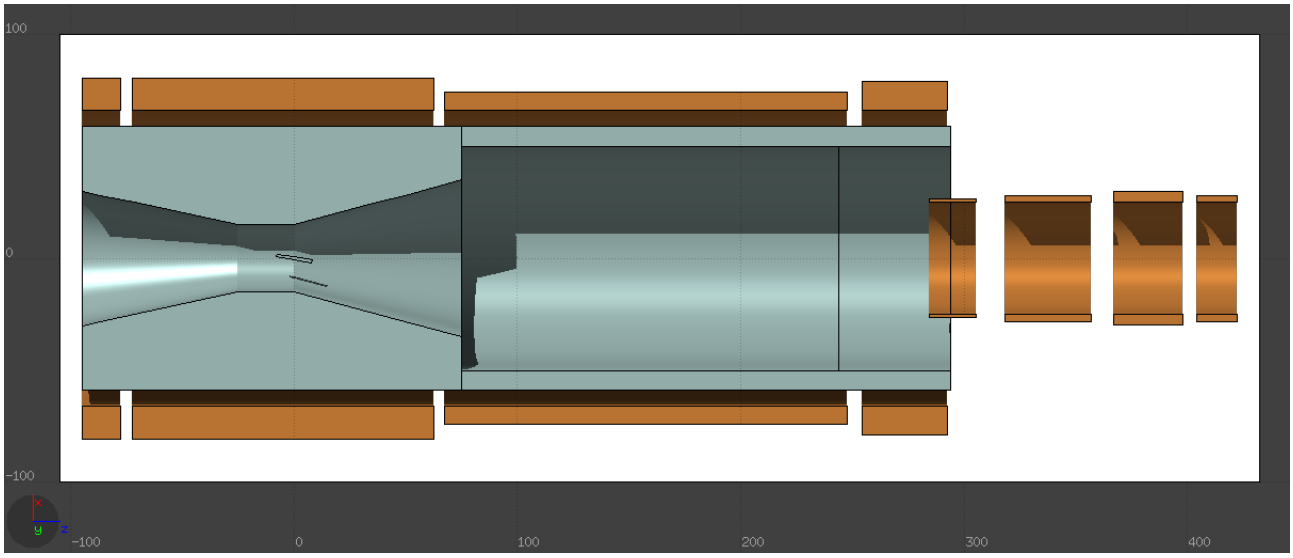

Figure 18.5: *FLUKA model of target and surrounding region, cutaways to show target at the origin of the coordinates.*

It is planned that geometric parameters can be read from ROOT geometry files that will be output by GEANT4 or from the source used to adjust this GEANT4 geometry.

While it is not possible to automatically translate GEANT4 geometry into FLUKA geometry, it may be possible to use FLUGG [104], an extension that replaces the geometry routines in FLUKA with calls to GEANT4.

Field maps are read from ASCII files using the same C code as used in the MARS COMET simulation. The C functions to interpolate the field at a given point are then called from a Fortran user routine that is linked into the FLUKA binary.

Currently the produced particles are written to an ASCII file that can be read in by GEANT4 for tracking through the rest of the experiment. The file has 1 line per output particle with columns for position x, y, z (mm), momentum x, y, z (MeV), time, particle id (PDG encoded), event id and weight.

It is planned to use ROOT files for these files, either by writing a converter that reads in the ASCII files, or by calling writing ROOT files in the output routine of FLUKA.

The FLUKA user license [105] requires each user to register to request a license in order to

download FLUKA and use it within ICEDUST. Though this is cost free for our uses, FLUKA must be acknowledged in publications.

MARS

MARS is a Monte Carlo generator developed at Fermilab that has been tuned to low energy pion data which is an important region of phase space for the COMET experiment. It will be used for both Monte Carlo event generation and for shielding calculations. MARS will also be one of the programs that will be used to calculate the radiation levels we can expect in the experimental hall. This will then be used to optimise the shielding geometry in order to minimise radiation exposure in certain areas. For this to be as accurate as possible, additional libraries are needed that contain low energy neutron data.

The two different uses of MARS require different sections of the geometry. For event generation, only the pion production target is necessary because, when comparing with hadron production models in other programs, it is preferable to remove any differences in magnetic field tracking and so particles from around the target are recorded.

For the shielding calculations the geometry of the whole experimental hall including solenoids, return yokes and concrete wall are required in order to accurately calculate dose rates in important areas. This geometry has been generated by SimG4 and exported as a ROOT geometry. This can then be imported into MARS, see Figure 18.6, ensuring that the same geometry is used and also simplifies maintaining the geometry.

Due to issues with licensing, it will not be possible to run MARS directly through the ICEDUST framework at any site. Currently MARS is licensed at UCL and KEK and it is possible to store the output of data produced at these sites in an ICEDUST compatible format ROOT file, which is easily distributable.

PHITS

PHITS (Particle and Heavy Ion Transport code System) is developed by JAEA for the calculation of particle transport and particle interaction. It can deal with the transport of almost all particles over a wide energy range and like FLUKA and MARS, PHITS is written in Fortran.

PHITS uses its own models for nuclear collisions and for hadron and neutron reactions, the Japanese nuclear library JENDL-4.0 is employed in the low energy region ($< 20\,\text{MeV}$). Between 20 MeV and 3 GeV, the INCL4.6, Bertini and INC-ELF model can be selected. Above 3 GeV, the Intra-nuclear cascade model JAM is used in PHITS. PHITS also has a different model called JQMD and JAMQMD for nucleus-nucleus collisions. The newest version of PHITS includes the EGS5 which can be used to simulate electromagnetic showers.

Charged particles are tracked using the COMET Phase-I field map and a ROOT output file is written containing all particles that pass through a surface around the target. An interface has been created to allow a particle distribution from a TURTLE simulation to be used as the primary particles.

The geometry of COMET phase-I experiment is created within PHITS based on the same design drawings as that used in SimG4, see Figure 18.7. It is currently not possible to directly import a ROOT geometry into PHITS.

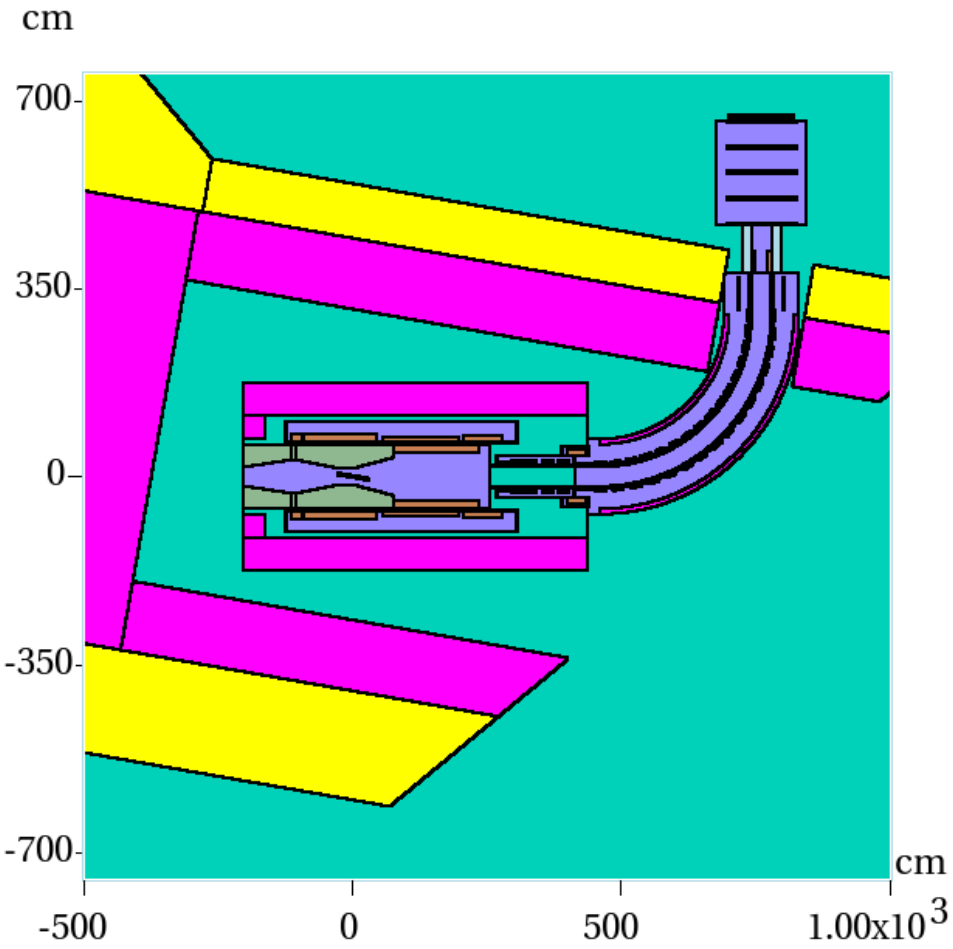

Figure 18.6: *Current geometry implementation of COMET Phase-I created in SimG4 and imported into MARS as a ROOT geometry.*

18.3.4 Refining Simulation Against Experimental Data

In order to achieve the single event sensitivity of Phase-I, it will be necessary to fully understand all source particles that could mimic an electron produced by muon to electron conversion. This requires accurate simulation of the experimental apparatus as well as understanding the production mechanisms of rare processes that produce signal-like electrons and ensuring that these are good model in the simulation.

It is important to make use of Phase-I to characterise the beam line and thus understand the transport characteristics of the curved solenoid channel in order to understand the background rates and validate the simulation. This can be done using a relatively simple detector to make flux measurements in the Phase-I beam line and by varying the magnetic fields and placing absorbers in the beam. Preliminary studies to show what sort of measurements can be done with Phase-I is presented in [106]. These results show that it is possible to alter the composition of the beam, by making simple changes to the magnetic field or using absorbers, and therefore understand the transport properties of the beam line better and will provide a way to ensure the simulation accurately models the experiment.

Important information will be provided by other experiments (e.g. AlCap) and beam tests (e.g. calorimeter resolution tests). The information from these will be fed back to improve the physics and detector descriptions in the offline software.

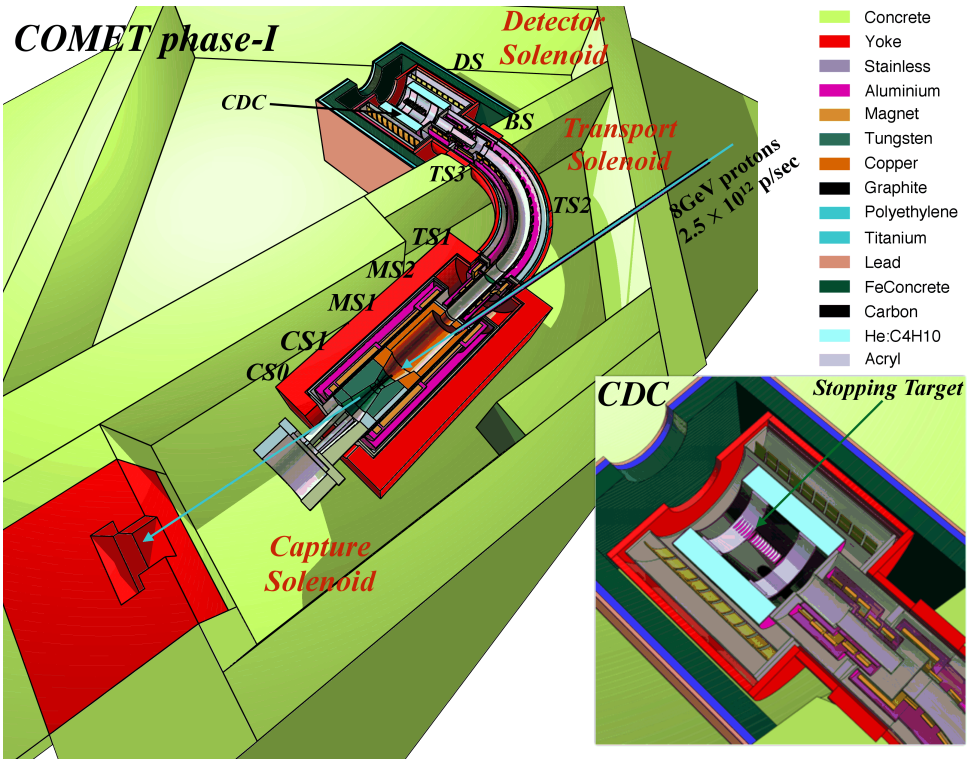

Figure 18.7: *Current geometry implementation of COMET Phase-I created in PHITS.*

18.4. Reconstruction

The aim of the reconstruction software is to take a collection of hits stored in a ROOT file, either from simulation or experimental data, and produce a collection of reconstructed objects such as tracks and clusters. This requires track or cluster finding and fitting code specific to each detector system.

The track fitting in ND280 was done using RecPack [107] but the interface was specified in a generalised way that can be easily adapted to other track fitting codes. GenFit [71] has been used for the CDC and straw tracker in stand-alone reconstruction studies. This is now integrated into ICEDUST, which provides:

- integration with SimG4;
- the ability to run on experimental data;
- integration with analysis codes;
- a simple interface to validated geometries and magnetic fields.

One important requirement of the ICEDUST framework is to provide a full audit trail that allows being able to recreate exactly an analysis plot. This requires persisting the precise process used by the reconstruction to create the reconstruction objects. This will obviously be different depending on which code is used, e.g. for track reconstruction. Thus, the minimal set of information required to fully specify the reconstruction process needs to be defined for each code. This can then be persisted in a database and used to tag data produced.

18.5. Future Plans and Schedule

In preparation for Phase-I data taking, three major releases of the offline software will be produced. The first two releases have been made and the current version is being used to tune reconstruction and analysis algorithms. The final release will be the version used to process data from Phase-I and will include a detailed geometry and field description based on measurements and engineering specifications. Figure 18.8 shows the schedule for the offline software including some of the major tasks and milestones.

With each major software release, there will also be the generation of large-scale MC data. This will be needed to debug the offline software as well as improving the experimental details of Phase-I, reconstruction algorithms and analysis code. In addition to producing data that will mimic the data from Phase-I, specific background modes will be simulated so that very rare processes can be studied in a resource-efficient way. The first of these MC production runs has been done and was used to debug the software and provide estimates of the computing resources required for future MC data production. These data sets will be used to develop reconstruction algorithms and analysis code and will provide estimates of the resources needed to process data from Phase-I, where the data rate is currently estimated to be 7 Tb/day for continuous running.

Grid computing resources will be used to generate and distribute the data. A similar production and distribution plan to that of the ND280 experiment will be used, though improvements to the computing infrastructure between J-PARC and KEK would be beneficial and discussions on this topic are on-going with the KEK computing centre.

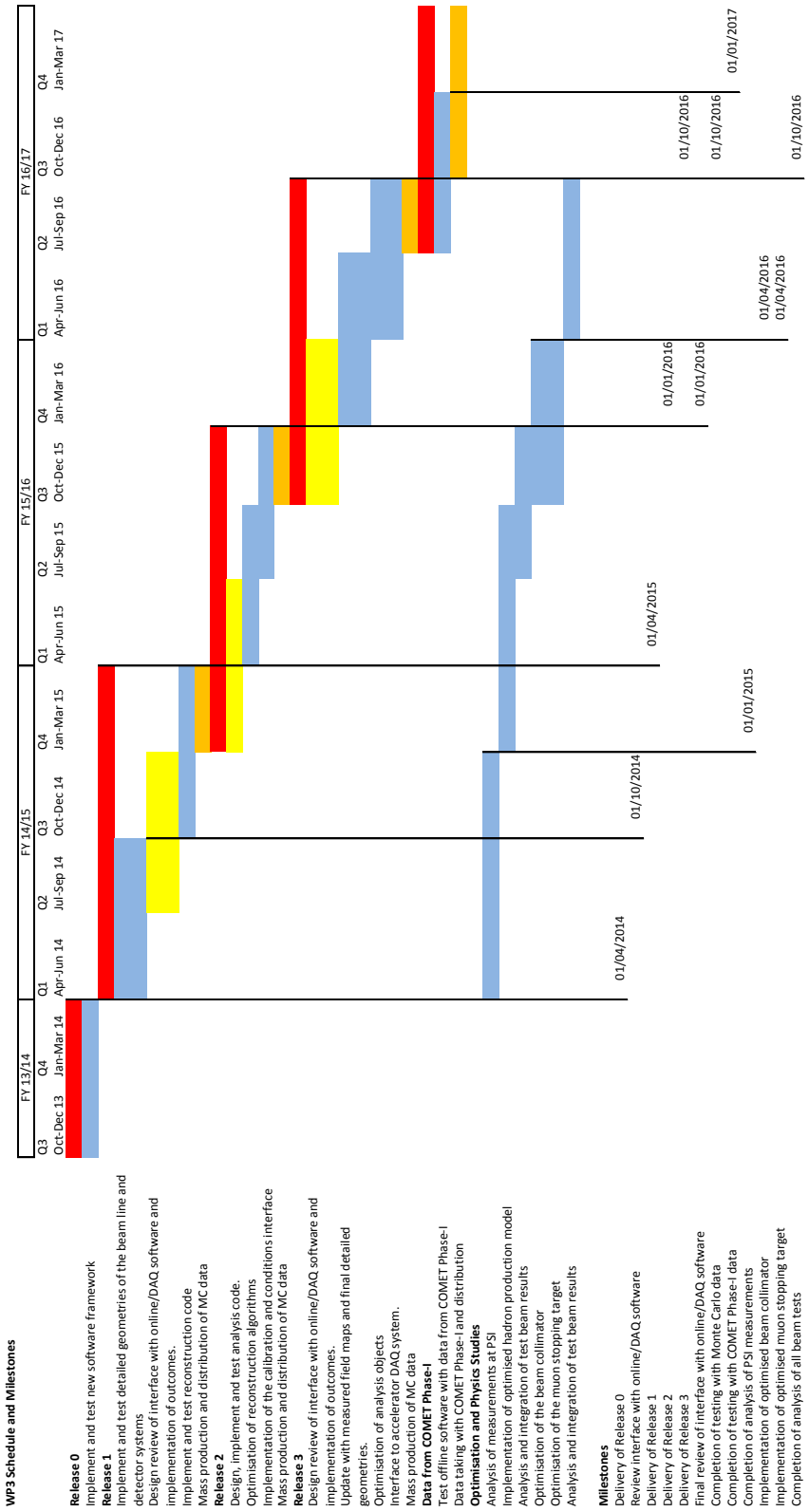

Figure 18.8: *Current schedule for the offline software showing the major tasks and milestones.*

Chapter 19

Physics Analysis Coordination

Currently, the focus of the physics analysis effort is to ensure that the development of the detector hardware, experiment infrastructure, software tools, and simulation studies and run-planning are progressing such that the goals of the experiment can be achieved, to allow real data, once it arrives, to be analysed promptly. Here we discuss the status of this work and the plans for the future.

19.1. Run plans

One ongoing effort is the compilation of a list of measurements to be made in both phases of the experiment. These include measurements which need to be made in support of the main physics measurements, such as beam intensity scans and dedicated detector calibrations.

For each type of measurement, we record its objective, the beam and detector configurations in which the data should be taken, the estimated length of time of data-taking and the analysis methods that need to be be employed, including any special tools that will need to be prepared. In many cases, simulation studies will required in order to refine the estimated data-taking time and analysis methods.

With this information, a detailed run plan will be produced, where beam time constraints will inevitably mean that we will not be able to accommodate all run types. In addition to this, the analysis results from these measurements may lead to different decisions being taken for subsequent data-taking—for example, an early study of the beam quality may lead to the need for more, or less, time spent on optimising the beam to reduce background rates. Such decision

Since beam time is allocated in competition with other experiments on the J-PARC Main Ring, it is imperative that the collaboration is able to put forward an efficient and well-motivated run plan.

19.2. Coordination

Analysis coordination during the construction phase applies to two broad categories of work: physics studies, mainly based on simulations, which help quantify and improve the physics reach of the experiment, inform any design decisions, and allow us to be ready to analyse data as soon as the experiment turns on; and oversight of ongoing construction preparation from an analysis perspective, to ensure that the goals of the experiment can be met. The latter includes

ensuring that the development of software tools occurs in a timely manner, and that decisions made regarding beam line and detector integration etc. are compatible with the needs of the different measurements that we intend to take.

19.2.1 Physics studies and software

Many inputs are required to perform the physics studies which determine the sensitivity of the experiment and allow us to be ready for the arrival of real data, including: a software framework that is fully tested for both simulation and real data; well-understood physics models for all aspects of the simulation, from hadronisation in the proton beam target and pion/muon beam interactions and the emission of particles from pion and muon captures on nuclei, and Geant4 versions; full detector and beam line geometries with means of accommodating real-world alignment offsets; magnetic field maps that are maintained to be up-to-date with respect to the designs for the solenoid and dipole magnets; the incorporation of detector test results into the calibration and decalibration methods in the software framework.

All of these aspects are currently undergoing improvement, and we will coordinate this effort such that changes are validated and the outputs of the physics studies are properly understood. It is also important that manpower is distributed appropriately, and that important areas of study are not overlooked.

Results from the current studies are presented in Section 20. However, as described in Section 18, a full ICEDUST-based study of Phase-I and II physics is ongoing and will be used to update the sensitivities and other aspects of the analysis preparations. The first full ICEDUST-based end-to-end physics sensitivity studies are expected in the second quarter of 2016.

The development of the software framework is closely tied to the analysis effort. The main ICEDUST framework passes real or simulated data through the calibration and reconstruction steps, and then outputs this information to configurable DSTs. The flexibility of the framework ensures that multiple algorithms can be implemented in parallel to allow cross-checking and comparisons to be performed between them. It is an analysis coordination task to make certain that there is enough redundancy for the most important algorithms, while also avoiding the concentration of too much effort in any particular area.

The output of ICEDUST will be used to perform high-level physics analyses. At this time, we choose a strategy where we do not write down the specifications for any high-level analysis software, as these ought to be driven by those who are performing these analyses, to meet the needs of the data at the time. In particular, there are several options for analysis software, such as the choice between using a ROOT-based framework, or making use of Python/iPython, a choice that we do not wish to impose on individual analysers at this time. However, we do require that analysis code is shared, so it can be tested fully and to avoid the redundant coding of similar algorithms.

19.2.2 Construction and development

Diverse considerations influence the progress of the subprojects across the experiment as they make progress to meet their goals, including cost and manpower, scheduling, engineering and safety. The impact on the experiment's physics potential of any decisions that are made must be evaluated at each step. This will require an understanding of the status of the physics sensitivity studies and possibly the use of dedicated simulation configurations, which will be done in coordination with those who are performing physics analyses as an analysis coordination

task.

Chapter 20

Physics Sensitivity and Background Estimations

The physics sensitivity and background estimations with the CyDet in COMET Phase-I are discussed. The single event sensitivity (SES) is determined for a given number of stopped muons, while taking into account all relevant efficiencies and acceptances in Section 20.1.˙ The different sources of backgrounds are identified along with their impact on the total expected background in Section 20.2.

20.1. Signal Sensitivity with CyDet

In order to estimate the physics sensitivity to $\mu-e$ conversion, the signal acceptance should be known. The signal acceptance of the CyDet is determined by its geometrical acceptance together with the track quality cuts and the acceptances of momentum and time windows of measurements. They are described in the following subsections.

20.1.1 Geometrical Acceptance

The detector configuration determines the geometrical acceptance of the CyDet. This includes the dimensions and positions of both the CDC and the CTH systems, along with configuration of a magnetic field. Based on the baseline design of the CDC and CTH systems, Figure 20.1 shows the distributions of longitudinal momenta (P_L) for the tracks which enter the CDC (open histogram), and further make two-fold coincidence of the CTH (blue histogram), and make four-fold coincidence (magenta histogram). The acceptance of the four-fold coincidence, which is mentioned in Table 13.11, is included. The plots at top and bottom are for single turn tracks and multiple turn tracks respectively. It is easy to understand that P_L should be larger for a single turn track to reach the CTH, whereas P_L is smaller for multiple turn tracks. The tracks to reach the CTH with a single turn and multiple turns are 0.21 and 0.13 with respect to all the tracks generated isotropically at the muon stopping target, yielding a sum of 0.34. The muon stopping distribution obtained from simulations was used. When the coincidence of hits of the CTH required, the acceptance is reduced. When the four fold coincidence is required (which corresponds to the histograms in magenta), the geometrical acceptance of single turn tracks and multiple turn tracks are 0.16 and 0.10 respectively (with respect to the total signal tracks generated isotropically). A sum of them is 0.26.

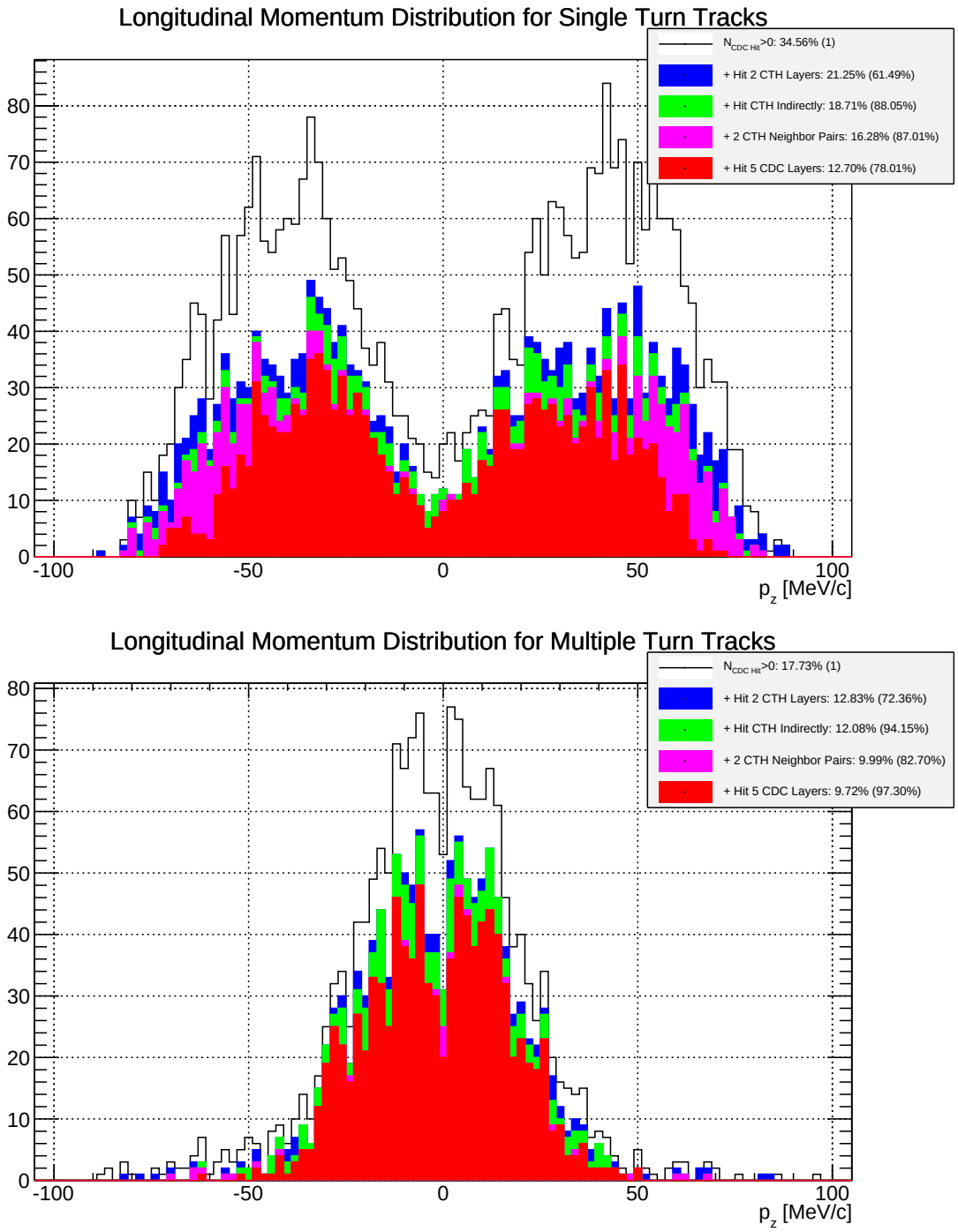

Figure 20.1: *Top: Distribution of longitudinal momentum (P_Z) of single turn tracks. Blue histogram is the tracks with two-fold coincidence of CTH, and magenta histogram is those with four-fold coincidence of CTH. Bottom; the same for multiple turn tracks.*

20.1.2 Track Quality Cuts

Several requirements are applied to candidate tracks before selection and reconstruction. This is to ensure only high quality tracks are considered. In particular, events with very low momentum resolution should be eliminated to reduce background contributions to the signal.

The hits selected by track finding are used for track fitting. In the tracking, the following requirements are made (see also in Section 13.5.2) ;

- tracks reaching the 5th sense layer (`NL5`),
- at least one whole turn in the CDC to be fitted is required (`NHIT`),
- number of degree of freedom greater than 30 (`NDF30`),
- normalized χ^2 less than two (χ^2), and
- hits in more than 3 consecutive layers at both entrance and exit of tracks (`CL3`).

The breakdown of the tracking quality cuts are given separately for single-turn tracks and multiple-turn tracks in Table 20.1. It is noted that the geometrical acceptances are taken from the previous section for single and multiple turn tracks separately.

	single turn tracks	multiple-turn tracks	single + multiple
Geometrical	0.16	0.10	0.26
`NL5`	0.78	0.98	
`NHIT` + `NDF30` + χ^2 + `CL3`	0.91	0.73	
total	0.11	0.072	0.18

Table 20.1: *Breakdown of the tracking quality cuts, together with the geometrical acceptance, separately for single turn and multiple turn tracks. These acceptance is normalized to all the signal tracks generated and emitted isotropically from the muon stopping target.*

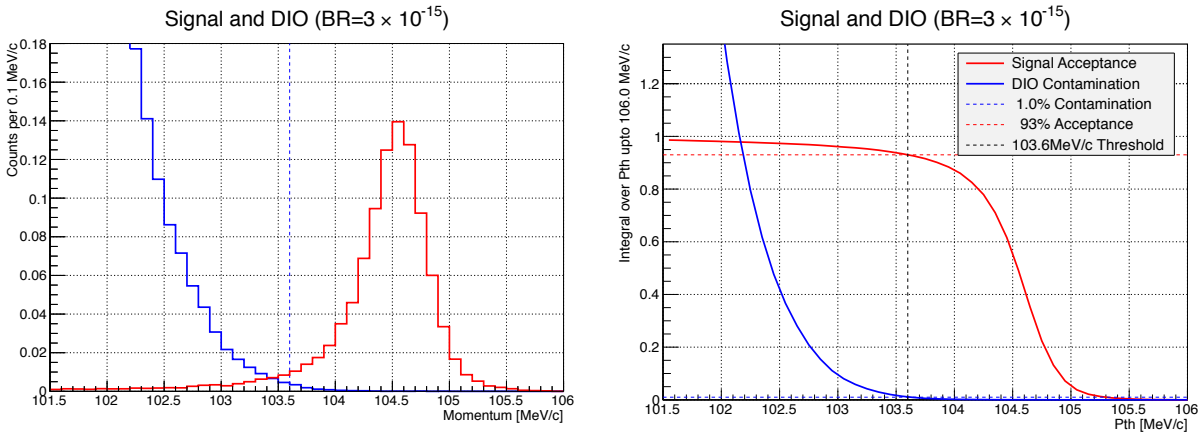

Figure 20.2: *Left: The momentum distributions for the reconstructed $\mu-e$ conversion signals and reconstructed DIO events. The vertical scale is normalized such that the integral of the signal curve is equal to one event. This assumes a branching ratio of $B(\mu N \to eN) = 3.1 \times 10^{-15}$. Right: The integrated fractions of the $\mu-e$ conversion signals and DIO events as a function of the lower bound of the integration range. The momentum window for signals is selected to be from 103.6 MeV/c to 106 MeV/c, yielding a signal acceptance of 0.93.*

20.1.3 Signal Momentum Window

A momentum cut can be used to reduce contaminations from background events such as DIO electrons. Figure 20.2 shows the momentum spectrum for the $\mu-e$ conversion signal events, together with the momentum spectrum for DIO electrons. These spectra are determined using

Monte Carlo simulations. In Figure 20.2, the vertical scale is normalized so that the integral of the signal event curve is one event at a branching ratio of $B(\mu N \to eN) = 3.1 \times 10^{-15}$. In this study, the momentum window is taken to be 103.6 MeV/c < P_e < 106.0 MeV/c, where P_e is the momentum of the electron. This cut is shown in Figure 20.3. According to this study, the signal acceptance of $\varepsilon_{\rm mom} = 0.93$ is obtained for a SES of 3.1×10^{-15}. A detailed description of the estimation of contamination from the DIO electrons is presented in Section 20.2.1.

20.1.4 Signal Time Window

The muons stopped in the aluminium muon-stopping targets have a lifetime of 864 ns. The $\mu-e$ conversion electrons can be measured between the proton pulses to avoid the beam-related backgrounds. However, some beam-related backgrounds can arrive late, after the prompt timing, such as pions in the muon beam. Therefore, the time window is chosen to start at 700 (500) ns after the prompt timing. This start timing will be optimized in the future offline analysis by using the real data.

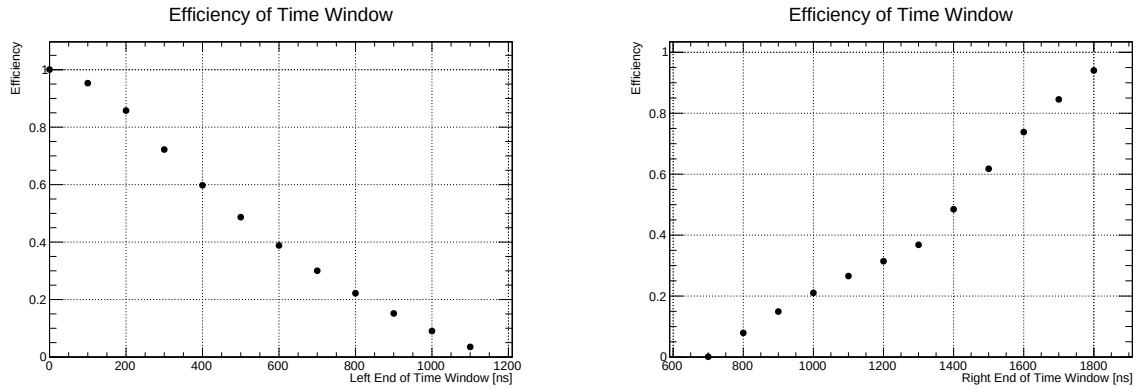

(a) Efficiency versus the start time of the time window with the stop time fixed at 1170 ns.

(b) Efficiency versus the stop time of the time window with the start time fixed at 700 ns.

Figure 20.3: *Acceptances of the time window of measurement of the time window as a function of (a) start time and (b) stop time. The width of the proton pulses of 100 ns is included. The periodic time structure is considered with bunch separation time* $T_{sep} = 1170ns$.

The acceptance due to the time window cut, $\varepsilon_{\rm time}$, can be given by,

$$\varepsilon_{\rm time} = \frac{N_{\rm time}}{N_{all}}, \tag{20.1}$$

$$N_{\rm time} = \sum_{i=1}^{n} \int_{t_1+T_{sep}(i-1)}^{t_2+T_{sep}(i-1)} N(t)dt, \tag{20.2}$$

which takes the contributions from the previous muon beam pulses into account. Here N_{all} is the number of the muons stopped in the target, $N_{\rm time}$ is the number of muons which can decay during the signal time window, T_{sep} is the time separation between the proton pulses, t_1 and t_2 are the start and end times of the signal window, and the index n corresponds to the window for the $n^{\rm th}$ advanced pulse. The distribution of the muon decays in time, $N(t)$, is obtained from the Monte Carlo simulations. Currently, the baseline design is that $t_1 = 700$ ns and $t_2 = 1170$ ns, and T_{sep} is 1170 ns. The signal acceptance of time window of measurement, $\varepsilon_{\rm time} = 0.30$ is obtained for the case of $T_1 = 700$ ns and $T_2 = 1170$ ns, as given in Figure 20.3. When the prompt beam background is less, the case of $T_1 = 500$ ns and $T_2 = 1170$ ns can become our option, where $\varepsilon_{\rm time} = 0.49$ is estimated.

20.1.5 Net Signal Acceptance

Thus the net acceptance for the $\mu-e$ conversion signal of $A_{\mu\text{-}e} = 0.041$ is obtained for $T_1 = 700$ ns and T_2=1170 ns, where appropriate numbers of the online event selection (see Section 16.1.3), the offline track finding efficiency (See Section 13.5.1) and DAQ efficiency (assumed) are considered. The breakdown of the acceptance is shown in Table 20.2.

Event selection	Value	Comments
Online event selection efficiency	0.9	Section 16.1.3
DAQ efficiency	0.9	
Track finding efficiency	0.99	Section 13.5.1
Geometrical acceptance + Track quality cuts	0.18	
Momentum window ($\varepsilon_{\rm mom}$)	0.93	103.6 MeV/c < P_e <106.0 MeV/c
Timing window ($\varepsilon_{\rm time}$)	0.3	700 ns < t < 1170 ns
Total	0.041	

Table 20.2: *Breakdown of the $\mu-e$ conversion signal acceptances.*

20.1.6 Single Event Sensitivity

The single event sensitivity (SES) aimed by COMET Phase-I and the required running time are described. The current upper limit on gold from SINDRUM-II is 7×10^{-13} [1]. The goal of COMET Phase-I is an improvement of a factor of 100 on aluminium over the current limit, namely,

$$B(\mu^- + {\rm Al} \to e^- + {\rm Al}) = 3 \times 10^{-15} \quad \text{(as SES) or} \tag{20.3}$$

$$< 7 \times 10^{-15} \quad \text{(as 90 \% C.L. upper limit).} \tag{20.4}$$

The SES is given by

$$B(\mu^- + {\rm Al} \to e^- + {\rm Al}) = \frac{1}{N_\mu \cdot f_{\rm cap} \cdot f_{\rm gnd} \cdot A_{\mu\text{-}e}}\,, \tag{20.5}$$

where N_μ is the number of muons stopped in the target. The fraction of captured muons to total muons on target $f_{\rm cap} = 0.61$ is taken, while the fraction of $\mu-e$ conversion to the ground state in the final state of $f_{\rm gnd} = 0.9$ is taken [22]. $A_{\mu\text{-}e} = 0.041$ is the net signal acceptance. To achieve SES=3×10^{-15}, $N_\mu = 1.5 \times 10^{16}$ is needed. By using the muon yield per proton of 4.7×10^{-4} in Section 8.5., a total number of protons on target (POT) of 3.2×10^{19} is needed. With the proton beam current of 0.4 μA, the measurement requires about 1.26×10^7 seconds, corresponding to about 146 days. Note that that the pion production yield may have an uncertainty of a factor of two or three, as shown in Section 8.1.2. The estimated running time might be uncertain accordingly.

20.2. Background Estimation with CyDet

The potential background sources in the search for the $\mu^- N \to e^- N$ conversion are grouped into four categories. These categories are intrinsic physics backgrounds, beam-related prompt

Intrinsic physics backgrounds		
1	Muon decays in orbit (DIO)	Bound muons decay in a muonic atom
2	Radiative muon capture (external)	$\mu^- + A \to \nu_\mu + A' + \gamma$, followed by $\gamma \to e^- + e^+$
3	Radiative muon capture (internal)	$\mu^- + A \to \nu_\mu + e^+ + e^- + A'$,
4*	Neutron emission after muon capture	$\mu^- + A \to \nu_\mu + A' + n$, and neutrons produce e^-
5*	Charged particle emission after muon capture	$\mu^- + A \to \nu_\mu + A' + p$ (or d or α), followed by charged particles produce e^-
Beam related prompt/delayed backgrounds		
6	Radiative pion capture (external)	$\pi^- + A \to \gamma + A'$, $\gamma \to e^- + e^+$
7	Radiative pion capture (internal)	$\pi^- + A \to e^+ + e^- + A'$
8	Beam electrons	e^- scattering off a muon stopping target
9	Muon decay in flight	μ^- decays in flight to produce e^-
10	Pion decay in flight	π^- decays in flight to produce e^-
11	Neutron induced backgrounds	neutrons hit material to produce e^-
12	$\overline{p}$ induced backgrounds	$\overline{p}$ hits material to produce e^-
Other backgrounds		
14	Cosmic-ray induced backgrounds	
15	Room neutron induced backgrounds	
16	False tracking	

Table 20.3: *A list of potential backgrounds for the search for the $\mu^- N \to e^- N$ conversion at the COMET experiment. The items with $*$ would not produce 100 MeV/c electrons but noise hits in the CyDet.*

backgrounds, beam-related delayed backgrounds, and other backgrounds. This last category includes cosmic-ray induced backgrounds, false tracking and so on.

The list of background sources is summarised in Table 20.3. The intrinsic physics backgrounds come from the muons stopped in the muon stopping target. Most of these can be rejected by the **detector resolution**, requiring the excellent momentum resolution in the CDC. One should note that the intrinsic physics backgrounds of 4 and 5 with $*$ in Table 20.3 cannot produce 100 MeV/c electrons. Instead, they can produce accidental tracks and hits in the CDC, which may be identified as a signal-like electron.

The beam-related prompt backgrounds originate from protons between the beam pulses. These are suppressed by the **proton extinction factor**. The beam-related delayed backgrounds are backgrounds originating from the main proton beam pulse and coming at a later time within the time window of measurement. These are suppressed by the **the delayed time window of the measurement**. In particular to remove pion backgrounds, a long muon beamline is needed.

In the following, the background estimations for COMET Phase-I are presented. The estimation studies can be grouped into two; one is based on the full `ICEDUST` simulations, and the second is based on some resampling started from the `ICEDUST` simulation data. For further reference, the former and latter are marked with (I) and (R) respectively. In the future when more computing power is available, the full `ICEDUST` data can be used.

20.2.1 Intrinsic physics backgrounds

Negative muons stopped in material are immediately trapped by the Coulomb potential of the nucleus of the material, and form a muonic atom, then cascade down to the $1s$ orbit of a muonic atom. From there the fate of the bound μ^- is dominated by two (Standard Model) allowed processes:

- muon decays in orbit (DIO), and
- nuclear muon capture (NMC).

Muon decays in orbit (I)

Muon DIO is a Michel decay, $\mu^- + N \to e^- \nu_\mu \overline{\nu}_e + N$, of muons that are bound in a muonic atom by the Coulomb potential of the nucleus N. In a free muon decay the electron momentum must be balanced against that of the neutrinos, but in DIO the nuclear recoil from the Michel decay allows the electron to carry much more energy. This causes the maximum energy of the e^- to exceed the end point energy of the ordinary Michel decay at rest (52.8 MeV), extending it to the momentum range of the $\mu{-}e$ conversion signal. The endpoint energy of DIO, $E_{\mu e}$, occurs when the neutrinos are produced at rest and (since neutrino masses are negligible) is the same as the $\mu{-}e$ conversion signal energy:

$$E_{\mu e} = m_\mu - B_\mu - E_{recoil} \tag{20.6}$$

where m_μ is the muon mass, and B_μ is the binding energy of the $1s$-state muonic atom, which depends on the species of nucleus. E_{recoil} is the nuclear recoil energy, and is generally small. It also depends on the nucleus, and is given by $E_{\rm rec} = (m_\mu - B_\mu)^2/(2m_N)$, where m_N is the mass of the recoiling nucleus, and is small. The endpoint energies $E_{\mu e}$ for different nuclei are given in Table 20.4 and shown in Figure 20.4. This is one of the dominant background sources.

Nucleus	Z	E_μ (MeV)	m_N (MeV)	$E_{\mu e}$ (MeV)
^{12}C	6	105.557	11188	105.06
^{27}Al	13	105.194	25133	104.973
^{28}Si	14	105.121	26162	104.91
^{48}Ti	22	104.394	44588	104.272

Table 20.4: *List of muon energies $E_\mu(= m_\mu - B_\mu)$, nuclear masses m_N, and endpoint energies $E_{\mu e}$ for a selection of nuclei.*

The momentum spectra of DIO electrons for aluminium have been calculated based on the model described in Refs. [25, 26, 27, 28]. Figure 20.5 shows the momentum spectrum of DIO electrons from aluminium. Figure. 20.6 shows the total rate of DIO spectrum for aluminium with energy above x (MeV) [25]. From this, it is concluded that in order to reduce the DIO contribution down to $O(10^{-16})$, the lower side of the momentum region for $\mu{-}e$ conversion signals should be above about 103.6 MeV for aluminium.

Using the spectrum in Ref. [25], DIO electrons are generated in a Monte Carlo simulation and their tracks are reconstructed with `Genfit2`. In Figure 20.7, the reconstructed momentum spectrum of DIO electrons is shown (blue line), normalised to the rate of a single $\mu{-}e$ conversion event at a branching fraction of 3×10^{-15}. This momentum spectrum is then integrated above the momentum threshold of the $\mu{-}e$ conversion signal region. The integrated fraction of signal events (for exactly one real $\mu{-}e$ event) as a function of momentum threshold is also shown (red

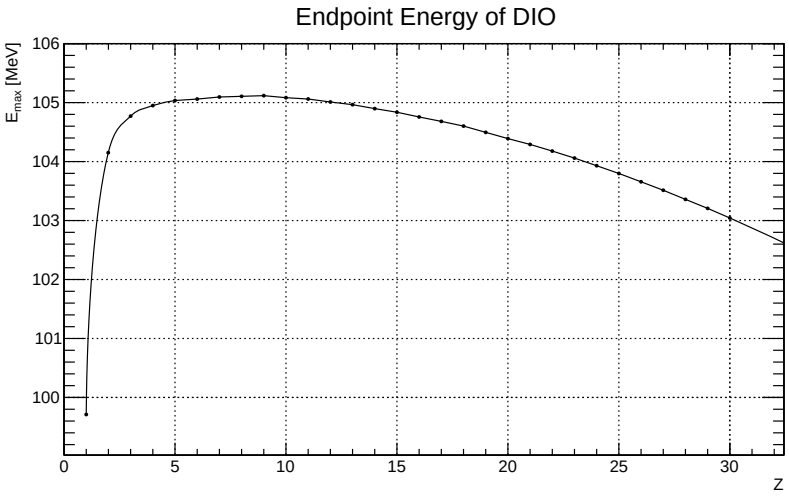

Figure 20.4: *DIO endpoint energy as a function of atomic number.*

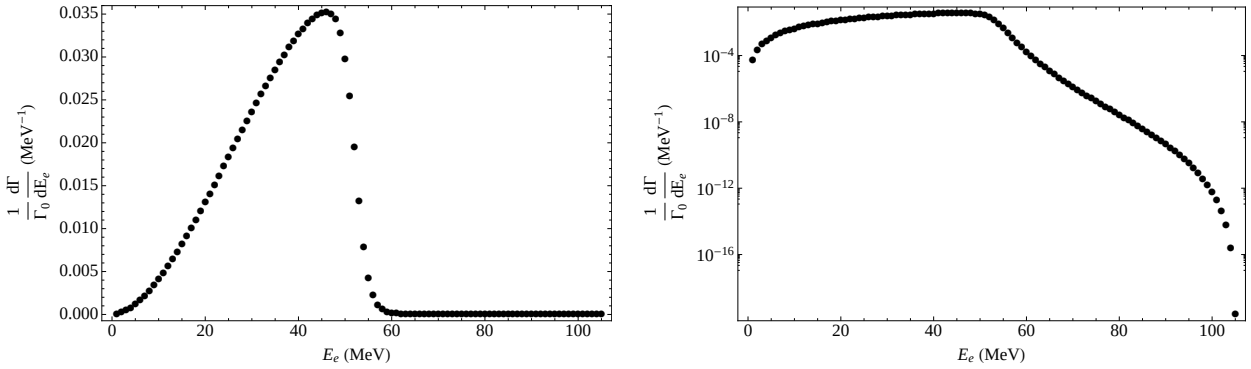

Figure 20.5: *DIO electron spectrum for Aluminium. The left is linear scale and the right is a logarithmic scale. From Ref.[25].*

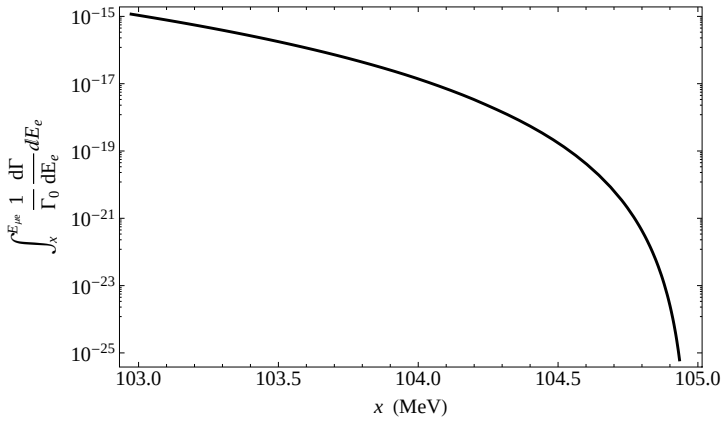

Figure 20.6: *Total rate of DIO for aluminium above the electron energy $x = E_e$ (MeV) value, normalised by the free muon decay rate from Ref.[25].*

line). As described before, this allows determination of an optimal momentum window cut at 103.6 MeV/c < P_e < 106 MeV/c for the $\mu-e$ conversion signals. In this momentum window, the fraction of DIO electrons in the signal region is 0.01 events, obtained for the single event sensitivity to $\mu-e$ conversion of 3×10^{-15}.

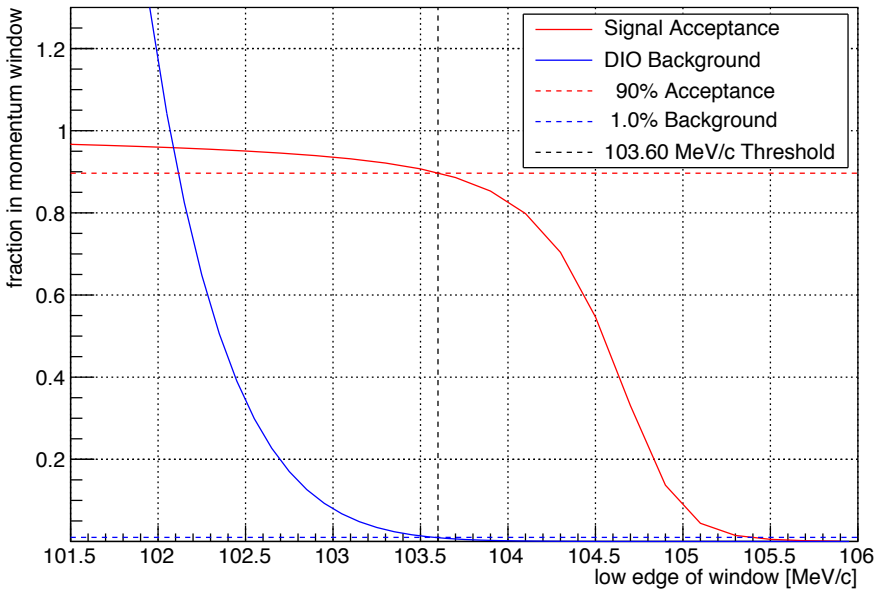

Figure 20.7: *Reconstructed DIO spectrum for aluminium, normalised to one single event of $\mu-e$ conversion with 3×10^{-15}. The red line shows the integrated event rate above the energy given. The lower edge of the momentum window of the signal is set to be 103.6 MeV.*

Radiative muon capture (R)

Muon nuclear capture (NMC) is analogous to electron capture. It is given by

$$\mu^- + N(A, Z) \rightarrow \nu_\mu + N(A, Z-1)\,. \tag{20.7}$$

The daughter nucleus produced by nuclear muon capture is usually in an excited state and may emit γ-rays, neutrons and charged particles through de-excitation. They can become sources of fake signals.

Radiative muon capture (RMC) is similar, the process being

$$\mu^- + N(A, Z) \rightarrow \nu_\mu + N(A, Z-1) + \gamma. \tag{20.8}$$

When this is followed by asymmetric e^+e^- conversion, or Compton scattering of the photon, it is one of the most important sources of intrinsic background events. We call this "external" conversion of RMC. There is another variation of RMC with internal conversion of the virtual photon

$$\mu^- + N(A, Z) \rightarrow \nu_\mu + N(A, Z-1) + e^+ + e^-, \tag{20.9}$$

which has a similar contribution to background events in cases when e^+e^- are asymmetric. We call this "internal" conversion of RMC.

Since the RMC background is one of the intrinsic physics background, the energy difference is the only method to remove it, as is the case for DIO. Neither the surviving rate of beam particles (pions, in particular) for the beam-related delayed background nor the proton extinction

factor for the beam-related prompt background can be applied for further suppression of RMC background. Because of this, the spectrum shape towards the endpoint is quite important to estimate this type of background.

For external process, the kinematic endpoint (E^{end}_{rmc}) of the emitted photon from RMC is given by

$$E^{\rm end}_{\rm rmc} \approx m_\mu - B_\mu - \Delta_{Z-1} - E_{recoil} = E_{\mu e} - \Delta_{Z-1}, \tag{20.10}$$

where m_μ is the muon mass, B_μ is the muon binding energy in a muonic atom, and E_{recoil} is the recoiling energy of the final nucleus. Δ_{Z-1} is a difference in the mass of the initial (A, Z) and final $(A, Z-1)$ nucleus involved in RMC. Therefore, an appropriate target with a large Δ_{Z-1} can be selected so as to keep a wide background-free region for the coherent signal. In aluminium the nuclear mass difference, $\Delta_{Z-1} = +3.12\,\text{MeV}$, and the RMC photon endpoint energy is 101.85 MeV. This is to be compared to the energy of $\mu-e$ conversion signal of $E_{\mu e} = 104.973\,\text{MeV}$. Table 20.5 shows the atomic mass difference for aluminium and magnesium. It is noted that to calculate the nuclear mass difference Δ_{Z-1} the one electron mass has to be taken care of when the numbers in table 20.5 are used. The energy difference for the aluminium case is 3.12 MeV. It is noted here that in a Ti target, $E^{\rm end}_{\rm rmc} = 89.7$ MeV and 91.4 MeV for ^{48}Ti and ^{46}Ti respectively [108], whereas $E_{\mu e}$ is 104.3 MeV.

Isotope	Mass
$^{27}_{13}$Al	26.98153 u
$^{27}_{12}$Mg	26.98434 u

Table 20.5: *Atomic masses for aluminium and magnesium, where 1u = 931 494 061 eV/c^2.*

The photon from RMC produces an electron by either Compton scattering or pair production. For Compton scattering, the maximum momentum of the electron emitted could be about $m_e/2 = 0.255\,\text{MeV}$ larger than the original photon momentum, when the electron scatters along the original photon direction and the scattered photon goes in the opposite. For pair production, the maximum momentum of the electron is about m_e smaller than the original photon momentum. Therefore, Compton scattering is more important than external pair production or RMC with internal conversion.

Nucleus(Z)	Nucleus($Z-1$)	Δ_{Z-1} (MeV)	$E^{end}_{\rm rmc}$ (MeV)	$E_{\mu e}$ (MeV)
^{27}Al	^{27}Mg	+ 3.12	101.85	104.973
^{48}Ti	^{48}Sc	+ 14.6	89.7	104.3

Table 20.6: *Endpoint energies of the photon emitted in RMC for various nuclei.*

The total background contribution from RMC for a single signal event is given by

$$\begin{aligned} N_{\rm RMC} &= N_{\rm proton} \times R_{\mu-{\rm stop}/p} \times B_{\rm RMC93} \\ &\quad \times P_{\gamma-e} \times A_{\rm geo} \times A_{\rm mom} \times A_{\rm time} \times \varepsilon_{\rm tracking}\,, \end{aligned} \tag{20.11}$$

where $N_{\rm proton}$ is the total number of protons on the pion production target; $R_{\mu-{\rm stop}/p}$ is the number of μ^- arriving at the muon stopping target per proton; $B_{\rm RMC93}$ is the branching ratio of RMC producing a photon with more than 93 MeV; $P_{\gamma-e}$ is the probability of conversion of the RMC photon to an electron in the signal region; $A_{\rm geo}$ is the detector acceptance of the RMC-originated electrons in the signal region; $A_{\rm mom}$ and $A_{\rm time}$ are the acceptances of momentum cut and timing cut, respectively; and $\varepsilon_{tracking}$ is the tracking efficiency.

So far there is no experimental data of the photon spectrum of RMC on aluminium near the endpoint. RMC on ^{27}Al [109, 110, 111, 112] is available, but not for the region of the endpoint energy. To estimate the contribution of RMC backgrounds, theoretical predictions must be used to extrapolate to the endpoint. The original theoretical prediction was given by Primakoff [113]. Later, another simpler formula for RMC by Hwang [114] based on the elementary particle approach in the Hwang–Primakoff theory was calculated. It is given by

$$R(x) = C(1 - 2x + 2x^2)x(1 - x)^2, \tag{20.12}$$

where $x = k/k_{\max}$, k is photon energy and C is a constant. Since no measured data is available, Eqn. (20.12) was used for the RMC spectrum prediction. To get the overall normalisation, C, the measured rates of RMC on aluminium were used. The measurements are given in Figure 20.8, from Ref. [112]. From this the partial rate of $E_\gamma \geq 57$ MeV of 1.83×10^{-5} per ordinary muon capture was chosen to determine the value of C. The result of this extrapolation is shown in Figure 20.9. From this histogram, the probability per muon capture of producing a photon with energy exceeding 93 MeV is estimated to be $B_{\mathrm{RMC93}} = 2.97 \times 10^{-7}$. It is noted that the RMC photon spectrum on aluminium should be measured experimentally at COMET Phase-I.

Element	Z	Early exp.	Döbeli [561]	TRIUMF	Armstrong [564]	Bergbusch [566]
^{12}C	6		2.7 (18)	2.3 (2)[d]		
^{16}O	8	3.8 (4)[a]	2.44 (47)	2.2 (2)[d]		1.67 (18)
^{27}Al	13		$1.83^{+0.55}_{-0.25}$		1.43 (13)	1.40 (11)
^{28}Si	14				1.93 (18)	2.09 (20)
^{40}Ca	20	2.07 (20)[b] 2.11 (14)[c]	2.30 (21)	2.11 (15)[d]	2.09 (19)	
Ti	22					1.30 (12)
Fe	26		1.71(17)			
^{58}Ni	28			1.48 (8)[e]		
^{60}Ni	28			1.39 (9)[e]		
^{62}Ni	28			1.05 (6)[e]		
Zr	40					1.31 (15)
Mo	42				1.11 (11)	
Ag	47					1.12 (13)
Sn	50				0.98 (9)	
^{165}Ho	67		0.75 (13)			
Pb	82				0.60 (7)	
^{209}Bi	83		0.62 (8)			

Figure 20.8: *Muon radiative capture on nuclei for $E_\gamma \geq 57$ MeV in units of 10^{-5} per ordinary muon capture. From Ref. [112].*

To find out how many energetic electrons would be generated by RMC photons in the CDC region, a `Geant4` simulation was used. The starting position is based on the stopping position distribution of muon in stopping target obtained from the muon beam study, with the assumption that RMC photons are emitted isotropically and the photon spectrum is given in Figure 20.9. Only high-energy photons (those whose energy is larger than 93 MeV) were generated. The electron spectrum resulting from RMC is shown in Figure 20.10, along with the DIO spectrum.

After smearing the momentum resolution, it is found that the number of RMC backgrounds to be in the momentum window of the signal is $N_{\mathrm{RMC}} = 0.0019$.

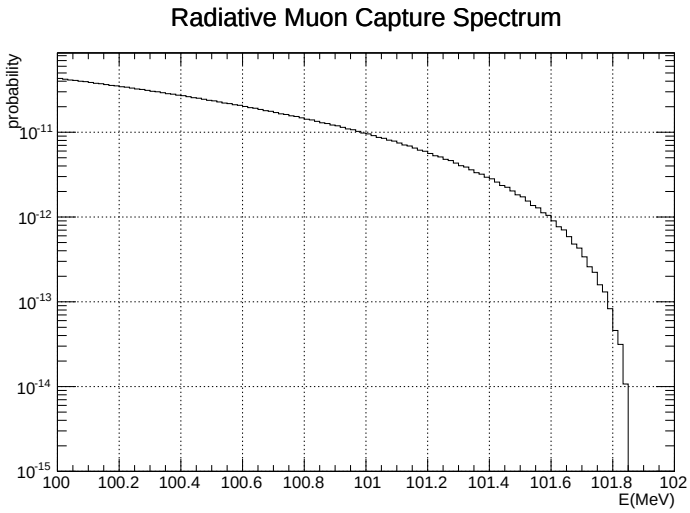

Figure 20.9: *Extrapolated momentum distribution of photons from RMC, based on theoretical prediction [114].*

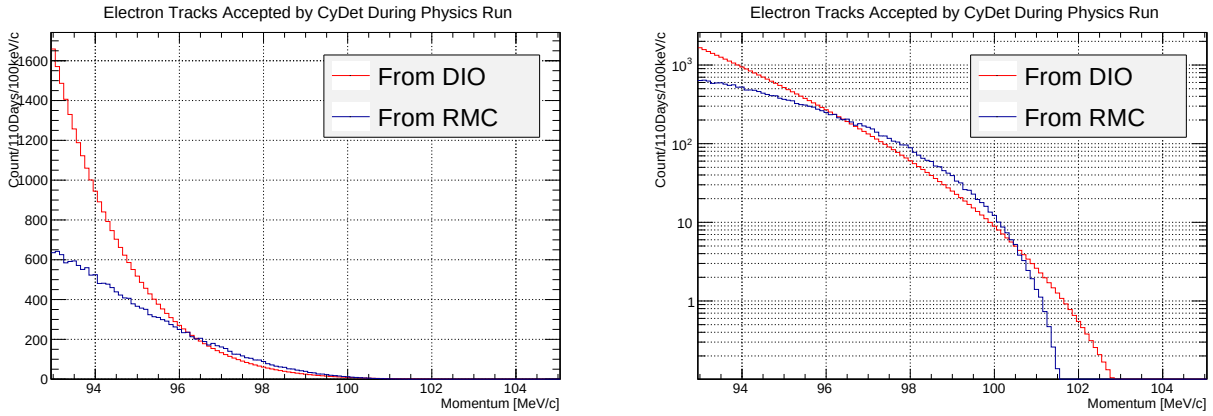

Figure 20.10: *Comparison of the rates and spectra between RMC and DIO, linear (left) and log (right) scales.*

20.2.2 Beam-related prompt backgrounds

The beam-induced prompt backgrounds arise from protons circulating in the MR buckets between the intended beam pulses. These backgrounds are suppressed by the proton beam extinction factor. A proton beam extinction factor, $R_{\text{extinction}}$ of 3×10^{-11} is used in the following background estimation, since that number was obtained from our recent experimental measurements at the J-PARC MR, as given in Section 4.6..

Radiative Pion Capture (R)

The radiative pion capture (RPC) background is caused by pions contaminating the muon beam. Those pions are stopped in the muon stopping target, then captured by an aluminum nucleus immediately to form an excited state of the daughter nucleus.

There are two processes, one directly produces a high energy γ ray and the other produces γ rays as an evaporative process of the excited daughter nucleus. For these processes, the

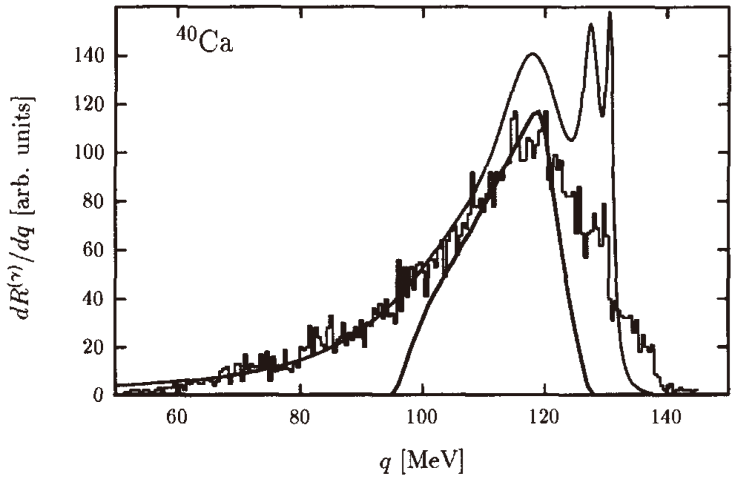

Figure 20.11: *Momentum distribution of γs from RPC. This figure was reprinted from [115]. The histogram is experimental data, and the lines are from two different theoretical models.*

probability of γ ray emission is as high as 2%. Some of the emitted γ rays convert into e^- and e^+ in the target or nearby material. If the e^+e^- pair creation occurs with an asymmetric energy distribution and the e^- has a high energy, it could mimic $\mu-e$ conversion signals. This is external conversion of a photon from RPC. There is also an internal conversion process for RPC, which contributes at almost same rate.

Nucleus	Measured branching ratio (%)		
^{12}C	1.84 ± 0.08,	1.92 ± 0.91,	1.6 ± 0.1
^{16}O	2.27 ± 0.24,	2.24 ± 0.48	
^{40}Ca	1.82 ± 0.05		

Table 20.7: *Experimentally measured branching ratios of radiative pion capture. Multiple values correspond to measurements by different experiments. The table was adapted from Table 4 in [115].*

The probability of γ emission and the energy spectrum of γs were extensively studied experimentally and theoretically for more than 20 years. According to [115], the probability of γ emission has very small Z dependence. It is almost 2% for C, O, and Ca as shown in Table 20.7. The energy of the γ from RPC ranges from 50 MeV to 140 MeV as shown in Figure 20.11. The overall shapes of the spectra are very similar in C, O, and Ca. Therefore, we implemented the experimentally obtained spectrum from Ca in our Monte Carlo code for this study.

The number of RPC backgrounds is expressed as

$$\begin{aligned} N_{\rm RPC} &= N_{\rm proton} \times R_{\rm extinction} \times R_{\pi-{\rm stop}/p} \times \\ &\quad B_{\rm RPC} \times P_{\gamma-e} \times A_{\rm geo} \times A_{\rm mom} \times A_{\rm time} \times \varepsilon_{\rm tracking}\,, \end{aligned} \tag{20.13}$$

where $N_{\rm proton}$ is the total number of protons on the pion production target; $R_{\rm extinction}$ is the proton beam extinction factor; $R_{\pi-{\rm stop}/p}$ is the number of π^-s arriving at the muon stopping target per proton; $B_{\rm RPC}$ is the branching ratio of radiative muon capture; $P_{\gamma-e}$ is the probability of conversion of the RPC photon to an electron of 105 MeV/c; $A_{\rm geo}$ is the detector acceptance of the RPC-originated electrons of 105 MeV/c; $A_{\rm mom}$ and $A_{\rm mom}$ are the acceptances of momentum cut and timing cut, respectively; and $\varepsilon_{\rm tracking}$ is the tracking efficiency. Parameters that have

to be evaluated specifically for the COMET Phase-I CDC are $R_{\pi-\mathrm{stop}/p}$, $P_{\gamma-e}$, A_{geometry}, and A_{tracking}.

From the muon beam simulation of COMET Phase-I, $R_{\pi-\mathrm{stop}/p} = 3.4 \times 10^{-6}$ at the target position, as shown in Section 8.5.. The stopping fraction of pions is around 0.9. The branching ratio of radiative pion capture, B_{RPC} was simulated for the COMET Phase-I CDC, based on the photon spectrum in Figure 20.11. The simulation started by generating RPC photons uniformly inside the muon stopping target, which were emitted isotropically. A total of 10^7 photon events were generated. Electrons and positrons were created by pair production, and also electrons were generated by Compton scattering. The photon conversion could occur anywhere in the detector, with the most important volumes being: at the muon stopping target (TG); at the CDC inner wall (IW) or outer wall (OW); in the CDC gas (GS); or in the CDC trigger counter (TR). Tracking was performed on events containing an electron whose momentum was higher than 90 MeV/c. In the COMET Phase-I CDC geometry, relative ratios of electrons between 102 MeV/c to 106 MeV/c occurring at different locations were found to be TG:IW:OW:GS:TR=19:2:22:1:4.Among these conversion locations, the electrons from the target (TG) and inner wall (IW) are most problematic as they cannot be distinguished from signal events. In the signal momentum region of 103.6 MeV/c to 106 MeV/c, there are 336 events occurring in the muon stopping target or CDC inner wall. In the end, these would give $P_{\gamma-e} \times A_{\mathrm{geometry}} \times A_{\mathrm{tracking}} = 3.9 \times 10^{-5}$. With 3×10^{19} protons on target, a total of 1.4×10^{-3} background events from the external conversion of radiative pion capture is obtained. The contribution from internal conversion is about the same as that of external conversion. Therefore, an expectation of 2.8×10^{-3} RPC events is estimated with a proton beam extinction factor of 3×10^{-11}.

Beam Electrons, Electrons from Muon and Pion Decays in Flight (R)

The beam electron background is caused by electrons contaminating the muon beam. The electrons in the muon beam mostly originate from decays of π^0s produced in proton interactions. Beam electrons can scatter off the muon-stopping target and fake the signal electrons if the electron momentum is in the signal region.

Similarly, decays of muons in flight during the muon transport system can produce energetic electrons that have sufficient momentum to fake a signal. For the decay electrons to have $p_{\mathrm{total}} > 102$ MeV/c, the muon momentum (p_μ) must exceed 77 MeV/c. Additionally, $\pi \to e + \nu$ decays of pions in flight are also a potential source of background. For pion decay electrons, the π momentum must exceed 60 MeV/c to make this a background process. It should be noted here that the branching ratio of $\pi \to e + \nu$ is about 1.2×10^{-4}.

The prompt background events from beam electrons, electrons from muon and pion decays in flight can be given by

$$N_{e-\mathrm{scat}} = N_{\mathrm{proton}} \times R_{\mathrm{extinction}} \times R_{e-\mathrm{beam}/p} \times R_{e-\mathrm{det}} \times P_{e-\mathrm{signal}}. \quad (20.14)$$

Monte Carlo beam simulations based on `ICEDUST` were made to estimate the energetic electrons in the muon beam. This includes the beam electrons and electrons from muon and pion decays in flight. After the beam collimator, the total number of electrons with momentum greater than 80 MeV/c is $R_{e-\mathrm{beam}/p} = 1.7 \times 10^{-5}$ per proton. It should be noted that an electron also needs to have transverse momentum, P_T, greater than 70 MeV/c to reach the CDC.

The electrons obtained from the Monte Carlo beam simulations are injected into the COMET Phase-I CDC to estimate the probability for them to reach the CDC. Out of 40,000 electrons, none of them reach the CDC, and therefore we estimate an upper limit of the product of

the probabilities of $R_{e-\mathrm{det}} \times P_{e-\mathrm{signal}} < 2.5 \times 10^{-5}$. Using $N_{\mathrm{proton}} = 3 \times 10^{19}$, the estimated background from beam electrons is less than 3.8×10^{-3}.

Background Induced by Beam Neutrons (R)

Some background events can be induced by high energy beam neutrons. These neutrons can pass through the muon beam line by continuously reflecting from its inner sides of the beam duct. In principle the neutrons which can produce electrons of 100 MeV must exceed its kinetic energy of 100 MeV. Using the `ICEDUST` simulation, the average transit time of those neutrons arriving at the muon stopping target was estimated to be around 300 ns, with far fewer arriving at the signal window start time of 700 ns. Therefore, this background is regarded as a prompt background.

Simulation studies show that the most probable process to produce a 100 MeV electron is π^0 production from energetic neutrons, followed by π^0 decay with photon conversion. Neutrons with kinetic energy of more than 180 MeV (corresponding to momentum more than 600 MeV/c) were produced and transported through the COMET Phase-I beamline to examine their rate and energy distributions. The rate $R_{n/p}$ of 10^{-5} neutrons per proton was obtained at the end of the first 90° bend. Using the `ICEDUST` simulation, a rate of $R_{\pi^0/n}$ of 7×10^{-8} was determined. In a simulation of 10^6 π^0s following the above kinetic distributions, 16 electrons fell into the signal region. From this, a rate of R_{e/π^0} of 1.6×10^{-6} is obtained. The prompt background rate N_{neutron} can be estimated by

$$N_{\mathrm{neutron}} = N_{\mathrm{proton}} \times R_{\mathrm{extinction}} \times R_{n/p} \times R_{\pi^0/n} \times R_{e/\pi^0} \tag{20.15}$$

This gives about 1×10^{-9}, so the neutron background through π^0s is expected to be negligible.

20.2.3 Beam-related delayed backgrounds

Beam-related delayed pion backgrounds (I)

The beam-related delayed backgrounds arise from slowly-arriving particles in the muon beamline. In general they traverse through the solenoids with a small pitch angle in their helical trajectories (namely a small P_T), and thereby arrive late. They have specific time distribution to their arrival and they are suppressed by the use of the delayed time window for measurement. In particular, it is critical to avoid delayed pions in the beam, since pions decays can easily produce 100 MeV/c electrons.

The pion survival rate is determined by the pion lifetime in flight. If the muon beamline is longer, the number of surviving pions is less. It should be noted that when a negative pion is stopped in the target, it is captured around the nucleus, then absorbed through the strong interaction. A stricter rejection of pions can be obtained by starting the signal window at later times after the beam pulse.

Figure 20.12 shows the pion survival rate as a function of the starting time of the signal window. In Figure 20.12 (Left), it can be seen that the pion arrival time distribution shows two components; one is an exponentially decreasing component and the other is a shoulder component starting after around 300 nsec. Figure 20.13 shows two-dimensional plots of momentum vs. arrival time for pions at the end of 90° bend (Left) and pions that pass the Bridge solenoid (Right). The pions with sufficient momenta arrive early and only the pions with low momenta come late but most of them are eliminated (by the vacuum window or others) before the Bridge

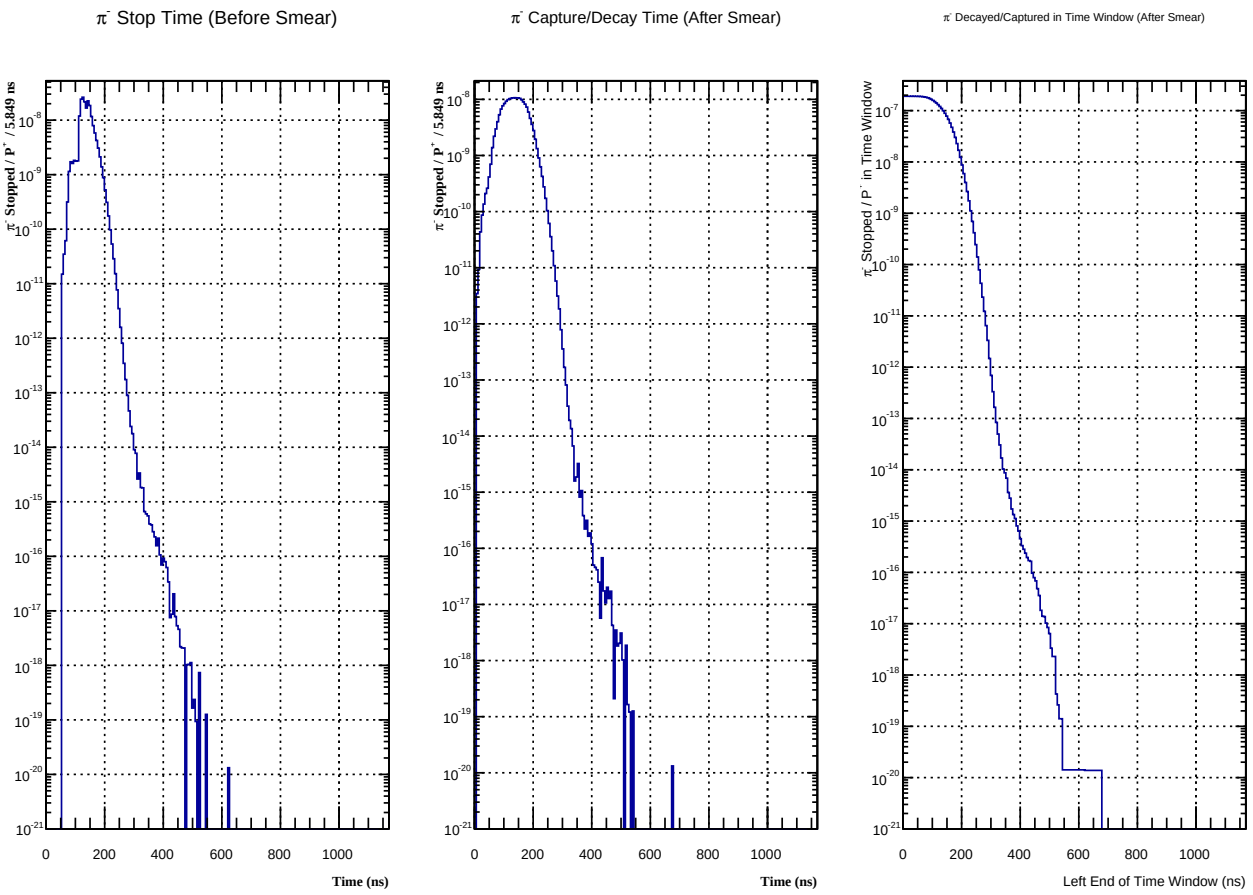

Figure 20.12: *[Left] Delay time distribution of the pion arrival. [Middle] Delay time distribution of the pion arrival with 100 ns square pulse distribution of proton pulse smeared. [Right] Pion survival rate as a function of the starting time of the time window of measurement.*

Solenoid. However it can be seen that some of the pions with high energy arrive even late, making the shoulder component. The reason for late arrivingl high energy pions may be related with a beam reflection effect. For example, Figure 20.14 shows a typical event display of such pions. It can be seen that the pion got scattered to upstream at the upstream vacuum window, then reflected to downstream again by a strong magnetic field near the Capture solenoid, and eventually pass through that vacuum window at a late arrival time. Since the vacuum windows cannot be removed owing to the safety reasons, it is difficult to reduce these shoulder component.

As a conclusion, from the right plot in Figure 20.12 it is learnt that, when the starting time is set to 700 (500) ns, a pion survival rate of 10^{-21} (10^{-18}) pions/proton is achieved. This is lower than the proton extinction $R_{\text{extinction}} = 3 \times 10^{-11}$. Therefore, the beam-related delayed backgrounds are expected to be below the level of prompt backgrounds. The best signal time window to used can be determined after some initial running to measure the the time distribution of pion arrival. The measured distribution can be used to optimise between the signal acceptance and background rejection.

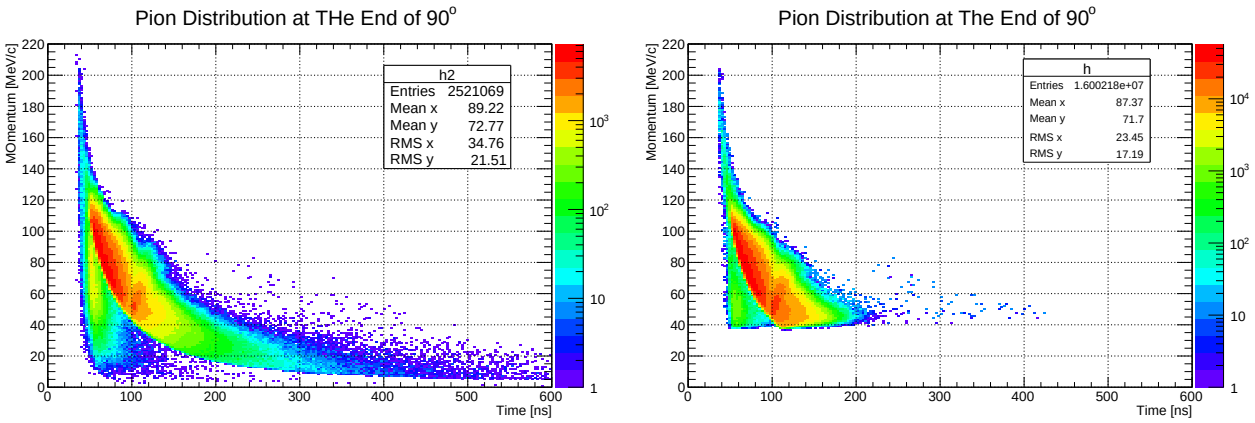

Figure 20.13: *Momentum versus arrival time distribution at the end of 90° bend of pions [Left] that arrived before the Bridge solenoid and [Right] that passed through the Bridge solenoid.*

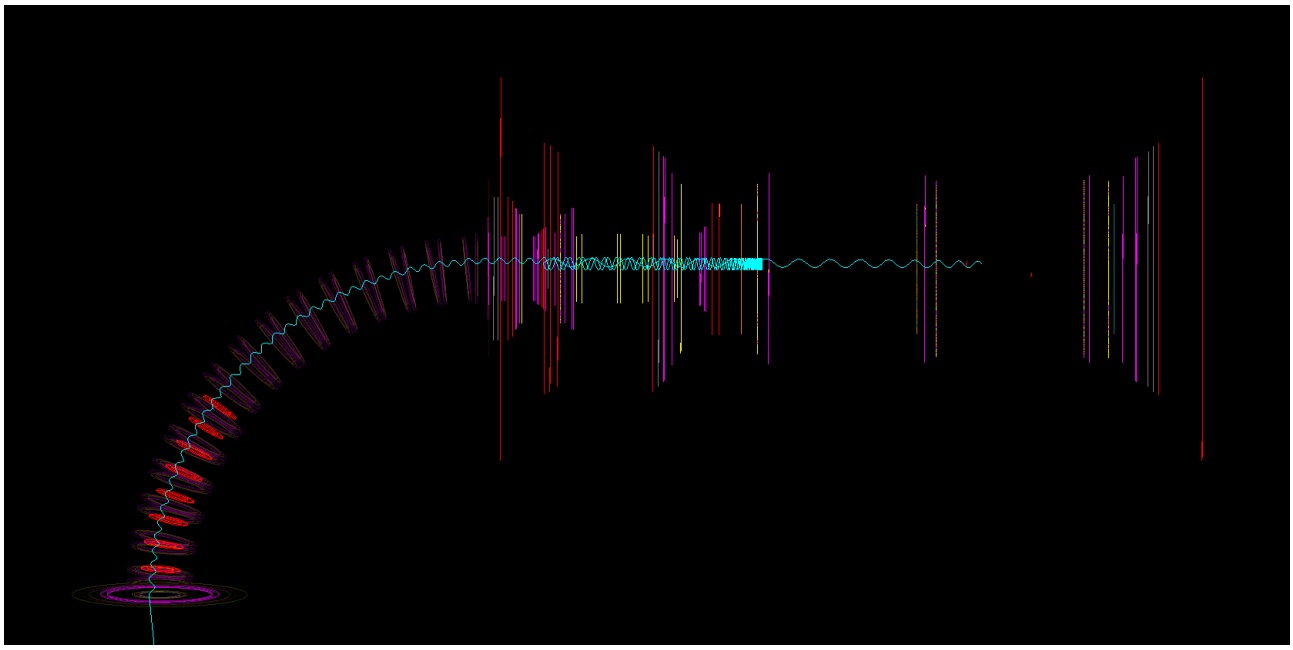

Figure 20.14: *An event display of a typical late arrival pion in the tail component.*

20.2.4 Antiproton induced backgrounds

Antiproton induced delayed backgrounds (I)

Antiprotons are another potential source of backgrounds. Owing to the charge selection in the curved muon beamline of COMET Phase-I, protons cannot reach the detector region, but antiprotons can. Also due to the momentum selection of the muon beamline, only those of low momentum can pass through the muon beamline. When antiprotons come to the detector region, they annihilate on materials releasing a large amount of energy and producing other energetic particles, including pions (which might produce 100 MeV/c electrons as a tertiary interaction) or directly producing 100 MeV/c electrons. These antiprotons have very low kinetic energy and low velocity. Therefore, they are not suppressed by the delayed time window of measurement.

There are several ways to suppress antiproton-induced backgrounds. They are

- reduction of the production rates of antiprotons by decreasing proton beam energy, and
- absorption in a thin absorber material placed in the muon beamline.

It is known that antiproton production has a strong dependence on incident proton energy. When the incident proton energy is lower, the production of antiprotons is reduced. The choice of a proton energy of 8 GeV is specifically to reduce the production rate of antiprotons, with keeping reasonably high rates of pion production.

The yield of antiprotons in the backward direction from an 8 GeV proton beam is not known. Early studies by the MECO experiment is shown in Figure 20.15, along with predictions using MARS. A rough estimate of the antiproton production per proton of 4×10^{-5} is obtained. The `ICEDUST` hadron generation codes are known not to have the reliable antiproton yields yet.

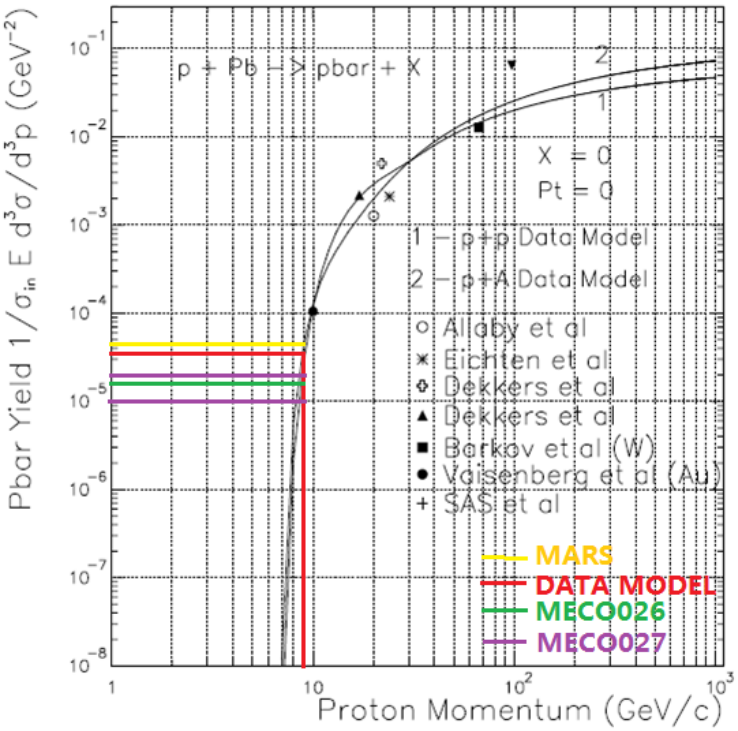

Figure 20.15: *Antiproton production yield per proton with 8 GeV protons, calculated by MARS.*

Consideration is also being given to installing two absorber foils in the muon beamline. One of them would be a 500 µm thick titanium foil with a diameter of 360 mm, and placed at the entrance of the curved muon transport solenoid. This foil would also serve a vacuum window (which is required by safety regulations) to separate the muon beamline and the proton beamline. The thickness of titanium is sufficient to maintain a pressure difference of one atmosphere. From simulations, it is found that it is better to annihilate antiprotons early in the transport stage, so that their transit time is minimised. The second absorber foil is 500 µm thick titanium with a diameter of 255 mm, and is placed at the front part of the Bridge Solenoid (BS). It also serves a vacuum window between the muon beamline and the detector region. It is also under investigation to place one more anti-proton absorber foil at the 45° position, but it has not been decided yet. With these absorbers placed in the muon beamline, low energy antiprotons which would come late are reduced by absorption and annihilation, as shown in Figure 20.16.

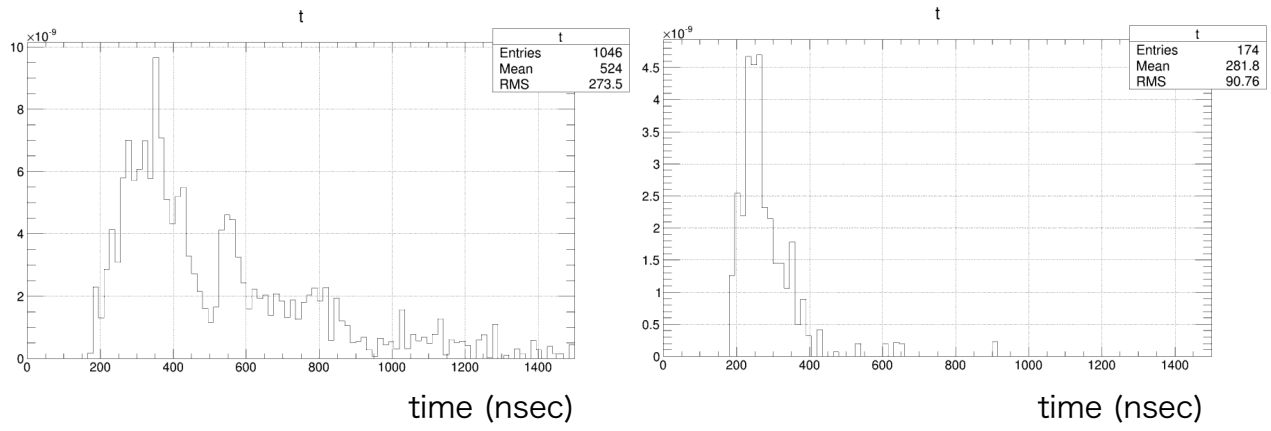

Figure 20.16: *Distribution of arrival time of antiprotons without antiproton absorber (left) and with antiproton absorber (right).*

It is known that the antiproton induced backgrounds can be grouped into two groups. They are

(1) late arriving high energy particles, giving signal-like tracks in the CyDet by scattering or decays and,
(2) late arriving pions stopped in the muon-stopping target, introducing signal-like tracks in the CyDet by RPC.

To study the contribution of (1), resampling of the events with different random seeds have been made many times to examine any 100 MeV/c electrons coming in the CyDet region. It is found that the time acceptance (using a signal window of 700 ns to 1170 ns) is 2×10^{-3} and the CyDet geometrical acceptance is less than 9×10^{-7}. A total net contribution of less than 3×10^{-4} is obtained. For the contribution of (2), the pions produced by antiprotons are resampled at the CyDet region. The distribution of arrival time of pions produced by antiprotons is shown in Figure 20.17. The rate of pions stopped in the measurement time window from 700 (500) ns to 1170 ns is found to be 4.9×10^{-17} (1.4×10^{-16}) per initial proton. With the use of the result of the RPC background estimation, a net contribution of 1.2×10^{-3} (3.5×10^{-3}) events is obtained.

20.2.5 Cosmic ray induced backgrounds

Cosmic ray muon induced backgrounds (I)

Cosmic ray induced backgrounds are one of the most important backgrounds. They can be divided into two categories:

- cosmic-ray muons that produce an electron which enters the detector, and
- cosmic-ray muons enter the detector and are misidentified as an electron.

To veto and eliminate cosmic-ray induced backgrounds, the Cosmic Ray Veto (CRV) system is installed to cover a large portion of the solid angle around the Detector Solenoid (DS), as discussed in Chapter 15. The CRV detector works as a veto with high efficiency of 10^{-4}, in an environment that has a large flux of neutrons. The COMET Phase-I detector is also required

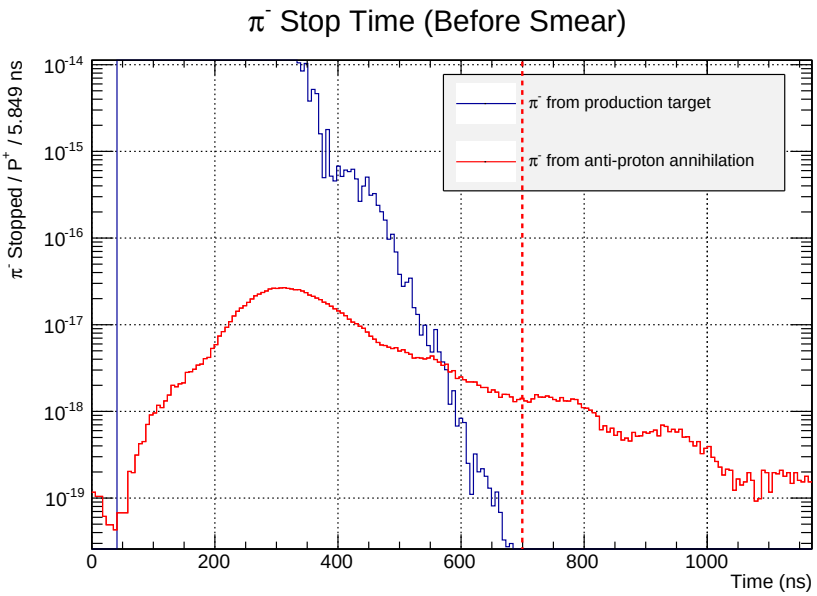

Figure 20.17: *Distribution of arrival time of pions produced by antiprotons. Those pions come late because of slowly-moving antiprotons.*

to have good particle identification to discriminate electrons from cosmic-ray muons. Signal tracks are required to hit the CTH, so the Cherenkov counters will serve as an active electron identification. It should be noted that the contribution of cosmic ray induced backgrounds is proportional to the total live running time, rather than the proton beam power.

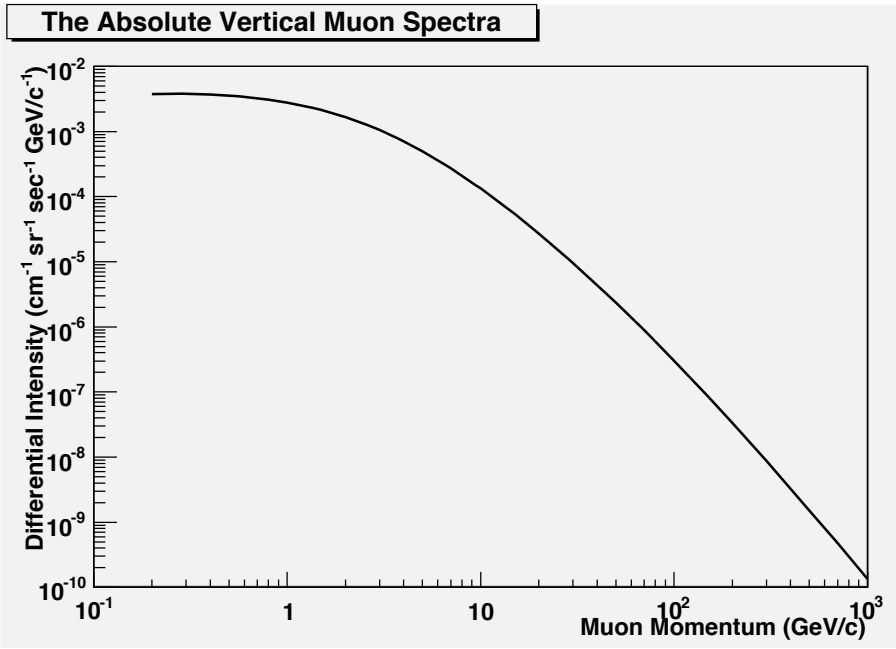

Figure 20.18: Energy spectrum of vertical (downward-going) cosmic ray muons at sea level.

In order to study cosmic ray induced backgrounds, two kinds of simulation studies are being considered. One is a general approach in which cosmic rays are generated widely around the COMET experimental hall. It is useful to examine the overall performance of the CRV and characteristics of cosmic ray induced backgrounds. The second is a focused approach, in which

some specific combinations of location and direction are chosen and cosmic rays are generated in these areas. In particular the second studies will be made for to the locations where cosmic ray veto is weak or does not provide complete coverage.

The general approach of is to use GEANT4 simulations to estimate the cosmic ray induced backgrounds. The vertical flux of cosmic muons at sea level is shown in Figure 20.18 [116]. The angular distribution of cosmic muons is known to be $\propto \cos^2\theta$ for typical muon energies ($\simeq 1\,\mathrm{GeV}$). The angular spectrum becomes steeper as the energy decreases and flattens as the energy increases. This data set of cosmic rays are based on a CERN input file,[1] which contains about 23 million $\mu^{\pm}$ events. A full air shower simulation code based on CORSIKA was used. 23 million cosmic ray events were generated over a $50 \times 50\mathrm{m}^2$ plane. Some event displays are shown in Figure 20.19. Among this sample, there was no event containing $\sim 100\,\mathrm{MeV}$ electrons in the CDC without being detectable by the CRV. There was one event where a cosmic ray muon produce a shower and one of the shower electrons scatters off the Bridge Solenoid (BS) enters the CDC, and hits the CTH. However, the electron lost much of its energy (which was originally below 80 MeV), and would not be mistaken for a signal electron.

It is noted that in the DS area, the CDC itself also serves as an active volume to detect cosmic ray muons, in addition to the CRV. A net veto inefficiency to identify cosmic rays and/or an associated shower should be much less than 10^{-4}.

Since one event came into the CDC from the BS area, we are running a focused simulation study on the BS area. 100 million cosmic ray events over a $2 \times 2\mathrm{m}^2$ region at the upstream of the CyDet were generated.[2] The area covers the BS coils. We found 35 events in which an electron of $85 \sim 110\,\mathrm{MeV}/c$ reaches the CDC. One example event is shown in Figure 20.20, where a cosmic-ray muon hit directly the CTH without hitting the CRV from upstream (left image), and created an electron of $80\,\mathrm{MeV}/c$ at the CTH with large transverse momentum (right image). None of the 35 events met the CTH trigger requirements and the track quality cuts. The BS area is close to the upstream CTH and it is therefore important to have additional veto system at the BS system (BS-CRV). With the assumption that the BS-CRV also has a veto inefficiency of 10^{-4}, a upper limit of background contribution is obtained to be ≤ 0.01 for a running period of the COMET Phase-I physics run. This estimate is currently limited by an available computing time, and can be improved once more computing resource is available.

Cosmic-ray run during and prior to the physics run It is noted that COMET will also be able to directly measure the cosmic-ray induced background using data collected during the J-PARC MR spill off time.

It will be useful to have a *cosmic-ray run* with the complete COMET Phase-I detector (with the CTH triggers), prior to the physics run without a proton beam. This *cosmic ray run* would provide an opportunity to study and determine any special arrangements to suppress cosmic-ray backgrounds further.

20.2.6 Summary of background estimations

Table 20.8 shows a summary of the estimated backgrounds. The total estimated background is about 0.032 events for a single event sensitivity of 3×10^{-15} with a proton extinction factor of 3×10^{-11}. If the proton extinction factor is improved, the expected background events are

[1] More recently, CORSIKA simulations of cosmic rays above J-PARC have been obtained from the T2K experiment, but were not available in time for this study.

[2] This data corresponds to a running period of 3 days.

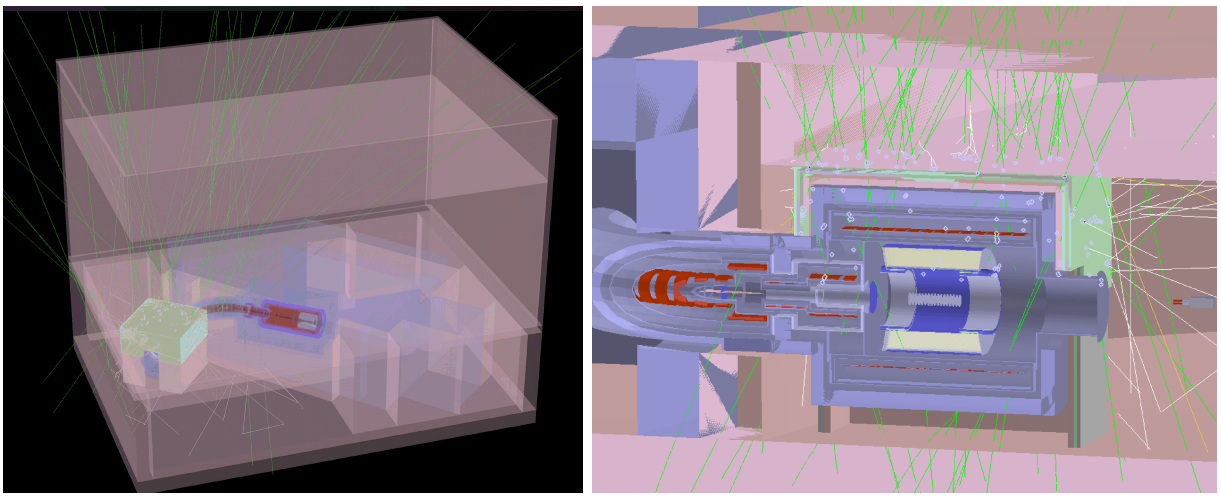

Figure 20.19: *Some cosmic event displays with 4000 events overlaid (left) and 13000 events overlaid (right). Cosmic rays were generated so as to pass through the whole COMET experimental hall volume.*

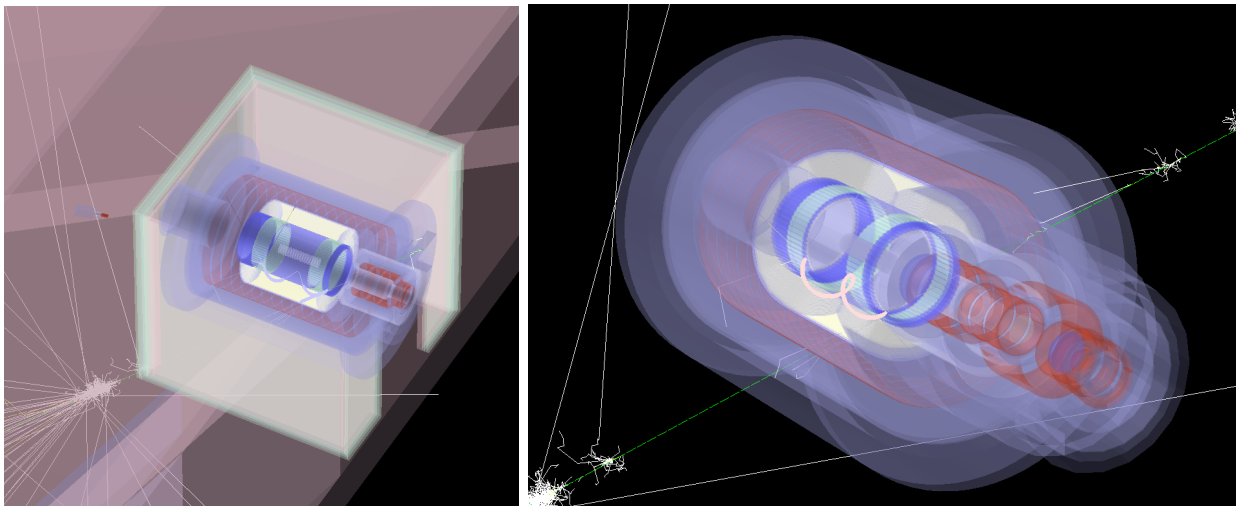

Figure 20.20: *One of the cosmic ray events which escapes the detection by the CRV and enters the BS region, creating an electron reaching the CDC. The same event shown for the whole detector region (left) and a zoomed view (right).*

further reduced.

Table 20.8: *Summary of the estimated background events for a single-event sensitivity of* 3×10^{-15} *in COMET Phase-I with a proton extinction factor of* 3×10^{-11}.

Type	Background	Estimated events
Physics	Muon decay in orbit	0.01
	Radiative muon capture	0.0019
	Neutron emission after muon capture	< 0.001
	Charged particle emission after muon capture	< 0.001
Prompt Beam	* Beam electrons	
	* Muon decay in flight	
	* Pion decay in flight	
	* Other beam particles	
	All (*) Combined	≤ 0.0038
	Radiative pion capture	0.0028
	Neutrons	$\sim 10^{-9}$
Delayed Beam	Beam electrons	~ 0
	Muon decay in flight	~ 0
	Pion decay in flight	~ 0
	Radiative pion capture	~ 0
	Anti-proton induced backgrounds	0.0012
Others	Cosmic rays†	< 0.01
Total		0.032

† This estimate is currently limited by computing resources.

Chapter 21

Beam Measurement Programmes

21.1. Pion/muon production and beam particles

There are no measurements of the pion production at backward angles with 8 GeV protons. Various hadron codes such as `MARS` and `Geant4 QGSP(BERT/BIC)` predict different production cross-sections which differ by more than a factor of two, as described in Section 8.1.2 in detail. In COMET Phase-I, the secondary and tertiary particles will be measured, by using the StrECAL which is placed downstream of the muon transport. As well as the desired muons and undecayed pions it will also sample antiprotons and electrons in the beam. This measurement is very important in terms of the sensitivity estimation since all the background estimation is based on these hadron codes. The measured **beam profile**, **rate**, and **timing structure**, as a function of energy for each kind of particle in the beam will provide a new input that can be used to tune hadron codes, and for more reliable estimation of the Phase-II sensitivity. It is noted that in order to translate the muon and pion yields from the graphite target to the tungsten target, the simulation programs are needed with proper identification of the hadron production code.

As shown in Figure 8.7 and Figure 8.9 in Chapter 8, many kinds of particles will reach the bore of the detector solenoid (DS). In order to perform a beam measurement for all of such particles by using the StrECAL detector in COMET Phase-I, we have to maximize a capability of particle identification (PID) of the StrECAL detector, using a restricted number of variables. Because the straw tracker consists largely of very light material, only a small energy loss is anticipated in the tracker. This is confirmed by the **GARFIELD** program, as shown in Figure 11.15. On its own, the energy loss information ($\mathrm{d}E/\mathrm{d}x$) is not enough to perform an effective PID. Since there are no any detectors dedicated to PID in the COMET detector apparatus, the PID is expected to be dominated by StrECAL detector, *i.e.* it is required to develop the alternative variables by the output of StrECAL. In this chapter, the development of such variables is described in addition to the discussion of beam measurement programme.

21.2. Particle identification (PID) by StrECAL

In order to evaluate the PID capability of StrECAL, a full Monte Carlo (MC) simulation was conducted by the `ICEDUST` (*cf.* Chapter 18) framework. Figure 21.1 shows the simulated events in StrECAL.

By using this full MC, alternative variables for PID by the StrECAL has been developed other than originally anticipated variables such as $\mathrm{d}E/\mathrm{d}x$ and E/p. For this development, the time

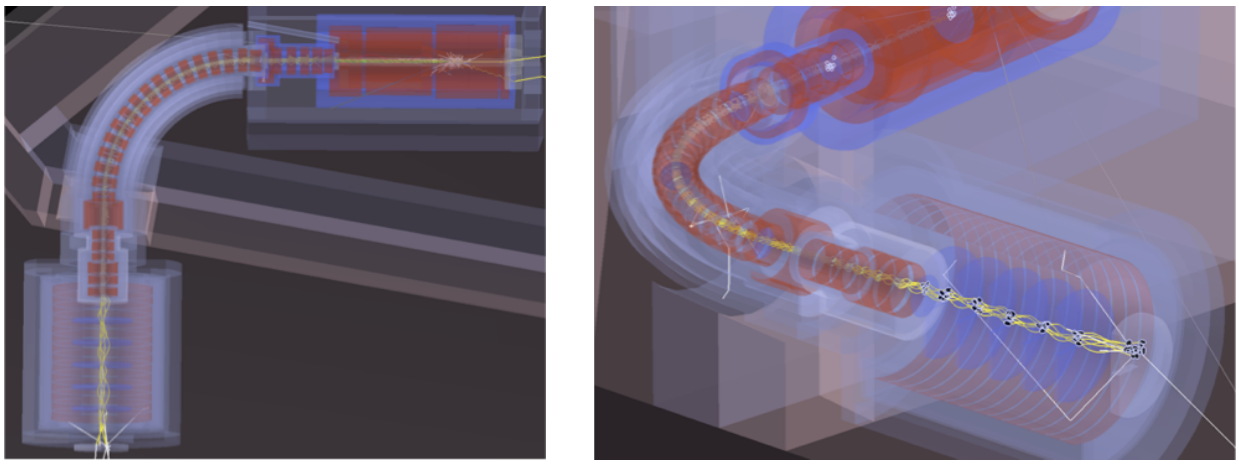

Figure 21.1: *Event displays of StrECAL full MC simulation by* `ICEDUST`

of particle flight within StrECAL detector (TOF) and the signal output from ECAL (ECAL-alone) have been investigated. TOF usually shows good PID performances, but it needs a certain distance of flight to have a clear discrimination among e, μ, π. In COMET Phase-I, various particles with various momenta would be transported to the detector region as shown in Figure 8.7 and Figure 8.9, so the capability of TOF as a PID is not clear, *i.e.* careful investigation by full MC is necessary. In case of TOF is not good enough for PID, more variable is required. The idea of ECAL-alone is to utilise the pulse shape difference of the ECAL output for PID among e, μ, π. However, such a pulse shape difference by LYSO crystal with 40-120 MeV/c particles has never been investigated precisely even for other high energy experiments. Then the dedicated test-beam campaign has been carried out at Paul Scherrer Institute (PSI) where could provide an intensive $e^{\pm}/\mu^{\pm}/\pi^{\pm}$ contaminated beam. The detail of test-beam campaign and its application for COMET Phase-I is described in Section 21.2.2.

In this investigation, target particles are "electron", "muon" and "pion" with the beam momenta of 40-120 MeV/c. The particles out of this range does not achieve to the stopping target in COMET Phase-II.

21.2.1 PID by time-of-flight (TOF)

In order to evaluate the PID performance by the TOF at StrECAL, dedicated MC was performed. In this MC, to investigate the accuracy of TOF measurement, thin plastic scintillation-fibre (Sci-Fi) detector, 250-μm-square, is placed just in front of the first station of straw tracker, as shown in Figure 21.2 (Left-Up). In this figure, TOF distributions between the Sci-Fi detector and ECAL for e^-, μ^-, π^- are shown with three different momenta, 55.9, 85.6 and 112.8 MeV/c, respectively. Particles are generated with the anticipated beam emittance so that they have a various emission angle distribution and its length of trajectory, *i.e.* the shown TOF is normalised by its length to have a clear particle discrimination. In this MC, the timing measurement accuracy is assumed to be 1.5 ns. As shown in this figure, electron can be eliminated from μ^-, π^- easily for 55.9 MeV/c. It is, however, not easy to discriminate μ^- and π^- perfectly, a certain tail parts are overlapped. For high momentum region such as higher than 100 MeV/c, even for electron discrimination is not perfectly possible as shown in Figure 21.2 (Right-Low). In consequence, the PID by TOF is somehow possible but not perfect. It is necessary to have alternative variable other than TOF.

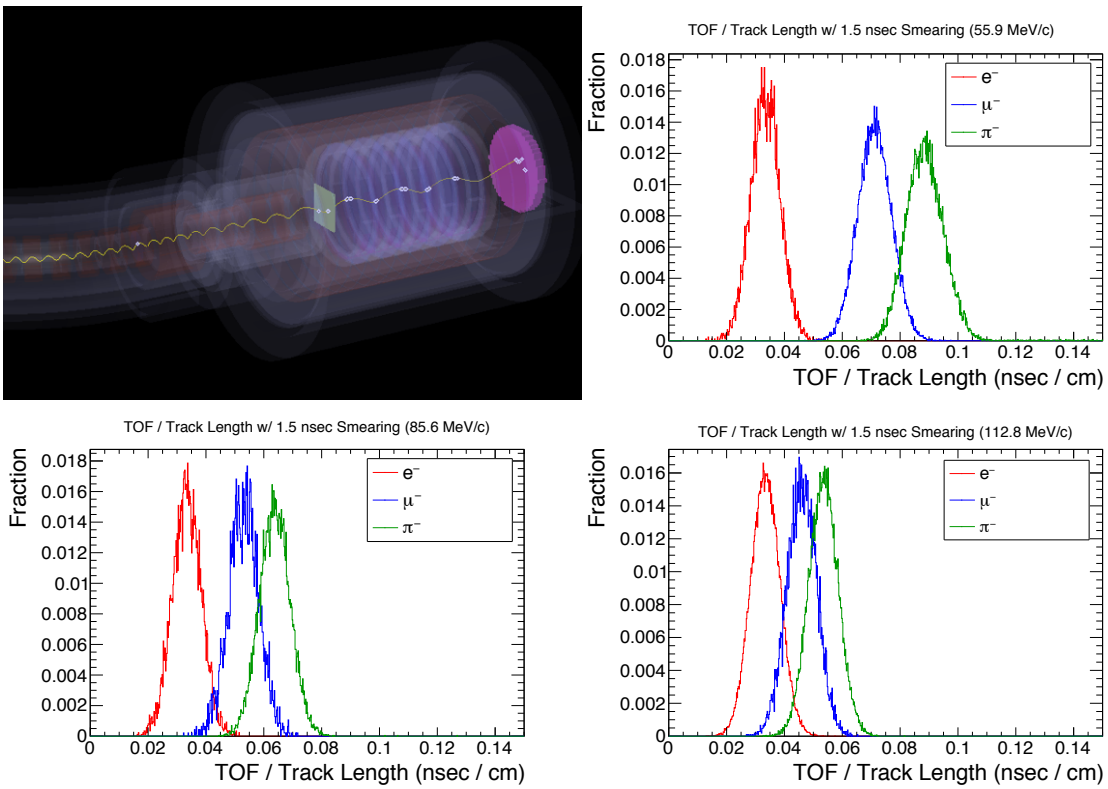

Figure 21.2: *StrECAL TOF simulation; (Left-Up) Event display of dedicated* `ICEDUST`*, (Right-Up) Normalized TOF with 55.9 MeV/c, (Left-Low) Normalized TOF with 85.6 MeV/c, (Right-Low) Normalized TOF with 112.8 MeV/c*

21.2.2 PID by ECAL-alone

In addition to TOF, another variable, "ECAL-alone", was also developed. The idea of ECAL-alone is to utilise the pulse shape difference of the ECAL output for PID among e, μ, π. However, such a pulse shape difference by LYSO crystal with 40-120 MeV/c particles has never been investigated precisely even for other high energy experiments. Then the dedicated test-beam campaign has been carried out at PSI where could provide an intensive $e^{\pm}/\mu^{\pm}/\pi^{\pm}$ contaminated beam. Figure 21.3 (Left) shows the experimental setup at PSI. In this test-beam, the experiment was conducted at the PiM1 beam line which is optimised to have more μ, π fraction in the beam. The beam momentum was set as 115 MeV/c, and the beam momentum was varied by putting various thickness lucite as a degrader. The first ECAL prototype, described in Figure 12.14, has been transported to PSI and placed just in front of the PiM1 beam window, so that the extracted beam to PiM1 was bombarded on ECAL prototype without any beam loss. The primary PID was performed by the beam line TOF which is the time difference between the beam extraction and the accelerator RF timing, as shown in Figure 21.3 (Right).

For the positive particles (e^+, μ^+ and π^+), it is obviously shown the decay chain of $\pi^+ - \mu^+ - e^+$ in the crystal, as shown in Figure 21.4 (Left). By combination of energy deposition information and this decay chain, PID for positive particles is reasonably realised. On the other hand, for the negative particles (e^-, μ^- and π^-), it is not so simple and not easy due to the complicated nuclear capture process. However, we can use this difficulty as an underhanded way to perform effective PID for negative particles. Due to the different process for nuclear capture of negative particles, the prompt energy fraction out of the total energy deposition in the crystal could have a finite difference among e^-, μ^- and π^-. For example, Figure 21.4 (Right) shows the

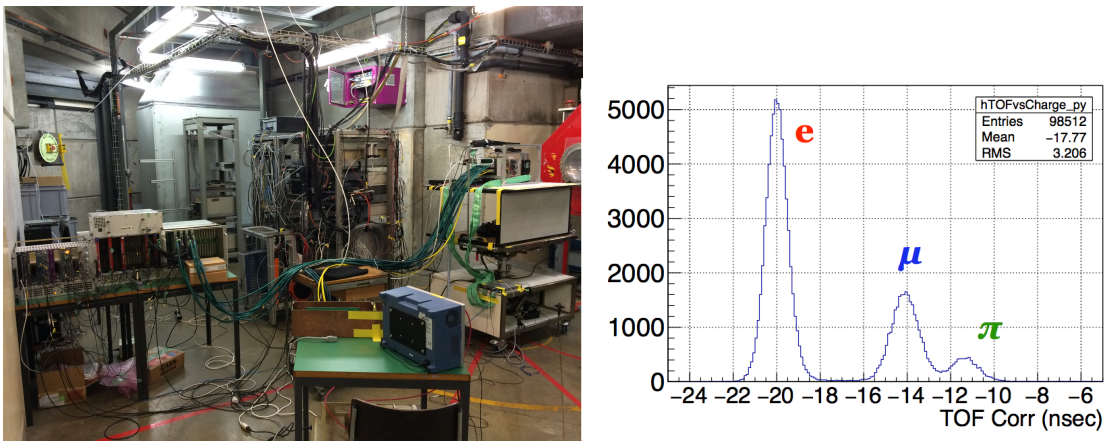

Figure 21.3: *PID demonstration by ECAL-alone at PSI. (Left) Set up, (Right) Primary PID by beam line TOF*

distribution of prompt energy deposit for three negative particles with 100 MeV/c. As shown in this plot, a certain difference can be seen even for μ and π. However, the difference is not clear since the nuclear capture process is complicated and not always same for each events. Even it is not perfect PID, the ECAL-alone can be utilised to help for PID. In consequence, it

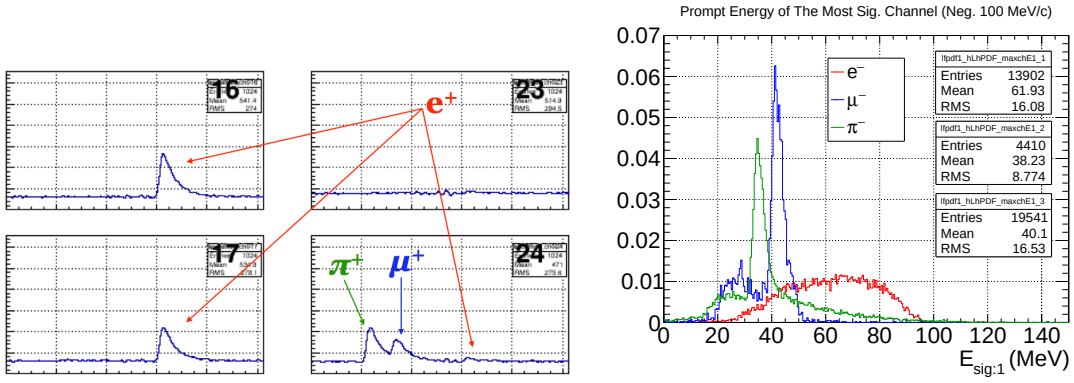

Figure 21.4: *ECAL-alone output. (Left) Observed decay chain of $\pi^+ - \mu^+ - e^+$, (Right) Distribution of the prompt energy deposition of negative particles*

would be worth to consider the combined analysis with "TOF" and "ECAL-alone".

21.2.3 PID power by StrECAL

As shown in the previous sub-sections, Section 21.2.1 and Section 21.2.2, TOF between the Sci-Fi detector and ECAL can perform PID somehow but not perfect, as well as the pulse shape difference of ECAL-alone output. Figure 21.5 shows the PID efficiency for negative particles, e^-, μ^- and π^-, by TOF only (Left) and ECAL-alone (Right). As obviously shown in the plot, TOF can discriminate each particle properly for low momenta region. On the other hand, ECAL-alone can recognise each particle properly for high momenta region. Hence, combined analysis would possibly compensate for each shortcomings. In order to demonstrate the idea of combined PID analysis, maximum likelihood analysis combining TOF and ECAL-alone was performed. In order to perform this demonstration, specially dedicated MC simulation was built. Because the precise and reliable physics process of the negative particle interaction

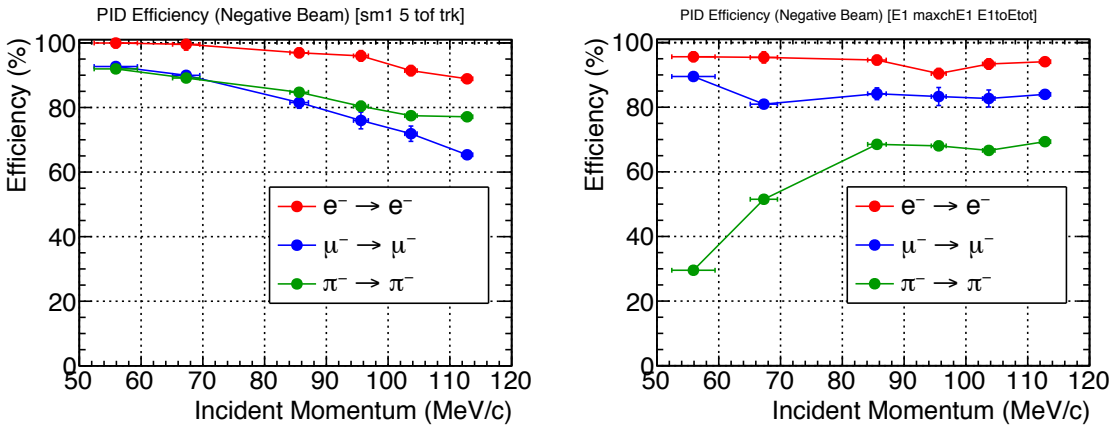

Figure 21.5: *PID efficiency for e, mu, pi, with 50-120 MeV/c. (Left) PID by TOF only, (Right) PID by ECAL-alone.*

with the LYSO crystal is not implemented in Geant4, the obtained data in the PSI test-beam campaign was quickly equipped into the `ICEDUST` framework just to reproduce the actual output for $e^{\pm}$, $\mu^{\pm}$ and $\pi^{\pm}$. First of combined analysis, PID for negative particles is demonstrated, and its result is shown in Figure 21.6. The left plot shows the result of combined analysis with the

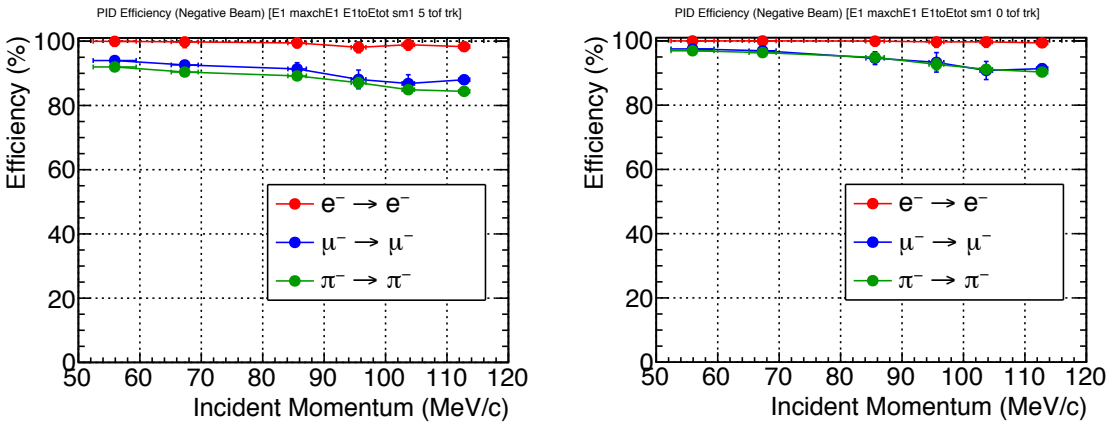

Figure 21.6: *Combined analysis by TOF and ECAL-alone for negative particles with 50-120 MeV/c. (Left) PID efficiencies by combined analysis with the timing resolution of 1.5 ns, (Right) with the timing resolution of 1.0 ns*

assumed timing resolution of 1.5 ns, and the right plot shows the efficiency with the timing resolution of 1.0 ns. As shown in both plots, PID efficiencies are dramatically improved from the plots in Figure 21.5, *i.e.* the expectation to compensate for each shortcoming of two method is successfully demonstrated. In addition, it is shown that a good timing resolution of TOF measurement can provide a further help. If the timing resolution of TOF measurement will achieve to 1.0 ns, all particles with all momentum range would be successfully identified with an efficiency of better than 90 %. It, however, would be better than 85 % even the timing resolution is just 1.5 ns.

Above results are demonstrated for negative particles. For the positive particles, e^{+}, μ^{+} and π^{+}, a better result than negative particle can be anticipated, since the ECAL-alone method with positive particle shows the better performance than the case of negative particle. Figure 21.7

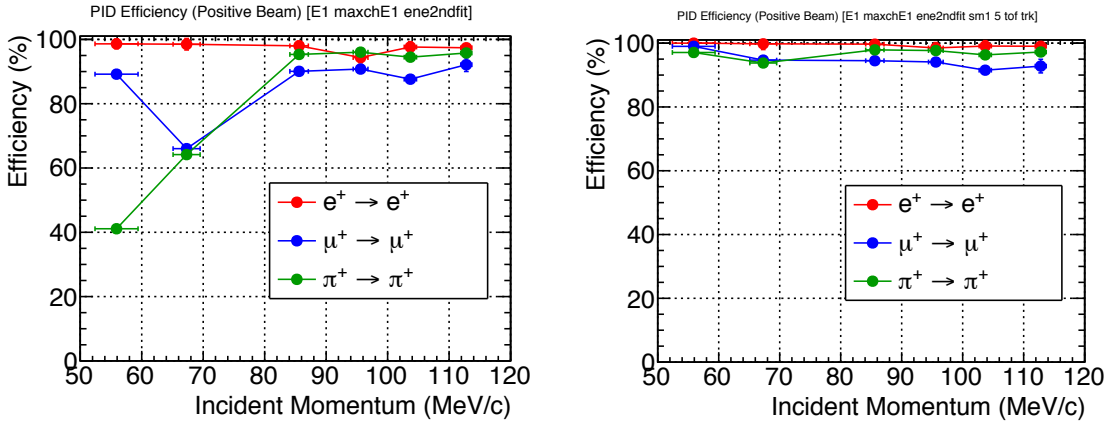

Figure 21.7: *Combined PID analysis for positive particle with 50-120 MeV/c. (Left) PID efficiencies by ECAL-alone for positive particle, (Right) Combined PID with ECAL-alone and TOF with assumed timing resolution of 1.5 ns*

(Left) shows the PID efficiency by ECAL-alone for positive particles with 50-120 MeV/c. As shown in the plot, the ECAL-alone method has a more efficient PID power for high momentum region than the case of negative particle. Thus the combined PID efficiency is better than 90 % for all particles with all momentum region even the timing resolution can achieve only 1.5 ns as shown in Figure 21.7 (Right).

In conclusion, StrECAL PID by the combined TOF and ECAL-alone is powerful enough to perform the COMET Phase-I beam measurement. A good timing resolution of TOF measurement is essential, the timing resolution of 1.0 ns is good enough, but the timing resolution of 1.5 ns is still acceptable. In order to obtain a good timing resolution of TOF measurement, involving the Sci-Fi detector in front of the first station of straw tracker is anticipated in this scenario. The realisation of TOF detector is described in Section 21.5..

21.3. Rate capability of StrECAL

To perform the beam measurement, momentum and profile measurement is one of the most important item. On the other hand, timing structure of the beam is also very important item for the beam measurement of COMET Phase-I, since the prompt timing which is right after the proton main bunch would contain so many background particles related to π decay, and also, small number of survived particles in the delayed timing would cause a severe background event for the $\mu^- N \to e^- N$ signature. Thus, the beam timing measurement is essential for beam measurement. In addition, momentum/profile measurement will be impossible with the normal beam power which is supposed to be 3.2 kW for COMET Phase-I. In order to consider the beam timing measurement, rate capability of StrECAL should be carefully investigated with a help of `ICEDUST` full simulation.

Obviously, beam intensity for Phase-I will be a serious problem. In order for the StrECAL to tolerate the remaining pion rate in the beam central region, beam power reduction should be considered. However, just reducing the beam power is not optimal, it would be more efficient to maintain the high power beam as high as possible but configure the StrECAL in such a way to decrease its sensitivity in the central region of the beam, *i.e.* “beam blocker” and “masked HV” was investigated.

21.3.1 Beam blocker

Since the muon transport line for Phase-I is not long enough and has only 90 deg bending, rate of transported beam to the detector section will be very high. However, the most of

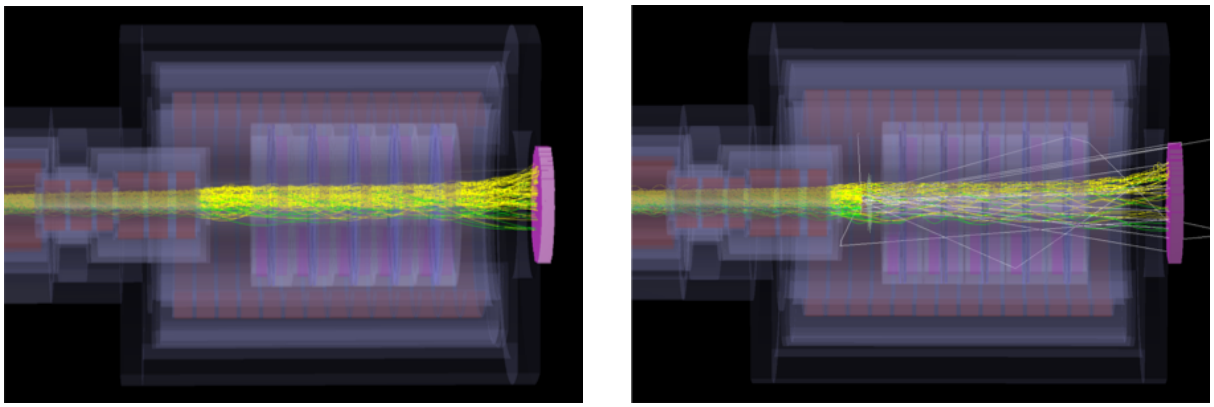

Figure 21.8: *Event display of StrECAL by the Full* `ICEDUST` *simulation, corresponding to the 3.2 kW beam. (Left) Normal condition, (Right) With the "Beam Blocker" of 20-mm-thick Tungsten disk.*

beam particles would be dominated by the central region; this is verified by the full `ICEDUST` simulation as shown in Figure 21.8 (Left). Thus it is worth to put the beam blocker in the central region of the beam. By the optimisation of the beam blocker size, material and position, it is shown that putting the 20-mm-thick Tungsten disk in front of the first station of straw tracker would be optimal, and the beam rate reduction is realised accordingly. Thanks to this beam blocker, beam rate is successfully reduced as shown in Figure 21.8 (Right).

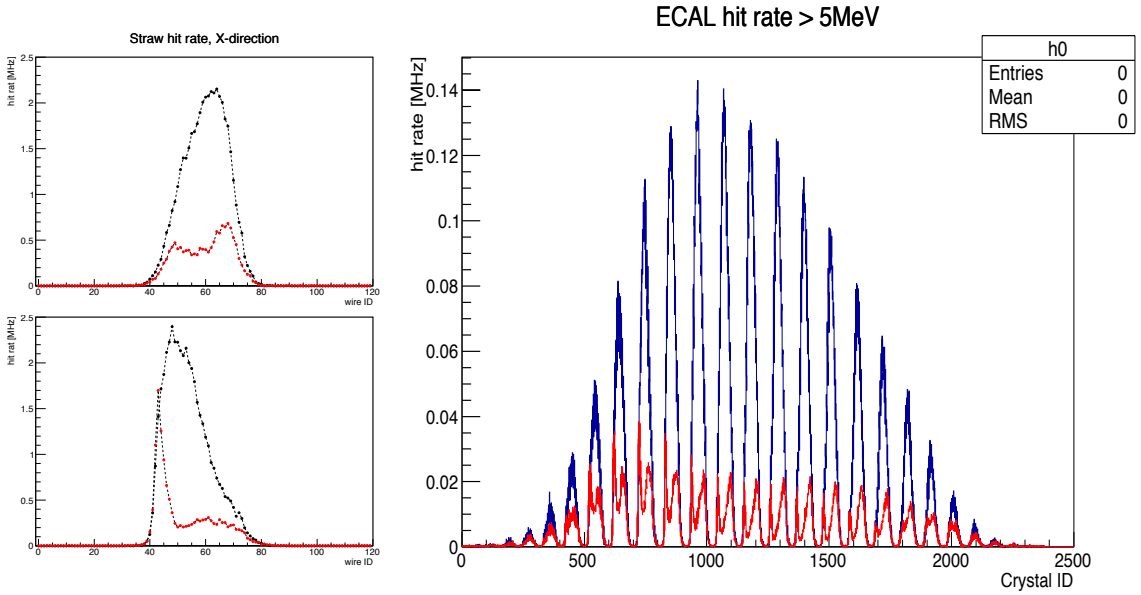

Figure 21.9: *Detector hit rates for StrECAL, red marker shows the rate with beam blocker. (Left-Up) Hit rate of straw x-axis, (Left-Low) Hit rate of straw y-axis, and (Right) Hit rate of ECAL*

Figure 21.9 shows the detector hit rates for StrECAL. Figure 21.9 (Left-Up) is x-axis hit rate of Straw and (Left-Low) is y-axis as well. Figure 21.9 (Right) shows the ECAL hit rate. For both, rate is indexed by channel ID, *i.e.* the wire ID and the crystal ID, and the red marker

shows the rate with beam blocker. Thus approximately factor 6 of rate reduction is achieved. It is, however, still very high; 1.5 GHz/straw and 40 MHz/crystal at highest. Further reduction is necessary.

21.3.2 Masked High Voltage

In order to make a further reduction on the detector hit rate without reducing the beam power, partially turning off the HV, so-called "Masked-HV", was investigated.

As described in Section 11.1.1 and schematically shown in Figure 11.1, straw tubes are grouped with 8 tubes in the straw-tracker station as a readout unit. HV distribution line and decoupling capacitor line are also attached to this grouped readout unit so that the HV-masking can be done by 8 channels as one unit. According to the optimisation by `ICEDUST` simulation, switching three units off, *i.e.* 24 channels off, is optimum to reduce the hit rate but to keep the tracking capability. Figure 21.10 shows the reconstructed momentum spectrum of electron, muon, and

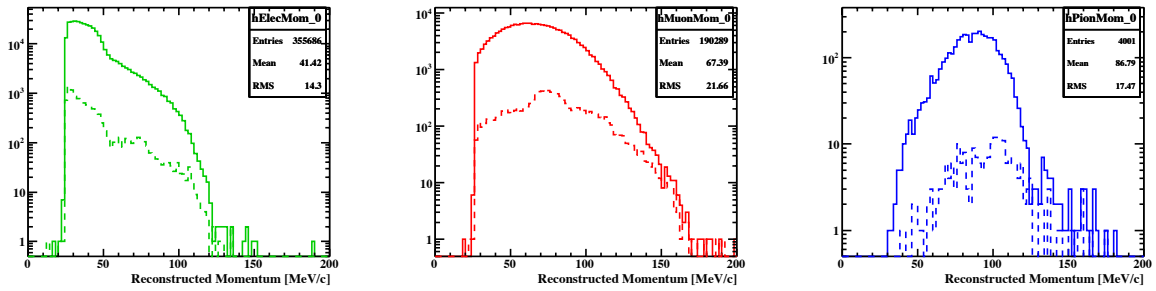

Figure 21.10: *Effect of "masked HV" on straw hit rate. (Left) Reconstructed momentum spectrum of electron, (Centre) muon, and (Right) pion*

pion, respectively, with masked-HV. Solid line is reconstructed without masked-HV, and dot line is reconstructed with masked-HV. As shown in spectra, a dramatically reduction of a factor of 100 is achieved by masking HV for three particles. And spectrum shape does not change so much, only low momentum part of electron spectrum changes. However, high momentum part, higher than 40 MeV/c, does not change, *i.e.* this is not a serious problem, since low momentum electron does not achieve the stopping target in Phase-II.

On the other hand, ECAL hit rate is not reduced effectively by masked-HV. As shown in Figure 21.9, putting the beam blocker reduces hit rate for a central part of beam in straw tracker, but a reduction of hit rate in ECAL is uniform. This is due to the gradient of magnetic field. After the fifth station of straw tracker, in other words, in front of ECAL, strength of magnetic field is lower than the central part of solenoid so that the beam is diverged in front of ECAL, as shown in Figure 21.8. That is why the hit rate reduction is uniform for ECAL while the central part is effectively suppressed in straw tracker. Due to this effect, masked-HV for the central part of ECAL does not reduce the hit rate effectively.

In consequence, masked-HV properly works for straw tracker, which reduces hit rate by a factor of 100. However, it does not function for ECAL effectively. Thus it is still desired to consider a beam power reduction to perform beam measurement for COMET Phase-I.

21.4. Beam measurement programme

The PID power and the rate capability of StrECAL was carefully investigated by the full MC simulation, `ICEDUST`. According to the result, PID can be done by combined analysis of "StrECAL-TOF" and "ECAL-alone" with a high PID efficiency. And the rate capability is still issue even beam blocker is placed in the beam and HV is masked to reduce the central part of beam distribution. Putting beam blocker reduces hit rate by a factor of 6 for StrECAL, the highest hit rate would be 1.5 GHz/tube and 40 MHz/crystal. Masking HV reduces hit rate by a factor of 100 for straw.

In this section, by reflecting these results, optimisation of the beam measurement programme is discussed.

21.4.1 Beam measurement strategy

Due to the rate capability of StrECAL, a certain reduction of beam power should be made. In order to keep the beam power as much as possible, the beam measurement will be done separately so that a part of measurement will be done with full beam power.

The programme is separated into two measurements; **"momentum/profile measurement"** and **"beam timing measurement"**. For the momentum/profile measurement, the goal is to reproduce the momentum spectrum (Figure 8.7) by the actual measurement. Thus this measurement needs a track reconstruction and a full PID, *i.e.* beam power reduction is essential. For the beam timing measurement, the goal is to reproduce the time spectrum (Figure 8.9) by the actual measurement. This can be done without track reconstruction, momentum information is not required at all. Thus this measurement can be done without spectrometer, detector solenoid and straw tracker will be turned off during this measurement. Then the measurement will be done with full beam power or with a partially reduced beam. Detailed plan is discussed in the following sub-sections.

21.4.2 Momentum/profile measurement

To measure the beam momentum/profile precisely, track/momentum reconstruction is necessary, *i.e.* rate capability is the most serious problem. In addition, the beam extraction from the J-PARC accelerator will be "bunched slow-extraction (SX)" as described in Chapter 4, thus the instantaneous rate would be very high. First, in order to avoid such a very high rate on the proton prompt timing, the momentum/profile measurement will be performed with normal SX so that the instantaneous rate would be small. However, even for normal SX beam, hit rate on ECAL is ∼10 MHz/crystal, it is still too high, *i.e.* beam power reduction is essential. If we require only one pile up in straw tube, this is corresponding to occupancy of 5 % and average number of hit of 20. This can be realised by a beam power reduction by a factor of 1000, the corresponding beam rate is 2×10^9 Proton-on-target (POT) /sec. If we allow two pile ups in straw tube, the allowed beam rate is 5×10^9 POT/sec, this can be realised by a beam power reduction by a factor of 500, For the beam power reduction of 1000, StrECAL hit rate is expected to be ∼10 kHz, this is somehow acceptable to make a trigger. Taking DAQ rate into account, 10 kHz is not acceptable. However, as discussed in Section 21.2.2, ECAL output can discriminate electron-like event so that the level-1 trigger can reduce the DAQ rate effectively by choosing μ/π-like event.

By assuming the normal SX and the beam rate of 2×10^9 POT/sec which is corresponding

to 1/1000 beam power reduction, DAQ time can be considered. In order to accumulate 1M negative pion events, DAQ net time would be 80 sec[1]. By including the DAQ/trigger tuning and a safety factor, 1 hour is enough. Concerning the positive pion, 1000 times longer time is needed since the positive pion yield is much smaller than negative pion, a factor of 1000, namely 80000 sec. However, just inverting the direction of dipole field, positive pion yield is also to be same as negative one, *i.e.* it is not necessary to have 80000 sec. Thus the positive pion spectrum can be extracted by i) 80000 sec (=22 hour) DAQ, or ii) 1 hour including tuning time with inverting dipole field. In any case, DAQ time of 1 day and a couple of spare days are enough for momentum/profile measurement.

21.4.3 Beam timing measurement

For the beam timing measurement, bunched SX is obviously necessary. However, the momentum information is not required at all, *i.e.* spectrometer is not necessary. This is big advantage to conduct this measurement. Detector solenoid and the straw tracker can be turned off during the beam timing measurement so that the hit rate would be dramatically reduced. By this scenario, full PID is not possible since the spectrometer would be turned off, but an "easy PID" is possible by ECAL-alone so that electron and muon/pion can be distinguished. Figure 21.11

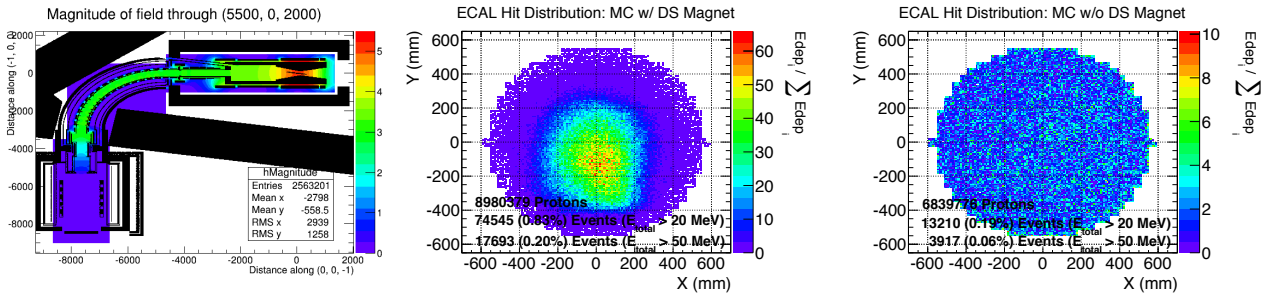

Figure 21.11: *Effect of no solenoid field. (Left) Magnetic field map, (Centre) ECAL hit distribution with magnetic field, and (Right) without magnetic field*

shows the effect of "no magnetic field" measurement. Figure 21.11 (Left) is the magnetic field map, only detector solenoid is turned off and all other magnets are on. Figure 21.11 (Centre) and (Right) is comparison of ECAL hit distribution for with and without magnetic field. As shown in this plot, hit distribution is expanded, and it is almost uniform if solenoid is turned off, *i.e.* hit rate is also reduced.

Figure 21.12 shows the comparison of momentum distribution with and without detector solenoid. As shown in this plot, no-solenoid run will result just scaling down the entries by a factor of 10, spectrum shape does not change for high momentum region, higher than 40 MeV/c. For low momentum region, lower than 40 MeV/c, the shape of spectrum changes but they are not interesting for Phase-II.

In consequence, beam timing measurement by ECAL-alone without magnetic field can be a solution. However, beam rate is still an issue, in particular, during the prompt timing. Thus the beam timing measurement would be separated into two sub-measurements, **prompt timing measurement** and **delayed timing measurement**.

[1] PID efficiency of 80 %, tracking efficiency of 90 %, trigger and DAQ efficiency of 90 % is assumed to estimate the DAQ time.

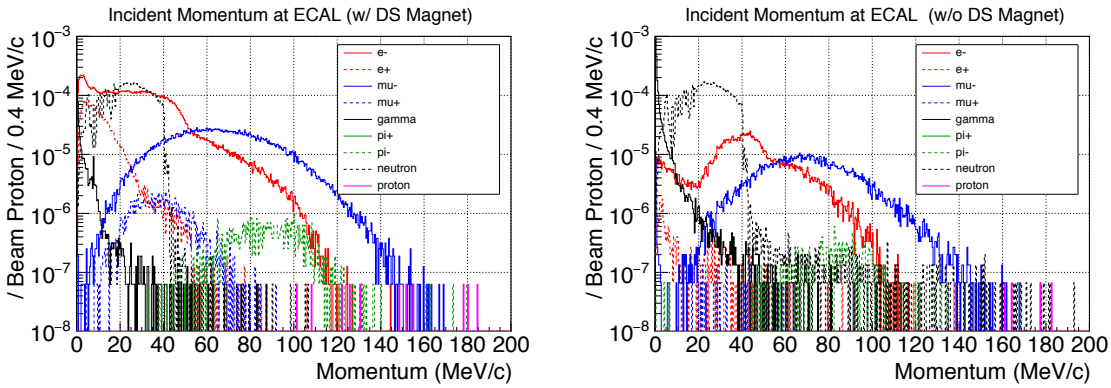

Figure 21.12: *Momentum distribution with and without magnetic field. (Left) With detector solenoid, (Right) without detector solenoid*

Prompt timing measurement

Due to the property of bunched SX, beam rate would be extremely high during the beam prompt timing (100 ns). However, the time structure of prompt beam should be carefully investigated for Phase-I beam measurement, especially right after the prompt timing. There is two possible scenario; i) reduce the beam intensity, or ii) mask the DAQ during the prompt timing of 100 ns. Based on the `ICEDUST` simulation with 5×10^8 POT, pion timing structure is

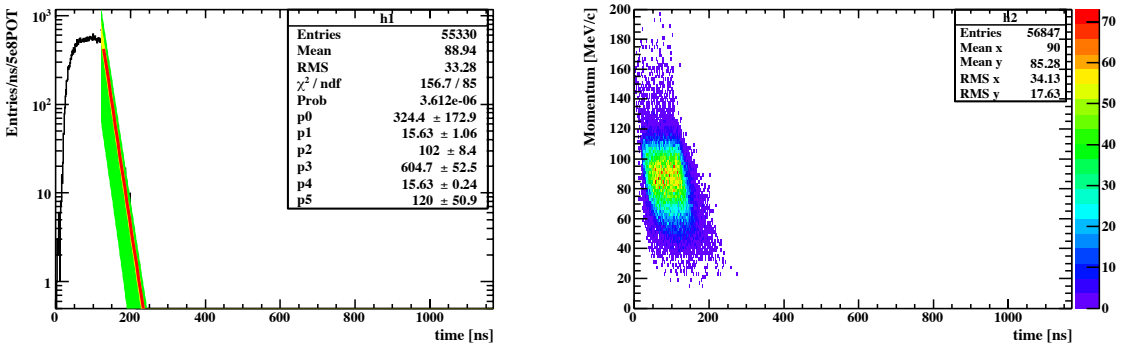

Figure 21.13: *Timing structure of pion. (Left) Simulated timing spectrum, (Right) Timing vs. Momentum*

simulated as shown in Figure 21.13. In order to have a clear spectrum, DAQ time of 3 days is needed with 1/100 beam rate.

Delayed timing measurement

One of the most important item of Phase-I beam measurement is careful investigation of the delayed particles. As described in Chapter 4, the DAQ window would wait long enough to be opened in order for no particle arrival into the DAQ window other than the signal electron, *i.e.* this "no-particle-arrival" should be demonstrated by Phase-I beam measurement. Based on the `ICEDUST` simulation with 5×10^8 POT, same as Figure 21.13, muon and electron timing structure is simulated as shown in Figure 21.14. DAQ will start after the prompt timing to see the delayed timing, hence the hit rate will be not a problem any more, *i.e.* delayed timing

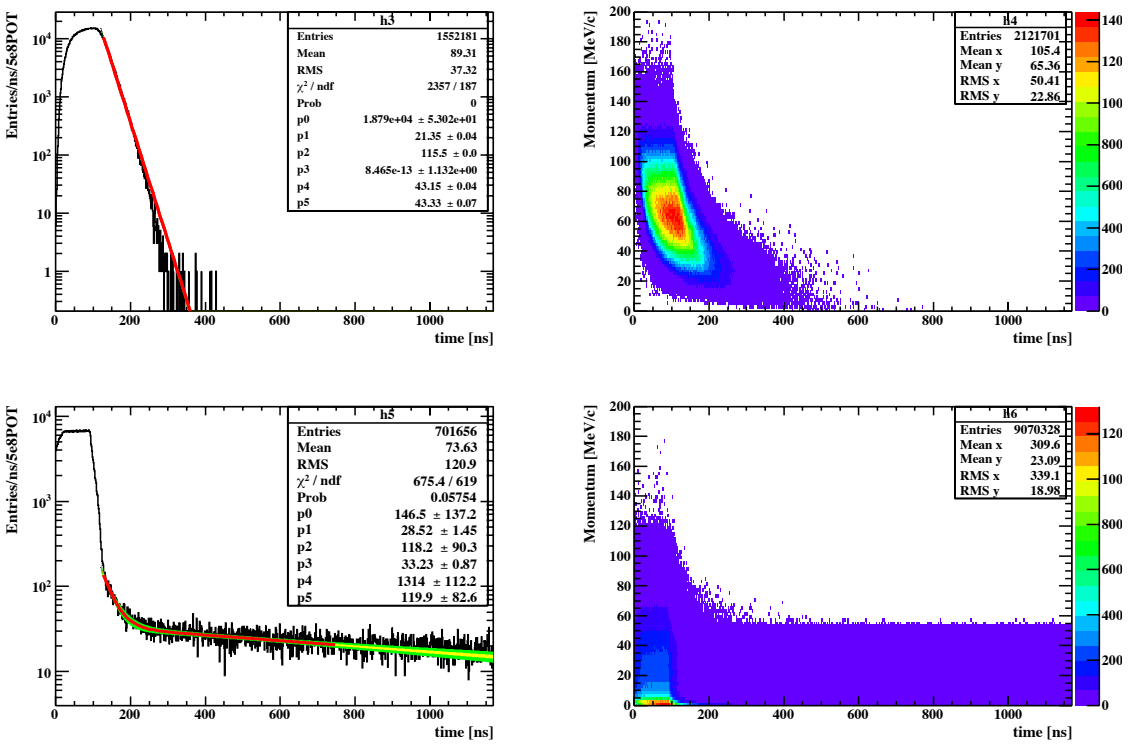

Figure 21.14: *Timing structure of muon and electron. (Left-Up) Simulated timing spectrum of muon, (Right-Up) Timing vs. Momentum of muon, (Left-Low) Simulated timing spectrum of electron, (Right-Low) Timing vs. Momentum of electron,*

measurement will be conducted with full beam power, 3.2 kW. The tail component is extracted by fitting the timing spectrum to the exponential function, as shown in Figure 21.14 (Left-Up). Based on this result, in order to accumulate an order of 1000 muons around 500 ns region, DAQ time of 60 hours is needed. Concerning the pion statistics, it is just a 3 % of fraction compared to muon statistics. As described above, only an easy-PID will be performed by the beam timing measurement, thus muon/pion combined timing spectrum will be measured.

On the other hand, much higher statistics is anticipated for electron, as shown in Figure 21.14 (Left-Low). In particular high momentum electron, higher than 80 MeV/c is especially interesting to estimate the background for Phase-II. In order to accumulate an order of 10000 of such a high momentum electron around 150 ns, just a quick DAQ of ∼200 sec is enough.

In consequence, 60 hours plus a certain tuning period is needed for delayed timing measurement, *i.e.* a week of dedicated period is necessary.

21.4.4 Summary of beam measurement programme

Here we summarise the beam measurement programme. In addition to the necessary DAQ period, some other dedicated period is also needed, *eg.* DAQ/trigger tuning, setup change over, beam power study, *etc.*, thus 2-3 weeks is reasonable for beam measurement programme.

Table 21.1: *Summary of beam measurement programme*

	Momentum measurement	Timing measurement
Detector	StrECAL + SciFi	ECAL-alone
Beam mode	Normal SX	Bunched SX
Detector solenoid	On	Off
Beam suppression	Beam blocker, Masked-HV	No beam suppression
PID	Full PID	Easy PID
Beam power	1/1000	1/100 (prompt), Full power (delayed)
DAQ period	1 day (+2 days for spare)	6 days (+1 week for spare)

21.5. Detector R&D for beam measurement

To finalise the detector configuration for beam measurement, some prototypings are ongoing. Mainly two prototypings were recently made; i) **Scintillating-fibre detector** (Sci-Fi), and ii) **StrECAL integration**.

21.5.1 Scintillating fibre detector

In order to complete the full PID for momentum/profile measurement, accuracy of timing measurement is essential, as described in Section 21.2.3. For this purpose, Sci-Fi detector is anticipated to be added to the StrECAL detector. The thickness of scintillation fibre is important. In order to obtain a good enough timing resolution, thickness should be thick enough so that an enough scintillation photon would be collected by a photon sensor. On the other hand, fibre thickness should be thin enough in order to keep the pion yield, otherwise no pion can arrive at ECAL, *i.e.* the thickness should be optimised.

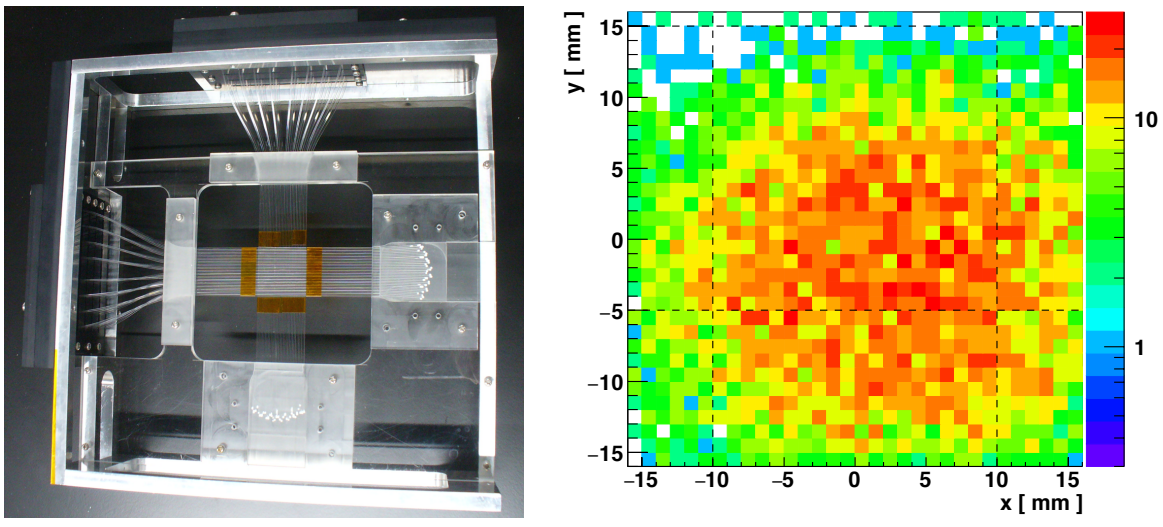

Figure 21.15: *Sci-Fi detector R&D. (Left) Prototype of Sci-Fi detector, (Right) obtained beam profile by Sci-Fi prototype.*

Sci-Fi prototype was built with 1 mm square scintillating fibre and MPPC readout as shown in Figure 21.15 (Left). This prototype was successfully used to obtain the beam profile for the straw tracker test-beam experiment, as described in Section 11.5.2 and shown in Figure 11.34.

The obtained beam profile is shown in Figure 21.15 (Right) and confirmed to have a good enough performances. However, 1 mm thick is too thick from the point of view of pion yield. According to the latest investigation by other experiments[2], 250-μm-fibre would be optimal.

Thinner fibre and vacuum compatibility will be tested by the next prototype in the second half of 2016.

21.5.2 StrECAL

At the end of test beam campaign at Tohoku university as described in in Section 11.5.2, the first integration test was performed to combine "Straw prototype" and "ECAL prototype" as "StrECAL" prototype. Figure 21.16 shows the integrated test with 100 MeV/c electron beam

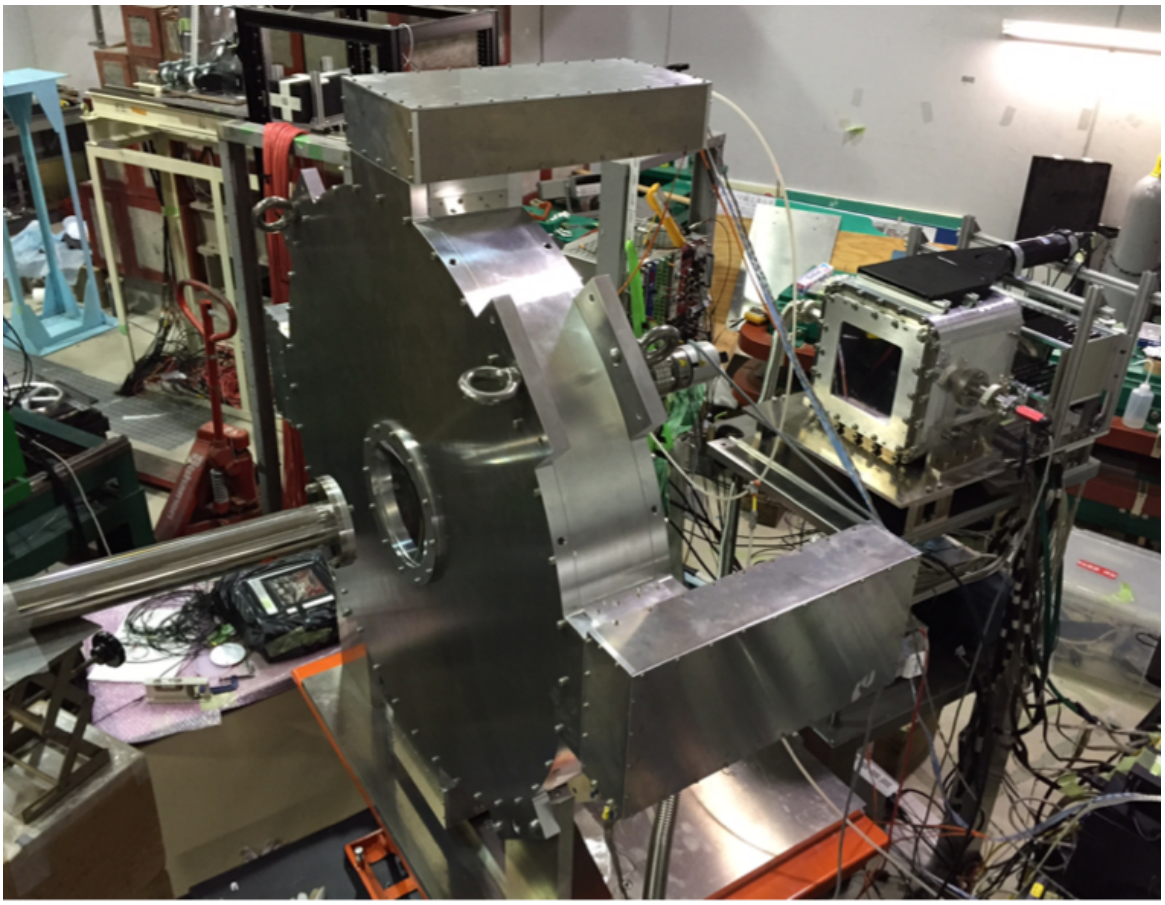

Figure 21.16: *StrECAL integrated test with beam.*

at Tohoku university in March 2016. The test was successfully done, the trigger signal was provided by ECAL, and the electron track was successfully reconstructed by straw using ECAL trigger. All the electronics chain for StrECAL was tested.

Due to the limitation of allowed beam period, only the pilot test could be performed. The detailed investigation such as performance study will be done in the second half of 2016. The test beam proposal to the Tohoku university was already approved.

[2] The latest information was provided by the private communication with MEG and Mu3e collaboration at PSI. According to their latest result, timing resolution of 500 ps for electron and 200 ps for muon was achieved with 250-μm-square fibres.

Chapter 22

Background Assessment Programs

Most of the background processes to the search for the $\mu-e$ conversion in aluminium have never been measured. The background estimations given in Section 20.2. are based on some assumptions on their rates and spectra, and therefore they have a large uncertainty. For COMET Phase-I, the measurement of background sources is one of the most important goals. In this chapter, assessment of backgrounds associated with muons (intrinsic physics background) is described. It is also noted that the assessment of the background processes is the most critical importance to COMET Phase-II.

Intrinsic Physics backgrounds	Status	Plan (section)
Muon decays in orbit (DIO)	endpoint not measured	by Phase-I (Section 22.1.)
Radiative muon capture	endpoint not measured	by Phase-I (Section 22.3.)
Neutron emission	not measured	by AlCap
Charged particle emission	measured (AlCap)	by AlCap (Section 22.4.)
Beam related backgrounds	Status	Plan
Radiative pion capture		
Beam electrons	not measured	by Phase-I
Muon decay in flight	not measured	by Phase-I
Pion decay in flight	not measured	by Phase-I
Neutron induced backgrounds	not measured	by Phase-I
$\overline{p}$ induced backgrounds	not known	by Phase-I
Other backgrounds	Status	Plan
Cosmic-ray induced backgrounds		by cosmic runs (Section 22.2.)
Room neutron induced backgrounds		

Table 22.1: *A list and status of potential backgrounds for the search for $\mu-e$ conversion. The COMET Phase-I experiment will measure most of the background sources, which have never been measured in the past, in sufficient precisions,*

22.1. Muon Decay in Orbit

There are no measured data of the muon decay in orbit (DIO) in the high-momentum region near the endpoint energy. This measurement cannot be done at any existing muon facility since

they are not powerful enough to produce the number of muons required. In COMET Phase-I, the CyDet will be used to measure the DIO electron spectrum precisely with a momentum resolution of about 200 keV. This measurement can be compared with the theoretical prediction. Once the DIO rate and spectrum are precisely measured, they can be used to monitor the total number of muons stopped in the muon stopping targets, as discussed in chapter 14.

22.2. Cosmic Ray Induced Background

Cosmic rays are known to be one of the important background sources, as discussed in Section 20.2.5. The contribution of cosmic ray induced background (CRB) is proportional to the total live running time, rather than the proton beam power. However, generation of a sufficient number of cosmic ray events in the simulation turns out very difficult. The data corresponding to the whole live running time is almost impossible to generate. Therefore, instead of relying fully on the simulation, we plan to study the CRB contribution by measurements using the COMET Phase-I detector. Namely, we can run the CyDet detector with the CTH triggers `without` a muon beam for a time period similar or longer to the live running beam time. If this *cosmic-ray run* can be carried out early before the physics run, it would provide an opportunity to study and determine any special additional arrangements to suppress cosmic-ray backgrounds further. According to the current schedule, the detector construction may be completed before the completion of the COMET beamline. If it is the case, we plan to have the *cosmic-ray run*, wishfully in early 2018 for about $6 \sim 8$ months, as described in Section 23.2.. It is noted that COMET will also be able to measure CRB using data collected during the J-PARC MR spill off time, but this is just a monitor of the CRB contributions during the physics run. The dedicate cosmic ray run is of critical importance to prepare and make further suppression of CRB before the beam time.

22.3. Radiative muon capture

There are no measurements of radiative muon capture (RMC) with photon energy in the region of the endpoint for aluminium. As with DIO, this measurement cannot be done at an existing muon facility since the number of muons required cannot be obtained. This measurement needs an energy resolution less than 1 MeV since the endpoint is about 3.06 MeV lower than the $\mu-e$ conversion signal. In COMET Phase-I, the CyDet can be used as a pair spectrometer with a photon converter to measure photon energies of 100 MeV with an energy resolution of about 200 keV.

The energy difference of the end point of RMC photon spectrum on $^{27}_{13}$Al and the $\mu-e$ conversion signal is 3.06 MeV. Because of this, the photon energy spectrum, in particular towards the end point, is best measured by a detector with energy resolution of less than 1 MeV. However, a 1% calorimeter energy resolution is challenging and the target for the COMET electron calorimeter (ECal) is $< 5\%$. Therefore, we are considering use of the CDC as a pair spectrometer, in which a photon converter is placed in front of the inner wall of the CDC. A photon converter could be a thin gold foil, or active material such as plastic scintillator.

We have performed Monte Carlo simulation of using the CDC as a pair spectrometer. The photon converter is 100 μm gold foil, placed in front of the inner wall of the CDC.

The geometrical acceptance and tracking efficiency turned out to be about 6.7% with the following tracking cuts:

- Reduced χ^2 is less than 2.
- The number of hits (hit cells) is greater than 20.
- Neither track reaches the outermost layer of the CDC.

Figure 22.1 shows reconstructed momenta and true momenta for $e^{\pm}$ after photon conversion, both separately and the sum of their momenta. It can be seen that the reconstructed momentum matches the true momentum quite well.

After reconstruction of tracks with the above cuts, the resolution on the summed energies of $e^{\pm}$ is found to be about 400 keV/c for a photon energy of 105 MeV. This meets our requirement of measuring RMC with an energy resolution of less than 1 MeV.

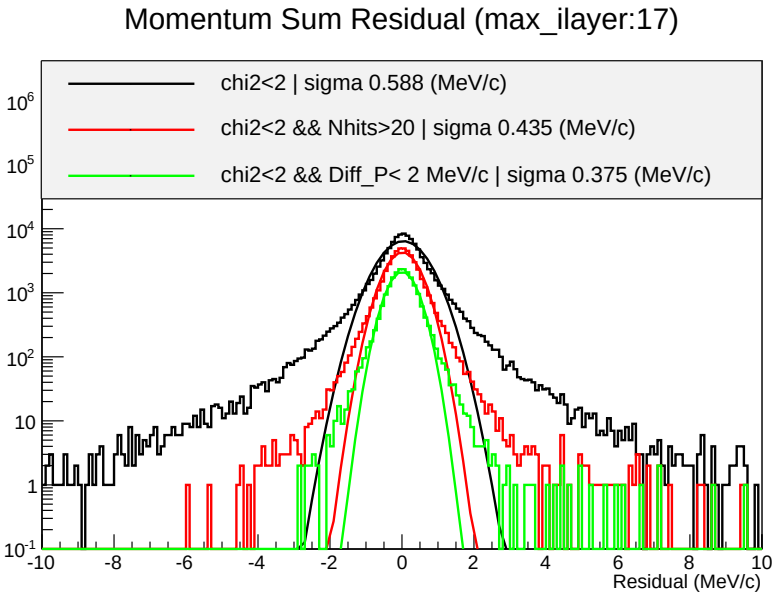

Figure 22.1: *Residual distribution of the momentum sum of the electron and positron. Histograms are for reconstructed events with chi-squared cut only (black), with chi-square and number of hit cut (red), and with chi-square, number of hit, and tail cut (green). Smooth curves show Gaussian fits to the corresponding histograms*

Rates A fast Monte Carlo simulation has been done to evaluate the measurement efficiency. The partial branching ratio of RMC on $^{27}_{13}$Al, where the photon energy is greater than 100 MeV is about 1.645×10^{-9}. The conversion efficiency with 100 μm gold foil is about 1.41%.

A combined geometrical acceptance and tracking efficiency of 6.7% is obtained from Monte Carlo simulation. Therefore, the net effective event rate R_{RMC} at the CDC for RMC photons whose energy is greater than 100 MeV can be expressed:

$$\begin{aligned} R_{\mathrm{RMC}} &= R_{\mathrm{muon}} \times f_{\mathrm{cap}} \times f_{\mathrm{he-photon}} \times f_{\mathrm{conv}} \times A_{\mathrm{geom}} \\ &= 1.3 \times 10^{9}\,/\mathrm{sec} \times 0.61 \times 1.645 \times 10^{-9} \times 0.0141 \times 0.067 \\ &= 0.0011\,/\mathrm{sec} \end{aligned} \tag{22.1}$$

where R_{muon}, f_{cap}, $f_{\mathrm{he-photon}}$, f_{conv}, A_{geom} are, respectively: the rates of muon stopping, fractions of muon capture, of production of a photon whose energy is greater than 100 MeV and of photon conversion, and the CDC geometrical acceptance. Here we assume that the muon yield of

$N_\mu = 1.2 \times 10^9$ /sec can be achieved. Therefore, the running time needed to accumulate 1000 events is

$$T = 1000/0.0011 = 8.8 \times 10^5 \,\text{sec}, \tag{22.2}$$

so measurement run of about 10 days would yield the desired 1000 events above 100 MeV. This exposure scales inversely to the muon yield per proton, and should be updated once this is more accurately known.

Trigger To use the CDC as a pair spectrometer, a special arrangement of the trigger hardware and software shall be needed, as the electrons may not pass the usual hodoscope trigger. One possibility is to trigger from CDC hits directly. The Belle-II front end readout board has such capability which we intend to use for the CyDet higher-level trigger, but we would need to write a different algorithm for this usage mode. An alternative method would be to place additional segmented tiles of plastic scintillator to trigger on events, using appropriate coincidences of hits. Further consideration will be needed, and should be informed by experience with the 'standard' configuration of the CyDet.

To summarise, in order to measure the RMC photon spectrum above 100 MeV in energy, we propose using the CDC as a pair spectrometer. It could achieve an energy resolution, for the sum of the $e^\pm$ energies, of about 400 MeV, which is sufficient for the measurement. The rate is also estimated assuming $R_{\text{muon}} = 1.3 \times 10^9$ /sec, which is also a reasonable running time. It should be noted that operating the CDC as a pair spectrometer with high energy resolution would provide opportunity to make other subsidiary measurements.

22.4. Proton Emission After Muon Capture

The maximum muon beam intensity that can be used in COMET Phase-I will be limited by the hit occupancy of the CDC. As described before, charged particles with transverse momentum, p_T, greater than 60 MeV/c are expected to reach the CDC. In this case, protons emitted after nuclear muon capture, namely $\mu^- + N \to N' + p + \nu_\mu$, were expected to be one of the major contributions to the CDC hit rate.

The energy spectrum of protons emitted after negative muon capture in aluminum has been measured by the AlCap experiment at PSI, a collaboration between COMET and Mu2e. A preliminary analysis shows that the proton emission probability per muon capture in aluminum in the energy range of 4 to 8 MeV is 0.017. Fitting the measured spectrum and extrapolating the fitted function gives a total emission rate per muon capture of 0.035. The proton spectrum peaks at around 3.7 MeV, then decreases exponentially with a decay constant of 2.5 MeV (see Figure 22.2). The fitted function is an empirical function as follows:

$$P(T) = A\left(1 - \frac{T_{\text{th}}}{T}\right)^\alpha \exp^{-\frac{T}{T_0}}, \tag{22.3}$$

where T is the kinetic energy in keV. The result of the fit gives $T_{\text{th}} = 1292.7$ keV, $\alpha = 3.26$, $T_0 = 2466.2$ keV, and a normalization factor of $A = 1.18 \times 10^{-4}$. A Month Carlo simulation was carried out to determine the hit rate of the CDC due to proton emission after muon nuclear capture. In this MC simulation, protons are generated isotropically with a spectrum from Eq. (22.3). The hit rate on a single cell is estimated to be 1.4 kHz. This is low enough for the normal operation of the CDC.

In COMET Phase-I, we can measure the rate and spectrum of proton emission after muon nuclear capture on aluminum more precisely than the AlCap with higher statistics. We might

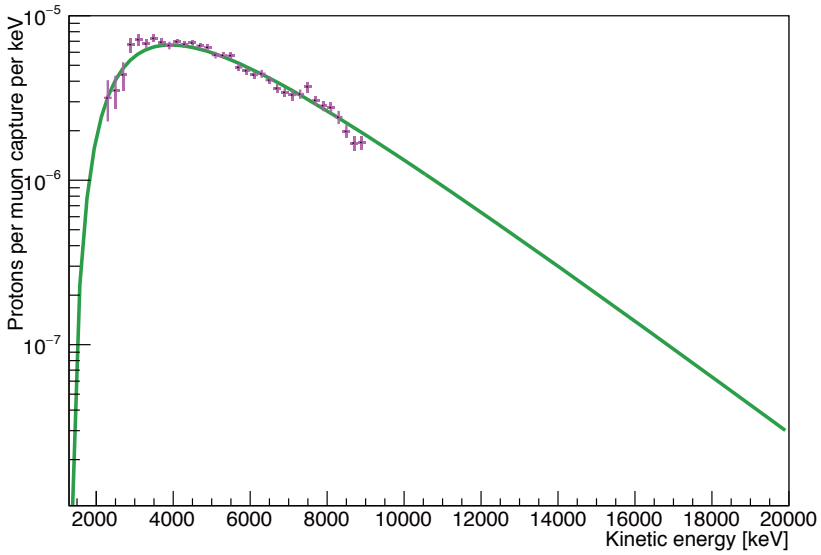

Figure 22.2: Energy spectrum of protons emitted after nuclear muon capture on aluminum. Data points are from the AlCap measurement in 2013, the solid line shows the fitted function.

also be able to measure deuterons, tritons, and ^{4}He. These results could be interesting for nuclear physics in their own right.

It is noted that the AlCap experiment had additional physics runs in 2015. The goals of these runs were to measure the rate and spectrum pf proton emission with more precision, as well as measurement of neutron emission. At the time of writing, analysis of these new data sets is ongoing.

Chapter 23

Cosmic Ray Run and Engineering Run

23.1. Cosmic Ray Run

As described in Section 20.2.5, the cosmic ray induced backgrounds could be one of the serious backgrounds, which is most difficult to estimate. In COMET Phase-I, the Cosmic Ray Veto (CRV) system is installed to eliminate the cosmic ray induced backgrounds. It covers a large portion of the solid angle around the Detector Solenoid (DS), as discussed in Chapter 15. Also the CDC which surrounds the muon stopping target would provide additional identification of cosmic rays coming into the detector. However, from simulations, it is known that when cosmic rays interact some materials outside the DS and the detector, electrons from the interaction still come into the detector and fake signal events. Some examples where cosmic ray muons interact with the materials in the Bridge Solenoid (BS) and electrons of 100 MeV/c produced from the interaction came into the CDC have been shown in Section 20.2.5. Other cases are events where cosmic muons interact with the downstream wall of the experimental hall, and electrons going upstream to the muon stopping target. There will be more unknown cases that cosmic ray muons produce fake signals. The estimation of such potential background events in simulations takes a huge computing power and time. Although we will make mass production of simulation data of cosmic rays for the study, we consider that it would be more convincing to have a special dedicated run with the use of the complete COMET Phase-I detector, without a muon beam. This is the main purpose of having the *cosmic ray run*.

The completion date of the COMET beam line is uncertain and depends on funding. However, it is likely that the detector system for COMET Phase-I might be possibly completed before the beam line completion. If this happens, the proposed *cosmic ray run* would fit well in the schedule and could be conducted prior to the physics run.

The plan of *cosmic ray run* is to run the complete COMET Phase-I detector with the CyDet detector and the CTH trigger without any muon beam for a long period. It is noted that the contribution of cosmic ray induced backgrounds is proportional to the total live running time. It would be good to have a running period of the *cosmic ray run* similar to the physics run of 150 days or more. The 150 days' data of the *cosmic ray run* is equivalent to 3 times the total live running time, with consideration of the duty factor (of 0.32). If we do not see any background events in the *cosmic ray run*, it would imply that this expectation of cosmic ray induced backgrounds is less than 0.3 events with the COMET Phase-I sensitivity. This would give more confidence before the COMET Phase-I data acquisition starts. Also during the physics run, we can collect additional data of 2 times the total live running time during the beam spill off time. If we do not see any signal events, by adding all the data (5 times the total live running time), the cosmic-ray induced background can be limited to be less than 0.2

events. If fake signal events were detected in the *cosmic ray run*, the repair and improvement are needed. Some supplemental detectors to study cosmic rays can be installed to monitor and study the pattern of fake signals, in particular along the beam axis. They should not be massive and not be a source of cosmic-ray induced backgrounds. Such detectors are still under consideration. We anticipate that the *cosmic ray run* can start after the completion of the COMET Phase-I detector, before the engineering run.

Tests of sub-detector systems with cosmic rays We plan to make commissioning of the sub-detector systems with cosmic rays, before the *cosmic ray run*. As an example, the CDC will be tested with cosmic rays, and it will start from summer 2016.

23.2. Engineering Run

As for the engineering run, we are planning to have several conditioning and measurements, including a physics pilot run, as follows. Table 23.1 is given as well.

Proton beam commissioning Conditioning and measurements of a 8 GeV proton beam will be made. For this purpose, the proton beam monitor of diamond detectors will be utilized together with other conventional proton beam monitors. It is also important to align the direction of a proton beam to the axis of the pion production target of 700 mm. The muon beam profile monitors made of plastic scintillating counters are placed at the end of the 90° bend to study a beam intensity, at least at the level of relative scale and a beam profile. This program will be conducted in the first week of the engineering run.

Momentum/profile measurement of beam particles The rates and momentum distributions of different beam particles are fundamental information of the beam. They will be measured by the StrECAL detector with particle identification (PID), as shown in Section 21.4.2. Plastic scintillating fiber detectors of 700 μm in diameter will be placed in front of the first station of the straw chambers to provide information of time of flight (TOF). The performance of PID together with TOF are described in Chapter 21. The covered range of momentum is from 55 MeV/c to 110 MeV/c. For this measurement, instead of using a bunched slow extraction, a normal slow extraction will be adopted to get a continuous beam. In addition, a proton beam intensity could be reduced by a factor of 500 or 1000 so as to make the hit rates of the StrECAL detector manageable. The measurements of positively-charged and negatively-charged beam particles will be investigated. The selection of the charge-sign of beam particles can be made by inverting the polarity of the correction dipole fields in the muon transport system. The data measured will be compared with the simulation results. This program will be conducted in the second week of the engineering run.

Time distribution of beam particles The time distribution of beam particles with respect to the beam prompt is also fundamental information of the beam. The measurement will be made only with ECAL, as shown in Section 21.4.3. Anti-protons in the muon beamline can also be measured at the same time. The measurement of time distributions can be grouped into two, one of which is to measure the delayed time distribution, and the other is to measure the prompt time distribution. The former can be made with a full intensity beam of 3.2 kW, whereas the latter can be done with a lower beam intensity such as 1/100. This program will

be conducted in the third week of the engineering run. In its implementation, the programs in the 3rd and 4th weeks can be combined together.

Rates of muons and pions stopped The CyDet detector can be installed for its commissioning. The CyDet trigger, together with the COTTRO system utilizing BDT, can be tested with a low intensity beam, as described in Section 16.1.4. The numbers of muons and pions stopped in the muon stopping target will be measured by detecting muonic and pionic X-rays respectively. The momentum ranges of muons and pions stopped are about 40 MeV/c or less. The beam intensity could be low so that the Ge detector could be in operation. At the same time, momentum spectrum of electrons from muon decays in orbit (DIO) will be measured simultaneously. The comparison with the two observables allows us to make the normalization of muons stopped by the DIO rate, even if a Ge detector is not in operation with a full beam intensity of 3.2 kW. Also the photon spectrum of radiative muon capture (RMC) on aluminum towards to the endpoint will be measured by using the CyDet as a pair spectrometer. The momentum calibration in the CyDet will be conducted as well. This program will be conducted in the fourth week of the engineering run. Since the detector needs to be exchanged from StrECAL to CyDet, a time for reinstallation is needed before the third and fourth week.

Physics pilot run Prior to the physics data acquisition, we like to have a physics pilot run for two weeks. This would allow for repairs and improvements to the apparatus if they are found to be needed after the analysis. The data taken for two weeks would provide a factor of ten (10) improvement over the current limit. This program will be conducted in the 5th and 6th weeks. After some data check or preliminary analysis completed, the physics run can start.

Week	Beam	Intensity	Detector	Measurement	Comments
1st	BX	low	PBM	proton beam commission	+muon beam monitor
2nd	SX	low	StrECAL	momentum/profile	TOF needed
3rd	BX	normal	StrECAL	time	ECAL only
4th	SX+BX	low	CyDet	muons and pions stopped	DIO and RMC
5th/6th	BX	normal	CyDet	physics pilot run	improvement of 10

Table 23.1: *Preliminary plan for run schedule.* BX *and* SX *stand for a bunched slow extraction and a normal slow extraction respectively. PBM is the proton beam monitor. Double horizontal lines separating the raws in the table indicates a potential time gap needed. For instance, some time separations will be needed between the 2nd/3rd and the 4th weeks since the detector has to be exchanged. The programs in the 3rd and 4th weeks can be combined in execution.*

Chapter 24

Infrastructure & Services

The COMET experiment will be located in its own building, which is connected to the NP hall (Figure 24.1). The building will consist of three floors: the basement, the ground floor and the

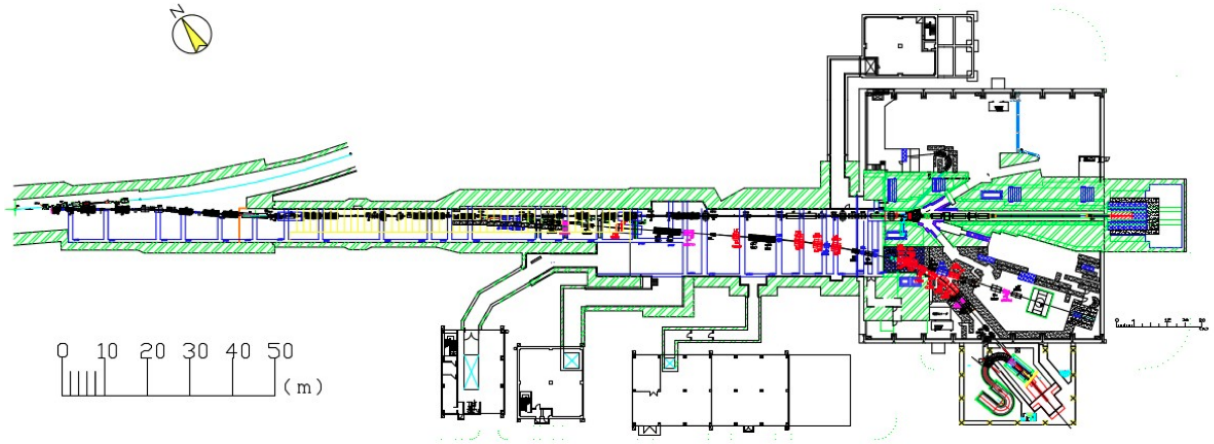

Figure 24.1: *The layout of the COMET hall annexed to the NP hall.*

control-room floor, and will house all COMET equipment except the helium compressor for the refrigerator. This will be housed in a separate building to the west of the COMET building. A machine room will be located in the building to house the necessary air-ventilation system with the appropriate filters as described below. The segmentation of the basement floor and a cross-section view of the building are shown in Figure 24.2.

The beamline and the main COMET apparatus will be on the basement level as shown in Figure 24.3. The beamline and pion capture solenoid will be heavily shielded with iron and concrete blocks. A hatch will connect this basement with the ground floor and this will be used to lower instruments into the experimental area from the ground floor.

Cryogenic equipment and power supplies for the superconducting magnets will be housed on the ground floor and a 40-ton crane will unload apparatus into the ground floor area. The upper floor will be used by COMET and the other experiments in the south area of the NP Hall. It will accommodate the control-rooms of all the experiments (and the beam channel group) and an air-conditioned computer server room.

The beamline and experimental area will be air-conditioned to ensure none of the apparatus overheats. A charcoal filter will be installed in the primary beamline area to filter out harmful, radioactive isotopes such as iodine and caesium. Standard dust-filtering systems will be installed

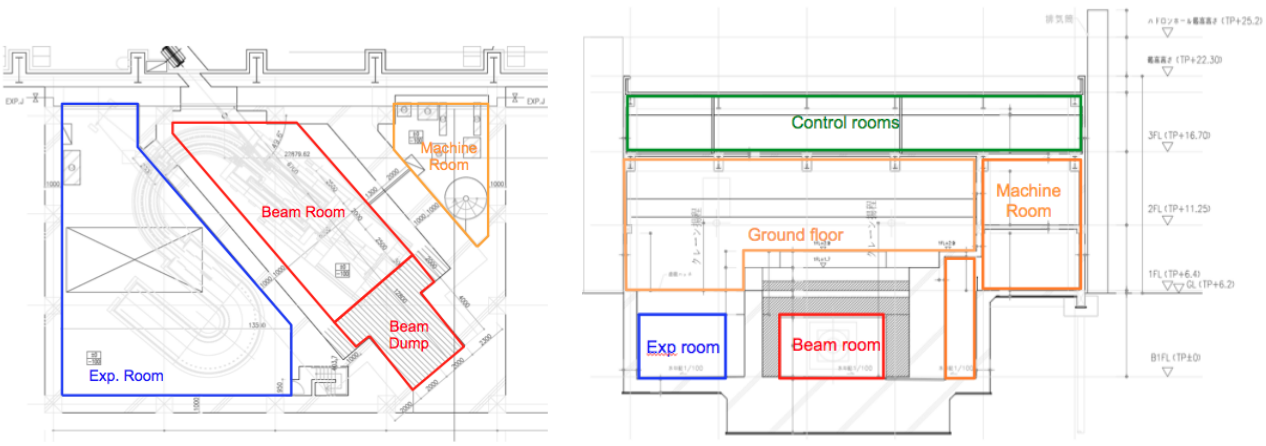

Figure 24.2: *The segmentation of the basement floor (left) and a cross-section view (right) of the COMET building.*

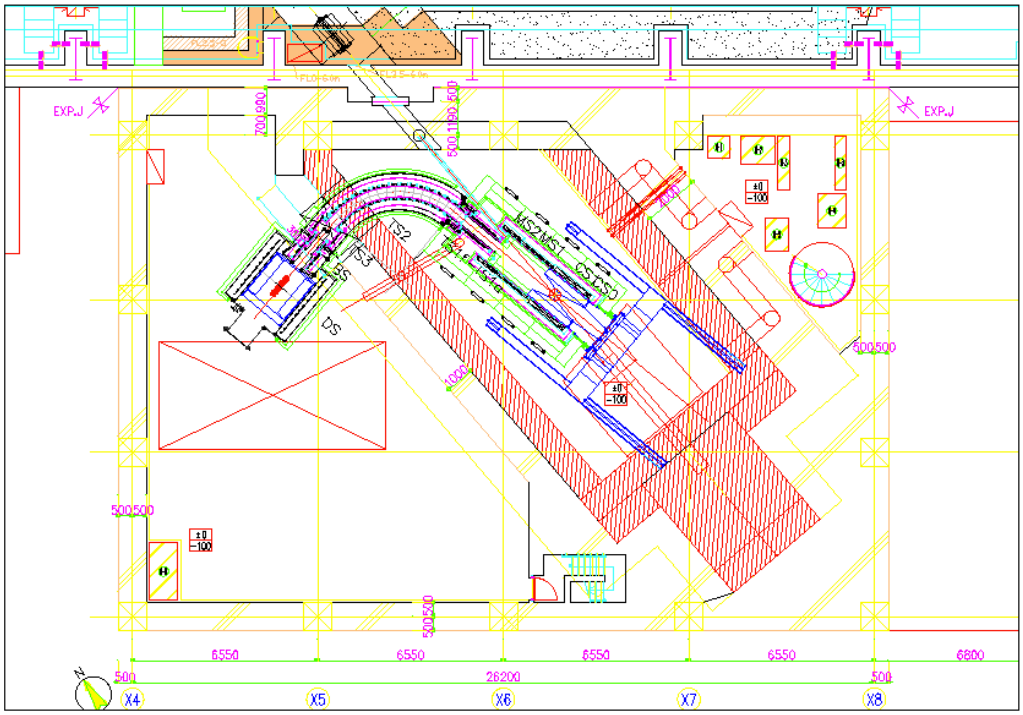

Figure 24.3: *The layout of the basement level of the COMET building that will house the beamline, target and pion capture solenoid, muon beam line, muon stopping target and detectors.*

elsewhere: the experimental area, the ground floor and the upper floor. In preparation for COMET Phase-II—where water will be used to cool the target, the pion capture solenoid radiation shield and the beam dump—a tank for the storage of activated cooling water will also be built.

Chapter 25

Radiation safety

The COMET building is being designed to ensure safe operation at the highest beam powers anticipated for Phase-II (56 kW). The thicknesses of all the concrete and iron walls are being designed to comply with Japan's radiation laws i.e. 11 mSv/hr (local maximum) and 5 mSv/hr (average) at the border of the ground soil and 25.0 μSv/hr at the borders where people may be present during operation. Radiation levels will be minimised in the control room since it is expected that people will spend prolonged periods in that area. It is also necessary to reduce the radiation level at the border of the controlled area (10 m away from the building wall) below 0.5 μSv/hr and at the border of the J-PARC facility area (60 m away from the building wall) below 50 μSv/yr. A new J-PARC design policy has been adopted in 2014 when we evaluated the doses using simulation. For the case of new buildings such as the COMET building it is necessary to include a safety factor of 2 due to possible insufficient modelling in the calculation. In addition it is mandatory to include an additional safety factor of 2 which originates from the ambiguity of the simulation code itself. Therefore we quote numbers in this report after multiplying the simulation results by a factor of 4 to be compared to regulation limits.

The building has been modelled (see Figure 25.1) using the MARS Monte Carlo simulation in order to evaluate the radiation doses. These doses are shown in Figure 25.2 and are below the legal thresholds at both soil and floor-level. Note that the dose in the machine room next to the primary beam line area is too high for people to stay there continuously. Thus access to the room during the beam operation will be controlled so that maintenance work of equipment can be conducted in the room safely enough. The dose at the J-PARC facility border is also confirmed to be well below the legal threshold. This dose evaluation at the J-PARC facility border is checked also by using simplified formulas for confirmation. Single Compton scattering by air of a gamma-ray flux of 0.026 μSv/h evaluated by the MARS simulation is considered to calculate the gamma-ray dose, and a response function of sky-shine dose called SHINE3 [117] is employed to calculate the neutron dose from the estimated neutron flux of 1.4 μSv/h above the COMET building. They are 1.5×10^{-4} μSv/h and 1.2×10^{-3} μSv/h, respectively at the border and are consistent with the MARS simulation results.

Neutron streaming through pipes and/or air ducts is considered in the design of their paths and shapes. Figure 25.3 shows an example of a calculation around the liquid-He transfer tube from the refrigerator on the ground floor to the magnet system on the basement floor. The streaming effect can be minimised by properly installing a crank structure along the path. It can be seen in this case that the neutron flux is suppressed by about 4 orders of magnitude along the path. Similar optimisations have been performed for all cases in the COMET building design.

Activation of the air and cooling water in the primary beam and experiment areas is estimated using the evaluated neutron flux by the MARS calculation and cross sections to produce ra-

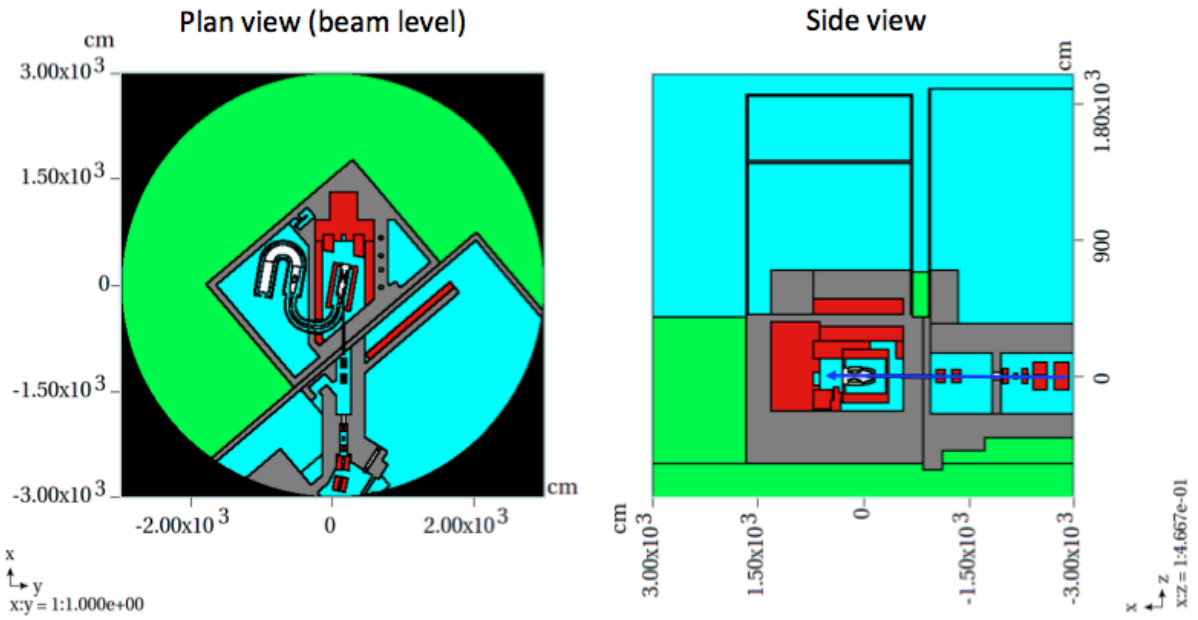

Figure 25.1: *The MARS model of the COMET apparatus and building.* [Left] *top view.* [Right] *side view.*

dioactive materials. Growth of the activation level is calculated as $R = N\,\Phi\,\sigma\,(1-\exp(-t/T))$ where R is activation level (Bq/cm^3), N is atom density (atoms/cm^3), Φ is the neutron flux evaluated by MARS (n/cm^2/sec), σ is cross section to produce a given radioactive material (cm^2/atom), and T is the lifetime of radioactive material (sec). The neutron flux (Φ) is conservatively determined to be 10^{10} (1/cm^2/sec) although the number varies from 2.0×10^9 to 9.7×10^9 (1/cm^2/sec) depending on the location. In this calculation, contributions from protons, muons, and pions are separately estimated and summed up to count the neutron flux. The estimated air activation level in Phase-I is summarized in Figure 25.4 for each nuclide as a function of time. Solid lines show activation levels of nuclide and dashed lines show decay of activated nuclide after the operations for 30 and 90 days stop. Thin solid lines indicate thresholds for air exhaust. Activation levels will decrease below thresholds in the primary beam area, except ^{3}H and ^{7}Be, 22.3 hours after the beam is stopped following 90-days of operation with 3.2 kW proton beam power. ^{7}Be can be reduced below the threshold with a filter with 99% efficiency in the exhaust line and thus does not cause any regulation issues. The ^{3}H level is above the threshold instantaneously, but the regulation only restricts the averaged amount of ^{3}H emission from an experiment over three months. Therefore by controlling the total amount of ^{3}H emission to the environment (exhausting the air from the primary beam area in 0.5 days) we can safely exhaust the air in the primary beam area (9.8×10^{-4} Bq/cc). In the experimental area, activation levels of all radioactive nuclides will be reduced below threshold in 10.7 hours after 90 days of operation. In Phase-II it will be necessary to wait for 30 hours and 18.3 hours for the primary beam and experimental areas respectively until activation levels of short-lifetime nuclides decrease below thresholds; it is also necessary to dilute the exhaust air of the primary beam area by ten times by volume of normal air. This procedure allows us to clear the regulations with an adequate margin. Note that here we suppose no humidity concentration occurs in the primary beam and experiment areas although in reality humidity might stay in concrete, and repeat evaporation and absorption during the operation cycle. Such humidity can be certainly the source of ^{3}H as HTO. Actually in the other facilities in J-PARC such HTO produced by neutron interactions with humidity is thought to be a dominant source of ^{3}H. In order to suppress such ^{3}H production, we consider in the COMET facility to cover

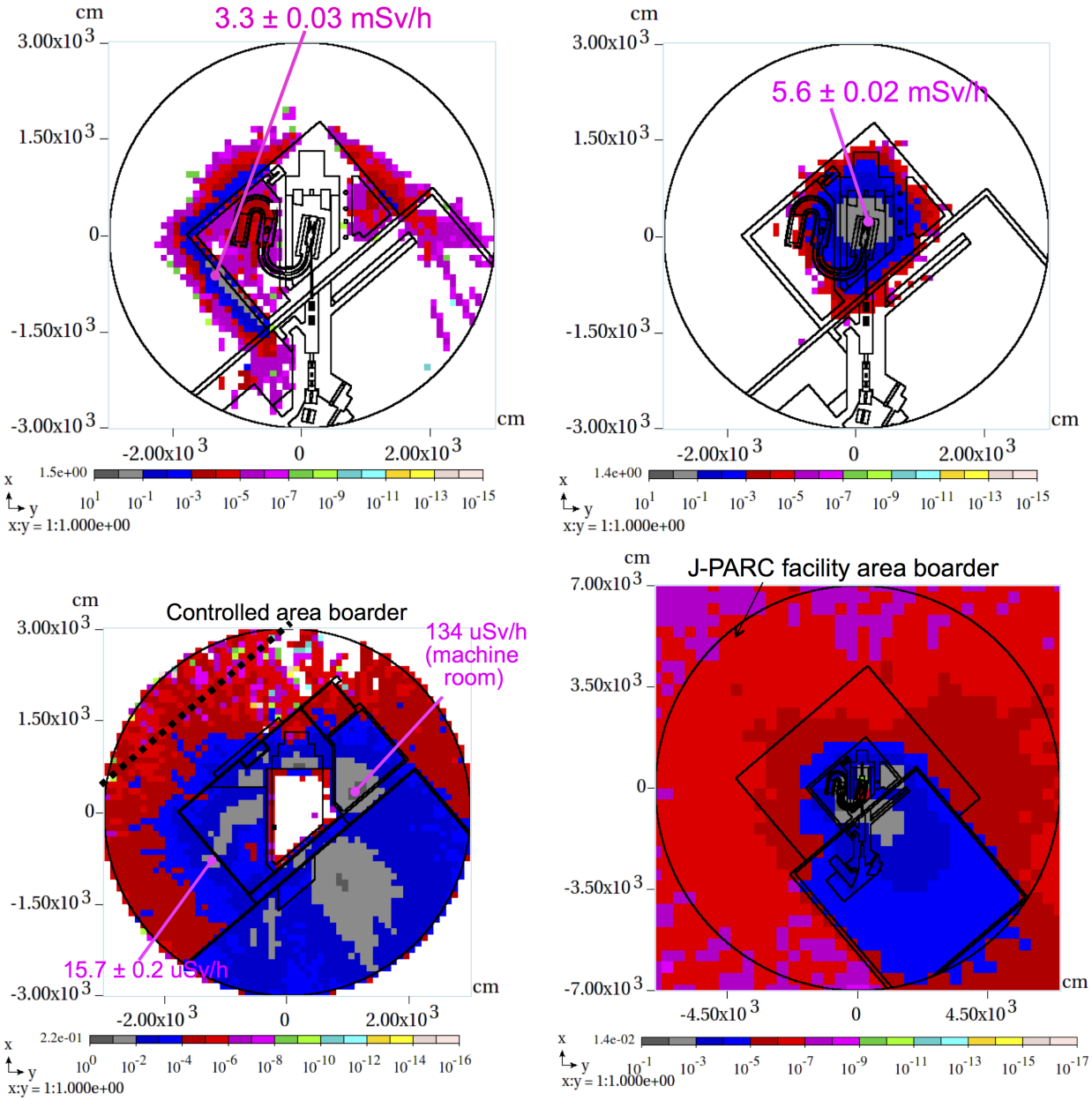

Figure 25.2: *The radiation doses for the COMET Phase-II beam intensity as calculated by MARS shown in the unit of mSv/h.* [Left top] *the dose at the primary beamline.* [Right top] *the dose below the concrete shield of the floor.* [Left bottom]*: the dose at the ground level.* [Right bottom]*: the dose at the J-PARC facility border.*

the surface of concrete walls with metal sheets. Further details need to be investigated after the construction is finished.

Water drainage in COMET Phase-I originates from the air-conditioning system. The water is produced only when the air-conditioning system is started after closing the primary beam and experimental areas and is free from activation. The water can be discarded before operations start and no drainage water will be produced after that. This is the plan for handling waste water in Phase-I.

Water activation has to be more carefully handled in Phase-II, where cooling water will be used for the pion production target, beam dump, and radiation shielding for the super-conducting magnet. Figure 25.5 shows activation levels of nuclides contained in water. As in the case of

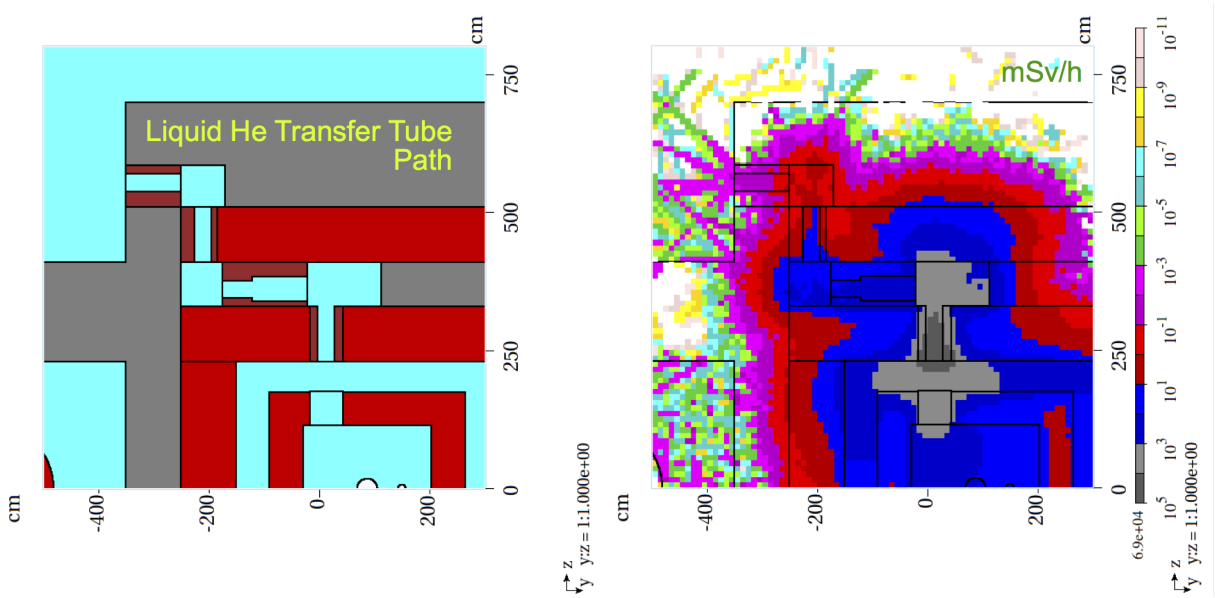

Figure 25.3: [Left] *The MARS model of the radiation shield around the liquid-He transfer tube and* [Right] *calculation result.*

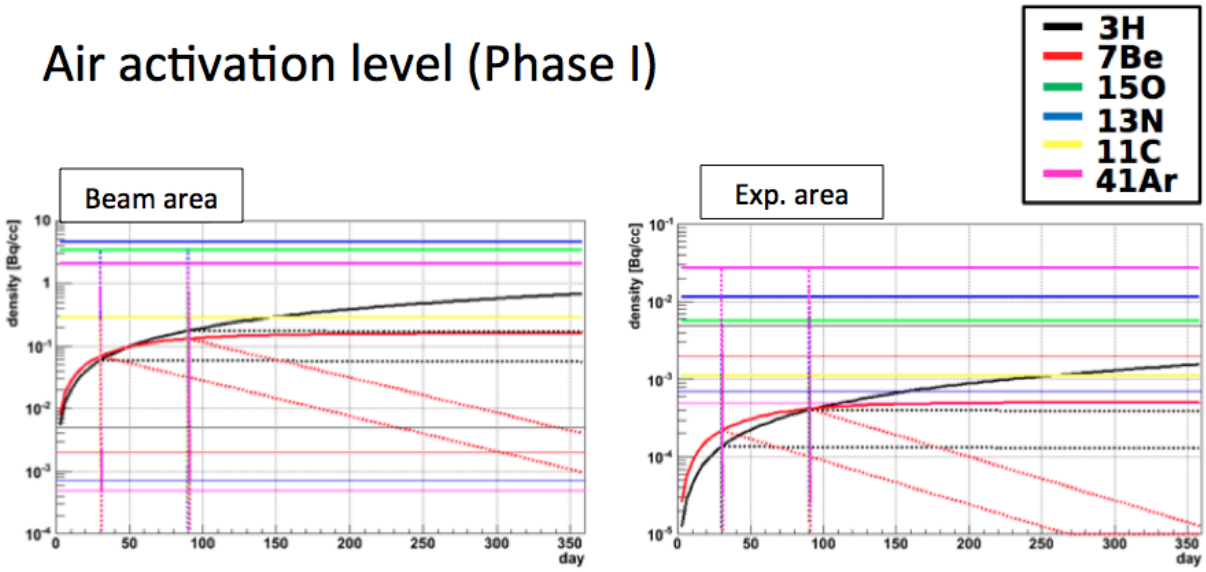

Figure 25.4: *Air activation levels as a function of time for Phase-I beam intensity. Solid lines show activation levels of nuclides and dashed lines show the decay of activated nuclides after operations for 30 and 90 days after beam stopping. Thin solid lines indicate thresholds for air exhaust.*

air activation, some nuclide activities are above the thresholds although these can be reduced with a filter (for ^{7}Be) and 10 times dilution (for ^{3}H). Other activation with short lifetimes can decay and be reduced well below the thresholds 5.4 hours after the beam stops so that we can discard the waste water safely.

Activated air circulated in the machine room for cooling purposes may cause an increase in radiation outside the COMET building. This effect is estimated in a simplified cylindrical model of the machine room using the MARS simulation. Activity contained in the circulating air is estimated as described above. It is assumed that 10 m^3 of air stays at the centre on both the ground and upper floors of the machine room. The thickness of the concrete wall is

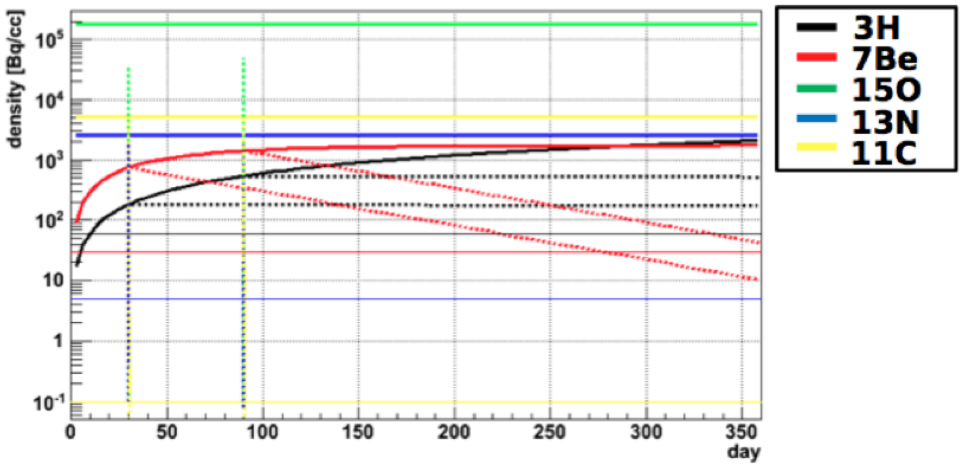

Figure 25.5: *Water activation levels as a function of time for Phase-II beam intensity. Solid lines show activation levels of nuclides and dashed lines show decay of activated nuclide after the operations for 30 and 90 days after beam stopping. Thin solid lines indicate thresholds for air exhaust.*

optimised to suppress the radiation dose outside the machine room sufficiently. Figure 25.6 summarises the doses at the surface of the room. All are below the regulation threshold; especially the radiation dose on the top of the second floor, where the control room is housed, is below 0.01 μSv/hr. It is also confirmed that these activations in the machine room do not provide significant dose (less than 1.0×10^{-3} μSv/hr) at the border of the J-PARC facility.

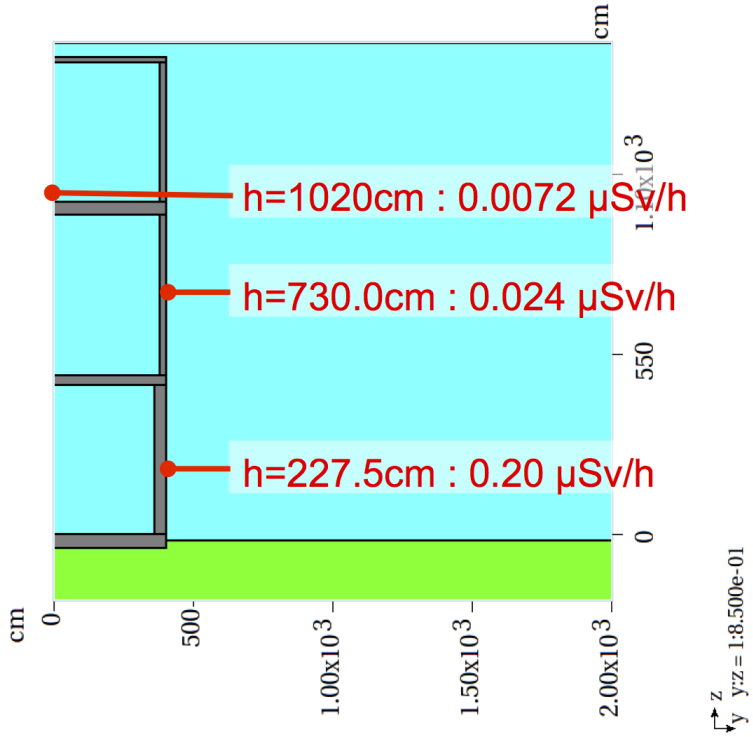

Figure 25.6: *Dose level outside the COMET building, estimated using a simplified cylindrical model of the machine room with activated air inside.*

Chapter 26

Management

Under the COMET constitution, the Spokesperson, the Project Manager and the Collaboration Board Chair serve on the Executive Committee which is responsible for the management of the experiment. The Collaboration Board consists of representatives of the participating institutions and is the body that has the ultimate power within the collaboration, including electing the Spokesperson and other members of the Management and can also modify the constitution.

Coordinators for each of the COMET sub-project systems have been assigned. The sub-project systems range, for instance, from the CyDet, the Straw and ECAL detectors to infrastructure, safety and software. A Technical Board is being formed from the sub-project coordinators which will discuss and optimize the design of the sub-project systems. Any major changes of the design will be discussed in the Technical Board and presented by the Project Manager to the Executive Committee for consideration and must be approved by the Collaboration Board.

The current COMET management (as of March 2016) is presented in Figure 26.1.

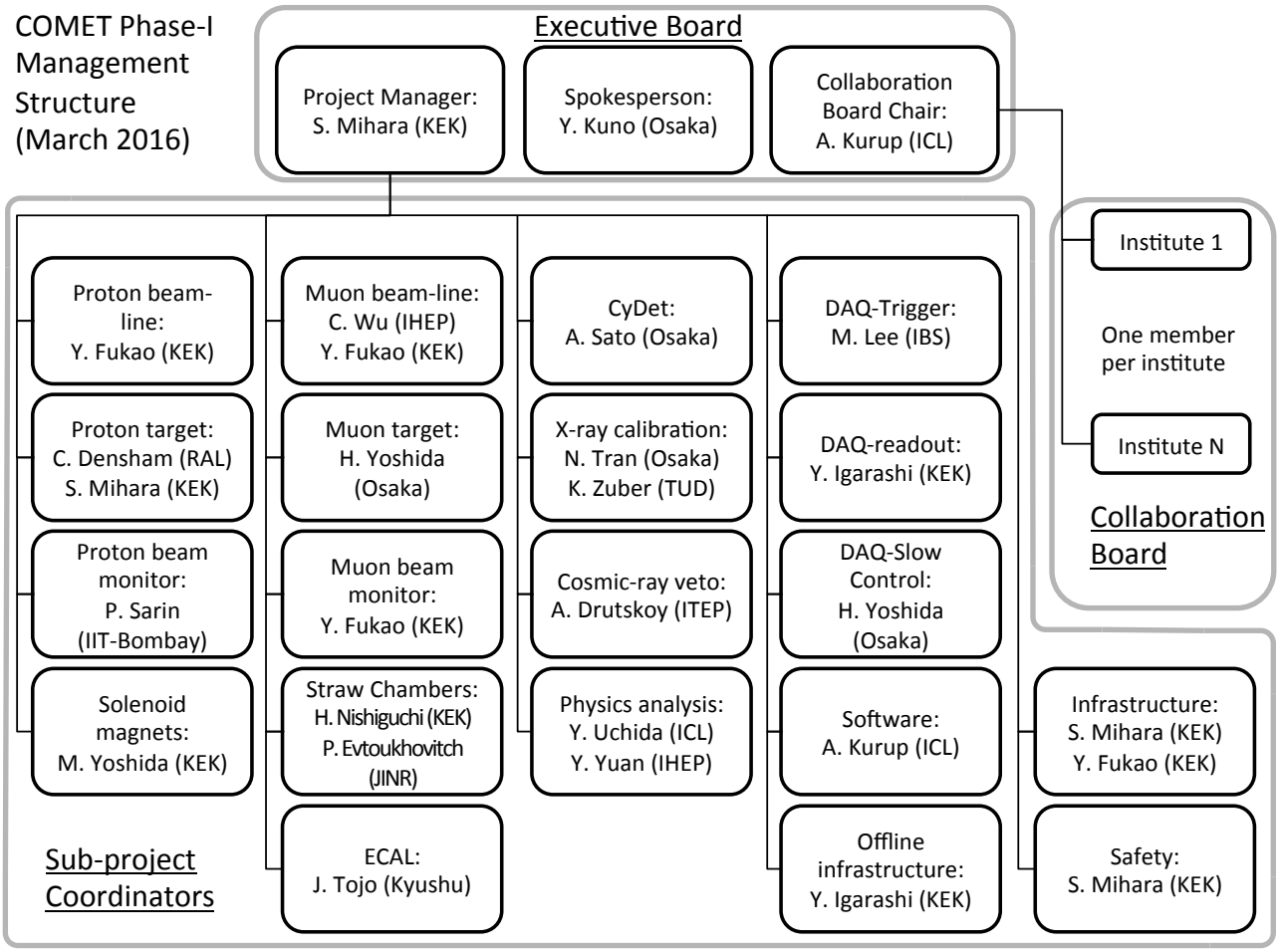

Figure 26.1: *COMET management (as of March 2016).*

Chapter 27

Cost

The proton beam line and muon beam line, including the proton target and proton dump, will be constructed by KEK. KEK has received a supplementary budget for Japanese fiscal year (JFY) 2012 for these beam lines. The necessary cost for constructing the beam line, including radiation shield and beam dump, is estimated to be 2,420,000 k JPY. This includes apparatus located in the primary beam line for the use in the high-p beam mode. The estimated cost for construction and installation of the magnet system is summarised in Table 27.1. The cost of the proton target includes the cost of a target insertion system. For the purpose of target replacement we additionally need a cask to safely house the used target and its holder, which can become highly radioactive.

Table 27.1: *Breakdown of the cost of the COMET magnet system. Transport solenoid installation has already completed in March 2015.*

Item	Cost (k JPY)
Capture solenoid	975,000
Capture solenoid return yoke	63,000
Radiation shield in the capture solenoid	424,000
Transport solenoid	307,520
Cryogenics and vacuum	81,310
Proton target	6,000
Total	1,856,830

The Japanese University groups in the COMET collaboration have received the Grant-in-Aid for Specially Promoted Research from JFY2013 for 5 years. The amount of the grant is about 433 million Japanese yen (JPY). The IHEP (Beijing) group in the COMET collaboration has received about 4 million RMB. These funds will be used to construct the CyDet and the detector solenoid. The estimate of detector costs is presented in Table 27.2. An R&D budget to develop the StrEcal detector has also been made available; a further funding request was made in 2015 for construction of the StrEcal detector. The total cost required for the StrEcal detector is strongly dependent on the number of crystals used in Phase I. In Table 27.3 the cost for the StrEcal detector is given with an assumption of 500 LYSO crystals in use in Phase I. This will cover about a quarter of the detector solenoid aperture. Because the COMET data acquisition system utilises a distributed front-end system, high-speed network switches are necessary in addition to front-end and online computers. Online storage will be used to

Table 27.2: *Breakdown of the cost of the CyDet and detector solenoid magnet.*

Sub detector	Item	Cost (k JPY)
CDC	mechanical structure	54,000
CDC	field-through and sense/field wires	57,600
CDC	wire stringing	12,000
CDC	readout electronics	75,000
CDC	trigger hodoscopes	5,000
Detector Solenoid	SC conductor	20,000
Detector Solenoid	coils and cryostat	250,000
Detector Solenoid	power supply and GM cooler	25,000
Total		498,000

Table 27.3: *Breakdown of the cost of the StrEcal.*

Sub detector	Item	Cost (k JPY)
Straw Tracker	module × 5	25,000
Straw Tracker	gas system (to be shared with CDC)	2,000
Straw Tracker	power supply	4,000
Ecal	crystal × 500	115,000
Ecal	photo sensors × 500	18,000
Ecal	structure	5,000
StrEcal	electronics	35,000
StrEcal	vacuum system	10,000
Total		214,000

store the data temporarily before it is sent to the KEK computing centre data storage system. A slow-control system with a unified standard across the whole experiment will be prepared to guarantee stable detector operation. The summary of necessary equipment for the data acquisition and slow-control system is given in Table 27.4.

Table 27.4: *Breakdown of the cost of the data acquisition and slow-control system.*

Item	Cost (k JPY)
Slow control hardware	4,000
Slow control computers and data server	800
Front-end network switch	6,000
Backend network switch	3,000
Online computers	3,600
Online storage	3,000
Front-end computers	8,750
Terminals and displays	1,200
Rack and cables	1,500
Total	31,850

Chapter 28

Schedule

The current schedule for the beam line and detector construction is presented in Figure 28.1. The construction of the beam line is highly dependent on the facility funding at J-PARC. The construction of the CyDet and StrEcal detectors is planned to be funded by "Grant-in-Aid for Specially Promoted Research" by JSPS in Japan, by JINR in Russia, by the NSFC in China, and by the Institute for Basic Science (IBS) in Korea. A significant part of these has been already approved and the construction is in progress. The current schedule is based on approval of further funding by JSPS in Japan and by other funding agencies in other countries. It is also necessary to obtain travel budget so that the COMET collaborators outside Japan can visit the J-PARC site for detector construction, conditioning and data acquisition. Changes in the allocated spending profile of these awards will potentially affect the detector construction schedule.

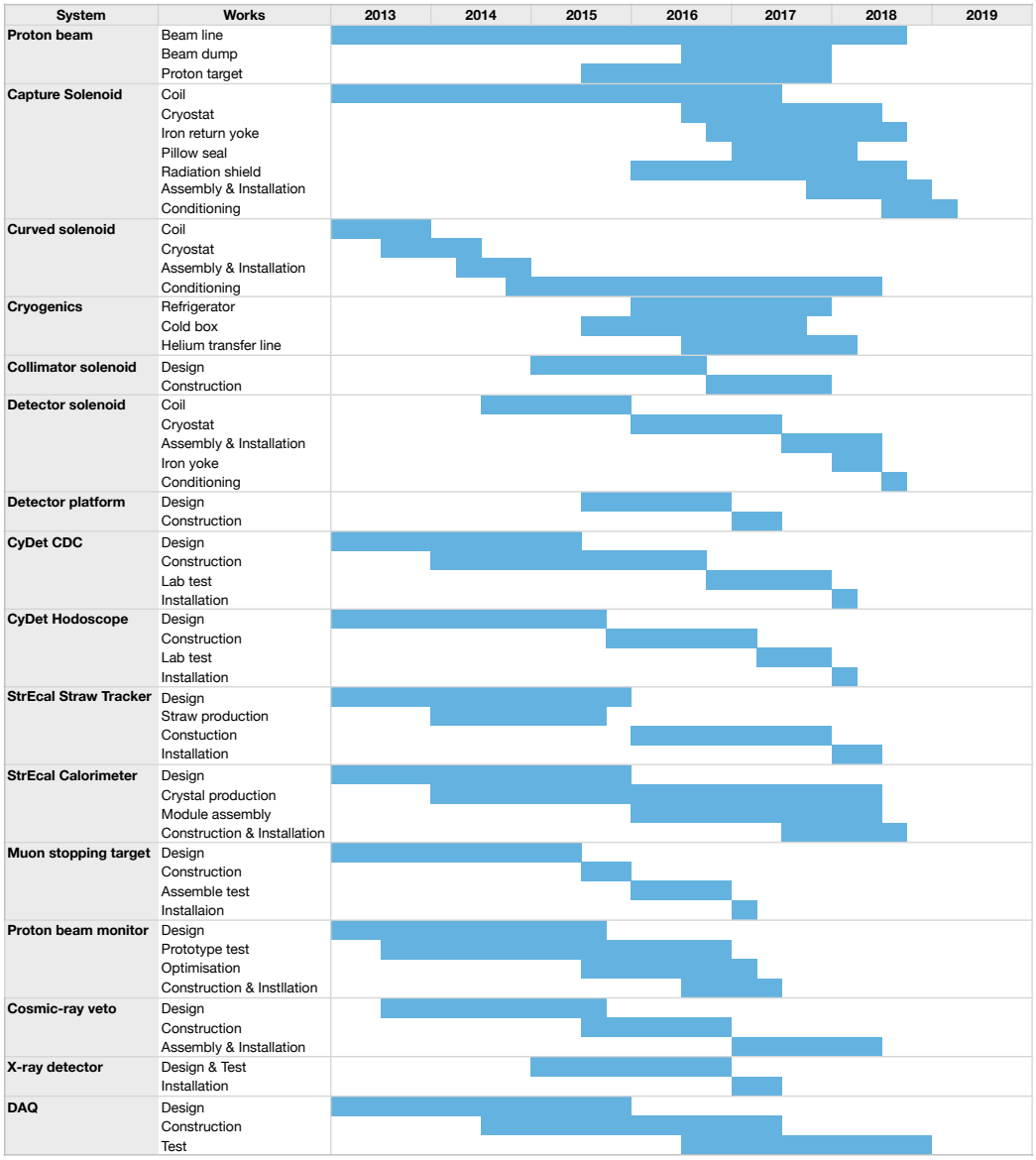

Figure 28.1: *Beamline and Detector construction schedule (in Japanese fiscal year).*

Chapter 29

Future Plans

COMET Phase-I is the first stage towards COMET Phase-II which has an anticipated single event sensitivity of 2.6×10^{-17}, a factor of 10,000 improvement. The COMET Phase-I detector will be augmented with prototypes of the Phase-II straw tracker and ECAL, that as well as allowing valuable experience with the detectors, will be used to characterise the beam and backgrounds to the $\mu-e$ conversion signal to ensure that the Phase-II goal can be realised. To be competitive with the Mu2e experiment at Fermilab, which plans to start its physics run in 2021 and run for three years to reach the goal, it is important to continue the R&D efforts required for Phase-II in parallel to the Phase-I running. It is noted that the COMET Phase-II detector is designed to take a muon beam intensity three time higher than the Mu2e, and one year physics running is sufficient to reach the goal. The successful operation of Phase-I and the timely production of physics results from Phase-I is key to ensure that additional funds can be obtained to construct the Phase-II beamline and detectors. Beginning Phase-I data-taking as soon possible is clearly of critical importance.

Acknowledgements This work is supported in part by the Japan Society of the Promotion of Science (JSPS) KAKENHI Grant No. 25000004; JSPS KAKENHI Grant No. 25003345; National Natural Science Foundation of China (NSFC) under Contracts Nos. 11125525, 11335009 and 11475208; Joint support of the NSFC-JSPS Scientific Cooperation Program; Institute for Basic Science of Korea (Contract number IBS-R017-D1-2016-a00); Ministry of Education and Science of the Russian Federation; Russian Fund for Basic Research grant RFBR-14-22-03071; the computing resources operated by Yandex Data Factory, Russia; the Science and Technology Facilities Council, United Kingdom; the use of Grid computing resources deployed and operated by GridPP, United Kingdom.

Appendix A

ICEDUST Conventions

A.1. ICEDUST Conventions: Summary

A.1.1 Framework Structuring

Projects

A project is a high-level grouping of packages, based on the packages' purpose, such as offline software, online monitors, data distribution, event display and so on.

```
PROJECTNAME/ -- packages/ --------- package1/
     |            |---------------- ....
     |
     |--------- mgr/ -------------- CMakeList.txt
     |            |---------------- ProjectConfig.cfg
     |
     |--------- documentation/ ---- cometDocOutput/
     |            |---------------- Conventions.pdf
     |            |---------------- ....
```

Packages (upon being checked-out, before building)

```
PACKAGENAME/ -- versionstring/ -- cmake/ (currently cmt)
                  |-------------- dox/
                  |-------------- README
                  | * optional *
                  |-------------- src/ (source code, header & implementation files )
                  |-------------- scripts/ ( stand alone utility scripts )
                  |-------------- app/ ( source for executables )
                  |-------------- constants/ ----- calibration_tables/
                  |                 | ------------- particle_distributions/
                  |
                  |-------------- configurations/ -- parameters.txt
                  |                 | -------------- run.cfg
                  |
                  | * external included packages contain a source tar file *
```

```
|-------------- package1_v1.tar.gz
```

A.1.2 Project and Package Naming

The five package functions are: Base, Sim, Calib, Recon, Analysis. *FUNCTION* in the names below should be replaced with one of these.

- Projects: *CamelCase*Project, eg OfflineProject.
- Meta Packages: comet*FUNCTION*, eg cometSim, cometBase, cometAnalysis
- Base packages: oa*CamelCase*, eg oaEvent, oaAnalysis
- High-Level physics packages: *FunctionCamelCase*, eg AnalysisTools, SimG4, CalibGlobal
- Included externals: UPPERCASE, eg ROOT, MYSQL
- Pure framework packages: Icedust*CamelCase* eg IcedustPolicy, IcedustDoc

See explanation in A.2.1

A.1.3 Repository

- A version string contains the version, release, and an optional patch number, eg v2r1 v2r1p2.
- External included packages may have an additional number to signify local patches, eg v5r34p01n02.
- Commits should only be made to the trunk, or a branch of a package or project, and not a tag.

A.1.4 Quality control

- New packages and projects must be accepted by the software group before being added to the repository.
- New package names must be based on these guidelines.

See explanation in A.2.2

A.1.5 Geometry Names and Numbers

- When code refers to a component of the geometry, it must use the relevant naming convention.
- Numbering of repeated components must agree with the numbering used in the real, physical system (eg. ECal crystals, Drift Chamber wires).

A.1.6 Filenames and Extensions

- Filenames should match contained classes (or the main, public class)
- Implementation files' names should only differ from the header file by their extension.
- File extensions :

	C	C++
Header	*filename*.h	*filename*.hxx
Implementation	*filename*.c	*filename*.cxx

	Python	Perl
Module	*filename*.py	*filename*.pl
Script	*filename*	*filename*
	filename.py	*filename*.pl

See explanation in A.2.3

A.1.7 Scripting Conventions

For all scripts who are directly executable:

python	`#!`	`/usr/bin/env python2`
shell	`#!`	`/bin/bash`
perl	`#!`	`/usr/bin/env perl`

See explanation in A.2.4

A.1.8 Executable Naming

- For executables providing standard functionality of a package, the name should be of the form *FunctionPackage* eg. RunSimG4, RunCalibApply, TestOAEvent, TestReconGlobal.
- The current list of these standard executable functionalities is: Run, Test, Validate.
- All other executables should use the package name followed by an underscore as a prefix: oaEvent_dump-event.

A.1.9 C++ Coding Conventions

See explanation in A.2.5

Class Conventions

	Prefix	Example	Comments
Standard classes	I	IExampleClass	
Abstract classes	IV	IVExampleBaseClass	
Exception classes	E	EExampleException	Must inherit (indirectly) from std::exception
Class data members	f	fMax, fDataPoint	Avoid public access, use private or protected
Class Methods	Capital	GetMax(), TwoFlushDump()	
Destructors			Always set as virtual
Sub-Class names		IMainClass::SubClass	If behaviour mimics an STL type, then name similarly eg. IMainClass::iterator

Namespaces

- Put all classes in the COMET:: namespace, although sub-namespaces can be used, eg: COMET::ECAL::.
- 'using namespace' directives must not be included in header files

Free Functions, Variables and Arguments

All functions, variables and arguments that are not part of a class (ie. free) must NOT use the class conventions, and should instead follow these:

	Prefix	Example	Comments
Functions	Lower case	`come_fly_with_me()`	underscores for long names
Variables & Parameters	Lower case	`myWay`	CamelCase for long names
Global Parameters	`g`		Avoid at all costs!!
enums	k	kSomeEnum	CamelCase for long names

Include Guards

- All header files must contain an include guard, to prevent multiple inclusion of the same file.
- All include guards should take the form: `[PACKAGE]_[FILENAME]`.
- Any non-alphanumeric characters in the filename should be replaced with underscores.
- For example, for IMCHit.hxx in oaEvent, use: `OAEVENT_IMCHIT_HXX`

Output and Error Messages

- Functions from ICOMETLog.hxx should be used instead of C++ STL output (std::cout) and error (std::cerr).
- This provides standard ways for dealing with verbosity and format.

Pointer/Memory Handling

- Bare pointers should almost never be returned.
- Use a IHandle instead (see below).

A.1.10 Documentation

- Each packages should contain a basic README file in it's top layer, describing it's purpose, the contents of its folders and where to find documentation.
- Package histories should be documented in doxygen markup in the `dox` directory of that package.
- All header files should be fully commented in doxygen markup.

- The package IcedustDoc is used to produce documentation from the source code. Its output can either be stored in the top-level documentation directory, or alongside the individual packages.
- All stand-alone documentation must have a version number and the date last updated just below the title.

A.1.11 Units and Constants

- HEPUnits.hxx defines the standard set of units and all derived ones and should be used for all output data.
- HEPConstants.hxx defines a set of useful constants, such as pi, the speed of light, standard temperature etc.
- Both these files are in the oaEvent package and all units are contained in the 'unit' namespace.
- The standard set of units is:

millimeter (mm)	positron charge (eplus)	luminous intensity (candela)
nanosecond (ns)	degree Kelvin (kelvin)	radian (rad)
Mega electron Volt (MeV)	the amount of substance (mole)	steradian (steradian)

A.2. ICEDUST Conventions: Explanation

Purpose:

It is common place in large scale computing projects to introduce coding conventions that standardize the way code looks, and how it is structured. No more is this as important as in particle physics computing projects where the software has to handle extremely large volumes of data. By agreeing a set of conventions and ensuring we all use them, code becomes more intelligible and potentially more efficient.

Difficulties in physics computing:

- Constant turn over of new physicists using the software
- Lot's of developers around the world with restricted communication
- Some developers have little experience of computing and software development

General Explanation:

The coding conventions for ICEDUST are largely built around the ROOT conventions, given that ROOT is so heavily used in the code. It also includes the experience and wisdom acquired from working on the nd280 framework, and so in many cases the conventions are similar.

A.2.1 Package naming

Tight package naming conventions were not well applied in the nd280 framework. This made the structure of the framework quite messy and difficult to understand for a newcomer.

The meaning of the five package categories is:

Meta Packages These packages serve only to cluster other packages together for the framework. They serve as a collection that can be used by CMake to build or check-out subsections of the framework. As a result, they contain little, if any, code or scripts of their own and probably only a CMakeList.txt file.

Base packages These are 'low-level' software elements and as such are used widely throughout the code. Examples are file format management packages, like oaEvent, oaRawEvent and oaAnalysis. In principle these packages could be reused for another experiment, because they contain very little COMET specific information.

High-Level physics packages These are the packages used to run the actual software and, together, provide the main set executables. They are the source of the physics information produced by the framework. This category contains 4 subdivisions, based on their functionality: Sim, Calib, Recon and Analysis.

Included externals These packages wrap external libraries and software into the framework. Upon checking out the package, there should only be a tar file and possibly a few patch files and scripts.

Pure framework packages These packages are framework management packages, with no knowledge of the experiment or it's data whatsoever. They purely provide tools for the framework to be controlled, such as repository access, package versioning, documentation building and so on.

A.2.2 Quality control

Whilst it is important to allow flexibility for everyone that works on the framework to work and produce as they feel necessary, the addition of a new package or project to the framework is big enough that we would like to have the project or package proposed and discussed before anything is committed. This should keep the framework tidier and better managed than otherwise.

A.2.3 Filenames and extensions

A python or perl script file is an executable file (has the executable bit set) and therefore contains a shebang on it's first line. Whether or not to use an extension for these files is left open to the developer.

A.2.4 Scripting Conventions

"`#!/bin/bash`" is the standard bash shebang. "`#! /bin/sh`" is bad because it could call a variety of shells.

Until recently, just "`#! /usr/bin/env python`" almost always gave you python 2 as the interpreter. Some systems are now beginning to use python3 as the default python, and require you to specify `python2`, if that's what you wanted. ICEDUST only supports Python 2, so all scripts should explicitly state this, in case they are used on a machine where python 3 is default.

A.2.5 C++ Coding Conventions

Packages that depend predominantly on external libraries may differ from these conventions in order to match the external library's conventions, eg. cometMC uses the GEANT4 conventions.

In general you should use the conventions defined by ROOT for c++ code (see `http://root.cern.ch/drupal/content/c-coding-conventions`). The conventions above take precedence over ROOT so that our conventions should be used instead of the ROOT one, where a conflict arises (eg. our code uses 'I' as a class prefix, whereas ROOT use 'T').

Include Guards

Include guards prevent a file being included twice, which would result in multiple definitions of the contained functions, classes and so on. Such a situation could easily arise if, for instance, a program included two files, but the second file itself already includes the first one. The typical solution (and the one used in ICEDUST) is to encase all the code in a header file in a set of preprocessor macros as such:

```
#ifndef INCLUDE_GUARD
#define INCLUDE_GUARD
//
// Code goes here
//
#endif  /* INCLUDE_GUARD */
```

Pointer and Memory Handling

Efficient memory management is very important when dealing with large amounts of data. Operations on pointers to deleted objects will cause runtime failures, such as seg faults, that could lose any processed data that was not yet saved. Similarly many calls to 'new' and 'delete' would result in slow code.

To solve this, the CHandle template class provides a 'smart' pointer that implements reference counting, so that the object it represents is only deleted once all its references are out of scope. This is great if several calling functions need to be able change the object because they can use it without worrying who 'owns' the memory that contains the object. See the oaEvent manual for more information on the CHandle class.

If on the other hand you only want a read-only, immutable version of the object, then a const pointer can be used instead of a CHandle. Information on const pointers and const_pointer casting in c++ is readily available online.

A.3. ICEDUST Conventions: Discussions

A.3.1 Project conventions

Use of Projects

Based on purpose:

- The suggested use of projects is to group packages by purpose (ie. Offline software, online monitoring, data distribution etc).
- In principle, a project would have very little dependency on another project, as there would be less need to interface between projects directly.
- The same package may be contained in two projects, (eg. the Online monitor project, which may need older versions of the same packages as the offline software).
- The way a project is managed in the repository would need consideration.
- Allowing people to checkout a subset of the packages within a project requires thought, and probably an extra script or two.

Based on functionality:

- We could alternatively group by functionality (ie. Analysis, Simulation, Reconstruction etc).
- This approach makes projects much more dependent on each other, and such relationship would need to be carefully defined.
- Packages such oaEvent and oaAnalysis that are used by many parts of the framework would want to go into a separate project.
- Therefore, Projects would depend directly on code and libraries found in other projects.
- Meta-packages could be removed completely.

RESOLUTION: Projects based on Purpose will be used

Top-level bin directory

- With this, the expectation was to simplify the PATH variable, and tidy up how executables are managed within a project.
- How do you manage packages with multiple versions stored concurrently?
- What happens when two executables have the same name?
- RESOLUTION: Top-level bin has been removed from the project layout

Top-level documentation directory

- Collects documentation in a directory at the top of the project, rather than storing it alongside the individual packages.
- Documents such as this one would be contained in there.

- In nd280, the package nd280Doc (now renamed to cometDoc) contains all the documentation, and is also responsible for running doxygen to produce the main documentation of the code.
- Documentation produced from code, via doxygen, would also be stored in this directory.
- What happens if there are two versions of a package stored concurrently? Where does that documentation get stored?
- RESOLUTION: Top-level documentation directory will be kept and cometDoc will be given an option to place output either alongside a package, or in this top-level directory.

A.3.2 Package conventions

Packages mainly involving external libraries

- Generalize statement that cometMC follows geant4 conventions in place of normal FRAMEWORK ones.
- All packages that depend predominantly on one external library should follow it's conventions.
- RESOLUTION: Now mention that all packages largely dependent on externals may differ to these conventions (previously, only mentioned cometMC).

doc/ dox subdirectory

- Discussion on whether this is necessary.
- RESOLUTION: Use 'dox' (change from doc).

High-level naming

- High level packages are currently subdivided into 4 categories functionality they provide (analysis, simulation etc). The recommended name for one of these packages is comet-FunctionName, ie cometSimMC for the monte carlo package, cometCalibApply.
- Does the comet prefix serve much purpose now we have the function after it?
- Without this, names would be shorter and simpler.
- RESOLUTION: Remove comet as a high-level package prefix

Project naming

- Projects are named with Icedust as a prefix. This clashes with framework management packages ie. IcedustOffline is a project, IcedustPolicy is a framework management package.
- RESOLUTION: Projects should use just Project as a suffix: eg. OfflineProject

dataFiles, controlFiles subdirectory

- Suggested that 'Files' is redundant.
- Maybe dataFiles -¿ staticData
- Tidy up the various kinds of runtime input and output files found in the framework.
- Data files to come from databases
- RESOLUTION: dataFiles → constants
- RESOLUTION: controlFiles → configurations

A.3.3 Scripting Conventions

Python Shebangs

- Do we want to require every python file to contain a shebang?
- As the 'file' command would use the shebang to identify the type of code, this will help this command out.
- At the moment the conventions state that only files intended to be executable should have a shebang.
- RESOLUTION: Only require shebangs in files that are to have their executable bit set.

Scripting Shebangs

- Should make sure people use `#! /bin/bash` and not `#! /bin/sh` or otherwise.
- RESOLUTION: Specify the shebang to be used for all major scripting languages

A.3.4 C++ conventions

Class data member prefix

- Alternatives to `f: '_', 'm_'`
- fData, _Data, m_Data
- _ may be confusable with system/ internal variables.
- RESOLUTION: Have stuck with f prefix.

Class and function prefixes

- Move away from 'T' for classes ?
  - Could help distinguish our code from ROOT code
  - Suggestion to use 'C'
- Files containing single 'free' functions should not use the class prefix (ie. 'T', 'C' etc).
- Namespaces should help distinguish the source of the code (COMET:: means it's not from ROOT or the STL etc)
- The mixin prefix 'TM' should be dropped - use documentation in stead.

- RESOLUTION: Switched from T prefix to C
- RESOLUTION: The mixin prefix 'TM' has been dropped - use documentation in stead.
- C clashes with COMET, which is prefixed to many classes.
- RESOLUTION: Switch to I instead of C

File extensions

- Implementation files should only ever differ from the header by the file extension.
- Using .hxx and .cxx allows shell globbing unlike .hh and .cc
- RESOLUTION: Made explicit how implementation files must have the same name as the header file.
- Add a convention for the file extension of c++ program files (files that contain the 'main' function used to create an executable)?
- RESOLUTION: Leave this out

Global variables / singleton classes

- Singleton classes were overused or misused in nd280
- Conventions should be careful of this.
- RESOLUTION: Suggest example classes should be used to write new classes.

Getters / setters policy

- Emphasize that thy should only be written when necessary
- If they don't act as regular getters or setters then a different name should be used.
- RESOLUTION: Suggest example classes should be used to write new classes.

Include statement placing

- Should we specify where these should be?
- All in header, or as few as possible in header?
- RESOLUTION: Left out of conventions

Comment formatting

- Develop a format for comments ?
- Coder's initials could be used to indicate who wrote what, and to make statements about future intentions
- Svn and Git both provide mechanisms to annotate code lines with the author, so probably not necessary in most cases.
- RESOLUTION: Ignored from Conventions

Code style

- Should code be automatically checked and reformatted, on commit?
- Programs such as astyle, http://sourceforge.net/projects/astyle/?source=navbar, could be used.
- RESOLUTION: Left out of conventions

Namespace

- At the moment all code is in a namespace called COMET.
- Should this now be ICEDUST or ID now that we've chosen ICEDUST as the framework name?
- RESOLUTION: Leave namespace as COMET.

Standard Output and Error

- TCOMETLog (in oaEvent) provides a standardised way to control all outputs from all packages
- Provides verbosity control and so on
- Therefore should not use std::cout or std::cerr and instead use these methods.
- RESOLUTION: Include statement of this in document

THandle and TBorrowed

- Only mention THandle
- This section needs expanding

A.3.5 Geometry naming and numbering

- Components that require numbering should make sure the numbering used in the code is consistent with the numbering used in real life.
- RESOLUTION: Added section that states this.

A.3.6 Units

- Do we wish to standardize the unit system employed as done in Geant4?
- Getters returning lengths, material densities, energies etc would all need to follow these guidelines.
- Do we instead just rely on clear documentation of each method?
- RESOLUTION: Mention using the HEPUnits.hxx class from oaEvent for unit standardisation.

A.3.7 Naming conventions for executables

- If a package has a 'run' executable it should name it in a standardised way.
- Likewise for 'testing' executables and any other common package applications.
- RESOLUTION: Add executable naming conventions to the document.

A.3.8 Other

- Capitalisation needs clarity in the conventions
- Give conventions for constants and enums, eg kSomeValue or kSOME_VALUE ? RESOLUTION: Have been added.

Bibliography

[1] W. H. Bertl, et al. (SINDRUM II). "A Search for muon to electron conversion in muonic gold." *Eur. Phys. J.*, C47:337, 2006. doi:10.1140/epjc/s2006-02582-x.

[2] R. M. Carey, et al. (Mu2e Collaboration). "Proposal to search for $\mu^- N \to e^- N$ with a single event sensitivity below 10^{-16}." FERMILAB-PROPOSAL 0973.

[3] R. Abrams, et al. (Mu2e Collaboration). "Mu2e Conceptual Design Report." `arXiv:1211.7019`.

[4] L. Bartoszek, et al. (Mu2e) FERMILAB-TM-2594, FERMILAB-DESIGN-2014-01. "Mu2e Technical Design Report." 2014. `1501.05241`.

[5] W. Altmannshofer, A. J. Buras, S. Gori, P. Paradisi, D. M. Straub TUM-HEP-727-09, MPP-2009-133. "Anatomy and Phenomenology of FCNC and CPV Effects in SUSY Theories." *Nucl. Phys.*, B830:17, 2010. doi:10.1016/j.nuclphysb.2009.12.019. `arXiv:0909.1333`.

[6] W. J. Marciano, T. Mori, J. Roney. "Charged Lepton Flavor Violation Experiments." *Ann.Rev.Nucl.Part.Sci.*, 58:315, 2008. doi:10.1146/annurev.nucl.58.110707.171126.

[7] A. de Gouvea. "(Charged) Lepton Flavor Violation." *Nucl.Phys. B (Proc. Suppl.)*, 188:303, 2009.

[8] O. Buchmueller, et al. "The CMSSM and NUHM1 in Light of 7 TeV LHC, B_S to $\mu^+\mu^-$ and XENON100 Data." 2012. `arXiv:1207.7315`.

[9] T. Hambye. "Lepton flavor violation in low-energy see-saw models." 2013. URL `http://bit.ly/19Wtken`.

[10] G. Feinberg, P. Kabir, S. Weinberg. "Transformation of muons into electrons." *Phys. Rev. Lett.*, 3:527, 1959. doi:10.1103/PhysRevLett.3.527.

[11] O. U. Shanker COO-3066-123. "Z Dependence of Coherent μe Conversion Rate in Anomalous Neutrinoless Muon Capture." *Phys. Rev.*, D20:1608, 1979. doi:10.1103/PhysRevD.20.1608.

[12] A. Czarnecki. "Using muons to probe for new physics." 1997. doi:10.1063/1.54452. [AIP Conf. Proc.415,252(1997)], `hep-ph/9710425`.

[13] A. Faessler, T. S. Kosmas, S. Kovalenko, J. D. Vergados. "Exotic mu e conversion in nuclei and R-parity violating supersymmetry." *Nucl. Phys.*, B587:25, 2000. doi:10.1016/S0550-3213(00)00446-6.

[14] T. S. Kosmas, S. Kovalenko, I. Schmidt USM-TH-111. "B quark mediated neutrinoless mu- - e- conversion in presence of R parity violation." *Phys. Lett.*, B519:78, 2001. doi: 10.1016/S0370-2693(01)01096-6. hep-ph/0107292.

[15] T. S. Kosmas, S. Kovalenko. "Lepton flavor violation: Constraints from exotic muon to electron conversion." *Phys. Atom. Nucl.*, 63:1158, 2000. doi:10.1134/1.855761. [Yad. Fiz.63N7,1234(2000)], hep-ph/0002070.

[16] P. Domin, S. Kovalenko, A. Faessler, F. Simkovic USM-TH-159. "Nuclear (mu-, e+) conversion mediated by Majorana neutrinos." *Phys. Rev.*, C70:065501, 2004. doi:10.1103/PhysRevC.70.065501. nucl-th/0409033.

[17] M. Gonzalez, T. Gutsche, J. C. Helo, S. Kovalenko, V. E. Lyubovitskij, et al. "Limits on lepton flavor violation from $\mu^- - e^-$ conversion." *Phys. Rev.*, D87(9):096020, 2013. doi:10.1103/PhysRevD.87.096020. 1303.0596.

[18] T. S. Kosmas, S. Kovalenko, I. Schmidt. "Nuclear muon- e- conversion in strange quark sea." *Phys. Lett.*, B511:203, 2001. doi:10.1016/S0370-2693(01)00657-8. hep-ph/0102101.

[19] F. Simkovic, V. E. Lyubovitskij, T. Gutsche, A. Faessler, S. Kovalenko. "Neutrino mediated muon electron conversion in nuclei revisited." *Phys. Lett.*, B544:121, 2002. doi:10.1016/S0370-2693(02)02466-8. hep-ph/0112277.

[20] T. S. Kosmas, J. D. Vergados. "Nuclear form-factors and closure approximation in the study of the (mu-, e-) conversion in nuclei." In "In *Thessaloniki 1990, Proceedings, Theoretical nuclear physics* 27-32.", 1990.

[21] T. S. Kosmas, J. D. Vergados, O. Civitarese, A. Faessler. "Study of the muon number violating (mu-, e-) conversion in a nucleus by using quasiparticle RPA." *Nucl. Phys.*, A570:637, 1994. doi:10.1016/0375-9474(94)90077-9.

[22] E. Oset, H. C. Chiang, T. S. Kosmas, A. Faessler, J. D. Vergados. "Coherent and incoherent (mu-,e-) conversion in nuclei and background from mu- decay in orbit." In "13th International Conference on Particles and Nuclei (PANIC 93) Perugia, Italy, June 28-July 2, 1993," pp. 271–272. 1993.

[23] R. Kitano, M. Koike, Y. Okada. "Detailed calculation of lepton flavor violating muon electron conversion rate for various nuclei." *Phys.Rev.*, D66:096002, 2002. doi:10.1103/PhysRevD.66.096002,10.1103/PhysRevD.76.059902. hep-ph/0203110.

[24] V. Cirigliano, R. Kitano, Y. Okada, P. Tuzon. "On the model discriminating power of $\mu \to e$ conversion in nuclei." *Phys.Rev.*, D80:013002, 2009. doi:10.1103/PhysRevD.80.013002. arXiv:0904.0957.

[25] A. Czarnecki, X. i Tormo, W. Marciano. "Muon decay in orbit: Spectrum of high-energy electrons." *Phys. Rev. D*, 84:013006, 2011.

[26] A. Czarnecki, M. Dowling, X. G. i. Tormo, W. J. Marciano, R. Szafron. "Michel decay spectrum for a muon bound to a nucleus." *Phys. Rev.*, D90(9):093002, 2014. doi:10.1103/PhysRevD.90.093002. 1406.3575.

[27] R. Szafron, A. Czarnecki ALBERTA-THY-9-15. "Shape function in QED and bound muon decays." *Phys. Rev.*, D92(5):053004, 2015. doi:10.1103/PhysRevD.92.053004. 1506.00975.

[28] R. Szafron, A. Czarnecki ALBERTA-THY-8-15, FERMILAB-PUB-15-205-PPD. "High-energy electrons from the muon decay in orbit: radiative corrections." *Phys. Lett.*, B753:61, 2016. doi:10.1016/j.physletb.2015.12.008. 1505.05237.

[29] D. A. Bryman, M. Blecher, K. Gotow, R. J. Powers. "Search for the reaction $\mu^- + Cu \to e^+ + Co$." *Phys. Rev. Lett.*, 28:1469, 1972. doi:10.1103/PhysRevLett.28.1469.

[30] A. Badertscher, et al. Print-81-0861 (BERN). "A Search for Muon - Electron and Muon - Positron Conversion in Sulfur." *Nucl. Phys.*, A377:406, 1982. doi:10.1016/0375-9474(82)90049-5.

[31] D. A. Bryman, et al. TRI-PP-85-14. "Search for μe Conversion in Ti." *Phys. Rev. Lett.*, 55:465, 1985. doi:10.1103/PhysRevLett.55.465.

[32] S. Ahmad, et al. TRI-PP-88-61. "Search for Muon-Electron and Muon-Positron Conversion." *Phys. Rev.*, D38:2102, 1988. doi:10.1103/PhysRevD.38.2102.

[33] C. Dohmen, et al. (SINDRUM II). "Test of lepton flavor conservation in $\mu \to e$ conversion on titanium." *Phys. Lett.*, B317:631, 1993. doi:10.1016/0370-2693(93)91383-X.

[34] W. Honecker, et al. (SINDRUM II). "Improved limit on the branching ratio of $\mu \to e$ conversion on lead." *Phys. Rev. Lett.*, 76:200, 1996. doi:10.1103/PhysRevLett.76.200.

[35] P. Wintz. "Results of the SINDRUM-II experiment." *Conf. Proc.*, C980420:534, 1998.

[36] M. Bachman (MECO Collaboration). "A Search for $\mu^- N \to e^- N$ with Sensitivity Below 10^{-16}, Muon to Electron COnversion." URL http://meco.ps.uci.edu/old/meco019.ps.

[37] J. Adam, et al. (MEG Collaboration). "The MEG detector for $\mu \to e + \gamma$ decay search." *Eur. Phys. J. C*, 73:2365, 2013. arXiv:1303.2348.

[38] J. Adam, et al. (MEG Collaboration). "New Constraint on the Existence of the $\mu^+ \to e^+ + \gamma$ Decay." *Phys. Rev. Lett.*, 110:201801, May 2013. doi:10.1103/PhysRevLett.110.201801.

[39] T. Sato, et al. "Particle and Heavy Ion Transport Code System PHITS." *J. Nucl. Sci. Technol.*, 50:9:913, 2013. Version 2.52.

[40] Y. Kanda, T. Momose, M. Taira. "Characterization of radiolytic products from air at a high-energy electron-positron storage ring." *Radiation Physics and Chemistry*, 48(1):49 , 1996. doi:http://dx.doi.org/10.1016/0969-806X(95)00430-6. URL http://www.sciencedirect.com/science/article/pii/0969806X95004306.

[41] P. Grybos. "Front-end electronics for multichannel semiconductor detector systems." *EuCARD Editorial Series on Accelerator Science*, 08, 2010.

[42] J. Isberg, et al. "High Carrier Mobility in Single-Crystal Plasma-Deposited Diamond." *Science*, 297:1670, 2002.

[43] K. Dolenc, et al. "Development of Beam Conditions Monitor for the ATLAS experiment." *CERN Document No. 1390440*, 2008. URL http://cds.cern.ch/record/1390440/files/.

[44] H. Kagan, S. Roe, P. Weilhammer (CERN RD42 Collaboration). "Development of Diamond Tracking Detectors for High Luminosity Experiments at the LHC." 2008. Status report, URL http://rd50.web.cern.ch/rd50/doc/status-reports/lhcc-2007-005-RD50-Statusreport.pdf.

[45] R. Akhmetshin, et al. (COMET Collaboration). "COMET Phase-I Technical Design Report." Sep 2014.

[46] D. Tromson, et al. "Influence of temperature on the response of diamond radiation detectors." *J. Appl. Physics*, 90:3:1608, 2001.

[47] C. D. Johnson. "The development and use of alumina ceramic fluorescent screens." *CERN Documents*, 1990.

[48] M. Moll, C. Joram, I. Mcgill (CERN bonding lab). "Irradiation test of STAYSTIK thermoplastic adhesive film no. 571." *CERN internal note*, 2002. URL https://bondlab-qa.web.cern.ch/bondlab-qa/STAYSTIK.html.

[49] M. Moll, C. Joram, I. Mcgill (CERN bonding lab). "Available epoxies for die attachment in high radiation high vacuum applications." *CERN internal note, CERN Stores catalog*, 2002. URL https://bondlab-qa.web.cern.ch/bondlab-qa/Die_attach.html.

[50] W. Bonivento, E. Collet, P. Imbert, C. deLaTaille. "Radiation hard micro-coaxial cables for the ATLAS liquid argon calorimeters." *Nuclear Instruments and Methods in Physics Research Section A: Accelerators, Spectrometers, Detectors and Associated Equipment*, 451:492, 2000. URL http://www.sciencedirect.com/science/article/pii/S0168900200003247.

[51] M. Mikuz, et al. (CERN RD42 Collaboration). "Diamond Sensors in HEP." *Proceedings of Science (ICHEP 2012)*, 524, 2012. URL http://pos.sissa.it/archive/conferences/174/524/ICHEP2012_524.pdf.

[52] S. Schnetzer, et al. (CERN RD42 Collaboration). "Diamond Sensors for Energy Frontier Experiments." *Proceedings of Science (Vertex 2013 Workshop)*, 029, 2013. URL http://pos.sissa.it/archive/conferences/198/029/Vertex2013_029.pdf.

[53] H. Jansen, et al. "Verification of the CNGS timing system using fast diamond detectors." *JINST*, 8:010117, 2013.

[54] M. Cerv, et al. "Diamond beam profile monitor for the COMET experiment at J-PARC." *JINST Proceedings of the PIXEL 2014 Workshop (forthcoming).*

[55] M. Friedl. "Diamond Detectors for Ionizing Radiation." *PhD thesis, University of Technology, Vienna*, 1999.

[56] M. Noy, et al. "TDCPix: Tracking for the NA62 GigaTracker." *Proceedings of the TWEPP 2014 workshop*, 2014.

[57] T. Bohlen, F. Cerutti, M. Chin, A. Fasso, A. Ferrari, et al. "The FLUKA Code: Developments and Challenges for High Energy and Medical Applications." *Nuclear Data Sheets*, 120:211, 2014.

[58] M. Noguchi, et al. "Production cross sections of tritium in high energy nuclear reactions with 12 GeV protons." *Int. J. Appl. Radiat. Isot.*, 42 (6):577, 1991.

[59] J. Fachinger, et al. "Decontamination of nuclear graphite." *Nucl. Eng. Des.*, 238:3086, 2008.

[60] J. A. Sawicki, et al. "Thermal release of tritium implanted in graphite studied by T(d,α)n nuclear reaction depth profiling analysis." *J. Nucl. Mater.*, 162-164:1019, 1989.

[61] R. Causey, T. Elleman, K. Verghese. "Hydrogen diffusion and solubility in pyrolytic carbon." *Carbon*, 17(4):323 , 1979. doi:http://dx.doi.org/10.1016/0008-6223(79)90003-4. URL `http://www.sciencedirect.com/science/article/pii/0008622379900034`.

[62] S. Makimura, N. Kawamura, K. M. Kojima, A. Koda, N. Kurosawa, et al. "Remote-controlled non-destructive measurement for thermal conductivity of highly radioactive isotropic graphite used as the muon production target at J-PARC/MUSE." *Journal of Nuclear Materials*, 450(1–3):110 , 2014. doi:http://dx.doi.org/10.1016/j.jnucmat.2013.10.019. Special Theme Issue on Spallation Materials Technology. Selected papers from the Eleventh International Workshop on Spallation Materials Technology (IWSMT-11), URL `http://www.sciencedirect.com/science/article/pii/S0022311513011677`.

[63] T. C. Collaboration KEK Report 2009-10 (Submitted to the J-PARC Physics Advisory Committee). "Conceptual Design Report for Experimental Search for Lepton Flavor Violating $\mu^- \to e^-$ Conversion at a Sensitivity of 10^{-16} with a Slow-Extracted Bunched Proton Beam (COMET)." 2009.

[64] S. Movchan. *Nucl. Instr. and Meth.*, A604:307, 2009.

[65] G. Xu, E. V. Hungerford. *IEEE Trans. on Nucl. Sci.*, 53:549, 2006.

[66] F. Sauli CERN-77-07. "Principles of Operation of Multiwire Proportional and Drift Chambers." *CERN-77-07*, 1977.

[67] I. Smirnov. "Interactions of particles with gases." URL `http://consult.cern.ch/writeup/heed`.

[68] S. Biagi. "Transport of electrons in gas mixture." URL `http://consult.cern.ch/writeup/magvoltz`.

[69] R. Veenhof. "Simulation of gaseous detectors." URL `http://garfield.web.cern.ch/garfield`.

[70] URL `https://garfieldpp.web.cern.ch/garfieldpp/`.

[71] C. Hoppner, S. Neubert, B. Ketzer, S. Paul. "A Novel Generic Framework for Track Fitting in Complex Detector Systems." *Nucl. Instrum. Meth.*, A620:518, 2010. doi:10.1016/j.nima.2010.03.136. `arXiv:0911.1008`.

[72] O. Sasaki, et al. (ATLAS TGC Collaboration). "Amplifier-Shaper-Discriminator ICs and ASD Boards."

[73] S. Ritt. *Nucl. Instr. Meth.*, A518:470, 2004.

[74] "The SiTCP firmware library." URL `http://www.bbtech.co.jp/en/products/sitcp-library/`.

[75] C. Grupen, I. Buvat, editors. *Handbook of particle detection and imaging, vol. 1 and vol.2*. Springer, Berlin, Germany, 2012. ISBN 9783642132704, 9783642132711. doi:10.1007/978-3-642-13271-1. URL `http://www.springer.com/978-3-642-13270-4`.

[76] ELGEN Technology. "EJ-228 and EJ-230 plastic scintillators." URL http://www.eljentechnology.com/index.php/products/plastic-scintillators/65-ej-230.

[77] Hamamatsu Photonics K.K. "H8409-70 photomultiplier tube assembly." URL http://www.hamamatsu.com/us/en/product/alpha/P/3002/H8409-70/index.html.

[78] S. Uno. "Drift Chamber for Super-Belle." *Super B Factory Workshop in Hawaii, Jan. 19-22, 2004*, 2004.

[79] F. Pedregosa, G. Varoquaux, A. Gramfort, V. Michel, B. Thirion, et al. "Scikit-learn: Machine Learning in Python." *Journal of Machine Learning Research*, 12:2825, 2011.

[80] J. H. Friedman. "Greedy Function Approximation: A Gradient Boosting Machine." *Annals of Statistics*, 29:1189, 2000.

[81] D. F. Measday, T. J. Stocki, B. A. Moftah, H. Tam. *Phys. Rev. C*, 76:035504, 2007.

[82] M. Angelone, M. Pillon, R. Faccini, D. Pinci, W. Baldini, et al. "Silicon photo-multiplier radiation hardness tests with a beam controlled neutron source." *Nuclear Instruments and Methods in Physics Research Section A: Accelerators, Spectrometers, Detectors and Associated Equipment*, 623(3):921 , 2010. doi:http://dx.doi.org/10.1016/j.nima.2010.07.057. URL http://www.sciencedirect.com/science/article/pii/S0168900210016712.

[83] "The FC7 project." URL https://espace.cern.ch/project-FC7/SitePages/Home.aspx.

[84] P. Moriera, et al. "The GBT Project." Proceedings of Topical Workshop on Electronics for Particle Physics (TWEPP). URL http://cdsweb.cern.ch/record/1185010?ln=en.

[85] "The Gigabit Link Interface Board (GLIB)." URL https://espace.cern.ch/project-GBLIB/public/default.aspx.

[86] PCI Industrial Computer Manufacturers Group (PICMG). "Introduction to MicroTCA." URL http://www.picmg.org/pdf/introductiontomicrotca.pdf.

[87] Uchida, T. and others. "Readout Electronics for the Central Drift Chamber of the Belle II Detector." Proceedings of the 2011 IEEE Nuclear Science Symposium, 23-29 October 2011, Valencia, Spain. doi:{10.1109/NSSMIC.2011.6154084}.

[88] "DisplayPort, High performance digital technology." URL http://www.displayport.org.

[89] "InfiniBand trade association." URL http://www.infinibandta.org.

[90] V. V. Gligorov, M. Williams. "Efficient, reliable and fast high-level triggering using a bonsai boosted decision tree." *Journal of Instrumentation*, 8(02):P02013, 2013. URL http://stacks.iop.org/1748-0221/8/i=02/a=P02013.

[91] B. P. Roe, H.-J. Yang, J. Zhu, Y. Liu, I. Stancu, et al. "Boosted decision trees as an alternative to artificial neural networks for particle identification." *Nucl. Instrum. Methods A*, 543(23):577 , 2005. doi:http://dx.doi.org/10.1016/j.nima.2004.12.018.

[92] S. Ritt, P. Amaudruz, K. Olchanski. "MIDAS: Maximum Integrated Data Acquisition System." URL http://midas.psi.ch.

[93] ""Experimental Physics and Industrial Control System (EPICS)"." URL http://www.aps.anl.gov/epics.

[94] Jean-Christophe DAVID, Detlef FILGES, Franz GALLMEIER, Mayeen KHANDAKER, Alexander KONOBEYEV, Sylvie LERAY, Guenter MANK, Alberto MENGONI, Rolf MICHEL, Naohiko OTUKA and Yair YARIV. "Benchmark of Spallation Models." *Progress in NUCLEAR SCIENCE and TECHNOLOGY*, 2:942, 2011.

[95] "Tandem Electrostatic Accelerator." URL http://www.research.kobe-u.ac.jp/fmsc-pbe/www/5sdh2/5sdh2_e.html.

[96] Yubin Zuo, Guoyou Tang, Zhiyu Guo, Jimei Guo, Yuyang Pei, Jianguo Xu, Hu Wang, Yuanong Lu. "Neutron yields of thick Be target bombarded with low energy deuterons." *Physics Procedia*, 60:220, 2014.

[97] S. Abe, and others 20p-F12-2. "Incident-energy dependency of secondary cosmic-ray neutron-induced soft errors." In "Proceedings of the 61st Spring Meeting," 2014.

[98] N. V. Mokhov, S. I. Striganov FERMILAB-CONF-07-008-AD. "MARS15 overview." *AIP Conf. Proc.*, 896:50, 2007. doi:10.1063/1.2720456.

[99] S. Agostinelli, et al. (GEANT4) SLAC-PUB-9350, FERMILAB-PUB-03-339. "GEANT4: A Simulation toolkit." *Nucl. Instrum. Meth.*, A506:250, 2003. doi:10.1016/S0168-9002(03)01368-8.

[100] K. Abe, et al. (T2K). "The T2K Experiment." *Nucl. Instrum. Meth.*, A659:106, 2011. doi:10.1016/j.nima.2011.06.067. arXiv:1106.1238.

[101] T. Lindner, C. McGrew (T2K ND280 Collaboration). "oaEvent Manual." URL http://www.hep.ph.ic.ac.uk/~bek07/comet/oaEvent/index.html.

[102] K. Niita, T. Sato, H. Nakashima, H. Iwase, H. Nose, et al. "PHITS: A particle and heavy ion transport code system." *Radiat. Meas.*, 41:1080, 2006. doi:10.1016/j.radmeas.2006.07.013.

[103] G. Battistoni, S. Muraro, P. R. Sala, F. Cerutti, A. Ferrari, et al. SLAC-REPRINT-2007-184. "The FLUKA code: Description and benchmarking." *AIP Conf. Proc.*, 896:31, 2007. doi:10.1063/1.2720455. [,31(2007)].

[104] A. Ferrari, P. R. Sala, A. Fasso, J. Ranft CERN-2005-010, SLAC-R-773, INFN-TC-05-11. "FLUKA: A multi-particle transport code (Program version 2005)." *CERN-2005-010, SLAC-R-773, INFN-TC-05-11*, 2005.

[105] P. Sala, S. Vanini. "FLUGG: FLUKA + Geant4 Geometry for Simulation in HEP." URL http://www.fluka.org/content/tools/flugg/.

[106] "FLUKA User License." URL http://www.fluka.org/fluka.php?id=license.

[107] A. Kurup, I. Puri, Y. Uchida, Y. Yap, R. Appleby, et al. "Large Emittance Beam Measurements for COMET Phase-I." In "Proceedings, 4th International Particle Accelerator Conference (IPAC 2013)," p. 2684. 2013. URL http://JACoW.org/IPAC2013/papers/wepea075.pdf.

[108] A. Cervera-Villanueva, J. J. Gomez-Cadenas, J. A. Hernando. "'RecPack' a reconstruction toolkit." *Nucl. Instrum. Meth.*, A534:180, 2004. doi:10.1016/j.nima.2004.07.074.

[109] J. Kaulard, et al. (SINDRUM II Collaboration). "Improved limit on the branching ratio of $\mu^- \rightarrow e^+$ conversion on titanium." *Phys.Lett.*, B422:334, 1998. doi: 10.1016/S0370-2693(97)01423-8.

[110] M. Dobeli, M. Doser, L. Van Elmbt, M. W. Schaad, P. Truoel, et al. "Radiative Muon Capture in Nuclei." *Phys. Rev.*, C37:1633, 1988. doi:10.1103/PhysRevC.37.1633.

[111] D. S. Armstrong, et al. TRI-PP-92-80. "Radiative muon capture on Al, Si, Ca, Mo, Sn, and Pb." *Phys. Rev.*, C46:1094, 1992. doi:10.1103/PhysRevC.46.1094.

[112] P. C. Bergbusch, et al. "Radiative muon capture on O, Al, Si, Ti, Zr, and Ag." *Phys. Rev.*, C59:2853, 1999. doi:10.1103/PhysRevC.59.2853.

[113] D. F. Measday. "The nuclear physics of muon capture." *Phys. Rept.*, 354:243, 2001. doi:10.1016/S0370-1573(01)00012-6.

[114] H. Primakoff. "Theory of Muon Capture." *Rev. Mod. Phys.*, 31(3):802 , 1959.

[115] W. Y. P. Hwang. "RADIATIVE MUON CAPTURE." *Phys. Rev.*, C22:233, 1980. doi: 10.1103/PhysRevC.22.233.

[116] J. E. Amaro, A. Lallena, J. Nieves. "Radiative pion capture in nuclei: A Continuum shell model approach." *Nucl.Phys.*, A623:529, 1997.

[117] O. C. Allkofer, K. Carstensen, D. W. Dau. "The absolute cosmic ray muon spectrum at sea level." *Phys. Lett.*, B36:425, 1971. doi:10.1016/0370-2693(71)90741-6.

[118] F. Masukawa, et al. JAEA-Data/Code 2006-024. "Development of SHINE3, simple code for high-energy neutron skyshine dose evaluation." *JAEA-Data/Code 2006-024*.